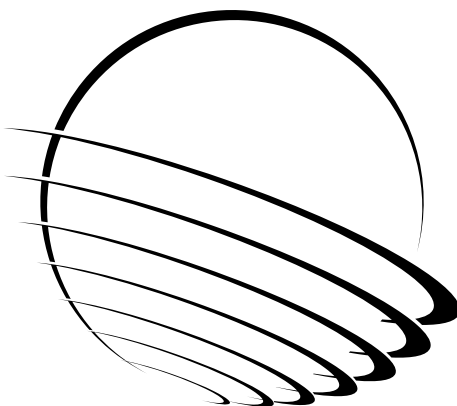




40th Aerospace Mechanisms Symposium

May 12-14, 2010



Proceedings of a symposium held at
Hilton Cocoa Beach Oceanfront Hotel, Cocoa Beach, FL
Hosted by the Kennedy Space Center and
Lockheed Martin Space Systems Company
Organized by the Mechanisms Education Association

Compiled/Edited by: Edward A. Boesiger

NASA STI Program ... in Profile

Since its founding, NASA has been dedicated to the advancement of aeronautics and space science. The NASA scientific and technical information (STI) program plays a key part in helping NASA maintain this important role.

The NASA STI program operates under the auspices of the Agency Chief Information Officer. It collects, organizes, provides for archiving, and disseminates NASA's STI. The NASA STI program provides access to the NASA Aeronautics and Space Database and its public interface, the NASA Technical Report Server, thus providing one of the largest collections of aeronautical and space science STI in the world. Results are published in both non-NASA channels and by NASA in the NASA STI Report Series, which includes the following report types:

- **TECHNICAL PUBLICATION.** Reports of completed research or a major significant phase of research that present the results of NASA Programs and include extensive data or theoretical analysis. Includes compilations of significant scientific and technical data and information deemed to be of continuing reference value. NASA counterpart of peer-reviewed formal professional papers but has less stringent limitations on manuscript length and extent of graphic presentations.
- **TECHNICAL MEMORANDUM.** Scientific and technical findings that are preliminary or of specialized interest, e.g., quick release reports, working papers, and bibliographies that contain minimal annotation. Does not contain extensive analysis.
- **CONTRACTOR REPORT.** Scientific and technical findings by NASA-sponsored contractors and grantees.

- **CONFERENCE PUBLICATION.** Collected papers from scientific and technical conferences, symposia, seminars, or other meetings sponsored or co-sponsored by NASA.
- **SPECIAL PUBLICATION.** Scientific, technical, or historical information from NASA programs, projects, and missions, often concerned with subjects having substantial public interest.
- **TECHNICAL TRANSLATION.** English-language translations of foreign scientific and technical material pertinent to NASA's mission.

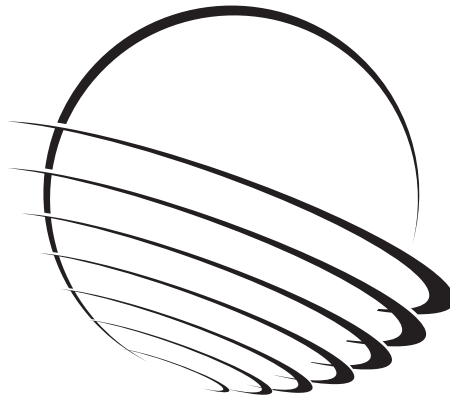
Specialized services also include organizing and publishing research results, distributing specialized research announcements and feeds, providing help desk and personal search support, and enabling data exchange services.

For more information about the NASA STI program, see the following:

- Access the NASA STI program home page at <http://www.sti.nasa.gov>
- E-mail your question via the Internet to help@sti.nasa.gov
- Fax your question to the NASA STI Help Desk at 443-757-5803
- Phone the NASA STI Help Desk at 443-757-5802
- Write to:
NASA STI Help Desk
NASA Center for AeroSpace Information
7115 Standard Drive
Hanover, MD 21076-1320

40th Aerospace Mechanisms Symposium

May 12-14, 2010



Proceedings of a symposium held at
Hilton Cocoa Beach Oceanfront Hotel, Cocoa Beach, FL
Hosted by the Kennedy Space Center and
Lockheed Martin Space Systems Company
Organized by the Mechanisms Education Association

Compiled/Edited by: Edward A. Boesiger

Acknowledgments

The high quality of this symposium is a result of the work of many people, and their efforts are gratefully acknowledged. This extends to voluntary members of the symposium organizing committee representing the eight NASA field centers, LMSSC, and the European Space Agency. Appreciation is also extended to the session chairs, the authors, and particularly the personnel at Kennedy Space Center responsible for the symposium arrangements and the publication of these proceedings. A sincere thank you also goes to the symposium executive committee and advisory committee who are responsible for the year to year management of the AMS, including paper processing and preparation of the program.

Special Thanks to:

Alan C. Littlefield, NASA KSC Host Chairman

Robert P. Mueller, NASA KSC Co-Host Chairman

Stuart H. Loewenthal, General Chairman, Lockheed Martin

Edward A. Boesiger, Operations Chairman, Lockheed Martin

David Mayall, KSC Symposium Organization Support

Jane M. Dumont, KSC Symposium Organization Support

Donna M. O'Neill, KSC Symposium Organization Support

ASRC Aerospace Graphics department

Available from:

NASA Center for AeroSpace Information

7115 Standard Drive

Hanover, MD 21076-1320

443-757-5802

This report is also available in electronic form at <http://www.sti.nasa.gov/> and <http://ntrs.nasa.gov/>

PREFACE

The Aerospace Mechanisms Symposium (AMS) provides a unique forum for those active in the design, production and use of aerospace mechanisms. A major focus is the reporting of problems and solutions associated with the development and flight certification of new mechanisms. Organized by the Mechanisms Education Association, responsibility for hosting the AMS is shared by the National Aeronautics and Space Administration and Lockheed Martin Space Systems Company (LMSSC). Now in its 40th symposium, the AMS continues to be well attended, attracting participants from both the U.S. and abroad.

The 40th AMS, hosted by the Kennedy Space Center (KSC) in Cocoa Beach, Florida, was held May 12, 13 and 14, 2010. During these three days, 38 papers were presented. Topics included gimbals and positioning mechanisms, CubeSats, actuators, Mars rovers, and Space Station mechanisms. Hardware displays during the supplier exhibit gave attendees an opportunity to meet with developers of current and future mechanism components.

The use of trade names of manufacturers in this publication does not constitute an official endorsement of such products or manufacturers, either expressed or implied, by the National Aeronautics and Space Administration.

CONTENTS

Symposium Schedule	ix
Symposium Organizing and Advisory Committees.....	xiv
Mars Science Laboratory Drill..... Avi Okon	1
Lightweight Low Force Rotary Percussive Coring Tool for Planetary Applications	17
Ross Hironaka & Scott Stanley	
A Novel Approach for a Low-Cost Deployable Antenna.....	31
Chris Amend, Michael Nurnberger, Paul Oppenheimer, Steve Koss & Bill Purdy	
A Completely New Type of Actuator -or- This Ain't Your Grandfather's Internal Combustion Engine	43
Brian Gore, Gary Hawkins, Peter Hess, Teresa Moore & Eric Fournier	
An Evaluation of Liquid, Solid, and Grease Lubricants for Space Mechanisms Using a Spiral Orbit Tribometer.....	59
Michael Buttery	
Qualification of a High Accuracy Dual-Axis Antenna Deployment and Trimming Mechanism	73
Alain Gossant & Francois Morichon	
Scanning Mechanism of the FY-3 Microwave Humidity Sounder.....	87
Manfred Schmid, Li Jing & Christian Hehr	
A Coarse Pointing Assembly for Optical Communication	99
Gerhard Székely, D. Blum, M. Humphries, A. Koller, D. Mussett, S. Schuler & P. Vogt	
Design and Development of Two-Axis Thruster Gimbal with Xenon Propellant Lines.....	109
Armond Asadurian	
Gravity-Offloading System for Large-Displacement Ground Testing of Spacecraft Mechanisms.....	119
Olyvia Han, David Kienholz, Paul Janzen & Scott Kidney	
Gimbals Drive and Control Electronics Design, Development and Testing of the LRO High Gain Antenna and Solar Array Systems	133
Boris Chernyakov & Kamal Thakore	
Fastener Capture Plate Technology to Contain On-Orbit Debris	147
Kevin Eisenhower	
Space Station Control Moment Gyroscope Lessons Learned.....	161
Charles Gurrisi, Raymond Seidel, Scott Dickerson, Stephen Didziulis, Peter Frantz & Kevin Ferguson	
International Space Station Powered Bolt Nut Anomaly and Failure Analysis Summary	177
Daniel Sievers & Harry Warden	
The International Space Station Solar Alpha Rotary Joint Anomaly Investigation	187
Elliot Harik, Justin McFatter, Daniel Sweeney, Carlos Enriquez, Deneen Taylor & David McCann	
Test Validation of the Repair to the Space Station Solar Alpha Rotary Joint.....	207
Curtis Allmon, Will Wilkinson & Stu Loewenthal	
Experimental Investigation of Forces Produced by Misaligned Steel Rollers.....	219
Timothy Krantz, Christopher DellaCorte & Michael Dube	

Mars Science Laboratory Sample Acquisition, Sample Processing and Handling: Subsystem Design and Test Challenge	233
Louise Jandura	
Mars Science Laboratory CHIMRA: A Device for Processing Powdered Martian Samples.....	249
Daniel Sunshine	
Performance of Regolith Feed Systems for Analog Field Tests of In-Situ Resource Utilization Oxygen Production Plants in Mauna Kea, Hawaii.....	263
Ivan Townsend, Robert Mueller & James Mantovani, Kris Zacny & Jack Craft	
Refined Gearbox Design for JSC's Chariot Lunar Rover	279
Steve Baumann & David Lewicki	
Nickel-Titanium Alloys: Corrosion "Proof" Alloys for Space Bearing, Components and Mechanism Applications	293
Christopher DellaCorte	
Gossamer Technology to De-Orbit LEO Non-Propulsion-Fitted Satellites	301
Christian Dupuy & O. Le Couls	
Preliminary Assessment of Seals for Dust Mitigation of Mechanical Components for Lunar Surface Systems.....	309
Irebert Delgado & Michael Handschuh	
Development of the Tri-ATHLETE Lunar Vehicle Prototype.....	317
Matt Heverly, Jaret Matthews, Matt Frost & Chris McQuin	
An Approach to Designing Passive Self-Leveling Landing Gear with Application to the Lunar Lander.....	327
Troy Rippere & Gloria Wiens	
Design and Manufacture of a Highly Reliable, Miniaturized and Low-Mass Shutter Mechanism	335
Markus Manhart, T. Zeh, G. Preißler, A. Hurni, G. Peter, I. Walter, J. Helbert, K. Multhaup & H. Hiesinger	
Miniaturized Single-Shot Valve and its Application to the ExoMars Pasteur Payload.....	341
Pierre Muller, Hartmut Henkel & Sabine Klinkner	
MoS ₂ -Filled PEEK Composite as a Self-Lubricating Material for Aerospace Applications.....	347
Geraldine Theiler & Thomas Gradt	
Evolution of the IBDM Structural Latch Development into a Generic Simplified Design	353
Kristiaan De Vriendt, Helder Dittmer & Davy Vrancken, Peter Urmston & Oscar Gracia	
Development of the Upgraded DC Brush Gear Motor for Spacebus Platforms	361
Robert Berning III & Olivier Viout	
Static Load Distribution in Ball Bearings	367
Mario Ricci	

BESST: A Miniature, Modular Radiometer	373
Robert Warden, William Good & Erik Baldwin-Stevens	
Development of an Actuator for Ambient to Cryo Application.....	389
Karen Menzel & Hans Jürgen Jung & Jörg Schmidt	
Development and Acceptance Testing of the Dual Wheel Mechanism for the Tunable Filter Imager Cryogenic Instrument on the JWS	401
Martin Leckie & Zakir Ahmad	
Xatcobeo: Small Mechanisms for CubeSat Satellites – Antenna and Solar Array Deployment.....	415
Jose Miguel Encinas Plaza, Jose Antonio Vilán Vilán, Fernando Aguado Agelet, Javier Barandiarán Mancheño, Miguel López Estévez, Cesar Martínez Fernández & Fany Sarmiento Ares	
Concept, Design, and Prototyping of XSAS: A High Power Extendable Solar Array for CubeSat Applications.....	431
Patrick Senatore, Andrew Klesh, Thomas Zurbuchen, Darren McKague & James Cutler	
Development of a Solar Array Drive Assembly for CubeSat	445
Mike Passaretti & Ron Hayes	

SYMPOSIUM SCHEDULE

WEDNESDAY, 12 MAY 2010

7:30 Wednesday Presenters' Breakfast

8:00 **CHECK-IN AND REFRESHMENTS**

8:30 **INTRODUCTORY REMARKS**

Alan Littlefield, Host Chairman
NASA Kennedy Space Flight Center, FL
Edward Boesiger, Operations Chairman
Lockheed Martin Space Systems, Sunnyvale, CA

CENTER WELCOME

Robert D. Cabana, Director
NASA Kennedy Space Center, FL

9:00 **SESSION I – DRILL IT, DEPLOY IT, LUBE IT**

Steve Kugelmann, Session Chair
United Space Alliance, Cocoa Beach, FL

- Mars Science Laboratory Drill
Avi Okon, Jet Propulsion Laboratory, Pasadena, CA
- Lightweight Low Force Rotary Percussive Coring Tool for Planetary Applications
Ross Hironaka, MDA ISI Space Division, Pasadena, CA; Scott Stanley, Techno Planet Inc., Northridge, CA
- A Novel Approach for a Low-Cost Deployable Antenna
Chris Amend, Michael Nurnberger, Paul Oppenheimer & Steve Koss, Naval Research Laboratory, Washington, DC; Bill Purdy, Purdy Engineering, Poolesville, MD
- A Completely New Type of Actuator -or- This Ain't Your Grandfather's Internal Combustion Engine
Brian Gore, Gary Hawkins, Peter Hess, Teresa Moore & Eric Fournier, The Aerospace Corporation, El Segundo, CA
- An Evaluation of Liquid, Solid, and Grease Lubricants for Space Mechanisms Using a Spiral Orbit Tribometer
Michael Buttery, The European Space Tribology Laboratory, ESR Technology, Warrington, UK

11:30 **LUNCH**

12:30 **SESSION II – GIMBALS**

Dave Messner, Session Chair
ATK-Able Engineering Company, Inc., Goleta, CA

- Qualification of a High Accuracy Dual-Axis Antenna Deployment and Trimming Mechanism
Alain Gossant, EADS Astrium, Stevenage, UK; Francois Morichon, EADS Astrium, Toulouse, France
- Scanning Mechanism of the FY-3 Microwave Humidity Sounder
Manfred Schmid & Christian Hehr, EADS Astrium GmbH, Friedrichshafen, Germany; Li Jing, Centre for Space Science and Applied Research, CAS, China
- A Coarse Pointing Assembly for Optical Communication
Gerhard Székely, D. Blum, M. Humphries, A. Koller, D. Mussett, S. Schuler & P. Vogt, RUAG Space AG, Zürich, Switzerland

2:00 **BREAK**

2:15 **SESSION III – GIMBALS TOO**

Hans Juergen Jung, Session Chair
EADS Astrium GmbH, Friedrichshafen, Germany

- Design and Development of Two-Axis Thruster Gimbal with Xenon Propellant Lines
Armond Asadurian, Moog Chatsworth Operations, Chatsworth, CA
- Gravity-Offloading System for Large-Displacement Ground Testing of Spacecraft Mechanisms
Olyvia Han, David Kienholz, Paul Janzen & Scott Kidney, CSA Engineering, Mountain View, CA
- Gimbals Drive and Control Electronics Design, Development and Testing of the LRO High Gain Antenna and Solar Array Systems
Boris Chernyakov, ATK Space Systems and Services, Beltsville, MD; Kamal Thakore, NASA Goddard Space Flight Center, Greenbelt, MD

4:00 **SPECIAL PRESENTATION**

Constellation Architecture and Ground Systems Development
Scott T. Colloredo, Chief Architect, Constellation Ground Systems, NASA Kennedy Space Center

6:00-10:30 **RECEPTION AT KSC**

6:00 Bus leaves the Hilton to KSC
Shuttle Experience ride
Dinner
8:15 IMAX movie
9:00 Exploration Space exhibit
10:00 Bus leaves KSC for hotel

THURSDAY, 13 MAY 2010

7:30 Thursday Presenters' Breakfast

8:30 **SESSION IV – SPACE STATION/EVA**

Kornel Nagy, Session Chair
NASA Johnson Space Center, Houston, TX

- Fastener Capture Plate Technology to Contain On-Orbit Debris
Kevin Eisenhower, Alliant Techsystems, Beltsville, MD
- Space Station Control Moment Gyroscope Lessons Learned
Charles Gurrisi, Raymond Seidel & Scott Dickerson, L-3 Communications Corporation Space & Navigation Division, Budd Lake, NJ; Stephen Didziulis & Peter Frantz, The Aerospace Corporation, El Segundo, CA; Kevin Ferguson, The Boeing Company, Houston, TX
- International Space Station Powered Bolt Nut Anomaly and Failure Analysis Summary
Daniel Sievers & Harry Warden, The Boeing Company, Huntsville, AL

10:00 **BREAK**

10:15 **SESSION V – SARJ**

David McCann, Session Chair
The Boeing Company, Houston, TX

- The International Space Station Solar Alpha Rotary Joint Anomaly Investigation
Elliot Harik, Justin McFatter, Carlos Enriquez & David McCann, The Boeing Company, Houston, TX; Daniel Sweeney & Deneen Taylor, NASA Johnson Space Center, Houston, TX
- Test Validation of the Repair to the Space Station Solar Alpha Rotary Joint
Curtis Allmon, Will Wilkinson & Stu Loewenthal, Lockheed Martin Space Systems Company, Sunnyvale, CA
- Experimental Investigation of Forces Produced by Misaligned Steel Rollers
Timothy Krantz & Christopher DellaCorte, NASA Glenn Research Center, Cleveland, OH; Michael Dube, NASA Goddard Space Flight Center, Greenbelt, MD

12:00 **LUNCH**

1:15 **SESSION VI – ROVERS**

Chris Voorhees, Session Chair
Jet Propulsion Laboratory, Pasadena, CA

- Mars Science Laboratory Sample Acquisition, Sample Processing and Handling: Subsystem Design and Test Challenge
Louise Jandura, Jet Propulsion Laboratory, Pasadena, CA
- Mars Science Laboratory CHIMRA: A Device for Processing Powdered Martian Samples
Daniel Sunshine, Jet Propulsion Laboratory, Pasadena, CA
- Performance of Regolith Feed Systems for Analog Field Tests of In-Situ Resource Utilization Oxygen Production Plants in Mauna Kea, Hawaii
Ivan Townsend, ASRC Aerospace, NASA Kennedy Space Center, FL; Robert Mueller & James Mantovani, NASA Kennedy Space Center, FL; Kris Zacny & Jack Craft, Honeybee Robotics Spacecraft Mechanisms Corporation, New York, NY
- Refined Gearbox Design for JSC's Chariot Lunar Rover
Steve Baumann & David Lewicki, NASA Glenn Research Center, Cleveland, OH

3:15 **BREAK**

3:30 **SESSION VII – A POTPOURRI OF POSTERS**

Bill Purdy, Session Chair
Purdy Engineering, Poolesville, MD

- Nickel-Titanium Alloys: Corrosion “Proof” Alloys for Space Bearing, Components and Mechanism Applications
Christopher DellaCorte, NASA Glenn Research Center, Cleveland, OH
- Gossamer Technology to De-Orbit LEO Non-Propulsion-Fitted Satellites
Christian Dupuy, Centre National D'Etudes Spatiales, Toulouse, France; O. Le Couls, EADS Astrium, Saint Médard en Jalles, France
- Preliminary Assessment of Seals for Dust Mitigation of Mechanical Components for Lunar Surface Systems
Irebert Delgado, NASA Glenn Research Center, Cleveland, OH; Michael Handschuh, Ohio State University, Columbus, OH
- Development of the Tri-ATHLETE Lunar Vehicle Prototype
Matt Heverly, Jaret Matthews, Matt Frost & Chris McQuin, Jet Propulsion Laboratory, Pasadena, CA
- An Approach to Designing Passive Self-Leveling Landing Gear with Application to the Lunar Lander
Troy Rippere & Gloria Wiens, University of Florida, Gainesville, FL
- Design and Manufacture of a Highly Reliable, Miniaturized and Low-Mass Shutter Mechanism
Markus Manhart, T. Zeh, G. Preißler & A. Hurni, Kayser-Threde GmbH, Munich, Germany; G. Peter, I. Walter & J. Helbert, Deutsches Zentrum für Luft- und Raumfahrt (DLR), Berlin, Germany; K. Multhaupt & H. Hiesinger, Institut für Planetologie, Westfälische Wilhelms-Universität, Münster, Germany
- Miniaturized Single-Shot Valve and its Application to the ExoMars Pasteur Payload
Pierre Muller, Hartmut Henkel & Sabine Klinkner, von Hoerner & Sulger GmbH, Schwetzingen, Germany
- MoS₂-Filled PEEK Composite as a Self-Lubricating Material for Aerospace Applications
Geraldine Theiler & Thomas Gradt, BAM Federal Institute for Materials Research & Testing, Berlin, Germany
- Evolution of the IBDM Structural Latch Development into a Generic Simplified Design
Kristiaan De Vriendt, Helder Dittmer & Davy Vrancken, Verhaert Space, Kruikebeke, Belgium; Peter Urmston & Oscar Gracia, ESA/ESTeC, Noordwijk, The Netherlands
- Development of the Upgraded DC Brush Gear Motor for Spacebus Platforms
Robert Berning III, Moog, Inc., Chatsworth, CA; Olivier Viout, Thales Alenia Space, Cannes la Bocca Cedex, France

6:30-9:30 **LUAU & DISPLAYS** – Hilton pool deck and display area

Invited component suppliers display current products and provide tutorials. Live music and food on the beach!

FRIDAY, 14 MAY 2010

7:30 Friday Presenters' Breakfast

8:30 **SESSION VIII – INSTRUMENTS**

Scott Strickland, Session Chair
The Boeing Company, Cocoa Beach, FL

- (Poster paper) Static Load Distribution in Ball Bearings
Mario Ricci, Instituto Nacional de Pesquisas Espaciais, São José dos Campos, São Paulo State, Brazil
- BESST: A Miniature, Modular Radiometer
Robert Warden, William Good & Erik Baldwin-Stevens, Ball Aerospace & Technologies, Boulder, CO
- Development of an Actuator for Ambient to Cryo Application
Karen Menzel & Hans Jürgen Jung, EADS Astrium GmbH, Friedrichshafen, Germany; Jörg Schmidt, PHYTRON-Elektronik GmbH, Gröbenzell, Germany
- Development and Acceptance Testing of the Dual Wheel Mechanism for the Tunable Filter Imager Cryogenic Instrument on the JWST
Martin Leckie & Zakir Ahmad, COM DEV, Ltd., Cambridge, Ontario, Canada

10:00 **BREAK**

10:15 **SESSION IX – SMALL SESSION ON SMALL SATELLITES**

Gloria Wiens, Session Chair
University of Florida, Gainesville, FL

- Xatcobeo: Small Mechanisms for CubeSat Satellites – Antenna and Solar Array Deployment
Jose Miguel Encinas Plaza, Javier Barandiarán Mancheño, Cesar Martínez Fernández & Fany Sarmiento Ares, Instituto Nacional de Técnica Aeroespacial (INTA), Madrid, Spain; Jose Antonio Vilán Vilán, Fernando Aguado Agelet & Miguel López Estévez, University of Vigo, Lagoas Marcosende, Spain
- Concept, Design, and Prototyping of XSAS: A High Power Extendable Solar Array for CubeSat Applications
Patrick Senatore, Andrew Klesh, Thomas Zurbuchen, Darren McKague & James Cutler, University of Michigan, Ann Arbor, MI
- Development of a Solar Array Drive Assembly for CubeSat
Mike Passaretti & Ron Hayes, Honeybee Robotics Spacecraft Mechanisms Corporation, New York, NY

11:45 **SPECIAL PRESENTATION**

NASA Kennedy Space Center Overview

12:15 **TECHNICAL SESSIONS CONCLUSION**

Stu Loewenthal, General Chairman, Lockheed Martin Space Systems, Sunnyvale, CA

- Herzl Award Presentation
- Closing Remarks

12:30 **LUNCH**

1:30-4:00 **FACILITY TOUR at KSC or Shuttle launch**

SYMPOSIUM ORGANIZING COMMITTEE

**Alan C. Littlefield, Host Chair NASA KSC
Robert P. Mueller, Co-Host Chair NASA KSC**

**Stuart H. Loewenthal, General Chairman, Lockheed Martin
Edward A. Boesiger, Operations Chairman, Lockheed Martin**

**Steven W. Baumann, NASA GRC
Carlton L. Foster, NASA MSFC
Claef F. Hakun, NASA GSFC
Christopher P. Hansen, NASA JSC
Wayne Jermstad, NASA JSC
Edward C. Litty, JPL
Gérard Migliorero, ESA/ESTeC
Fred G. Martwick, NASA ARC
Donald H. McQueen, Jr., NASA MSFC
Wilfredo Morales, NASA GRC
Fred B. Oswald, NASA GRC
Minh Phan, NASA GSFC
Donald R. Sevilla, JPL
Mark F. Turner, NASA ARC
Robin Tutterow, NASA LaRC
James E. Wells, NASA LaRC**

SYMPOSIUM ADVISORY COMMITTEE

**Ronald E. Mancini, NASA ARC (ret)
Stewart C. Meyers, NASA GSFC (ret)
William C. Schneider, NASA JSC (ret)**

Mars Science Laboratory Drill

Avi B. Okon*

Abstract

The Drill for the Mars Science Laboratory mission is a rotary-percussive sample acquisition device with an emphasis on toughness and robustness to handle the harsh environment on Mars. The unique challenges associated with autonomous drilling from a mobile robot are addressed. A highly compressed development schedule dictated a modular design architecture that satisfies the functional and load requirements while allowing independent development and testing of the Drill subassemblies. The Drill consists of four actuated mechanisms: a spindle that rotates the bit, a chuck that releases and engages bits, a novel voice-coil-based percussion mechanism that hammers the bit, and a linear translation mechanism. The Drill has three passive mechanisms: a replaceable bit assembly that acquires and collects sample, a contact sensor / stabilizer mechanism, and, lastly a flex harness service loop. This paper describes the various mechanisms that makeup the Drill and discusses the solutions to their unique design and development challenges.

Introduction

The Mars Science Laboratory (MSL), scheduled to launch in the fall of 2011, is part of a long-term effort of robotic exploration of Mars that will assess whether Mars ever was, or is still today, an environment able to support microbial life. The MSL rover features the most advanced robotic Sample Acquisition, Sample Processing and Handling [1] (SA/SPaH) subsystem ever sent to another planet (see Figures 1a and 1b). The major elements of the SA/SPaH subsystem are a Robotic Arm (RA) with a tool and instrument laden turret. The tools are: a sample acquisition Drill, scooping, sieving and portioning device called CHIMRA [2], and the Dust Removal Tool (DRT). The instruments are the APXS and MAHLI.

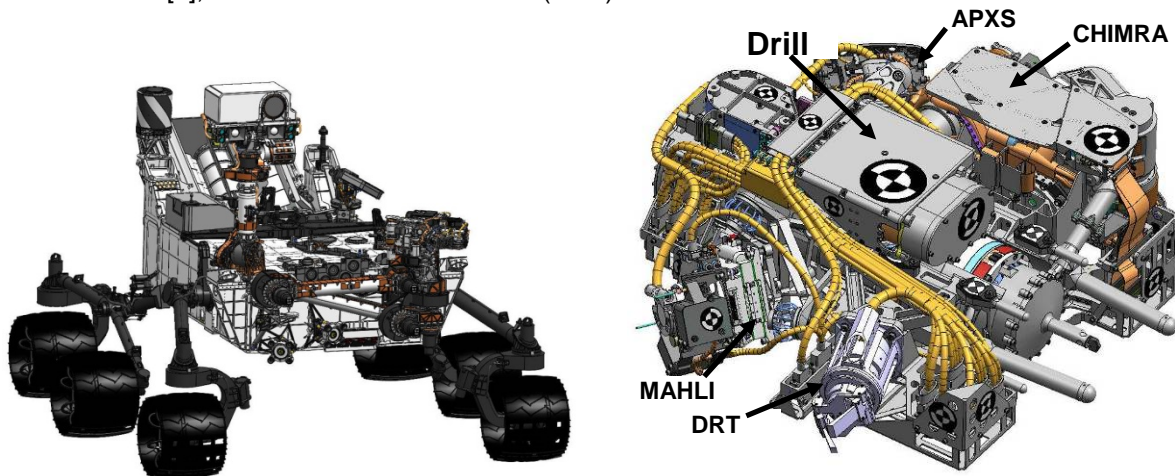


Figure 1. (a) MSL Rover (b) SA/SPaH Turret

The primary sample acquisition element of SA/SPaH is the Drill (see Figure 2) which collects powdered samples from various rock types (from clays to massive basalts) at depths up to 50 mm below the surface. The Drill then transfers the powdered sample to a processing device, the CHIMRA, which subsequently delivers sieved and apportioned samples to the science instruments housed in the belly of

* Jet Propulsion Laboratory, California Institute of Technology, Pasadena, CA

the rover. A typical sample acquisition operation with the Drill is described as follows. The Drill is placed in contact with the target rock by the SA/SPaH RA. A telemetry switch indicates contact has been made. The Drill is then preloaded onto the target by the RA for increased stability, reducing the likelihood of shifting during the operation. The Drill acquires the sample by rotating and hammering while maintaining a desired weight on the bit. Upon the completion of sample acquisition, the Drill retracts from the hole to a stow configuration and is disengaged from the rock by the RA. Lastly, through a combination of gravity manipulations by the RA and vibration environment generated by the Drill percussion mechanism, the sample is transferred from the Drill to the CHIMRA for further preparation.

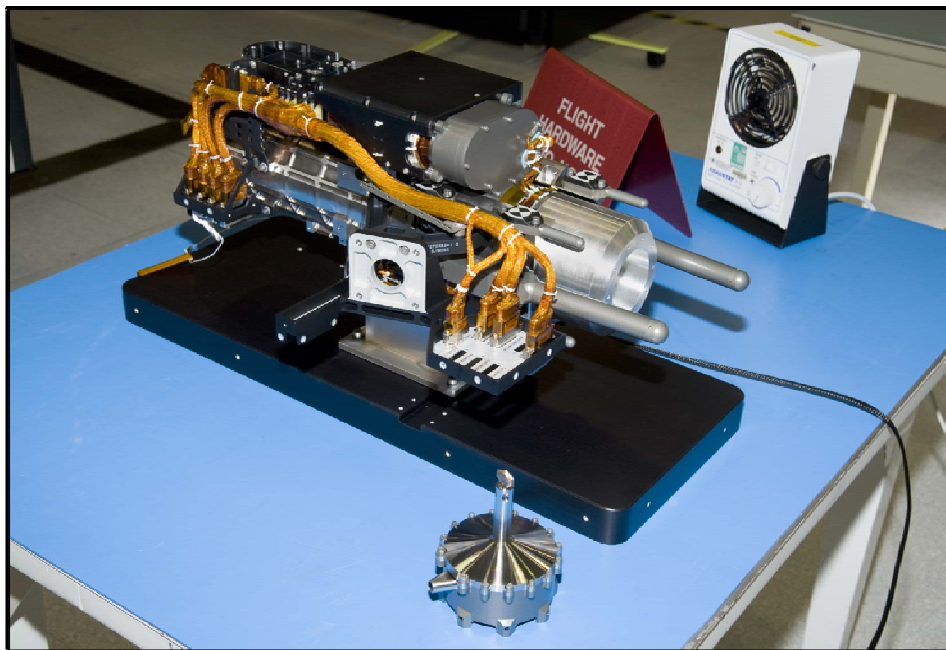


Figure 2. Engineering Model MSL Drill, Bit Assembly in Foreground (some of the turret brackets are attached to the housing and a ground adapter is chucked)

Drill System Development

Though the primary design objective of the Drill is the reliable acquisition of samples from rocks of various strength and composition, many aspects of the design (especially its mass and volume) were driven not by its primary function, but from the dreadful things that could happen while on the surface of Mars. What follows are some of the device's more pertinent design drivers.

Live long and drill – that's a requirement!

The Drill is designed to provide 81 samples for the science payload on MSL. To meet the strict cross contamination requirement across the sampling system, the Drill must also provide samples for dilution cleaning: the acquisition of a pre-sample for the sole purpose of flushing the residual of the previous sample from the entire sample path. This, in effect, doubles the drilling depth requirement. Since drilling on Mars is inherently a dry process, a rotary percussive drill was implemented after development testing showed that it produced significantly less bit wear than a rotary drag bit type (especially on rock with high compressive strength). Even still, in order to show margin to the life requirement, the Drill has the ability to replace a worn bit with a fresh one during the mission. Additionally, since sample flows solely within the bit, the ability to jettison a clogged bit adds another level of robustness.

Two spare bit assemblies, housed in their own bit box assemblies, are mounted to the front panel of the rover. A clever bit exchange method, which uses three active elements of the Drill (translation, rotation

and the chuck), enables the bit boxes to be passive devices while minimizing the impact to the Drill's volume and mass. The success of this execution is evident by the presence of only two additional features on the Drill for the sole purpose of bit exchange: the retaining features on the bit and the alignment posts on the contact sensor assembly for docking the Drill to the bit box.

It's a dirty and dangerous job...

The collection of extraterrestrial samples from a mobile robot on rough terrain poses the unique challenge of ensuring reliability and robustness in a highly indeterminate environment. One example is the sustained and maintenance-free operation in a dirty environment. Wherever possible, the moving components were placed internally within the sealed Drill housing, otherwise they were designed to be tolerant of dirt. The specific implementation of the latter will be discussed in the subsequent sections.

Since many highly valued science targets on Mars such as outcroppings are located on rough and steep terrain, the MSL rover has been designed to acquire samples from sloped surface up to 20 degrees. The compressed development schedule required the generation of a load case that could be defined and articulated relatively quickly. Without any ensured friction between the rover wheels and the surface of Mars, a worst-case load scenario was generated: a complete loss of friction at the rover wheels on a 20-degree slope while the tip of the bit was locked to the surface. One component of the Drill could not be designed to show positive margin for this load case: the bit. To meet this requirement the bit diameter would have to grow considerably, increasing the volume of sample collected. Larger cavities would be needed to process the additional sample causing the turret to exceed its volume allocation. Since the failure of one mechanical component cannot be counted on to protect the others downstream, all the non-replaceable elements of the Drill have been designed and will be qualified to the worst-case loads. Throughout the remainder of the paper, it will be shown how this single requirement drove the overall volume, structural design and required capability of many of the mechanisms of the Drill.

Live long (reemphasis) – even if you can't drill

Penetrating the surface from a *mobile* robot requires that a single mechanism fault in the Drill cannot result in the anchoring of the entire rover to the Martian surface; and the bit being “stuck” in a rock is not a mechanism fault – it is part of the process. This requirement flowed into two capabilities: (1) generate a large force to extract a stuck bit and (2) release the bit subjected to the worst-case load scenario. These functions are entirely independent throughout the system (including being powered by separate electronic drivers) such that a loss of one function will not preclude the operation of the other. Defining a “stuck” bit is somewhat of a slippery slope – pun intended. Lacking a more accurate definition of stuck, it was the intent of the Drill design to provide a sufficient retraction force to dead-pull the bit without percussion from a rock while under the worst-case load scenario. However, development testing showed that the force to extract a bit while subjected to 40% of the worst-case load scenario was higher than the maximum capability of the Drill. Mass and volume constraints of the turret precluded additional capability. However, a promising result observed in the force time history plots showed a stick-slip phenomenon which implies that the load required may be significantly reduced by hammering the end of the bit – a capability that the Drill has. This conservative test case was based on the assumption that the flight system would do nothing to alleviate the loads on the bit. It is emphasized that the flight system must carefully assess risk when sampling on steep and uncertain terrain.

Divide and conquer

Through a series of unfortunate events, the brunt of the design and implementation of the Drill started mid-summer of 2007 when the completion of the conceptual design kicked-off an intense effort to meet a launch date of fall 2009 (prior to the slip to 2011). As a result, a large emphasis of the Drill design architecture was placed on modularity allowing various mechanisms of the Drill to reach design maturity relatively independently. This approach demanded heavy coordination of interfaces; however, by keeping the interfaces simple and avoiding an overly intertwined design, the process was streamlined by only requiring the consensus of two mechanism engineers with the cognizant engineer providing review, arbitration and concurrence.

The modular approach was not exclusive to the design phase. A team of supporting engineers, working closely with the flight hardware engineers, designed, built and executed twelve Drill Development Tests (DDT) across several test platforms starting in September 2007 and completing in June 2008 (see Table 1). DDT-3 through 6 were performed using a prototype drill, mounted to a robot arm, that was functionally equivalent to the flight Drill featuring: a flight-like bit assembly, chuck (passive), spindle, voice coil actuated percussion mechanism, representative stabilizer kinematics and a weigh-on-bit force sensor. Drilling tests (DDT-3) in various rock types with natural surfaces generated the design requirements for: spindle torque and speed, impact energy, and weight-on-bit. This test activity also yielded algorithms for autonomous drilling that will be implemented in flight system software. Other test platforms utilized duplicate prototype Drill subassemblies so that those tests could be performed in parallel.

Table 1. A list of completed Drill Development Tests indicating the usage of flight-like prototype mechanisms: bit assembly (B), spindle (S), chuck (C), percussion (P)
Italicized text indicates tests performed using an arm-mounted prototype Drill

DDT-1 Cold Spindle / Bit Drag (B,S)	DDT-2 Bit Exchange (pickup only) (B,S,C)
<i>DDT-3 Drilling Parameters (B,S,C,P)</i>	<i>DDT-4 Drilling from a Compliant Arm (B,S,C,P)</i>
<i>DDT-5 Dynamic Environment due to Drilling (B,S,C,P)</i>	<i>DDT-6 Bit Life (B,S,C,P)</i>
DDT-7 Sample Flow in Low Pressure (B,C,P)	DDT-8 Bit Release Under Load (B,C)
DDT-9 Sampling at Low Pressure (B,S,P)	DDT-10 Bit Retraction Force (B – tube and bit only)
DDT-11 Force Sensor PQV	DDT-12 Percussion Cable Cycle Life

Lastly, the modular design extends into flight Drill integration and testing. All the mechanisms in the Drill are fully assembled and qualification tested prior to being integrated into the Drill top level assembly. Thus, some of the lessons learned during the assembly and test of one Drill sub-mechanism was preemptively applied to others. Some of these discoveries included: manufacturing defects, cabling process errors, chamber frost mitigation and electronic ground support equipment operation.

Drill Design Description

Autonomous sample acquisition is a complex process that requires a device with high functional density. The Drill is comprised of 7 sub-elements depicted in Figure 3. Starting at the business end of the Drill, there is a bit assembly that cuts the rock and collects the sample (Figure 3a). Supporting the bit is a subassembly comprised of a chuck mechanism (Figure 3b) to engage and release the new and worn bits, respectively, and a spindle mechanism (Figure 3c) to rotate the bit. Just aft of that, is a percussion mechanism (Figure 3d) which generates hammer blows to break the rock and create the dynamic environment used to fluidize the powdered sample. The aforementioned components are mounted to a translation mechanism (Figure 3e) which provides linear motion and senses weight-on-bit with a force sensor. There is a passive contact sensor / stabilizer mechanism (Figure 3f) that secures the Drill's position on the rock surface, and flex harness management hardware (Figure 3g) to provide the power and signals to the translating components. The remainder of this paper describes the Drill mechanisms, highlights how their design features enable the execution of reliable extraterrestrial drilling, and expands on various design challenges.

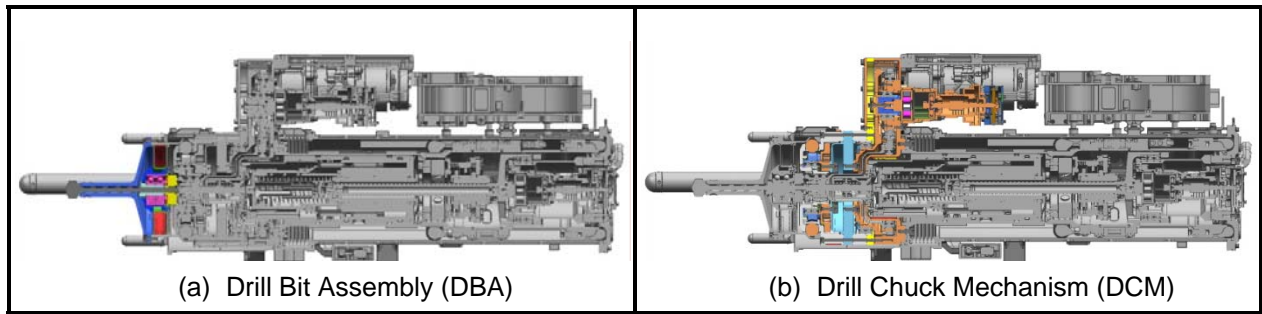


Figure 3 a-b. Depictions of the Drill Sub-Assemblies

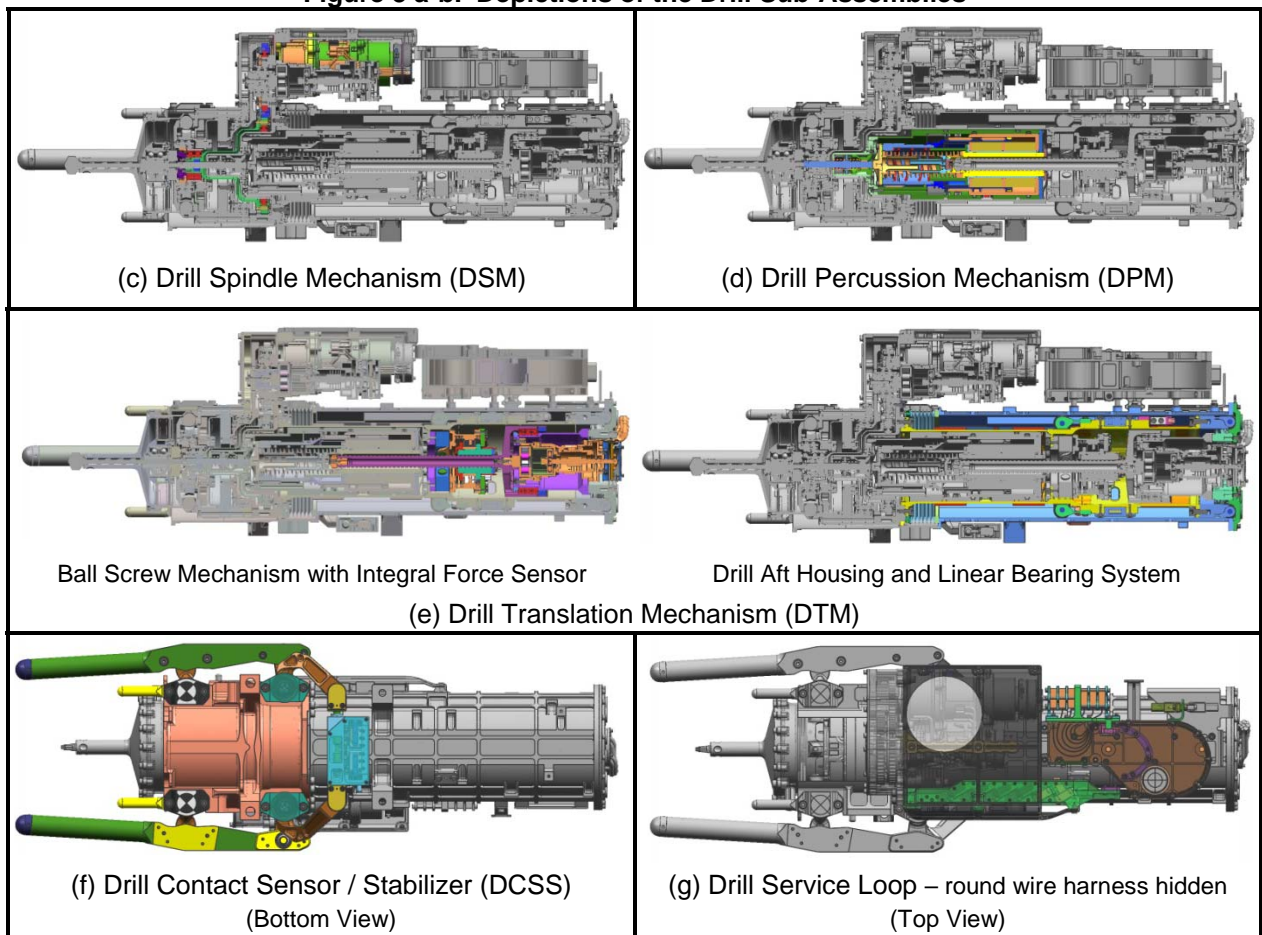


Figure 3 c-g. Depictions of the Drill Sub-Assemblies (cont.)

Development and Design of the Drill Mechanisms

Drill Bit Assembly

The Drill Bit Assembly (DBA) is a passive device which is rotated and hammered in order to cut rock (i.e. science targets) and collect the cuttings (powder) in a sample chamber until ready for transfer to the CHIMRA. The DBA (Figure 4a) consists of a 5/8-in (~16-mm) commercial hammer drill bit whose shank has been turned down and machined with deep flutes designed for aggressive cutting removal. Surrounding the shank of the bit is a thick walled maraging steel collection tube allowing the powdered

sample to be augured up the hole into the sample chamber. For robustness purposes, the wall thickness of the DBA was maximized while still ensuring effective sample collection. There are four recesses in the bit tube that are used to retain the fresh bits in their bit box (Figure 4a).

The rotating bit is supported by a back-to-back duplex bearing pair within a housing that is connected to the outer DBA housing by two titanium diaphragms. These bearings, the only ones on the Drill in the sample flow, are protected by a spring energized seal and an integrated shield that diverts the ingested powdered sample from the moving interface (Figure 4b).

The DBA diaphragms provide radial constraint of the rotating bit and form the sample chambers. The axial compliance of the diaphragms (combined with anvil springs in the Drill Percussion Mechanism) reacts the weight on bit generated by the Drill Translation Mechanism. Between the diaphragms there is a sample exit tube from which the sample is transferred to the CHIMRA. To ensure that all sample is retained no matter the orientation of the Drill with respect to gravity during sampling, the pass-through from the forward to the aft chamber resides opposite to the exit tube (Figure 4b).

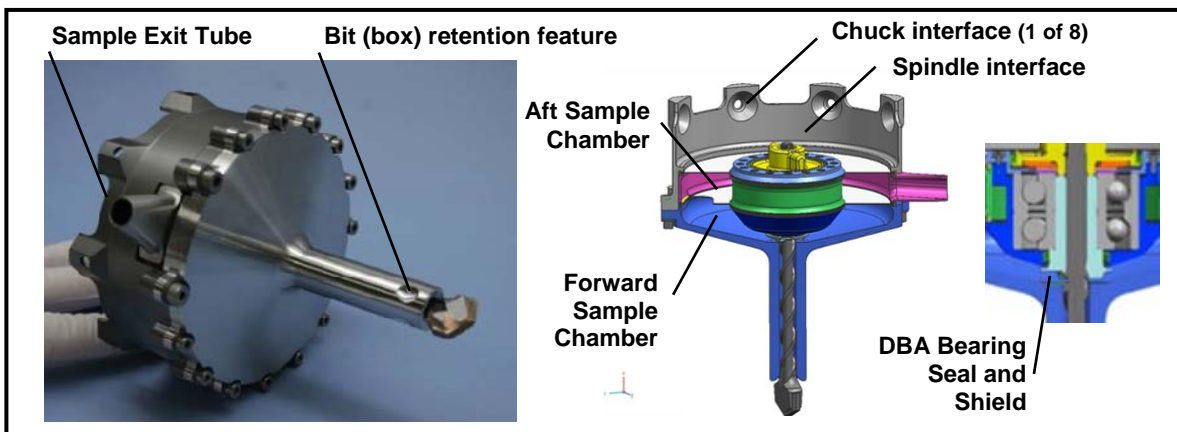


Figure 4. (a) EM Drill Bit Assembly (b) Sample paths and interfaces of the DBA

The DBA interfaces to the rest of the Drill via eight circumferential, conical recesses in its housing and a torque coupling affixed to the end of the bit shank. There are through holes at the bottom of each recess so that any Martian dust accumulated on spare bits stored on the rover can be pushed outward when a fresh bit is acquired. The DBA interface to the Drill has a small prescribed amount of free play. This both allows the DBA to find its natural path into the rock and decouples most of the cyclic radial load due to the bit-rock interaction from being transmitted to the rest of the Drill.

Lesson learned:

Mechanism components that operate in a dirty environment require some or all of the following features: dedicated pathways for the flow of particles, cavities that can receive debris, and compliant elements to accommodate the presence of junk. In addition to the DBA, these features were implemented in the Drill Chuck Mechanism and the switch assembly of the Drill Contact Sensor / Stabilizer.

Drill Spindle Mechanism

The Drill Spindle Mechanism (DSM), nested within the Chuck / Spindle Sub-assembly (Figure 5) provides the torque to rotate the bit for drilling and unlocking the fresh bit assemblies from the bit box. The mechanism is actuated by an electrically-commutated gearmotor that drives the spindle shaft via a spur geartrain. The output shaft is support by a bearing pair at the nose (near the torque coupling to the bit) and a single deep groove bearing at the rear (under the spindle gear). The maximum mean contact stress in the bearings is kept low to prevent lube degradation. Mounted to the shaft is a dirt-tolerant torque coupling that transmits torque to the bit. The coupling accommodates axial, radial and angular motion

between the bit and spindle shaft to permit the following functions: the transmission of the hammer blow directly onto the bit, the mating of a fresh bit, and release of the bit both in free space and under load.

Drill Chuck Mechanism

The Drill Chuck Mechanism (DCM), also residing within the Chuck / Spindle Sub-assembly (Figure 5), enables the Drill to release worn bits and take hold of fresh ones stored on the rover front panel. The design driver not only included the requirement to survive the worst-case load scenario but also to release the bit while subjected to it. The DCM is a dirt tolerant ball lock device that consists of eight stainless steel balls that are pushed out radially by a rotary cam. The cam is actuated via a drivetrain consisting of an electrically-commutated gearmotor with a power-off brake, a single spur gear stage and a harmonic drive. This mechanism underwent substantial high fidelity development testing with a prototype 12-ball chuck mechanism (DDT-8). The objectives were to:

1. Verify cam mechanism tolerance to airborne dust particles and self-generated rock particles, and demonstrate the effectiveness of its seals.
2. Measure the torque requirement to release under the worst-case load scenario with and without the presence of various types of rock particulate.
3. Estimate the coefficient of friction at the ball interfaces to more accurately evaluate the peak contact stress.

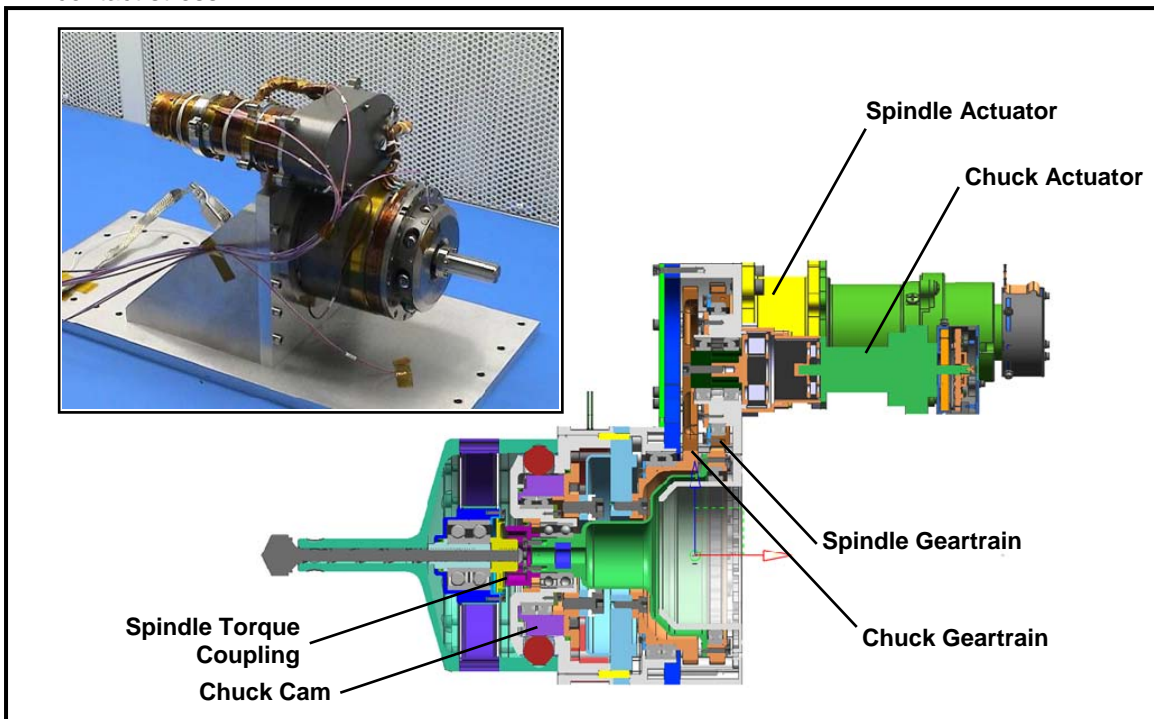


**Figure 5. Chuck / Spindle Subassembly with Bit Assembly
(inset: EM Unit Ready for Spindle Thermal Dyno Test)**

The mechanism demonstrated 4X life operation, fully loaded, with the ball cavities filled with both fine and coarse Martian regolith simulant with sufficient torque margin (Figure 6a). Even corundum particles introduced were crushed easily. However, the coefficient of friction estimated from the test results showed that the contact stresses on the cam was above the material allowable. This was verified upon disassembly and inspection of the cam where local surface deformation was found. Additionally, there were tracks where the Lub-Lock 4306 dry lubricant was worn away (Figure 6b). The analysis also showed that the highest stress was on the sloped portion of the cam profile. To lower the contact stress the cam surface curvature was reduced by decreasing the number of balls from twelve to eight. However, the analysis still showed that this was insufficient, so a conforming curvature shape was also implemented on

the cam to reduce the contact stress. The new cam design with an improved dry lubricant process was tested again to 5X life (Figure 6c) with the same dirt tolerance conclusion and no detriment to the cam surface.

Lesson learned:

High-fidelity development test hardware is worth its weight in unobtainium. Although the initial development test results show that there was sufficient torque margin at end of life, it was deemed inappropriate to implement a design that would degrade under expected operational conditions especially with the likely unknown unknowns associated with planetary exploration.

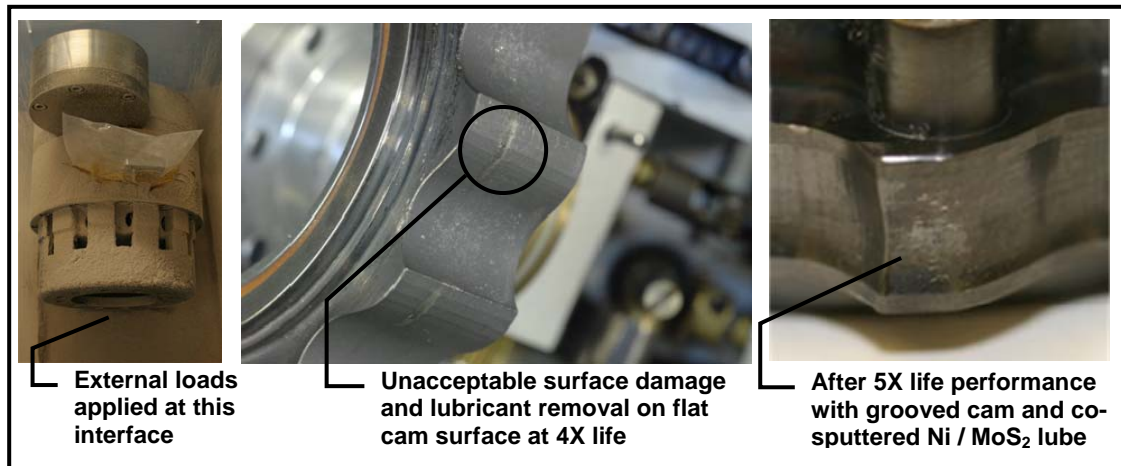


Figure 6. (a) Development Test DCM Dirty Testing (b) Post Test Flat Cam Surface (c) Post Test Grooved Cam Surface

Drill Percussion Mechanism

The Drill Percussion Mechanism (DPM) generates the impact needed to break the rock and the dynamic (vibration) environment required to move powdered sample through the DBA (Figure 7). The DPM is a functionally simple device consisting primarily of a hammer assembly, a spring, and a housing assembly. The DPM is actuated by a long-stroke voice coil developed by BEI Kimko Magnetics. It is wound with bifilar magnet wire providing graceful degradation in the case of an open winding.

The 0.4-kg hammer assembly strikes the end of a spring-suspended anvil rod that remains stationary and in contact with the end of the bit. The anvil spring rate is one half of the axial spring rate of the DBA such that it supports one third of the weight on bit. The percussion action is a transfer of momentum from the moving hammer, through the anvil in the form of a stress wave, then through the bit and ultimately to the rock. The DPM operates at 1800 blows-per-minute with variable impact energies from 0.05 to 0.8 Joules.

There are three integral linear bearing rails with polished hard anodized surfaces in the aluminum housing of the DPM. Spring elements are used across most of the interfaces within and external to the mechanism to accommodate the various coefficients of thermal expansion. The percussion housing features grooves that contain internal and external radial expansion spring pairs to accommodate relative radial dimensional variations to the steel voice coil magnet field assembly mounted within it and the titanium tube it is mounted within, respectively. In the axial direction, dedicated wave springs ensure that preloads are maintained and thermally induced stresses are minimized between the following: the percussion housing and the rest of the Drill, the voice coil field assembly and field cable guide, and the percussion housing and the voice coil field assembly. The last spring also functions as the retraction hardstop absorbing the residual kinetic energy if the hammer exceeds its nominal range of motion.

The hammer assembly is comprised of a maraging steel hammer head fastened to an aluminum flexure body which is adjoined to the voice coil bobbin (windings) via a threaded joint and structural adhesive.

The hammer head has three tabs that engage the retraction hardstop. The flexure body has these features: a splice cavity where the harness is connected to the voice coil magnetic wire, a permanent magnet assembly which activates a bank of reed switch sensors, and three flexure suspended DU bearing segments. An inverted DU bearing is bonded to the end of the voice coil bobbin providing an aft support bearing surface which rides along the inner surface of the voice coil magnetic field outer pole piece. The aft bearing ensures that only dedicated wear components are in contact. DU bearings were selected for their high wear life and low service temperature; the latter reduces the required heater power for the cold operation of this mechanism. Beryllium Copper was selected for the bobbin material.

Within the hammer assembly there is the main spring of the mechanism which provides two functions: (1) it stores the work done by the voice coil on the upstroke for delivery on the downstroke and (2) it captures the rebound energy from previous impact for use on the next impact. The voice coil actuator simply needs to recoup the energy lost during the impact (causing rock fracturing) and internal mechanism losses. One technical challenge discovered on the prototype percussion mechanism was spring surge of the main spring. The original springs were failing prematurely due to the proximity of the spring's natural frequency with the operating frequency. This was solved by changing the spring material to one with a lower shear modulus, lower density and high fatigue strength. The new spring allowed a large amount of stored energy while maintaining an appropriately large separation between the operating frequency and its natural frequency.

Inside the main spring, the voice coil harness is routed within a unique helical cable guide assembly whose helix direction is opposite of the main spring. Inspired by a telephone handset cord, the design controls the location of the harness, provides significant stroke while minimizing wire strain, and has a very low spring rate. To avoid contact with the main spring, the inner diameter of the cable guide helix is control by a split, fingered mandrel integrated into the moving hammer head and stationary side of the cable guide assembly. The outer diameter of the main spring is controlled by the inner surface of the flexure housing. During assembly of the mechanism, the clearances were verified to ensure there will always be a gap between the two components.

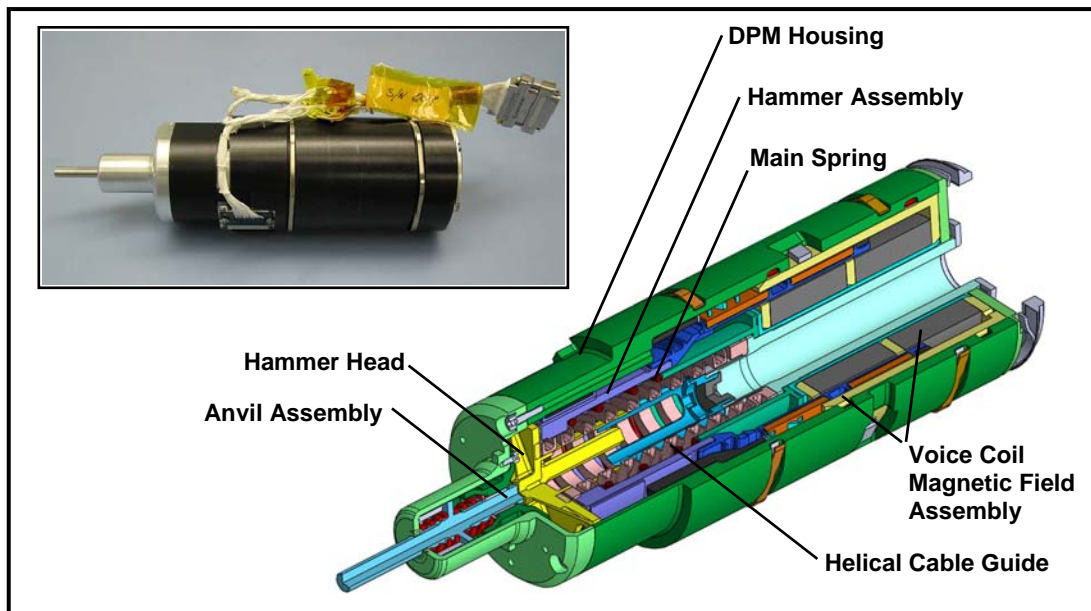


Figure 7. Drill Percussion Mechanism

Another challenge were eddy currents due to the electrically conductive voice coil bobbin material moving quickly through a magnetic field. This manifested itself as a velocity dependent loss force (i.e., viscous damping) that had to be eliminated for efficient operation. The solution implemented was to cut axial slots in the bobbin in the area that was exposed to the magnetic field. The slots were then filled with non-

conductive structural adhesive. This increased the effective electrical resistance of the bobbin in the appropriate direction without compromising the thermal conductive properties of the bobbin. When implemented on the prototype mechanism, there was no measurable performance difference between the slotted Be-Cu bobbin and a polymeric one.

The voice coil drive method is quite different to the electrically commutated motors that power the rest of actuators in the Drill. Due to its late development in the MSL project life cycle, the voice coil actuator needed to be compatible with the existing motor drive electronic hardware. Additionally, the tight packaging constraints and the severe percussive (shock) environment precluded the implementation of a sensor for closed loop feedback control of the DPM. The challenge remained to develop a drive method that did not require sensory feedback.

The DPM is driven by an open loop voltage waveform. Near the impact, the voltage waveform is set to zero so the hammer will coast just prior to and after the impact. This zero voltage zone, called the coast period, provides a tolerance to perturbations in the hammer motion cycle. This prevents the voice coil from fighting the motion of the hammer. Otherwise, the voice coil could be quite inefficient using energy and generating heat to slow down the hammer. The voltage values are defined such that the voice coil generates a prescribed force to retract (upstroke force) and extend the hammer (downstroke force). The forces are defined during a tuning procedure to create a desired percussion output: kinetic energy level just prior to the impact. A position sensor was used to determine the kinetic energy; it was removed before the installation of the DPM into the Drill top-level assembly. During tuning, the two forces are also modulated to adjust the timing of impacts such that they occur in the middle of the coast period.

For a desired impact hammer velocity and assumed rebound velocity, the motion profile of the hammer (i.e. position and velocity time history) is estimated *a priori* (Figure 8). Using a discretized motion profile, the desired actuator force, $F_{desired}$, the voice coil force constant, K_F , (back-emf, K_V , constant equivalently) as a function of hammer position, x , and the total roundtrip resistance of winding circuit, R_{total} , the voltage waveform is defined as follows:

$$V = I_{desired} \times R_{total} + V_{emf}$$

$$V_k = F_{desired}/K_F(x_k) \times R_{total} + \dot{x}_k \times K_V(x_k)$$

where k is the index of the voltage table

The voice coil winding temperature, and thus resistance, will increase due to self heating during operation. The temperature of the windings is modeled onboard by the flight system software to prevent overheating and to estimate the resistance parameter for the voltage waveform. The DPM tuning process yields two tables: desired current draw and the feed-forward back-emf voltage compensation.

A project schedule constraint mandated the use of a voltage driver for the voice coil to minimize the impact to the rover avionics development. Fortunately, the voltage drive method features inherent speed regulation and a reduced sensitivity to variations of the voice coil force constant. If the velocity of the hammer is lower than expected, the voice coil will draw more current and thus output more force. This is equivalent to having a built in proportional feedback controller on hammer velocity. One source of velocity error is the variation of impact coefficient of restitution due to rock strength. In a current driver, a drop in the force constant (K_F) would directly result in a voice coil output force. In an open loop current driver system, the known sources of K_F variation would require compensation complicating the software implementation. With the voltage drive, a decrease in K_F (and thus force generation of the actuator) is counteracted by a lowering of the back-emf voltage generated by the windings. Since the unreduced back-emf is compensated for in the voltage waveform, this “found” voltage is converted into additional current to generate more force. Some sources of K_F variation are the presence of the steel ball screw within the bore of the voice coil field assembly (which varies with Drill feed position) and voice coil magnet temperature.

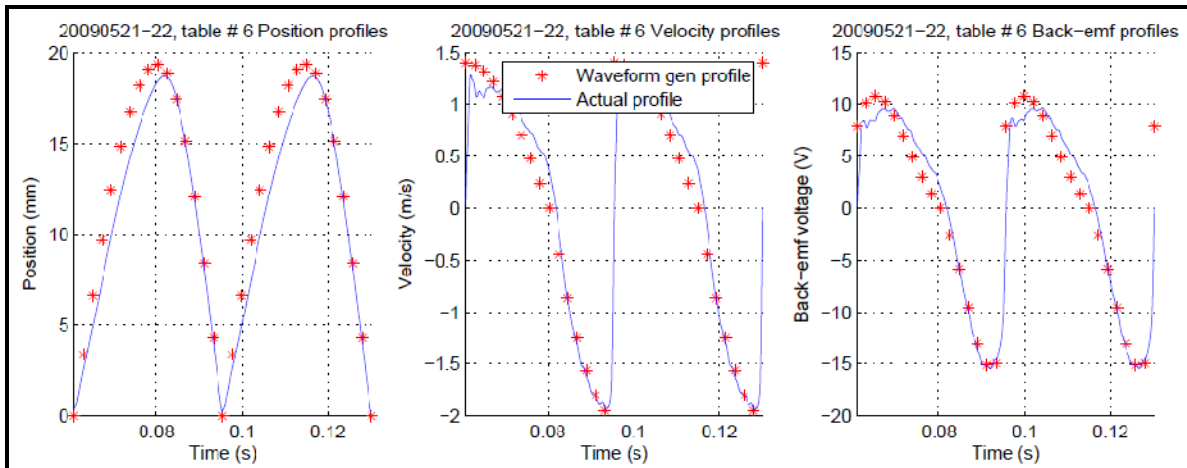


Figure 8. Actual versus predicted hammer position, velocity and back-emf voltage

A misunderstanding occurred during the specification of the voice coil driver when the term “tri-state” was used to describe the desired function during the coast period. This resulted in back-emf voltage induced current during the coast period which effectively dynamically braked the voice coil – dissipating kinetic energy (bad) in the form of joule heat (worse). By the time the problem was discovered, the firmware on the driver could not be changed without a major cost and schedule impact. Fortunately, a work-around was discovered: by commanding a low voltage to retract the hammer (instead of zero), the desired effect could be achieved.

Lessons learned: (1) What can appear to be clear communication across disciplines can often be quite nebulous. For example: one expression or word can have different meanings depending on the individual's interpretation. Exhaustive interaction (and often repetition – especially in high stress situations) with diagrams and simplistic explanations are the surest bet for success. (2) Sometime external project constraints can yield serendipitous outcomes as was the case with the voltage-drive method.

Lastly, mounted to the DPM housing is a series of six normally open reed switch sensors which provide coarse hammer position telemetry. The small reed switches are robust to large dynamic environments and were easily integrated into the existing rover avionics. The switches are activated by a magnet mounted to the hammer assembly. The activation regions of the adjacent switches overlap providing up to 12 position states. Figure 9 shows reed switch performance across the mechanism range of motion. These sensors provide the only direct telemetry of the hammer motion and thus are useful for operational diagnostics. These sensors are not used for feedback control. Additionally, drilling various rock types during the development test program has shown a correlation between max hammer motion and rock strength. If this carries over to the flight Drill, these sensors may also provide interesting science data about the composition of the Martian rock.

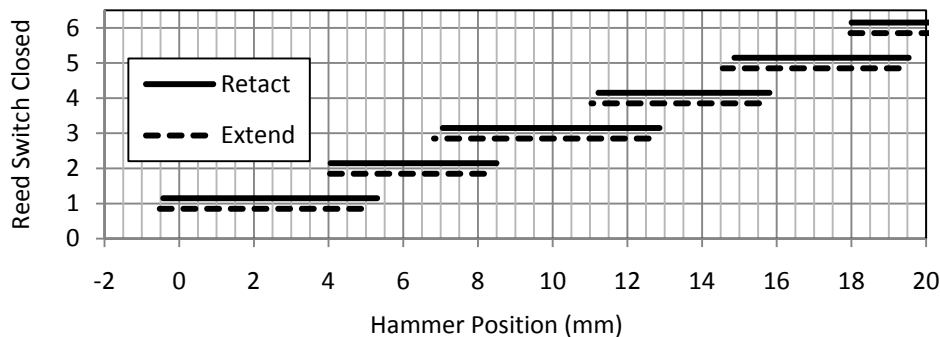


Figure 9. Reed switch data across the DPM stroke

Drill Translation Mechanism

The Drill Translation Mechanism (DTM) provides the linear motion of the bit, spindle, chuck and percussion Drill subassemblies for the following functions: maintaining 120-N weight-on-bit (WOB) during sample acquisition, generating a large retraction force to extract the bit from the hole, and mating to a fresh bit in the bit box. The DTM is comprised of:

1. Aft housing assembly that forms the linear bearing rails (Figure 10).
2. A translation tube that is populated with various bearing elements (Figure 10).
3. A ball screw mechanism with an integrated force sensor (Figure 11).

The Percussion and Chuck / Spindle Sub-assemblies are installed into and integrated onto the end of the translation tube, respectively. A welded metal bellows mounted between the translation tube and the aft housing seals the internal components to protect them from Martian dirt.

To support side and cross-moment loads, the linear bearing system uses two sets of 6 pairs of needle roller bearings mounted to the translation tube that ride on the flat internal surfaces of the aft housing. The arrangement of these bearing sets, which drives length and diameter of the Drill, was dictated by the worst-case load scenario. Torsion loads are supported by a two-stage bearing system: one set provides low axial drag and the other supports high loads. Testing across the qualification operation temperature of $\pm 70^{\circ}\text{C}$ resulted in axial drag force less than 5 N for sample acquisition operation, thus yielding a low disturbance to the WOB measurement.

The dual bridge force sensor provides redundant measurement of the low weight-on-bit since the nominal axial load is too low to be observed in the actuator current telemetry. The inner diameter of force sensor is axially clamped to the ball nut. The force sensor outer diameter is axially constrained between two preloaded wave springs. These springs serve a few functions:

1. Provide additional compliance to lower the WOB feedback control bandwidth requirement
2. Allow the high retraction load to be shunted around the sensor.
3. Isolate the science instruments mounted to the Drill aft housing from the dynamic environment generated by the Drill.

The force sensor and wave springs are housed in a gimbal assembly which couples the translation mechanism to the translation tube. The gimbal isolates the ball screw and force sensor from radial and bending loads.

The ball screw mechanism consists of a custom ball screw supported by a high axial capacity bearing set at one end. It is actuated by an equivalent electrically-commutated gearmotor with a power-off brake as the DCM. To reduce the overall length of the Drill, the ball screw bearings also support the output of the gearmotor. This not only reduced the volume by removing a set of redundant bearings (in the actuator gearbox), but also eliminated the need for a coupling component between the gearbox and the ball screw. The ball nut torque is reacted by a flange mounted anti-rotation roller assembly. The range of the motion of the DTM in the aft direction is limited by the contact of rotation hardstop features on the nut and the screw.

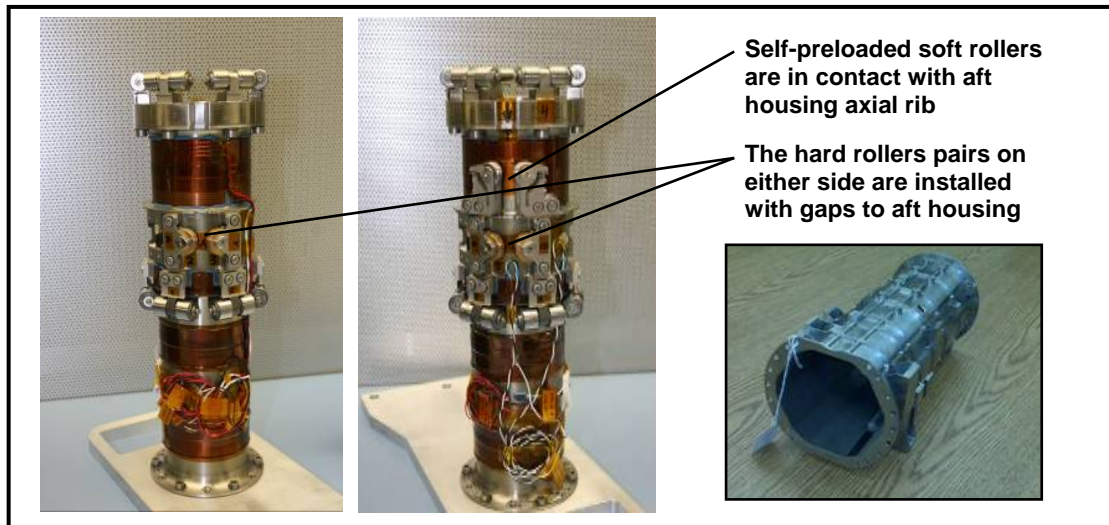


**Figure 10. Translation Tube with Rollers and Thermal Hardware
(inset: an aft housing ready for dimensional inspection)**

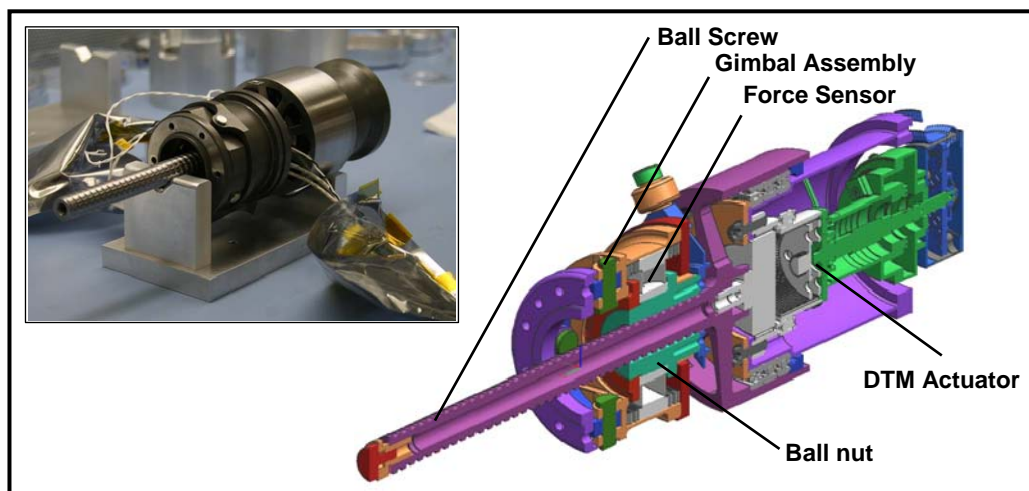


Figure 11. Ball Screw Mechanism with Integral Force Sensor

Figure 12 shows the DTM undergoing two of its qualification tests. One test demonstrates margin against the maximum axial and side loads expected during sample acquisition. The other is a characterization of the retraction force generation capability of the DTM; the device is shown lifting 10,012 N at -70°C.

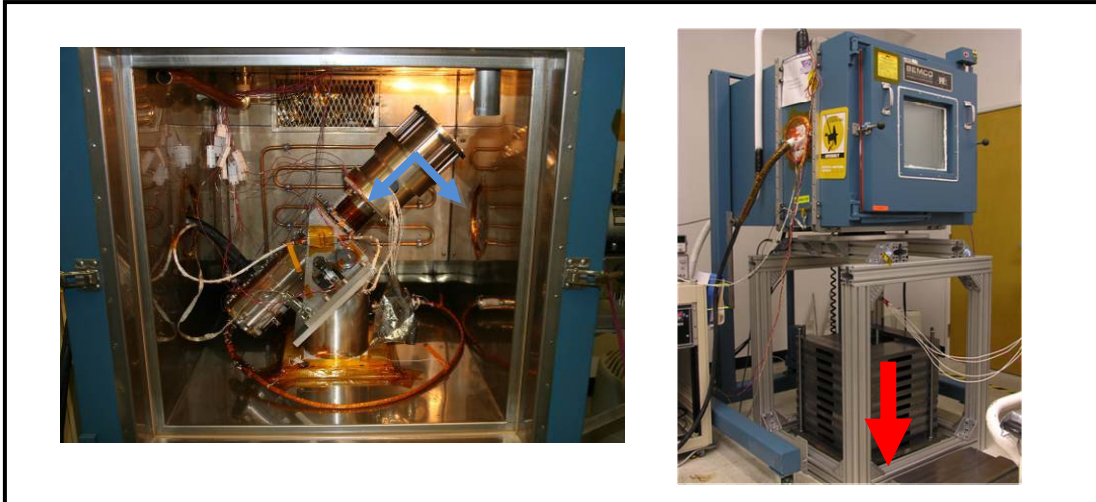


Figure 12. Two of the DTM Qualification Tests: (left) Margin under Drilling Loads and (right) Retraction Force Capability Characterization (Lifting 10,000 N at -70°C)

Drill Contact Sensor / Stabilizer

The Drill Contact Sensor / Stabilizer (DCSS) is a passive mechanism that indicates the placement of the Drill on a target rock (Figure 13). The articulating two point-contact design of the DCSS accommodates a combination of target surface height variations between the contact points and Drill axis misalignment to the surface normal. The DCSS will indicate contact if and only if both prong tips are in contact with the target. Once preloaded to the target by the Robotic Arm, the DCSS stabilizes the Drill by locking out 4 degrees-of-freedom (3 translational DOFs and a rotational DOF about the bit axis) between the Drill and the target. This device is conceptually similar to the contact sensor implemented on the Mars Exploration Rover for the Rock Abrasion Tool [3]. The DCSS consists of two counter articulating spring-loaded 4-bar linkages interconnected by a coupler assembly. The coupler assembly consists of a piston with cam surfaces that actuate two micro switches. The two prongs of the DCSS and the Drill forward housing structure make up the coupler links and ground link, respectively. The total linkage is centered by counter-acting clock springs mounted in the aft links' lower joint assembly. These springs also reset the coupler piston thus eliminating the need for a return spring within the coupler sub-assembly. The springs are machined (rather than hand wound) to ensure there is no coil rubbing which would add undesired friction. They also have spline features on the inner and outer diameter that allow fine adjustment of the spring preload.

A low and consistent switch trigger force will yield more reliable preloading by the robotic arm. This presents a conflicting requirement for the DCSS: the return spring force should be high enough to ensure the release of the switches but not so large as to drive the trigger force above 40 N. The solution was to seal the moving elements: including all rotary joints and the piston of the coupler with felt seals. This would ensure that the Martian dirt would not foul up the device and keep its performance consistent. The return springs were then preloaded to ensure sufficient margin to un-trigger the contact switches against the total measured friction in the assembly.

Another design challenge for DCSS was structural capacity. One of the drivers was, once again, the worst-case load scenario: the rover can hang off one prong on a 20 degrees Martian zero-friction slope. However, the biggest driver was the Translation Mechanism retraction force which is reacted back to the rock by the DCSS. The loads in the links of the four-bar can get quite severe especially when the DCSS is in its fully articulated configuration. This is compounded with the tight packaging constraints of the turret (Figure 1b); the DCSS is the closest neighbor to the DRT and CHIMRA. Through the use of high strength materials, spherical bearings at each joint, and clever link geometry the device meets the load

requirement with positive margin. Lastly, integrated onto the housings of the DCSS forward joints are four alignment posts that enable the Drill to dock with the bit box.

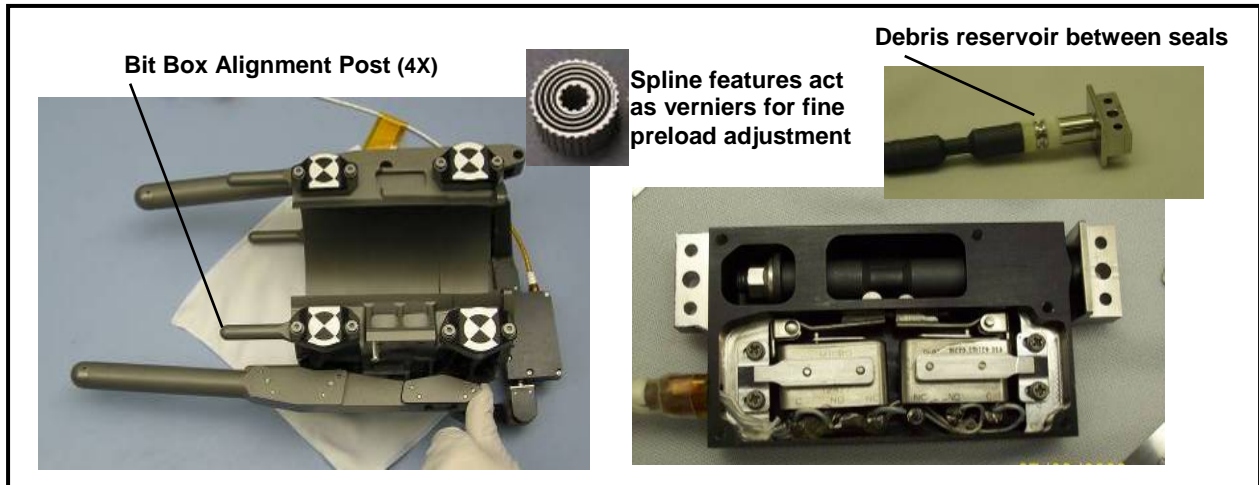


Figure 13. (a) Drill Contact Sensor / Stabilizer Assembly at full articulation (inset: Return Spring) (b) Compressed DCSS Coupler w/o Cover (inset: Coupler Piston with Seals)

Conclusion

At the time of writing this paper the Qualification Model and Flight Model Drill mechanism subassemblies are being tested across the qualification operating temperature range (-70°C to +70°C for most components, colder for the DPM, DCSS and DBA). The Engineering Model (EM) Drill assembly has been functionally tested at ambient conditions and integrated at the next higher level of assembly – onto the Robotic Arm as part of the Turret. There it was subjected to a sub-system level test to characterize the self-generated dynamic environment used for sample flow within the Drill and CHIMRA. Over the next few months, the EM Drill will be mounted to another manipulator to undergo abbreviated drilling and sample transfer testing at low pressure.

Acknowledgements

The work described in this paper was performed by the Jet Propulsion Laboratory, California Institute of Technology, under contract with the National Aeronautics and Space Administration.

Developing the Drill and producing it for flight is an enormous undertaking that relies on personal dedication and sacrifice. This author has been blessed with a fantastic team of hardware engineers who have worked tirelessly for years to reach this point: Kyle Brown (Chuck, Spindle and Bit), Ian Cady (Percussion), Matt Haberland (Contact Sensor / Stabilizer), Kerry Klein (Translation Mechanism), Kristo Kriechbaum (Percussion), Justin Lin (Chuck, Spindle and Bit) and Paul McGrath (Translation Mechanism). Jack Aldrich, Mark Balzer, Richard Barela, John Bousman, Kevin Burke, Louise Jandura, Mike Johnson, Brett Kennedy, David Levine, Joe Melko, Suparna Mukherjee, Matt Orzewalla, Frank Ramirez, Dave Putnam, Don Sevilla, Lori Shiraishi, Jeff Umland, Robert Uyeda, Max Von Der Heydt and Chris Voorhees have also contributed to the Drill development.

References

1. Jandura, Louise. "Mars Science Laboratory Sample Acquisition, Sample Processing and Handling: Subsystem Design and Test Challenges." *Proceedings of the 40th Aerospace Mechanisms Symposium*, (May 2010).
2. Sunshine, Dan. "Mars Science Laboratory CHIMRA: A Device for Processing Powdered Martian Samples." *Proceedings of the 40th Aerospace Mechanisms Symposium*, (May 2010).
3. Myrick, Thomas, Davis, Kiel and Wilson, Jack "Rock Abrasion Tool." *Proceedings of the 37th Aerospace Mechanisms Symposium*, (May 2004).

Lightweight Low Force Rotary Percussive Coring Tool for Planetary Applications

Ross Hironaka* and Scott Stanley**

Abstract

A prototype low-force rotary-percussive rock coring tool for use in acquiring samples for geological surveys in future planetary missions was developed. The coring tool could eventually enable a lightweight robotic system to operate from a relatively small (less than 200 kg) mobile or fixed platform to acquire and cache Mars or other planetary rock samples for eventual return to Earth for analysis. To gain insight needed to design an integrated coring tool, the coring ability of commercially available coring bits was evaluated for effectiveness of varying key parameters: weight-on-bit, rotation speed, percussive rate and force. Trade studies were performed for different methods of breaking a core at its base and for retaining the core in a sleeve to facilitate sample transfer. This led to a custom coring tool design which incorporated coring, core breakage, core retention, and core extraction functions. The coring tool was tested on several types of rock and demonstrated the overall feasibility of this approach for robotic rock sample acquisition.

Introduction

Current science for Mars and lunar exploration demands that small diameter rock cores be acquired for geologic evaluation. Tools to acquire these cores must be lightweight, draw minimal power, and induce low loads on their robotic platforms. Unfortunately, no tools have yet been produced that meet these requirements and produce a viable core. Tools developed to date are often complex, require large power and mass budgets, demand down forces beyond the capabilities of anticipated landers and rovers, and either take an inordinate amount of time to generate a core or introduce excessive energy into the core sample, pulverizing it.

A rotary-percussive mechanism for rock drilling offers promise in addressing these requirements. Delivering hammer blows to a drill bit allows rock to be chiseled away as opposed to being worn down by friction alone. This can significantly reduce the amount of down-force, or weight-on-bit (WOB), required as well as offer savings in power consumption.

In addition to raw coring ability, there are other challenges in coring tool design that must be addressed for successful sample acquisition. A means of breaking off generated cores from the parent rock must be included. The design must also provide a practical and reliable means for extracting and handling the generated cores. These are not trivial problems. Common rocks of interest, particularly sedimentary types, are easily fractured during the core generation process. This can cause mechanisms to bind or jam, foiling sample retrieval efforts. In addition, for maximum geological significance, science demands maintaining the order in which fractured rock core pieces are acquired. Finally, the ability to replace worn drill bits is an important consideration for the coring tool design because some rocks of interest, such as basalt and sandstone, are particularly abrasive. A mechanism that allows for bit change-out must be designed to work in concert with the rotary-percussive and core handling mechanisms.

This paper details the development of a rotary-percussive coring tool design that addresses core generation, break-off, containment, and retrieval.

* MDA ISI Space Division, Pasadena, CA

** Techno Planet Inc., Northridge, CA

Corer Tool Background

The Low-force Sample Acquisition System (LSAS)

Previous design efforts were leveraged during the development of the rotary-percussive coring tool. In 2006, the Space Division of MDA Information Systems, Inc. (formerly Alliance Spacesystems) produced a rotary percussive drill designed for space use under a NASA-funded Mars Instrument Development Program (MIDP) project – the Low-force Sample Acquisition System (LSAS) in Figure 1. The flight-like drill prototype that was the end result of the project successfully drilled and acquired 1-cm³ sample fines from a variety of rocks and soils, including the hardest anticipated Martian rock (basalt) and frozen soil. This ability was demonstrated in ambient conditions and in a thermal/vacuum chamber replicating Mars pressure and extreme temperatures. The rotary percussive approach was demonstrated to be simple, robust, and highly efficient in power and mass.

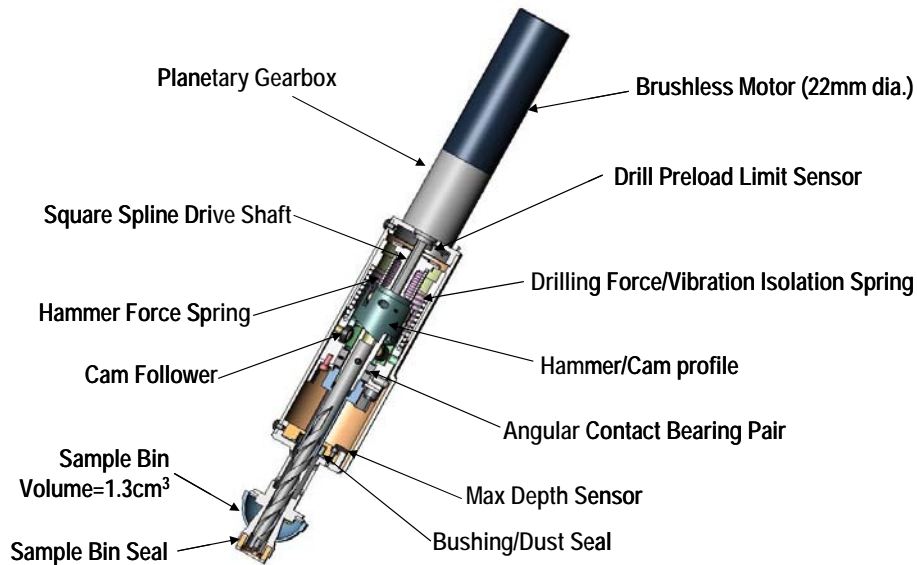


Figure 1. Original Low-Force Sample Acquisition System (LSAS)

The successful performance of the LSAS drilling system, along with the difficulties encountered by existing coring devices, led MDA Information Systems to consider applying LSAS and its rotary percussive action to the coring problem. The LSAS prototype was simply adapted to accommodate a commercial coring bit (see Figure 2), and no attempt was made to optimize the drill for the new coring operating conditions. The results were surprisingly positive. When drilling in limestone, 1-cm-diameter cores were readily produced up to 1 cm long in as little as 20 minutes while mounted on a rover-mounted robotic arm. The drill readily began coring without a pilot hole, probably because of the low applied force and compliance of the robotic arm/rover platform.

SBIR 2006 Phase 1

Following the encouraging results with the modified LSAS drill, a Phase 1 SBIR effort commenced in 2006 that took this heritage device and expanded its potential to include coring against a variety of rock materials anticipated to be encountered on Mars. An industry and literature search was conducted to identify best practices in rotary percussive coring, and commercial off-the-shelf (COTS) bits were located for test. An extensive test program was performed to evaluate these bits with accompanying performance parameters such as rotational speed, WOB, hammer frequency, and hammer force. Through the use of a breadboard fixture (see Figure 3), coring bit designs and coring parameters were evaluated to identify optimum combinations. The breadboard fixture, with separate motors for driving rotary and hammering action, allowed drilling parameters to be independently varied during testing.

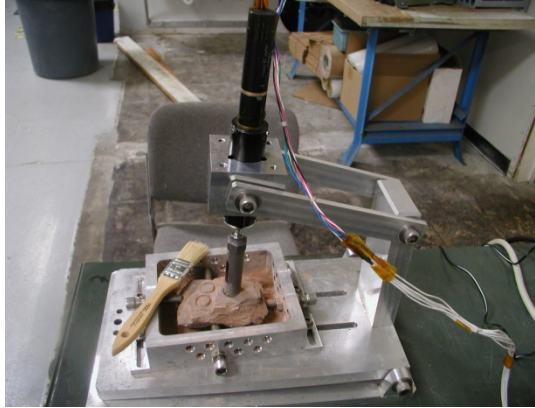


Figure 2. Modified LSAS in Test Fixture with Commercial Coring Bit

Phase 1 results indicated that the primary goal of producing a 1-cm-diameter, 10-cm-long core¹ from a variety of rocks, including hard basalt was achievable, though not without complications. The commercial coring bits exhibited rapid dulling, particularly with basalt and sandstone. This suggested the importance of a bit change-out mechanism and/or the need for further bit refinement. Also, the bit and associated performance parameters required to core basalt are evidently too aggressive for softer materials, particularly layered rock structures, resulting in broken or even pulverized cores. As a result, a conceptual corer was designed that included a bit change mechanism concept and a means of modifying the percussive force. Finally, it was found that relatively large amounts of power, approximately 90 watts, were needed to generate the cores. Although a specific power target was not established at the time of Phase 1 testing, it was clear this was in excess of current rover capacity. Mission requirements were to later baseline 65 watts as the targeted value, an intimidating goal in view of the Phase 1 data.

SBIR 2006 Phase 2

The Phase 2 effort evolved the conceptual design developed in Phase 1 by evaluating each function (coring, break-off, retention, and transfer), building prototypes, and ultimately generating an integrated prototype coring mechanism incorporating each detail function. In addition to the 65-watt power consumption target, mission requirements later defined in the project included a 5-kg mass budget for the integrated corer, coring performance yielding 5-6 cm long corer samples within a Martian day, and a corer WOB no greater than 50 N. This paper focuses on the Phase 2 design efforts to achieve such a corer.

Development of the Corer

The Phase 2 work plan was divided into four primary sections: (1) development of a custom coring bit, (2) core handling mechanisms development, (3) prototype corer development, and (4) corer testing.

(1) Custom Coring Bit Development

The majority of the coring bit data from Phase 1 were produced from tests with the COTS coring bit that showed the most promise for core generation, a 1-inch (25-mm) diameter coring bit from Milwaukee, P/N 48-20-5005. These coring bits are designed for the drilling of holes, not for the generation of intact rock cores. Nonetheless, the Milwaukee bits successfully yielded cores in testing, though the cores were occasionally fractured. Also, the generated cores were 1.5 cm in diameter, substantially larger than the targeted 1 cm.

The objective of the coring bit development was to thus produce a custom coring bit capable of consistently generating intact 1 cm diameter cores. A targeted core length was defined at 6 cm based on the latest mission requirements from the science community. The coring bit development was performed in parallel with the core handling mechanisms development so that the coring bit could be designed to

¹ Original mission requirements dictated a 1 cm x 10 cm long core, and later eased to 5-6 cm long.

accommodate the anticipated coring handling implementation. This necessitated designing a coring bit with a relatively large cutting annulus to yield the space required by the core handling mechanisms.

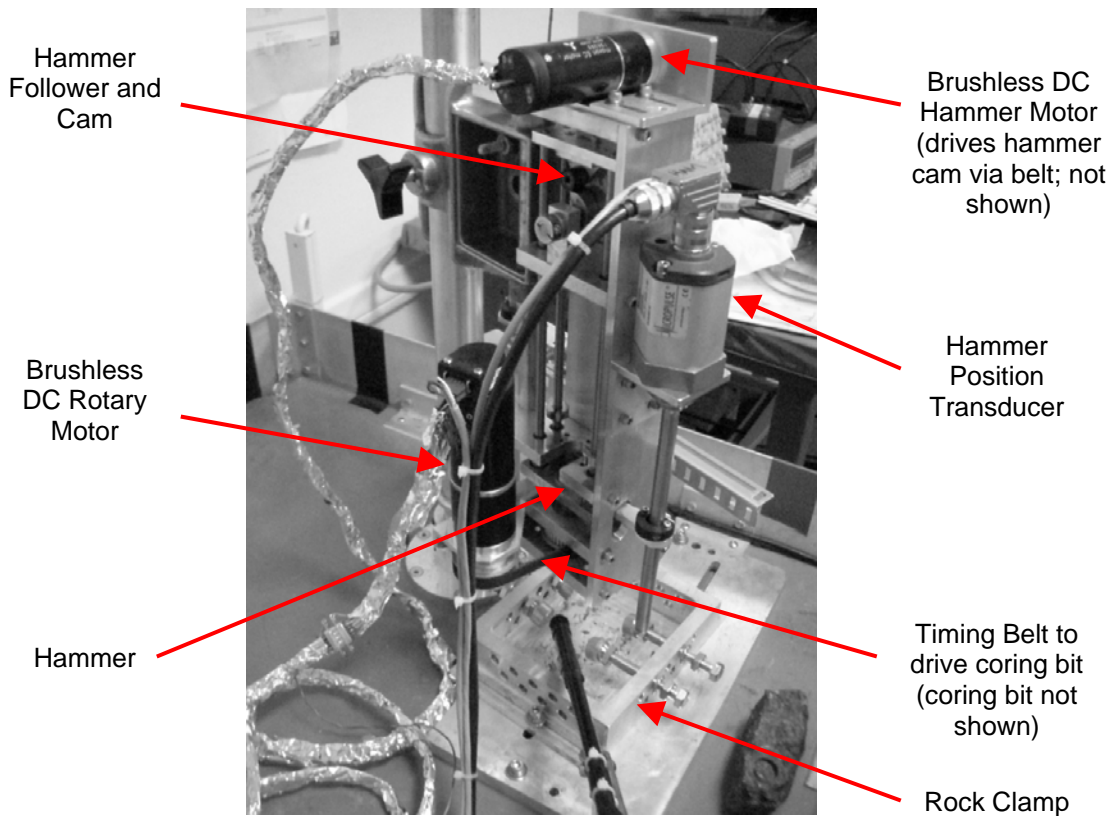


Figure 3. Drilling Breadboard Fixture Used for Coring Bit Evaluations.

A bit design expert was consulted to assist in the analysis of earlier coring results obtained with COTS bits and to develop a custom coring bit design specifically for this application. After two iterations, a successful bit design was obtained to core targeted rock materials.

The first custom coring bit, Revision A, used a single sloping cutting tooth profile as shown in Figure 4. The cutting teeth were fabricated from grade C2 carbide. This coring bit cored basalt successfully, though chipping of the carbide was observed. Unfortunately, the bit had stability issues in softer materials. The bit tended to wander, breaking the softer cores into numerous pieces. On a positive note, the flutes designed into the tool body were effective in carrying away rock fines. In previous testing with non-fluted COTS coring bits, a shop vacuum was used to clear away the fines, and debris clearance was anticipated to be much more of a challenge than was actually encountered.

Revision B, the next coring bit design iteration, addressed the stability issues found in the previous version. This design used a crown-shaped symmetrical tooth profile. A different grade of carbide, GC-012F by General Carbide, was used in an attempt to improve the cutting teeth life and reduce chipping. This coring bit design solved the stability issues in soft rock and still cored basalt well, though the teeth still chipped when coring basalt and even iron spot brick. Nonetheless, because this coring bit design cored well and the chipping did not cause a significant difference in coring performance, it was decided to proceed with this basic design and focus remaining project resources on the development of the integrated corer.



Figure 4. Revision “A” (left) and “B” (right) Coring Bits with Basalt Cores

(2) Core Handling Mechanisms

The core handling mechanisms identified in Phase I – core retention, break-off, and ejection – required prototyping and testing to verify their suitability. This reduced the risk of a possibly failing subassembly to negate the total design and effort.

Core breakage from the parent rock material was a major concern from the beginning of Phase 2 since it was not explored during the Phase 1 effort, which focused primarily on coring. A number of concepts for breaking cores were investigated, including scoring the base of the core to weaken the rock. A Milwaukee 48-20-5005 coring bit was modified to provide a means of scoring existing core samples at the base of the core. This method looked promising as the forces required to snap the rock core were found to be minimal. However, the concept was eventually discarded because of the complexity involved with integrating such a device into the corer design.

Next, a collet concept was conceived to break the rock core samples. Two different design approaches were considered and explored, shown in Figure 5. The first was a conventional axial collet much like the type of collet found in a machine shop. This was tested on rock samples in a variety of rock breakage modes: tension, bending, and compression. The other collet concept used nested eccentric tubes that generated a shearing force on the rock core when the tubes were rotated with respect to each other. Mechanisms were designed and built to test these concepts, and both methods were found to be effective. Both approaches required approximately the same amount of input torque to snap rock samples. In the end, the eccentric collet concept was selected as the core breakage method of choice because it was observed that the concept would be easier to implement into an integrated corer design, and that it would be simpler and more tolerant of stray rock particles.

During testing with the collet mechanisms, input torques and displacements were measured and recorded to characterize the forces and strains required to break the rock cores reliably. These results then helped define the design parameters for the integrated corer.

(3) Prototype Corer Development

Development of a fully integrated corer prototype was performed following the successful demonstration of the individual core handling mechanisms. As mentioned earlier, it was decided that the integrated corer should be designed to utilize the eccentric collet concept based on the results of the testing with the core

handling mechanisms. However, the problem of containing and transferring the core sample remained unaddressed. A containment sleeve was attractive with the realization that many cores would not be intact, and maintaining the order of the pieces of a disrupted core is a requirement. However, designing provisions for a sleeve into the integrated corer without interfering with the breakage mechanism and providing a clear exit path out of the corer for the sleeve was a challenge. Analysis of the dimensions of the rock cores generated during the core breakage testing revealed that only a very small clearance typically existed between the outside diameter of the rock cores and the inside diameter of the coring bits. The clearance was so minimal that it became clear that ejection of the containment sleeve out the front of a coring bit would be impractical because it would necessitate a containment sleeve of nearly zero wall thickness.

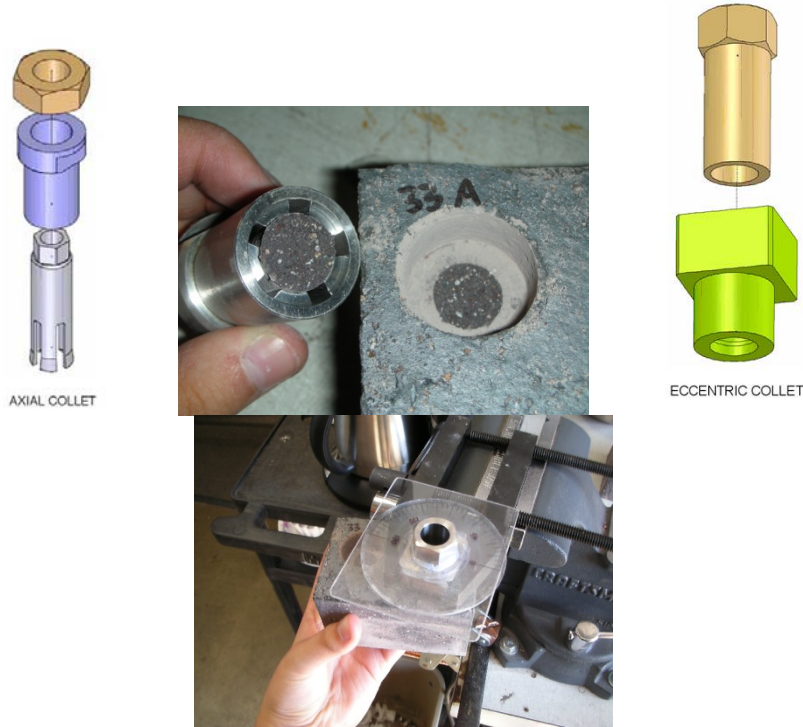


Figure 5. Core Breakage Collet Prototypes

Consideration was thus given to an integrated corer design that allowed the ejection of the rock core containment sleeve out the rear of the assembly. This concept was compatible with the eccentric collet breakage design, and seemed the most straightforward in achieving all of the corer objectives of coring, breakage, retention, and ejection. Because there was a clear exit path through the entire corer assembly, an external plunger mechanism to push the sleeve containing the corer could be housed in the sample system on the base platform to “ramrod” the sample out the rear of the corer. This significantly simplified the integrated corer assembly and also incrementally simplified the requirements of the robotic arm to which the corer would be mounted by reducing mass and required electrical connections.

Other design considerations were addressed prior to finalizing the overall concept of the integrated corer design. A decision was made to use a single motor to drive a spring-loaded rotary-percussive cam mechanism, much like the original LSAS drill. Although it was desirable to have the flexibility of independent control over the hammer and rotary functions in the manner of the drilling breadboard fixture, the single-motor rotary-percussive mechanism offered simplicity and low mass. An additional motor was incorporated in the design to accomplish core break-off. While it appeared possible to leverage the rotary-percussive motor to achieve this function and save mass, it was much more straightforward to add a second motor. See Figures 6 and 7 for CAD views of the prototype design.

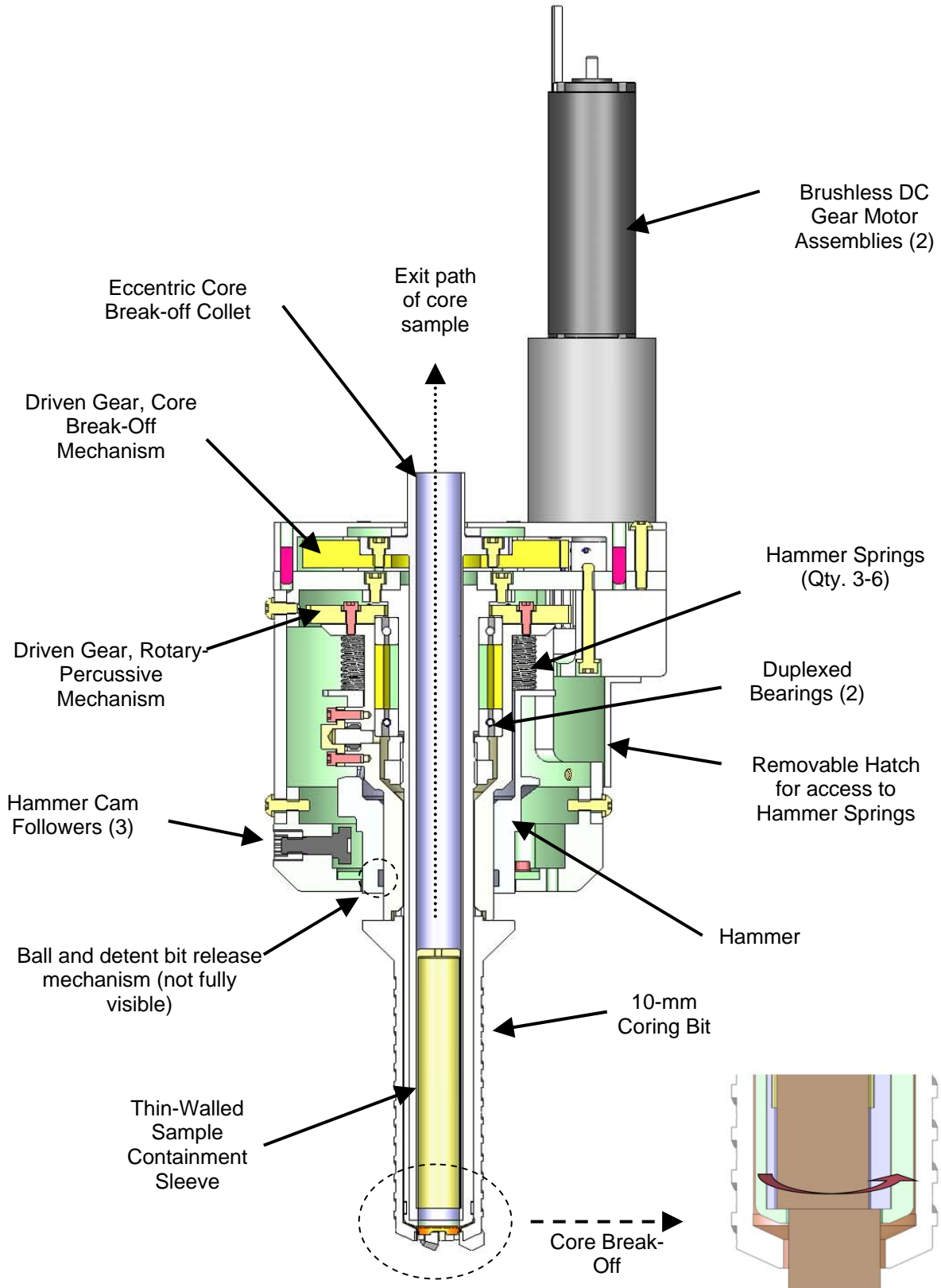


Figure 6. Integrated Corer Prototype Cross-Section

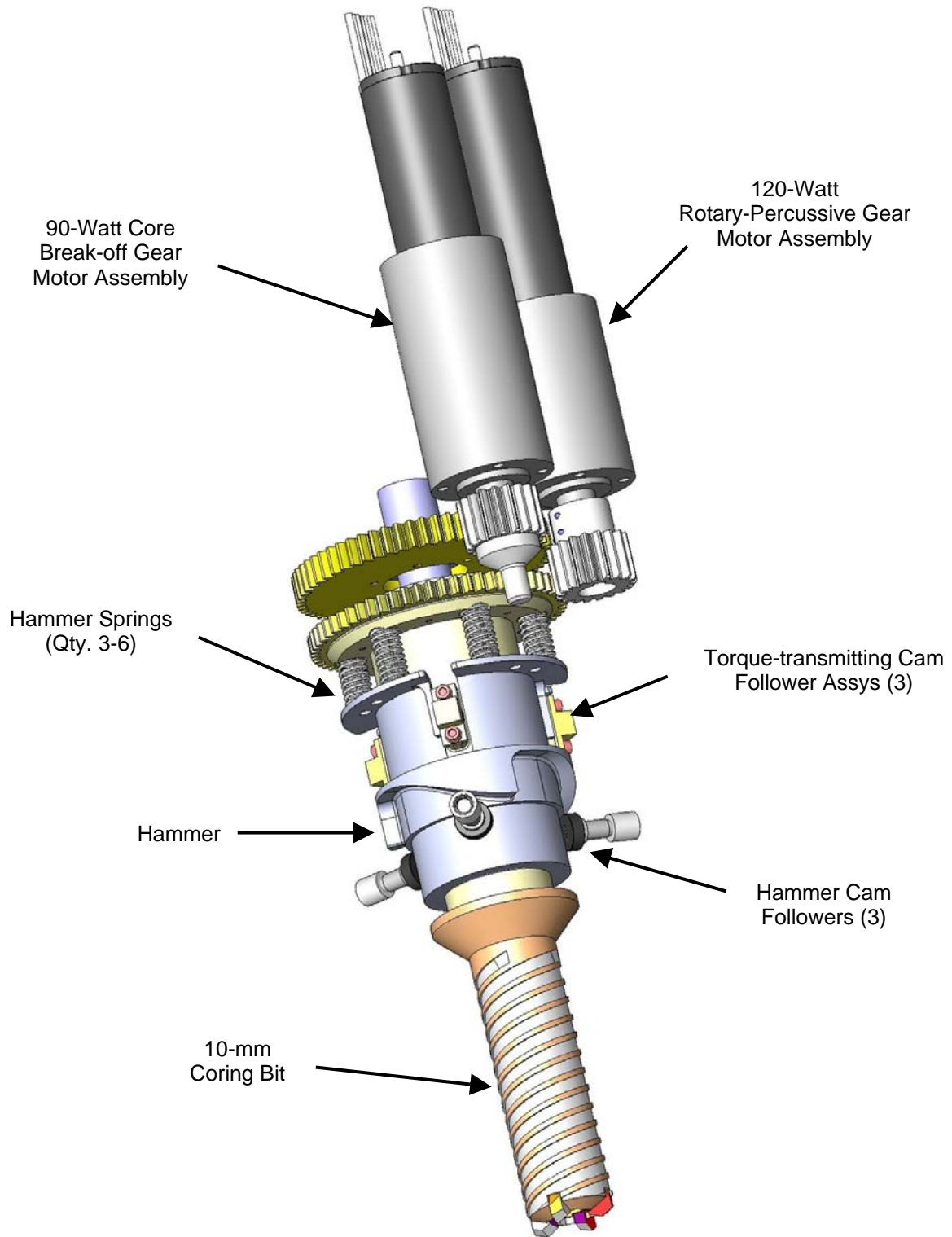
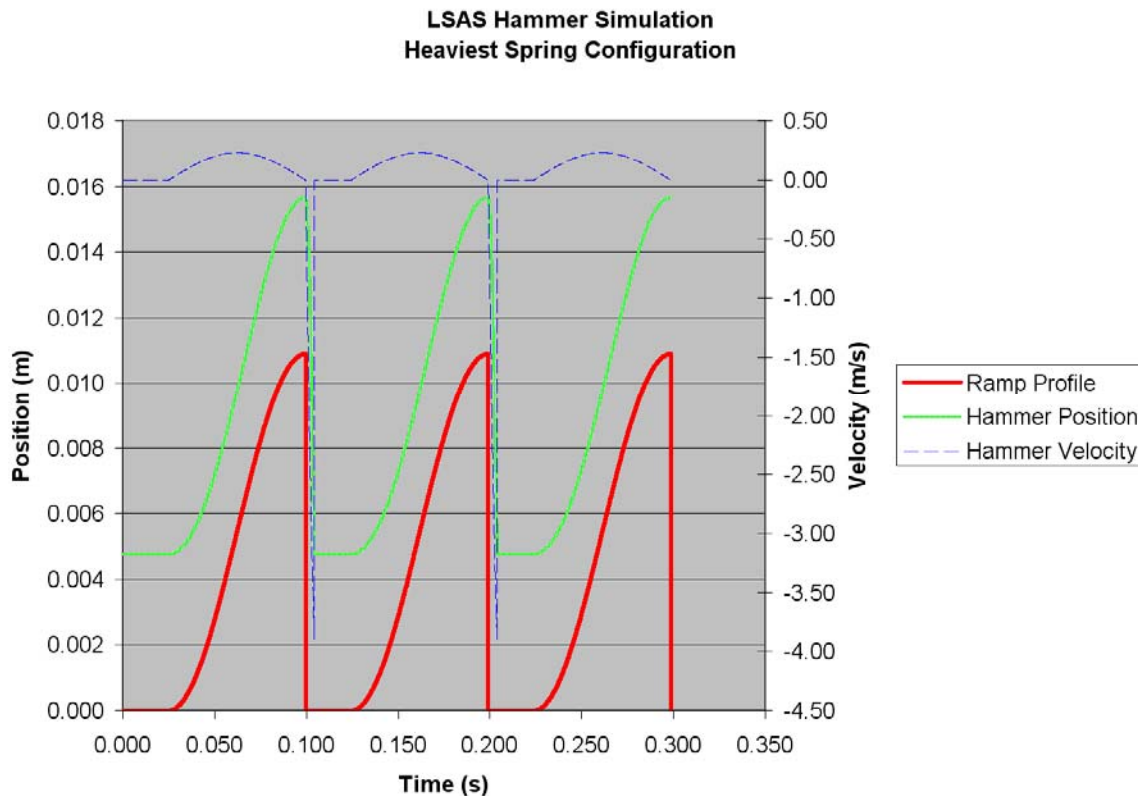


Figure 7. Integrated Corer Prototype (housings omitted)

A limited amount of analysis was performed prior to finalizing the integrated corer design. In view of the successful coring achieved with the breadboard fixture, the rotary-percussive motor and gear drive mechanisms were sized on the integrated corer to achieve the maximum hammering energies investigated with the breadboard fixture. Because gaining an understanding of the coring problem was deemed more important than strict mass reduction of the integrated corer prototype, the motors were sized with extra torque margins to ensure that all data points of interest could be obtained during testing. Finally, attention was given to developing efficient hammer cam profiles to minimize the amount of power required by the integrated corer. The hammer cam profile was modeled and simulations run (see Figure 8) in order to optimize the shape of the cam profile and to ensure that correct timing of the hammer strikes was obtained.



It became clear during the cam profile analysis that a rotary-percussive mechanism can only operate within a narrow speed range and still be effective. If the mechanism rotates too slowly, the hammer loses energy by not being cleanly released by the cam mechanism. If the rotary-percussive mechanism rotates too fast, the hammer can be picked up before contact with the coring bit takes place.

An additional design concern regarded the mounting of the corer to the robotic arm or test fixturing. Early concepts assumed that advancing the unit down the coring axis could be accomplished by coordinated movements of the robotic arm joints. However, work performed on another project showed that low velocity, coordinated moves were very difficult and required positioning accuracy and control beyond the capabilities of current robotic arms. Power requirements were also quite high because all arm joint motors were energized along with the corer. In response, the simple solution of mounting the corer to linear slides with preload springs was implemented. The arm would press the corer against the target rock and preload the springs. The arm motors would be turned off, engaging the joint brakes. Coring would then begin and the corer assembly would be advanced by the preload springs. The preload springs could be re-compressed by shutting off the corer and advancing the robotic arm, then the process repeated until

the desired core length was achieved. See Figure 9 for the completed Integrated Corer Prototype mounted on spring-loaded linear guides.



Figure 9. Integrated Corer Prototype

(4) Corer Testing

The integrated corer prototype was then functionally tested in a laboratory environment with a variety of rock samples. See Table 1 for a summary of the results. The tests were narrow in scope because of the limited funds remaining on the program. However, the testing was adequate to demonstrate the successful performance of the integrated corer against the rock types anticipated to be encountered on Mars. It is hoped that additional more comprehensive testing be performed in the future as funding becomes available.

Coring Performance

Sandstone: This material had been found to be very abrasive and hard on the coring bits in the past, and this experience was repeated during testing with the integrated corer. Run 3H with a virgin coring bit through sandstone started to reach a performance plateau towards the end of the run. The coring bit teeth, while not fractured as during the runs with basalt, exhibited substantially worn cutting edges at the conclusion of the run.

Basalt: All coring bit runs in basalt produced chipping of the teeth, as evident in Figure 10. In two extreme cases - Runs 2I and 3I - the brazed joints on some of the cutting teeth failed as shown in Figure 11, causing the coring bits to lose cutting teeth. In the case of Run 3I, two adjacent cutting teeth were lost, resulting in a large side load to be imparted onto the generated core and causing it to inadvertently snap from the parent rock material. This occurred with the corer set for maximum hammer energy (1.09 J per blow)². Subsequent Run 4I was performed with reduced hammer energy (0.61 J per blow) with much better results. One possible reason for failure was that the highest hammering energy was too aggressive on the coring bit teeth. In addition, the current coring bit design had cutting teeth that overhang the coring bit body by a substantial amount, making the teeth susceptible to failure. A future design change to the coring bit should be considered to minimize this overhang.

Shale: Coring penetration rate was the highest of the three materials tested, and the coring bit was in good condition at the end of the run.

² "Hammer energy" used here refers to the approximate change in potential energy the hammer springs experience between two points: (A) when the hammer is fully "up" (cocked) and (B) when it first strikes the coring bit. This is not the same amount of energy that is actually transferred to the coring bit and imparted to the rock, which would require extended detail analysis to predict. However, hammer potential energy was an easily calculated, convenient reference when comparing the different hammering settings.

Table 1. Corer Prototype Test Summary

Test ID	Rock Material	Required Electrical Power, W	Speed Range, rpm	Theoretical Hammer Potential Energy, J	Weight On Bit Range, N	Total Coring Bit Penetration, mm	Average Penetration Rate, mm/min	Core Breakoff Achieved	Core Sample(s) Retrieved in Containment Sleeve
1H	Sandstone	18-32.2	131-199	0.21-0.42	78.6-83.0	9.04	0.0747	No	No attempt to sleeve core samples.
2H	Sandstone	25.9-27.1	193-202	0.61	49.2-59.1	13.72	0.229	No	(1) ϕ 9.61 mm x 2.58 mm thk (1) ϕ 9.78 mm x 2.72 mm thk
3H	Sandstone	28.3-33.8	189-201	0.61	55.2-68.4	24.36	0.0727	No	(1) ϕ 9.60 mm x 3.32 mm thk (1) ϕ 9.79 mm x 2.68 mm thk (1) ϕ 9.85 mm x 4.66 mm thk (1) ϕ 9.78 mm x 3.24 mm thk
1J	Shale	26.2-30.5	191-201	0.61	51.2-68.3	25.93	0.370	No	(1) ϕ 10.30 mm x 9.16 mm thk
1I	Basalt	28.6-30.2	192-199	0.61	56.0-59.3	4.55	0.1467	No	None (too short to break off)
2I	Basalt	38.4-46.8	188-200	1.09	59.7-68.3	9.16	0.1017	No	None (too short to break off)
3I	Basalt	36.2	190	1.09	65.8	--	--	No	None (bit failure caused generated core to prematurely break off)
4I	Basalt	33.6-60.0	189-199	0.61	61.7-101	18.16	0.1316	Yes	(1) ϕ 9.68 mm x 11.55 mm thk



Figure 10. New Bit and Chipped Bit after Basalt Testing



Figure 11. Failed Bit after High Energy Basalt Testing

Overall, as shown in Table 2, the coring penetration rates were lower than observed during the coring bit development testing with the breadboard fixture. This was not surprising because of the inherent hammer/rotation phase drift that prevented a rapidly-repeating strike pattern from developing. The breadboard fixture contained separate rotary and percussion motors which were run open loop and always drifted with respect to each other. This was naturally conducive to preventing a rapidly repeating strike pattern. Indeed, on many rock samples cored by the integrated corer prototype, deep strike marks were seen in the rock that was suggestive of a repeating strike pattern. Performance could have been improved if a design feature had been introduced to shift the hammer/rotary phasing relationship. This could have been in the form of separate drive and hammer motors, a cam device to oscillate the LSAS Corer with respect to the robotic arm, or a number of other mechanical options.

Table 2. Prototype Corer Penetration Rate

	Average Penetration Rate, mm/min	
	Corer Prototype	Breadboard Testing
Sandstone	0.0727-0.229	15.812
Shale	0.370	6.789
Basalt	0.1017-0.1467	2.817

The low input power required to core, even in the most aggressive setups, was a pleasant surprise. Approximately 90 watts were required to core effectively with the breadboard fixture. During all of the representative runs with the corer prototype, power consumption was below 50 watts. Even in the one extreme case where the weight on bit was taken to a very high level (Run 4I), the maximum current draw was still only 2.5 amps (60 watts). To ensure conservatively that data could be collected in any likely test condition, the corer prototype was designed around a 120-watt motor. Further mass reduction could have been possible from motor substitution alone.

One of the primary differences in power consumption between the breadboard fixture and the integrated corer prototype was initially thought to be caused by the lower WOB used with the most recent testing. However, the high WOB settings investigated during Run 4I suggested this was not the case. It is suspected that the keys to the high efficiency of the current corer were the use of ball bearing cam followers for lifting the hammer mechanism (the original LSAS Corer Prototype used bushings), a hammer mechanism that did not slow down the rotation speed of the coring bit at every strike, a freely moving hammer mechanism, and careful tailoring of the hammer cam profile. In contrast, the hammer on the breadboard fixture did not rotate with the coring bit, causing loss of bit speed each time the hammer struck the shank of the bit. The hammer on the breadboard fixture also had excessive frictional losses.

Differences in the dynamics of the core bit fluting were noticeable during testing with the corer. In some cases the fluting appeared to be very effective removing debris, with rock fines being ejected with such velocity that they actually became airborne. In other cases, the rock fines tended to gather around the coring bit. One variable not previously explored is vibration of the overall test setup, helping to cause the dispersal of the fines. Indeed, when a rather large rock sample was used, the fines did not disperse in a similar manner to a nearly identical test setup that used a smaller rock that had fractured during the test. It was suggested that vibration of the small rock fragments helped with the fines dispersal. It appeared that more realistic testing (e.g. testing in the field on large in-situ rocks) might have yielded results that are more applicable.

Core Handling

With the exception of the one basalt sample (see Figure 12), all of the coring runs yielded core samples that were either too short to be snapped by the eccentric collet breakage feature, or the rock samples were already fractured. In the latter case, despite the core already being broken, the eccentric collet still retained the captured pieces in the order they were produced. In all four cases of obtaining captured rock pieces via the eccentric collet, the pieces were retained and successfully inserted into the thin-walled containment sleeve.

In all cases of successful rock sample retrieval, loose rock was found to remain with the parent rock. In some cases, a substantial amount of rock core was unaccounted for when comparing the length of the retrieved samples versus the leftover rock. It was evident that some of the cored rock is pulverized during the core generation process. It would have been useful to understand why this was happening to maximize the yield of retrieved rock cores and to avoid potential problems with debris jamming. The addition of a passive sample retention feature to the open end of the containment sleeve could have been a possibility.

Because of schedule and budget constraints, the core breakage mechanism was tested only against a sample of basalt, the most challenging material of interest for this application. Though this test demonstrated the success of the breakage function against the strongest sample type, it would have been more rigorous to perform testing against all types of anticipated rocks and measure the actual strain displacements needed to break the cores reliably. Having a statistically significant amount of breakage data could have enabled the development of a smaller, more compact design. A conservatively large amount of eccentricity was designed in the collet breakage mechanism to ensure success. However, this makes the corer larger and more massive, and the coring bit annulus subsequently larger, thus requiring more power during coring.



Figure 12. Containment Sleeve at Rear of Integrated Corer (left), Sleeve with Basalt Core (right).

Conclusions and Recommendations

Most, though not all, of the goals for the integrated corer were met and the results are encouraging. The 65-watt power requirement, previously thought to be insurmountable because of the high power consumption seen with the breadboard fixture, is clearly achievable. The low WOB target of 50 N was exceeded during test, but this was primarily caused by an oversight in the setting of the preload springs. Based on the relative ineffectiveness of higher WOB values briefly explored during testing, it is believed that sufficient coring performance is achievable with a lower WOB provided other measures are taken to improve coring performance.

Improved coring performance is likely achievable with design changes to alter the hammer/rotary phasing relationship in the integrated corer, since the coring bits cored much more efficiently on the breadboard fixture than in the integrated corer. The coring bits were the same in both cases, but the natural drift between hammering and rotary action on the breadboard is a major differentiator. Indeed, witness marks

on rock samples cored by the integrated corer reflect the rapidly-repeating strike pattern. A variable strike pattern will erode the rock more efficiently.

The performance and life of the coring bits can definitely be improved. A bit design with an asymmetrical tooth spacing arrangement would also help to avoid a rapidly-repeating strike pattern. Other cutting teeth geometry and material variations could be investigated to help address the robustness issue since the basic bit configuration is defined.

The containment sleeve concept was demonstrated to be effective along with the rear exit path of the contained sample. The eccentric core break-off/retaining feature likewise worked successfully. However, more statistically significant testing must be done to determine how well these mechanisms perform over time with varied rock materials.

A mass goal of less than 5 kg was established when requirements were re-baselined early in the program. The final configuration was significantly under this goal, the corer weighing 2.5 kg without mounting features. This leaves considerable room for future improvements which could include increased margins (though the motors in particular are currently oversized), and additional functionality such as motorized tool change, additional spare bits or bits for other functions, etc. The low mass also potentially reduces strength and stiffness requirements for the robotic arm or other mount device, resulting in further mass savings. Depending on the actual mission application, the motors could be readily reoriented at a 90° angle or even doubled back upon the assembly to reduce length.

Though commercial components were used, the design has a direct path to flight with vacuum and temperature compatible materials and lubricant. The current prototype is capable of environmental testing in a laboratory environment.

Early component and subassembly testing certainly reduced risk. Individual testing of the core handling mechanisms allowed definition of the design parameters needed to complete the integrated corer design while giving confidence that the integrated corer would function successfully.

Additional telemetry and improved data are required for fully understanding the rotary-percussive problem. As mentioned earlier, the analysis done while designing the hammer cam profile on the integrated corer yielded insight to the critical timing nature of the rotary-percussive mechanism. A rotary-percussive mechanism can only operate within a narrow speed range and still be effective. Excessive hammer energy losses can occur if the mechanism rotates too slowly, and rotating too fast can prevent the hammer from contacting the bit. The rotary-percussive events occur over a period of milliseconds. Having hammer position and/or impact feedback, for example, would enable better assessment of what is really happening in the mechanism and prevent erroneous conclusions.

Acknowledgements

The authors would like to thank Paul Backes of JPL and Adam Armstrong, Jason Bardis, Jason Bean, Amanda Bright, Dan DiBiase, Rene Espinosa, Richard Fleischner, Jay Harland, Brett Lindenfeld, Richard McKenzie, Roy Nakagawa, Bill Reed, Stephanie Smith, and Chris Thayer of the Space Division of MDA Information Systems, Inc. for their work and support on this project.

References

1. Ng, T.C. & Yung, K.L. "Mars Rock Corer and Planetary Micro Sampling Tools." *Proceedings of the 33rd Lunar and Planetary Science Conference*, (2002).
2. Fleischner, R. "Concurrent Actuator Development for the Mars Exploration Rover Instrument Deployment Device." *Proceedings of 10th European Space Mechanisms and Tribology Symposium*, (2003).
3. Maurer, William C. *Novel Drilling Techniques*. New York: Pergamon Press, ©1979

A Novel Approach for a Low-Cost Deployable Antenna

Chris Amend*, Michael Nurnberger*, Paul Oppenheimer*, Steve Koss* and Bill Purdy**

Abstract

The Naval Research Laboratory (NRL) has designed, built, and fully qualified a low cost, low Passive Intermodulation (PIM) 12-foot (3.66-m) diameter deployable ultra high frequency (UHF) antenna for the Tacsat-4 program. The design utilized novel approaches in reflector material and capacitive coupling techniques. This paper discusses major design trades, unique design characteristics, and lessons learned from the development of the Tacsat-4 deployable antenna. This antenna development was sponsored by the Office of Naval Research.

Introduction

The Tacsat-4 satellite is part of a series of fast-paced, low-cost missions for the Operational Responsive Space (ORS) initiative. The spacecraft bus, funded by the Office of the Secretary of Defense, was designed, built and tested by a team consisting of both NRL and Johns Hopkins University Applied Physics Laboratory. The payload, Comm-X, is funded by the Office of Naval Research and will provide Communications-on-the-Move (COTM), Blue Force Tracking (BFT), and Data Exfiltration to the user community. The COTM capability provides UHF legacy radio support and a Mobile User Objective System (MUOS) like channel bit (but not MUOS-like capability) for early testing. The BFT capability collects existing UHF devices with tasking priority expected for underserved areas. The Data Exfiltration capability focuses on data collection from Navy buoys, which are typically remotely located on the seas and in littorals. The Tacsat-4 payload operates in a bent pipe fashion, working directly with legacy radios and/or sensors and ground terminals. Tacsat-4 has several ORS system-level objectives including using a prototype bus to mature spacecraft bus standards for acquisition and to fly in a "low" highly elliptical orbit (HEO), enabling a new set of ORS missions that require dwell, such as communications. The deployable antenna on the CommX payload was designed to provide UHF capability from the HEO orbit to the ground such that no active pointing was required by any ground assets.

Design Requirements

The Comm-X UHF antenna is a parabolic reflector with an f/D of 0.425 and operates over a frequency range of 240 MHz to 420 MHz. The reflector surface accuracy of the antenna was designed such that the root mean square (RMS) of the surface was within 6.35 mm (0.25 inch) of the ideal parabola. This RMS requirement, very loose compared to many industry standard reflectors, is sufficient because of the wavelength/frequency that the payload operates at. The antenna was designed to fit within the stowed envelope of the Minotaur IV launch vehicle. The antenna mass allocation was 27 kg (60 lb) with a stowed first mode of >60 Hz and deployed first mode >5 Hz. The Comm-X antenna was designed as a Class D mission, and scheduled to be completed within 12 months for $< \$4M$.

The selected orbit of the TacSat-4 satellite is 700 km x 12,050 km with an inclination of 63.4 degrees. The UHF antenna is unshielded and is required to withstand 100 MRad of total ionized dose radiation in this orbit. Additionally, the antenna will be required to withstand the thermal environments imposed by the HEO orbit (-150 deg C to +150 deg C).

* Naval Research Laboratory, Washington, DC

** Purdy Engineering, Poolesville, MD

The mission required that the antenna would be capable of transmitting and receiving multiple carriers simultaneously. In order to meet this requirement, the antenna is designed to be low PIM. PIM effectively raises the noise floor of the receiver system, reducing the sensitivity of the system.



Figure 1: Stowed TacSat-4 UHF Antenna



Figure 2: Deployed TacSat-4 UHF Reflector on Comm-X Payload

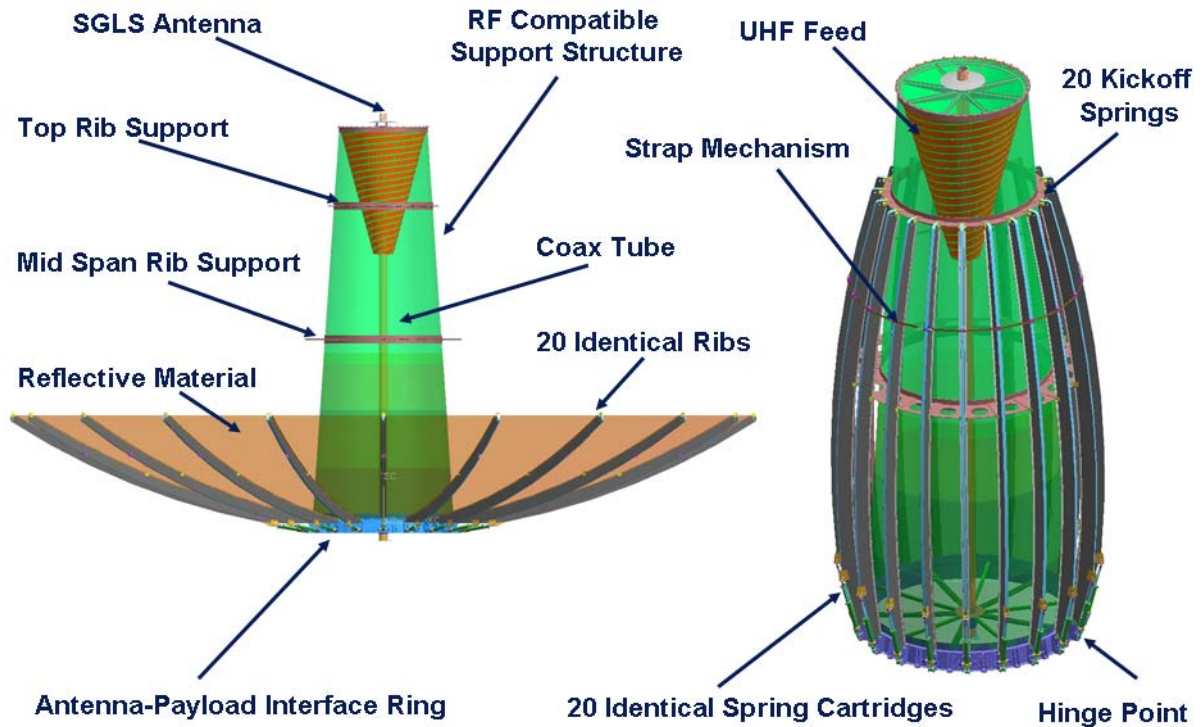


Figure 3: Tacsat-4 UHF Antenna Design

Major Design Trades

Make vs. Buy

The initial design trade of the antenna was a make versus buy decision. Several of the recognized private industry providers of space qualified reflectors were approached and provided ROM estimates for meeting the TacSat-4 antenna design requirements. Several companies provided estimates for building an antenna; however, no vendor could meet the design requirements within the schedule and budget constraints of the program. The industry estimates were approximately two to five times the available schedule and budget. Additionally, because of the extremely aggressive schedule of the program, most necessary derived requirements were determined in parallel, not serially, with the antenna development. It was therefore decided that the UHF antenna would be built in house at the NRL to meet the program's budgeted cost and schedule.

Deployment Schemes

Several deployment schemes were initially traded for the antenna. The two best options were a tensioning band around the deployable ribs and a top release "pie plate" approach which would release the ribs from the tips. It became apparent that the deployment approach would affect the relative sizing of the fixed and deployable portions of the reflector.

The "pie plate" approach required that the deployable ribs would need to reach above the UHF feed of the reflector to meet RF and PIM requirements (no metal in RF field). This meant that either the fixed portion of the reflector would be smaller than structurally desired or the ribs would need to be unnecessarily long to reach the top of the UHF feed. The release band approach allowed flexibility of fixed and deployable reflector sizing enabling the design to be optimized for mass and stiffness. The band design also did not require any additional metal in the RF field once deployed. For these reasons a release band design was used for the antenna.

Further analysis proved that a band located at a midpoint between two circumferential rings with v-block interfaces provided the highest stiffness and least complex design. These rings and v-blocks were fabricated from Ultem 2300[®] to provide necessary strength and tribology for reliable release while meeting RF requirements.

The release device selection and band design was a complex and essential part of the antenna development. Thermal knives and other flight-qualified separation mechanisms were traded for the release device. Program requirements did not allow the use of any pyrotechnic devices and therefore were not included in the trade space. A low-mass release device was needed to minimize deployment dynamics differences between all ribs. Furthermore, because of the length of the band (~2.5 m or 100 inches) and the kinematics of the deployment, it was decided to deploy the band in two halves rather than one long piece (shown in Figure 4 and Figure 5). This was done to minimize possible snagging and friction forces. A TiNi Aerospace Frangibolt[®] device was selected for the release of the band. A single device was selected to release both band halves over two devices because of complexity and risk implications on the antenna design. Early full-scale breadboard testing of the release concept ensured confidence in the release design approach for proper function as well as working out band tightening techniques.

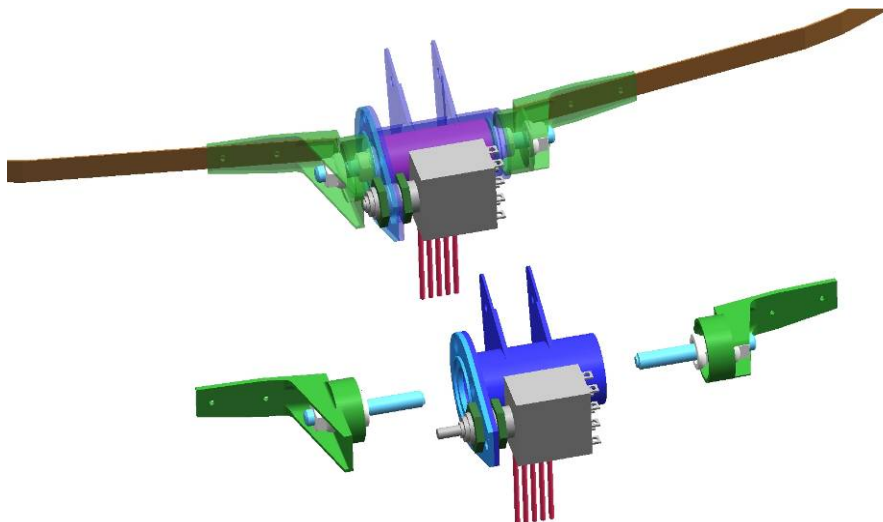


Figure 4: Release Device Assembly



Figure 5: Deployment Band Breadboard Fixture

Reflective Material

The reflective material for the antenna was a major design driver and yielded a novel design approach. The low PIM requirement, required surface accuracy, survival temperature, radiation environment, and stowed packaging all factored into the material selection trade space. PIM is generated by loose or “dirty” metal to metal contacts in the RF field. A low-PIM reflector required that any metal to metal contacts would need to be avoided if possible and closely analyzed where necessary.

There are many proven deployable reflector designs which use a woven metallic mesh material and achieve much tighter surface accuracies. In this type of design, the material must be managed very carefully to maintain the tension of the mesh in order to maintain low PIM. This is accomplished through an intricate design adjusted through a labor intensive process to meet RF performance requirements. The material is also expensive and is not readily available for purchase. For TacSat-4, the cost and schedule ROMs showed that this design approach would not be feasible, nor was it required to meet the looser UHF tolerances for surface accuracy.

The goal of the TacSat-4 antenna design was to take advantage of the very loose RMS requirements in order to lower the complexity, and in turn cost of the antenna. A gore approach was selected using several smaller reflector pieces that were joined together using capacitive coupling into a single reflector while avoiding any metal to metal contacts. The novel approach used Kapton[®]-Copper flex circuit material. Each gore is made of a sandwich material with Kapton on the outside and a soft copper grid in the middle. The copper thickness was selected so that it was three skin depths over the frequency range of the antenna; so the gores acted as a RF reflector. It was important to minimize the amount of copper used in the design in order to achieve the required mechanical performance of the gore material as well as minimize the mass of the reflector. The flex circuit material has been used in space applications previously but not in this manner. To gain confidence and qualify the material, several small material samples were thermally cycled in vacuum and exposed to expected radiation levels. Additionally, Kapton[®] material was fit on a scaled antenna model to evaluate the behavior of the stowing and deploying process necessary for the deployable reflector. As a result of this testing, small through-holes were added to the gore design with the intent to better allow out of plane bending and relieve stress concentrations when stowing the reflector. It was thought that the holes would also have the secondary benefits of both reducing the part mass and reducing air drag during deployments in air. The grid selection and hole size were limited by RF requirements on the reflector. The EDU gore design is shown in Figure 6. The part size was driven by available raw material and manufacturability of the part which in turn drove the number of deployable ribs. Flex circuits are readily available in standard panel sizes, but not in the length and

width of the antenna gores. An industry survey showed there were a limited number of vendors that were capable of processing parts of this size. There was a learning curve for handling and tooling the antenna gores mostly due to the cover-lay process in the part manufacturing.

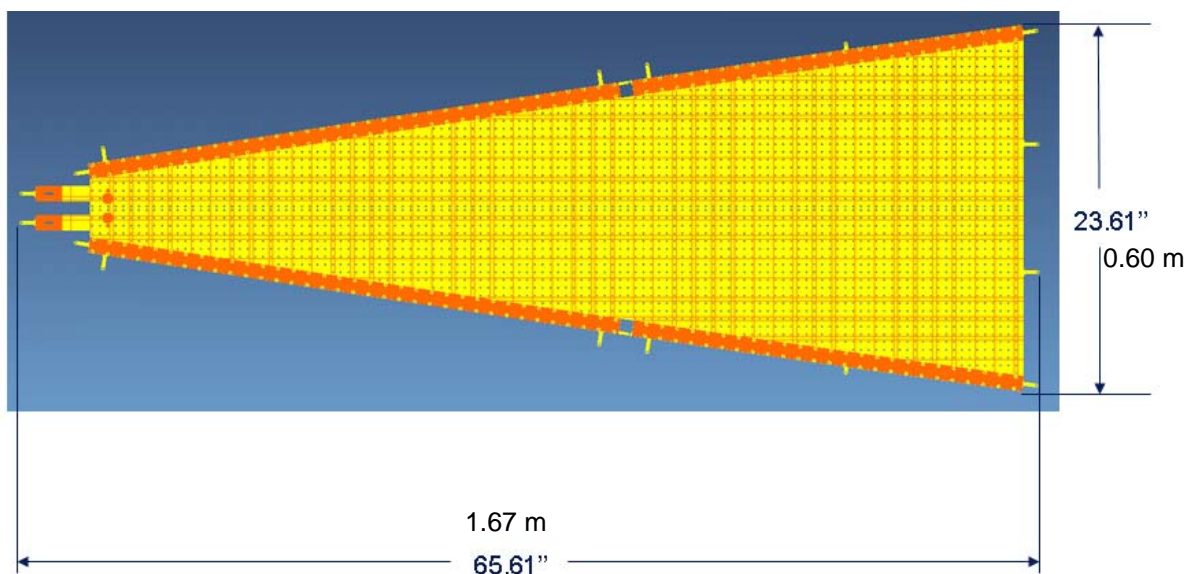


Figure 6: EDU Gore Layout

Gore Fasteners

As previously stated, the low PIM requirements on the antenna forced a capacitive coupling approach throughout the antenna design. This capacitive coupling relies on an even preload to be maintained on all RF joints, which includes the joints between individual gores. Many fasteners were used to maintain the equal preload required across the entire joint. These fasteners hold the reflector gores to each other and to the ribs.

There are over 2000 fasteners used to hold the reflector gores both together and to the individual antenna ribs. Standard metallic fasteners were not an option because of the mass and RF implications. Several non-metallic space-qualified materials were traded to find a suitable substitute for metal in the fasteners. Additionally both socket and pan head screws were evaluated. Pull testing and radiation testing were done on the top two choices of the trade. After testing, socket head Ultem 2300[®] was selected for the material of the fasteners, washers, and nuts for attaching gores. The screws needed to be fabricated in a special run, and the end cost was roughly \$4 per fastener. The fasteners were not as strong as metal fasteners so free running nuts were used to keep the running torque as low as possible. A torquing technique was developed and each fastener was staked for backout prevention.

Gravity Offloading

The 60-Hz stiffness and 27-kg (60-lb) mass requirements for the antenna meant that materials and parts would need to be light weighted and optimized for on orbit deployment loads. However, because of the ground testing requirements and program budget, a highly complex gravity offloading scheme was equally unfeasible. It was critical to show sufficient deployment force and energy margin to qualify the new design using as relatively simple ground testing fixtures to meet cost and schedule goals. As a result the antenna was designed to withstand ± 0.3 g deployment forces. This required that a gravity offloading fixture be designed in order to test both positive and negative deployment force and energy margins. Testing was performed in both air and thermal vacuum (TVAC).

The final gravity offloader design was a single plate with individual mechanisms interfacing with each of the deployable ribs of the antenna. Each rib offloader had a cam profile fit to match the theoretical gravity

forces of the deploying geometry of the antenna that was calculated by kinematic modeling. The offloading force was provided by compression springs that were interchangeable, allowing offloading forces to be varied quickly and different equivalent offloading to be tested easily. This offloader design was straightforward and adjustable; however it interfaced to the base ring of the antenna and was incapable of being used once the antenna was integrated to the rest of the satellite. This meant that the antenna would need to be completely qualified before delivery to the system. "Pop and catch" deployment tests instead of full deployments were done for all system level antenna deployment testing.



Figure 7: Gravity Offloading Fixture

EDU Antenna

An engineering development unit (EDU) was fabricated and fully tested in order to gain confidence in the antenna design. The EDU antenna was the full scale flight design and was completed in February of 2007. Testing included in air deployment testing, baseline RF patterns and PIM measurement, surface RMS measurements, three axis quasi static and random vibration, TVAC cycling and deployment testing, and finally post environmental RF pattern and PIM measurements. In total, the EDU antenna had a total of 22 open/close cycles including 4 in air and 3 TVAC deployment tests.

The EDU antenna passed all tests, however there were several noteworthy lessons learned:

Spring Cartridge Lock Pins

Initial deployment testing and surface mapping revealed that the locking mechanisms in the spring cartridge design did not function as intended. The design did not adequately take out the end of travel slop of the rib. The problem was found to be a combination of both tolerance stack-up of all of the rotating surfaces and the large moment arm of the deployed rib. This issue needed to be fixed in order to meet the deployed frequency (>5-Hz first mode) requirement. To fix the problem, it was decided to remove the

latch feature on all of the spring cartridges allowing the spring travel to bottom out on an existing secondary impact spring. This design change utilized existing parts and also removed the complexity and potential single point failures of the antenna's latch features. The new spring cartridge design solved the issue, met surface tolerance requirements, and was implemented as the baseline for the remaining testing and subsequent antenna builds.

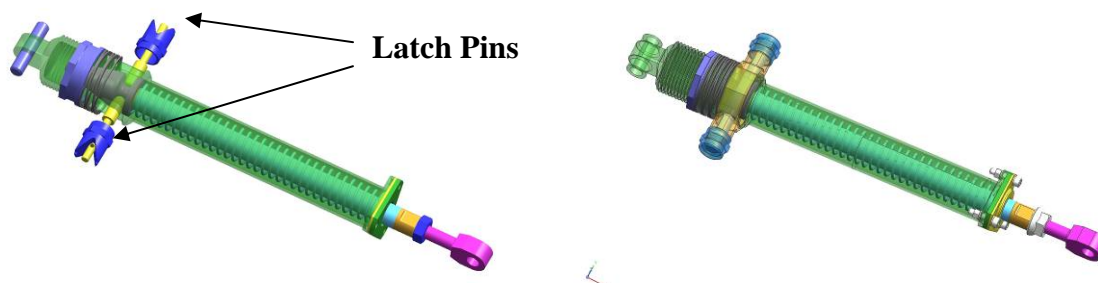


Figure 8: Spring Cartridge With (Left) and Without (Right) Latch

Reflector cracking

The EDU reflector gore material developed cracks. These cracks were caused through the folding of the reflector associated with stowing. The cracks initiated at the edge of the through holes in the gores and once initiated ran from one hole to another. All cracking was similar in location and type on all gores of the reflector and worse in areas that were required to package tighter for stowing. This cracking was reproduced with sub-scale material samples and was shown to be worse once exposed to thermal cycling.

The through holes were put into the gores using a drilling process that is standard in the flex circuit and printed circuit board industry. Testing of samples without holes proved to largely solve the cracking issue. Additionally, there was no compelling requirement (air drag, easier to fold, lighter) to keep the holes. For these reasons the holes were removed for the FM antenna. The copper trace width was also reduced in an effort to improve material compliance and lower the mass of the gores. This was a low risk change given the RF data from the EDU testing.

Release Strap Development

A test fixture, shown in Figure 5, was developed early on in the development to address a number of deployment strap concerns. There were concerns that special attention would need to be taken to control the band tensioning to avoid destruction of the ribs and/or feed support through twisting or excessive and/or uneven loading. A prototype deployment strap was heavily instrumented with strain gauges between every rib to examine the band tension uniformity and how easily the band slid on the Ultem band guides. A process was developed to step the band tension up gradually and work the loading around the ribs by lifting the band off the Ultem blocks for a uniform distribution. A flight band tensioning procedure was developed with expected torque values and correlating band tensions. This early testing enabled removal of the strain gauges for the flight unit eliminating multiple snag hazards. The strain gauges were also initially required to verify and correlate the structural analysis of band behavior and performance of the stowed antenna during launch. Testing showed that uniform rib gapping force was the critical parameter affected by band tension. This uniform rib gapping force could be maintained by controlling the band tension to ± 13 N (3 lbf). Instead of using the strain gauges, a handheld force gauge was used to apply the theoretical gapping force. If the rib did not gap under that load, the band was sufficiently tensioned.

Upon actuation, energy stored in the Frangibolt fastener and strap tension is released into the bands. Initial prototype testing revealed there was sufficient energy for the two band end fittings to contact on the opposite side of the structure and possibly tangle, thus possibly preventing a full deployment. If the bands

did not contact, they would spring back into the deploying antenna. A damping method was required to absorb some of the energy to prevent the ends from striking the gores or payload and becoming entangled. The ultimate solution was to attach two welding rods to the Elgiloy band with heat shrink tubing as a damper/stiffener. The solution was tested with a 1G gravity assist to prove the end fittings would never come into contact.

Reflector CTE

During TVAC testing of the EDU antenna, a cold spike test was conducted to demonstrate survivability and performance at the coldest predicted temperatures. During the test, the antenna was taken cold (~ -50 deg C) and deployed with ~ 0.3 g offload giving a worst case energy deployment. After the deployment was completed, the shrouds of the chamber were set to -150 deg C and the antenna was allowed to be exposed to a cold spike. The reflector has very low thermal mass and quickly moves with the shrouds of the chamber while the rest of the antenna remains within survival temperature limits. The purpose of the test is to show that the EDU gores were properly designed for on orbit coefficient of thermal expansion (CTE) effects. The reflector material is made primarily of Kapton[®] which has a fairly high CTE. This is a potential issue because if the reflector material shrinks too much it would go taut and would exert force on the deployable ribs. This force would act to move the ribs back towards the stowed condition, altering the deployed shape of the antenna. Without a latch, the ribs could move enough to change the shape and/or pointing of the antenna as a function of temperature. The advertised CTE of the reflector material is 25 ppm/degC and the gore was sized such that the extreme cold temperature would not allow the gores to go tight while meeting RMS requirements at the predicted hot condition. During the cold spike test, it was visually observed that the deployed ribs did move in the stowing direction indicating that the reflective material did get tight. More slack gore was added to solve this issue. This in turn adversely affected the RMS of the reflector surface at hotter temperatures. The solution to this problem was to loosen the RMS requirement of the reflector to 12.7 mm (0.50 in) RMS, resulting in a link margin reduction of ~ 0.2 dB, which was deemed acceptable by the program. The flight gores added 6.35 mm (0.25 in) additional material from rib to rib which proved to solve the CTE issue.

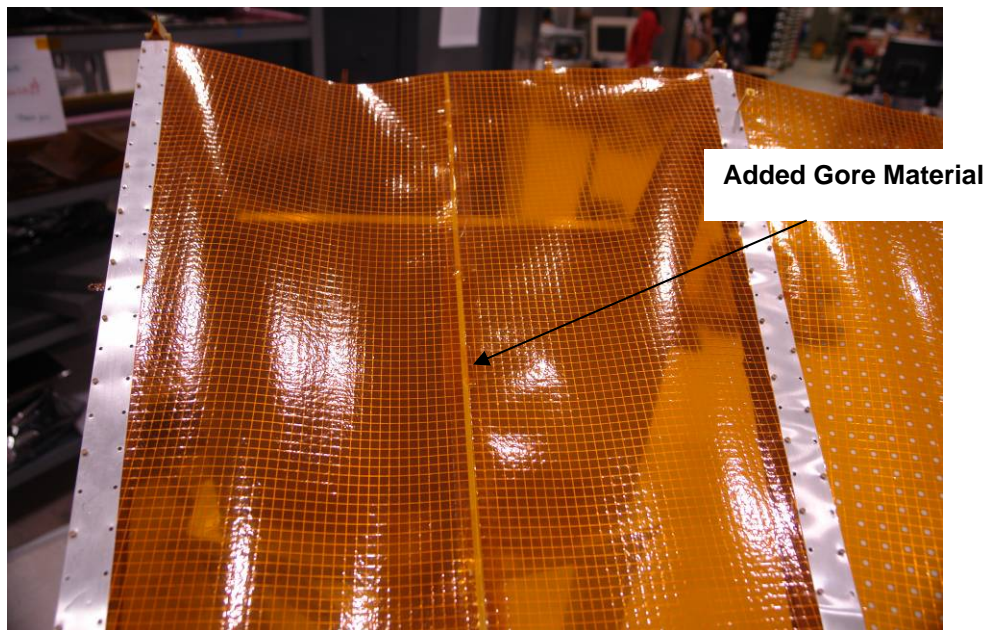


Figure 9: Mockup FM Gore with Added Material

Gravity Offloading Issues

Deployment testing showed that the gravity offloading was not acting as intended. This problem presented itself as the antenna stopping short of the fully open position. The deployment force required to

gap the gravity offloader in the deployed position was measured and compared to the theoretical model. These measurements showed a discrepancy between predicted and as-built gravity offloading forces at the open position. Further analysis showed that the as-built gravity offloader force profile was offset which resulted in both under-offloading in some positions and over-offloading in other positions over the antenna deployment. The issue was traced to a small link chain that was used to transfer the offloading spring force over the cam profile and onto the antenna rib. The chain restricted movement along the profile of the offloading cam. The “as-built” offloader design was capable of testing either energy margin or force at fully deployed position but not both simultaneously. The offloader was used in the “as-built” configuration for all remaining testing and was adjusted accordingly to get the desired energy or force offload.

Surface Mapping

The reflector was mapped using laser scanning photogrammetry; a technique which is often used in reverse engineering applications. Because of cost limitations the antenna was mapped at room temperature in a “cup sideways” orientation only; that is the boresight of the antenna is parallel to the ground. The loose RMS accuracy required of this antenna allowed this simplified measurement setup to be used. The surface accuracy of the antenna was loose enough that the antenna met the requirement even with the 1g sag of the reflector. Several setups were used to record the shape of the reflector and the data was processed to find the RMS deviation of the antenna from the ideal parabola. The antenna RMS deviation was measured to be 6.35 mm (0.25 in) from the theoretical surface. The measurement technique worked well, however it was necessary to find a laser scanner that was capable of imaging a surface with optical properties of both the Kapton used for the EDU antenna and the germanium sputtered Kapton[®] used for flight model (FM) antenna. The laser scanner that was found to be adequate was a Cyrax 2500.

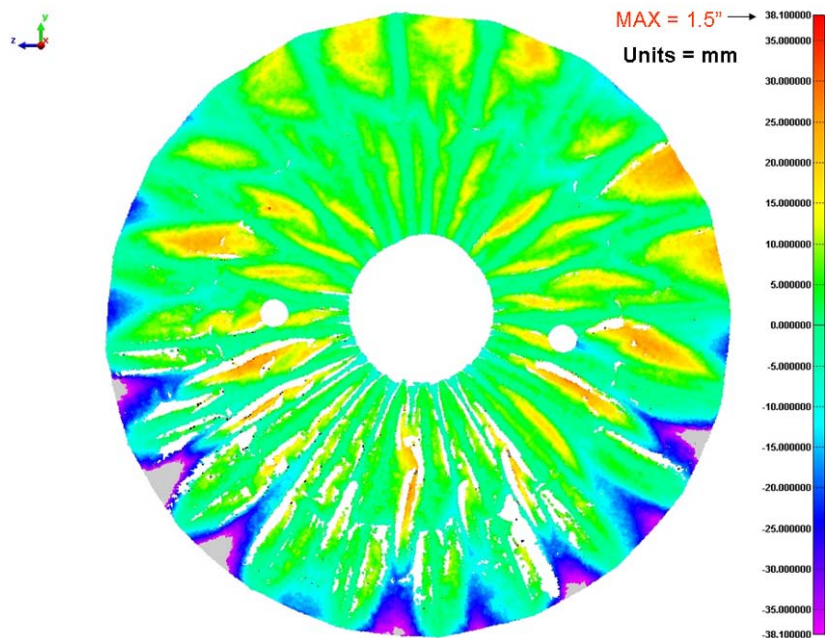


Figure 10: Surface Mapping Results

FM Antenna

The FM antenna was built following the completion of all EDU testing. The flight antenna incorporated the lessons learned on the EDU antenna discussed in this paper including changes to the spring cartridges, gores, and deployment strap. The FM antenna went through identical mechanical and RF and PIM testing as the EDU antenna. This included in-air deployments, surface mapping, RF and PIM performance

testing, quasi static and random vibration testing, TVAC (thermal cycling, deployment testing, cold spike) testing, final surface mapping, and post environmental RF performance testing. The antenna passed all tests and was delivered for system integration and testing. All of the design changes made from the EDU antenna did improve the performance of the antenna. The FM antenna has a measured surface accuracy of 8.1 mm (0.32 in) RMS and has seen a total of ~30 open/close cycles, including 3 TVAC deployments and 6 in air deployments.

There were additional lessons learned through the build and testing of the FM antenna:

Gore Cracking

In total the gores on the FM antenna behaved much better than the EDU gores. The additional material added solved the CTE issue that was found on the EDU antenna. Secondly removing the through holes substantially improved the cracking issue that was seen on the EDU antenna. However, as expected, the FM gores were stiffer and proved to be slightly more difficult to stow. After ~20 open/close cycles some minor gore cracks have developed. These cracks were very small (pin holes to 1.6-mm (1/16-in) long), and developed in areas where the reflective material was forced to bend in multiple planes creating “kinks” through the stowing action. This phenomenon can be observed by bending a piece of paper in a similar fashion. The effect is that a stress point develops and this point has a very tight bend radius. These stress points are worked over time from opening and stowing the antenna and eventually a small pin hole develops in the material. When left unchecked the pin hole developed into a small crack/tear in order to relieve the stress in the material. To combat this issue, a patching procedure was developed and tested. Small (25 mm x 25 mm) germanium sputtered black Kapton tape was placed over the problem areas on both sides of the reflector. This method proved to stop the propagation of the crack without adversely affecting the RF performance or the material behavior during the stowing process. In some cases preventative patches were placed in areas showing beginning signs of crack development.

Several design changes were considered to solve the cracking problem. These potential changes included changing the gore geometry to give the localized stress areas additional material, using thinner Kapton in the flex circuit to lower the gore bending stiffness, using a different type of Kapton that could have better resistance to this type of stress, and increasing the f/D of the reflector. In the end these changes were not necessary because the patches proved adequate to meet the mission requirements.

Overall the flex circuit gore material proved to be fairly robust to work with. The material did work very well in order to meet the low PIM requirements and was easy to handle and manipulate in order to stow the antenna while meeting the surface accuracy requirement of the reflector.

Conclusions

The Naval Research Laboratory has developed a novel design approach for a low-cost, low-PIM, deployable UHF antenna. The design has been fully qualified and will launch as part of the Tacsat-4 satellite in 2010. This new technology is directly applicable to other sub four-meter deployable antennas at UHF and may have application for other missions at higher frequencies.

A Completely New Type of Actuator -or- This Ain't Your Grandfather's Internal Combustion Engine

Brian W. Gore*, Gary F. Hawkins*, Peter A. Hess*, Teresa A. Moore* and Eric W. Fournier*

Abstract

A completely new type of actuator – one that is proposed for use in a variety of environments from sea to land to air to space – has been designed, patented, built, and tested. The actuator is loosely based on the principle of the internal combustion engine, except that it is a completely closed system, only requiring electrical input, and the working fuel is water. This paper outlines the theory behind the electrolysis- and ignition-based cycle upon which the actuator operates and describes the performance capability test apparatus and results for the actuator. A mechanism application that harnessed the unit's power to twist a scaled rotor blade is also highlighted.

Introduction

Traditional electro-chemical actuators use electrolysis to produce hydrogen and oxygen to generate pressure that can be used for mechanical work. These actuators can create substantial forces over large strokes but are inefficient and relatively slow. The Aerospace Corporation developed an actuator in which the hydrogen and oxygen are produced electrochemically and then ignited when actuation is desired. The process takes place in a closed volume so the water produced during combustion is contained and used again. The actuator essentially acts as a power amplifier that converts a low electrical power into stored chemical energy. The stored chemical energy can then be rapidly released (~10 ms) to produce high mechanical power in the actuator.

The advantage of this device is the extremely high energy density that can be safely stored, then delivered instantaneously. It is essentially a power amplifier – a low level of power can be input over an extended period of time, then quickly reclaimed, on the order of single-digit milliseconds. The time duration of the actuation pressure pulse can be controlled from tens of microseconds to tens of milliseconds by adding variable quantities of inert “buffer” gas, which slows down the thermal activity during combustion. In the design space of energy density vs. speed of operation, this actuator lies outside the current state-of-the-art envelope, as shown in Figure 1.

* The Aerospace Corporation, El Segundo, CA

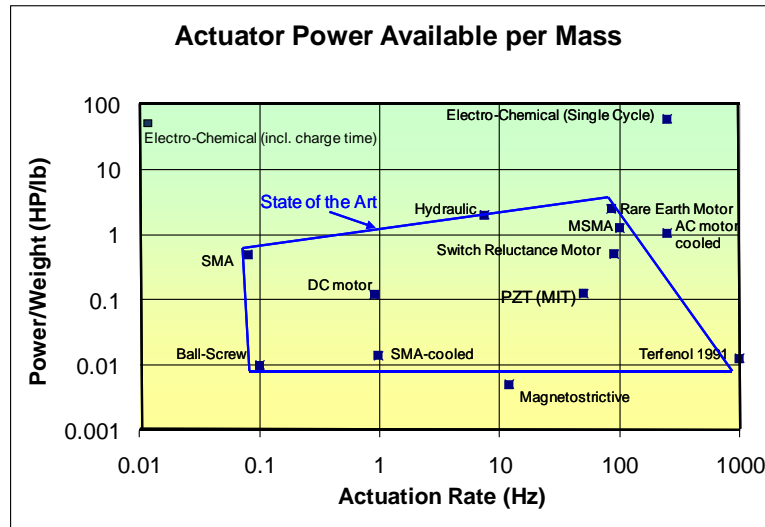


Figure 1. Actuator Specific Power vs. Actuation Rate for State Of The Art (Courtesy Of Bell Helicopter)

The heart of the closed-cell electrolysis/combustion cycle (shown in Figure 2) uses Nafion[®] material submerged in a small, fixed amount of water, which does not require replenishment.

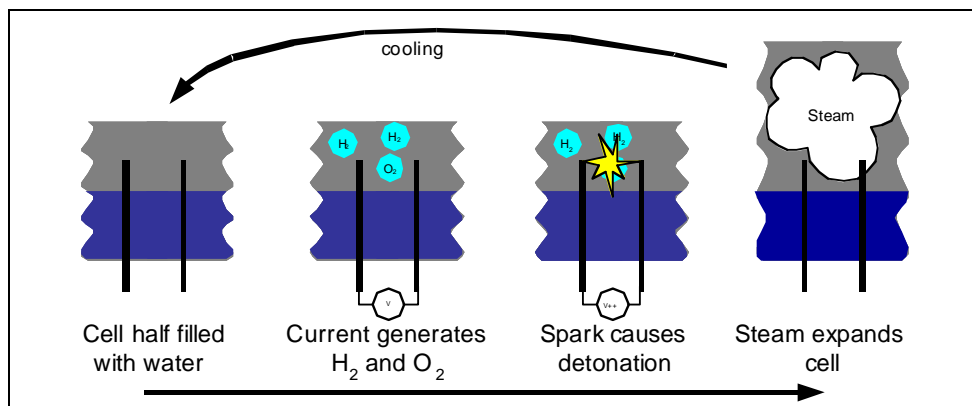


Figure 2. Schematic Drawing of the Actuation Cycle

When an electric current is passed through the Nafion[®], the surrounding water undergoes electrolysis to produce hydrogen and oxygen molecules that bubble to the surface as gases. Both gases are contained within the common volume until a spark- or glow-plug is energized which then ignites the hydrogen in the system, using oxygen as the oxidizer. A large pressure pulse results from the combustion, from which mechanical work can be extracted, similar to that in a piston/cylinder system of an automobile's internal combustion engine. The difference between the two is that there is no exhaust; after combustion of the hydrogen and oxygen, the reactants are transformed into high-pressure steam that eventually condenses back into water, collecting in the reservoir. The process can continue to cycle, as long as electricity is provided to the Nafion[®] to drive the electrolysis.

Development of Prototype Actuator

A typical experiment during the actuator development cycle used a prototype actuator unit, shown in Figure 3, which was not optimized for weight or volume. The actuator was a piston and cylinder arrangement that pushed against a spring typically used in automotive applications. Electrolysis was performed using 7.5 W (3.75 volts and 2.0 amps) for 180 seconds, followed by ignition.



Figure 3. Piston/Cylinder Actuator (Left), And Spring It Compressed (Right) During Actuation

The resulting force and displacement profiles are shown in Figure 4. The force peaked at approximately 2.60 kN (580 lb), while pushing 1.8 cm (0.7 in) against the 145 kN/m (825 lb/in) steel compression spring. The force curve (Delta Load, in black) was measured by a load cell at the fixed end of the spring and contains additional temporal structure due to compression waves generated within the spring. The full-width-at-half-maximum duration of the force pulse was approximately 5.5 ms. Peak internal pressures of 31 MPa (4500 psi) have been attained inside the cylinder and are limited only by the strength of the cylinder itself, not the electrolysis/ignition process.

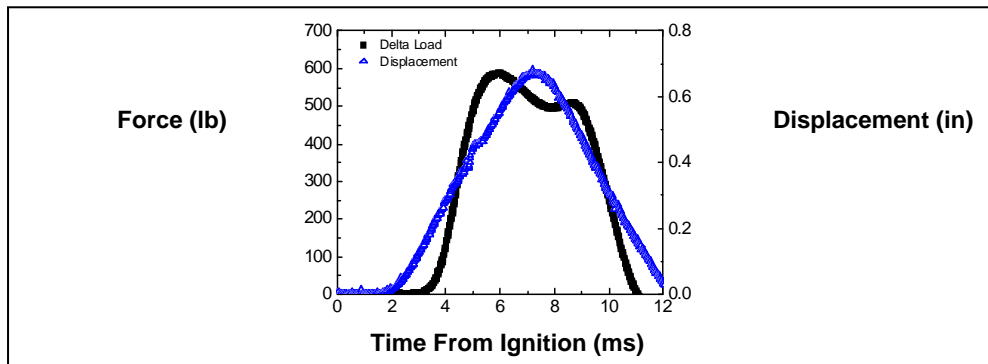


Figure 4. Load and Displacement of the Actuator Pictured in Figure 3

This example demonstrated the application of 7.5 W for 180 seconds and the achievement of >2500 W of instantaneous usable power. Again, the amount of safe potential energy stored, and power delivered, by the combusting hydrogen and oxygen is only limited by the structural integrity of the cylinder. Gas generation rate is proportional to electrolysis current; the more time-integrated current that is used, the more gas will be generated in a given time, and the more power will be available.

Development of Trigger-based Power Meter

One of the other metrics in this development effort was to determine and maximize the specific power of the actuator, with a goal of 16.7 kW/kg (50 hp/lb). Initially, the piston/cylinder pictured in Figure 3 was used with an original test “bomb” mounted to its underside as the combustion chamber (also not optimized for weight, but used readily available, off-the-shelf parts). A power density for that combination of parts – about 13.1 kW/kg (39 hp/lb) – was calculated through knowledge of pressure, surface area, and piston velocity/acceleration.

A custom, lighter-weight chamber was then designed and built for the purpose of lowering the entire Electrolysis Combustion Actuator (ECA) device’s mass, thus increasing the overall specific power density of the device. This lightweight ECA (195 g/0.43 lb) consists of a thin-walled gas generator and ignition

chamber, has ports for the igniter and buffer gas inlet, and has feed-throughs for gas generation. It replaces the original, heavy flange-based CVR (Constant Volume Reactor), (1.42 kg/3.14 lb). Figure 5 shows a close-up of the newly built, lightweight ECA chamber.



Figure 5. Lightweight Electrolysis Combustion Actuator (ECA)

A special test fixture was also developed. The fixture design needed to restrain the stroke of the piston from the build-up of pressure during the electrolysis phase, but possess a trigger function to allow the piston to begin to stroke instantly after ignition. The goal was to make this a passive device, rather than to try to incorporate a complicated feedback release system. The trigger device in Figure 6 was designed. It uses the basic principle of a quick-disconnect, ball release mechanism which will not allow relative motion until a specifically-applied external force is present; in this case, that force comes from the pressure pulse above and beyond the electrolysis static pressure. Rollers were used instead of spherical balls to allow for greater Hertzian contact load capability without brinelling. Accommodations were made for a variable-sized spacer to allow for different threshold pressures at which the device would release.

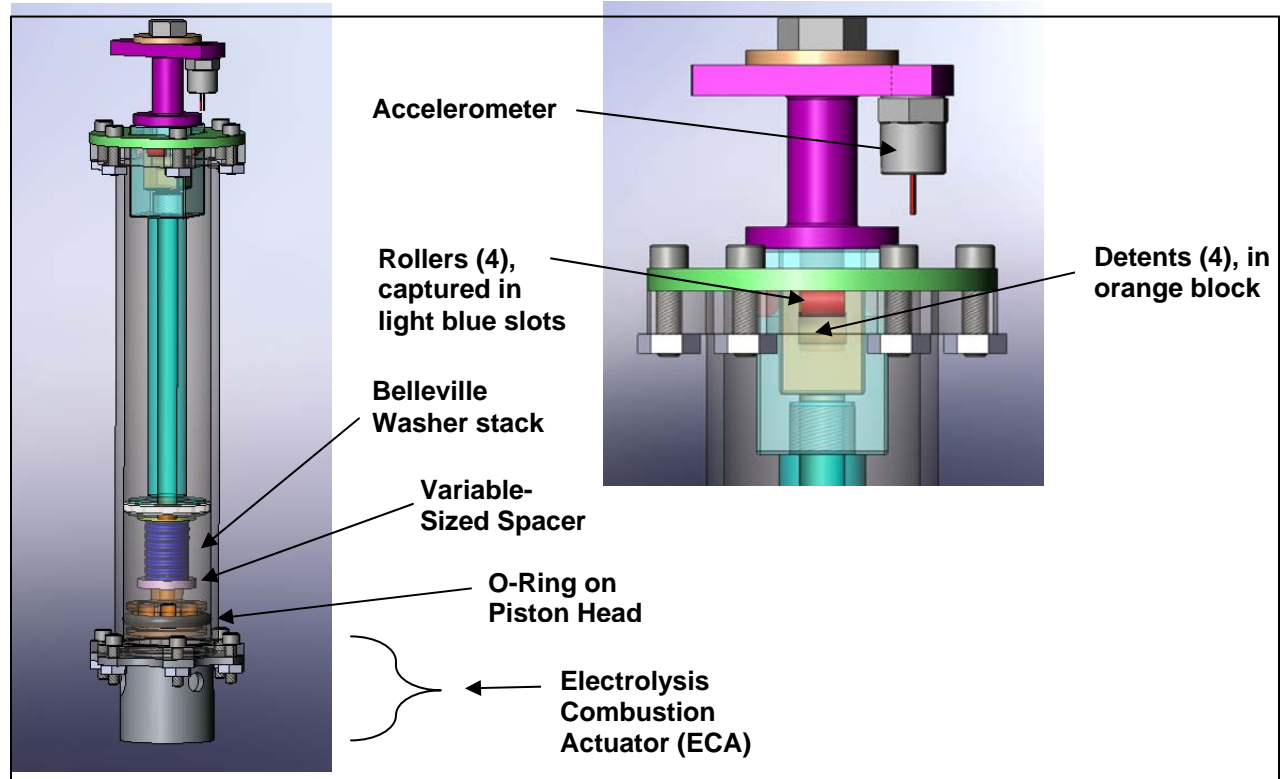


Figure 6. Quick-Disconnect Ball Release Test Fixture

The following derivation was used to calculate the horsepower being generated by the actuator on the moving mass inside the test fixture:

$$\begin{aligned} \text{Power} &= \text{Energy} / \text{time} \\ \text{Power} &= \text{Force} * \text{distance} / \text{time} \\ \text{Power} &= \text{Moving mass} * \text{acceleration} * \text{distance} / \text{time} \\ \text{Power} &= \text{Moving mass} * \text{acceleration} * \text{velocity} \end{aligned} \quad [1]$$

For the test, the moving mass in the apparatus (everything except the gray and green structural pieces) in Figure 6 was 0.2 kg (0.45 lb). The total displacement allowed before an external crushable device was impacted was 9.65 cm (3.8 in). Note that the device itself has an allowable stroke of 1.7 cm (4.6 in).

Figure 7 is a picture of the entire assembled test fixture hardware, including the ball release trigger mechanism and the ECA. Note the inclusion of the accelerometer mount at the top which serves a dual purpose as both a structural mount for the accelerometer, and also as a hard stop for the moving mass as it impacts the external crushable honeycomb unit mounted to the rigid test stand above.

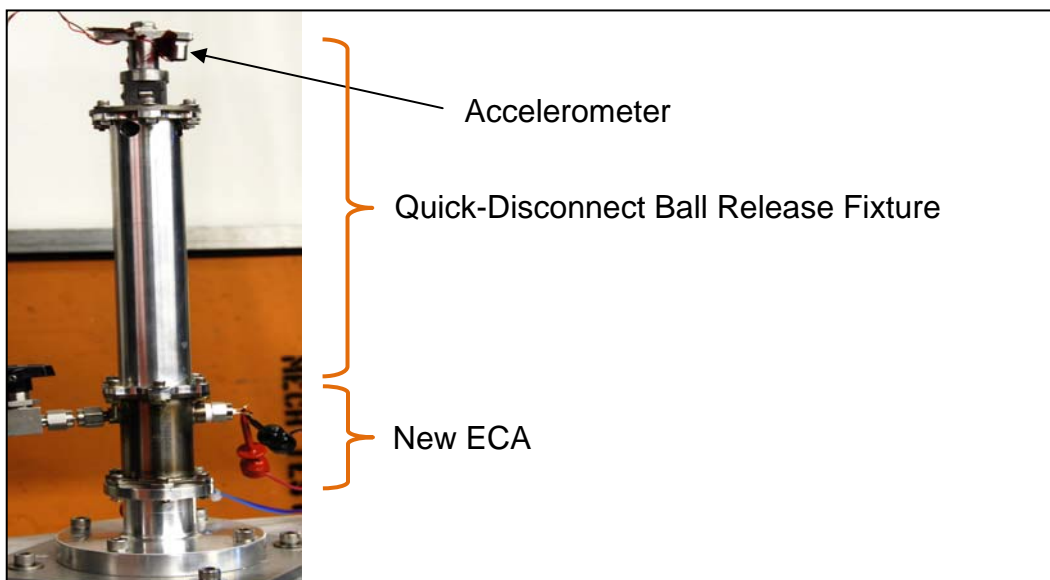


Figure 7. Complete Peak Power Density Test Fixture

Figure 8 depicts the entire test station where the specific power measurements were made. It includes the location of the test fixture on the stand, the crushable shock absorber, and the black and white measurement scale. The calibrated scale was placed behind the fixture and used as a reference to easily determine position and velocity from the high speed video camera output.

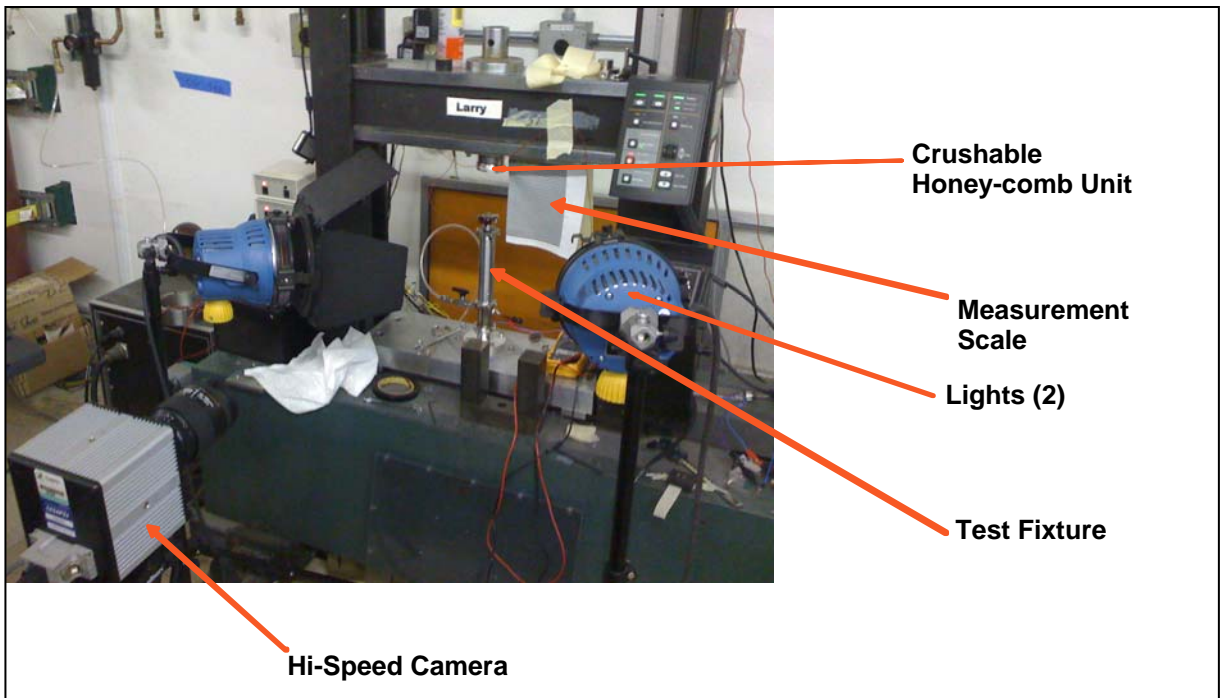


Figure 8. Peak Power Density Experimental Test Setup at The Aerospace Corporation

Figure 9 shows the first frame of the high-speed video. The accelerometer mount can be seen at the bottom of the frame, with a clear horizontal edge to use as a reference on the vertically moving part. The measurement scale is shown along the right side, and the crushable device is at the top of the frame.

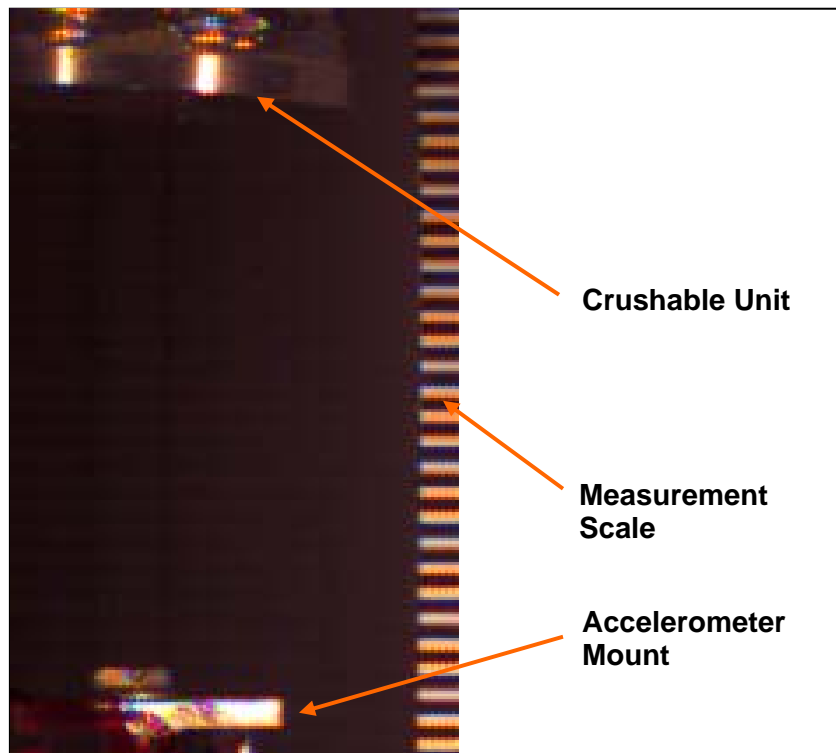


Figure 9. First Frame of Peak Power Testing High-Speed Video

Each of the measurement marks (black or white) was measured to be 2.08 mm (0.082 in) (average of many stripes divided by the number of them), and the observation points taken from the video were to count the number of marks travelled by the accelerometer stand in each frame (=0.1 ms).

The actual “run-for-record” utilized 1.38 MPa (200 psig) of argon buffer gas in the chamber, and about 0.48 MPa (70 psi) of electrolysis-generated H₂ and O₂. When combusted, the gases propelled the moving mass a distance of 9.58 cm (3.77 in) in 2.9 ms and compressed the crushable device (which had a 26–36 kN (6000-8000 lb) crush load) approximately 0.5 cm (0.2 in). That translates to an average velocity of 33 m/s (1300 in/s), which for reference is almost 119 km/hr (74 mph). The raw displacement-vs.-time data were surprisingly smooth, but when differentiated to obtain velocity and then again to obtain acceleration, the data became increasingly noisy. To solve this problem, a best-fit polynomial was found to represent the displacement-time data, which could then be more easily differentiated. Since the displacement and velocity are initially zero, the constant and first-order coefficients of a fourth-order polynomial were forced to be zero, and the result was Equation 2.

$$D = 51,746,636,636 \cdot t^4 - 396,904,167 \cdot t^3 + 1192091 \cdot t^2 \quad [2]$$

where: D = displacement (in), and t = time (s)

This polynomial had an R² correlation of 0.9997 to the raw displacement data. With such a strong correlation factor, the best-fit method is strongly supported. The plot in Figure 10 was created after Equation 2 was differentiated for velocity and then again for acceleration. The non-zero acceleration is real, since there is a force acting on the body (from the combustion) before it starts to move.

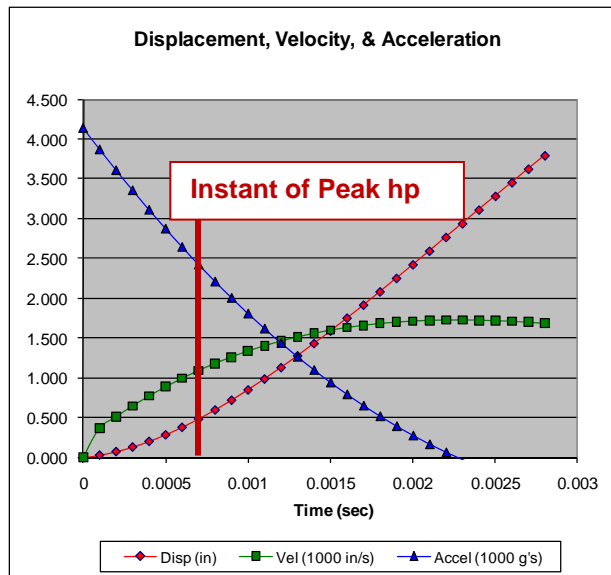


Figure 10. Displacement, Velocity, & Acceleration of Moving Mass

As illustrated in Figure 10, the peak of instantaneous horsepower occurred approximately 0.7 ms after the start of motion and was calculated, using Equation 1, to be 134 kW (180 hp). The maximum velocity achieved before the end-of-travel impact was almost 160 km/hr (100 mph). However, since the milestone to be met was specific power, not total power, that value had to be divided by the mass of the entire device that produced it. The total mass of test fixture’s mechanism/cylinder (all of the hardware above the “New ECA” in Figure 7), is 0.39 kg (0.85 lb) with the moving portion at 0.20 kg (0.45 lb) and the fixed portion at 0.18 kg (0.40 lb). The mass of that ECA is 0.43 lb (the old CVR “bomb” was 1.42 kg (3.14 lb), for reference). Therefore, the calculation of the demonstrated peak specific power is

$$180 \text{ hp} / (0.85 + 0.43) \text{ lb} = \underline{141 \text{ hp/lb (47.1 kW/kg)}}, \quad [3]$$

which was nearly triple the milestone objective of 16.7 kW/kg (50 hp/lb). Moreover, the instantaneous specific power, again using Equation 1 at each time-step, was plotted throughout the usable stroke of the test fixture, and is shown in Figure 11.

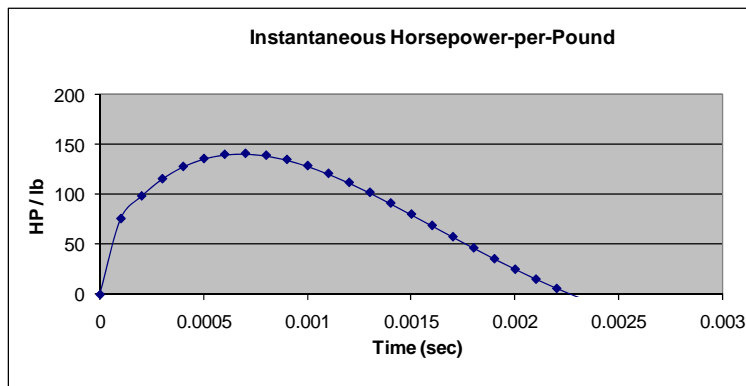


Figure 11. Specific Power Throughout Test Fixture Stroke

The important conclusion to draw from Figure 11 is that the specific power exceeded the milestone of 16.7 kW/kg (50 hp/lb) for virtually the entire effective stroke. Two different methods were originally used to curve-fit the displacement-time data, resulting in some variation in the calculation of peak power. The other method resulted in a peak of 57.1 kW/kg (171 hp/lb), or about 20% higher. The more conservative results are published here, but there should be recognition of some small level of uncertainty.

Even more power may be available with the existing setup, since only mid-sized adjustment spacers (shown in Figure 6) were used in the release/trigger mechanism; higher initial pressure (and thus final combustion pressure) could be achieved with the current hardware. Some minor fixture wear from usage was observed at this stage of the program, but nothing appeared to be detrimental to the demonstrated performance.

Practical Actuator Application Description

After proving that the state of the art in actuator technology could be exceeded, the next goal for the project was to develop a practical application for such an actuator. That application was to use the actuator, in concert with a power transfer mechanism assembly, to twist a scale prototype rotor blade. Twisting such a blade in flight was intended to improve the performance at multiple points in the performance envelope.

The actuator designed and developed for the rotor blade twist mechanism is a bidirectional electrochemical-combustive actuator designed to provide the mechanical force to twist and untwist the blade. The actuator body has mounting points and is sized to mount in the interior of the blade. The end of the piston shaft has a threaded connection to couple the actuator to the blade's internal twist mechanism. Electrical control wires extend from the actuator through the interior of the blade to its root end. Connections to external control electronics can be made from there.

The actuator design incorporates two electrochemical-combustive units that act on a single piston to provide activation in two directions. In typical blade operation the electrochemical-combustive units would be activated alternatively. One electrochemical-combustive unit serves to extend the piston shaft, while the other serves to withdraw it.

The electrochemical-combustive units operate in two phases. In the first, or "charge," phase the electrochemical unit generates combustible gas. Then in the "fire" phase, the igniter initiates the combustive process and the resulting sudden pressure pulse drives the piston, producing motion of the shaft. The force exerted by the actuator can be adjusted by varying the duration of the "charge" time.

Operation of the actuator requires power at constant current for each electrochemical unit to “charge” and power at different constant current for each igniter to “fire.”

The electrochemical-combustive units contain pressurized argon gas that modifies the combustion and heat transfer characteristics which, in turn, optimizes the transfer of energy of combustion to piston motion. The electrochemical-combustive units have valves that allow the argon pressure to be adjusted prior to initial use and during maintenance.

The electrochemical-combustive units also contain water to keep the electrochemical components submerged. In a spinning rotor blade, known water position is achieved by centrifugal force. In the testing environment, water position is achieved by orienting the actuator vertically with the piston shaft at the bottom.

Figure 12 shows a cross section of the actuator with the piston, shaft, and components of the two electrochemical-combustive units labeled. Note that the combustion chamber of the number 1 unit is above the piston, and the combustion chamber of the number 2 unit is the volume around the shaft. The volumes of these two chambers are approximately equal. The 3-D rendering on the right is shown at a slight angle to better show the piston shaft. The mounting rod, rendered in light green, is located near the bottom protruding to the right. The electrochemical units are shown in dark blue. The igniters and argon fill valves are shown in brown.

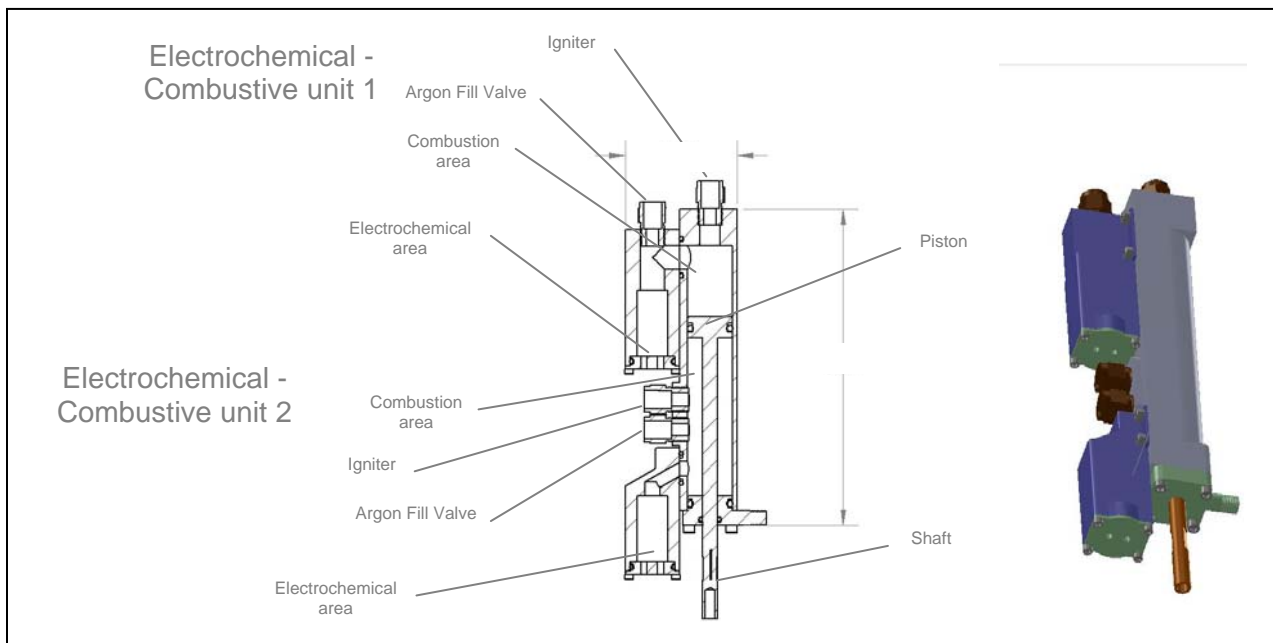


Figure 12. Bidirectional Actuator for the Rotor Blade Application

Figure 13 is a photograph of the actuator development hardware in a laboratory test stand. The photo shows black tubes and fittings connected to the argon fill valves. These valves are used to fill the electrochemical combustive units with argon and would be removed for normal operation in the blade. Note the electrical wires (white, yellow, blue) connected to each igniter and to the electrochemical areas.



Figure 13. Actuator Development Hardware in Laboratory Test Stand

Design of Twisting Tilt-Rotor Blade and Mechanism

The Aerospace Corporation's initial concepts of the rotor blade design involved a split spar and a semi-flexible trailing edge that would let the blade twist by shearing the two spar members. Since a robust design could not close around the open trailing edge, an alternative was pursued. The team noticed that shearing the two spar members also produced a slight separation between them. Using that knowledge, the team pondered that the reverse methodology should also hold, i.e., separation of the members would result in some amount of shear (and thus twist in the blade). That supposition proved to be true and is the principle that led to the design of the twist mechanism described below.

The mechanism design is based on a pin-follower, cam-based, detent shuttle concept. A CAD drawing of the mechanical system inside the blade was created, as shown in Figure 14 (some aspects not to scale).

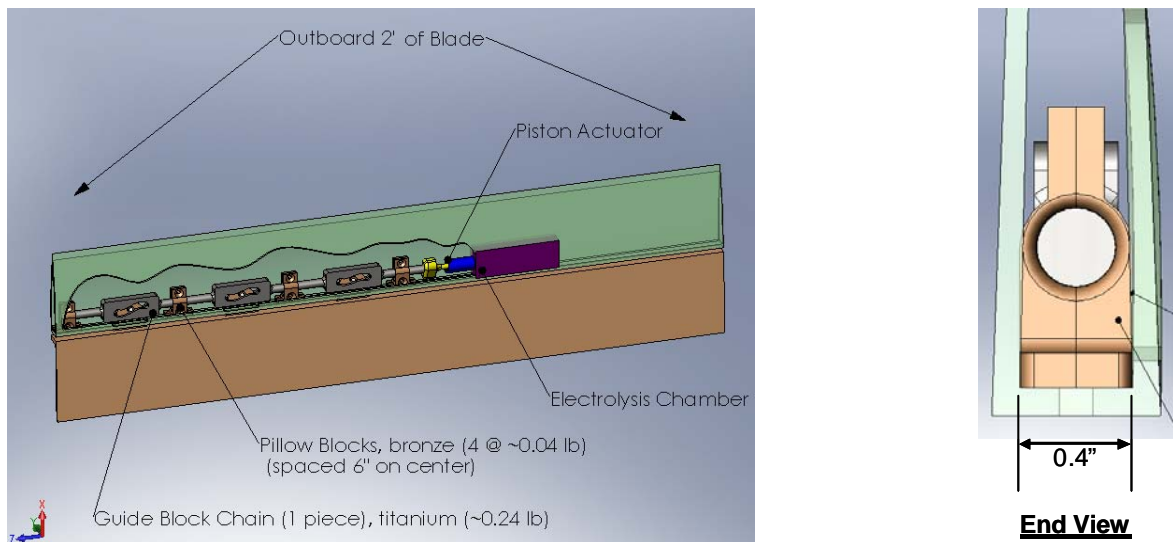


Figure 14. Preliminary CAD Representation of Twist Mechanism Inside Blade

A single actuator (in purple and blue) drives three cam mechanisms with detents in series inside the prototype blade section; the cam mechanisms, which possess respectively different profiles to produce an overall gradient deflection in the blade, are located on 15-cm (6-inch) centers to distribute the load. This preliminary design layout drawing also resulted in a first-order approximation of the size and weight of the actuator/mechanism assembly. The electrolysis/combustion team initially estimated the actuator would weigh approximately 0.2 kg (0.5 lb). Including the other masses shown in Figure 14 for which The Aerospace Corporation was responsible (actuator and power transfer mechanism), the weight goal levied for the entire subsystem was 0.45 kg (1.0 lb) plus miscellaneous attachment hardware. The weight goal was a large challenge, as one can see from the packing factor in the end view in Figure 14. The weight of the actuator development hardware shown in Figure 13 was approximately 0.59 kg (1.3 lb), which was significantly over its allocated weight. However, the mechanism portion of the assembly weighed just under its 0.2 kg (0.5 lb) allocation, so the final overall assembly weighed approximately 0.82 kg (1.8 lb).

The next step in the process was the creation of a multi-body dynamic model of the system, using Dynamic Analysis and Design System (DADS), a commercially available multi-body dynamics software. DADS aided in the evaluation of necessary actuator pressure and load to twist the rotor blade. Cam profile shapes, friction, and local blade stiffnesses were all incorporated into the model. Figure 15 shows images from the DADS model. The view is looking from the top of the blade downward, similar to Figure 14. The forward spar structure is in green (fixed reference frame), and the aft spar structure, which gets separated (and thus twists the blade via the previous discussion) is in orange. The pin (in red) is fixed to a lug mounted to the aft spar, which protrudes through an access hole in the forward spar. The actuator moves the guide blocks (shown in blue, and constrained to a fixed distance from the forward spar by pillow blocks) to the left and right. As it does so, it forces the red pin (and aft spar) fore and aft relative to the forward spar through the cam profile. In the model, the pin slides in the cam groove with an assumed friction coefficient of 0.1 (sliding but lubricated condition). Initial designs considered the inclusion of a rolling element bearing at this joint, but that option was quickly ruled out due to the very tight volume constraints and relatively large loads; Hertzian contact stresses were prohibitive. The purple model springs between the forward and aft spars represent the torsional stiffness of the blade at each cam location. Using the blade's finite element model results of applied deflections at each cam location and their respectively required forces, values were calculated for use as spring constants. Note that the three cams are slightly different in the amount of forward/aft spar separation that they produce (3.81, 2.54, and 1.27 mm (0.150, 0.100, and 0.050 in)). This separation gradient is what actually produces the twist in the blade.

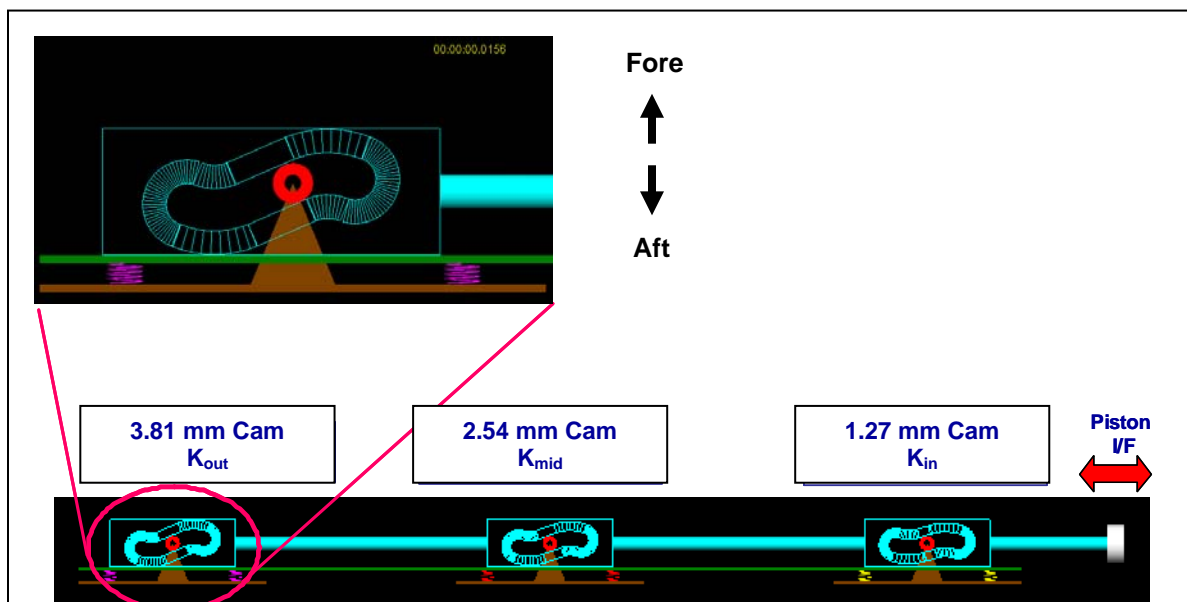


Figure 15. Screen Images of DADS Model

After the DADS model was created, several investigative runs were performed to determine the necessary force profile, specifically peak force and duration, to be delivered by the actuator. A series of spike-and-decay force pulses with a 0.002 second full-width-at-half-max (0.012 second overall) were used, since that was the general pulse shape from the actuator development testing, and the amplitude was varied. According to the simulation, a 5.17 MPa (1.47 kN) [750 psi (331 lb)] peak pulse was not successful in actuating the mechanism past the detent, but a 6.89 MPa (1000 psi) pulse was successful. With the latter pulse shape, the end-to-end actuation was predicted to be 0.004 s; a higher, 10.34 MPa (1.97 kN) [1500 psi (442 lb)] pulse was predicted to actuate in 0.002 second.

So the actuator was tuned to the correct pressure profile using appropriate levels of buffer gas and electrolysis parameters, and the tilt mechanism hardware was built. A test fixture was also built at The Aerospace Corporation to simulate the DADS model (which in turn, simulated the rotor blade) with custom-designed stacks of Belleville washers at each of the three cam locations. Given additional sources of fixture friction not accounted for in the DADS model, such as lug alignment rod sliding and pillow blocks rubbing with the connecting rods, the actual hardware and test fixture actuation time of 0.007 second was within the expected range of uncertainty. After the hardware was working satisfactorily on that fixture, it was sent to Bell Helicopter for integration into their blade, as shown in Figure 16.

A total of thirty actuations were conducted at Bell during integration bench testing, in order to properly configure the actuator with the correct electrolysis time and current, buffer gas pressure, etc. An additional thirteen actuations were conducted during the “run for record” (referred to as the Demonstration).

Three of the thirty bench test actuations ended on the up-stop (cams moving inboard in blade); and seven of the actuations ended on the down stop (cams moving outboard in blade); the remainder started or stopped somewhere in mid-stroke. There was only one bench test in which the actuator/mechanism traveled the full stroke, from up-stop to down-stop, which resulted in a total of 4 degrees of twist. This amount of twist met the goal of the project. High-speed video was used to capture the twisting events, with the beginning and ending frames showing total blade tip motion with respect to a protractor, as presented for one example in Figure 17.

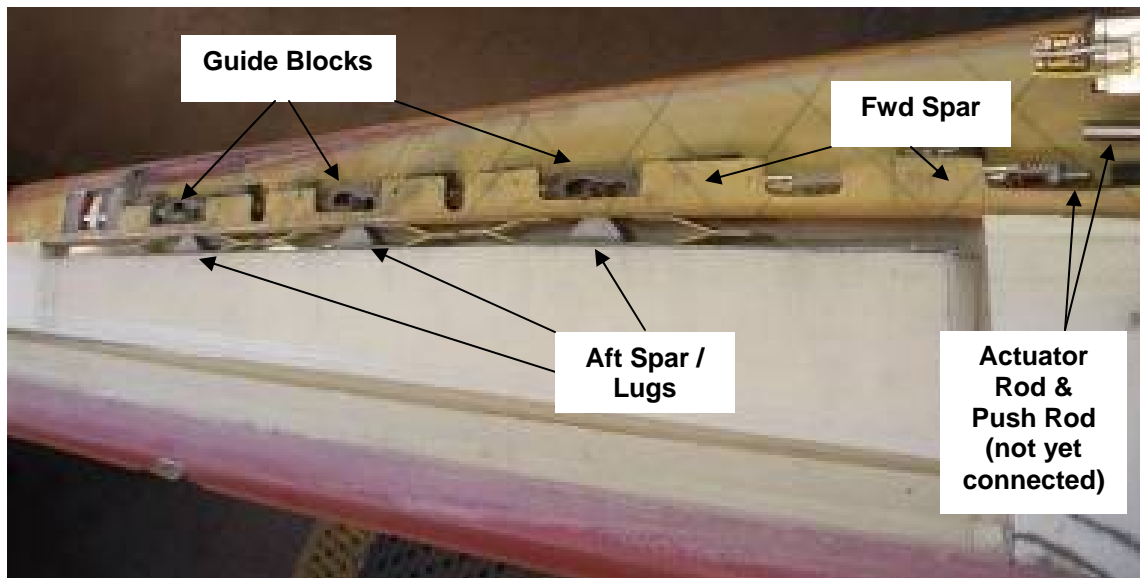


Figure 16. Cams and Rods Installed In Blade Spar Prior To Installation of Upper Skin

Once the team felt comfortable with the setup of the actuator and mechanism, the formal Demonstration for the DARPA customer was executed. Of the thirteen actuations conducted during the Demonstration, all but the first one traveled the full stroke, stop-to-stop (the first was actuated from the mid-point, since

that is the installation configuration). However, those actuations only averaged about 2.5 degrees of blade twist.

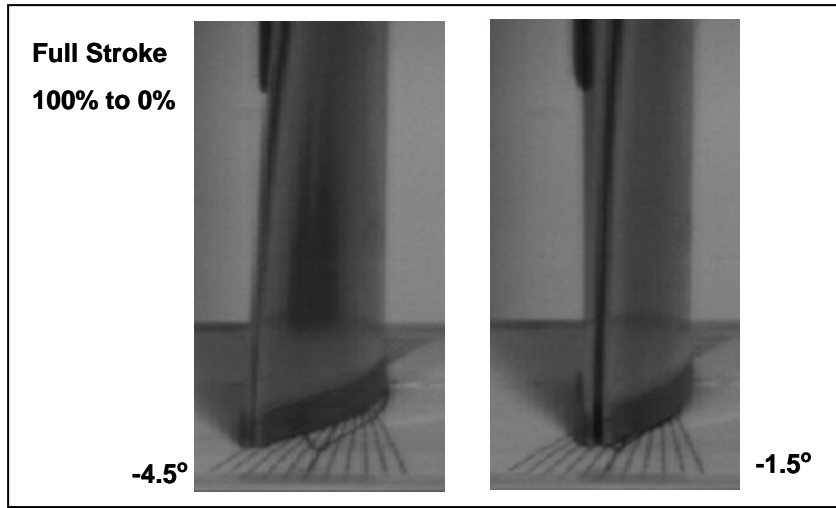


Figure 17. Beginning and End Frames from High Speed Video for Typical Sequence

After the Demonstration, the blade was X-rayed to determine if any internal failures occurred. The results, shown in Figure 18 indicate that the rods in the most outboard cam may have been previously bent. Some of the curvature seen in the X-rays is due to a “fisheye” effect because of projecting a point-source onto a flat receiver. However, the intersection of the inboard rod and Cam 1 does not appear to be perpendicular.

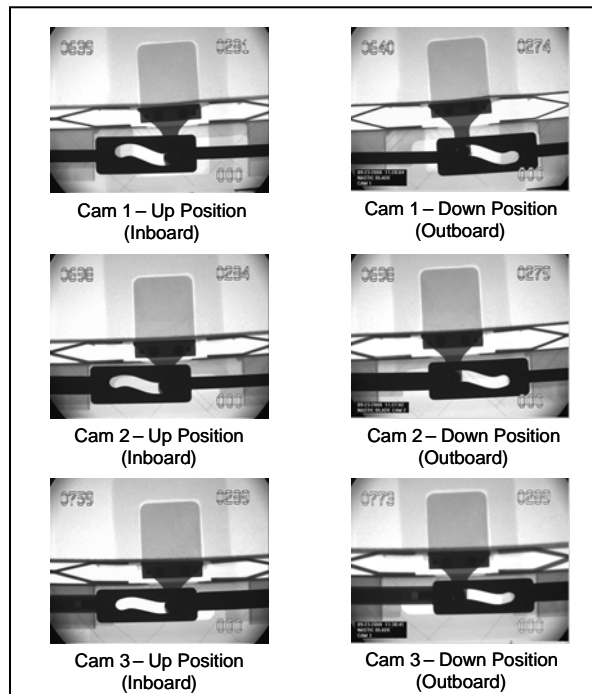


Figure 18. Post-Demonstration X-Ray Results

Post-Demonstration Evaluation

The actuator proved to have more than sufficient force to actuate the mechanism assembly. The loads in the Demonstration tended to be a little over 2.2-kN (500-lb) tension for moving the cams inboard in the blade and around 1.78-kN (400-lb) compression for moving the cams outboard. These forces are roughly what the DADS model predicted (1.5-2.0 kN (330-440 lb) minimum for a successful actuation), but are slightly higher in reality due to the additional friction features in the real hardware.

When the model used lumped masses at each of the lug locations to simulate the mass of the twisting blade, and used a pulse of 6.89 MPa (1000 psi) over 2 ms (full-width, half-max) it predicted a profile shown by the red curve in Figure 19, for actuator push rod load vs. time. That analytical curve is overlaid onto one of the successful bench test sequences for comparison.

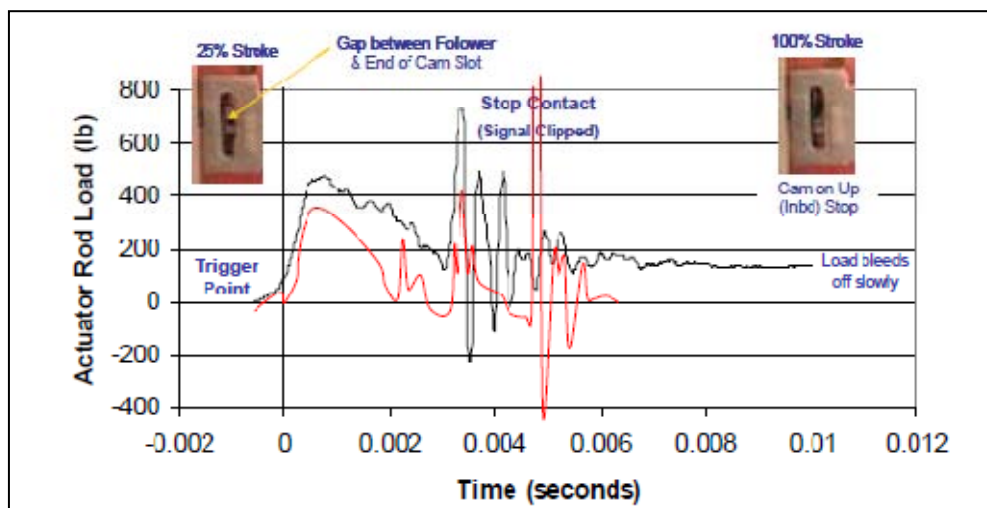


Figure 19. DADS Output (Red) Overlaid Onto Bell Test Data for Sequence 30

Lessons Learned

1. Electrolysis/combustion actuators can be used successfully to achieve a higher specific power than other currently available technologies.
2. Electrolysis time and buffer gas volume can be used to effectively tune the combustion pulse in both peak magnitude and time duration to meet specific application needs.
3. Intelligent solutions can sometimes unexpectedly result from lofty goals. The actuator goal of 16.7 kW/kg (50 hp/lb) was chosen because it was 1-2 orders of magnitude above what had ever been produced previously. Initially thought by the research team to be unattainable, that "stretch" goal drove the team to produce innovative hardware.
4. Non-metallic materials should always be part of the design trade space. Some spacecraft and launch vehicle engineers can be lulled into the familiarity of metals and their properties, but lessons can be learned from the air vehicle industry which might be just as concerned or more about light weight solutions. The pillow blocks, made out of a sintered polyamide, were a wise choice for strength, weight, and low friction.
5. Befriend the machine shop experts. Present them with reasonable designs and more importantly, reasonable deadlines. Similarly, solicit their input during the design phase, not after it has been frozen. Chances are, they have seen many different design solutions and may have different ideas to offer.

Summary/Conclusion

Extremely powerful, reusable actuators can be constructed by generating hydrogen and oxygen through electrolysis and then igniting the gas mixture when actuation is desired. The amount and rate of gas generated is simply a function of electrolysis current and time; the more Coulombs delivered, the more gas will be generated, and the more power will be available.

This technology was applied beyond the theoretical environment to achieve both goals for which the team set out to achieve. A test fixture was created to measure the instantaneous specific power of the device, which was measured at over 46.8 kW/kg (140 hp/lb), or three times the proposed goal. This result demonstrated that this type of actuator is outside the current state of actuator performance in terms of power density. Furthermore, a practical application of using such an actuator to twist a prototype rotor blade was identified, and a development actuator and power transfer mechanism were built. The goal to achieve 4 degrees of blade twist was realized with the development hardware.

Acknowledgments

The authors would like to thank the Defense Advanced Research Project Agency for their guidance and support of this research, which was part of a project led by Dr. Louis Centolanza entitled "Controllable Active Materials Via Internally Generated Pressure," under U.S. Army Research, Development, and Engineering Command (RDECom) contract W911W6-05-C-0015. In addition, Dr. Michael J. O'Brien (materials), Aldrich R. De La Cruz (FEM modeling), and Dr. Brian M. Gable (materials and heat treating) were all instrumental in helping the project. The authors also wish to acknowledge the excellent assistance of Nolan Phillips, Ernie Powell, Joe Tzeng, and the entire Bell Helicopter partner team.

An Evaluation of Liquid, Solid, and Grease Lubricants for Space Mechanisms Using a Spiral Orbit Tribometer

Michael Buttery*

Abstract

We present the findings of the test program performed by The European Space Tribology Laboratory (ESTL) to evaluate the performance (friction and lifetime) of a number of space lubricants under vacuum using a Spiral Orbit Tribometer (SOT). Focus was given to a comparison of various popular space oils, a comparison study between the old and new MAPLUB grease formulations, and the performance of commonly used solid lubricants under various conditions.

Tests demonstrated that the lifetimes of hydrocarbon NYE oils 2001 & 2001A outperformed those of the perfluoropolyalkylether (PFPE) oils Fomblin Z25 & Z60, though these pairs displayed similar behavior. This relationship was also generally seen for greases; with the lifetimes of the multiple alkylated cyclopentane (MAC)-based greases being extended in comparison to the PFPE-based greases. Testing on greases also demonstrated similar performance between the old (-a) and new (-b) formulations when considering PFPE-based MAPLUB greases, and indeed for all tested PFPE-based non-MAPLUB greases, but significantly shorter lifetimes for the new formulations when considering MAC-based MAPLUB greases. MAPLUB MAC greases containing molybdenum disulphide (MoS_2) thickener were also found to display reduced lifetimes.

For solid lubricants, lead displayed significantly extended lifetimes over MoS_2 , speculated to be caused by redistribution of lead from the ball onto all contact surfaces during the test. Friction coefficients were seen to be some 2.5x higher for lead than for MoS_2 under similar conditions, a result that corresponds well with conventional bearing tests.

The work described was performed under contract for the European Space Agency as part of the Tribology Applications Program, with all funding for testing and apparatus provided by European Space Agency (ESA).

Introduction

Selection of an appropriate lubricant is a vitally important stage of mechanism design. Due consideration must be given to the lubricant properties such as lifetime, friction coefficient, and vapor pressure to avoid unforeseen mechanism failure, a potentially disastrous consequence. As such there is a great need to accurately understand the behavior of space lubricants, and to comparatively assess their performance under representative test conditions. This paper details the findings of a test program performed by ESTL to assess the performance of a number of space lubricants (liquid, grease and solid), using a Spiral Orbit Tribometer.

Two commonly used space oils are Fomblin Z25, a Z-type PFPE oil, and the MAC oil NYE 2001A. Additionally the oil NYE 2001 is also frequently used; an oil similar in composition to that of 2001A, but containing phosphate ester boundary lubricants and antioxidant additives to improve this oil's boundary lubrication performance.

* The European Space Tribology Laboratory (ESTL), ESR Technology, Warrington, UK

During a recent ESA-funded research program, the PFPE oil Fomblin Z60 was highlighted as having exceedingly low vapor pressure, with predicted oil loss by evaporation approximately three orders of magnitude lower than that of Fomblin Z25 at room temperature [1]. Subsequent bearing testing at ESTL found the oil displayed similar lifetimes to those observed with Z25 bearings [2]. Friction coefficients were demonstrated in the range 0.1 – 0.15, with the Z60 displaying slightly higher torque, consistent with the higher viscosity of this oil. During the work described in this paper, a detailed study of these oils was carried out to assess their comparative friction and lifetimes under differing conditions.

In addition to oils, this work program investigated the performance of space-based grease lubricants, focusing upon the MAPLUB grease range. The MAPLUB range provides a series of high performance greases for space applications, developed in collaboration with CNES (Centre National d'Etudes Spatiales). These greases are available under a range of formulations, and are described using a 5-digit reference, e.g. PF100. Grease consistency depends upon both thickener and base oil, and is related to the grease's deformation by an applied force.

- The two letters indicate the base oil
 - PF for Perfluoropolyalkylether oil (Fomblin Z25)
 - SH for Synthetic Hydrocarbon oil (NYE 2001A)
- The first two figures correspond to the grease consistency
 - 10 for low consistency
 - 05 for very low consistency
- The final figure specifies the type of additive filler
 - 0 for PTFE only
 - 1 for PTFE and molybdenum disulphide (MoS₂)

Due to a change in laws regarding CFC products, the formulation of these greases has recently changed, resulting in a change in product index (e.g. PF100-a changed to PF100-b). For the old (-a) greases, the PTFE was procured as a powder suspended in a solvent, whilst in the new (-b) formulation the PTFE is procured as a dry powder [3]. It cannot be assumed that the performance of these new greases can be extrapolated from the performance of the old, and thus a comparison study was required. The remaining greases tested included Castrol Braycote 601EF, Braycote 601EF Micronic, and NYE Rheolube 2000. The Braycote greases consist of Brayco 815Z oil suspended within a PTFE thickener, and have strong heritage within the space industry. The Micronic designation indicates the grease has been extruded through a screen pack filter to remove PTFE particles larger than one micron. NYE Rheolube 2000 is a sodium complex-soap-thickened, medium-viscosity MAC grease based upon the oil NYE 2001.

In addition, two commonly used solid lubricants were included within this study. The selected lubricants were sputtered MoS₂, and lead, applied as a thin film. Between them, these two lubricants account for a large majority of solid lubrication for space and have a heritage of successful applications.

Scope of work

This paper covers the friction and lifetime performance of the space lubricants listed in Table 1 under vacuum, assessed with a Spiral Orbit Tribometer.

Table 1. Lubricants covered within the scope of this work

Lubricant	State	Base Oil
Fomblin Z25	Oil	--
Fomblin Z60	Oil	--
NYE 2001 (with additives)	Oil	--
NYE 2001A (without additives)	Oil	--
MAPLUB PF100-a	Grease	Fomblin Z25
MAPLUB PF100-b	Grease	Fomblin Z25
MAPLUB PF101-a	Grease	Fomblin Z25
MAPLUB PF101-b	Grease	Fomblin Z25

MAPLUB SH050-a	Grease	NYE 2001A
MAPLUB SH100-b	Grease	NYE 2001A
MAPLUB SH051-a	Grease	NYE 2001A
MAPLUB SH101-b	Grease	NYE 2001A
Braycote 601EF	Grease	Castrol Brayco 815Z
Braycote 601EF Micronic	Grease	Castrol Brayco 815Z
Rheolube 2000	Grease	NYE 2001
Sputtered MoS ₂	Solid	--
Sputtered Lead	Solid	--

Apparatus

Spiral Orbit Tribometer

The Spiral Orbit Tribometer is a test facility developed by NASA Glenn Research Center and recently purchased by ESTL to advance the assessment of lubricants and coatings for space applications. The facility reproduces the kinematics of an angular contact bearing, and allows for the evaluation of friction and degradation rates (i.e. consumption) of lubricants in detail.

The Spiral Orbit Tribometer is essentially a thrust bearing, with a single ball held between two interchangeable flat plates, located within a vacuum chamber. A load is applied to the top plate via a spring-loaded linear translator. The lower plate rotates via a motor located outside the chamber, causing the ball to move in a spiral path with a radius ~21 mm. This configuration causes the ball to spiral outwards, and a fixed guide plate is positioned to keep the ball within the flat plates and to maintain a repeatable orbit. The region of each orbit for which the ball is in contact with the guide plate is denoted as the scrub (see Figure 1). A force transducer behind the guide plate measures the force exerted by the ball onto the guide plate. From this the friction coefficient for each orbit is found, and can be plotted to give the performance of the lubricant over time (Figure 2).

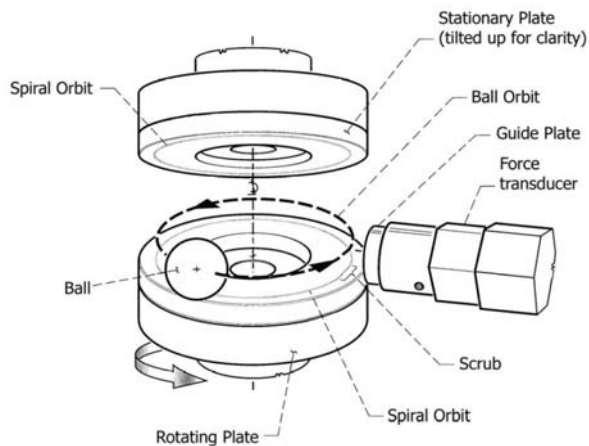


Figure 1. Internal arrangement of SOT, showing flat and guide plates

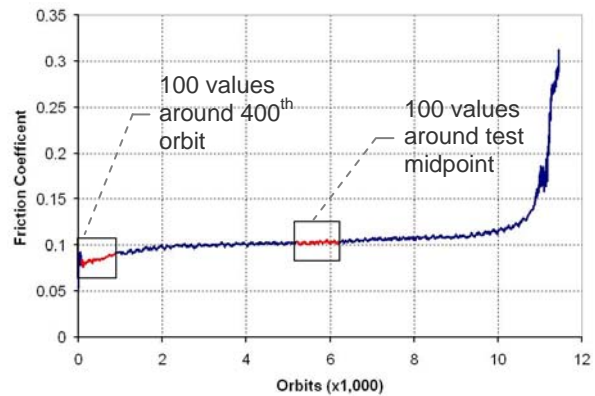


Figure 2. Typical friction plot created with SOT (using grease MAPLUB PF100-b) showing typical regions sampled for friction coefficients

The arrangement of the SOT allows the ball to experience rolling, sliding and pivoting – motions experienced by a ball in an angular contact bearing. This allows for a more representative testing of a lubricant than conventional pin-on-disc testing, which only recreates sliding motion.

Samples

Test plates were supplied along with the SOT by Spiralab LLC, Cleveland, OH. All samples (flat and guide plates) were manufactured from 440C stainless steel, and polished to a surface roughness

$R_a < 0.05$ microns. Balls used were either 12.7 mm (1/2 inch) or 7.14 mm (9/32 inch) diameter, manufactured of 440C and 52100 steel respectively, depending on the requirements of the particular test, explained in more detail below.

Controllers

The SOT is controlled by a supplied laptop PC, running a Labview-based data acquisition program.

Procedures

Sample preparation

Due to the limited number of test specimen sets, it proved necessary to re-prepare used samples for subsequent testing. This was performed by the National Centre of Tribology. Samples were polished using a diamond paste solution mixed with Meta-Di, a water-based diamond suspension solvent, on a 6-micron polishing disc. Samples were cleaned before and after polishing in methanol, and dried using a hot air blower with dry cotton wool. Balls were not reused for multiple tests.

Prior to testing all balls and plates were solvent cleaned in a Kerry cleaning plant using Lenium ES solvent in accordance with standard ESTL practice.

Lubrication

Lubrication was applied to the balls only. Liquid lubrication was achieved through the preparation of a solution of lubricant diluted in an appropriate solvent, of a known concentration. This solution was applied directly to a rotating ball, and the solvent allowed to evaporate from the ball's surface. The amount of lubricant was determined using a high accuracy 6-point microbalance (accurate to 1 μg). A typical lubricant amount of 50 μg was applied for each test.

For grease lubrication, the ball was weighed dry and a minimal amount of grease (less than 1 mm^3) applied directly to the surface. The ball was then rolled successively between three pairs of solvent cleaned Ultra Clean Level 100 Polyethylene tubing, stretched over Petri dishes, to evenly distribute the grease (Figure 4). The ball was subsequently re-weighed, with the weight change being the grease uptake. A typical lubricant amount of 50 μg was applied for each test.

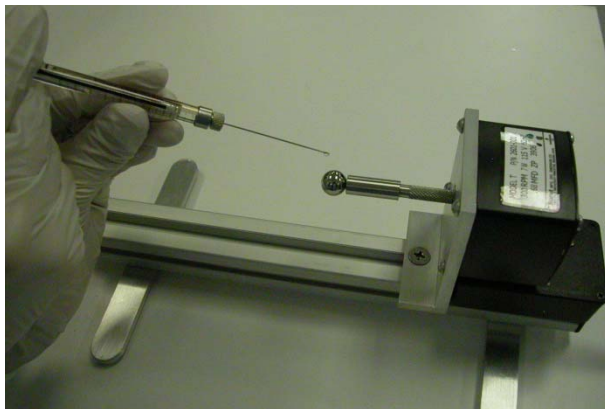


Figure 3. Liquid lubrication – application of oil-solvent solution directly to the ball

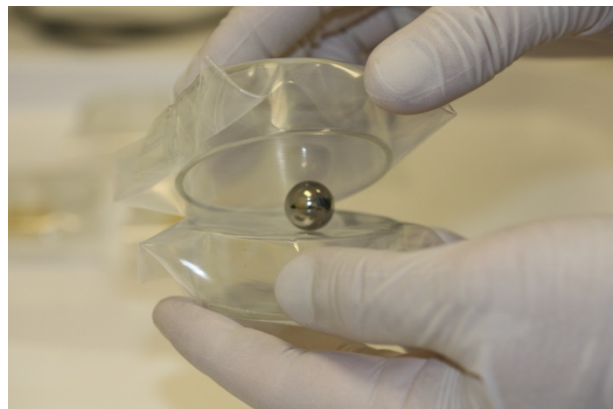


Figure 4. Grease lubrication – grease lubrication through rolling between polyethylene sheets

Solid lubrication was performed with ESTL's sputter coating rig, coating the balls only, to a desired thickness. The coating thicknesses were assessed using a calibrated X-Ray Fluorescence (XRF) measurement system, taking 20 measurements of 60 seconds for each coating run. Coating thicknesses for each test are detailed below.

Test Program

Testing was performed using the SOT under vacuum ($<1.3 \times 10^{-4}$ Pa, 10^{-6} torr) at room temperature (~ 23 deg.C). Tests ran until the friction coefficient exceeded 0.3 for three consecutive orbits, and which point the motion was halted by an automatic trigger. Other test details are given in the relevant sections below.

Liquid lubricant assessment

Tests on each liquid lubricant were performed over a range of mean contact stresses (1.00 – 1.75GPa). For all but the highest contact stress, a 440C ball of 12.7-mm diameter was used (a smaller 7.14-mm ball of 52100 steel was used to achieve the higher contact stresses without exceeding the limit of the linear translator). Tests on the Fomblin oils were performed at 30 RPM, and increased to 100 RPM for the NYE oils due to the expected longer lifetimes of these oils. Preliminary testing at ESTL using Z25 demonstrated no apparent dependence of lifetime upon ball size or rotation speed for this lubricant within this range.

Grease lubricant assessment

Grease lubricant tests were performed using a 12.7-mm diameter 440C steel ball, rotated at 100 RPM and loaded to 1.50 GPa mean contact stress. A minimum of three tests were performed for each grease formulation, and results presented in Table 2 show the mean values.

Solid lubricant assessment

For all solid lubricant tests, a 52100 steel ball of 7.14 mm diameter and rotation speed of 100 RPM was used. For MoS₂, the coating thickness was varied with constant mean contact stress. For lead, the mean contact stress was varied with constant coating thickness.

Table 2. Test matrix for solid lubricant tests

Lubricant (thin solid film)	Coating thickness (Angstroms)	Mean contact stress (GPa)
MoS ₂	800	1.50
MoS ₂	2300	1.50
MoS ₂	5300	1.50
Lead	850	1.50
Lead	850	1.75
Lead	850	2.00

Liquid Lubricant Assessment

The frictional behavior of all oils tested was broadly similar. Start-up friction values were typically $\mu = 0.1$. Steady state friction is then maintained until rapidly increasing to above $\mu = 0.3$ (see example Figure 2). This increase in friction is accompanied by a slight increase in chamber pressure, indicating the presence of volatile constituents – an expected observation as the lubricant degrades [4]. Figures 5 & 6 show the lifetime and friction coefficients of the test oils as a function of mean contact stress. Lifetimes are normalized to orbits/microgram of lubricant. Steady state friction coefficients are calculated by averaging 100 readings around the 400th orbit of each test, to allow for comparison with previous results.

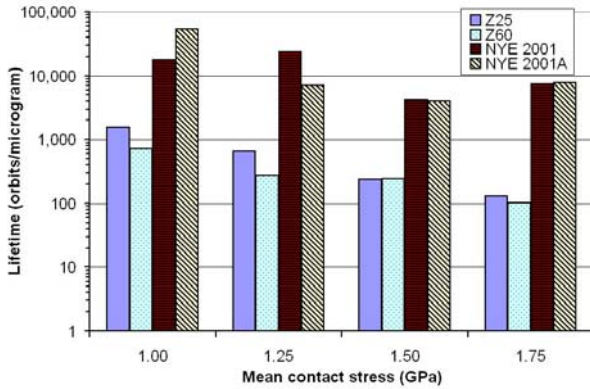


Figure 5. Lifetimes of liquid lubricants as a function of contact stress

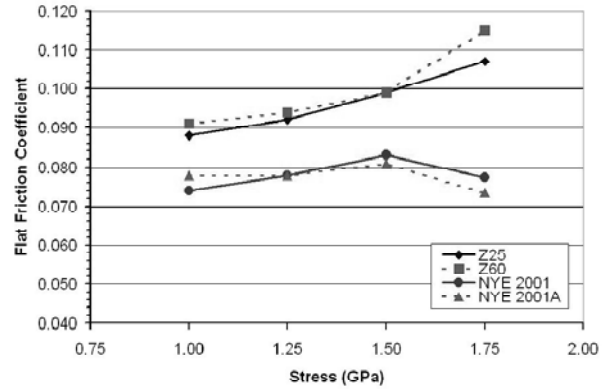


Figure 6. Friction coefficients (assessed at 400th orbit) of liquid lubricants as a function of contact stress

Lifetimes were found to be much reduced for the PFPE oils (Fomblin Z25 & Z60) in comparison to the MAC oils NYE 2001 & 2001A, a result previously seen for these oils under boundary lubrication conditions [5], as well as from past experiences with bearing tests at ESTL, operating in both boundary and mixed lubrication modes [6]. There is also a small but clear distinction in the friction coefficients of the two groups. A comparison of this data with previous studies performed using a SOT by NASA on the lubricants Z25 and 2001A [7, 8] reveals good correlation between the friction and lifetimes of 2001A, but poor correlation when considering the lifetimes of Z25 oil. Lifetimes of Z25 measured by ESTL are some 3x greater than those found in [8]. The likely cause of this discrepancy lies in the differing sample cleaning techniques between the two studies, as surface condition is thought to play a significant role in the degradation rates of PFPEs [9].

The performance of Z60 was very similar to that of Z25, with slightly reduced lifetimes and comparable friction coefficients. Similar results have been observed for these Fomblin oils in non-boundary lubricating conditions [2]. No significant difference was observed between the two NYE oils under the test conditions. This result is curious when we consider that the oil NYE 2001 contains additives to improve this lubricant's boundary performance. However, it is proposed that due to the minimal amounts of oil tested within the SOT (typically 50 µg), resulting in only a few atomic layers of lubricant on the ball's surface, these additives are not replenished once they are removed from the contact zone. Typically there is an oil reservoir present to replace the additives.

All oils displayed a decrease in lifetime, and a corresponding slight increase in friction coefficient, with increasing contact stress, an effect similarly seen in previous studies using a SOT [7]. This behavior demonstrates the sensitivity of these lubricants to contact stress when operating under boundary lubrication conditions. The cause of the potentially anomalous results seen for the MAC oils running at 1.75 GPa is not clear.

Post-test inspection of the samples showed markings on the flat and guide plates from the running of the ball. Inspection with a low powered optical microscope revealed these marks to consist of brown material deposited away from the ball tracks; consistent with the residue of the consumed lubricant.

Grease Lubricant Assessment

Figures 7 & 8 show respectively the lifetime and friction coefficients of the assessed greases. Lifetimes are normalized to orbits/microgram of lubricant, and friction coefficients are taken as the mean of 100 readings around the 400th orbit, and the midpoint of each test (Figure 2). Mean contact stress for all grease tests was 1.50 GPa.

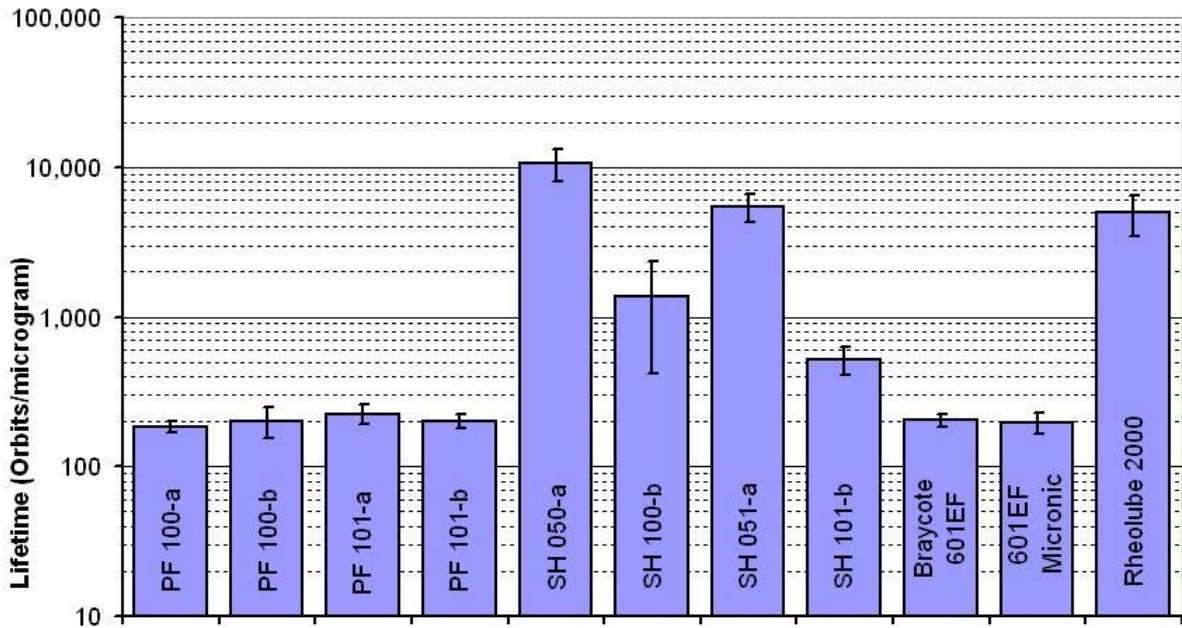


Figure 7. Lifetimes of various greases assessed under vacuum at 1.50 GPa mean contact stress

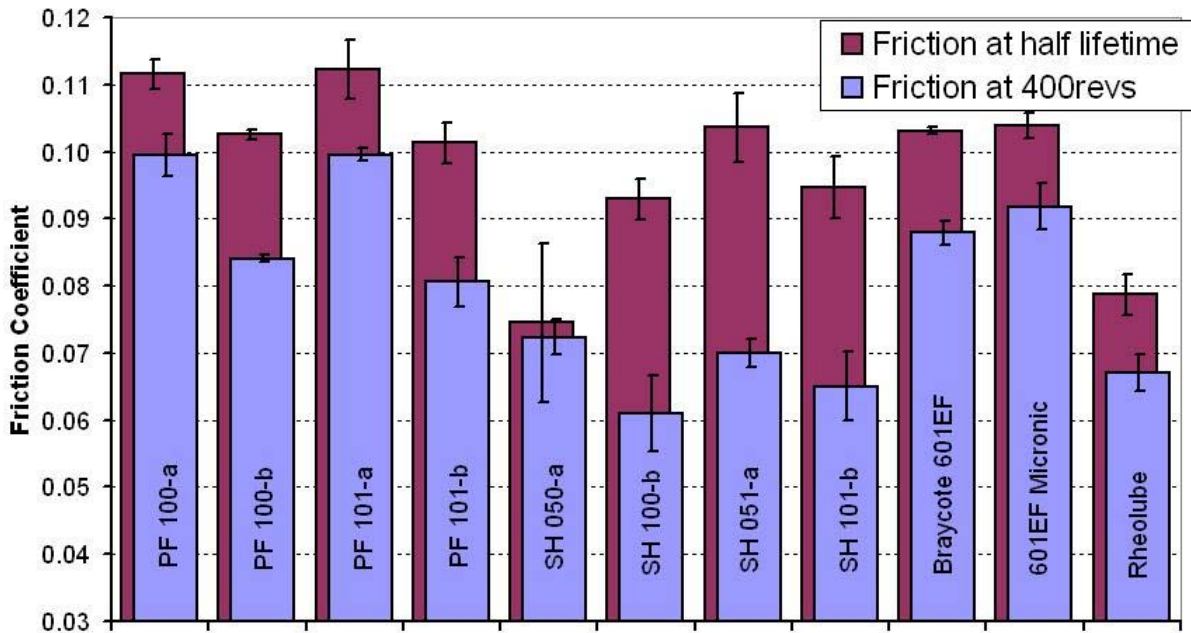


Figure 8. Friction coefficients (assessed at 400th orbit and mid-test) of various greases assessed under vacuum at 1.50 GPa mean contact stress

In general, friction profiles generated from grease lubrication were similar to those of the base oils, with long periods of low friction before a comparatively rapid increase to failure. It was observed that the increase of friction coefficient during the test was more progressive for the MAC greases in comparison to

the PFPE-based greases. This effect has been observed previously when testing greases using a SOT [10, 11].

All tested PFPE-based greases showed little variation in lifetime, with a value of ~200 orbits/ μg for all greases (Figure 7). This value is significantly increased in comparison to studies performed at NASA under similar conditions (30-40 orbits/ μg) [11, 12], and as stated above, this is believed to be a consequence of the differing cleaning techniques implemented. Considering lifetime the inclusion of MoS_2 filler was not found to cause a significant effect, nor was a difference observed between the old (-a) and new (-b) MAPLUB formulations, nor indeed between Braycote 601EF and 601EF Micronic.

Considering the friction coefficients (Figure 8) we find the new MAPLUB PFPE greases display lower friction coefficients than their comparative old formulation greases. This difference is most exaggerated in the early stages of the test. When plotting friction coefficient against orbits, it is seen that the new (-b) greases undergo a change in gradient after a few thousand revolutions (Figure 9), not seen for the old (-a) greases (Figure 10). This difference in the frictional behavior of the greases is the cause of the lower friction coefficients for the new PFPE greases, and is seen when considering greases both with and without MoS_2 filler. The friction coefficients of the Braycote greases fall somewhere between the old and new MAPLUB formulations.

Lifetimes for MAC greases were greatly extended in comparison to the PFPE greases, again in agreement with bearing grease tests at ESTL. Lifetimes for new formulation MAPLUB greases (-b) were seen to be reduced by an order of magnitude in comparison to the old (-a). It is thought this difference can be attributed to the greater viscosities of the new formulations, hampering the re-introduction of grease into the contact surfaces during the tests. In addition, lifetimes for greases containing MoS_2 thickener were found to be less than those containing only PTFE (e.g., SH101/100 and SH050/051). This result is interesting when we consider that the MoS_2 content of these greases is ~1% by volume. Given the minimal amount of grease used per test (~50 μg) it is somewhat surprising to see the addition of such a small amount of MoS_2 apparently effecting the lifetimes to such a degree.

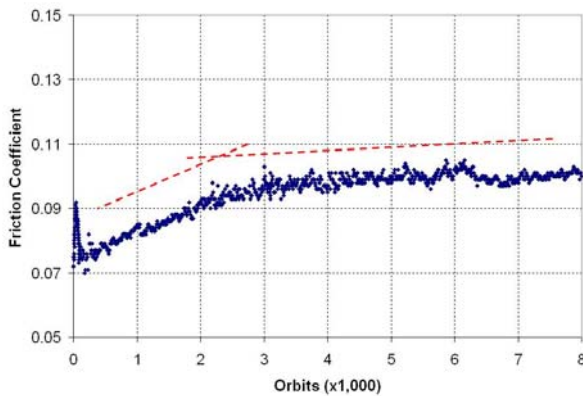


Figure 9. Early stages of PH101-b test, displaying change in gradient around 2,500 orbits

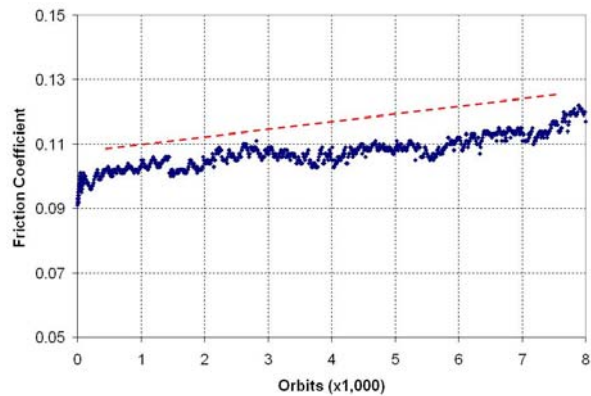


Figure 10. Early stages of PF101-a test, no gradient change

Rheolube 2000 was found to have similar friction to that of the MAC-based MAPLUB greases. This finding is akin to that found in [13], where the performance of low-speed bearings showed comparable torque for Rheolube 2000 and MAPLUB SH050-a & SH051-a. Bearing tests at ESTL have also demonstrated lower torque for Rheolube than Braycote 601 when rotating at low speeds [14], again in accordance with the results generated with the SOT.

Inspection of the samples post-test revealed brown deposits away from the ball track, similar in appearance to those of the base oils, consistent with the degraded lubricants.

Comparison with base oils

The performance of greases in comparison to their base oils is given in Table 3. Values for the oil Castrol 815Z are taken from the SOT commissioning tests performed by ESTL upon delivery of the facility. From the values in Table 3, we see that the performances of the MAPLUB PFPE greases are similar to those of their base oil when considering lifetime, and that the friction coefficients for Z25 fall somewhere between the old and new MAPLUB grease formulations. The change in gradient (demonstrated in Figure 9) is not seen for the base oil. The performance of the Braycote greases is also similar to their base oil Castrol 815Z.

Table 3. Friction and lifetimes of greases and oils assessed at 1.50 GPa mean contact stress under vacuum in the SOT, 100 RPM rotation speed (with the exception of the Z25 oil, performed at 30 RPM)

Grease	Base oil	Lifetime (Orbits/ μ g)	Friction @ 400 th orbit	Friction @ half lifetime
--	Fomblin Z25	239	0.099	0.106
MAPLUB PF 100-a	Fomblin Z25	184	0.100	0.112
MAPLUB PF 100-b	Fomblin Z25	201	0.084	0.103
MAPLUB PF 101-a	Fomblin Z25	225	0.100	0.112
MAPLUB PF 100-b	Fomblin Z25	201	0.081	0.101
--	NYE 2001A	3,937	0.081	0.090
MAPLUB SH 050-a	NYE 2001A	10,653	0.072	0.075
MAPLUB SH 100-b	NYE 2001A	1,376	0.061	0.093
MAPLUB SH 051-a	NYE 2001A	5,492	0.070	0.104
MAPLUB SH 101-b	NYE 2001A	522	0.065	0.095
--	Castrol 815Z	233	0.093	0.104
Braycote 601EF	Castrol 815Z	203	0.088	0.103
Braycote 601EF Micronic	Castrol 815Z	198	0.092	0.104
--	NYE 2001	4,189	0.083	0.090
Rheolube 2000	NYE 2001	4,946	0.067	0.079

MAC MAPLUB greases were varied in comparison to their base oil NYE 2001A when considering both lifetime and friction coefficient. However, friction coefficients were observed to be lower for these greases in comparison to NYE 2001A when considering the early stages of the tests. The grease based on the NYE 2001 oil, Rheolube 2000, gave a similar lifetime, and slightly reduced friction coefficient than that of its base oil. Similar lifetimes of NYE 2001 and Rheolube 2000 (as well as Castrol 815Z and Braycote 601EF) have previously been observed when using the SOT [15].

Solid Lubricant Assessment

Tests on MoS₂ and lead displayed similar behavior to the liquid lubricants, characterized by a long period of low friction before a dramatic increase to failure. In all cases the running-in period to low friction was relatively short in comparison to bearing tests, which can display high torque for many thousands of revolutions. Summaries of lifetimes and friction coefficients for MoS₂ (as a function of coating thickness) and lead (as a function of mean contact stress) are plotted in Figures 11 to 14. Friction coefficients were found from the mean of 100 readings around the 100,000th orbit for MoS₂, and 1,000,000th orbit for lead.

MoS₂

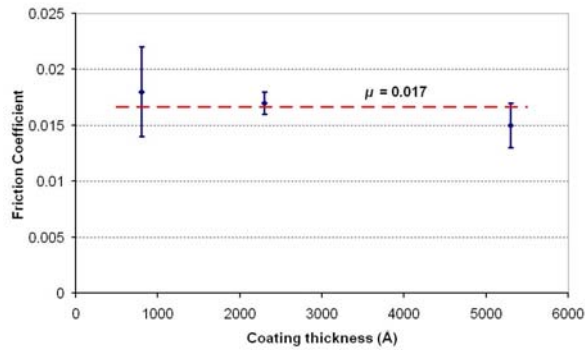


Figure 11. Friction coefficients (assessed at ~100,000th orbit) of MoS₂ as a function of coating thickness

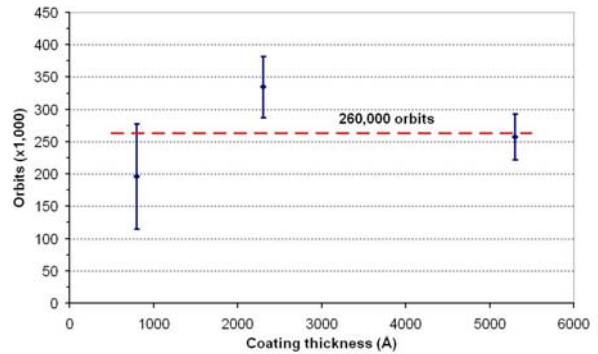


Figure 12. Lifetimes of MoS₂ as a function of coating thickness

For MoS₂ a mean friction coefficient of $\mu = 0.017$ was found, with little variation across the assessed coating thickness range 850 – 5,300Å (Figure 11). In addition, the lifetime of the coating is also not observed to be dependent upon coating thickness within this range, displaying a mean of 260,000 orbits (Figure 12). It is speculated that a greater initial thickness of MoS₂ applied to the ball merely results in greater volumes of lubricant material being lost in the early stages of rolling, with the ball running on a much thinner coating for the majority of its lifetime. X-Ray Fluorescence analysis of the post-test samples revealed no MoS₂ remaining on the ball and loose debris pushed clear of the ball track, demonstrating failure in these cases is caused by removal of MoS₂ by the actions of rolling, sliding and pivoting.

The frictional performance of thin films of lead was found not to vary with increasing contact stress, with a mean of $\mu = 0.046$ found over the tested contact stress range (Figure 13). This friction coefficient is some 2.5x higher than the value found for MoS₂ under similar conditions, a relationship which corresponds well with results from angular contact bearing tests [14]. Lifetimes were seen to decrease with increasing contact stress, an expected behavior, with the lowest stress test (1.50 GPa mean contact stress) being stopped at +3.5million orbits showing no indication of failure (Figure 14).

Lead

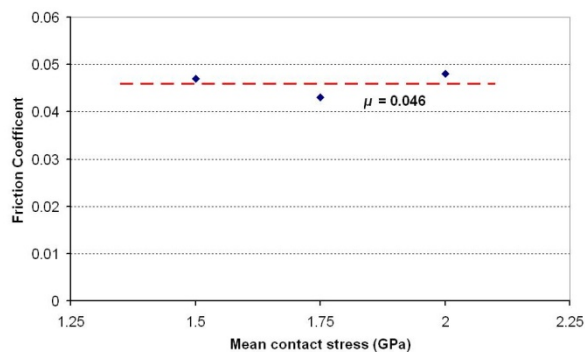


Figure 13. Friction coefficients (assessed at ~1,000,000th orbit) of lead as a function of mean contact stress

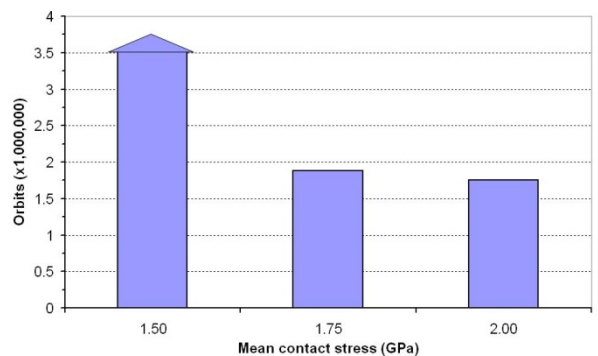


Figure 14. Lifetimes of lead as a function of mean contact stress

Under similar conditions, the lifetimes displayed by thin lead films were extended an order of magnitude in comparison to MoS₂. Similar extension of life when using lead lubrication is seen in angular contact bearing tests [14]. This result demonstrates well the ability of the SOT to assess the performance of thin solid film lubricants in comparison to other tribometers, particularly pin-on-disc (POD) tribometers, which

are capable of only simulating sliding motion. Figures 15 & 16 demonstrate the difference in lifetime gained from these two methods, with the result from the SOT (Figure 15) being a much more accurate model of the behavior seen in angular contact bearings.

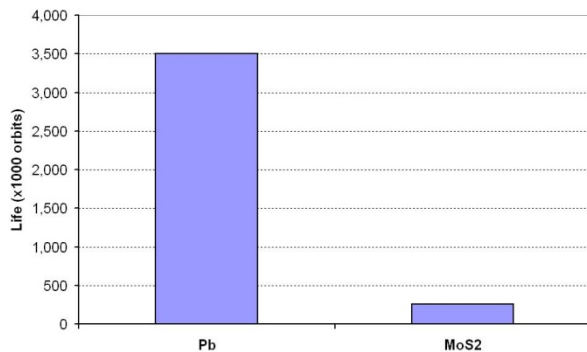


Figure 15. Lifetimes of thin solid films (ball only) as assessed with a SOT

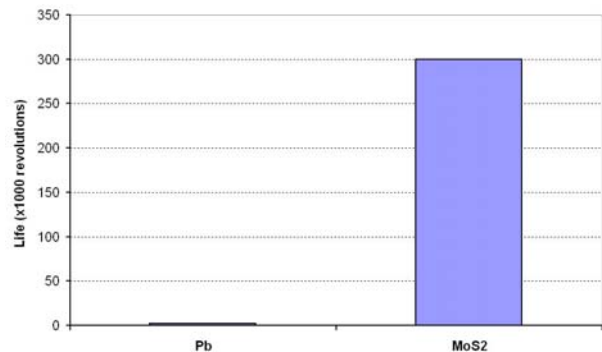


Figure 16. Lifetimes of thin solid films as assessed with a POD tribometer

XRF analysis of the samples used in the 1.50-GPa lead test (+3.5 million orbit lifetime) revealed less than 100 Å of lead remaining on the ball (Figure 17), reduced from the originally deposited 850 Å. Additionally, low but finite lead readings were given in the ball tracks on the flat plates, with the highest readings given in the scrub region (Figure 18). Accurate thickness measurements could not be taken in the ball tracks as the XRF measurement area has a greater diameter than the width of the track (>1 mm). These results lead to the theory that during the test lead is re-distributed from the surface of the ball onto all contact surfaces, promoted by the ductile nature of the lead in comparison to the more friable MoS₂. It is speculated that this process is the cause of the order of magnitude extension in life displayed by lead over MoS₂ running under similar conditions.

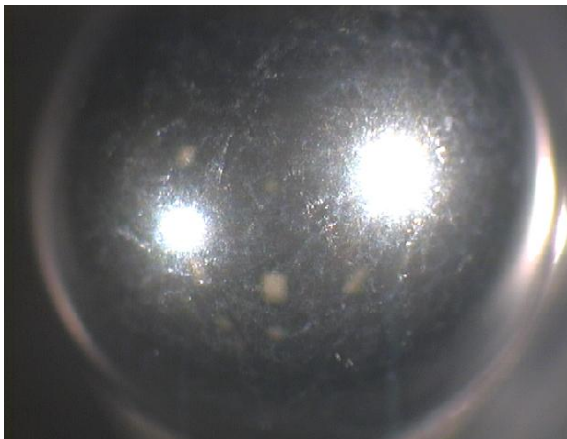


Figure 17. Ball from 1.50-GPa contact stress test on lead, displaying lead mottles on surface. XRF analysis read ~100 Å lead remaining

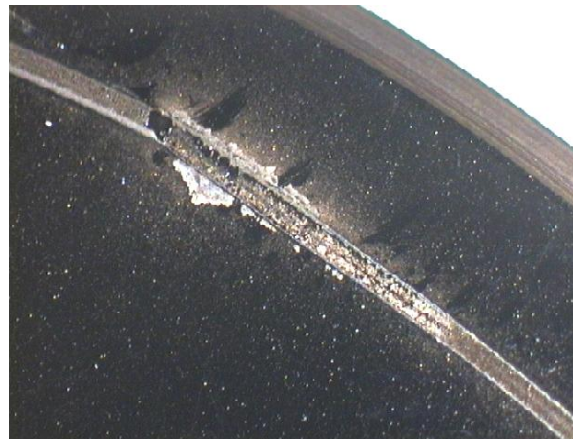


Figure 18. Flat plate (top) from 1.50-GPa contact stress test on lead, displaying lead deposits in scrub region and ball track

Conclusions

The following conclusions are drawn in relation to the tested oils. These conclusions are specific to these lubricants operating under boundary lubrication conditions at ambient temperatures.

- The lifetimes of the hydrocarbons NYE 2001 & 2001A outperform those of the PFPEs Fomblin Z25 & Z60.
- The steady state friction yielded by the tested NYE oils is slightly less than that yielded by the PFPEs at a given contact stress.
- The performance of NYE 2001 is similar to that of NYE 2001A.
- The performance of Fomblin Z60 is similar to that of Z25, with the Z60 oil displaying slightly shorter lifetimes and marginally greater steady-state friction coefficients.
- Increasing contact stress results in decrease in lubricant lifetime.

The following conclusions are drawn in relation to the tested greases.

- Lifetimes are longer, and friction coefficients generally lower for MAC-based greases in comparison to PFPE-based greases under these conditions.
- Little variation in lifetime was found for PFPE-based greases, with all tested greases displaying ~200 orbits/ μg
- Friction coefficients were found to be slightly lower for the new (-b) formulation PFPE-based MAPLUB greases in comparison to the old (-a). This difference was observed to be largest in the early stages of running
- Lifetimes of MAC-based MAPLUB greases were an order of magnitude lower for the new formulations in comparison to the old, suspected to be due to the higher viscosities of the new greases.
- MAC MAPLUB greases containing MoS_2 thickener were found to display reduced lifetimes in comparison to those with only PTFE thickener.
- Braycote 601EF and Braycote 601EF Micronic gave virtually identical lifetimes and friction coefficients.
- The performances of the greases were generally similar to those of their base oils, with the exception being the MAC based MAPLUB greases.

The following conclusions are drawn in relation to the tested solid lubricants.

- Lifetimes of lead coatings are greatly extended in comparison with MoS_2 of similar coating thickness, due to the re-distribution of the lubricant over the test surfaces.
- Lead displays a steady state friction coefficient ~2.5x greater than MoS_2 , comparable to results from ESTL bearing tests.
- The performance of MoS_2 is not dependent upon coating thickness within the range tested, with no strong relationship when considering lifetime or friction.
- The lifetime of lead decreases with increasing load/contact stress.

The Spiral Orbit Tribometer performs well in such investigations. It enables comparative life and friction assessments to be performed on a variety of lubricants on much shorter timescales than conventional ball bearing tests.

Acknowledgements

The author acknowledges Mr. Mark J. Jansen (Spiralab/University of Toledo, OH), Mr. William R. Jones, Jr. (Spiralab/NASA Glenn Research Center, OH) and Mr. Stephen V. Pepper (Spiralab/NASA Glenn Research Center, OH) for their continued guidance, knowledge and advice.

The author also acknowledges Mrs. Helen Hunter, Mr. Ian Pleavin, and Mr. Alan Swift (National Center of Tribology/ESR Technology) for their help in the preparation of test samples.

The work described was performed under contract for the European Space Agency

References

1. Anderson, M. J., 'Review and Identification of European Space-Compatible Oils', ESA-ESTL-TM-0021 (2005)
2. Cropper, M. & Anderson, M. J., 'An Assessment of an Ultra-low Vapor Pressure Oil (Fomblin Z60)', ESA-ESTL-TM-0043 01- (2007)
3. Sicre, J., et al. 'Perpetuation of MAPLUB Grease Range', Proc. 13th ESMATS Symp. SP-670 (2009)
4. Jones, W. R., et al. 'A New Apparatus to Evaluate Lubricants for Space Applications – The Spiral Orbit Tribometer (SOT)', NASA/TM-2000-209935 (2000)
5. Price, W. B. & Cunningham, J. M., 'Boundary Lubricant Tester: Pre-Failure Degradation of Lubricants', ESTL-TM-146 (1994)
6. ESTL, 'Space Tribology Handbook, 4th Edition' (2007)
7. Jansen, M. J., et al. 'Relative Lifetimes of Several Space Liquid Lubricants Using a Vacuum Spiral Orbit Tribometer (SOT)', NASA/TM-2001-210966 (2001)
8. Pepper, S. V., & Kingsbury E. P., 'Spiral Orbit Tribometry II – Evaluation of Three Liquid Lubricants in Vacuum' Trib. Trans. (2003)
9. Jansen, M. J., et al. 'Evaluation of Non-Ozone-Depleting-Chemical Cleaning Methods for Space Mechanisms Using a Vacuum Spiral Orbit Rolling Contact Tribometer', NASA/TM-2000-210050 (2000)
10. Marchetti, M., et al. 'Tribological Performance of Some Pennzane® based Greases for Vacuum Applications', NASA/TM-2002-211373 (2002)
11. Marchetti, M., Jones, W. R. & Sicre, J., 'Relative Lifetimes of MAPLUB® Greases for Space Applications', NASA/TM-2002-211875 (2002)
12. Lo, C. J., et al. 'Use of Cumulative Degradation Factor Prediction and Life Test Result of the Thruster Gimbal Assembly Actuator for the Dawn Flight Project', Proc. 12th ESMATS Symp. SP-653 (2007)
13. Watters, R. B. & Roberts, E. W., 'Torque Behavior of Low-Speed Greased Bearings', ESTL-TM-248 (2003)
14. Cunningham, J. & Swales, G., 'Evaluation of the Torque Performance of a Range of Space-Compatible Greases as a Function of Temperature, Speed & Grease Quantity', ESTL-TM-197 (1997)
15. Marchetti, M., et al. 'Preliminary Evaluation of Greases for Space Mechanisms Using a Vacuum Spiral Orbit Tribometer', NASA/TM-2001-211157 (2001)

Qualification of a High Accuracy Dual-Axis Antenna Deployment and Trimming Mechanism

Alain Gossant* and Francois Morichon**

Abstract

The Antenna Deployment and Trimming Mechanism Mark 2 (ADTM Mk2) has been developed to answer today's need for a generic antenna deployment and high accuracy pointing mechanism, allowing RF sensing applications and easier dual deployments configurations.

This paper presents the design and evolution from its predecessor, the experience of the design team from kick off to qualification and batch manufacture, as well as some lessons learned from ramping up "mass-production" capabilities while implementing customer driven changes.

Introduction

Astrium has manufactured and flown ADTM units for the past 20 years, from an initial deployment-only mechanism developed for the Orion program to today's Eurostar E3000 ADTM family. The Antenna ADTM Mk2 is an evolution of the original ADTM Mk1. Although it uses Mk1 building blocks to minimize risks associated with the development of a new product, it incorporates major evolutions and is the new baseline for Astrium latest generation of Eurostar E3000 telecom satellites.

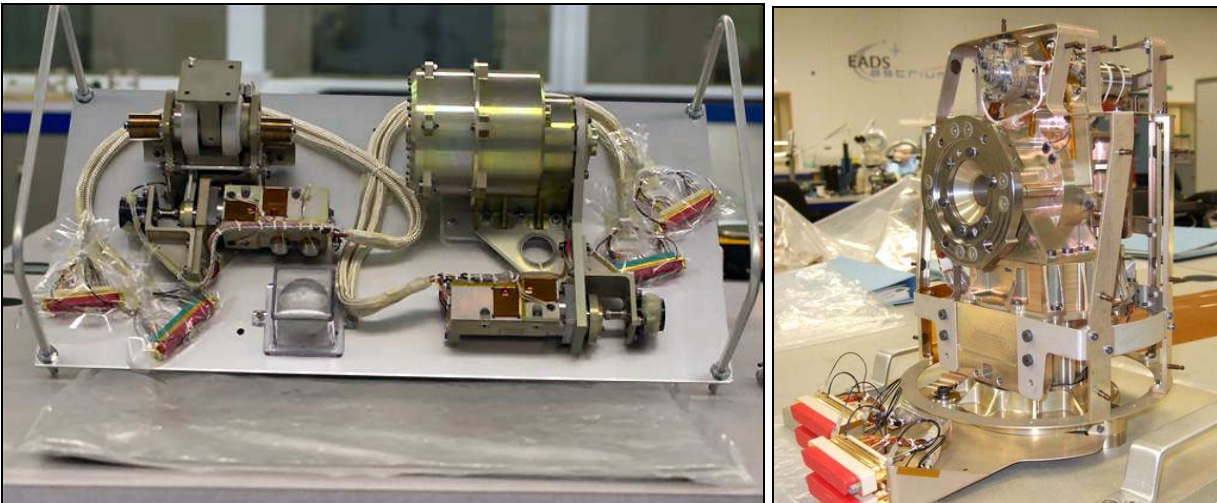


Figure 1: Left = ADTM Mk1 (one-axis), Right = ADTM Mk2 (two-axes) (without MLI fitted)

The ADTM Mk1 is used to deploy large antenna reflectors that are stowed on the spacecraft walls during launch. It is composed of an active trunnion (motive source for pitch deployment and trimming) and a passive trunnion (passive pitch deployment follower and motive source for roll trimming). Deployment is ensured by a passive spring-loaded motor, while each trimming axis is powered by a stepper motor gearbox (SMG).

* EADS Astrium, Stevenage, UK

** EADS Astrium, Toulouse, France

The new ADTM Mk2 is made of two identical one-axis Rotary Actuators (RAs) mounted together (each powered by a CDA Intercorp stepper motor gearbox), with added antenna and spacecraft interfaces as well as MLI enclosure. It has been developed to fulfil the following requirements difficult to achieve with the previous Mk1 version:

- ✓ Compatible with large 2.6+ m diameter antenna reflectors;
- ✓ Compatible with sequenced deployments (complete control of both deployment axes movements), allowing dual antenna deployments. The Mk1 version was single-axis using a passive spring motor for deployment, only capable of a one-off deployment to a mechanical stop;
- ✓ High resolution of 0.0025 °/step over the full range of motion, continuous trimming / re-pointing over the lifetime of the spacecraft, thus compatible with RF sensing applications and/or mission reconfiguration, allowing steering the antenna beam on different Earth locations as requested by the mission management (related to the operators needs);
- ✓ Manufacturing process and number of parts are minimized.

At the time of writing this paper, the ADTM Mk2 Qualification Model has been manufactured and has completed a significant portion of its planned qualification testing.

Table 1: ADTM Mk2 Main Characteristics

Weight: 7.7 kg (includes 2 RAs, spacecraft interface, antenna interface, harness + connectors, MLI)					
Size: 240 x 240 x 290 mm (without connectors)					
Axes: <ul style="list-style-type: none"> · 2 perpendicular RAs, used for deployment and trimming / pointing functions · 120° movement range on each RA · 0.0025 °/step on the whole angular range 					
Operating temperatures: <ul style="list-style-type: none"> · Bulk temperatures: Operational: -25°C to +105°C, Survival: -55°C to +125°C · Antenna interface thermally decoupled from antenna due to a custom thermal washer. Eurostar E3000 typical operational temperature ranges are -95°C to +115°C for antenna side and -10°C to +70°C for spacecraft side. 					
Power consumption: <15 W including thermal control (one axis command)					
Available Output Torque: At least 20 N-m (including 200% margin, or 60 N-m without margin) across the whole operating temperature range.					
Backlash: None up to a minimum of 7 N-m					
Load Capacity (Min):		Axial	Torque	Shear	Bending
	Structure Interface	1600 N	100 Nm	1800 N	240 Nm
	Reflector Interface	1600 N	100 Nm	1800 N	120 Nm
Stiffness: >10,000 Nm/rad around deployment X and Y axes, >40,000 Nm/rad around remaining Z axis					

Design

General Description

The Roll RA controls the deployment and trimming functions of the ADTM Mk2 in the spacecraft antenna roll direction; the rotation axis is perpendicular to the spacecraft wall.

The Pitch RA controls the deployment and trimming functions of the ADTM Mk2 in the spacecraft antenna pitch direction; the rotation axis is parallel to the spacecraft wall and adjusting the antenna pitch. This axis is not fixed with regards to the spacecraft coordinate system but rotates during roll motion.

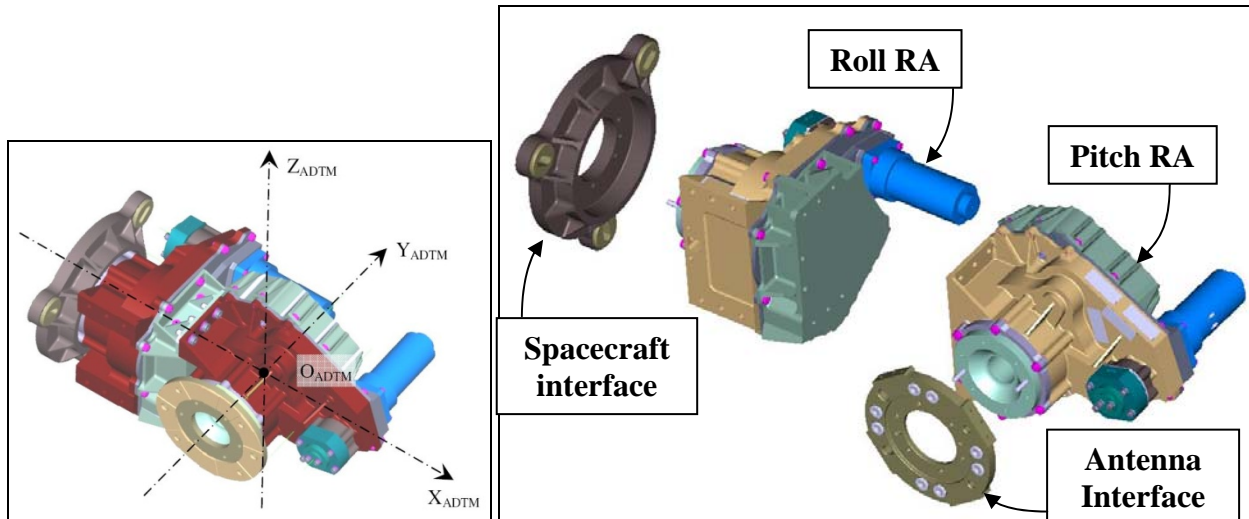


Figure 2: ADTM Mk2 General Description

Key Elements

- Each RA is composed of building blocks from the ADTM Mk1, but re-arranged and providing different functions:
 - ✓ a stepper motor gearbox (SMG) from CDA Intercorp (Florida, USA) providing the active motion for both deployment and trimming functions on Mk2, was used for trimming function only on Mk1,
 - ✓ a spring motor used as an anti-backlash device on Mk2, was performing the main deployment function on Mk1,
 - ✓ a potentiometer monitoring the SMG output shaft (no direct measurement of the RA output shaft)
- spacecraft interface,
- antenna interface, insulating the ADTM Mk2 from the antenna thermally (low thermal distortion)
- thermal control

Anti-backlash



Figure 3: Anti-backlash Spring Motor

The spring motor design here is one where springs are attached to a central torque drum with screws and naturally wound around the storage drums due to their curling treatment. When the torque drum is rotated away from its rest position, an almost constant torque is applied on the torque drum axis throughout the motion range.

In the ADTM Mk2, the spring motor acts as an anti-backlash device, mounted such that it will act in a counter-clockwise direction. Backlash can so only occur when the RA is subjected to a clockwise torque exceeding the spring motor constant preload torque. The size of this spring motor is the limiting factor for

the travel range; 120° range is enough for today's deployment and trimming requirements, and this range can easily be extended by increasing the number of torque drum allowable rotations.

Harness

The harness on the ADTM Mk2 has been designed to accommodate all ADTM Mk2 movements within the space allocated, so that the harness on the satellite side is fixed. This has been accommodated by creating a relaxation loop as shown in Figure 4, allowing $\pm 60^\circ$ rotation around the RA1 roll axis (vertical axis in Fig. 4).

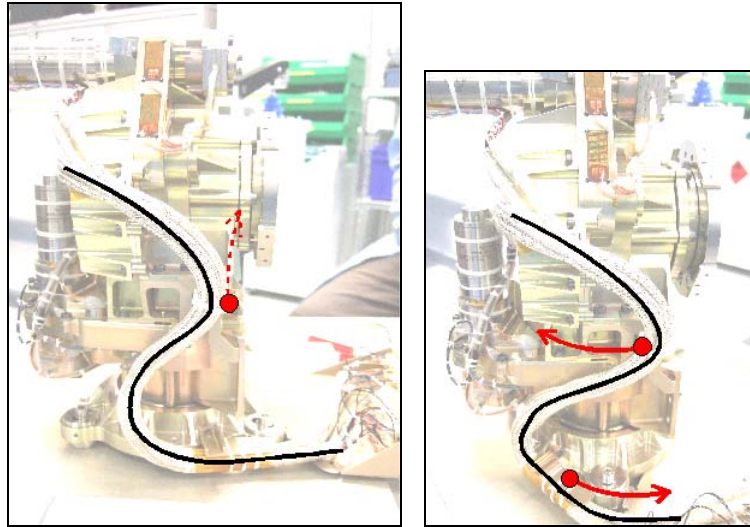


Figure 4: Harness Relaxation Loop,
Left = Roll at reference position, Right = Roll at -60° position

As seen in Figure 4, there are two fixing points, the harness being formed in a loop allowing the RA1 roll rotations. The top mounting point is a pivot point, minimizing harness stress within the whole movement range. The lower bracket is a fixed line contact bracket, guiding the harness loop in the restricted available space.

- ✓ Reference position (left picture on Figure 4): the harness is in its most relaxed position as set during manufacture, and as shown on the left picture the harness is lightly stressing the RA1 roll actuator vertically. This load is easily handled by the RA1 roll output shaft mounted on a duplex pair bearing.
- ✓ 0 to +60° (not shown on Figure 4): the harness loop deploys but the loop itself is remaining similar (similar radius all the way), the top pivot point following the harness thus minimizing torsional stress. The harness is acting similarly as in the reference position, without added torsional stress.
- ✓ 0 to -60° (right picture on Figure 4): although the harness loop is following the movement and the top pivot point minimizes stress, the bottom fixed line contact bracket is forcing the loop to stay in the same location, which decreases the loop radius and therefore increases the torsion stress on the RA1 roll output shaft (spacecraft interface), acting clockwise.

Tests have been carried out using a rapid prototyped ADTM Mk2 with a proper harness routing but with sliding surfaces instead of a duplex pair bearing, and the worst-case torque measured was less than 0.3 N-m, which is not adding significant loads compared to the anti-backlash spring motor and load requirements.

Design Board: The Key Ideas leading to Higher Stiffness

Achievement of high stiffness has been a key target set in the ADTM Mk2 design specification.

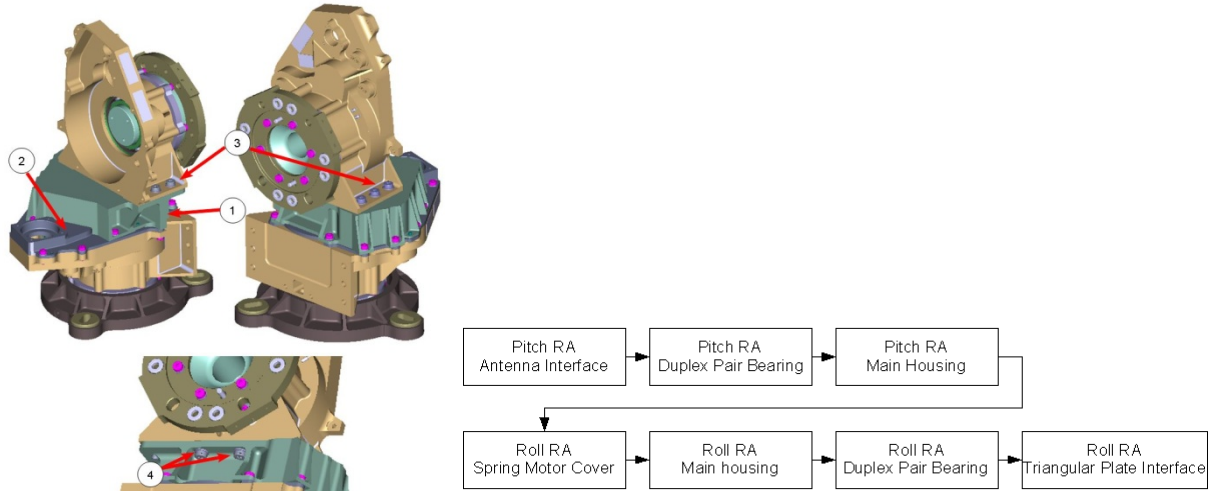


Figure 5: Load Path

Every intermediate part in the load path is another flexibility introduced in the system, so the number of parts used in the load path is minimized to achieve a high global stiffness goal:

- ✓ At position 1 in Figure 5, the preliminary design of the ADTM Mk2 used an additional inter-RA bracket, necessary because of the geometry of the RA and the required relative positions of the roll and pitch RAs (perpendicular crossing axes). It has been determined by stress analysis that growing the roll spring motor cover achieved the same position function but with a higher stiffness.
- ✓ Position 2 in Figure 5 designates the intermediate plate used as the SMG and spring motor mounting bracket. The preliminary design was using a smaller spring motor cover, bolted to this plate, itself bolted to the main housing. Due to the required high loads going through the load path, this roll RA intermediate plate was acting as a flexible membrane, reducing the global stiffness. To avoid this limitation, the spring motor cover has been extended to the main housing border, and bolts are all directly screwed from the spring motor cover, through the intermediate plate, to the main housing. This resulted in much improved stiffness response, with an acceptable mass increase.

Specified stiffness was also achieved during design phase by further structural improvements:

- ✓ Webs have been strategically placed to improve reinforcement of the structure in relatively high load areas. Similarly, thicknesses have also been increased in the higher stress areas.
- ✓ Position 3 in Figure 5 highlights the "legs" of the RAs main housing, used to mount the pitch RA onto the roll RA. These are very similar to the ADTM Mk1 active trunnion design. They are fairly far apart to ensure good moment stiffness results around the pitch Y axis; the right stiffness around the other axes is achieved by adding two screws at position 4 in Figure 5, better linking the pitch RA to the stiff roll RA spring motor cover. This solution was much better in terms of manufacturing, mass and volume than for example having additional brackets between the two actuators.
- ✓ The preliminary design of the triangular plate interface with the spacecraft was flat, and with only 3 attachment points (to allow better accommodation on the spacecraft), it was acting as a membrane. It has been reinforced as much as possible within the ADTM Mk2 volume and movements constraints by adding a thick cylinder plus webs all around. It is now a very stiff bracket (see Table 1) comparing favorably with the duplex pair bearing stiffness.

"Mass Production"

Gearing towards Mass Production

The ADTM Mk2 has been developed to better answer dual deployment requirements, which is now becoming the standard. This means that instead of one large antenna per East/West spacecraft wall, two large antennas are to be deployed on each wall. A few spacecraft were equipped with ADTM mk1 for dual deployments but as it is a single deployment axis mechanism, heavy and voluminous support structures were needed to have the right orientation of the mounting plane of the mechanisms.

Once qualified, the ADTM mk2 is intended to become the baseline deployment mechanism for E3000 spacecraft. It has to cope with any mission, meaning it has to have a fine angular resolution of 0.0025° on the whole angular range, be compatible with the top floor antenna environment (earth-facing wall), and fulfil the most severe missions like RF-sensing missions requiring in-orbit daily trimming operations over the whole lifetime of 15 years.

Therefore, the number of ADTMs required per spacecraft has at least doubled compared to Mk1, and production of this equipment needed to be scaled up to cope with the demand. The design and development phase of the ADTM mk2 was done taking into account the expectations of the first customers. Today (18 months later), we have successfully passed all major reviews and are close to the end of qualification. The first batch of 20 units is in manufacturing and delivery and another half from the next batch2 production has been sold. This has been a fast-paced development, only possible thanks to the dedication of the team and the close co-engineering we developed with our internal and external customers.

Electrical Ground Support Equipment (EGSE)

The ADTM mk1 is a "passive" mechanism for deployment which is driven by springs; only the trimming function is done using electrical actuations. The ADTM mk2 requires electrical actuations whatever the operation: deployment or trimming, and this on a wider angular range. Although the number of ADTM per spacecraft has increased, the specification requires a lot more data about performance of the units and family data comparison than in the past with the Mk1. It has been very challenging to conceive, manufacture and validate a new EGSE within the short time between kick-off and the first tests.

To cope with the increased amount of tests, data and analyses now required, three identical EGSE have been developed in parallel to the ADTM Mk2, each capable of testing up to four ADTMs in parallel (consistent with most dual deployments spacecraft where four antennas are to be deployed), enabling the automation of most of the functional tests performed on the ADTM Mk2, recording all data and pass / fail status in a spreadsheet.

The EGSE units programmed under Labview environment produce extremely useful data. The amount of data collected today is large (~0.5 GB per functional test per unit) but is currently necessary to clearly understand and characterize the behavior of the ADTM. It is planned to make a data reduction exercise in the future once we have a clear understanding of what parameters are important to monitor.

Design Lessons Learned

Load through the output shaft

A duplex pair bearing supports the RA output shaft. It is designed to survive the specification worst case design loads. These have continuously increased throughout the project, exceeding the initial allowable design loads. This led to modifications of the preliminary design of some of the screwed joints within the RA.

These screws are used to preload the RA output shaft duplex pair bearing and retain a gear onto this shaft. Due to increased torsional loads requirements, these were not strong enough to eliminate sliding between the gear and the output shaft during spacecraft launch; up to 2.5 degrees shift can occur. The

solution implemented during detailed design phase was to add shear pins and corresponding hole / slot at the gear / output shaft interface, as well as to increase the size of the screws allowing higher preload, and therefore increasing the sliding threshold. The lesson here is to always allow enough contingency overall to cope with likely increased requirements and to recognize the benefit of shear pins which are less dependent on the bolted joint to prevent sliding.

Harness Routing

The overall azimuth movement range is 120°. This movement is composed of long strokes at beginning of life (deployments during ground tests, then in-space deployment after up to 6 years ground storage), and then subsequent small movements over the lifetime (15 years in-orbit). These small movements are daily continuous for Radio Frequencies (RF) sensing applications.

The harness design has been chosen mainly due to the volume constraints requirements, and include a relaxation loop (left picture of Figure 4). Design of the relaxation loop has been greatly accelerated and proven to be a good concept due to the use of rapid prototyping early in the project. However, both RAs being identical, they have the same harness length, leading to different connectors positions. A tooling bracket is used at ADTM Mk2 level to ensure each RA harness achieves the same positions consistently. Integration at ADTM Mk2 level of two RAs proved difficult to consistently achieve these positions, due to small variations of the cabling inside the harness. Harness bending / routing reflects these variations, and influences significantly the end position of the connectors. A solution for this was to implement longer wires with temporary connectors at RA level for tests, and cut to length at ADTM Mk2 level then wire the final flight connectors.

Qualification

Qualification Status

At the time of writing this document, initial functional and post mechanical (i.e. vibration & shock) tests have been performed on the qualification model and some flight models (FMs). Functional tests consist of RA torsional stiffness measurements (including backlash threshold verification), resistances + insulation + grounding measurements, axes perpendicularity and coning measurements, full sweep motion over the complete angular range of both RAs (for step size accuracy and repeatability), minimum start-up voltage (for torque margin analysis) and hysteresis performance across the operating range.

Thermal Balance has been performed on the qualification model and thermal model correlation performed. Thermal Vacuum tests have been performed on both qualification model and the first four FMs. The qualification model will continue to final functional tests and life test sequence.

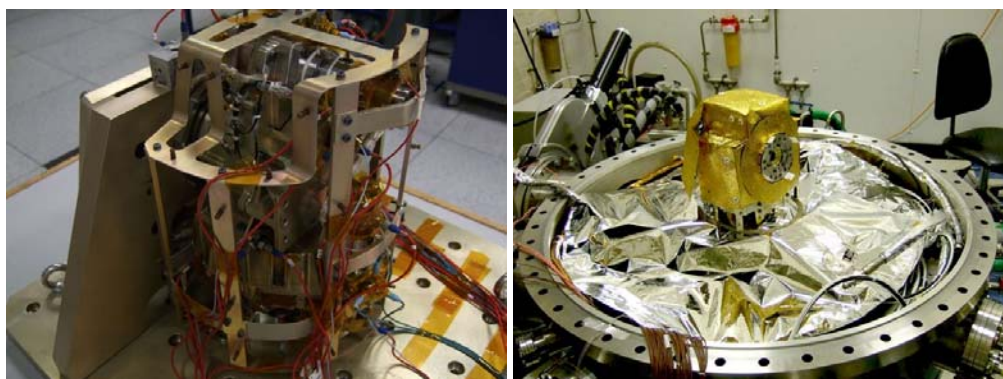


Figure 6: ADTM Mk2, Left = Vibrations and Shocks Setup, Right = Thermal Balance Preparation

Coning and Stiffness results

The requirements for coning and stiffness measurements have been met; Figure 7 shows a few pictures representative of the performance achieved.

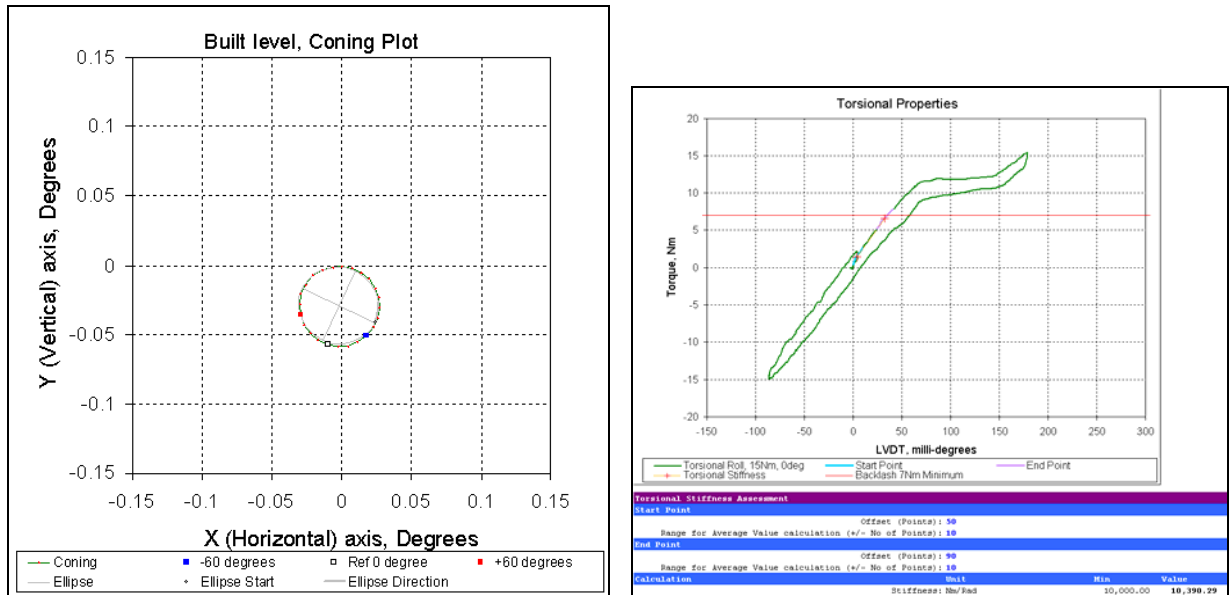


Figure 7: Left = Coning measurement, Right = Stiffness + Backlash measurements

Tests Lessons Learned

Step size Accuracy

The step size accuracy is one of the key functional parameters of the ADTM Mk2 when used for RF sensing missions. The performance of the closed control loop system is indeed improved when the dispersion of the step size is low. The knowledge of the step size accuracy is therefore fundamental and has to be characterized during qualification and acceptance tests.

To measure all the steps sizes (which are nominally 0.0025° /step) with the required resolution, a 22-bit encoder (resolving down to $360^\circ/2^{22} \approx 0.000086^\circ$, which is 3.4% of the nominal step size) mounted on the output shaft of the monitored axis was selected. Measurements are made during a full sweep cycle of the 120° angular range in functional tests, an example is shown below in Figure 8.

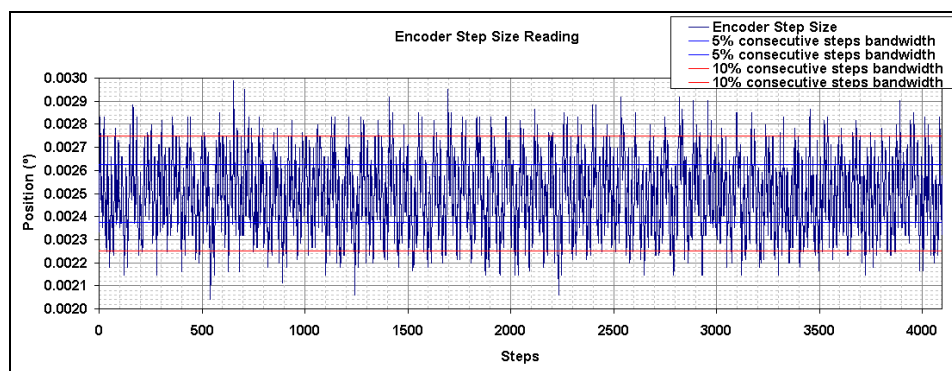


Figure 8: Encoder Step Size Reading during Motion

Zooming on Figure 8, some repeatable frequencies seem to occur, as seen in Figure 9.

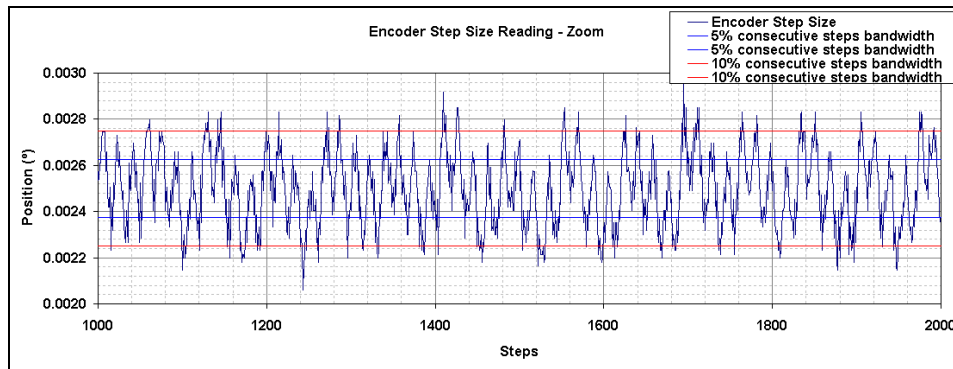


Figure 9: Encoder Step Size Reading during Motion, Zoomed In

Further investigating this in an Excel spreadsheet and using the discrete Fourier Transform by FFT on the encoder and ADTM Mk2 potentiometer readings, the plots shown in Figure 10 were produced.

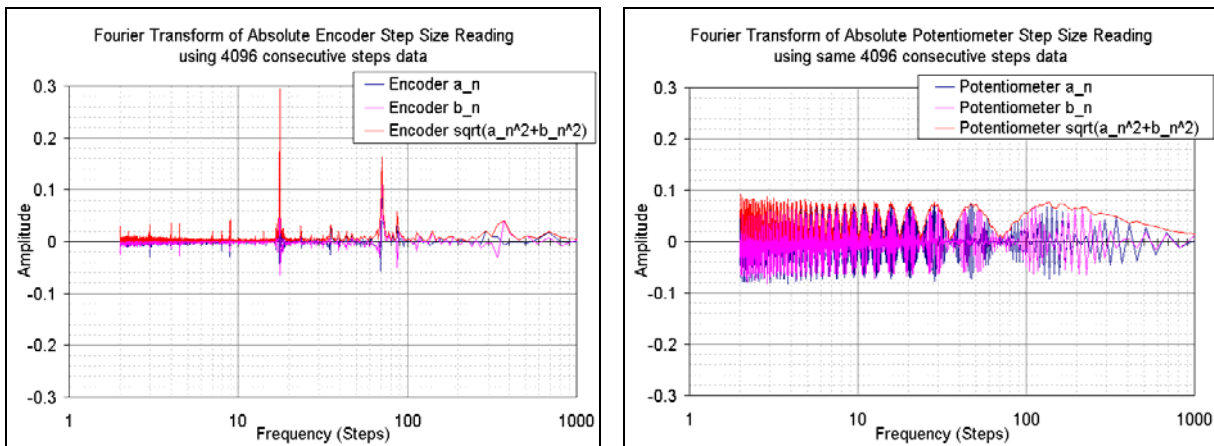


Figure 10: Fourier Transform of step size over 4096 consecutive steps, left = Encoder Fourier transform, right = Potentiometer Fourier transform

The Fourier transform on potentiometer data does not yield exploitable results (aberration from the FFT algorithm, no frequency detected in the noise of the potentiometer reading), but the FFT on the encoder data does make the frequencies very easy to read.

Further thoughts on the root cause lead to calculate all the ADTM gearboxes tooth to tooth frequencies, which converted back to output step size are the following: 1.125, 8.889, 54, 360, 2400steps.

The FFT analysis tool in MS Excel is limited by the maximum of 4096 samples. This leads to a frequency analysis only possible in the range 2 to 2048 steps (if taking 4096 consecutive steps), with a very rough resolution in the higher steps frequencies and a good resolution in the lower steps frequencies. So in the identified frequencies above, the 1.125 and 2400 steps one won't be visible. Note: to increase resolution on higher steps frequencies, it is possible to analyze 16384 steps modulo 4 (i.e., 4096 samples), but this method cannot be extended indefinitely as we will then hit the maximum mechanical range of the ADTM Mk2.

In the left plot of Figure 10, only 8.889 and 360 can be identified, 54 does not appear.

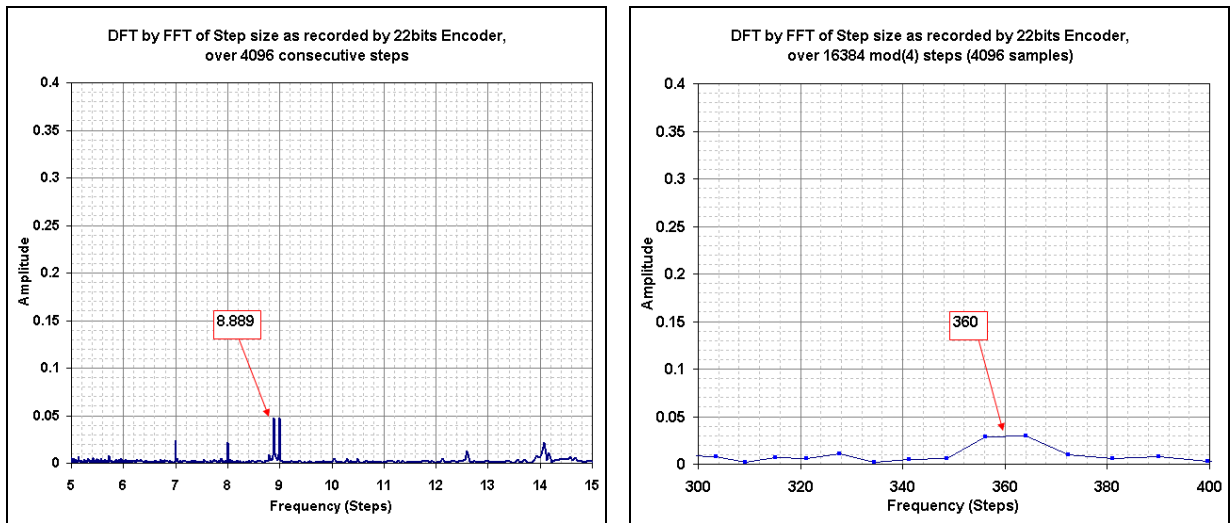


Figure 11: Fourier Transform, Zoom-In

However, this does not explain the much higher amplitude frequencies found in the left plot of Figure 10. Looking now at the encoder itself, it returns a 22-bit position with normal binary numbers. Calculating the relationship between bits number and the equivalent steps length, the frequencies shown in Table 2 appear.

Table 2: Relationship between Encoder bits and Steps Frequency

Encoder Bit	Bit Changes over 360°	Angle per Bit Change	Steps per Bit Change
22	4194304	8.58307E-05	0.034332275
21	2097152	0.000171661	0.068664551
20	1048576	0.000343323	0.137329102
19	524288	0.000686646	0.274658203
18	262144	0.001373291	0.549316406
17	131072	0.002746582	1.098632813
16	65536	0.005493164	2.197265625
15	32768	0.010986328	4.39453125
14	16384	0.021972656	8.7890625
13	8192	0.043945313	17.578125
12	4096	0.087890625	35.15625
11	2048	0.17578125	70.3125
10	1024	0.3515625	140.625
9	512	0.703125	281.25
8	256	1.40625	562.5
7	128	2.8125	1125
6	64	5.625	2250
5	32	11.25	4500
4	16	22.5	9000
3	8	45	18000
2	4	90	36000
1	2	180	72000

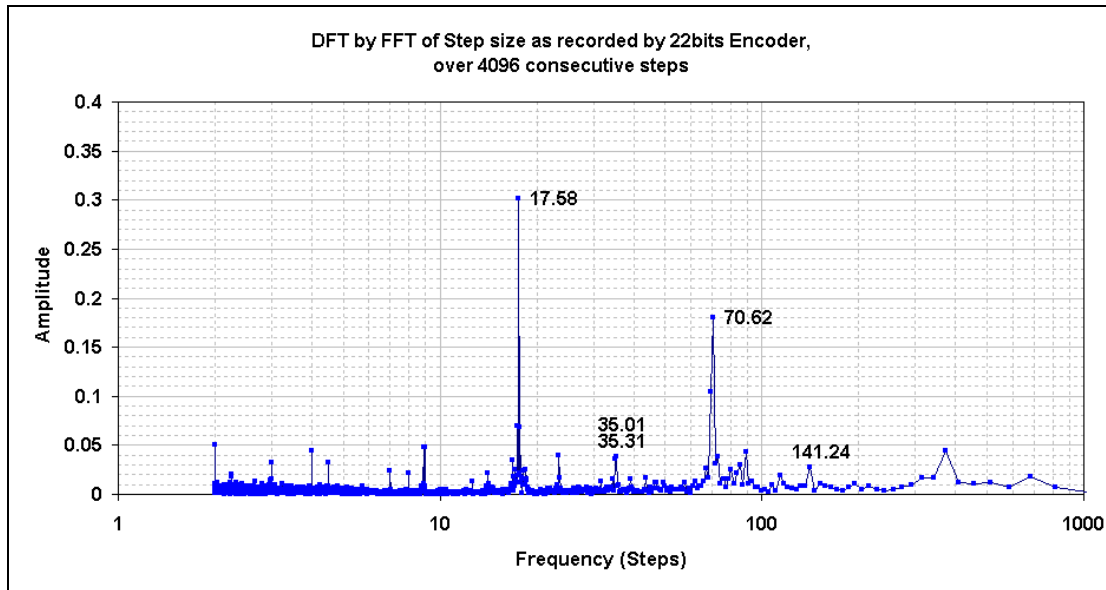


Figure 12: Fourier Transform, Zoom-In bis

Looking back to Figure 10, some of these frequencies do appear in the readings. In particular, in Figure 12, the amplitude seen at the positions corresponding to the 11th bit (70.31 steps) and 13th bit (17.58) are the major contributors to the error recorded by the encoder. Thus it seems that most of the error recorded by the encoder during functional tests is actually generated by the encoder itself. Looking in detail at the encoder technology used, it appears that only the first 11 bits are real mechanical bits, and the rest of the bits are interpolated using sine / cosine signals in the encoder. Therefore, it would appear that the interpolation algorithm used has some edges effects that are very significant compared to the data read resolution.

There is a lesson learned here: we should not select high precision measuring equipment only based on claimed accuracy by the supplier, but should also qualify such equipment beforehand. In this case, the supplier claimed a much finer absolute accuracy than what we are actually seeing using the FFT function, and this is repeatable on all the encoders we have bought for mass production tests. At the time of writing this document, alternative measurement equipments are being investigated, but we now have a better understanding of our current test equipment and may be able to correct data after calibration, although this is an on-going activity as well.

Despite the disturbances of the step size accuracy introduced by the test encoder, the ADTM mk2 performances have been proven to be compliant with the targeted flight applications.

Thermal Vacuum (TVAC) Tests with an Inertia

When testing the qualification model in a TVAC configuration (after thermal balance), it was initially planned to attach the pitch output shaft to a rigid inertia to simulate the worst case antenna load. To achieve this, a 90 kg-m² inertia was to be used outside the chamber, with a shaft linking it to the ADTM unit via a feed-through on the top of the TVAC chamber. The main interest for this inertia was to be able to measure hysteresis, and preliminary tests proved that the pass-through seal had too large an influence on the results to be of any use, as shown in Figure 13.

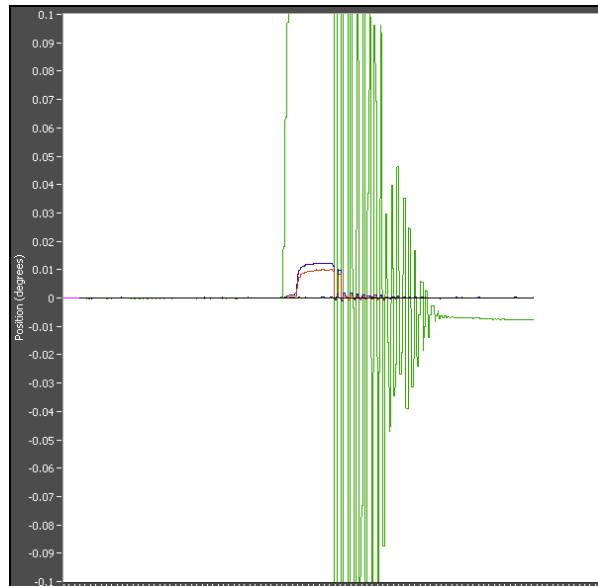


Figure 13: Inertia Test

On the Figure 13, the inertia was loaded to apply ~ 25 -Nm load on the ADTM shaft, and then released free, the idea being to make a quick verification of the frequency response of the setup. The green line is the inertia movement read by the encoder, and the other lines are the prime and redundant potentiometer monitoring the SMG movements. This test enables us to measure a few things:

- ✓ First the backlash measured on the potentiometers when loading the inertia corresponds to the SMG backlash, which is apparent when the applied load on the RA output shaft is compensating the spring motor anti-backlash device (>7 Nm). The backlash measured on the SMG here is $\sim 0.01^\circ$, or 4 steps.
- ✓ The other interesting information from this plot is the hysteresis of the inertia: after the test, it settled about 4 steps away (according to the encoder) from its start position. So here again, the lesson learned is that to measure sensible data on very small movement, it is necessary to really think through all the possible causes of friction that would influence significantly the results (here: passing through a TVAC chamber seal).
- ✓ And finally, zooming in the data it is possible to extract the length of a cycle of the inertia during motion, which corresponds to the natural frequency of the system. Here it was measured to be at ~ 1.15 Hz.

Conclusion

The ADTM Mk2 has been a challenging program. New mass production test equipment has been developed and is still being improved to cope with the higher demand (more than double from Mk1 versions). Qualification and flight productions have been and still are running in parallel successfully, thanks to the good cooperation between the prime customer and the ADTM team.

First qualification test results were as expected and demonstrated the robustness of ADTM mk2 design. Some lessons have been learned along the way, such as design improvement rationale and also test equipment selection and calibration, such as encoder accuracies. Combination of analyses and units tests results are being collected to allow family data to be built up and presented (as is being requested more and more by our customers). Production is on its way!

Even if today the ADTM Mk2 fulfils the most stringent requirements for the current flight missions, the anticipated evolution of these missions continues to require better performances like a smaller step size

or increase of the angular range. The lessons learned during the development of the ADTM Mk2 will be invaluable to complete the development on time and on cost of a mechanism with higher performances.



Figure 14: ADTM Mk2 Project Team

Scanning Mechanism of the FY-3 Microwave Humidity Sounder

Manfred Schmid^{*}, Li Jing^{**} and Christian Hehr^{*}

Abstract

Astrium GmbH Germany, developed the scanning equipment for the instrument package of the Micro-Wave Humidity Sounder (MWHS) flying on the FY-3 meteorological satellite (FY means Feng Yun, Wind and Cloud) in a sun-synchronized orbit of 850-km altitude and at an inclination of 98.8°. The scanning mechanism rotates at variable velocity comprising several acceleration / deceleration phases during each revolution.

The Scanning Mechanism contains two output shafts, each rotating a parabolic offset Antenna Reflector. The mechanism is operated in closed loop by means of redundant control electronics.

Introduction

MWHS is a sounding radiometer for measurement of global atmospheric water vapour profiles. An Engineering Qualification Model was developed and qualified and a first Flight Model was launched early 2008. The system is now working for more than two years successful in orbit.

A second Flight Model of the Antenna Scanning Mechanism and of its associated control electronics was built and delivered to the customer for application on the follow-on spacecraft that will be launched by the end of 2010.

Instrument Description

The operating frequencies of MWHS include both the atmospheric transparent window at 150 GHz and the water vapor absorbing lines around 183.31 GHz. The 150-GHz radiometer has two polarizations (V and H) and the 183.31 radiometer has three channels (from ± 1 to ± 7 GHz around 183.31 GHz).

The instrument comprises four major functional units, namely the Antenna Scanning Mechanism (ASM) with Antenna Reflectors and Feed Horns, the Motor Control Drive Electronics (MCDE), the Front-end Receiver with Receiver Electronics and the Instrument Electronics Unit. An Instrument block diagram is shown in Figure 1.

The scanning equipment (shown in the center of Fig. 1) includes the Scanning Mechanism, the Antenna Reflectors and the Feed Horns, all mounted to a base-plate on top of the instrument.

^{*} EADS Astrium GmbH Satellites, Friedrichshafen, Germany

^{**} Centre for Space Science and Applied Research, CAS, China

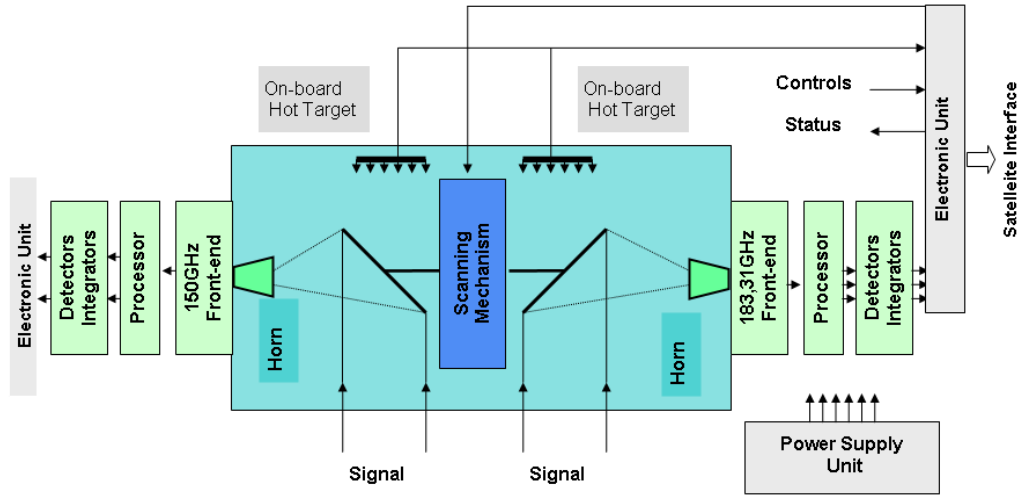


Figure 1. Instrument Block Diagram

The arrangement of the MWHS instrument on the spacecraft is shown in Figure 2. The Scanning Unit is mounted on top of the instrument electronics compartment (shown in Figure 2 on the right side). Figure 3 depicts a typical picture taken by MWHS, showing the global brightness temperature.

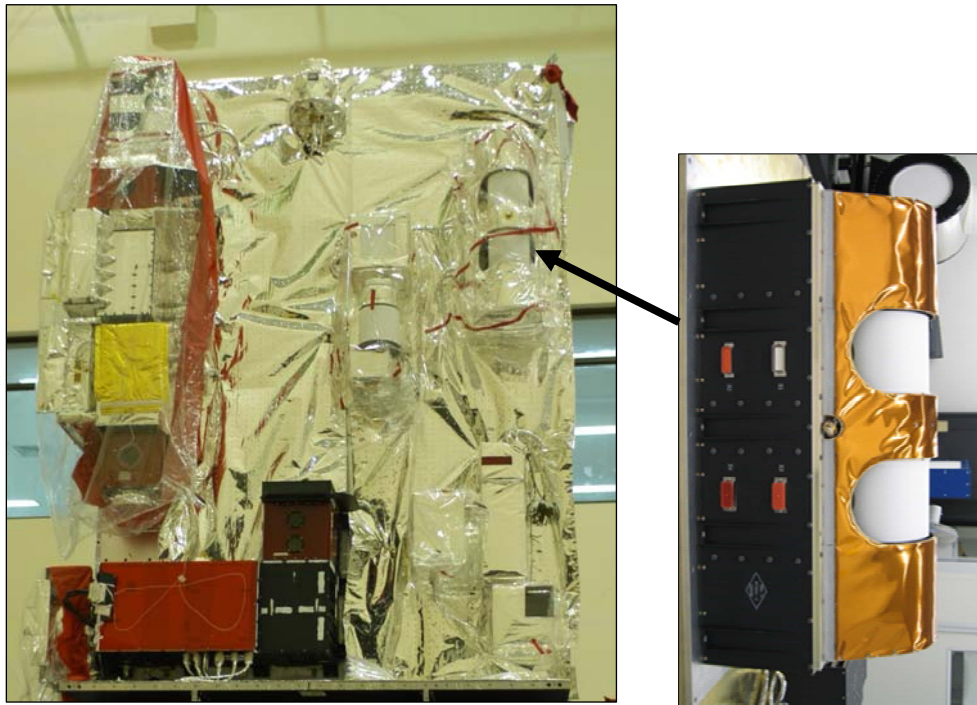


Figure 2. MWHS Instrument Configuration on FY-3 Spacecraft

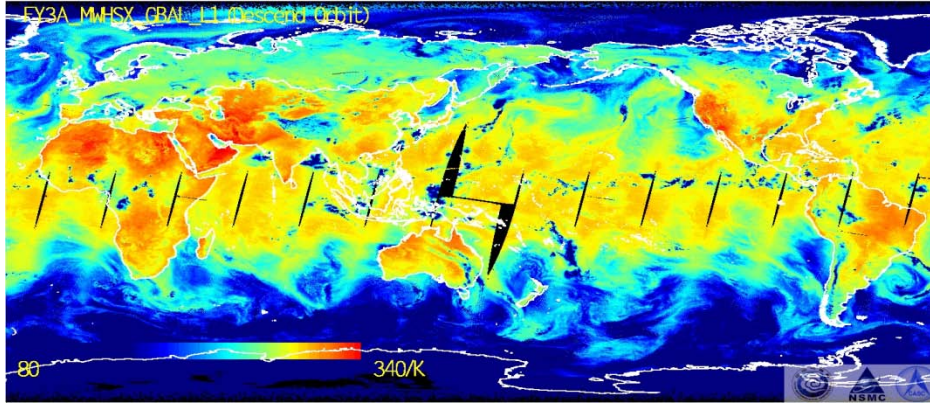


Figure 3. Global Brightness Temperature taken by MWHS

Key Requirements

Major mechanism functional performance characteristics are the scan velocity constancy, the scanning time accuracy, the pointing accuracy (calibration), and the capability to accelerate/decelerate the Antenna Reflectors within a minimum time in order to maximize the observation time during each scan period.

Switch-over capability between three different scanning modes is provided. There is the nominal scan mode with its variable speed, a constant velocity mode without hot/cold calibration, and the possibility to stop the scan at each arbitrary position. The equipment orbit life requirement of 3 years leads to about 36 million mechanism revolutions at nominal operation.

A summary of the key requirements is shown in Table 1.

Table 1. Key Requirements

Requirement	Value
Orbit Altitude	836 km
Swath Width	2700 km
Spatial resolution (Nadir)	15 km
Power consumption	< 18W
Power Supply	DC: 27V, ±12V, +5V
Mass	15 kg (overall, incl Base Plate and thermal H/W)
Environmental temperature	-30° ~ +55°C
Life	>Three Years
Viewing Angle (Earth Scan)	+/-53.35°
Scanning speed error (during earth scan)	1 %
Pointing Accuracy	<0.1 deg
Scanning Period	2.667 s ± 50 ms
Scan profile	Scheme 1: Nominal Scan profile Scheme 2: constant speed in 2.667 s period Scheme 3: stop at any position
Operation Frequency	150 and 183 GHz

The nominal operational instrument rotation speed is variable (hot calibration, cold calibration, earth scan and motion between these three angular ranges). The earth scan takes 1.71 s for 106.7 deg. of scan angle.

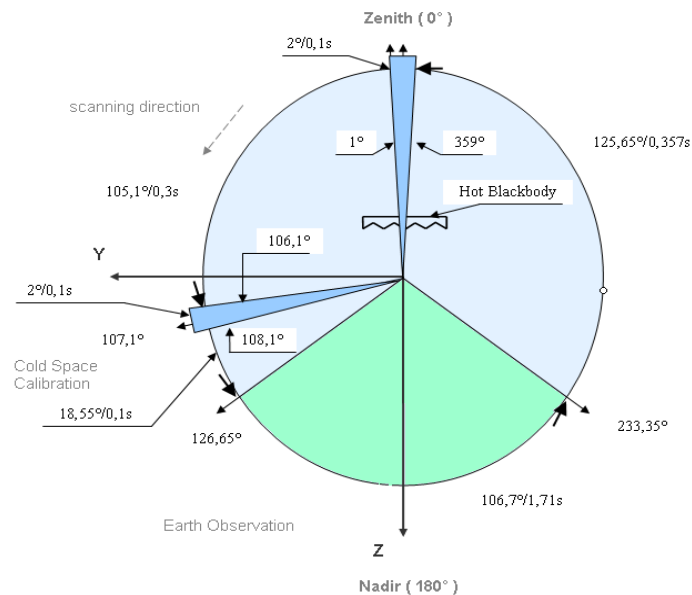


Figure 4. Scan Profile

Scan Mechanism Overview and Configuration

The Antenna Scan Mechanism uses a Base Plate on top of which the Scan Drive Unit is mounted. The Scan Drive Unit comprises a brushless DC Motor with redundant stators and a redundant 17-bit optical encoder for closed loop velocity, respectively position control. The controller is FPGA based and included into the Motor Control Drive Electronics (MCDE). The motor carries two output shafts. One Antenna Reflector is mounted to each of the output shafts in order to allow simultaneous and synchronous rotation of both reflectors. The incoming signal is focused via the two reflectors to the focal planes of the overall three Feed Horns mounted to support structures on either end of the Base Plate.

Some important design features are:

- The mechanism is equipped with two pairs of pre-loaded ball bearings in face to face arrangement. In combination with the direct drive, the output motion is free of backlash and hysteresis.
- A very good scan speed performance (low speed error) is achieved by the controller using sine commutation and by mechanical optimization of the motors for low detent torque.
- The mechanism is designed for high dynamic performance (high reflector acceleration) and energy efficiency. This implies minimization of the moment of inertia of the rotating masses.
- The flexible control electronics interface allows fine definition and rotational adjustment of the reflector mechanical zero position even on the spacecraft level.

The rotating mass' moment of inertia ($<0.007 \text{ kg}\cdot\text{m}^2$) was minimized, not only to avoid a momentum compensation drive in the mechanism which would have increased the mechanism complexity, but also to minimize for power consumption and to provide maximum reflector acceleration capability, leading to a maximum of useful earth observation time. This goal was achieved by designing light weight antenna reflectors from aluminium with an attached lightweight thermal shield ("barrel"), rotating together with the reflectors.

Since the Drive Unit carries the rotating Antenna Reflectors, it has to be aligned with high accuracy with respect to the Feed Horns (Front Ends) mounted to both sides of the Drive Unit. Due to the fact that the base plate thickness was limited to 20 mm maximum, special attention had to be paid to limit the mechanical and thermal deflection of the Base Plate especially in combination with the attachment interface on instrument side. After specifying the interface planarity on Instrument side, the AI base plate was designed as a milled structure with stiffening ribs, closed by a thin Al cover plate attached to its bottom by means of screws and dowel pins in order to achieve a box-type structure providing good bending but also adequate torsion stiffness at low sensitivity against thermal gradients.

Figure 5 shows the arrangement of the Scan Drive Unit and Antenna Reflectors on the Base Plate. The Front Ends with Antenna Horns are mounted to each end of the Base Plate.

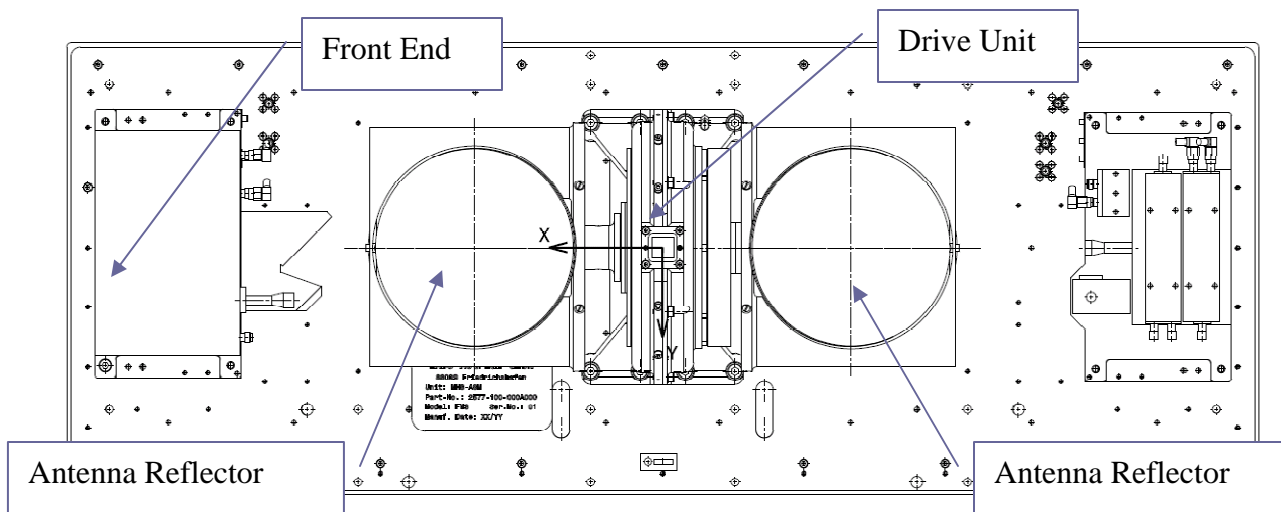


Figure 5. Top View of Antenna Scan Mechanism (ASM)

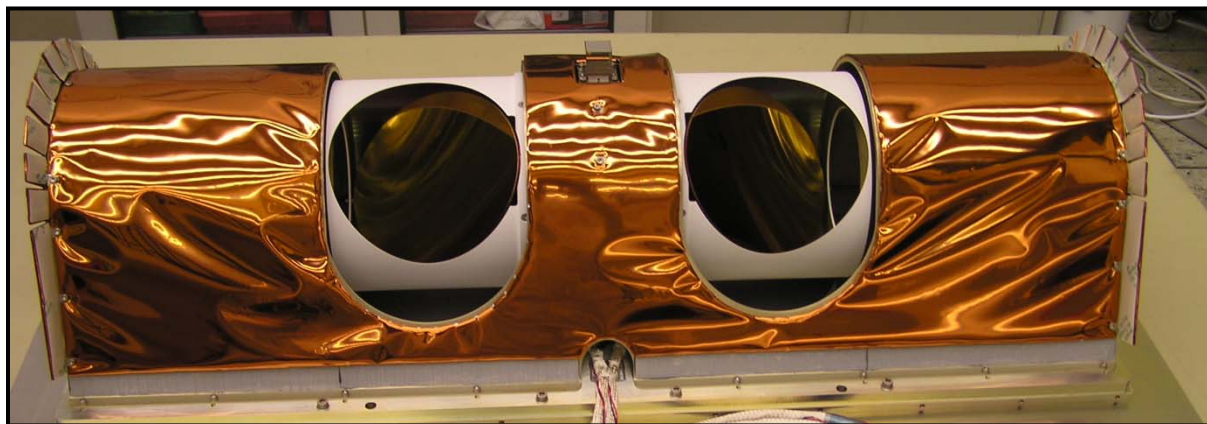


Figure 6. Scan Drive Mechanism Complete (ASM).

Drive Unit

The Drive Unit is built up with a titanium Housing and a steel Shaft interfacing the two Antenna Reflectors. The material combination was chosen to optimize for minimum mass and good thermal match at temperature extremes. The Optical Encoder for motor commutation and position feedback is mounted to one side of the Drive Unit Housing. The Drive Unit is mounted via its footprint to the structural Base Plate.

Two pairs of preloaded thin ring angular contact ball bearings with a contact angle of 20° in face to face arrangement are used in the ASM. The outer bearing diameter is about 50 mm. The number of balls is 24 per bearing and the ball diameter is 3.175 mm. Bearing material is stainless steel 440 C equipped with phenolic resin cages, lubricated with Fomblin Z 25. The bearing preload is 650 N.

The brushless DC motor is designed for a maximum output torque of 2.3 Nm at 27 V. The motor has independent stators so to provide redundancy and to allow adjustment of the two stators in rotational direction with respect to each other. This feature was included in order to further optimize the system in view of the high required velocity constancy. By rotational adjustment of the redundant stator with respect to the main stator, an additional minimization of the overall detent torque could be realized.

Motor commutation and position feedback to the controller is provided by an optical 17-bit encoder in redundant configuration.

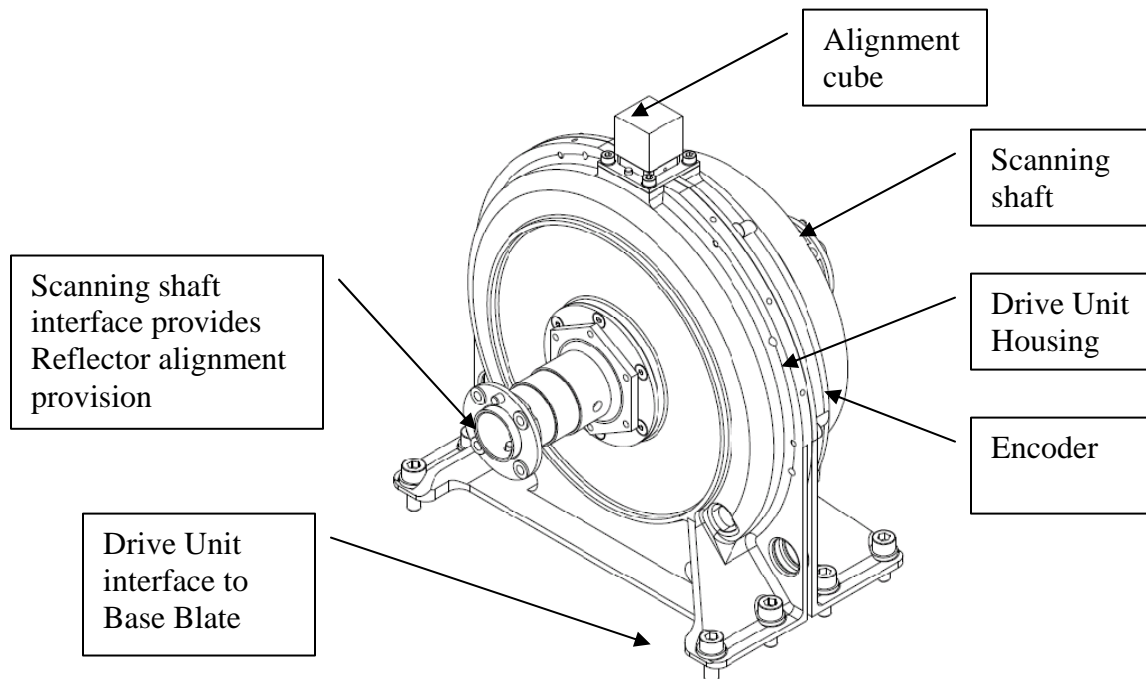


Figure 7. Drive Unit (Drive Module)

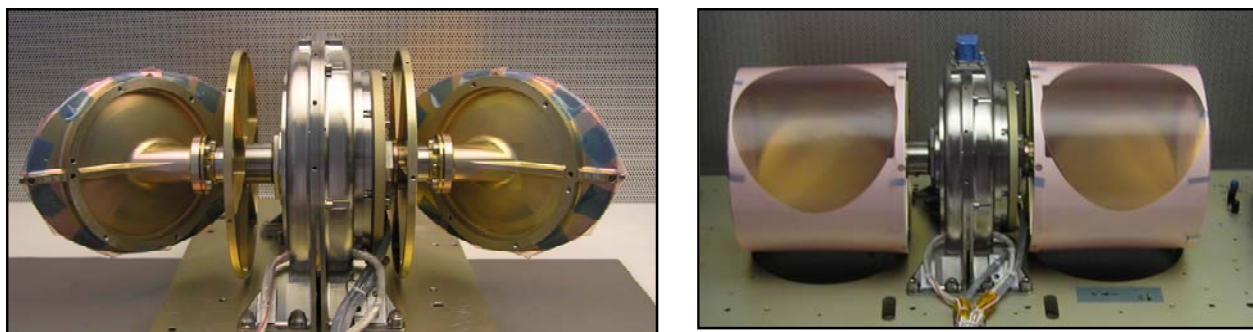


Figure 8. Drive Unit with Reflectors and Thermal Baffle (AIT protection mounted)

Antenna Reflectors

The two Antenna Reflectors are designed from aluminium. The required rms value is 5 μm minimum. This value was exceeded by splitting the manufacturing process into several individual sub tasks at different specialized suppliers. The coordination of the related tasks was followed and closely supported in order to minimize the technical and subsequent programmatic risks. The major working steps were:

- Coarse manufacturing of the Reflectors (at leaving additional material on the Reflector surface for later fine turning)
- Heat treatment of the pre-shaped Reflectors
- Intermediate fine surface manufacturing
- Inspection of Quality including surface accuracy measurement
- Cleaning process
- Final surface shaping with diamond tool
- Inspection of quality including surface accuracy measurement
- Cleaning process
- Pre- and post surface treatment by applying gold coating

Motor Control Electronics

The Motor Control Electronics (MCDE) is designed as a completely cold redundant unit, each part acting to the main respectively redundant motor stator and receiving feedback from the redundant high resolution encoders. The controller is implemented into the FPGA.

The MCDE is a two-channel, 3-phase, brushless DC motor controller, which has been especially adapted to MWSH. It has linear power stages for extremely accurate, wide-bandwidth and high precision tracking control. It incorporates redundancy both in the power stage and the encoder input. It employs extensive use of FPGA logic, which have been adapted to support serial interface protocols, sequencing, digital velocity and position control, profile generation, redundancy management etc.

The power stages are linear (non-switching) and are designed to operate at 27V and at a peak current of up to 2A. These power stages possess two current sensors in the output phases to support full sine-wave commutation, which ensures optimum torque and velocity control characteristics. The use of linear power control and precise control of the operational current guarantees an excellent performance at low drift, high bandwidth and high linearity.

Control of the MCDE is by means of a serial bus interface, which also feeds status information back to the host. In addition there are two enable and status signals for each of the redundant power stages and encoder feedback channels.

Specific Development and Test Issues

Mass and Inertia Minimization of Welded Baffle

In order to achieve the required scan performance (minimum time between the operational points which are earth scan, cold and hot calibration), the system had to be designed for maximum acceleration capability. Since the available torque is limited by the available motor power, the moment of inertia of the rotating part of the mechanism had to be minimized.

This was achieved firstly by designing light weight Reflectors. However, for thermal reasons a cylindrical thermal baffle ("barrel") surrounding the Reflectors was needed in order to keep the Reflector temperature as stable as possible. The thermal baffles (two of them) provide significant contribution to the overall moment of inertia and its mass and radius had therefore to be minimized. Consequently the baffle was designed as a very thin walled structural cylinder (1-mm wall thickness) manufactured out of a bent aluminium plate and stiffened up by means of a radial ring at its one end (close to the Front Ends). The

cylinder and stiffening ring were manufactured and connected by electron beam welding in order to simplify the manufacturing process. The other end of the baffle was attached via screws to a circular plate attached between Drive Unit and Antenna Reflectors (see Figure 8).

During vibration testing, a failure of the electron weld seam was identified, so that a re-design of the thermal baffle was necessary. In order to solve the issue, it was decided to manufacture the Baffle structure in a sophisticated manufacturing process from one piece of aluminium so to avoid any welding seams and the critical welding process (Figure 9). The subsequently repeated vibration test was successfully passed without any problem.



Figure 9. Thermal Baffles Manufactured as Monolithic Structure (Originally Welded)

Minimization of Motor Detent Torque

According to the requirement, a maximum scan speed error of 1% shall be realized. In order to achieve this value, the motor Control Electronic commands the Brushless DC motor in sine control. However, due to the fact that the motor detent torque plays also an important role in achieving good velocity stability, additional measures to reduce the detent torque were identified. The mechanism contains two independent motor stators for redundancy reasons. An overall detent torque of up to ± 25 Nmm was expected on basis of analysis for the two stators. It was found that by rotation of one of the two stators by half a stator slot pitch (corresponding to 2.5 deg rotation), the detent torque could be significantly reduced to a maximum of ± 15 Nmm. This design feature was consequently included into the design to further optimize for minimum velocity disturbances.

Detent Torque

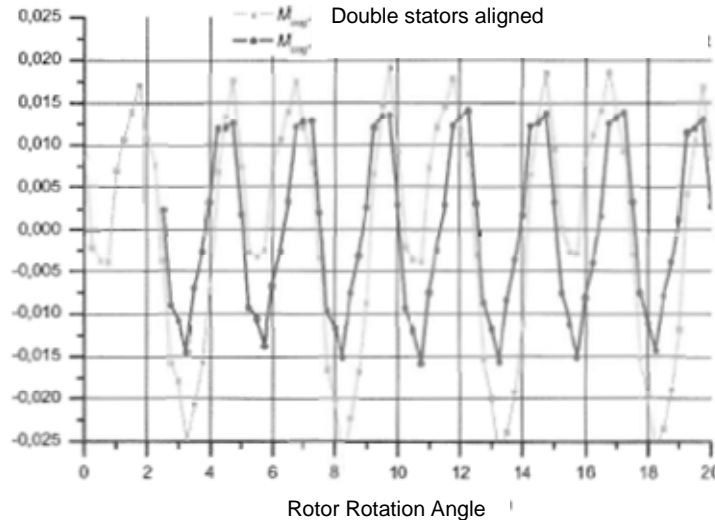


Figure 10. Minimization of Motor Detent Torque

Alignment Concept

Based on the existing tolerance chain between Drive Unit and Base Plate, Drive Shafts and Reflector and between Base Plate and Feed Horn (Mounting Brackets), the implementation of a suitable alignment concept was mandatory in order to fulfil the pointing and performance requirements.

In order to cope with the schedule constraints during the integration and test phase, it would have been favorable to avoid as far as possible a time intensive alignment concept. For example, concepts using in situ shimming and adjustment of the individual components during the integration and test process are time and effort intensive.

Therefore, two alignment alternatives were discussed in this context: one was to manufacture the relevant mating parts with sufficiently high accuracy in order to avoid shims wherever possible. This alternative was found not to be adequate, since the involved tolerance chains did not allow to manufacture the individual parts with sufficiently high precision without high additional effort.

The second alternative was to provide active adjustment and alignment provisions already by design, so to allow alignment by means of suitable adjustment screws after integration. This alternative was skipped due to the fact that it added high design complexity, imposed stiffness and load capability limitations and would have increased mass and moment of inertia. Therefore it was decided to go for a conventional shimming approach and to adjust first the Reflectors about two axis in the interface between Drive shaft and Reflector and then to shim the feed horn support structures with respect to the Reflectors.

The correct Reflector alignment with respect to the feed horn was supported by using Reflector best fit analysis data as an input for the 3D measuring machine during the reflector alignment process.

A zero referencing possibility in rotational direction was additionally implemented in the electronics command interface in order to allow for compensation of rotational misalignment of the Reflectors between the S/C mechanical and electrical zero.

Encoder Supply Voltage

During the last environmental test which was the common TV test of ASM (Mechanism) and MCDE (Electronics), an error was observed in the main path of the equipment. The observed phenomenon was a randomly occurring incorrect start command execution of the scanning function after switching from the redundant to the main path.

The error was observed at first during cold TV condition in the main equipment path however it could later be reproduced also on the redundant path and also after cross-strapping between main electronics and redundant mechanism. Therefore, it was concluded that a systematic random error had to be considered.

After detailed check of the electronics function and also of the mechanism integrity, the detailed root cause investigation led to the suspicion that the error must be produced by the power supply used during equipment test. It was proven by test, that the probability to reproduce the random error was depending on the actually used power supply unit.

Therefore the power supply characteristics were investigated in detail and it was found that the encoder supply voltage (5 V) provided to the encoder had a rise time of >20 ms. Detailed discussion with the encoder supplier led to the conclusion that this fact could cause a starting issue in the encoder ASIC. The RC part of the ASIC has time constant of <10 ms so that the encoder start-up could not always be executed in a reliable manner.

As a consequence a switch box was integrated into the output line of the power supply so to allow switching the encoder voltage by a separate command after switching on the power supply in order to guarantee a voltage rise time of < 5 ms. By including the additional switch box, the scanner start up issue was solved and the TV test was successfully repeated.

Scan Performance during Ground Test

The key functional performance requirements of the Antenna Scan Mechanism are its high velocity constancy during the earth scan period and the requested minimum time consumption for the motion time between two earth scans (hot/cold calibration and movement between these positions) in order to maximize the useful observation time. This was achieved by optimizing the motor dimension and its output torque and dynamics in combination with a minimized moment of inertia of the rotating masses.

The achieved measured velocity and acceleration profile of two subsequent scan periods is shown in Figure 11. The maximum angular velocity ω is about 9 rad/s, the maximum achieved acceleration is about 150 rad/s² while the maximum deceleration is up to 180 rad/s² (deceleration is supported by bearing friction torque).

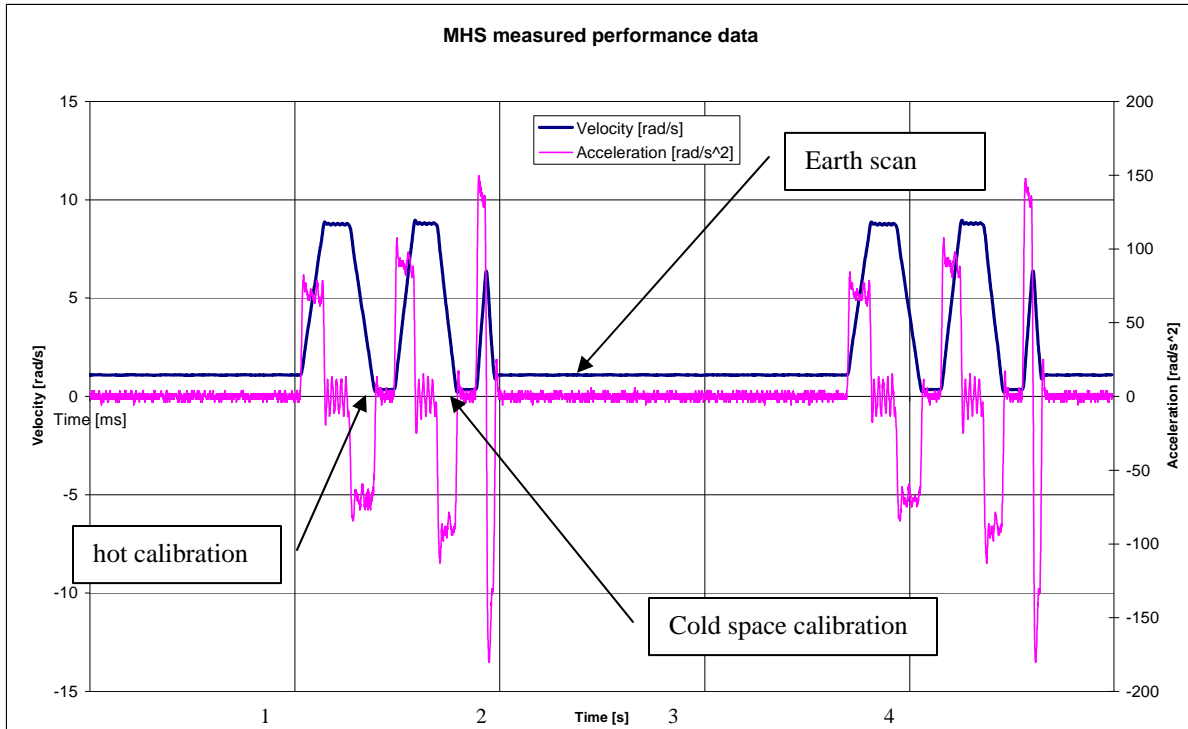


Figure 11. Measured Performance Data (Velocity and Acceleration)

Orbit Performance

The temperature variation of the mechanism over the orbit was analyzed during the development phase. The housekeeping data obtained during the mission show good correlation to the analysis. An active thermal heater concept for the instrument is not needed due to a trimming radiator. The available orbit data of the mechanism demonstrate that the 183 GHz Front-end remains at a very stable temperature of 12°C over one orbit while the 150 GHz Front-end temperature varies between 20 and 22°C.

In Figure 12, the average current needed to drive the scan mechanism is plotted over time. Since the current needed to drive the system is a good indicator of the mechanism health status and especially of its bearings, such data are extremely helpful to gain information for similar flight designs requesting non-uniform bearing rotation.

As can be seen, the current is at about 0.37 A during a first orbital run-in phase lasting for about 3 months. After this time, the current decreases to about 0.35 A and finally to an average value of about 0.34 A after a time of about 9 months. The overall number of scans performed within the time frame shown in Figure 12 amounts to about 16.5 million revs (almost half of the nominal operational life).

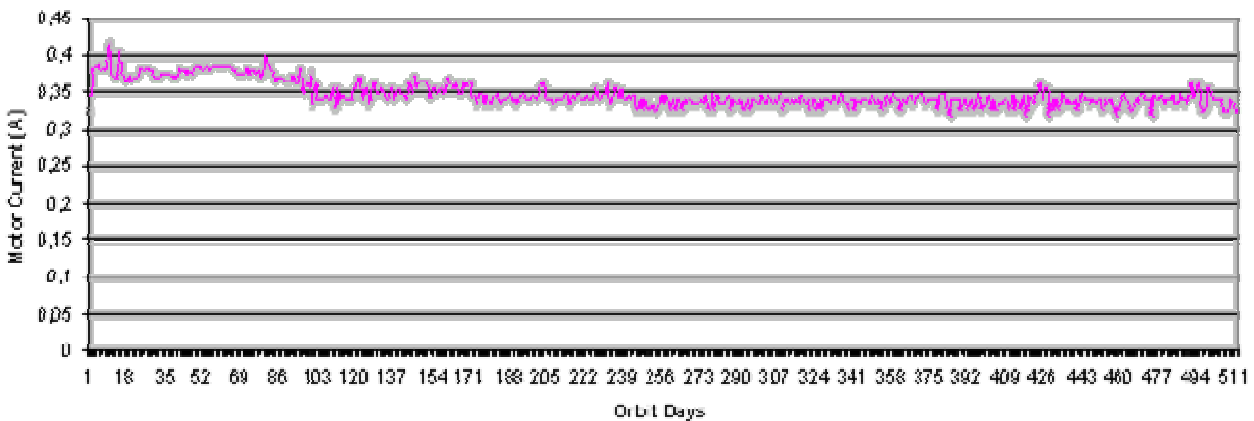


Figure 12. Motor Current Curve from June 2008 to Nov 2009.

Conclusions and Lessons Learned

Electron beam welded connections (electron beam) were found to be not adequate for the application and should be carefully investigated in view of their load capability and durability under the given vibration loads. If possible, alternative solutions should be considered.

Alignment concepts using accurately manufactured parts provide schedule advantage over alignment concepts using shimming methods, however depending on tolerance chains they are often hard to be realized. Actively adjustable shimming provisions, e.g., alignment screws, etc., suffer from mass and stiffness constraints and add design complexity. Therefore, the conventional in situ shimming method using shim washers during integration and test process was found to be the most effective one.

The detent torque of the motor using two independent motor stators could be reduced by turning one of the redundant motor stators by half a stator slot pitch with respect to the other in order to smoothen the overall detent torque amplitude.

The output characteristics (voltage rise time) of power supplies might be important for the correct operation of sensitive equipment (e.g., optical encoders). The voltage rise time of power supplies and potential requirements from equipment side should be carefully cross checked before using standard power supplies on sensitive equipment.

The drive concept using liquid lubrication and two pairs of thin ring ball bearings in face-to-face arrangement provides good life performance at continuous extreme acceleration / deceleration conditions as in the presented application. Based on the available current housekeeping data, the current is very stable over time and no bearing degradation which would result in a higher torque /current level is observed after 2 years of continuous scanning operation (24 million revs).

A Coarse Pointing Assembly for Optical Communication

G. Székely¹, D. Blum*, M. Humphries*, A. Koller*, D. Mussett*, S. Schuler* and P. Vogt*

Abstract

In the framework of a contract with the European Space Agency, RUAG Space are developing a Coarse Pointing Assembly for an Optical Communication Terminal with the goal to enable high-bandwidth data exchange between GEO and/or LEO satellites as well as to earth-bound ground stations. This paper describes some development and testing aspects of such a high precision opto-mechanical device, with emphasis on the influence of requirements on the final design, the usage of a Bearing Active Preload System, some of the lessons learned on the BAPS implementation, the selection of a flex print design as rotary harness and some aspects of functional and environmental testing.

Introduction

In the framework of the European Space Agency's (ESA) Artes V long-term technology development initiative, RUAG Space is developing a Coarse Pointing Assembly (CPA) for an Optical Communication Terminal.

The main requirements for the CPA can be summarized as follows:

- full hemispherical pointing range
- high absolute pointing accuracy: $\pm 270 \mu\text{rad}$ under TV conditions
- very low jitter: $< 2 \mu\text{rad RMS}$
- high reflectivity, minimal wave front distortion, as well as maximum stray light suppression of the optical components in the CPA
- challenging environmental requirements in the form of
 - high accelerations during take-off on various launchers
 - very large temperature ranges derived from a broad spectrum of thermal load cases
 - optics and electronics components sustaining a tough radiation environment during 15 years in-orbit life

Full hemispherical pointing is achieved by a two-axis azimuth/elevation design – a commonly encountered solution for such pointing devices. Arranged at a 90° angle to each other, each actuator stage carries a flat mirror mounted at 45° with respect to its axis of rotation. With this arrangement, each mirror deflects the optical beam by 90° effectively resulting in the required pointing range.

From the very beginning, it was clear that the jitter and pointing performance could only be realized by minimizing friction and stick-slip effects. Besides utilizing ultra-precision bearings and brushless DC motors operated in closed-loop control with a high-resolution optical encoder, the CPA's actuator stage performance was pivotally enhanced by integrating a Bearing Active Preload System (BAPS).

The BAPS offers on one hand a high and stiff preload state for launch, providing high tolerance to the above mentioned challenging launch loads. On the other hand, the BAPS can be actively transitioned to a low and soft bearing preload state for in-orbit operation, enabling smooth, low-jitter movements during beam tracking, as well as allowing for relatively large thermal gradients across the bearings, which is especially important for GEO applications, where the interior of the CPA might be exposed to the sun. Finally, minimization of friction was tackled by implementing the harness from the azimuth to the elevation

¹ RUAG Space AG, Zürich, Switzerland

axis as a flex print design rather than slip rings, roller rings, or conventional cable wraps. These elements brought together the mechanization aspects of the CPA design.

The mirror units were designed to exhibit minimum susceptibility towards thermo-mechanical disturbances. While being of pure Beryllium for weight reasons, the design solution eventually chosen was a highly optimized mirror shape on an innovative iso-static mounting construct.

The high structural loading capacity while maintaining a mass as low as possible was achieved by using AlBeMet or Titanium for all major structural parts.

In the subsequent sections, first, the main components of the CPA are introduced. Following the description how the ambitious requirements were successfully accommodated in the design of the CPA, some lessons learnt concerning the implementation of a BAPS and a flex print cable wrap are discussed before some of the tested achievements of the CPA are presented.

Background

A multi-purpose Optical Communication Laser Terminal is being developed by TESAT Spacecom, Backnang, Germany. The terminal – capable of simultaneous data transmission and reception – is intended for high-bandwidth data transfer between telecommunication satellites operating on different ranges of orbits. The envisaged links (GEO-GEO, GEO-LEO and LEO-LEO, and to ground stations) are foreseen to be established by laser beams. The entire terminal is a highly complex system consisting of tightly interacting subsystems involving mechanical, thermal, optical, and electro-optical elements. In this context, RUAG Space supplies the full chain of front end optics, i.e. CPA and telescope.

Origin of Design-Driving Requirements

The design-driving requirements for the CPA originated from the combination of the wide range of target applications, i.e. operating orbits, as well as the logical need for getting the terminal on the satellite to its in-orbit station. The following points illustrate the origin of the major CPA requirements.

- Pointing-Range: For pure GEO-GEO link applications, a much simpler CPA design could be conceived (Ref. 1) where the required pointing range is much less, especially in elevation. However, if GEO-LEO or LEO-LEO link capability is required, high pointing range with relatively large rotation speeds and fast acquisition times become necessary.
- Pointing Accuracy: When initiating contact between two satellites, the beam is pointed towards the target terminal based on inertial navigation data provided from the satellite to the CPA drive electronics. In a GEO-GEO scenario the involved satellites may be as far as 60'000 km apart, hence directly requiring a high pointing accuracy. For GEO-LEO or LEO-LEO situations an absolute pointing knowledge is essential. The relative velocities of the involved communication terminals may be quite high. With mutual line of sight contact limited to as little as 20 minutes fast beam acquisition is crucial. This furthermore, dictates the need for a high-pointing accuracy even at moderately high-speeds.
- Low Jitter: Maximization of the transfer power is essential to maintaining high data throughput. Therefore, the optical beam has to be kept as stable as possible, hence directly dictating the need for "jitter as low as possible" at zero velocity as well as under constant movement. In fact, jitter must therefore be minimized both cross-axis and in plane

Thermal Stability:	During operation, the CPA may point in the direction of the sun or to deep space for quite long durations. The operational thermal range of the CPA poses a true challenge for material choice and component or design selection. Furthermore, thermo-mechanical stability throughout the operation at these temperature extremes must be guaranteed.
Radiation Hardness:	Telecom satellites operating in GEO orbits have generally a comparatively large life time, often 15 years or more. Thus, radiation hardness of the equipment must be very high, which reduces the number of choices for electronic components and surface coatings of mechanical or optical parts, or may even impose the need for shielding.
High Load Capability:	To enhance versatility and extend the scope of application, the quasi-static loads have been chosen accordingly.

CPA Design Overview

General Overview

Figure 1 shows the assembled CPA without the MLI thermal cover.

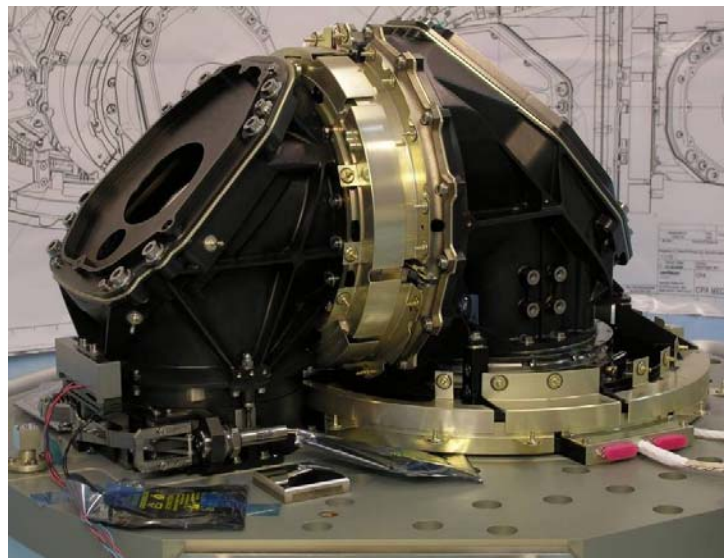


Figure 1. Assembled CPA without MLI protection

As shown in Figure 2, the CPA consists of the following main elements:

- Azimuth Actuator Assembly, containing a bearing set, a BAPS, a brushless DC motor and an optical encoder. This assembly is explained in more detail further on in the text.
- Azimuth Supporting Structure, an ultra light weighted AlBeMet structure that connects the Azimuth Actuator to the Elevation Actuator and supports the Azimuth Mirror Assembly
- Cable Wrap, for transmission of power and signals over one rotation axis to the next.
- Azimuth Mirror Assembly, which is composed of the Azimuth Beryllium Mirror with a high-reflectivity coating, its iso-static support and the Azimuth Mirror Support.
- Elevation Actuator Assembly, same concept as the Azimuth Actuator Assembly.
- Elevation Support Structure, same concept as the Azimuth Support Structure.
- Elevation Mirror Assembly, same concept as the Azimuth Mirror Assembly.
- Park Position Assembly (PPA) incl. Launch Lock, where the functions of the Launch Lock are to rotationally lock the CPA and to increase the first Eigenfrequency to the minimum required value.

Making use of significant synergies, the two Actuator Assemblies have been designed to be identical.

Further elements that are not shown in the figures are the Multi-Layer-Insulation and thin film heaters, which enable the thermal control of the CPA.

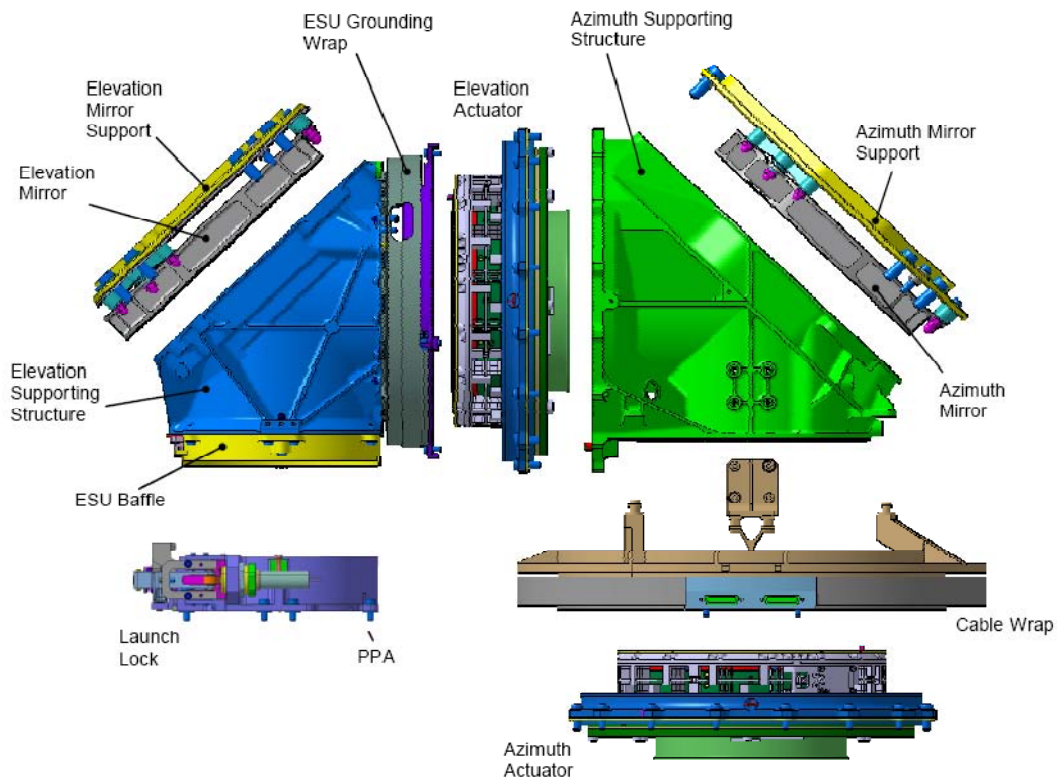


Figure 2. CPA exploded view

Actuator Units

The CPA mechanism core components are the two Actuator Assemblies. The requirements to these assemblies can be summarized as follows:

- Provide the rotation possibility with a bearing system that has:
 - a minimum of resistance torque
 - very low torque noise
 - a long life in terms of time duration as well as number of cycles
 - a high tolerance of quite large temperature gradients across the bearings, which is especially important for the GEO applications
- Allow the optical beam to pass through the centre of the CPA.
- Include the brushless DC motor
- Include the 24-bit resolution optical encoder
- Withstand the challenging launch loads.

Typically, the first point can be reached through a soft and low preloaded bearing system (see Ref. 1). However, this is in contradiction to the last point, which generally asks for stiff, highly preloaded systems preventing too much gapping in the bearings. Together with ESR Technologies, the solution to this challenge was found by using an evolution of their original Bearing Active Preload System (BAPS) QM (see Ref. 2). The BAPS can be considered a bearing housing consisting of a monolithic titanium structure of three coaxial rings which are joined by pairs of thin, blade-like flex-struts as shown in Fig. 3. The upper and lower rings are interfaced to the bearings to be preloaded whereas the middle 'synchro-ring' can be rotated through a small angle (typically $\sim 10\text{-}15\text{mrad}$), thus deforming the flex-struts and axially displacing

the upper ring with respect to the lower (typically by 30-100 μm) so changing preload whilst retaining tight control of the bearing ring planarity.

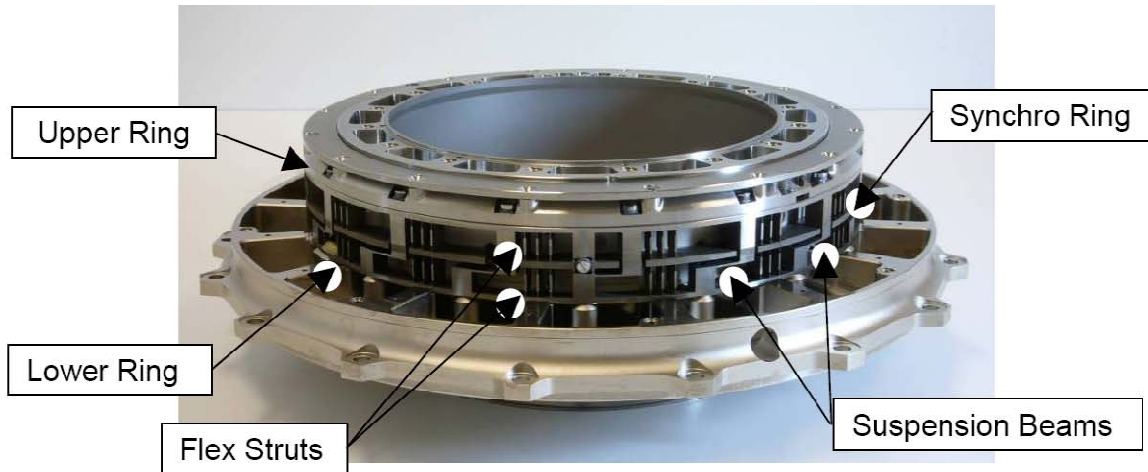


Figure 3. Actuator Unit with BAPS

In the high preload state for launch the flex-struts are slightly deformed from the nominal as-manufactured fully straight 'Top Dead Centre' (TDC) position as shown in Fig 4. In order to actuate the device a torque or tangential force is applied to the synchro-ring causing its rotational displacement past the straight strut position "Top Dead Centre" (TDC) initially to low-preload balance point (which is optimally low preload stiffness since the synchro-ring is un-restrained) at which point the residual preload in the bearing system is balanced by the elasticity of the flex-struts in bending.

The BAPS structure is inherently stiff and stable in the high preload state for launch when the flex-struts are relatively lightly stressed even by launch vibration loads. The struts also serve to synchronize the motion so that the parallelism of the axial motion of the upper and lower bearing housing is extremely high.

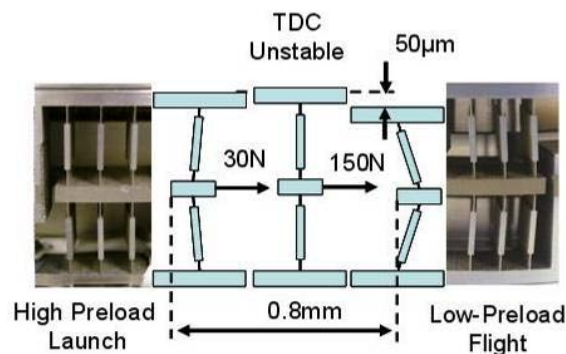


Figure 4. Preload States of BAPS

Thus, the BAPS provides an ideal solution for the application, and eliminates the compromise required with a passive system. In the high-preload state, it provides high stiffness for launch in order to prevent bearing gapping, a concern for bearings of the highest surface finish quality, and in order to protect the close clearance between the rotating and static discs of the high precision encoders from touching. On-orbit, the BAPS is switched to low preload and low stiffness in order to provide very low inherent sensitivity to thermal strains, and low torque noise in absolute terms.

The specified design load parameters to the BAPS are shown in Table 1.

Table 1. Specified Design Load Parameters of the BAPS

Parameter	Value
Maximum High Preload	~ 4000N
Min Low Preload	~ 350N
Quasi-Static Launch Loads	5650N
Quasi-Static Bending Moments	770Nm
Quasi-Static Angular accelerations around rot. axis	2500 rad/s ²

The actuation of the BAPS from high to low preload is achieved by a bi-directional Shape Memory Alloy (SMA) actuator, which engages into the synchro ring with an SMA contact. The SMA actuator activates upon introduction of heat into the heater plate. When power is switched off, the SMA contact returns to its original position and leaves the synchro-ring free, such that the BAPS is in a minimum energy balance preload condition. The resetting of the BAPS is done manually.

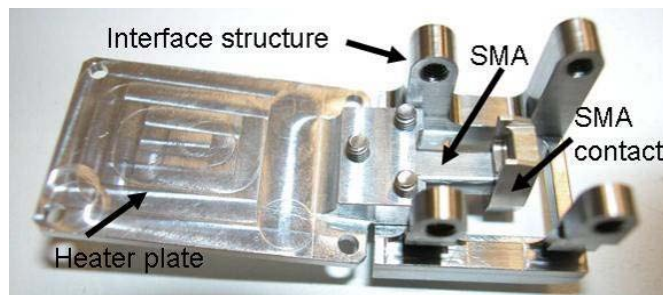


Figure 5. BAPS SMA Actuator

In order to allow for a large optical beam in the center of the mechanism in combination with low torque noise, the previous experience (see Ref. 1) has been recalled and thin section angular contact ball bearings are utilized in back-to-back configuration. Ceramic load carrying balls are used with undersized steel spacer balls. The bearings are lubricated with Fomblin Z25.

As mentioned above, the motion is enabled by a brushless DC torque motor. The motor has dual windings for redundancy reasons. A frameless design has been selected in order to minimize mass. It has to be noted, that the volume constraints are very stringent. In order to minimize the length and diameter of the system, the motor is placed between the central Hollow Shaft and the BAPS structure.

Finally, the actuator units are equipped with 24-bit Optical Encoders from Codechamp, which allow for a very smooth control and hence contribute to the achievement of the jitter requirements in motion direction.

Cable Wrap

A major challenge for many multi-axis motion systems, especially with large angular motion ranges, is the transmission of power and signals over one rotation axis to the next. In order to keep the design simple and close to previous heritage, a flex print design has been utilized in Omega configuration (see also Ref. 1). However, the number of transferred lines is much larger than used in Ref. 1 and the EMC shielding requirements are more complex. Hence, a flex print consisting of three ribbons has been implemented. One advantage of this design is that the power lines and the sensitive encoder signals can be routed over different ribbons, providing naturally better protection from interference. Again, for redundancy reasons, the flex print exists in primary and redundant configuration in the CPA.

Launch Lock

When utilizing a BAPS, a launch lock system in the classical sense of a launch protection system or a bearing off-load system is not required. The reasons for implementing a launch lock into the CPA nonetheless are the following:

- The COG of the rotating parts, especially around azimuth axis, is out of center. Hence, lateral accelerations can cause rotational movements, which need to be prevented.
- With the introduction of a pure rotational lock, the required minimum Eigenfrequency of the CPA could not be met, mainly due to the nodding and bending modes across to the azimuth axis.
-

For the launch lock design key design drivers were minimizing the required volume and the particular location of the CPA with respect to the terminal's support structure. The CPA is placed with its azimuth axis onto the centre of this support structure and in launch configuration the elevation axis points to one of the supported corners of the plate.

In summary, the requirements to the implemented launch lock are:

- Provide a rotational lock to both axes
- Increase the Eigenfrequency of the CPA above the min. required
- Do not bypass loads of the support structure via the CPA bearings
- Only use one actuator that can be reset and reused during ground testing
- Minimize the overall used volume

The final implementation is shown in Figure 6. The rotation locking is achieved by a latch that engages with a lock on the moveable part of the ESU structure. In addition, the latch positively preloads the Elevation structure into the flex supported contacts on either side, which thus stop rotational motion around the Elevation Axis. The preloading is achieved by a lock spring. The release of the system is performed by a HOP actuator and monitored by micro-switches. With this design, all of the above mentioned requirements are met.

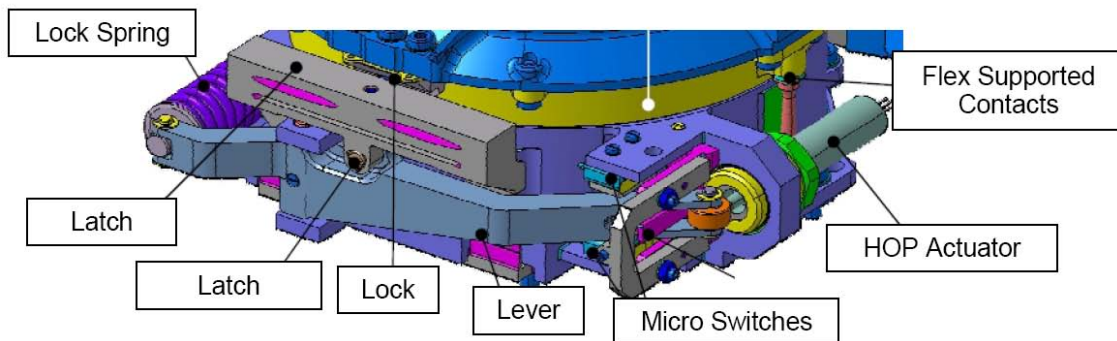


Figure 6. Launch Lock

Optical Elements

Along with the mechanization units, the performance of the mirrors is of critical importance. Figure 7 depicts the azimuth mirror assembly in its holding jig ready for integration on the CPA. The core of the mirrors is of pure Beryllium coated with Nickel. The Nickel is then polished to the required surface quality of around 10 nm RMS and later covered with a protective silver coating. The key performance characteristics of the optical coating are high reflectivity in the target frequency band (>99.5%) and polarization efficiency (>0.99). One particularly noteworthy aspect of the mirror units is the iso-static mounting concept. While providing the necessary stability, stiffness, and strength for the high launch loads, the mounting concept also provides thermal decoupling and by this means high tolerance towards thermo-mechanical influences.

Maximized stray light suppression is achieved by blackening all elements in the optical path. Thereby, the establishment of stable processes for black Titanium and black Nickel on AIBeMet proved to be veritable challenges. Eventually, both key processes were successfully space qualified.

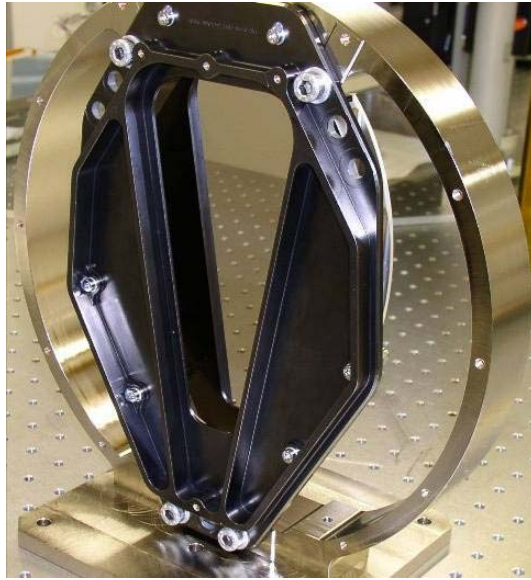


Figure 7. The azimuth mirror unit ready for integration on the CPA.

Achieved CPA Major Performance Characteristics

The CPA is currently under testing. Based on analyses and tests performed so far the following performance data can be reported:

Pointing Range:	$\pm 175^\circ$ (azimuth), $-20/+200^\circ$ (elevation)
Pointing Accuracy:	$\pm 270 \mu\text{rad}$, under TV conditions
Jitter performance:	$\leq 2 \mu\text{rad RMS}$
Mass:	$< 15.2 \text{ kg}$ including MLI and cables
1st Eigenfrequency:	$> 180\text{Hz}$
Max. power consumption:	$< 5\text{W}$
The following environmental conditions are covered:	
Quasi-static Launch loads:	70 g
Vertical Random Inputs:	15.2 g RMS
Lateral Random Inputs:	9.6 g RMS
Operational Temperature Range:	-30°C to $+45^\circ\text{C}$ at interface
Non-Operational Temperature Range:	-30°C to $+ 55^\circ\text{C}$ at interface
Operation Temperature Tolerance:	Geo-Geo continuous operation, direct view of the sun; cold operation in earth shadow, view of deep space.
Max. thermal gradients across bearings:	-11°C to $+11^\circ\text{C}$
Operational life time:	$> 15 \text{ years}$

Various sub-unit level tests have been performed so far, among which the most interesting is the torque and torque noise test. Figure 8 shows that the bearing system, running at low preload, has a mean resistive torque of $< 0.04 \text{ Nm}$ and that the torque at high preload is $\sim 0.2 \text{ Nm}$ (i.e., factor of 5). It also can be seen, that the torque noise is in the order of 0.01 Nm peak to peak or 0.003 Nm RMS .

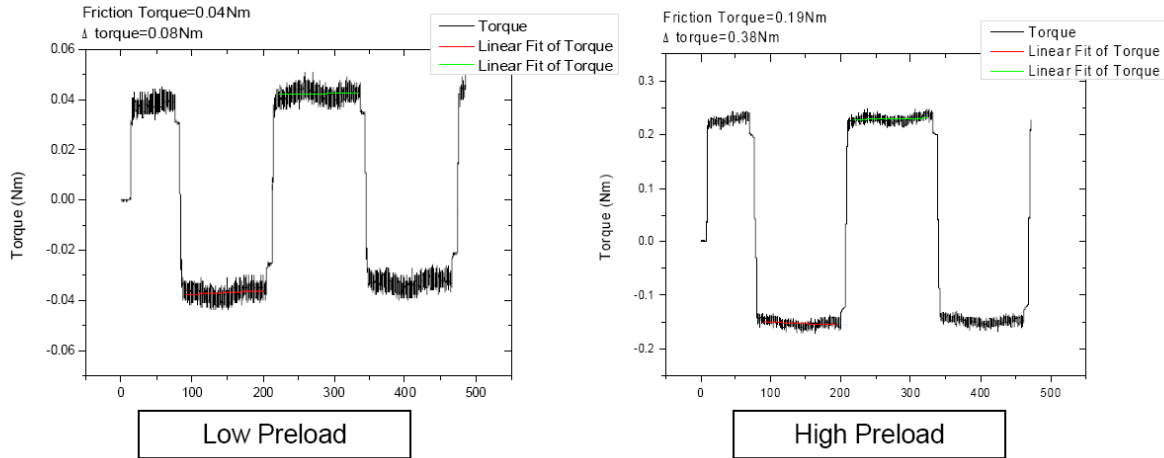


Figure 8. Torque and Torque noise measurements

Figure 9 shows the achieved in plane and out of plane random vibration input levels:

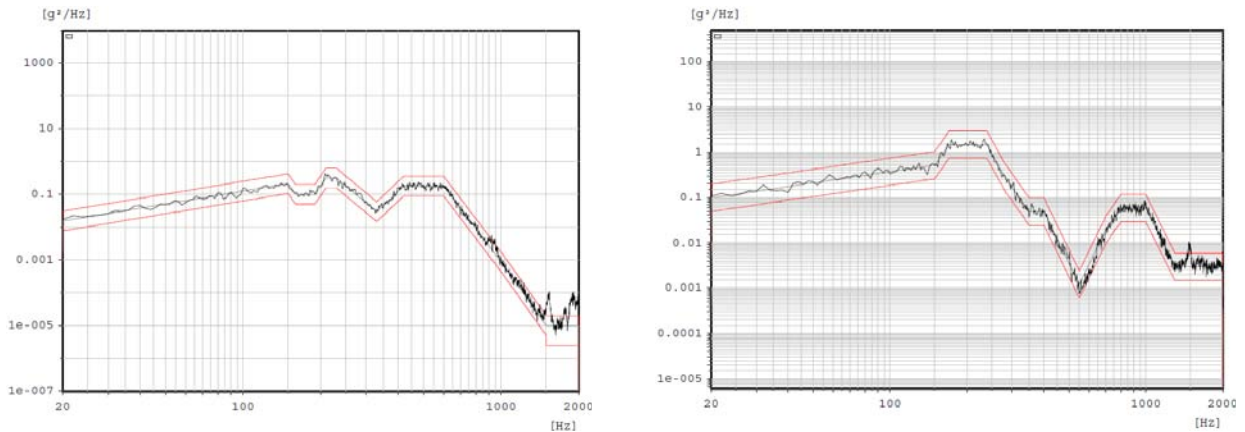


Figure 9. Random vibration tests: achieved inputs in plane (left side) and out of plane (right side)

Lessons Learned

During previous phases, RUAG has achieved considerable success in optimizing and further developing existing designs to meet the above discussed tight requirements. Some examples are discussed in the subsequent sections.

Flex Prints for Rotary Power / Signal Transfer

As mentioned above, the cable wrap of the CPA is made of flex prints. This solution was chosen based on heritage with the previously developed CPA (see Ref. 1). For this CPA, three ribbons are staggered on either side and connected to the same connector. This led to the situation that initially manufactured prints formed bumps and buckles and their roll-down had impacts on the torque noise of the global system, which would reduce the smoothness and thus the accuracy of the CPA. Therefore, RUAG Space improved the design together with the manufacturer. Subsequently the optimal shape of the flex prints was found.

Bearing Active Preload System (BAPS)

Many of the lessons learned on the BAPS, especially the ones concerning manufacturing and assembly are presented in Ref. 2 and will not be repeated here. However, there are some major lessons from the usage of such a BAPS that will be discussed below.

For the CPA application with the very high requirements on torque noise, life, jitter etc. the BAPS is an ideal solution. The measurements done so far can only confirm and justify its implementation.

One major challenge turned out to be the used SMA actuator. This actuator type was chosen due to very tight volumetric/geometric constraints. Several optimization loops were performed and a specific screening process has been introduced in order to obtain a qualified solution.

Conclusions

The CPA currently under testing at RUAG Space has been presented in this paper. It has been shown, that the very tight requirements can be met by a highly optimized design providing multi-purpose usability. The main performance characteristics have been reported among which the low torque noise and the sustainability of high launch loads shall be pointed out.

For future “coarse” pointing mechanisms it is recommended to use a BAPS (Ref. 2).

References

1. Mussett D., et al. (2003) “Contraves Optical Terminal – Coarse Pointing Assembly (CPA)”. In Proc. 10th European Space Mechanisms and Tribology Symposium (San Sebastian). (Ed. R.A. Harris) ESA SP524, ESA Publications Division, European Space Agency, Noordwijk, The Netherlands
2. S.D. Lewis et al. (2009) “Development of an Adjustable Bearing Preload Enabled – Optical Terminal”. In Proc. 13th European Space Mechanisms and Tribology Symposium (Vienna). (Ed. H. Lacoste) ESA SP670, ESA Publications Division, European Space Agency, Noordwijk, The Netherlands

Acknowledgements

Special thanks are due to ESR Technologies (ESTL) for their development of the BAPS, the numerous hours spent for their work and their constant support.

Also thanks are due to the team of TESAT Spacecom for their continued interest and involvement during the development of this product. Furthermore, the German Aerospace Center (DLR) and the Swiss Space Office (SSO) vigorously drive the development of optical communication forward with their support.

Last but not least, it shall be acknowledged with a hearty “thank you”, that the author team listed in this paper would not have been able to accomplish this exceptional feat without the constant support of the rest of CPA team as well as the management at RUAG Space with their high motivation and perseverance.

Design and Development of a Two-Axis Thruster Gimbal with Xenon Propellant Lines

Armond Asadurian^{*}

Abstract

A Two-Axis Thruster Gimbal was developed for a two degree-of-freedom tip-tilt gimbal application. This light weight gimbal mechanism is equipped with flexible xenon propellant lines and features numerous thermal control features for all its critical components.

Unique thermal profiles and operating environments have been the key design drivers for this mechanism which is fully tolerant of extreme space environmental conditions. Providing thermal controls that are compatible with flexible components and are also capable of surviving launch vibration within this gimbal mechanism has proven to be especially demanding, requiring creativity and significant development effort. Some of these features, design drivers, and lessons learned will be examined herein.

Introduction

The construction of the Thruster Gimbal is modular, as seen in the exploded view of Figure 1. It is comprised of subassemblies in order to facilitate fabrication and assembly and to allow subassembly-level testing. This construction expedites the manufacturing process for the entire Thruster Gimbal Assembly. The modular structural components of the gimbal are the Inboard Platform, the Outboard Platform, and the Gimbal Ring, which is the intermediate gimbal member. Other modular components are the two Rotary Actuators and the Tubing Assembly.

The basic gimbal structure consists of the Inboard and the Outboard Platforms joined together through the Gimbal Ring. The Gimbal Ring is joined to the Inboard Platform on a single pivot axis through two sets of preloaded angular contact bearings. This articulation is the Azimuth axis. Its two points of support are the actuator output bearing set, housed within the Azimuth actuator, and the opposing bearing set, housed in the yoke arm of the Inboard Platform. Both bearing sets are preloaded angular contact pairs, providing rigid and accurate location of the Gimbal Ring.

The actuator bearing set is a duplex set preloaded to meet stiffness and load requirements, while the bearing set on the opposite side is a more compliant duplex set, to meet load and stiffness requirements while accommodating any misalignments. This arrangement is duplicated on the orthogonal Elevation axis. The Elevation actuator is mounted to the yoke arm of the Outboard Platform, with the gimbal ring again attached to the actuator output member. The second bearing pair is again mounted in the opposite yoke arm, supporting the other side of the Outboard Platform on the gimbal ring. Orthogonality of the two separate and independent axes is therefore established by the gimbal ring. This configuration forms a true gimbal, with the axes intersecting at the center of the gimbal ring. The dimension from the interface surfaces of the platforms to the rotational centerlines is common, and therefore the gimbal axes are located at a midpoint between the inboard and outboard platform interface surfaces.

The true gimbal configuration utilizing an open intermediate member (the Gimbal Ring) results in a large clear space on the central axis of the unit. This space is used to accommodate a set of flexible xenon propellant lines, which are routed from the inboard interface to the outboard interface. The size and shape

^{*} Moog Chatsworth Operations, Chatsworth, CA

of the clearance volume has been thoroughly analyzed to ensure sufficient clearance between the Gimbal Ring and the coiled propellant lines over the full combined range of angular travel of both gimbal axes.

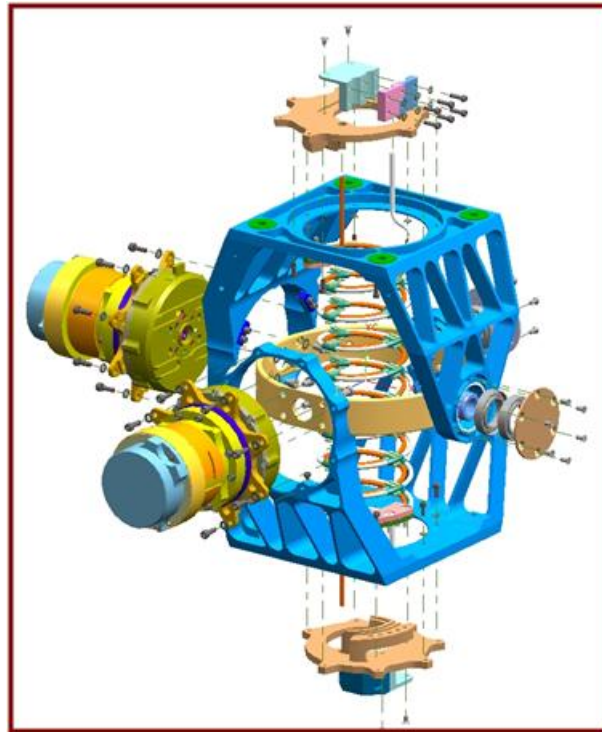


Figure 1. Modular Construction

Rotary Actuator

Two rotary actuators are provided for the articulation of the Thruster Gimbal (Figure 2). The rotary actuators consist of four-phase unipolar stepper motors coupled with Harmonic Drive gear transmissions. These actuators are also configured with large output flanges mounted on preloaded duplex bearing set. This bearing mounting provides a high degree of moment stiffness while causing minimum drag torque reflected to the motor, at the input of the Harmonic Drive gear reducer. A potentiometer is provided for position telemetry. It is located in the rear section of the actuator, with the potentiometer wipers directly connected to a shaft that extends through the length of the actuator from the output flange. Since the output of the actuator is attached to the inboard/outboard platform of the thruster gimbal, the position indication of the potentiometer located inside the actuator correlates directly with the gimbal axis angle.

Inboard and Outboard Platform

The Inboard and Outboard Platforms are almost identical components, with the exception of the mounting hole patterns designed to accommodate spacecraft and thruster mounting interfaces (Figure 3). Other differences between the Inboard and Outboard Platforms are the use of different materials for the mounting spacers, which will be discussed in the “Thermal Control Features” section. Materials for these brackets were selected carefully, due to the requirement for low weight and the critical dimensional requirements for orthogonality and parallelism of the gimbal axes

For simplicity and light weight, the brackets were designed as one-piece machined parts. The basic U-shape and the extensive lightweighting employed in the design mean that a large amount of the original billet material is removed in machining to the net shape. The need for stability of certain critical dimensions in the finished parts- required for gimbal performance- resulted in special design

considerations. In addition to light weight, a material exhibiting good dimensional stability over time was needed. After researching the available materials, a 7000-series aluminum was selected as having the best combination of properties. This material demonstrated high dimensional stability in the finished brackets.



Figure 2. Elevation and Azimuth Rotary Actuators with Heaters

A number of other design features were incorporated to produce a high stiffness-to-weight ratio. These features were carefully implemented in order to avoid weak points in the structure and to avoid interferences over the large articulation range of the gimbal.

Gimbal Ring

The Gimbal Ring is the structural member connecting the Inboard and Outboard Platforms of the Thruster Gimbal (Figure 3). It is in the load path and is a critical structural component.

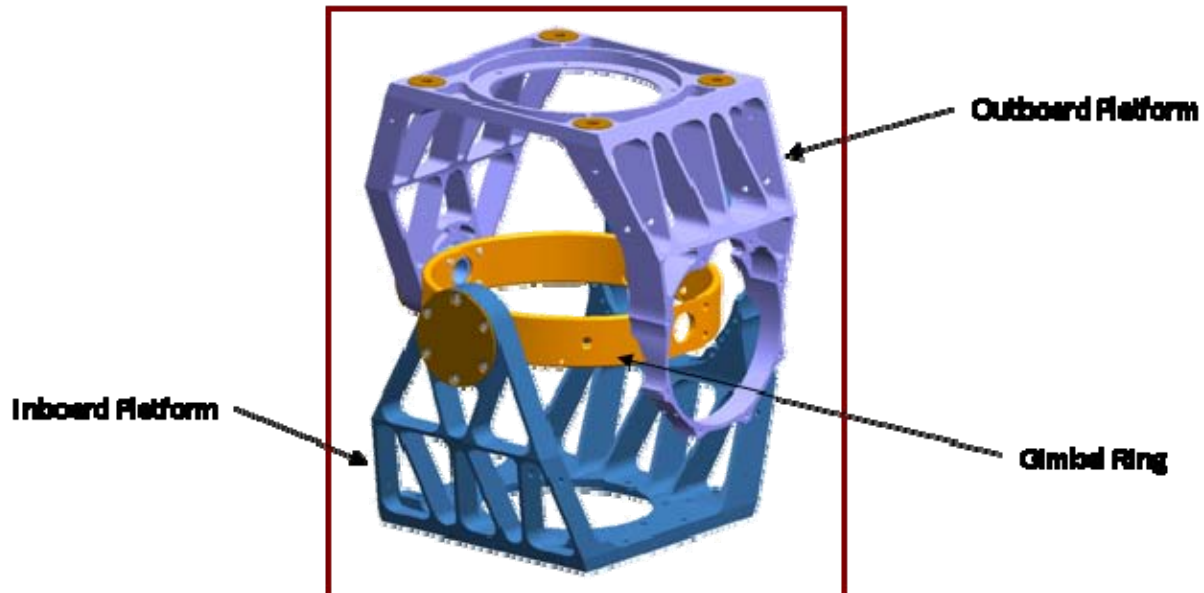


Figure 3. Inboard and Outboard Platform with the Gimbal Ring

The gimbal ring is designed as a large round annular structure, creating a circular clearance volume in the center of the gimbal. Although changing in shape, that volume remains clear over the full articulation

range of the gimbal, and can be used for routing the flexible propellant tubing across the gimbal. Early in the gimbal development, it was realized that the propellant tubing design would dictate the size of the clearance volume and therefore the size of the gimbal ring. For light weight and high stiffness, it was desirable to minimize the size of the gimbal ring. However, design of the metal propellant tubing coils for adequate flexibility required a relatively large coil diameter and therefore a larger gimbal ring.

These opposing requirements were resolved through an unorthodox approach to design and material selection. Material selection was the more powerful tool, since the geometry of the gimbal ring is constrained by gimbal and propellant coil dimensions. Available materials were surveyed for the relevant properties, primarily density and bending modulus. Traditionally, titanium alloy has been the material of choice for high stiffness and light weight. In terms of specific stiffness (stiffness per unit mass), however, titanium is similar to other material choices. A more creative approach to material selection was needed.

To best meet the design requirements for the Gimbal Ring, Moog selected an aluminum grade containing reinforced composite material. To produce the gimbal ring, a near-net-shape ring of the material was first forged. Using the material supplier's recommended cutting and fabricating techniques, that billet was then machined to produce the one-piece Gimbal Ring structure.

Propellant Line Assembly

From the fluid system design standpoint, cleanliness and smoothness of the interior surfaces were the driving requirements for the Xenon propellant tubing. A stainless steel alloy was selected as the tubing material. A small tube diameter supports the small required flow rate, and a nominal wall thickness was adequate to contain system pressure. From the gimbal design standpoint, flexibility of the tubing was most important.

Full articulation of the thruster gimbal is ± 35 degrees, on both axes, from the symmetrical or zero position. The metal propellant line assembly must accommodate that range of motion. To incorporate the necessary flexibility into the tubing assembly, the geometry of a large helical coil was selected. The tubing coils can accommodate both axial (stretching/compression) and lateral (bending) deflections. The height of the gimbal and the inside diameter of the gimbal ring allowed a tubing coil design which can accommodate the maximum deflections with acceptable material stresses in the tubing and low torque loads induced on the gimbal actuators.

The geometry of the tubing coil is that of a soft helical spring constrained only at its ends- a necessary feature in the gimbal application. Vibration input to such a structure can induce a large response, and this was a major concern with the tubing coil.

The fluid system design for the thrusters requires two Xenon supply lines. This feature was used to design a vibration-resistant tubing coil assembly. The two lines were designed as concentric coils having the same number of turns end-to-end. The difference in coil diameters resulted to separate natural frequencies for the two coils, and it was thought that tying the two together at intervals would force a response at a different frequency and much lower amplitude (Figure 6, Figure 6a).

An experiment was conducted on an engineering prototype with the inner and outer propellant lines coupled together at every 90 degrees around the coils. Exposure to random vibration showed response at a single frequency, as intended. However, amplitude of the response was still unacceptably high, achieving only a partial solution to the problem.

The vibration concern with the propellant tubing coils arises only at launch, and the stowed configuration of the gimbal at launch is not at the symmetrical or zero position, but rather at the fully articulated position; i.e., $+36$ degrees rotation on both the X and Y axes. In that gimbal configuration, it was found that the coils could be tied to gimbal structure in order to limit and control the vibration response. Properly spaced flexible tension members performed this function in the launch configuration, and then went slack

in all operational configurations of the gimbal, not interfering with coil movement. This solution was implemented simply with tie cords spaced at optimum locations on the tubing assembly (Figure 7). These two design measures produced a tubing assembly with the flexibility to allow full gimbal deflection and the support needed to withstand launch vibration.

Another requirement on the propellant line assembly was maintenance of tubing temperatures conducive to proper performance of the xenon propellant, and therefore heaters were required. Adhesive-backed film heating elements are normally used for this function; however, the 1/8-inch (3.2-mm) diameter propellant tubing did not offer sufficient flat areas for application of the heaters. Further, the tubing coils flex in operation, compromising adhesion of such heaters. A different solution was needed.

The heating elements to be used require flexibility similar to the flexibility of the tubing coils themselves. Therefore, resistive heater wires formed into coils matching the tubing coils were fabricated. The heater wires were sandwiched between two layers of insulating Kapton film (Figure 5).



Figure 4. Outer Propellant Tubing with Heater



Figure 5. Inner Propellant Tubing with Heater

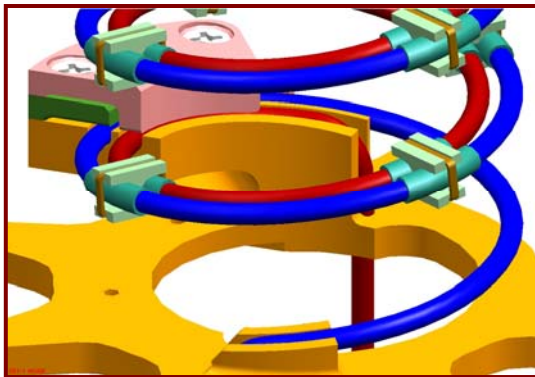


Figure 6. Propellant Line Assembly with Spacers

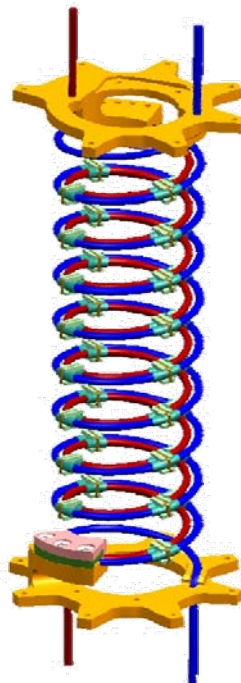


Figure 6a. Propellant Line Assembly

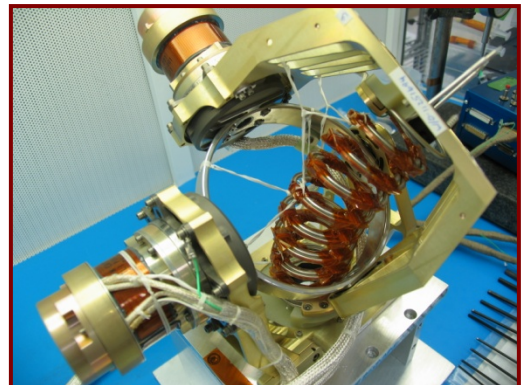


Figure 7. Fully Articulated Assembly with Restraining Cords

Thermal Control Features

The operating environment of the Thruster Gimbal presents a number of challenging thermal design problems. As discussed above, the propellant supply lines are furnished with heaters. Heaters are also provided for the gimbal actuators. For temperature monitoring and control, thermistors are located on the propellant lines near the Inboard and Outboard Platforms as well as on the actuators.

The location of the thruster gimbals on the spacecraft is such that they are exposed to extreme temperatures and temperature gradients. In the worst case, the gradient from Inboard to Outboard can be as high as 100 deg C. This extreme thermal condition was mitigated by tailoring thermal conductivity at the gimbal interfaces. At the Inboard Platform interface with the spacecraft, a set of four aluminum spacers were used to promote conductivity. At the Outer Platform interface with the thruster assembly, four spacers were used to limit heat transfer from or to the thruster assembly and to promote isothermality of the gimbal structure.

The spacecraft operating scenario results in the Thruster Gimbal being exposed to a deep space view, and the resulting extreme cold, for extended periods of time. A flexible multilayer insulation blanket encapsulating the entire gimbal was used to protect against the resulting radiant heat loss, and, again to promote isothermality of the gimbal. Innovative design of the Multilayer Insulation Blanket (MLI) was required to accommodate the large travel angles of the gimbal. A camera bellows type of construction was used, and was found to offer minimum additional torque load on the gimbal actuators (Figure 8).



Figure 8. Multilayer Insulation (MLI) Blanket

General Performance of the Thruster Gimbal

Thruster Gimbal Specifications	
Physical Characteristics	
Dimensions	22.23 x 12.7 x 12.7 cm (8.75 x 5 x 5 in)
Weight	< 5 kg (11 lb)
Payload Weight	22.7 kg (50 lb) (externally supported)
Performance	
Total rational range of travel	±36.5 degrees in two axis
Angular resolution of gimbal	0.01125 degree
Angular velocity	1 deg/sec (nominal)
Angular accuracy of gimbal	Under 0.02 degree
Operating temperature range	-20° C to +80° C
Power Requirements	
Power Consumption	22 watts max. per actuator

Lessons Learned

The motor in the elevation and azimuth actuators is a four-phase 1.8-degree hybrid stepper, wound for unipolar excitation. The motor design has high magnetic efficiency, allowing it to produce high output torque and unpowered holding torque at relatively low power levels. The high magnetic efficiency results in part from a small motor air gap. The air gap is the radial clearance between teeth on the moving rotor and opposing teeth on the stationary stator core. Although it is important to maintain a small air gap in order to achieve optimal motor performance, it is equally critical to ensure that the clearance between parts in the air gap is maintained. It was recognized early in the development phase that diligent measures would be required to insure consistent air gap dimensions in production units. All elements affecting air gap variations were thoroughly analyzed and a Critical Clearance Analysis report, based on worst case values, was generated.

Approximately 26 actuators were produced (some shown on the completed gimbals in Figure 9). In thermal cycle testing, one axis of a thruster gimbal stopped operating during a high temperature portion of the cycle. As a troubleshooting step, the chamber temperature was lowered. The affected actuator then resumed normal operation. The preliminary conclusion was that the anomaly was temperature-related.



Figure 9. Completed Gimbals

The gimbal was disassembled and the problem traced to one of the actuators. Actuator disassembly then further isolated the cause of the problem to the motor. Motor disassembly showed rub marks on the rotor with matching marks on the stator. These marks were consistent with a condition causing the rotor-to-stator clearance to be lost, with resultant physical contact.

The Critical Clearance Analysis was revisited, and no errors in the methodology or calculations were found. However, it was noted that the analysis assumed a uniform coating of insulating material thickness on the critical rotor and stator surfaces. This assumption was investigated further.

The magnetic materials susceptible to corrosion are protected by a thin film of epoxy material- a so-called 'wash coat'- which forms a barrier coating over the otherwise vulnerable surfaces.

Wash coat application is a standard and well established process used on virtually all Moog motors. However, the majority of motors produced are of the three-phase permanent magnet stepper design, with relatively larger air gaps not requiring extremely tight control on coating thickness.

The conclusion of the investigation was that the actual thickness of the wash coat in places exceeded dimensions assumed in the Critical Clearance Analysis and, together with differing thermal expansion coefficients and/or thermal gradients in the motor assembly at high temperatures, caused the closure of the air gap and resulting stoppage of the motor. Figure 10 and Figure 11 demonstrate the radial location where the air gap closure occurred.



Figure 9. Rotor

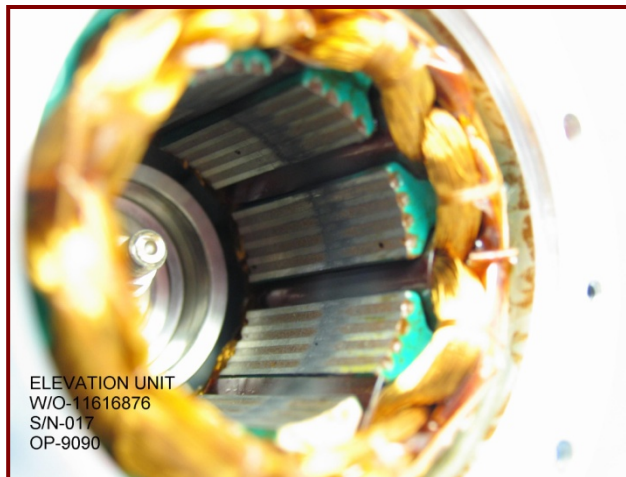


Figure 10. Stator

Conclusion

Design and development of the Two-axis Thruster Gimbal was completed largely free of interruptions and course corrections. However, a significant number of up-front analyses were precipitated by the stringent operating, performance, and weight requirements. In addition, a Monte Carlo analysis was performed to predict performance in simulations using randomly selected thermal and operating parameters. To further ensure successful production of flight hardware, several Engineering units of varying degrees of complexity were built and tested. By the conclusion of the Final Design Review, an extraordinary amount of analytical and test data had been accumulated, indicating a well conceived and low risk design approach.

A large part of the development effort was focused on the mitigation and suppression of, and compensation for, the extreme thermal conditions to which the gimbal would be exposed. Heaters which could be mounted on moving and flexing members were developed, as well as complex, flexing thermal blankets designed to contain thermal energy and promote isothermality. Aggressive weight reduction measures were also implemented in order to achieve an optimized design with adequate margin.

Unique testing methods were developed, enabling testing of the Thruster Gimbal with simulated payload and launch lock mechanisms in order to emulate flight-like test conditions with high fidelity.

Despite the up-front development effort and the extensive analyses performed to lower and/or eliminate risk, an oversight in process selection allowed a test anomaly to occur. A motor fabrication process commonly used for Moog motors, but inappropriate for the optimized Thruster Gimbal motors, was used. The process was modified to specifically address the unique characteristics of the Thruster Gimbal. Numerous other process improvements were implemented as well as the specific testing measures used to isolate and correct the observed anomaly.

Moog has successfully produced a number of the Thruster Gimbals, and has recently concluded a second life test program, demonstrating 2X life. This follows the original life test program which successfully demonstrated 1.5X life.

Acknowledgements

The author wishes to acknowledge James Hammond, Steve Mallonee and Ruben Nalbandian of Moog for their contributions in the design and development of the Two-axis Thruster Gimbal.

The author expresses his sincere appreciation to Dave Putnam of Lockheed Martin Space Systems for his significant contribution in the development of the Thruster Gimbal and his hands-on involvement during the complex Qualification Testing phase of the program.

Gravity-Offloading System for Large-Displacement Ground Testing of Spacecraft Mechanisms

Olyvia Han*, David Kienholz*, Paul Janzen* and Scott Kidney*

Abstract

Gravity offloading of deployable spacecraft mechanisms during ground testing is a long-standing problem. Deployable structures which are usually too weak to support their own weight under gravity require a means of gravity offloading as they unfurl. Conventional solutions to this problem have been helium-filled balloons or mechanical pulley/counterweight systems. These approaches, however, suffer from the deleterious effects of added inertia or friction forces. The changing form factor of the deployable structure itself and the need to track the trajectory of the center of gravity also pose a challenge to these conventional technologies. This paper presents a novel testing apparatus for high-fidelity zero-gravity simulation for special application to deployable space structures such as solar arrays, magnetometer booms, and robotic arms in class 100,000 clean room environments.

Introduction

The WAGM (Walking Anti-Gravity Machine) is an active approach to gravity offloading of space structures that deploy in three degrees of freedom. At its heart is the proven AGM (Anti-Gravity-Machine) technology [1][2] – a single degree-of-freedom gravity offloading device that supports a wide range of payload weight over several centimeters or more of vertical travel with arbitrarily low stiffness, zero static deflection, minimal added mass, freedom from spurious modes, and perhaps most importantly, zero friction. The deployable payload in the present WAGM application is single-point suspended from the AGM via a load cable. The AGM is itself mounted onto a pair of commercial off-the-shelf sealed linear belt drive tracking stages. Horizontal drag forces on the payload are minimized by an active system that actuates the linear belt drive stages such that the AGM is centered over the payload and the load cable is kept close to vertical as the payload moves under its own power. The horizontal and vertical systems work together to deliver gravity offloading for arbitrary trajectories of the payload with a total range of motion of about 2 meters (6 feet) in all three spatial directions, with capability to scale up to greater distances in each direction. In particular, one horizontal direction can have an arbitrarily long range of motion, a feature that would be useful for testing of unfolding solar arrays or extending booms.

Comparison to Conventional Gravity Offloaders

A common approach to gravity offloading deployable structures ignores the most difficult DOF (vertical) and is restricted to applications involving only translation in one or two horizontal degrees of freedom. In this approach, overhead air bearings or ball bearing dollies moving in the horizontal direction(s) carry the payload weight as it deploys [3]. Often, the payload itself must pull the dollies or air bearings along. This approach is limiting in that it not only artificially constrains the vertical degree of freedom but also imposes artificial lateral drag forces on the payload.

Buoyancy systems using floats in a water tank can deliver a large range of horizontal motion. However, in addition to logistical and cleanliness problems, they suffer from a high level of viscous damping as well as excessive vertical stiffness. Overhead helium balloons solve some of these problems but add a minimum of 16% of the payload mass, an important limitation in dynamic testing.

* CSA Engineering, Mountain View, CA

Other gravity offloading approaches use support from above cable arrangements that place a simple linear spring in series with each cable. Unfortunately the very low stiffness required of the spring poses the problem of static sag. This makes suspension cable systems only practical for vertical displacements on the scale of centimeters, which is inadequate for deployment testing. The WAGM utilizes established AGM technology to deliver vertical gravity offloading with zero static sag and air spring stiffness limited only by the volume of the external volume connected to the AGM.



Figure 1: Mechanical gravity offloader

In its first application, WAGM replaced the mechanical pulley and counterweight gravity offloader shown in Figure 1. The pulley and counterweight were attached to a moving trolley which rode on a guide rail. The guide rail was attached by a hinge to the side of the spacecraft. The customer expressed dissatisfaction with the fact that the counterweight overhung the payload, the system took a long time to set up and required bolting test equipment to the side of the spacecraft, and most deleteriously, the need for the deploying payload to pull the “jib crane” around and to move the counterweight inertia compromised torque margin measurements. Torque margin of the deployment system is an important criterion to the customer as it is fundamental to on-orbit reliability. In tests on the WAGM, friction in the vertical direction at the payload end of the load cable was measured to be on the order of 0.25 – 0.35% of payload weight.¹ In the horizontal degrees of freedom, drag forces were measured to be just 0.5% of payload weight at payload speeds of 1.59 mm/s (0.0625 in/s). Moreover, interfacing to expensive flight hardware is kept to a minimum as the deploying payload under test is single point suspended from a light load cable with no other interface between the WAGM and any part of the spacecraft. The latter advantage greatly reduces setup and test time, an important factor since tests are performed with the spacecraft very close to completion and the tests on the critical schedule path.

¹ The AGM itself is completely frictionless. The measured friction is added by the 4:1 displacement amplifying mechanism described later.

Requirements and System Architecture

The WAGM was commissioned to offload the weight of a deployable robotic arm during ground testing. The requirements were:

- Minimal friction
- Minimal setup time
- Minimal interfacing to spacecraft
- Offloading force of 355.86 N (80 lb) with an offload accuracy of ± 89 mN (± 0.02 lb) in x, y, z
- Insensitivity to set-up or set-up repeatability

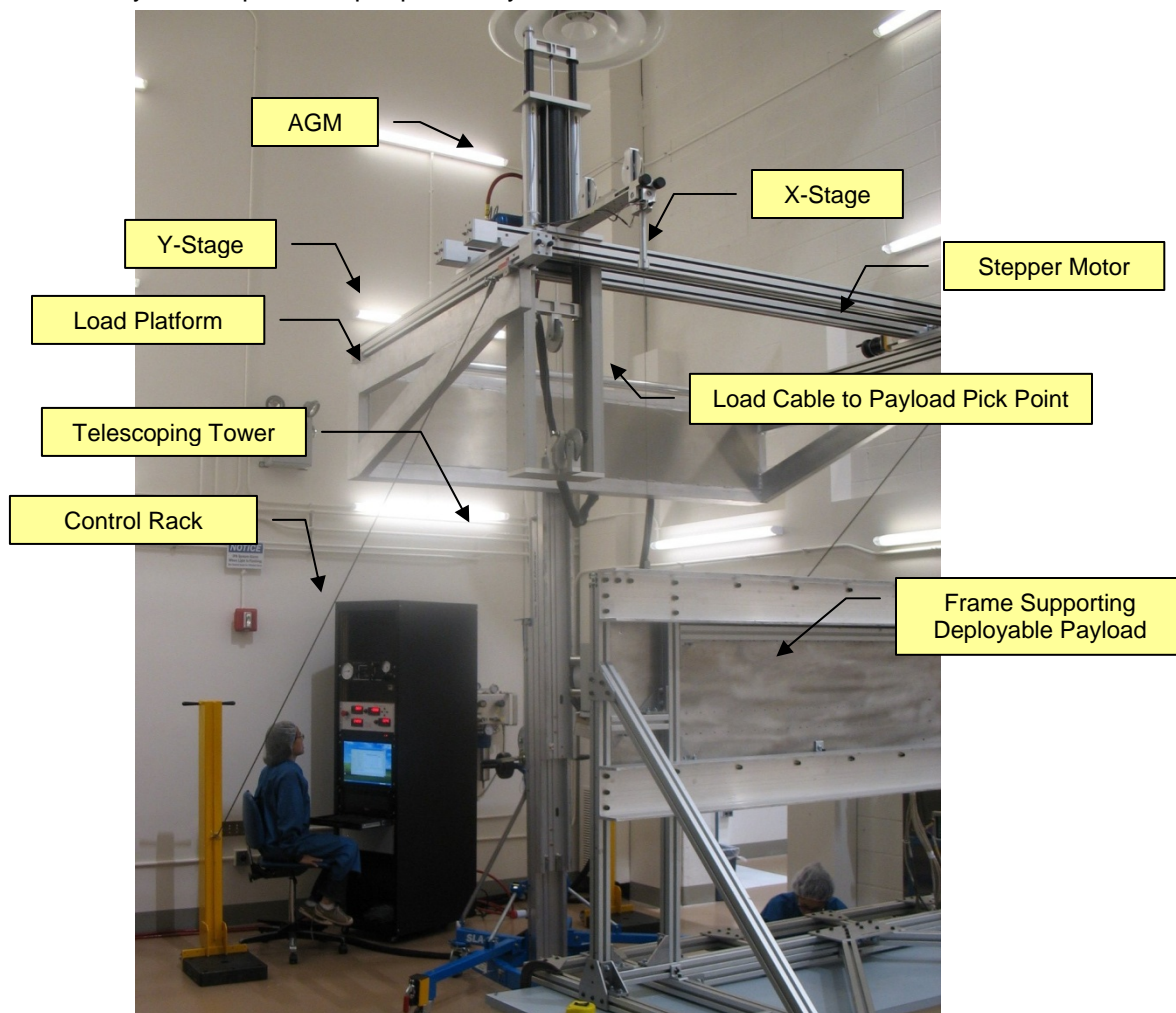


Figure 2: WAGM during acceptance testing at customer site

Figure 2 shows the WAGM during acceptance testing at the customer site. The WAGM is composed of five main subsystems.

- The gravity offloading device (AGM) that carries the weight and accommodates vertical motion of the payload.
- An X-Y stage system comprised of sealed linear belt drives that move the AGM horizontally to keep the load cable vertical during active tracking. The X-Y stages are driven by a pair of commercial off-the-shelf stepper motors.
- A COTS industrial lift whose fork has been replaced by a custom load platform onto which the X-Y stages are mounted. The industrial lift has a telescoping tower that allows for coarse adjustment of the height of the load platform. The base of the lift is equipped with casters that allow the entire assembly to be rolled into place.

- A control rack containing signal conditioning for sensors, drive electronics for the X-Y stage motors, and the control computer with its peripherals (not shown in Figure 2).
- Triangulated stiffening elements to stiffen the telescoping tower in yaw and roll (not shown in Figure 2). These will be discussed in the Lessons Learned section.

Operating Principles

At the heart of the WAGM is the proven AGM (Anti-Gravity Machine) technology. The AGM is essentially a pressure-regulated air spring. It is shown schematically in Figure 3.

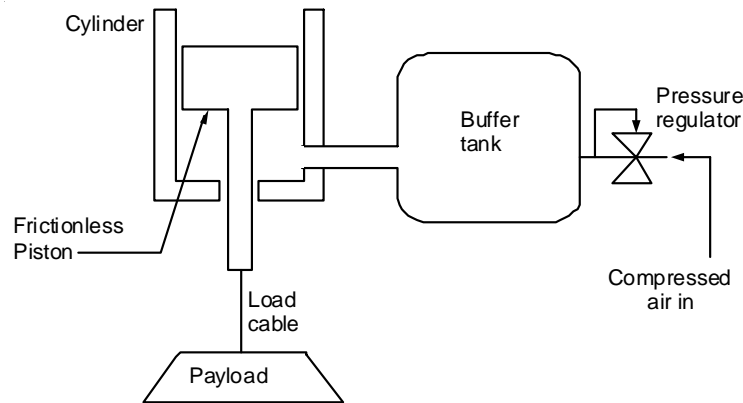


Figure 3: Operating principle of the AGM

The load is supported by force developed by an air piston that moves vertically in a closely fitted cylinder. The piston is of a special type that combines the functions of a piston and an air bearing. Air circuitry within the piston produces a very thin air film between the piston skirt and the cylinder wall, thus eliminating all friction while providing a force capacity equal to the piston area times the cylinder air pressure.

Figure 4 shows two detail views of the AGM. The piston lifts against a moving carriage (shown in red) that rides vertically on four conventional air journal bearings that completely eliminate friction between the frame and moving carriage. The volume below the piston is pressurized with air by a precision manual pressure regulator. For slow vertical motions of the piston, the pressure regulator vents air into or out of the cylinder and buffer tank to keep the pressure constant. The buffer tank assists in this function by reducing the effective stiffness of the air spring for small motions, even if they are rapid. The effective stiffness of the air spring can be reduced significantly by simply increasing the size of the external volume in the buffer tank. The tank also slows down the response of the piston pressure when the regulator set point is changed, thus making the device more tractable and easier to “dial in” to a desired pressure.

The lower end of the moving carriage connects to a cable-and-pulley motion amplifier. The amplifier allows the 45.7 cm (18 in) vertical stroke of the air cylinder to produce a 182.9 cm (72 in) vertical displacement at the end of the load cable attached to the payload. The cable-and-pulley motion amplifier is required because the piston and cylinder of the AGM require extremely close dimensional tolerances to function correctly. This limits the length of cylinder that can be fabricated and hence the working stroke of the AGM. Fortunately, the AGM has much greater force capacity than needed for the application. In general, the AGM force and stroke capabilities can be matched to the requirements of the load by using a simple displacement multiplier composed of a load cable and three pulleys. The principle is illustrated on the right in Figure 5. In the interest of minimizing friction and wear in the cable, the pulley diameter is about 80 times the diameter of the cable².

² The nominal standard for aircraft control cables is a minimum ratio of 35:1.

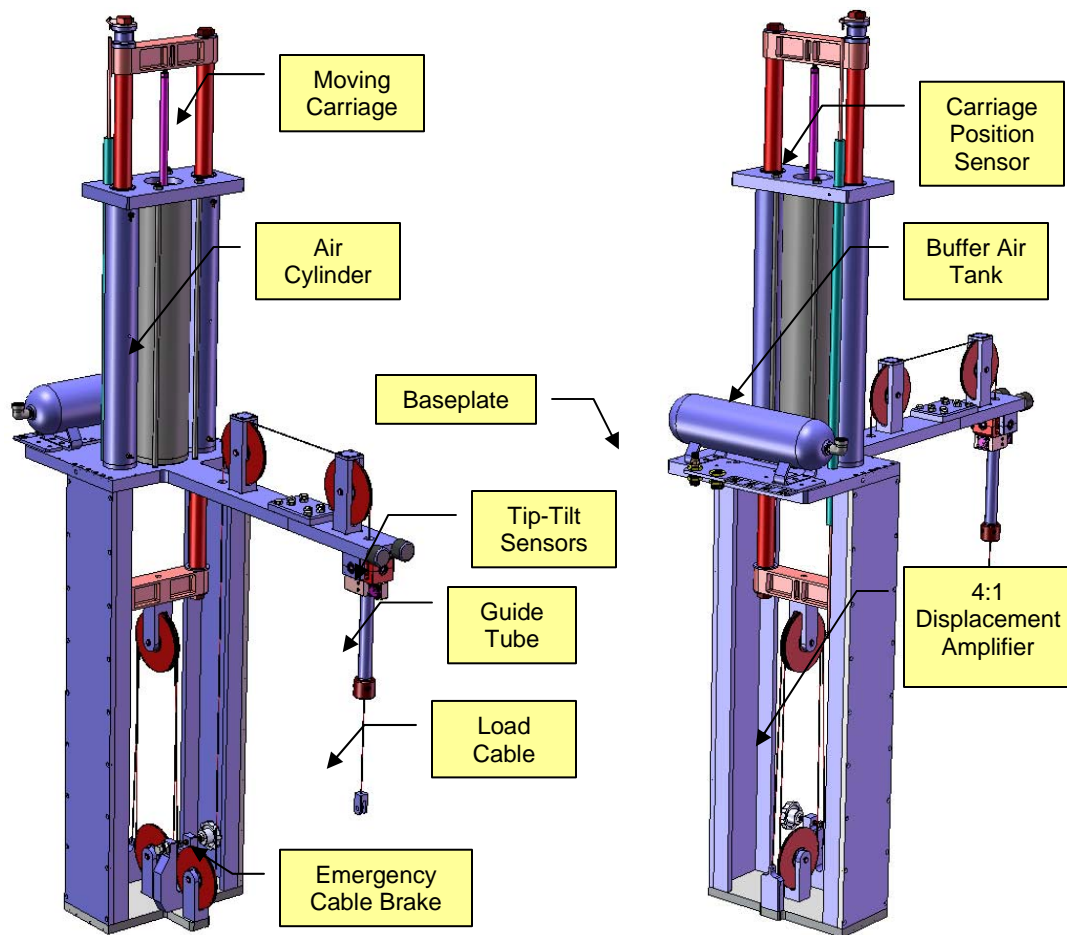


Figure 4: AGM detail

During active tracking, horizontal forces on the payload are minimized by an active system that keeps the AGM centered over the payload such that the load cable is kept very close to vertical as the payload moves. The key to doing this is a system for sensing the load cable angle relative to true vertical. This is done by routing the load cable up and over two additional pulleys and down through a guide tube as shown in Figure 6. The guide tube is part of a larger angle-sensing mechanism: the upper end of the guide tube is fixed to the lower yoke of a precision universal joint (the upper yoke of the universal joint is fixed to the baseplate of the AGM) into which are mounted two high-sensitivity, DC-coupled accelerometers (i.e. tip-tilt sensors) with their sensing axes oriented normal to the guide tube. As the payload moves horizontally the load cable departs from vertical, pulling the lower end of the guide tube with it. The DC-coupled accelerometers produce output signals proportional to the tube's deviation angle from vertical (for small angles). Using band-limiting lowpass filters in the signal conditioning, the accelerometers have a resolution noise floor of about 1 micro-g, corresponding to 1 micro-radian of angle for small angles of the guide tube around vertical. The signals from the accelerometers are gained up to a sensitivity of 200 volts/radian. The ± 10 volt range at the amplifier output then corresponds to a measurement range of ± 50 milliradians. The basic advantage of the sensing method is that it is unaffected by small deviations of the load platform from horizontal, as will inevitably be caused by flexing of the platform and the tower under load.

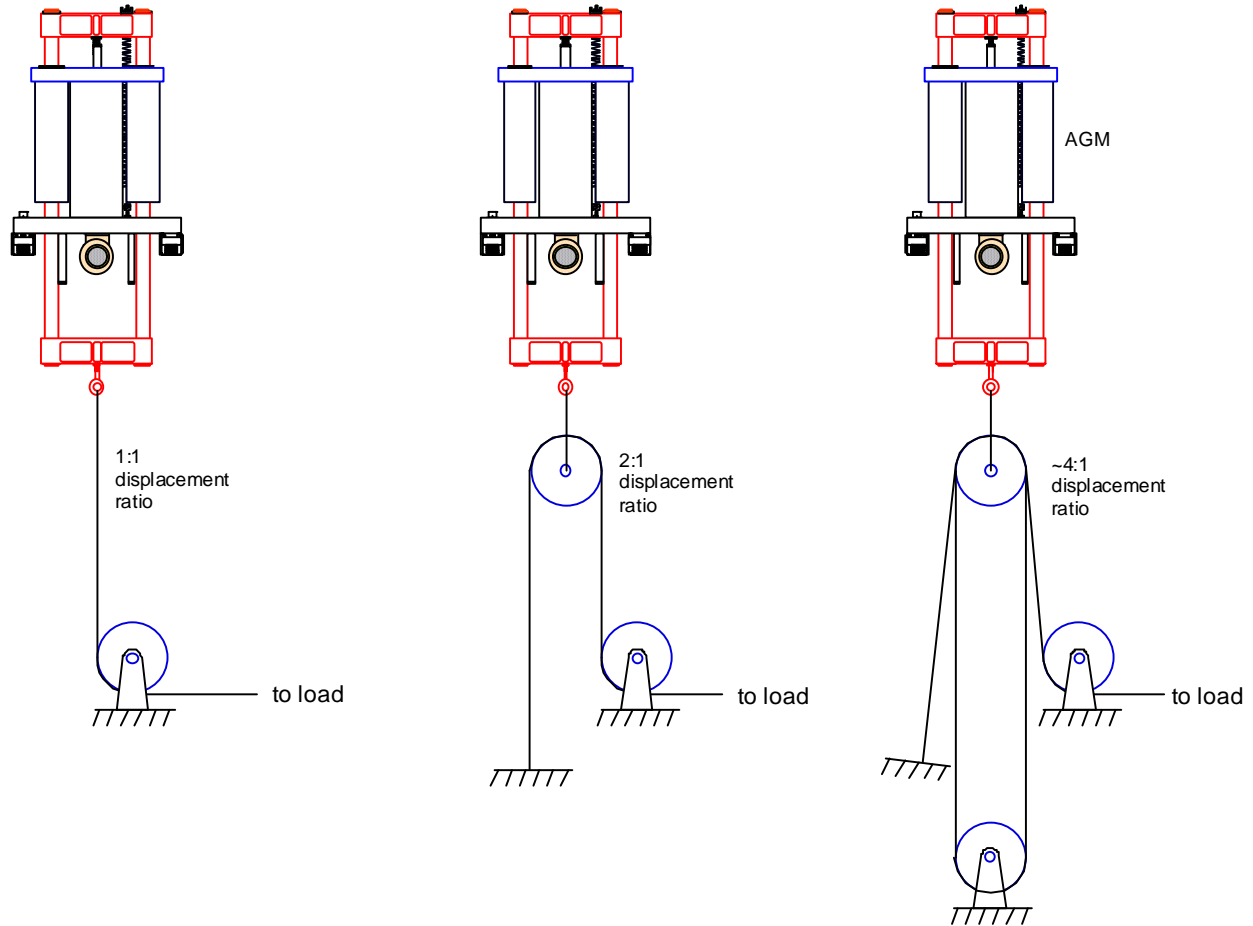


Figure 5: Cable-and-pulley displacement multipliers. The WAGM uses the 4:1 system.

The deviation angles are filtered through an analog anti-aliasing filter module before being digitized by a packaged motor controller card. Inside the motor controller card a feedback loop outputs step and direction commands to the stepper motors to position the X-Y stages such that the tip-tilt sensor is maintained directly over the payload, keeping the load cable as vertical as possible and minimizing the deviation angles. A 1-Hz low-pass digital filtering onboard the controller card is included in the feedback loop to keep the system stable and to prevent the control loop from amplifying ambient ground vibration and noise in the accelerometer signals. It is important to note that the controller only has control authority over the movement of the X-Y stages. It has no control authority over the AGM piston pressure or the AGM piston displacement. This is because the AGM is a constant force device; once the AGM cylinder pressure is set the uplift force on the payload remains essentially constant over the vertical range of motion.

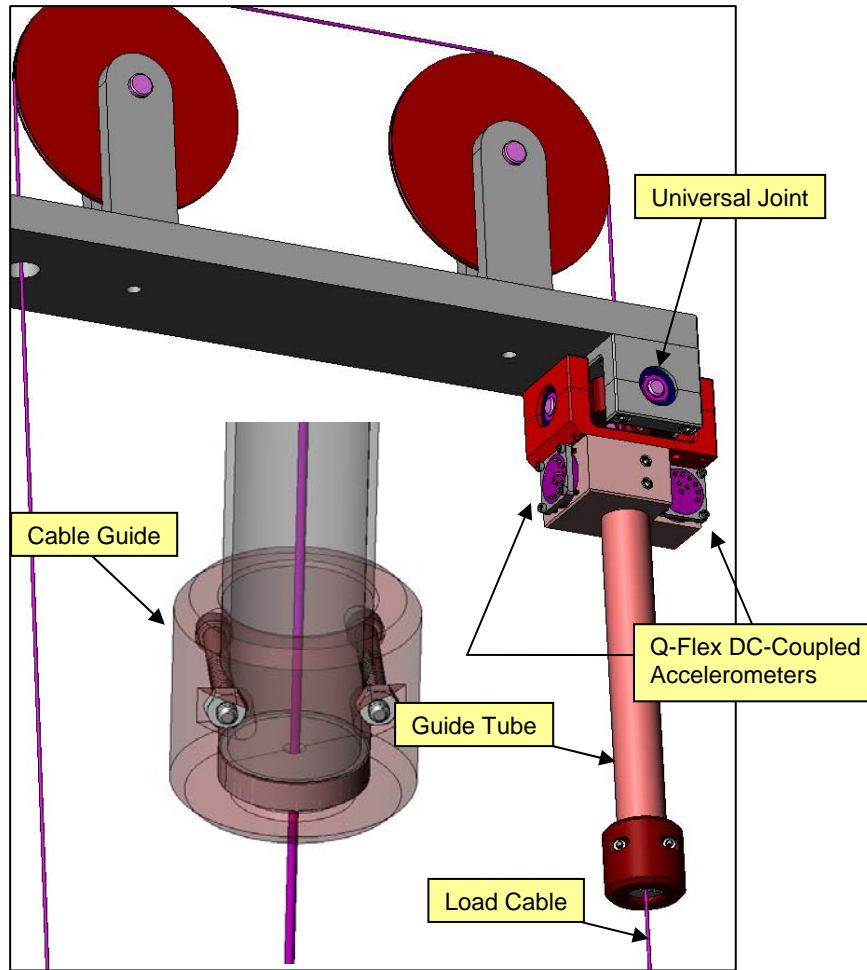


Figure 6: Q-flex DC coupled accelerometers, cable guide, and payload pick point

Figure 7 shows the control system block diagram for one translational axis. A difference in the horizontal position of the pick point relative to the AGM creates an off-vertical angle in the load cable that is sensed by the tip-tilt sensor. The analog tip-tilt sensor output is digitized and digitally low-pass filtered with a cutoff frequency of 1 Hz. Proportional gain is then applied to generate a velocity command (stepper counts/sec) that is digitally filtered and then integrated. Stepper counts are turned into engineering units and a gain is applied that accounts for the cable length variation as the pick point translates vertically. The result is the setpoint for the native position control loop running on the card. Both control loops are executed at a 2-kHz update rate.

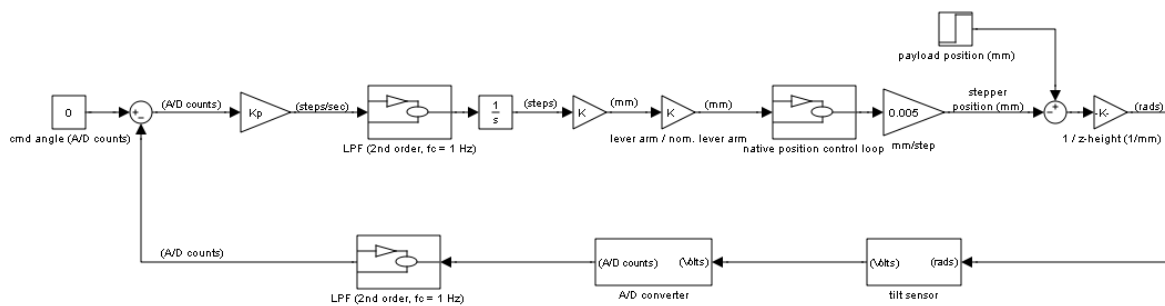


Figure 7: Control system block diagram

Test Results

Friction Tests

Figure 8 shows the WAGM set up for friction tests. Calibrated weights totaling 360.26 N (80.99 lb) were suspended from the load cable. The pressure in the AGM cylinder was adjusted to “float” the load such that the vertically moving carriage of the AGM was stationary and within its working stroke. The air



Figure 8: WAGM supporting 360.26-N (80.99-lb) payload

pressure was then increased very slowly and the pressure P_u (psig) was noted at which the load just began to move upward. The pressure was then reduced very slowly and the pressure P_d (psig) was noted at which it just began to move downward. The friction force referred to the payload end of the load cable was then calculated according to:

$$L_f = A_p (P_u - P_d) / 2N \quad (1)$$

where:

L_f = friction force in lb

A_p = piston area in in^2 (6.157 in^2 (39.72 cm^2))

N = displacement multiplier ratio of pulley system (4.0:1)

The piston pressure in psig was read from the digital panel meter of the WAGM control console (Figure 9). The pressure sensing channel had previously been calibrated against a primary pressure standard. Motion was detected via the digital readout from the carriage position sensor. A displacement change of at least 0.0508 mm (0.002 in) (twice the least-count of the meter) was taken to indicate that friction had been overcome and the carriage had moved.



Figure 9: Piston pressure in psig (lower left) and carriage position from center in inches (upper left) on the control console. Tip-tilt sensor outputs in milliradians are displayed on the other two readouts.

The test was repeated numerous times at payloads of 360.26 N (80.99 lb) and 249.06 N (55.99 lb). Results are shown in Table 1. Each cell of the table contains two numbers. The upper number is a pressure, either P_u or P_d . The lower number is the carriage position at which the pressure was recorded, in inches from the vertical center of travel.

Table 1: Friction test results

Payload = 360.26 N (80.99 lb) Bearing pressure = 210 kPa (30.5 psig)		
P_u k Pa (psig)	P_d kPa (psig)	Friction N (lbf)
Carriage Z cm (in)	Carriage Z cm (in)	
391.23 (56.743) 18.331 (7.217)	390.48 (56.635) 18.326 (7.215)	0.369 (0.083)
390.55 (56.644) -10.419 (-4.102)	389.31 (56.464)	0.618 (0.139)
390.55 (56.644) -10.419 (-4.102)	391.01 (56.711) -10.414 (-4.1)	-0.231 (-0.052)
390.43 (56.772) -10.411 (-4.099)	390.48 (56.634) -10.416 (-4.101)	0.472 (0.106)
391.55 (56.789) -10.409 (-4.098)	390.48 (56.634) -10.416 (-4.101)	0.529 (0.119)
391.52 (56.785) -10.409 (-4.098)	389.94 (56.556) -10.416 (-4.101)	0.783 (0.176)

Payload = 360.26 N (80.99 lb) Bearing pressure = 210 kPa (30.5 psig)		
P_u kPa (psig)	P_d kPa (psig)	Friction N (lbf)
Carriage Z cm (in)	Carriage Z cm (in)	
278.71 (40.424) 0.813 (0.320)	279.48 (40.535) 0.826 (0.325)	-0.378 (-0.085)
278.62 (40.410) 0.815 (0.321)	279.49 (40.536) 0.823 (0.324)	-0.431 (-0.097)
278.62 (40.410) 0.815 (0.321)	279.50 (40.538) 0.833 (0.328)	-0.436 (-0.098)

As usual in friction testing, there is considerable scatter in the results. However, a typical value for vertical friction referred to the payload end of the load cable was 0.445 N (0.1 lb). A lower payload value resulted in less scatter but did not necessarily reduce the friction force. This is probably because a certain portion of the friction comes from cable flexing rather than bearing friction in the pulleys.

In addition to friction, the uplift force accuracy is limited by the resolution of the ultra-precision regulator. By test it was found that, with practice, the pressure could be changed in increments as small as 69 Pa (0.010 psi). This resulted in a force resolution of 69 Pa (0.01 psi) $\times A_p / 4 = 0.67$ N (0.015 lb) due to the pressure regulator. The uplift force accuracy is the combination of the friction and the force resolution due to the pressure regulator, or ± 0.53 N (± 0.12 lb).

Friction tests were also conducted on the AGM alone, without the 4x displacement multiplier. Figure 10 shows the AGM configured for this test. The 4x multiplier mechanism is removed, as is the lower plate that normally supports two pulleys of the multiplier. A load of 711.7 N (160 lb) is suspended directly from the lower cross-member of the AGM carriage. The piston pressure is then adjusted to an equilibrium value just sufficient to “float” the load. Piston pressure and carriage position are monitored via the digital panel meters of the control console (Figure 9). The test method then proceeds in the same way as the aforementioned friction test with the displacement amplifier. It was found that, even with the ultra-precision pressure regulator, the piston pressure could not be adjusted accurately enough to maintain a perfect equilibrium. The carriage would always rise or fall very slowly. This is typical behavior for an AGM. It indicates that friction, if there is any at all, is less than the product of the piston area and the pressure regulator resolution. For a pressure resolution of 35-69 Pa (0.005-0.010 psi) (typical for this type of ultra-precision regulator), the friction force is less than 138 mN (0.031 lb) at the offloader carriage or less than 36 mN (0.008 lb) at the payload end of the load cable when using the 4x multiplier. For practical purposes, the friction referred to the payload end of the load cable due to the AGM itself can be taken as zero.

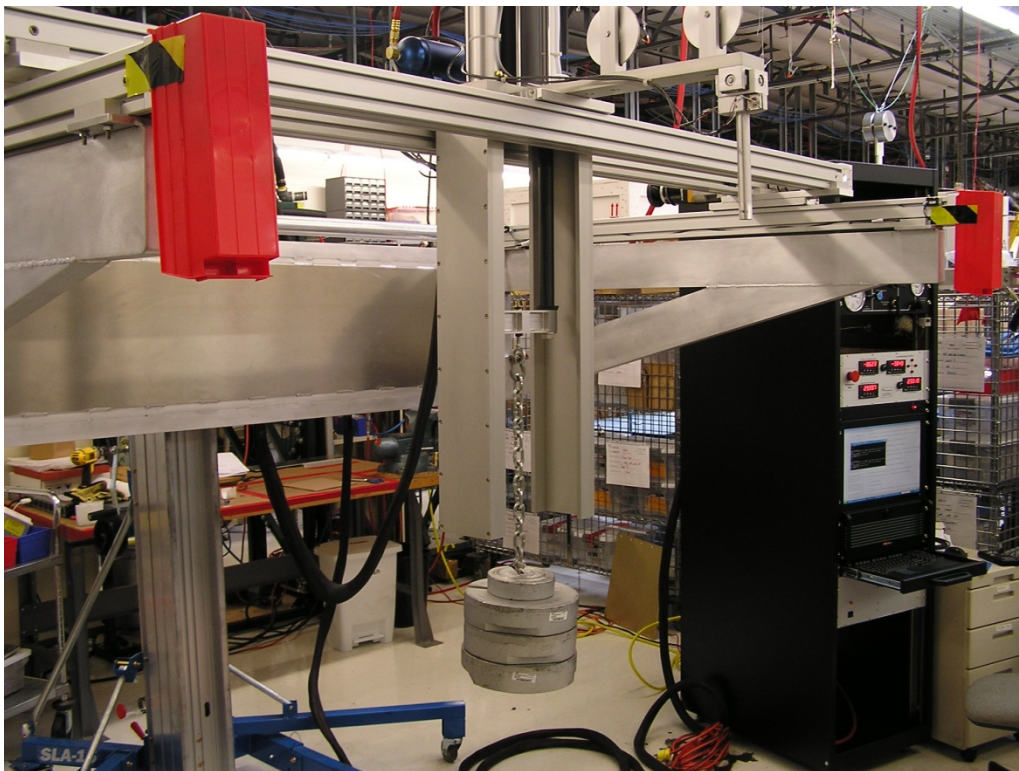


Figure 10: Friction test of AGM alone, without 4x displacement multiplier

Proof Load Testing

Figure 11 shows the WAGM set up for proof load testing. The goal was to demonstrate that the WAGM could support a load of 711.7 N (160 lb) at the payload end of the load cable without sustaining visible damage and retain all functionality. There was no requirement for the AGM to float the proof load nor was there a requirement for the X-Y stages to be moving while supporting the proof load.

For the test, the XY stages were both positioned at their outermost locations. That is, the Y stage was positioned as far as possible from the tower and the X stage was positioned at either travel limit. The AGM was depressurized and the supply pressure to the air bearings was set to its normal value of 206.842×10^3 Pa (30 psig). The tower was extended high enough so that a weight pan could be hung from the payload end of the load cable without the pan touching the floor. At least 711.7 N (160 lb) of weights were placed on the weight pan and the entire system was examined for signs of distress. The weights were left in place for a minimum of five minutes and then removed.

Figure 11 shows the WAGM with 716.1 N (160.99 lb) of certified weights hung from the payload end of the load cable. The XY stage was at one outboard “corner” of its range of motion, per the test requirement. No damage was visible or otherwise apparent during or following the proof load test, nor was any effect on performance detected during the remaining tests.



Figure 11: WAGM undergoing proof load test

X-Y Tracking Accuracy

The customer requested that the offload force resolution be less than 89 mN (0.02 lb) in all three spatial directions. Friction tests and review of the pressure regulator resolution showed that 534 mN (0.12 lb) of vertical force resolution was possible. In the horizontal degrees of freedom this requirement is a function of the payload weight and the angular tracking error when the payload is moving at constant velocity. For a maximum payload weight of 355.8 N (80 lb) and a maximum payload speed of 1.59 mm/s (0.0625 in/s)

this translated into less than 0.25 milliradian allowable steady state angular deviation of the cable guide tube, an aggressive goal to be sure.

CSA conducted a so-called 'box test' to determine the steady state angular tracking error at the maximum payload speed. A box test exercises the robotic arm through its entire range of motion in all three spatial directions. Prior to start, a dummy weight was hung from the load cable and the tip tilt sensors were zeroed. The WAGM custom software generates a log of pressure, position, and angle at a 2-Hz sampling frequency. This sampling frequency is sufficient because as mentioned previously the tip-tilt sensor signals are fed through anti-alias filters before digitization by the controller card, whereupon the signals are then further digitally low-pass filtered onboard the controller card at a cutoff frequency of 1 Hz. The data logged over the entire box test trajectory were plotted against time in order to determine the steady state x-y tracking accuracy as a function of robot arm speed.

The upper panel of Figure 12 shows both the raw signals of X-Z angle and Y-Z angle taken directly from the WAGM software log, as well as the signals post-processed in MATLAB with zero phase shifting digital filtering at 1 Hz for better visualization of the mean underlying angular errors. The lower panel of Figure 12 shows the trajectory of the payload in all three coordinate directions. The Z-trajectory in the lower panel reflects the length of the load cable from the universal joint to the pick point on the payload. Figure 12 shows that the steady state angular tracking error is a function of the payload speed. This is because the feedback control loop utilizes only proportional control (see Figure 7). Integral control was not utilized because it was found that the integral gain required to have any significant effect within the deployment time made the system unstable.

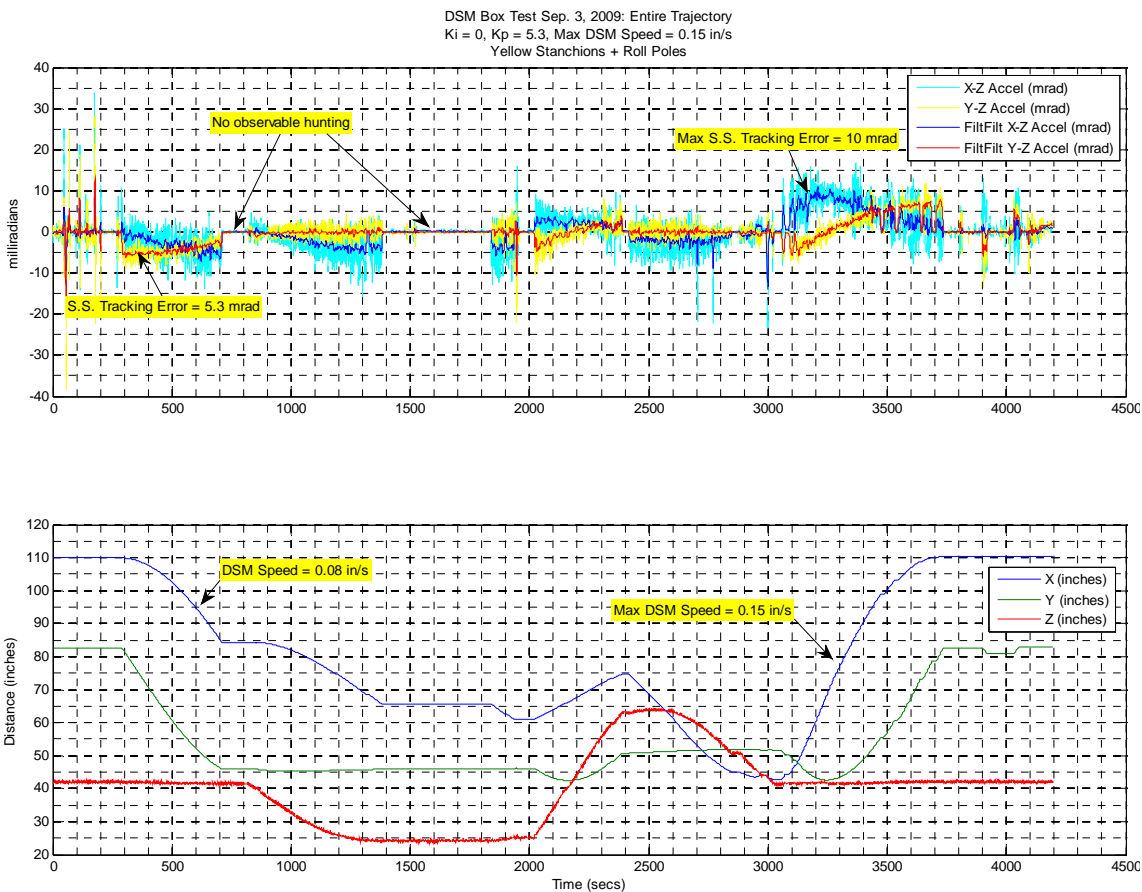


Figure 12: Angular tracking error vs. payload speed during a box test

Figure 12 shows that at a payload speed of 3.81 mm/s (0.15 in/s) the steady state tracking error approached 10 milliradians. Close to the contractual maximum payload speed of 1.6 mm/s (0.0625 in/s) the steady state tracking error was around 5 milliradians. For a maximum payload weight of 355.8 N (80 lb), this corresponds to a lateral drag force of just 1.779 N (0.4 lb).

Lessons Learned

Free play in the stages of the COTS telescoping tower presented some significant challenges during development. Free play around the vertical axis of the telescoping tower produced a yaw mode that interacted unfavorably with the horizontal active tracking system. Free play in the roll direction gave rise to a sudden shift of the load platform as the AGM traversed over center in the X-direction.

To mitigate the control engagement of the yaw mode two anchor stanchions and a set of guy cables were added to stiffen the tower in yaw. To eliminate load platform shifting two telescoping poles were installed beneath the tines of the load platform to stiffen the tower in roll. The customer deemed the set-up repeatability of these stiffening elements insufficient however, and so another stiffening solution was devised that lent itself to greater repeatability of setup.



Figure 13: Pair of triangulated roll poles to stiffen telescoping tower of industrial lift

The solution implemented was a pair of telescoping tubes that triangulate the structure (Figure 13). The telescoping tubing retracts and extends automatically with the raising and lowering of the load platform.

The two sections of each tube are clamped together once the load platform is at the desired height. The setup is straightforward and repeatable with the use of a torque wrench to pre-load the triangulating members.

Refashioning COTS equipment for use in an application for which it was not originally intended should be approached with caution. Such use often depends on characteristics of the COTS equipment that are not usually important (free play of the tower in yaw and roll) and may therefore not be well controlled in design and manufacture. This is the risk that comes with the cost savings motivating the use of COTS equipment. In hindsight, the problems with the tower could have been solved at the design stage by simply using two towers, one lifting at each rear corner of the load platform. More attention to tower stiffness could potentially allow the X-Y control system to be stable at higher gains and possibly with integral gain, thus giving higher tracking accuracy.

Conclusions

WAGM is the first proven three-DOF gravity offloading system of its kind to deliver high fidelity zero-gravity simulation over large displacements with very low set-up time. Its very simple interface to the payload suggests that it could be used for zero-g simulation with a wide variety of deployable structures and other uses as well. Potential applications of WAGM include:

- Ground testing of deployable spacecraft structures
- Pick and placement of heavy, sensitive equipment (e.g., during spacecraft installation)
- Gravity offloading of human subjects for injury rehabilitation or to study the effects of zero-gravity conditions on the musculoskeletal system

With its improvements over existing technologies in zero-gravity simulation fidelity, set-up time, and extended range of motion, it is easy to envision many applications for WAGM at significant cost savings to the user in terms of set-up time, testing time, and accurate system validation.

References

- [1] Kienholz, D., Crawley, E., Harvey, T., "Very Low Frequency Suspension Systems for Dynamic Testing," Proc. 30th Structures, Structural Dynamics, and Materials Conference, Mobile, AL, April 1989
- [2] Kienholz, D., "A Suspension System for Simulating Unconstrained Boundary Conditions," Proc. 12th Int'l Modal Analysis Conf., Honolulu, HI, February, 1994
- [3] Tanimoto, R., Moore, A., MacDonald, D., Thomas, S., Murray, A., Polanco, O., Agnes, G., "Model and Test Validation of Gravity Offload System," Proc. 48th AIAA/ASME/ASCE/AHS/ASC Structures, Structural Dynamics, and Materials Conf., Honolulu, HI, April, 2007
- [4] Corey, R. L. and Pidgeon, D. J., "Electric Propulsion at Space Systems Loral," IEPC-2009-270, 31st International Electric Propulsion Conference, MI, 2009

Gimbals Drive and Control Electronics Design, Development and Testing of the LRO High Gain Antenna and Solar Array Systems

Boris Chernyakov* and Kamal Thakore**

Abstract

Launched June 18, 2009 on an Atlas V rocket, NASA's Lunar Reconnaissance Orbiter (LRO) is the first step in NASA's Vision for Space Exploration program and for a human return to the Moon. The spacecraft (SC) carries a wide variety of scientific instruments and provides an extraordinary opportunity to study the lunar landscape at resolutions and over time scales never achieved before. The spacecraft systems are designed to enable achievement of LRO's mission requirements. To that end, LRO's mechanical system employed two two-axis gimbal assemblies used to drive the deployment and articulation of the Solar Array System (SAS) and the High Gain Antenna System (HGAS). This paper describes the design, development, integration, and testing of Gimbal Control Electronics (GCE) and Actuators for both the HGAS and SAS systems, as well as flight testing during the on-orbit commissioning phase and lessons learned.

Introduction

In January 2004, the President of the United States unveiled the Vision for Space Exploration which charted the path for the return of humans to the Moon and deep space. The first milestone in that plan was an unmanned lunar orbiter to be launched in late 2008. By late 2004, that first mission had become the Lunar Reconnaissance Orbiter, and as 2005 began, development had started at NASA's Goddard Space Flight Center.

With a goal launch date of end of 2008, the mission had only four years to be developed from concept to launch. In addition, the primary mission required that the spacecraft remain in a nominal 50-km polar mapping orbit for a minimum of one year, collecting data over the entire lunar surface under all possible lighting conditions; imposing challenging constraints on SC design. Schedule, cost, mission, and reliability requirements manifested themselves in every aspect of the LRO design.

To meet the needs of a discovery-class mission with an accelerated development schedule, the development, fabrication and testing of the LRO GCE and Actuator subsystems was inevitably fast-paced. Schedule needs of the overall mission required that the GCE/Actuator subsystems provide reliable, environmentally tested flight hardware within 15 months of specification release; just in time for SC integration and test (I&T) activities. Figure 1 shows the layout of the integrated spacecraft, with fully deployed HGAS and SAS.

This paper will discuss the overall design, development, integration, testing (ground and flight), and lessons learned for the GCE and Actuator subsystems of both the HGAS and SAS.

* ATK Space Systems and Services, Beltsville, MD

** NASA Goddard Space Flight Center, Greenbelt, MD

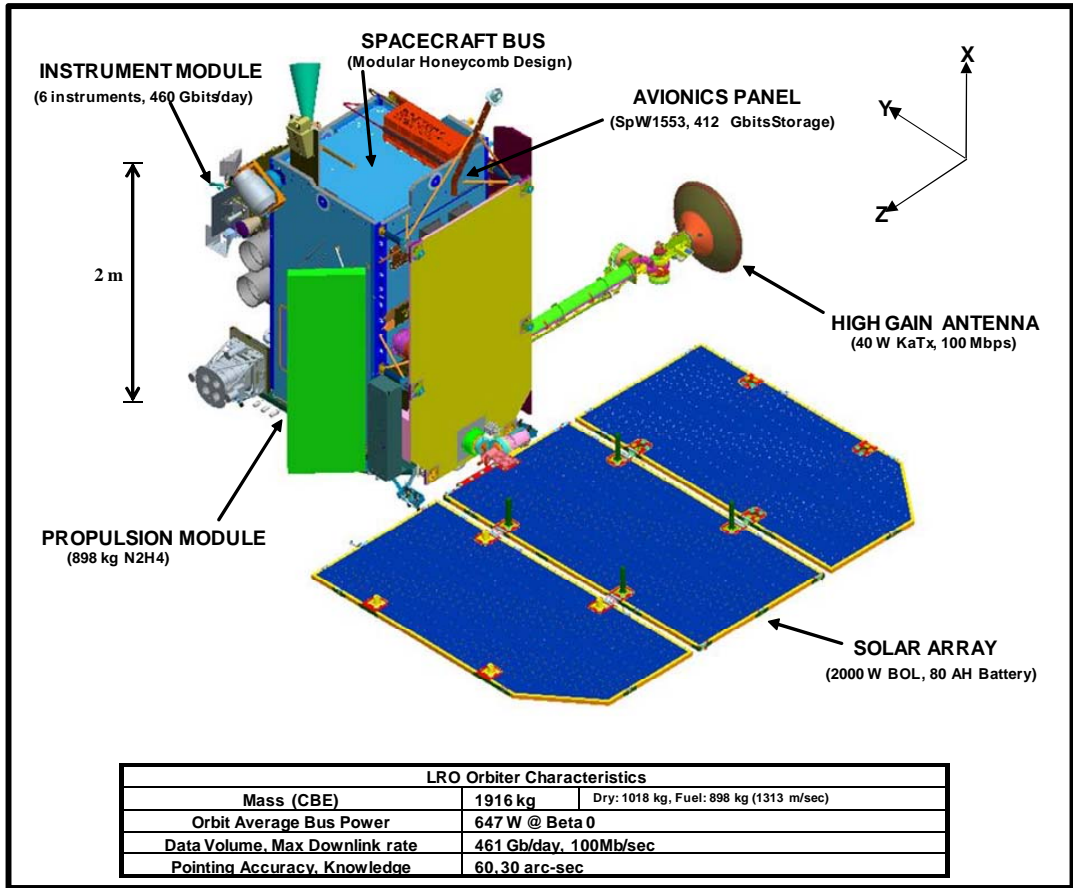


Figure 1. LRO Spacecraft with Deployed Solar Arrays and High Gain Antenna

Design

As described in the Introduction portion of this paper, the Gimbal Control Electronics and Actuator subsystems of the LRO are intended to enable the primary mission objectives, and were required to meet cost, reliability and schedule constraints imposed by the class and short development time of the overall mission.

On LRO, the function of the GCE is to control and drive dual-axis redundant actuators on the SAS and HGAS. The Solar Array System GCE drive enables mechanical rotation of 90° on one actuator and 180° on the other, allowing the Solar Arrays to track the sun in two axes and provide a reliable power source for the Orbiter. The HGAS GCE subsystem drives 180° rotation on both axes, enabling the high-gain antenna to point toward Earth whenever it is in view (providing maximum time for data downlinking and ground system communications). Two redundant, dual disk, incremental encoders – one on the input (fine) and one on the output (coarse) – are integral to the actuator assembly for both the HGAS and SAS GCE subsystems. These encoders provide fine and coarse incremental position sensing with respect to a unique home/reference position located at the center of travel. They also provide a logical state change for each physical motor cardinal step taken, thereby providing an output resolution equal to the cardinal step size. A pictorial view of the LRO actuators and the internal layout of the fine and coarse encoders are shown in Figure 2. HGAS and SAS gimbal systems can be seen in Figure 3.

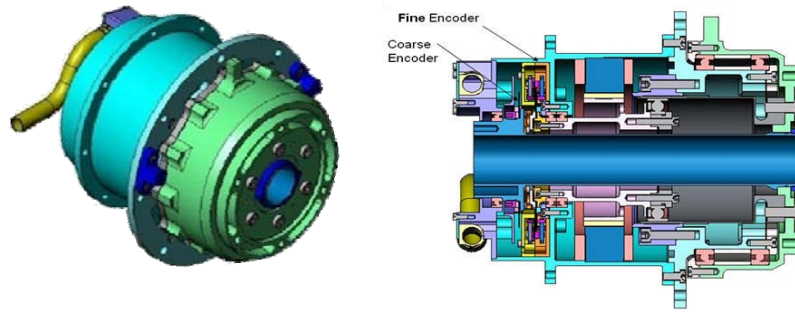


Figure 2. LRO HGAS and SAS gimbal actuators

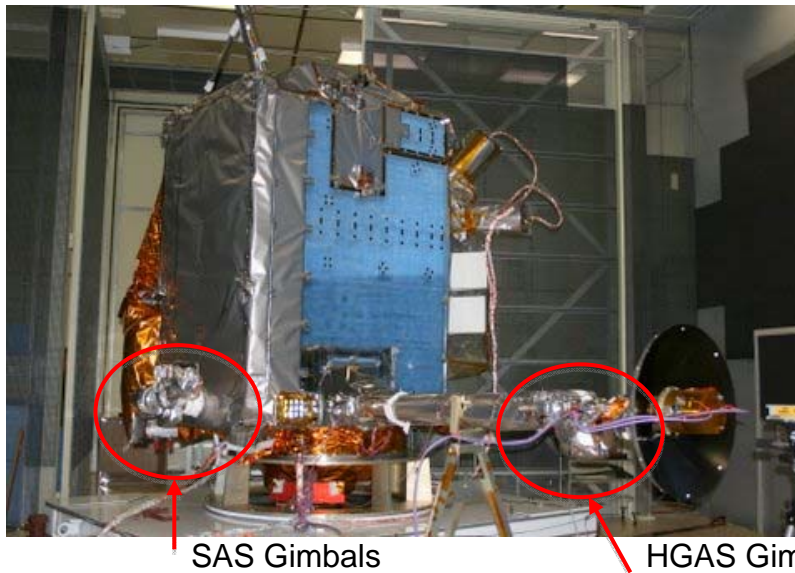


Figure 3. LRO S/C in the EMI chamber with a removed SA and fully deployed HGA

The GCE/Actuator subsystems consisted of two engineering development units (EDU), three flight boxes, two commercial actuators, and five flight actuators. Each electronics box provides a fully redundant two-axis control or drive for the three-phase harmonic drive actuators.

These gimbal assemblies, including the Gimbal Control Electronics (GCE) and harmonic drive actuators used for the SC deployables were developed by a team comprised of engineers from Goddard Space Flight Center (GSFC), Alliant TechSystems (ATK), Broad Reach Engineering (BRE) and Sierra Nevada Corporation (SNC).

Actuator Selection

In order to meet reliability and schedule constraints, the project leveraged available technologies and in-production hardware, and strove for overall simplicity of design wherever possible. To ensure that reliable, environmentally tested GCE/Actuator subsystems were delivered in time for SC I&T activities, the project selected SNC Actuators, identical to those developed for the Solar Dynamic Observatory (SDO) spacecraft.

These actuators had been extensively tested during SDO High Gain System integration, with performance characteristics shown to meet the basic requirements for LRO's mission. The actuator interfaces were also well understood, allowing subsystem and interfacing system designs to proceed rapidly. In addition, these actuators provided the internal redundancy required by LRO's mission.

Although the HGAS and SAS inertias differ by a factor of fifty, the analysis showed that the actuators could easily achieve the required torque margins for both systems with optimized motor drive control electronics. Given that the SNC Actuators met the needs of both the HGAS and the SAS, and could take advantage of the development and testing for SDO, these actuators were selected for use on LRO over more optimized but more schedule intensive actuators.

Drive Electronics Selection/Design

Due to the wide range of operational constraints imposed by a lunar mission, such as a challenging thermal environment and the need for extensive ground testing in a 1g environment, a drive electronics system with multiple set points was selected to provide flexibility.

In addition, it was found that the drive system needed to allow micro-stepping with multiple resolution options for micro-step rates. Accurate tracking of the sun on two axes required that the solar arrays be driven at a rate of 7 pulses per second (pps), and their large inertias added the risk that spacecraft jitter may have caused violation of pointing budgets. To minimize the potential effects of SAS tracking on spacecraft stability, the GCE assembly (Figure 4) was designed to provide the capability for micro-stepping at multiple resolutions.

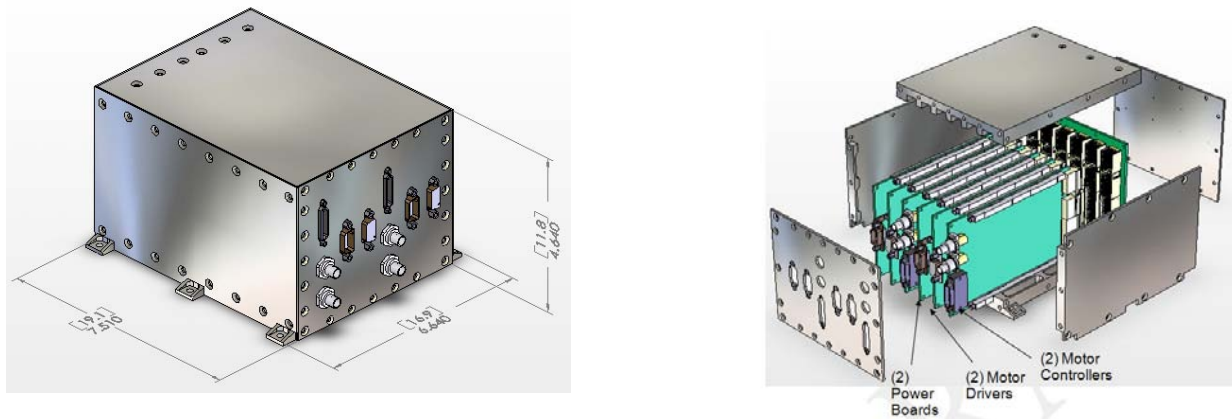


Figure 4. LRO Gimbal Control Electronics Box

GCE Design

To take advantage of the inherent internal redundancy of the SNC actuators, and to improve the reliability of two critical SC control subsystems, the GCE subsystem was designed as a 100% redundant electronics box. The GCE subsystem is comprised of two identical controllers, two identical Motor Driver Boards, two identical DC to DC Converter Boards, two backplanes and the chassis. The spacecraft provides the subsystem a 31-Volt Direct Current (VDC) nominal voltage and Primary/Redundant Side Enabled pulsed discrete commanding to the subsystem. The GCE communicates with the SC via the MIL-STD-1553B bus. A block diagram of the GCE is shown below in Figure 5.

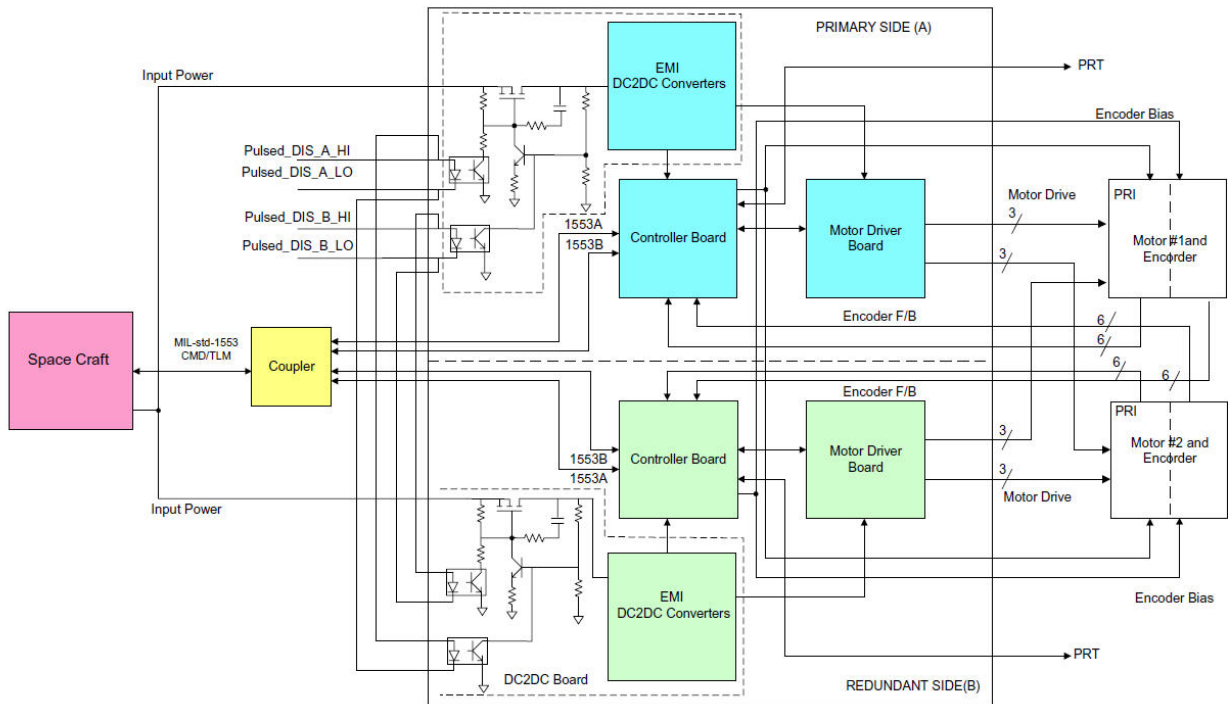


Figure 5. LRO GCE block diagram

The GCE design maximizes internal mode control capability while minimizing command and control interfaces with the flight software. Major communications and control functions are accomplished by two Field Programmable Gate Arrays (FPGAs). One of these is located on the Controller Card to provide SC command and telemetry interfaces, processing of critical and housekeeping GCE telemetry, operational positioning controls, and automated positioning controls. The other FPGA is located on the Motor Driver card, and controls the stepper motors' commutation sequences, micro-stepping capabilities, programmable power set points, and closed loop current control.

To allow minimal power dissipation in the gimbals, and to provide flexibility in selection of an optimum drive, the GCE design utilized a constant current drive system with pulse width modulated control. The system offers eight current set points ranging between 200 and 390 mA. Operational step rates are commandable in the range of 0 to 67 cardinal steps/sec for flight operation and 0 to 150 steps/sec for laboratory and ground testing. The system also enabled optional micro-stepping, allowing commanding of micro-step resolutions from 0 (1 cardinal step) to 6 (64 cardinal steps), to minimize the effect of tracking motions on spacecraft jitter. Internal electronics condition the actuator motor and output optical encoder signals, providing a closed loop control with resolution of 0.0075° per cardinal step.

The GCE uses five distinct command modes to execute gimbal control; the GCE mode state diagram is shown in Figure 6. In addition to the basic commanding of the gimbals, the GCE also monitors gimbal execution and positional accuracy by way of operational error flags; the Position Error and Step Error flags. During the initialization mode, the GCE sets the "Home" position to 0, and the Position Error flag is checked every time the "Home" marker is crossed to verify that the current position is at 0 counts. Any deviation from 0 indicates positional accuracy violation. The Step Error flag is generated if encoder feedback indicates that the actuator failed to complete a command for the motor to take a step. These operational error flags ensure that the gimbals can be accurately commanded and controlled. The GCE also provides high resolution temperature monitoring for multiple PRT (platinum resistance thermometer)/Thermistor sensors for various LRO SC hardware components.

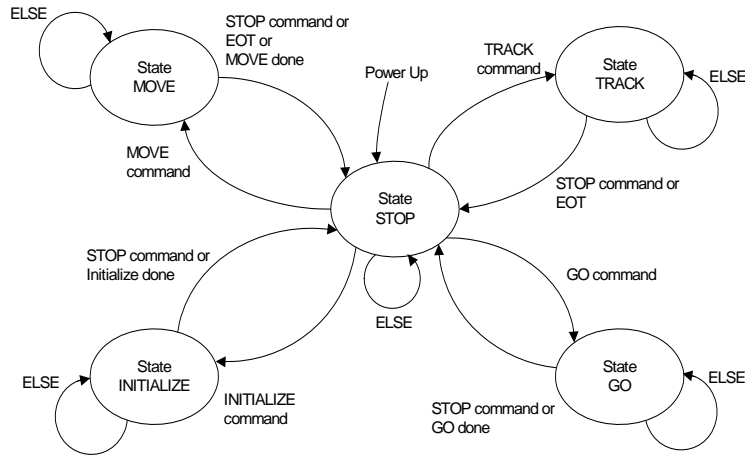


Figure 6. GCE Mode State Diagram

Technical Problems and Solutions

As with all spaceflight hardware, design of the GCE/Actuator subsystems presented many technical challenges. Not only did the systems need to meet flight requirements, they also needed to be able to be efficiently and thoroughly tested in all operational modes.

Re-circulating Current and Motor Current Measurement Distortion

One such challenge was presented by the need to provide an accurate motor current measurement in a pulse modulated system with multiple actuator drive current settings, while operating from an unregulated power bus.

Specifics of the pulse width modulation control produce a re-circulating current (supplied by the actuator coils during dead time), bypassing a sense resistor. Figure 7 shows one possible re-circulating current condition, with all motor driver switches set on HIGH.

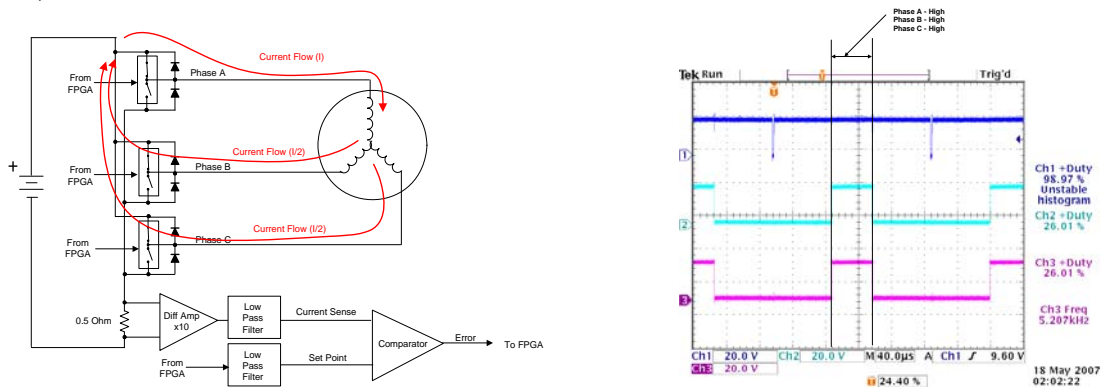


Figure 7. GCE shunt current monitoring, all motor driver switches on HIGH

When all the motor driver switches are set on HIGH, the current is supplied by the actuator coils, re-circulating to the power supply and therefore bypassing the sense resistor. The current then decays based on the time constant of the actuator coils ($t = 100\text{mH}/69\text{W} = 1.4\text{ms}$), reducing the shunt current measurement, and distorting the motor current value.

To resolve the problems related to the re-circulating current, the FPGA measures the dead-time using knowledge of the pulse width modulated (PWM) duty cycles. The FPGA calculates the measured current error by computing the amount of measured current distortion (% of time the current is measured) from knowledge of the PWM duty cycles. The commanded set point is then continuously adjusted by multiplying the power set point by the shunt measurement distortion factor, reported in the telemetry as a “power scale factor”. Figure 8 shows a simplified model of the current control mode with “dead-time compensation”.

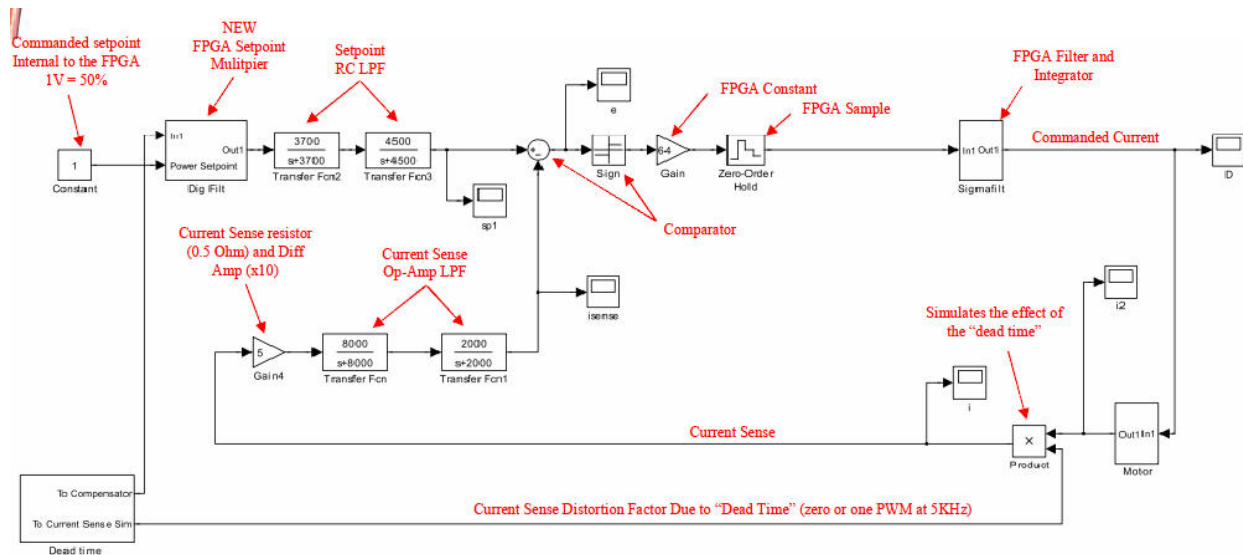


Figure 8. GCE Current Control Mode

Power Return Electromagnetic Interference/Radio Frequency Interference

Another challenge was presented by the design of the gimbal drive electronics power returns. These drive electronics required that the primary (spacecraft) power returns be connected to the secondary returns, and therefore must be isolated from the chassis. To satisfy LRO’s EMI/RFI requirements, low noise PRT conditioning circuits were utilized and many other design considerations were implemented.

When the GCE/Actuator subsystem EDU was initially EMI tested, analysis showed significant EMI violations and excessive noise. To resolve the violations and decrease the noise, many modifications to the EDU were made. These included redesign of the power distribution to the motor drive electronics, implementation of constant current source circuitry for temperature monitoring, and a partial re-layout of printed circuit cards. Final EMI and functional testing verified that these design changes successfully resolved all EMI and noise related issues.

Component and System Level Tests

Systems level testing of the HGAS and SAS was particularly critical to mission success. In order to conduct multiple, and often simultaneous, tests, many combinations of flight hardware, commercial equivalents, and Ground Support Equipment configurations were identified, with specific harnesses fabricated.

Although all GCE subsystem testing was done with a dedicated lab-view setup, all system and SC level GCE testing was conducted with Integrated Test and Operations System (ITOS) driven test racks. ITOS would be used in flight for commanding and telemetry monitoring, and provided a flight like ground control environment for testing. Use of the ITOS test racks for testing also allowed the team to develop and become familiarized with ground station telemetry and control pages, used throughout system and Orbiter integration and testing, and in flight. Two sample GCE/Gimbal telemetry pages are shown below in

Figures 9 and 10; Figure 9 shows a gimbal telemetry display built in an ITOS Java environment, and Figure 10 shows a typical GCE telemetry page.

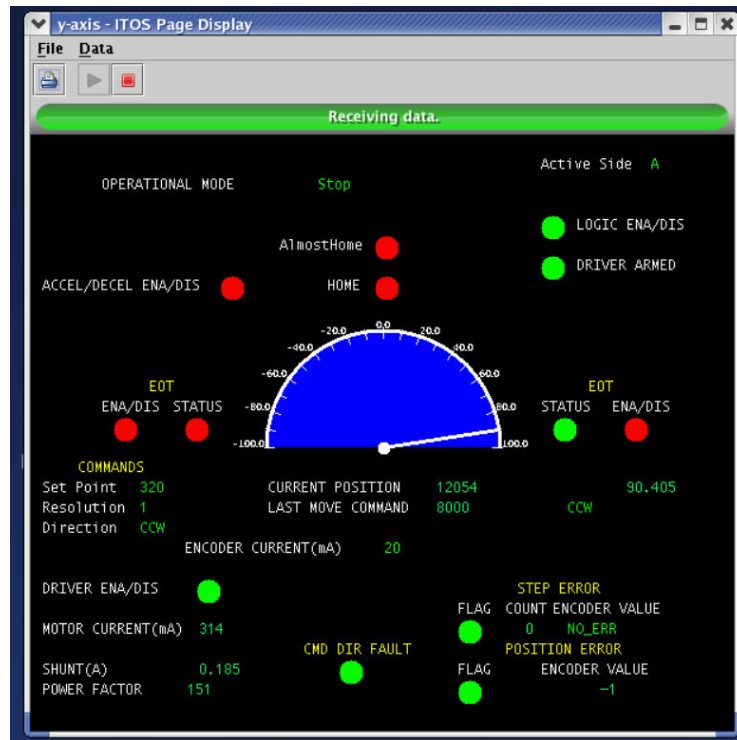


Figure 9. Sample Y-axis Gimbal Telemetry Display



Figure 10. Sample ITOS GCE Telemetry Screen

Specialized test configurations allowed various detailed characterizations of subsystem elements to be developed. This was particularly useful in the case of the HGAS actuators. Although the SAS flight software (FSW) could be ground tested with flight gimbals without solar array panels attached, the HGAS FSW and tracking and control algorithms fully verified in a 1G environment and was mostly conducted with the set of commercial (but otherwise flight like) actuators. Therefore it was critical to characterize the flight units prior to integrating them into the gimbals assembly.

The characterization of the GCE/Actuator components prior to flight was especially helpful in the identification and isolation of the source of one specific anomaly encountered during flight operations. Figure 11 shows the results of test characterizations for HGAS flight actuator encoder responses when operating at a 67 pps step rate in clockwise (CW) and counterclockwise (CCW) directions. The distinct differences of the signal waveforms illustrated here will be addressed in the Flight Operations section of this paper.

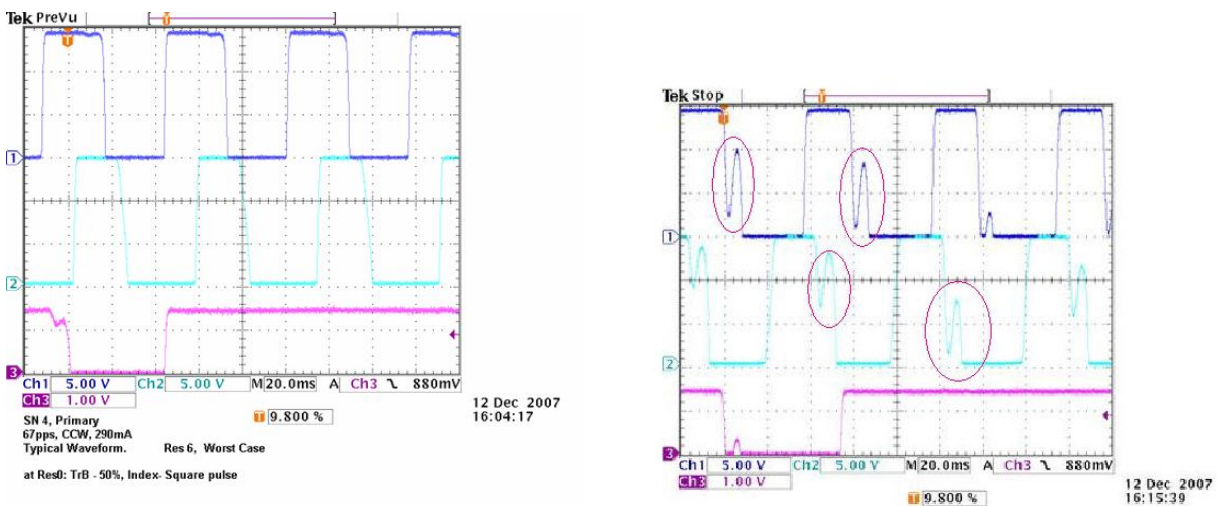


Figure 11. LRO HGAS Actuator Encoder responses at a 67 pps step rate (Left: CCW, Right: CW)

To conduct the necessary HGAS Range of Motion tests with LRO's flight antenna, a special sequence of coordinated motions and tracking rates were developed. These special sequences were intended to enable testing of the entire end-of-travel to end-of-travel range of motions for all quadrants of the two-axis gimbals while avoiding "zippering" in the 1G environment. These special motion sequences and tracking rates were developed from calculations and analysis of torque capabilities that allowed determination of safe start and end positions, while enabling the ground test to exercise slew and tracking rates. Specific current set points for each motion were established to produce a combination of single and dual gimbals motions for the test that would minimize the time required to complete any individual test. These motions were run numerous times during the integration and environmental testing of the spacecraft. The HGAS Range of Motion Profile is shown in Figure 12.

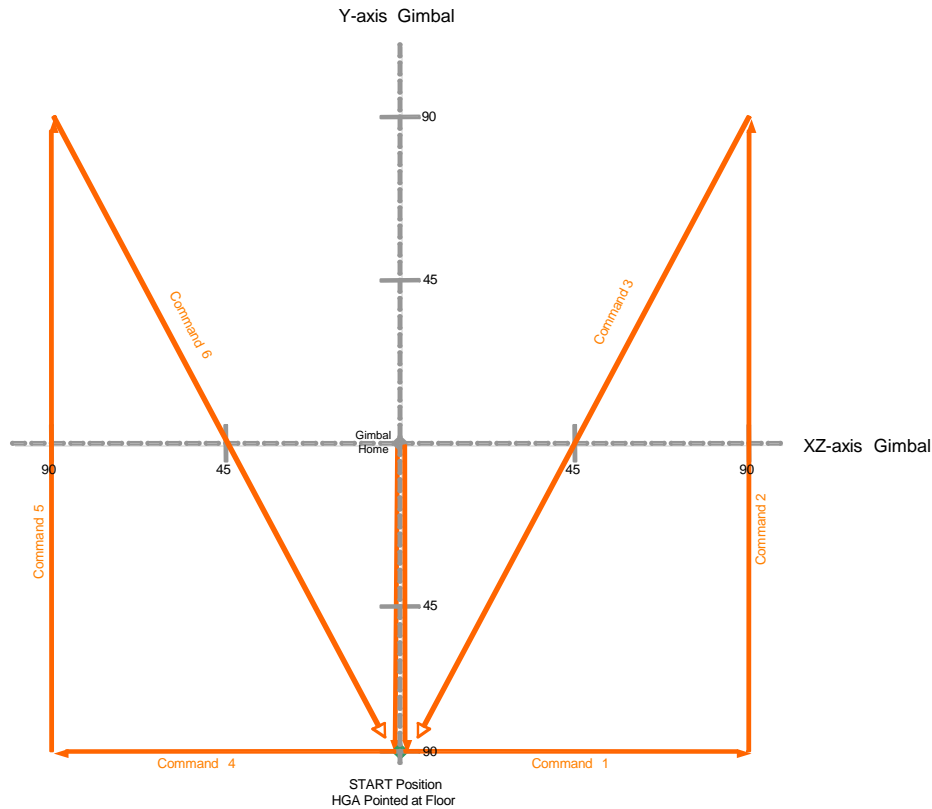


Figure 12. HGAS Range of Motion test profile

Lessons Learned

Although numerous potential improvements to GCE/Actuator requirements, design and operation were realized during the many hours of HGAS, SAS and SC testing, integration and operation, only a few of the most significant are discussed below.

Lack of loadable "Position Register"

One potential improvement to the system would be to have a pre-loadable position register. This would simplify laboratory development and ground level testing, as well as eliminate some confusion when gimbals are deliberately positioned to certain angles prior to system shut down. With a pre-loadable position register, on power up the GCE could be loaded with the default value. If knowledge of absolute position is required for follow-up tests, the register could be pre-loaded with the value corresponding to an actual position, and any further movement, even without system initialization, would reflect absolute gimbal position. In a 1G environment, the initialization is sometimes an undesirable mode, and can be a time consuming operation. Use of pre-loaded position register can be utilized to save time and avoid undesirable operation modes.

An alternative solution may also be the addition of non-volatile memory, where specific system parameters can be maintained at all times.

Acceleration/Deceleration Profiles

One of the original requirements imposed on the GCE by the LRO Design Specification was that acceleration (Accel) and deceleration (Decel) ramping profiles be internally generated. At the time the Design Specification was developed (early in LRO's project life), ACS tracking requirements and controls were not fully defined, making it difficult to establish requirements for the Accel/Decel profiles. As a result,

it was later found that meeting the specified requirement of no greater than 2 seconds ramping timing to move the high-inertia Solar Array was extremely difficult.

Satisfying the Accel/Decel profile requirements while maintaining the necessary micro stepping resolution, and meeting the requirement to always finish motions at the cardinal step was very challenging. This requirement also presented complications in FPGA implementation of multiple micro-step resolutions and rates. Although the problem was resolved for 90% of possible combinations of micro-stepping resolutions and step rates, the function ended up disabled as LRO's FSW employs its own acceleration and deceleration algorithms. In LRO's case, hard-coded Accel/Decel profiles did not match with control algorithms and were not useful as a tool to reduce SC disturbance.

In addition, LRO's system utilized micro-stepping based on cardinal steps rather than pure micro-stepping; in the LRO system, the micro-stepping was incorporated within the cardinal step and was required to stop at each cardinal step. Implementing Accel/Decel profiles in this system used a large percentage of FPGA capabilities, and made design alterations extremely difficult.

Based on the difficulties encountered, and the ability to provide acceleration/deceleration algorithms via FSW, it may not be practical to hard code Accel/Decel profiles into the GCE.

Constant Current vs. Constant Voltage Drive

Although the use of a constant current motor drive in the system does offer some benefits, it is not clear if these benefits outweigh the complexities they introduce into the system, especially while meeting current (and torque) requirements at Hot and Cold conditions with high set points.

Comparatively, the a constant voltage stepper motor drive delivers better performance at a given set point; the power delivered to the motor in a "Cold" environment is greater than that in a "Hot" environment, providing more balanced torque margins at various ambient conditions.

The constant current drive also introduces complications in accurate monitoring of the actuator current in a pulse-width modulation scheme (as discussed earlier), due to the fact that the sense resistor does not measure the re-circulating ("freewheeling") current flowing in the motor.

Taking these considerations into account, a constant voltage drive may be more appropriate for use in similar conditions.

Two Encoder Current Options

LRO's GCE design specification required two set points for encoder LED excitation. Although this was a proven and uncomplicated circuit implementation, it appears to be excessive requirement for a mission of LRO's duration and radiation environment, especially without including the capability to measure possible read-head performance degradation. Additional command and control functions required significant analysis and testing during GCE development and SC testing. This requirement should be re-visited for similar applications.

HGAS and SAS Flight Operation and Performance

Both the HGAS and SAS subsystems were shown to perform exceptionally well from deployment through slewing and tracking operations at various operational currents and stepping rates.

No Position Errors

No position errors were seen in any mode for either the SAS or HGAS gimbals from launch throughout the commissioning phase. From HGAS and SAS deployment, through the first month and a half of operation, the gimbals were operated at the nominal micro-step and current levels determined to provide required torque margins, satisfy GEVS Gold Compliance, and provide reliable operation in safe hold mode. For the SAS, nominal micro-step resolution is 16 micro-steps per cardinal step at a Y-axis current

of 320 mA and a Z-axis current of 220 mA. For the HGAS, the nominal micro-step resolution is 16 micro-steps per cardinal step with a motor current of 240 mA on both axes.

Single Step Errors

Although no position errors were encountered, a few single step errors were detected on both systems at the beginning of tracking motions immediately after the initialization sequence. A step error is an inherent feature of the actuator harmonic drive which, occasionally during the first few steps of motion, results in the motor encoder not detecting a step within the time the GCE expects to see a transition. The step errors did not result in any position errors. These single step errors during the gimbal operation are a good indication of the balance between the motor current, encoder LED current and encoder alignment.

SAS Actuator Power Dissipation Reduction

The SAS Y-axis actuator operations also underwent on-orbit testing on July 1, 2009. Prior to testing, analyses were conducted for the worst-case inertia of 321 N-m-s² (2841 in-lb-s²). By reducing the torque factor to 1.25, it was determined that a 240-mA operational current would provide a positive torque margin for the Y-axis actuator. Analyses also showed that slightly increasing the parameter "Number of steps to accelerate inertia to full speed" conservatively set to 15 (with approximately 2:1 margin,) would result in stable operation with both 200-mA and 220-mA currents.

On-orbit testing was executed at both 200 mA and 200 mA for both SAS gimbals, exercised over the full range of motion, and demonstrated reliable, error free operation. To add additional margin, the decision was made to set the Y-axis operational current to 240 mA, reducing actuator power dissipation from approximately 5.5 W to 3.0 W.

The on-orbit testing, and the implementation of the test and analysis findings, was in response to Thermal team requests to minimize motor power dissipations effects on SAS Y-axis actuator temperature.

Delta Angle Violation Anomaly

A single type anomaly, initially detected by the Guidance, Navigation and Control (GN&C) team, was occasionally observed on the HGAS gimbals during slewing operations at 67 pps in the CW direction, referred to as a Delta Angle Violation (DAV). The first HGAS DAV happened at 2009-170-01:07:30.43345. DAV flags are generated by the FSW if the difference between two consecutive samples of position telemetry data, sampled at 200-ms intervals, exceeds 14 counts, which corresponds to the fastest allowable rate of 67 steps per second. The source of this error was traced to the **flight** actuator's encoder operation associated with misalignment and amplified by the operation in the micro stepping mode. This also explains why the error was never seen during ground tests or simulations, during which the **commercial** encoders were used.

The anomaly mechanism can easily be seen by analyzing the plots shown in Figure 11. When the GCE reads a proper track transition (level change exceeds the conditioning circuitry threshold) it updates the position counter by increasing the count for CW corresponding transition or decreases it for the CCW corresponding transition. When the "wobble" occurs, it causes the GCE to increase the counter on the lowering transition prior to the "wobble." It then decreases it on the "wobble-up" transition (since this is the proper CCW corresponding transition). This results in the net zero count change with the following "wobble-down" transition producing a legitimate step count. If the position telemetry counter is sampled prior to the "offsetting wobble" it would produce an extra step count, which should happen at a later time. A similar scenario could occur on either the A or B track. Since the position counter is sampled asynchronously with the DAV flag, occasional violations are produced.

This anomaly can be easily resolved by switching from micro-stepping (which is not required for the HGAS operation) to cardinal stepping, but since this anomaly does not affect gimbal operation or the control algorithm, the HGAS operational mode was not changed.

Effects of Micro-Stepping on Spacecraft Jitter

Further testing was conducted to study the effect of various micro-step resolutions on SC jitter. The plots in Figure 13 show the motor winding currents at 2 micro-step and 32 micro-step resolutions, and indicate why some improvement of SC jitter at higher micro-step resolutions was expected.

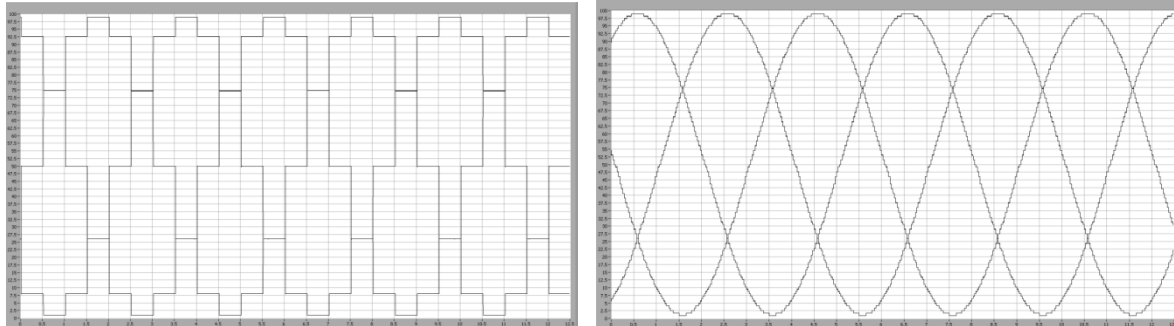


Figure 13. Actuator winding currents at 2 (left) and 32 (right) micro-steps per cardinal step modes

In addition, a Gimbal Step Resolution Experiment was conducted on the LRO Solar Array Gimbals to determine the effects of the different step resolutions on spacecraft Jitter and Attitude Error. The test entailed running the Solar Array gimbals in track mode, using three different step rates or resolutions: cardinal, 16 micro-step, and 32 micro-step. The experiment was conducted on consecutive orbits in the sequence indicated in Table 1.

Table 1. Timeline for SA Gimbal step resolution experiment

Test Timeline	
Time	Event
2009-183-21:42:00	SA Y Gimbal stopped, commanded to cardinal stepping
2009-184-01:07:44	SA Y Gimbal stopped, commanded to micro step with resolution of 32
2009-184-03:00:00	SA Y Gimbal stopped, commanded to micro step with resolution of 16

To analyze the data, MATLAB was used to generate a Power Spectral Density (PSD) plot of the Spacecraft Body Rates for each of the three test cases. In order to obtain more information about the difference between the spacecraft’s response to various gimbal micro-step resolutions, the time history of the Attitude Error and IRU rates was calculated. The variance in the data is shown in Table 2 for SC body rates and Table 3 for Attitude Error.

Table 2. Variance for SC Body Rates for full data set

Body Rates (asec/sec)	X Variance	Y Variance	Z Variance
Cardinal	27.4473	110.3259	8.2311
Micro 16	20.9319	113.7145	8.0349
Micro 32	22.2692	84.5873	7.4360

Table 3. Variance for SC Attitude Error for full data set

Attitude Error (asec)	X Variance	Y Variance	Z Variance
Cardinal	16.1147	21.4523	4.8761
Micro 16	4.4508	13.0828	2.1641
Micro 32	2.5229	8.2906	2.2742

After analysis of the results, it was determined use of the 32 micro-step resolution significantly improves attitude and jitter performance, in comparison to use of cardinal stepping.

Conclusion

On-time hardware delivery, successful SC integration and test, and six months of successful on-orbit testing and operation have demonstrated that the GCE/Actuator team, and the overall LRO Project team, used a viable approach for the rapid design, development and integration of critical spacecraft subsystems.

Acknowledgements

The authors would like to recognize many individuals instrumental to the successful design, development, testing, and integration of the LRO GCE/Actuator subsystems. The Pala Manhas, Praful Petal, Chris Hodge, and the entire BRE GCE team not only provided the development and timely delivery of the gimbal control electronics, but also all necessary support during SC operation. HGAS and SAS mechanical engineers Adam Matuszeski (GSFC), Greg Martins (GSFC), and Mike Hersh (Sigma) were all critical to mission success. SNC's Jeff Moser and GSFC's Joe Schepis provided essential support in resolving all actuator related issues. ACS analyst Gerardo Cruz provided analysis and evaluation of on-orbit jitter and attitude stability tests. LRO Systems Engineering support from Dave Everett (GSFC), Michael Pryzby (ATK), and Steve Andrews (GSFC) provided indispensable guidance and oversight during development and critical support during environmental tests and orbital simulations. There are numerous others to mention that are also appreciated for their efforts.

References

Technical Memo: LRO SA and HGA Systems Torque Margins Analysis.
Technical Memo: Step Stability Margin Assessment, J. Schepis, GSFC
Technical Memo: Analysis of results from Solar Array Gimbal Step Resolution Experiment, G. Cruz-Ortiz

Fastener Capture Plate Technology to Contain On-Orbit Debris

Kevin Eisenhower*

Abstract

The Fastener Capture Plate technology was developed to solve the problem of capturing loose hardware and small fasteners, items that were not originally intended to be disengaged in microgravity, thus preventing them from becoming space debris. This technology was incorporated into astronaut tools designed and successfully used on NASA's Hubble Space Telescope Servicing Mission #4. The technology's ultimate benefit is that it allows a very time-efficient method for disengaging fasteners and removing hardware while minimizing the chances of losing parts or generating debris. The technology aims to simplify the manual labor required of the operator. It does so by optimizing visibility and access to the work site and minimizing the operator's need to be concerned with debris while performing the operations. It has a range of unique features that were developed to minimize task time, as well as maximize the ease and confidence of the astronaut operator. This paper describes the technology and the astronaut tools developed specifically for a complicated on-orbit repair, and it includes photographs of the hardware being used in outer space.

Introduction

Background of Problem

Confronted with the unique challenge of fixing a failed electronics board inside the Hubble Space Telescope (HST), NASA got the job done thanks to astronauts equipped with new tools and technologies. Servicing Mission #4 (SM4) occurred in May of 2009 and was a complete success. The failed electronics board was inside one of HST's many instruments, the Space Telescope Imaging Spectrograph (STIS). Accessing the board meant getting behind an aluminum Front Panel that was held in place with 111 fasteners, ranging from #4 countersunk to #4 and #8 socket head caps screws, with many having washers. It also meant worksite preparation by removing parts such as a handrail that blocked access to the Front Panel. To make things even more challenging, during the late stages of mission planning another instrument, the Advanced Camera for Surveys (ACS), had an electrical failure requiring four more electronics boards be removed.

Replacing entire instruments was not an option in this case, so NASA set off to replace just the failed electronics boards. This meant performing on-orbit surgery, but if any one of those fasteners had come free inside the telescope it could have been very detrimental to the telescope's functionality. Technologies, tools, and techniques had to be developed to avoid such a situation and ensure the mission would be successful.

Problem Solution – Tools

Four tool designs were developed and fabricated for HST SM4, each incorporating the same general fastener capture technology but for distinctly different work sites. These tools are the STIS Fastener Capture Plate (Figure 1), the ACS Fastener Capture Plate (Figure 2), the Handrail Removal Tool (Figure 3), and the Clamp Removal Tool (Figure 4).

* Alliant Techsystems, Beltsville, MD



Figure 1 – STIS Fastener Capture Plate



Figure 2 – ACS Fastener Capture Plate



Figure 3 – Handrail Removal Tool

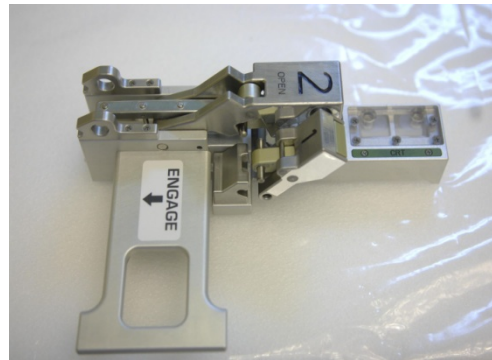


Figure 4 – Clamp Removal Tool

General Tool Description

A typical solution to the loose fastener problem would be to disengage, remove, and discard each fastener one-by-one. This would involve multiple tools used in concert, for example, grabbing the fastener with one tool while it is being disengaged with a second tool and then disposing of it into a trash bag or third tool. Stowing the released fastener is another complicated operation during which there is risk of losing the fastener. The tools invented simplify the problem by reducing the number of tools operated simultaneously and by removing the risky operation of stowing the fastener.

With the new tools, each tool is permanently attached to its worksite by the operator. This allows the operator to have both hands free. Each tool has clear windows with holes that line up with the fasteners that are to be removed. These holes allow the operator to insert a screwdriver-type bit through the window to unscrew each fastener. Behind each window is a gap, which creates a pocket or cavity for the fastener to fall in to after it is unscrewed. In some cases, a compliant gel material fills in the gap to grab the head of the released fastener. The holes in the window are small enough that the fastener cannot escape, but large enough for the bit to pass through. This concept is pictured with the Handrail Removal Tool in Figure 5.

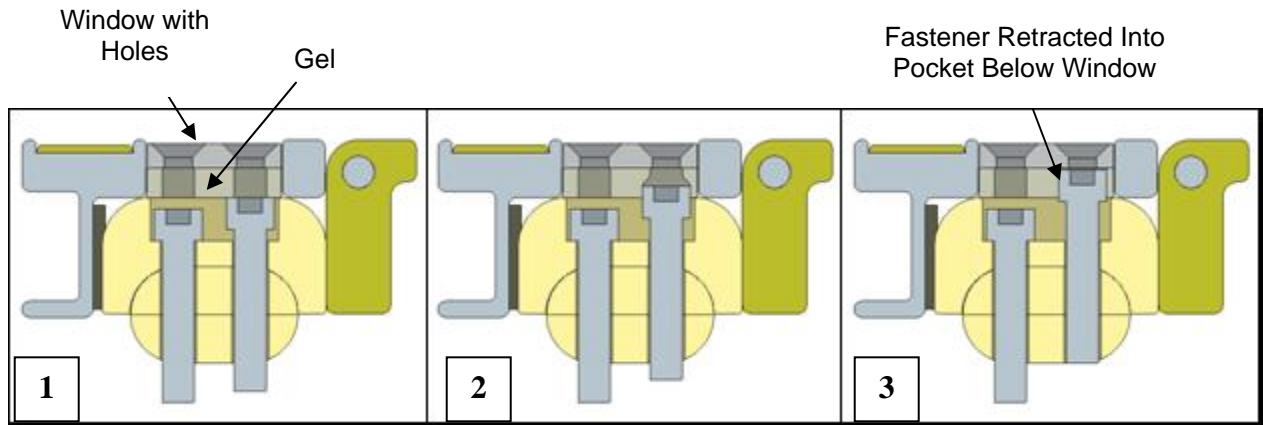


Figure 5 – Profile View of Fastener Capture Windows Concept



Figure 6 – Photograph from an Evaluation of the Fastener Capture Windows Concept

Unique Tool Features

Some unique features of the technology that give it advantages over prior fastener removal methods are listed below. All the listed features were intended and developed to minimize task time, as well as maximize the ease and confidence of the astronaut operator.

- 1) The action of disengaging fasteners is not automated but rather allows the operator full control and feedback.
- 2) The fasteners can be completely disregarded after they are disengaged. They do not need to be grabbed, stowed or cleaned up.
- 3) The tool can be attached in place just once and does not need to be handled or moved around the work site. It then can be used as the handling interface for the removed hardware.
- 4) The loosened fasteners are positively captured at all times and cannot come free without ultimate structural failure.
- 5) The tool minimizes particulate debris, even if a fastener were to be drilled out.
- 6) The tool can prevent a loosened fastener from incidental thread re-engagement with its mating part.
- 7) The tool can keep the loosened fastener positioned for easy re-engagement if necessary.

Tool Design

Tool Design Overview

The STIS Fastener Capture Plate tool is shown with labeled components in Figure 7. The other fastener capture tools created for the HST SM4 mission have similar features but differing geometries and capture different amounts of fasteners.

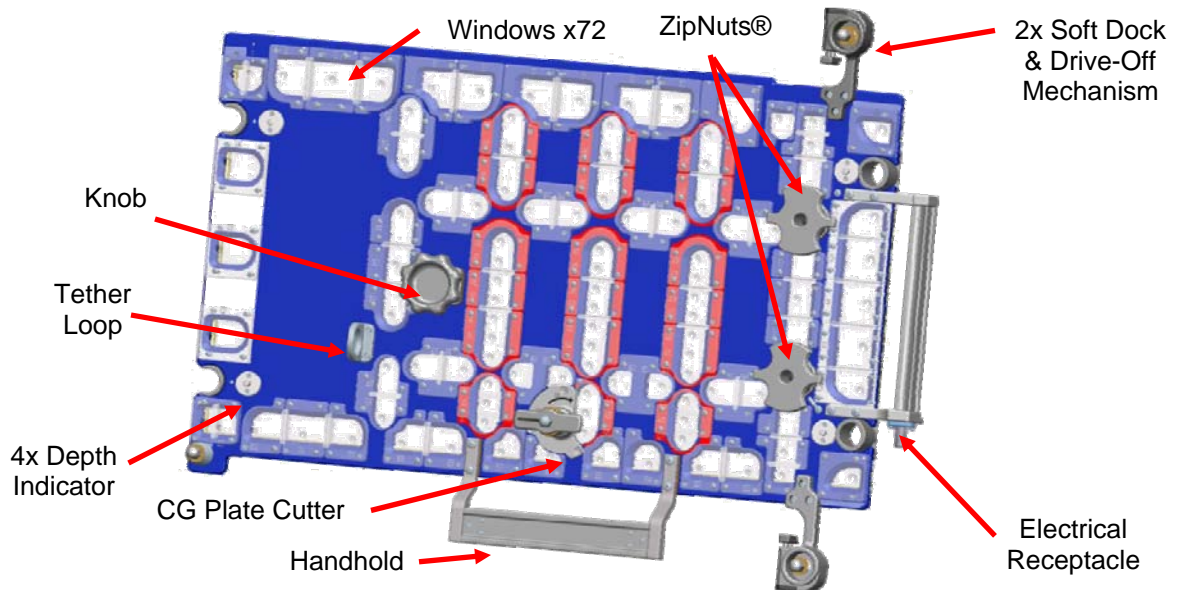


Figure 7 – STIS Fastener Capture Plate Overview

The STIS Fastener Capture Plate attaches to the front side of the STIS instrument, shown in Figure 8. The attachment mechanism is not detailed here, but the Fastener Capture Plate is essentially anchored at its four corners to the STIS Front Panel. The Front Panel, detailed in Figure 9, needs to be removed to gain access to the failed electronics board.

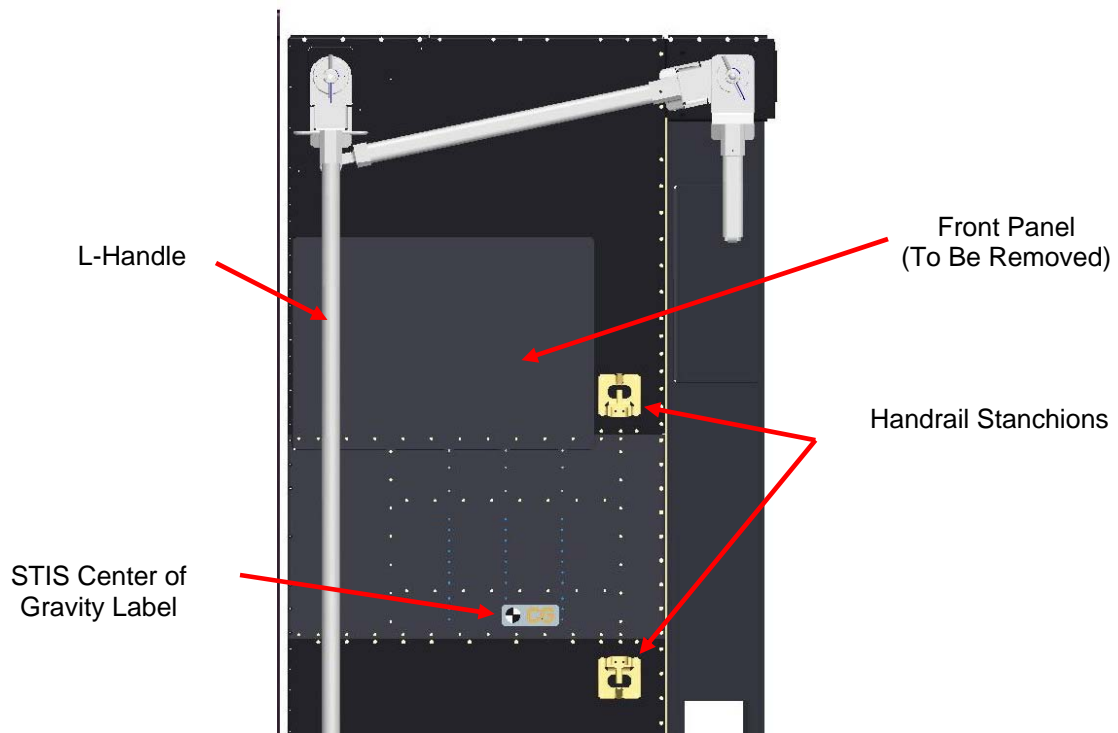


Figure 8 – STIS Fastener Capture Plate Worksite – STIS Front Panel

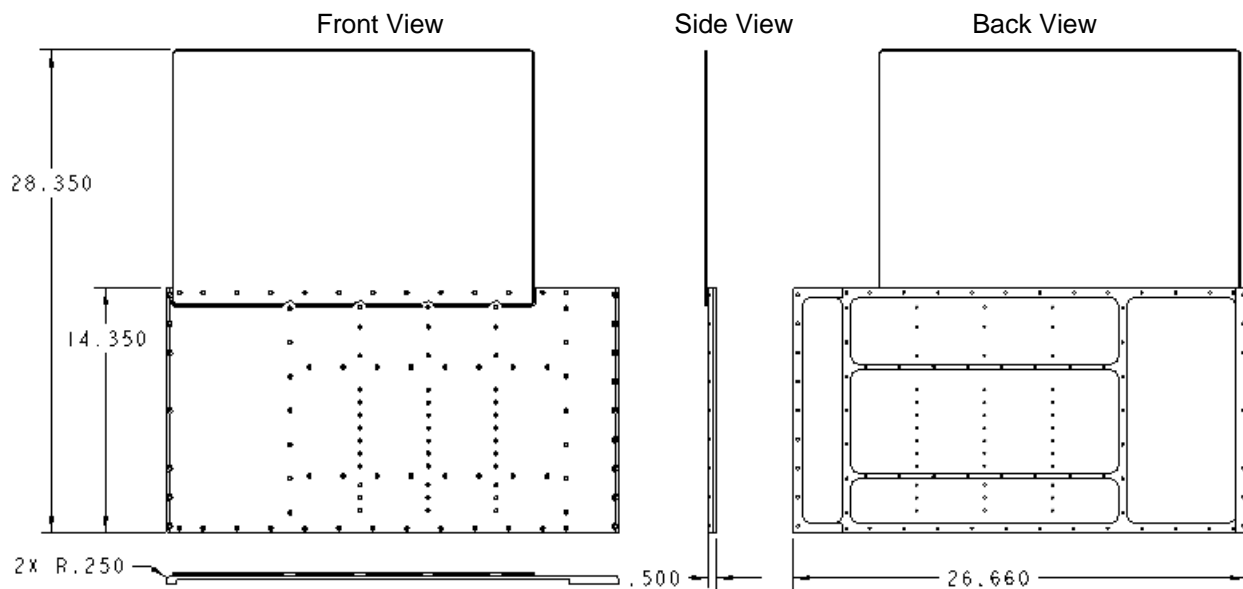


Figure 9 – STIS Front Panel Details (dimensions are in inches)

The layout of the 111 fasteners holding the Front Panel on can be seen in Figure 10. There are three types of fasteners, two having washers, the details of which can be found in Table 1.

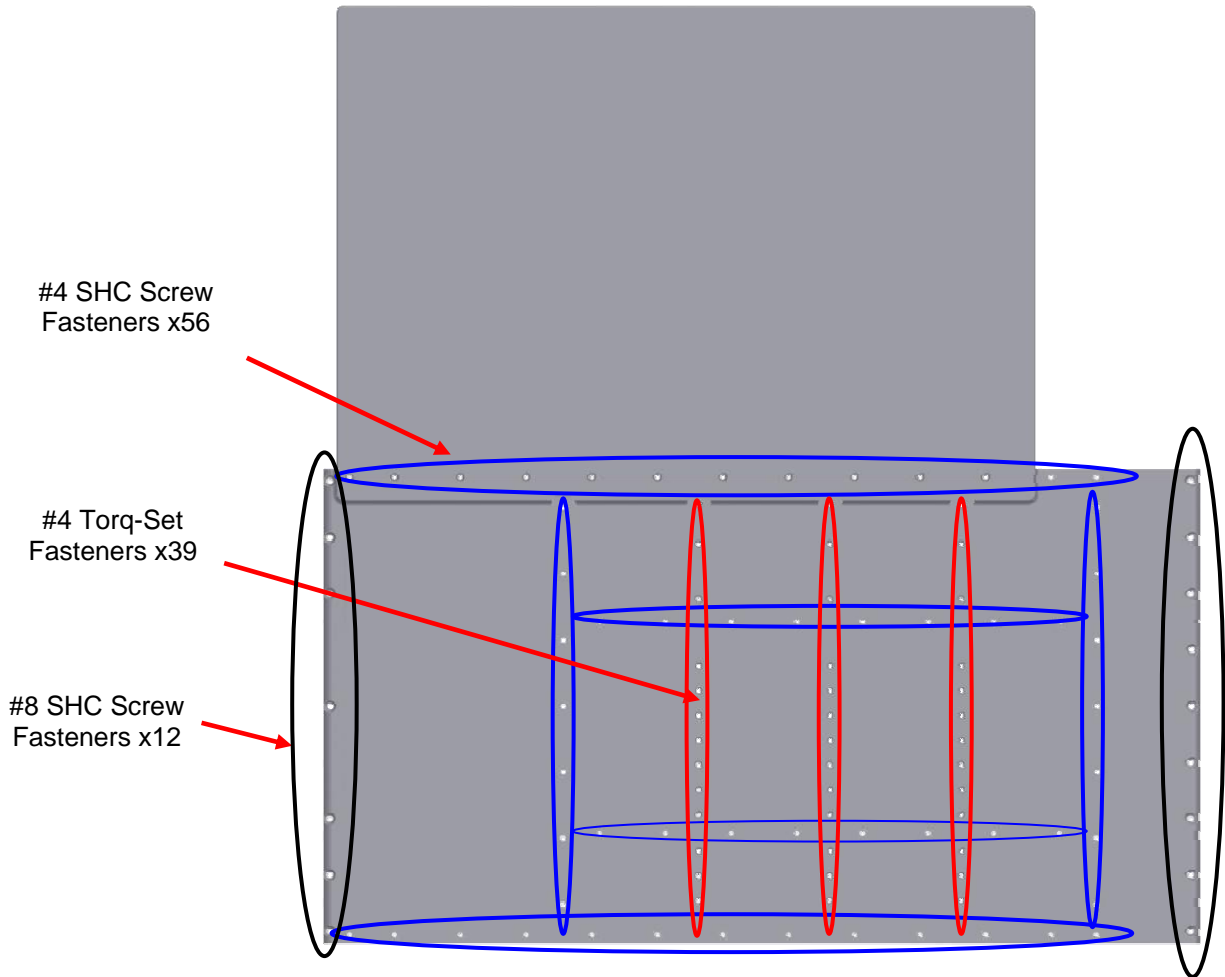


Figure 10 – STIS Front Panel Fastener Layout

Table 1 – STIS Front Panel Fastener Details

Fastener Type	Qty	Size (inches)	Specification / Part Number
#4 Torq-Set Screw	39	0.112-40, 3/8 inch long	NAS 1189E04T6K
#4 Socket Head Cap Screw	56	0.112-40, 7/16 inch long	NAS 1352E04LE7
#4 Reduced Diameter Washer	56	0.125 ID	NAS 620C4
#8 Socket Head Cap Screw	12	0.164-32, 1/2 inch long	NAS 1352N08LL8
#8 Reduced Diameter Washer	12	0.179 ID	NAS 620C8

When attached in place on STIS, the default position of the Fastener Capture Plate aligns its clear windows and holes with the Front Panel fastener locations. The colors on the tool (red, white and blue) help the operator differentiate between the different types of fasteners. Each fastener also has an alpha-numeric label. This allows an operations monitor to take note of what fasteners have and have not yet been removed, so as to make sure none get omitted. These colors and labels can be seen in Figure 11.

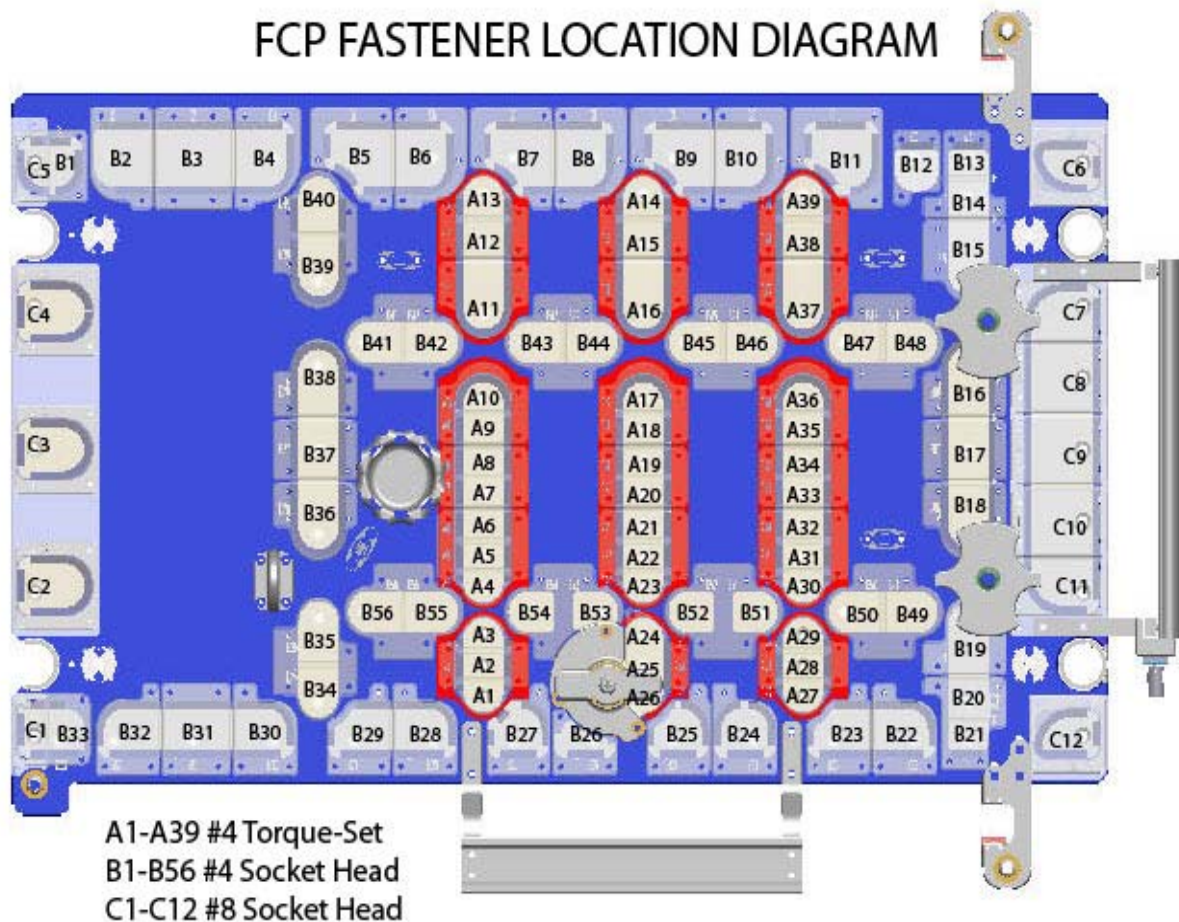


Figure 11 – STIS Fastener Capture Plate Fastener Labels

Tool Operation

Before the STIS FCP can be installed, the worksite needs to be prepared. This involves removing a handrail and a radiator clamp that block access to the Front Panel. Both of these items are held in place with fasteners, which must also be disengaged, captured, and removed. This is accomplished with the Handrail Removal Tool and the Clamp Removal Tool. These tools function with similar fastener capturing technology as the Fastener Capture Plate. Removing the handrail leaves behind the handrail's stanchions, seen in Figure 8. The handrail and clamp are removed and stowed in trash bags. Then anchor points must be installed onto the worksite for attaching the FCP.

These anchor points are created by removing four fasteners from the Front Panel, one at each corner, and replacing them with custom studs. Once they are in place, the FCP can be installed. Figure 12 shows

FCP installation. First, the FCP is positioned in place and the left side is lowered beneath the L-Handle. Second, the right side can be lowered such that the studs align with their mating holes in the FCP. Then third, the four corresponding nuts can be tightened onto the four studs, essentially fastening the FCP in place on top of the Front Panel.

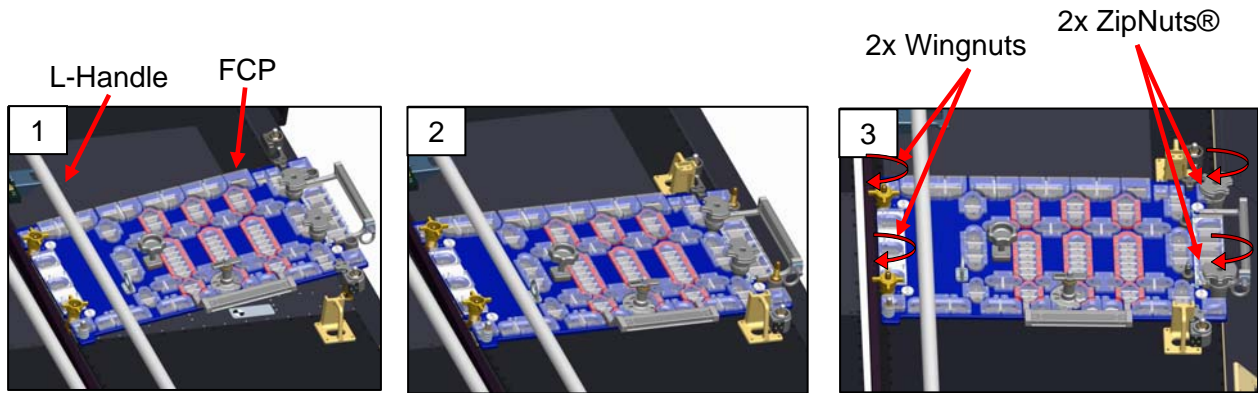


Figure 12 – STIS FCP Installation

In order to tighten the four nuts, the operator may need to let go of the FCP. In microgravity, this could allow the FCP to float freely and become misaligned. To prevent this, the FCP has a “soft dock” mechanism that holds it in place temporarily. This mechanism is essentially two spring-loaded plungers that interface with the handrail stanchions at the worksite, shown in Figure 13.

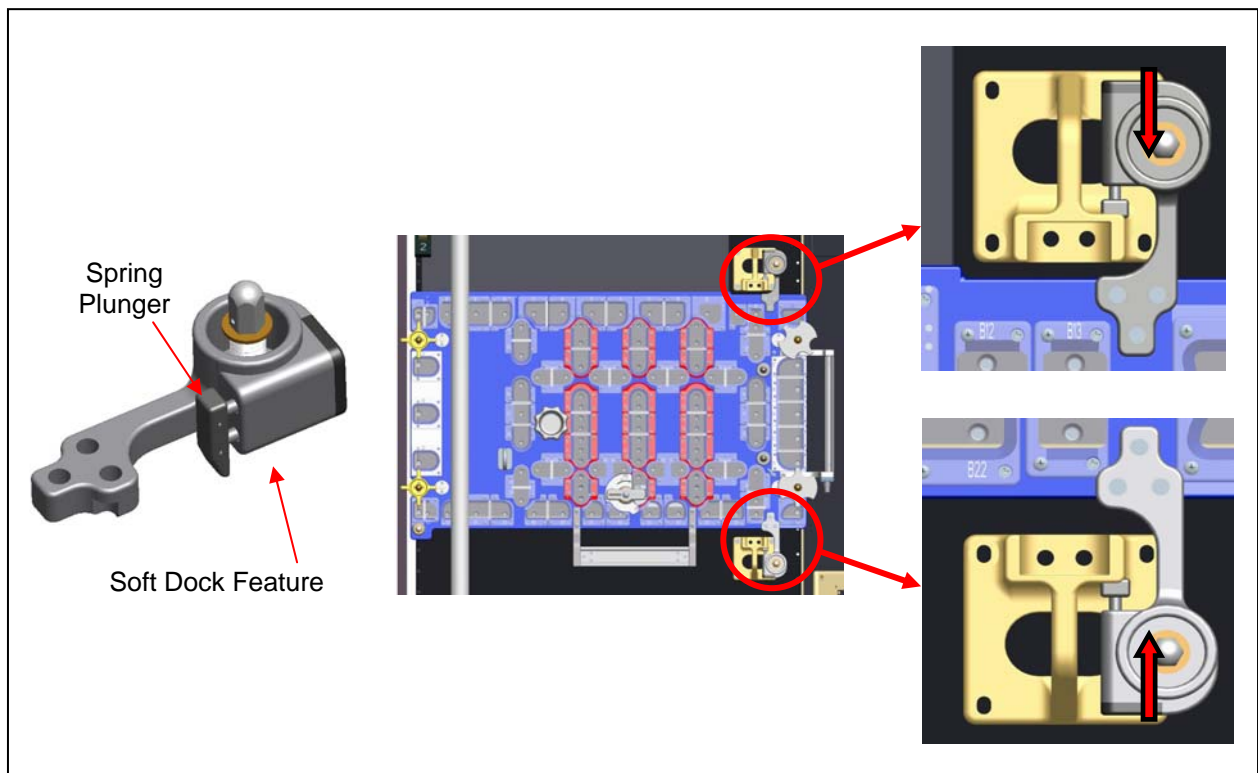


Figure 13 – STIS FCP Soft Dock Details

Once the FCP is fully installed, the task of removing the remaining 107 fasteners and the Front Panel can begin. Each fastener can be disengaged by a bit through an Access Hole in the windows in the FCP. The Access Hole will assist alignment within specified tolerances of the screw heads once the FCP is installed properly. Figure 14 shows a detailed view of the window design. Some windows may have multiple Access Holes, and some Access Holes may have countersinks to help guide the bit into place.

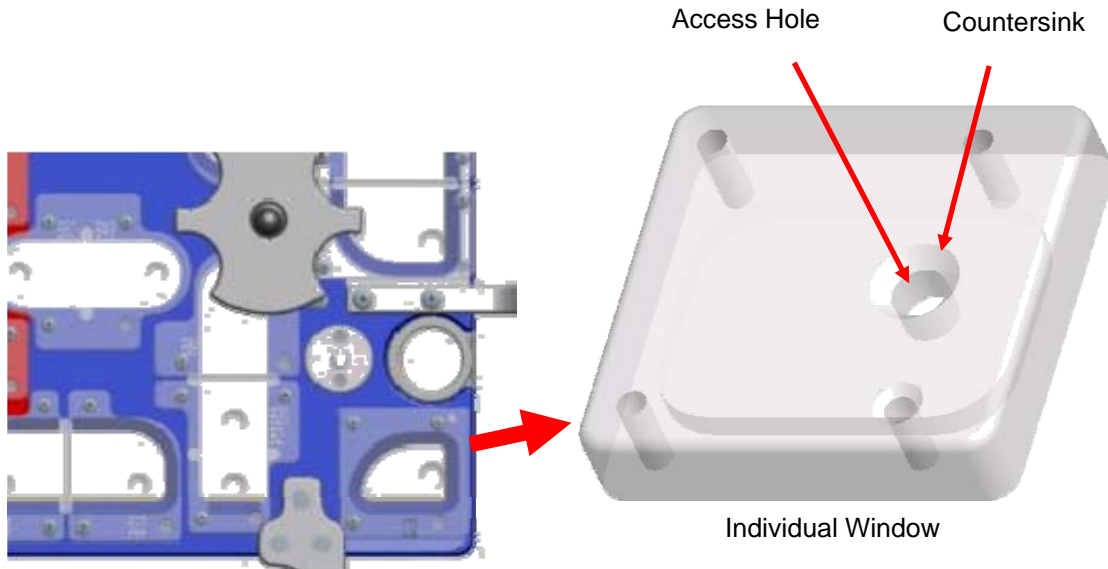


Figure 14 – Close-Up View of an FCP Window Component

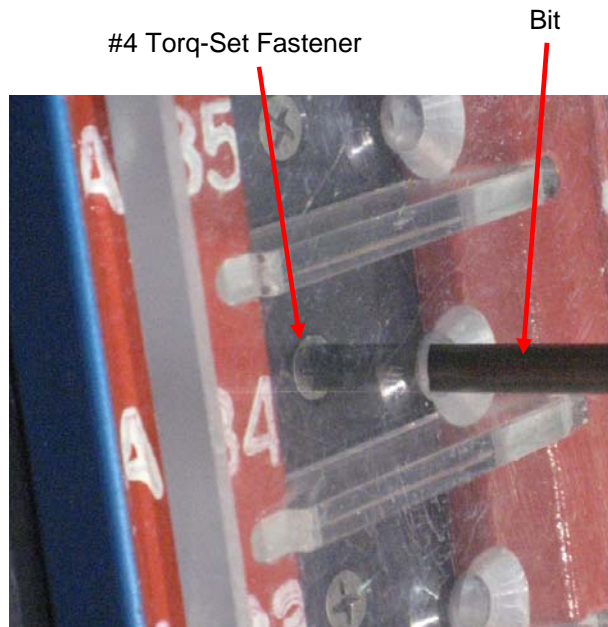


Figure 15 – Close-Up View of a Fastener Being Disengaged Through a Window

Once all 111 fasteners have been disengaged, the Front Panel is disconnected from the STIS instrument but still directly attached to the FCP tool via the four studs. Since the FCP is still “soft docked” to the handrail stanchions, it will not float away. The operator can use both hands to move the tool / Front Panel assembly away from the worksite.

Tool Design Considerations

Design of the fastener capture technology involved many tests, prototype iterations, and trade-offs. Many design considerations involved deciding how to deal with possible anomalies and common fastener problems, such as stripped head recesses. A problem encountered often on Earth is when, after a fastener is fully disengaged, its last thread incidentally re-engages with its mating female thread. One solution implemented was having a soft, compliant material within the fastener cavity that holds the fastener in place after it is disengaged. This is illustrated in Figure 16 in a cross-section view of the Handrail Removal Tool. This concept can also be utilized if the design needs to allow the fasteners to be re-engaged, because the fastener is held fairly stationary for bit re-engagement. Design details that must be taken into consideration include particle contamination, optimal geometries, and adequate compliant material durometer.

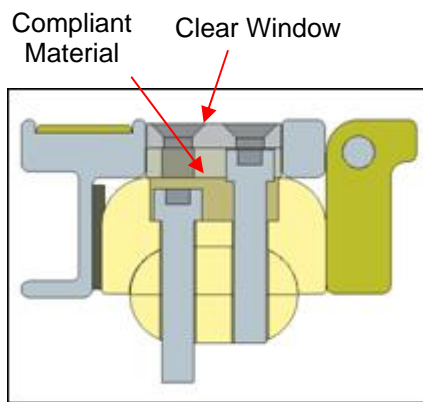


Figure 16 – Illustration of Fastener Cavity Compliant Material Concept

Accessibility and operator visibility of the worksite are major design considerations. The fastener capture technology works best when the operator can see the fastener heads clearly and closely without obstruction. This makes it easier to determine if the screwdriver bit is properly engaged, recognize if a fastener is turning properly, and realizing the fastener is all the way out. The geometry necessary for implementing this does not always align with other essential design features, leading to important trade-off decisions.

Whether or not the screwdriver bits already exist or still are in design stage must factor into the tool design. Reach and access evaluations may deem the bit must engage a fastener at a slight angle. Also material strength analysis may influence the bit's diameter and other geometries. The Access Holes in the tools must accommodate these types of variables.

In order to ensure the fasteners and washers are properly contained, the tool's geometry is important but also its position relative to the fasteners and mating surfaces. For the STIS Fastener Capture Plate, this is dependent upon the four anchor points and proper installation. The operator must be given some sort of feedback that the tool is installed properly, meaning sufficient enough to guarantee successful functionality. This feedback is provided by Depth Indicators on the FCP that tell the operator that the tool is seated flush enough to its mating surface such that there are no gaps to allow fasteners to escape.

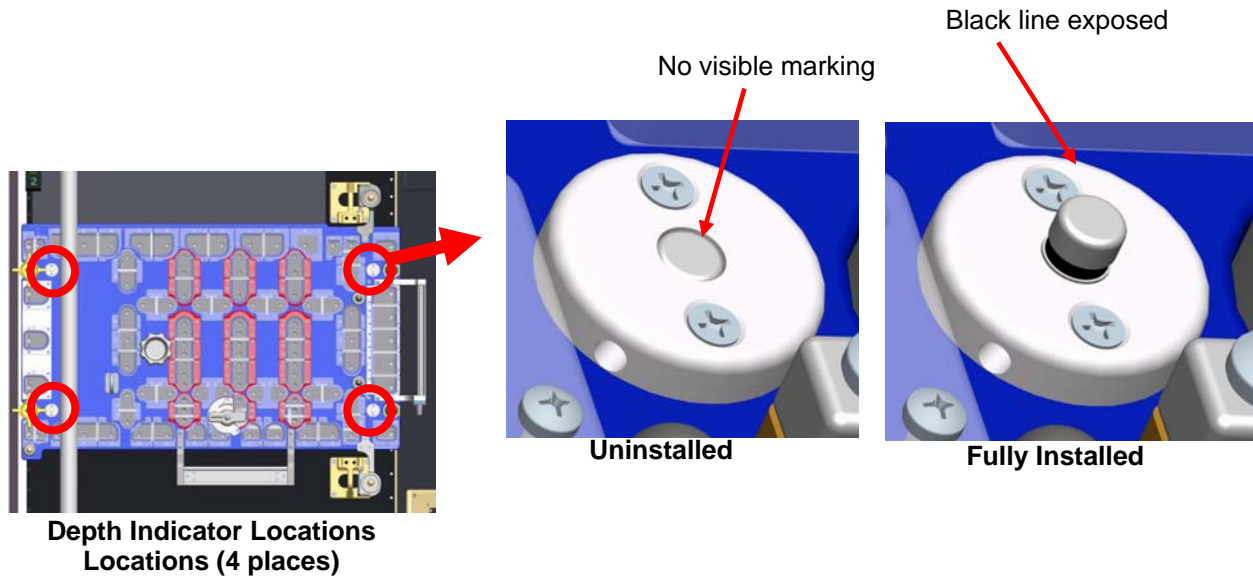


Figure 17 – Illustration of Depth Indicators

Due to tolerance stack-ups and anomalies, it would be impossible to guarantee that the FCP is installed exactly flush with its mating surface. Therefore, some compliance must be built into the system. This is accomplished with a gasket barrier around the perimeter of the underside of the tool. The compliant gasket creates a seal at the mating interface, providing containment to prevent disengaged fasteners or washers from getting free.

A potential problem of significant concern early on in the design phase was the presence of a Center of Gravity label on the Front Panel that covered up some of the fasteners that needed to be removed. The label is a sticker made of sheet metal and is not simply removable by hand. A lot of testing was employed to come up with a solution. Drilling through the label was evaluated, as well as a mechanism for peeling it off. In the end, included in the STIS FCP is a mechanism for cutting the label in a manner that removed just enough label material to reveal the fasteners it covered up.

Another design requirement of the STIS FCP involved providing the operator a means of prying the Front Panel off with enough force to overcome a sticky gasket that is holding it in place underneath. This was accomplished by including a power tool driven Drive-Off Mechanism that could be actuated if the force was too much to overcome by hand.

Tool Development and Evaluation

The fastener capture technology was developed through many tool design reviews as well as evaluation and testing of prototypes. Many of these evaluations occurred at the NASA Neutral Buoyancy Lab, where astronauts train and practice for EVA's underwater to help simulate zero-gravity. Early prototypes of the tools allowed the operators to make the following deductions:

- Removal of the Front Panel and fasteners should be done by an EVA crewmember and not an automated tool.
- Each fastener at the worksite is accessible to be removed individually.
- Use of the fastener capture technology of the FCP was preferable to removing and stowing each fastener individually.
- Disengaging the fasteners would require a clear line-of-sight to each fastener.
- An astronaut in a spacesuit could accomplish removal of all fasteners without being over-fatigued.
- Operators demonstrated the ability to diagnose and remove a stuck fastener.
- Demonstrated reliable operation of the Center of Gravity Label Cutter.

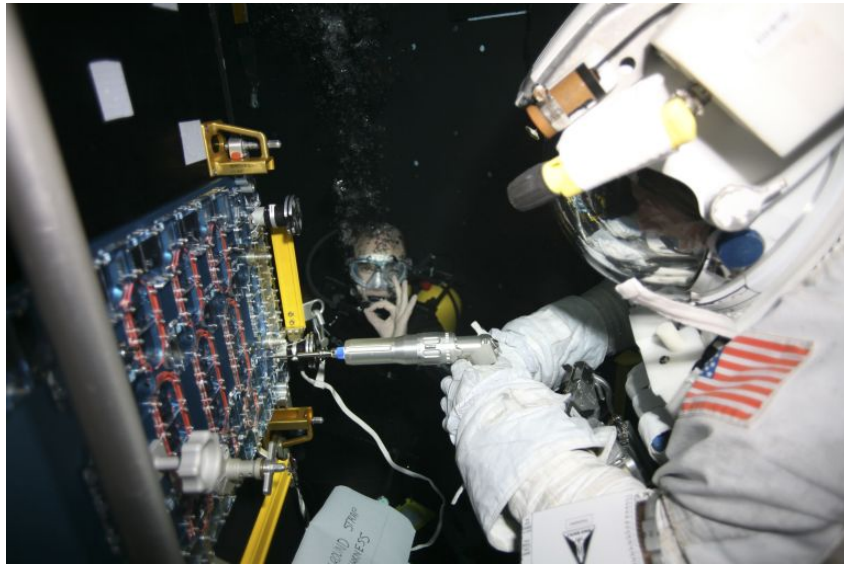


Figure 18 – STIS FCP Being Evaluated Underwater at the Neutral Buoyancy Lab

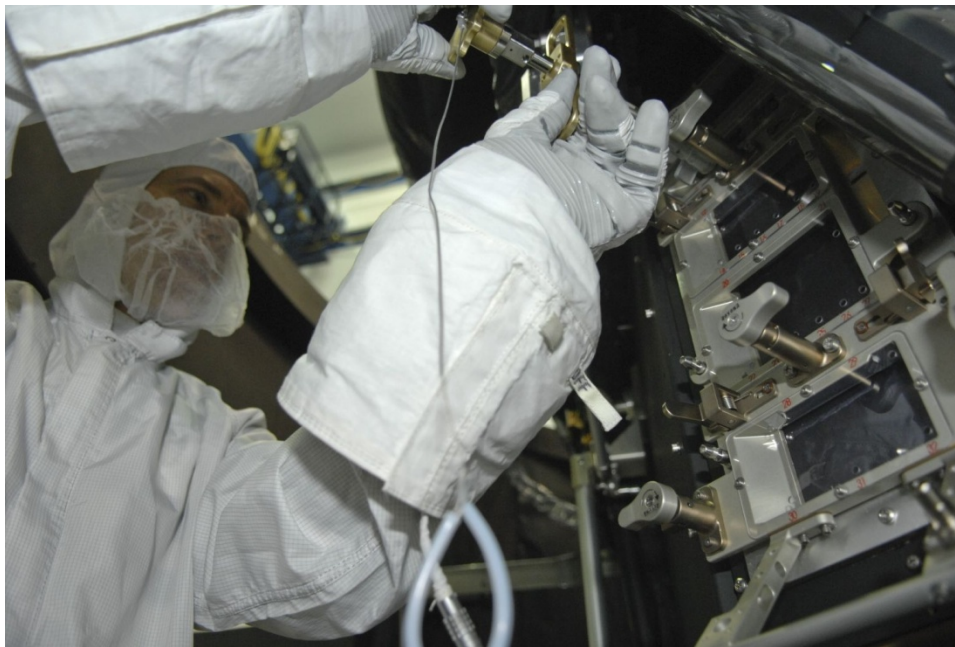
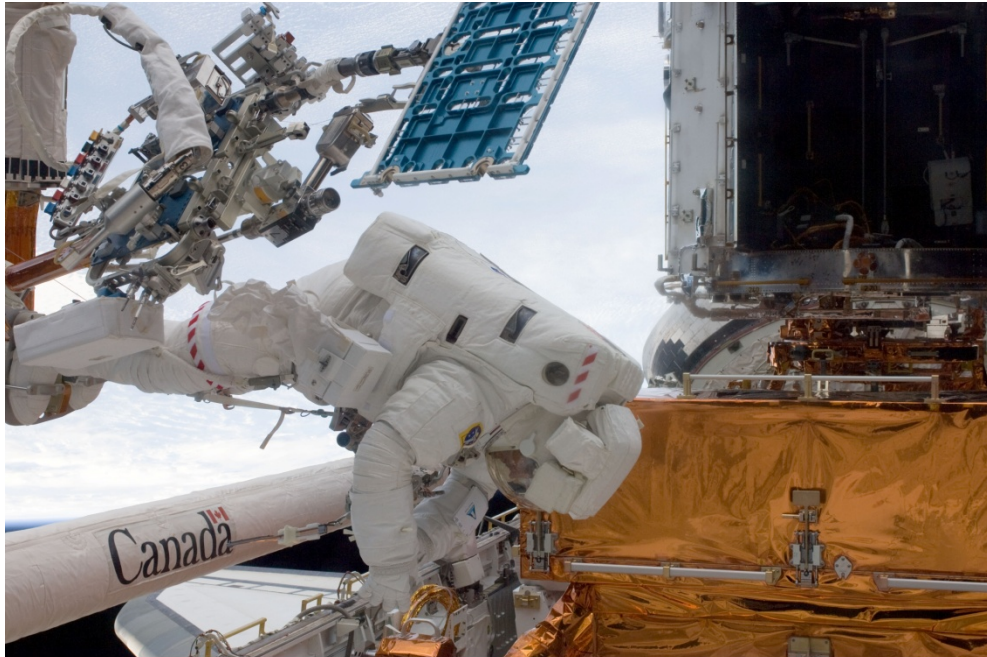


Figure 19 – ACS FCP Being Evaluated on a Mockup

On-Orbit Tool Performance

HST SM4 occurred in May of 2009 and was a complete success. The failed electronics boards inside both STIS and ACS instruments were replaced on-orbit. The fastener capture tools contained all removed fasteners as designed. Images of the tools on-orbit can be seen in Figures 20, 21, and 22.



S125E008744

Figure 20 – STIS FCP Being Translated to the Worksite On-Orbit

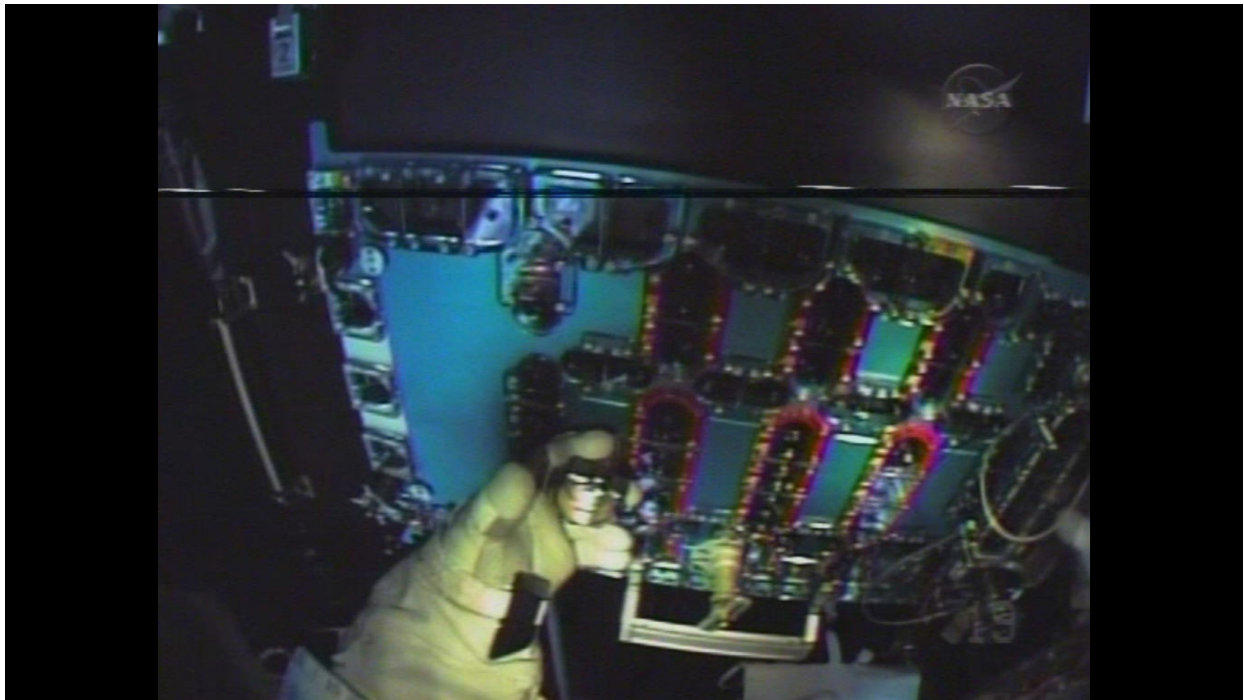


Figure 21 – STIS FCP Being Installed On-Orbit



Figure 22 – Handrail Removal Tool Installed on Handrail On-Orbit

Summary

The Fastener Capture Plate technology proved that it could solve the problem of capturing fasteners that were not originally intended to be disengaged on-orbit in microgravity, specifically for NASA's Hubble Space Telescope Servicing Mission #4. The technology demonstrated a very time-efficient method for disengaging fasteners and removing hardware while minimizing the chances of losing parts or generating debris. The four astronaut tools that implement this concept were used successfully on-orbit. There were many design variables determined for overcoming anomalies, maximizing operator efficiency, and minimizing space debris. This technology and the research put into developing the tools could be utilized in any future need for on-orbit repairs where space debris and contamination is a concern.

Acknowledgements

The development of the Fastener Capture Plate technology, related EVA tools, and STIS Repair engineering would not have been possible without the thoughtful work of Jon Penn, Tim Horner, Matt Ashmore, Torrie Kelly, Hans Raven, Kristoff Paulson, Mike Cortina, Jill McGuire, and Justin Cassidy. Thank you for your help and insight.

References

1. NASA Human Spaceflight: Gallery. <<http://spaceflight.nasa.gov/gallery>>
2. NASA: Hubble Space Telescope. <http://www.nasa.gov/mission_pages/hubble/main/index.html>

Space Station Control Moment Gyroscope Lessons Learned

Charles Gurrisi*, Raymond Seidel[†], Scott Dickerson*, Stephen Didziulis**,
Peter Frantz** and Kevin Ferguson***

Abstract

Four 4760 Nms (3510 ft-lbf-s) Double Gimbal Control Moment Gyroscopes (DGCMG) with unlimited gimbal freedom about each axis were adopted by the International Space Station (ISS) Program as the non-propulsive solution for continuous attitude control. These CMGs with a life expectancy of approximately 10 years contain a flywheel spinning at 691 rad/s (6600 rpm) and can produce an output torque of 258 Nm (190 ft-lbf)¹. One CMG unexpectedly failed after approximately 1.3 years and one developed anomalous behavior after approximately six years. Both units were returned to earth for failure investigation.

This paper describes the Space Station Double Gimbal Control Moment Gyroscope design, on-orbit telemetry signatures and a summary of the results of both failure investigations. The lessons learned from these combined sources have led to improvements in the design that will provide CMGs with greater reliability to assure the success of the Space Station. These lessons learned and design improvements are not only applicable to CMGs but can be applied to spacecraft mechanisms in general.

Introduction ²

The International Space Station (ISS) is currently the largest man-made object to ever orbit the Earth and represents one of the greatest engineering and integration efforts the National Aeronautics and Space Administration (NASA) has ever undertaken. The Guidance, Navigation, and Control (GN&C) system is composed of both a US non-propulsive attitude control system and a Russian thruster attitude control system. Nominal operations are conducted under US control using its four Control Moment Gyroscopes (CMGs), shown in Figure 1, with the Russian system providing momentum desaturation through thruster assists. When configured for completely non-propulsive control, the CMGs provide the ISS with the micro-gravity environment that is required for science payloads.

The US GN&C system uses a one-, two-, or three-axis Torque Equilibrium Attitude (TEA) seeking controller to minimize the amount of momentum required to maintain attitude control. Due to thermal issues with external components, several of the assembly stages require a biased attitude to minimize sun exposure to specific surface regions. Analysis of the momentum necessary to maintain the required attitude envelope has shown that the momentum of four CMGs is required for much of the assembly phase.

This paper describes the configuration of the ISS CMGs, their operations, a description of CMG1's "hard" bearing failure after approximately 1.3 years of operation. Included also are the findings for CMG3's "soft failure" that led to its removal from service and the corresponding most probable causes and lessons learned.

* L-3 Communications Corporation Space & Navigation Division, Budd Lake, NJ

** The Aerospace Corporation, El Segundo, CA

*** The Boeing Company, Houston TX

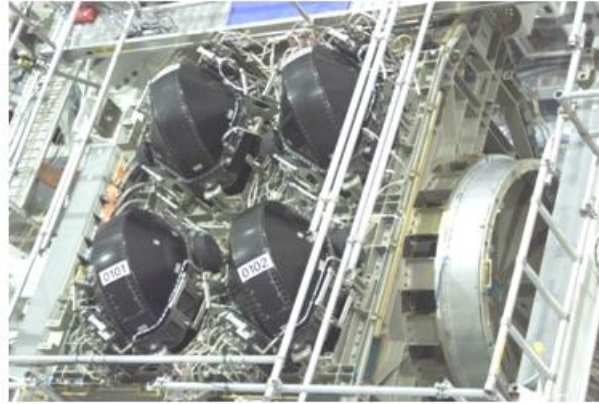


Figure 1. CMGs 1-4 Mounted on Z1 Truss

Space Station Z1/CMG Configuration²

The four CMGs operate as momentum storage devices that exchange momentum with the ISS through induced gyroscopic torques. These torques are created by a motor-driven constant-speed momentum flywheel mounted inside two orthogonal gimbals. Both gimbals have torquer motors and position resolvers mounted on the rotational axis and move by use of a gear train system. The momentum flywheel is mounted inside the inner gimbal and is supported by bearings mounted on each side of the flywheel. This configuration is shown in Figure 2. Double Gimbal CMGs were selected for the ISS because of the spherical momentum envelope. The control law is heuristic with no singularities and should the active number of CMGs change, the entire momentum envelope varies in proportion to the initial momentum sphere.³

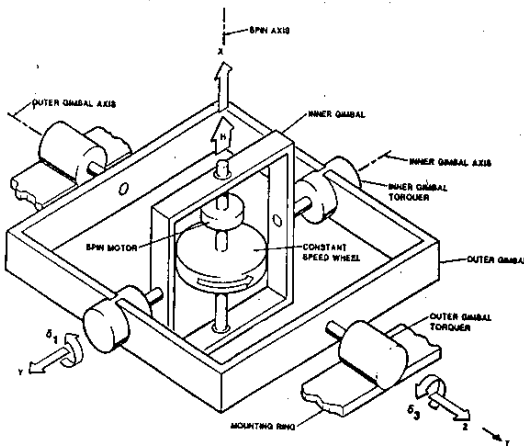


Figure 2. CMG Gimbal and Flywheel Assembly

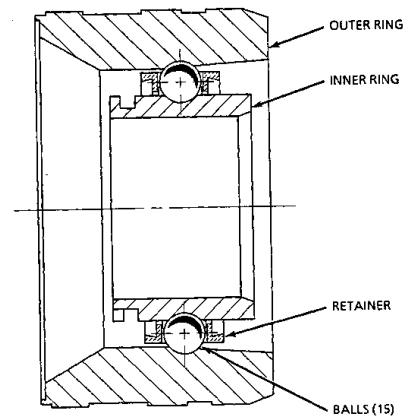


Figure 3. CMG Spin Bearing Assembly

The flywheel is mounted on two spin bearings, one on the Spin Motor (SM) side, and one on the Hall Resolver (HR) side. The Spin Motor is a low torque motor mounted on the spin axis with a control loop to maintain the commanded wheel-speed. The Hall Resolver provides digital wheel-speeds for downlinking via telemetry. The Spin Motor Command Current (SMCC) ranges from 0 to 1.6 Amps and nominally averages 0.37 Amps. The SMCC varies due to viscosity changes in the spin bearing lubricant caused by thermal variations and high gimbal rates that induce radial loads on the spin bearings. The SMCC is used as an indicator of spin bearing health and status.

An accelerometer is mounted to the inner gimbal of each CMG to monitor flywheel unbalance. The accelerometer signal is filtered to a bandwidth of 20 to 120 Hz to eliminate frequencies/disturbances not associated with the flywheel unbalance frequency.

The Spin Bearings, shown in Figure 3, are single angular-contact ball bearings with modified inner and outer races. There are 15 steel balls mounted in a retainer to maintain consistent ball motion. The spin bearings are lubricated with KG80, a super refined mineral oil, in an active oiler system. Pairs of cartridge heaters mounted near the outer race of each bearing are provided to maintain the lubricant above the pour point temperature and in the range of 15.6°C to 26.7°C (60°F to 80°F) during cold orbital conditions.

Space Station Operational History

ISS Assembly

Assembly of the ISS began in November, 1998, with the first Russian component, the Functional Cargo Block. Since then, the ISS has expanded with the addition of many sections, several of which are of international origin. Major components include Node 1 (a connector module), the Russian Service Module, the Z1 Truss, the US Laboratory Module, a Canadian robotic arm, the Integrated Truss Structure with eleven segments, four sets of solar arrays, Node 2, the European Space Agency Columbus module, and the Japanese Experiment Module. Node 3 will be added in early 2010. Russian components were transported via their own launch vehicles. All other components were carried into orbit using the US Shuttle Transportation System (STS). The ISS has been permanently inhabited by international crews since October, 2000.



Figure 4. International Space Station, Present Configuration

To date, the ISS has flown in three different orbital attitudes:

- *X Body Axis on the Velocity Vector ($\pm XVV$)*, also referred to as Local Vertical, Local Horizontal (LVLH). The ISS design is optimized for this attitude for microgravity, altitude re-boosts, and vehicle dockings, hence this is the primary flight attitude. Normally the +XVV attitude is flown, but during docked Space Shuttle missions, the attitude is changed to -XVV to allow for the Space Shuttle to not be in the forward velocity direction to avoid the potential for micro-meteorite debris.
- *X-Principle Axis Perpendicular to the Orbit Plane ($\pm X-POP$)* was utilized during early Space Station construction since full solar array capability was not achieved until Flight 12A. During certain solar beta angles, ISS would be maneuvered to this attitude to allow the existing solar arrays to point more directly to the sun.
- *Y Body Axis on the Velocity Vector ($\pm YVV$)* is a similar but alternate attitude from the $\pm XVV$ attitude. During YVV, the Space Station is rotated 90 degrees from the typical $\pm XVV$ attitude. This attitude was

useful during early construction when full solar array capability was unavailable, but due to other constraints, it was not desirable to operate at the higher temperature X-POP attitude.

Since assembly Flight 12A in September 2006, the $\pm YVV$ and $\pm X$ -POP attitudes are no longer used, although in future unique situations, they may be used as contingency attitudes.

GN&C Operational CMG Usage

Prior to CMG activation, the ISS attitude control was accomplished using thrusters. Thrusters are now used as a backup for CMG control, for large attitude maneuvers, or for translational control.

Nominal quiescent operations are handled by the CMGs using a concept known as momentum management. A Momentum Manager controller is designed to perform via the following two methods: (1) seeking the TEA by finding the attitude having the lowest momentum, and (2) maintaining a particular attitude by expending the appropriate amount of momentum to bias that attitude. Usually, controllers combine a TEA-seeker in one ISS body axis (pitch) with an attitude bias for the other two axes (yaw and roll).

GN&C software maintains a given attitude by commanding the CMG inner and outer gimbals to specific locations. This positions the individual momentum contributions from the CMG flywheel spin axes to provide a total momentum vector for vehicle control. External torque disturbances on the vehicle can be countered by moving the vector as appropriate.

If a disturbance torque imparts a momentum that is greater than the total combined control momentum, the CMGs 'saturate', having expended all available momentum to counter the disturbance. The controller commands thruster firings to 'desaturate' the CMGs, or unload the momentum to a specified value. The CMG gimbals are then re-positioned to attain a lower total momentum. A CMG desaturation happens quickly, and may result in rates of gimbal rotation that are substantially higher than those needed for quiescent operations having low or non-existent disturbance torques. The CMG desaturation function can be disabled, and attitude control is then handed completely over to the thrusters in the case of CMG momentum saturation.

CMG Operational History

The original four CMGs were launched on the Z-1 Truss, Mission STS-92, ISS Flight 3A, on October 11, 2000. They remained dormant and unpowered for a few months until being activated on February 12, 2001 during Space Station Flight 5A. On June 8, 2002, CMG1 developed a problem and failed resulting in 3 operational CMGs. Operations using a 3-CMG control configuration was required until a spare replaced the failed CMG1 on August 1, 2005 during Space Shuttle Flight LF-1. The ISS then continued to operate under 4-CMG control until CMG3 exhibited signs of distress. The initial CMG1 Failure Root Cause Investigation together with the CMG3 experience led to the development of on-orbit monitoring criteria intended to identify problems and prevent a hard failure. An additional benefit of implementing these criteria was to preserve the hardware for re-use and subsequent forensic analysis. On October 10, 2006 CMG3 was shut down because the unbalance sensor had reached the shut-down criterion. It was then taken out of service but remained on the Z1 Truss with the Electrical Assembly (EA) and heaters enabled, until it was removed on August 13, 2007. A 3-CMG control configuration was again implemented for attitude control. During CMG3's non-operational time period, various diagnostic tests were performed to support the joint L-3 S&N, Boeing, and NASA decision to remove and replace CMG3. This "soft failed" CMG was replaced by another ground spare on August 12, 2007 during Space Shuttle Flight 13A-1 and the ISS was restored to a 4-CMG control system.

The CMG1 investigation identified high gimbal rates as a contributor to the failure. During the earlier stages of ISS assembly, CMG gimbal angular velocity was restricted by CMG firmware to a maximum rate of 0.054 rad/s (3.1 deg/s). Following the two CMG failures, GN&C engineers limited all CMG gimbal

rates to 0.014 rad/s (0.8 deg/s) within the GN&C software. Acceleration was originally restricted only by the CMG firmware was similarly limited to 0.0007 rad/s² (0.04 deg/s²) by the GN&C software. These limits were imposed with intent to potentially benefit CMG health, but still allow satisfactory vehicle attitude control.

CMG3 showed short periods of elevated accelerometer activity between the CMG1 failure and the CMG3 soft-failure. Concern over these signatures resulted in the implementation of several operational limitations intended to lower the gimbal angular rates of motion that were believed to be triggering the disturbances. The limitations included significant restrictions on attitude control methods that required nominal CMG momentum desaturations, limited values for the gimbal rotation rates used to manually positioning the CMGs (especially CMG3), and temporary cessation of use of the X-POP flight attitude. X-POP in particular was found to impart cyclical gimbal rates at an order of magnitude greater than the LVLH flight attitudes for quiescent operations

On-Orbit Failure Description and Signature²

CMG1 "Hard" Spin Bearing Failure

At the end of May 2002; the ISS was in a high solar beta X-POP period. The ISS attitude was transitioned from X-POP to LVLH on June 7th, several hours prior to shuttle docking. In order to accomplish this re-orientation and docking, large gimbal rates within design requirements were imparted to the CMG due to desaturations. Approximately 6 hours after the docking at ~23:00 on GMT Day 158, 2002, CMG1's Spin Motor Command Current (SMCC), the indicator of the combined bearing torques, started increasing over a 14-minute period. This increase in SMCC was later concluded to be the start of the failure. The increase in SMCC was caused by an increase in the Hall Resolver side bearing torque. This was confirmed by the increase in bearing temperature that indicated the Hall Resolver side bearing may be in distress. During the course of the next 15 hours, CMG1 showed signs of good and bad bearing performance, with the ultimate failure occurring at 14:57 on GMT Day 159, 2002. Several hours after docking, the flight control team noted a flag that indicated the accelerometer on CMG1 had measured 0.5 Gs. The rise in SMCC and associated Hall Resolver temperature was repeated twice during the next 16 hours. Then, following a 30-minute period with no ground communication, telemetry showed that the CMG1 SMCC was at its maximum value, 1.6 Amps, and the wheel-speed was decreasing. After several seconds of maximum current and wheel-speed reduction, Fault Detection and Isolation software declared the CMG failed and automatically shut down the Spin Motor. Normal shut down would result in the flywheel speed decelerating to 0 rad/s in approximately 12 hours. However, during this event, the flywheel stopped 72 minutes after Spin Motor shutdown because of the bearing failed condition. During this run-down period, the Hall Resolver bearing temperature exceeded the maximum telemetry value of 93°C (199.4°F) while the Spin Motor bearing temperature reached only ~30°C (86°F), indicating major distress in the Hall Resolver bearing. Data was retrieved from the on-board data recorders to fill in the missing telemetry for analysis purposes. The timeline of events is given with SMCC and spin bearing temperatures shown in Figure 5, Figure 6 and Figure 7. The CMG1 was later returned to L-3 for disassembly and formal failure investigation.

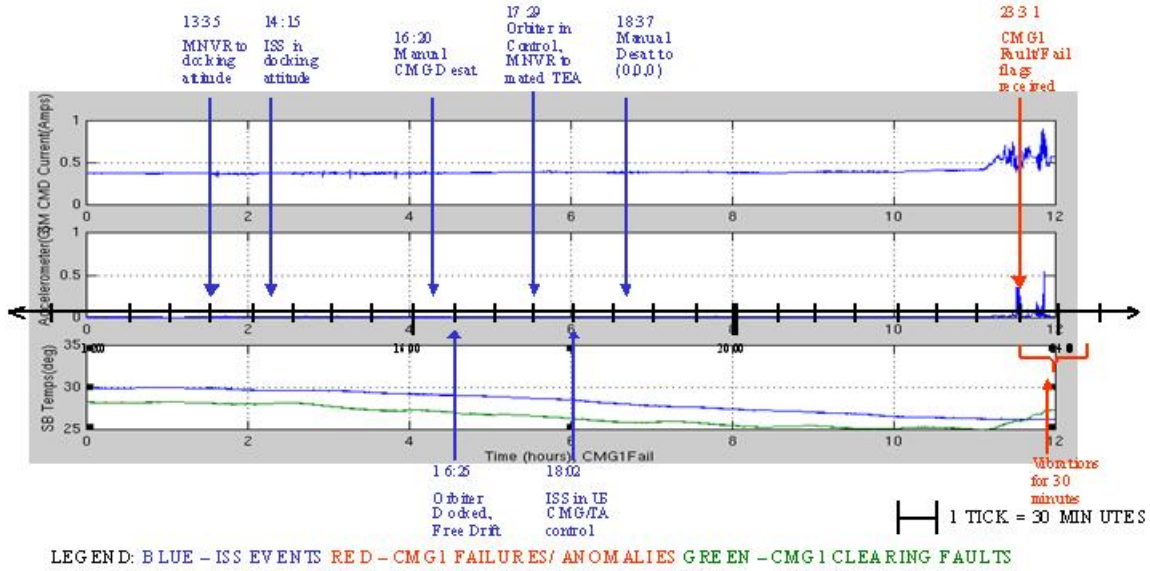


Figure 5. First Indication of Anomalous Behavior GMT 158/2002/12:00-24:00

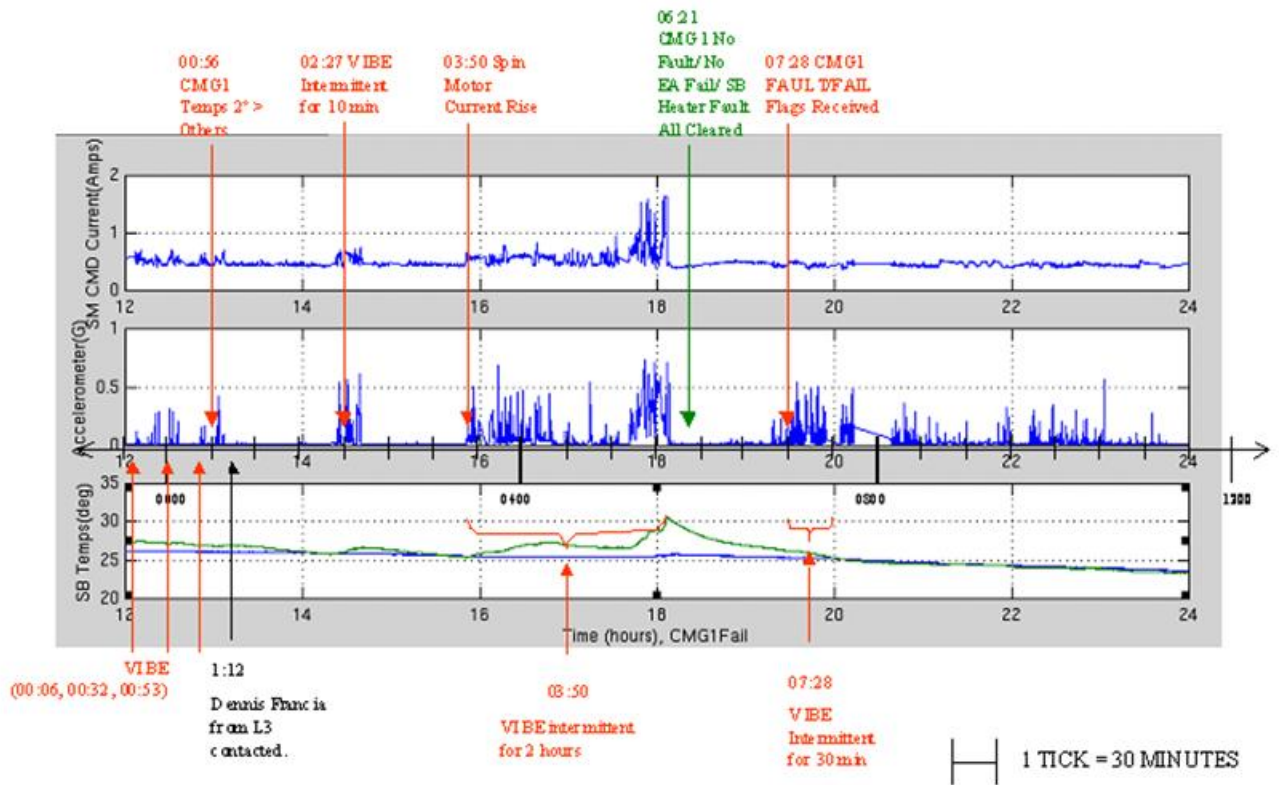


Figure 6. Erratic Behavior after Anomaly GMT 159/2002/00:00-12:00

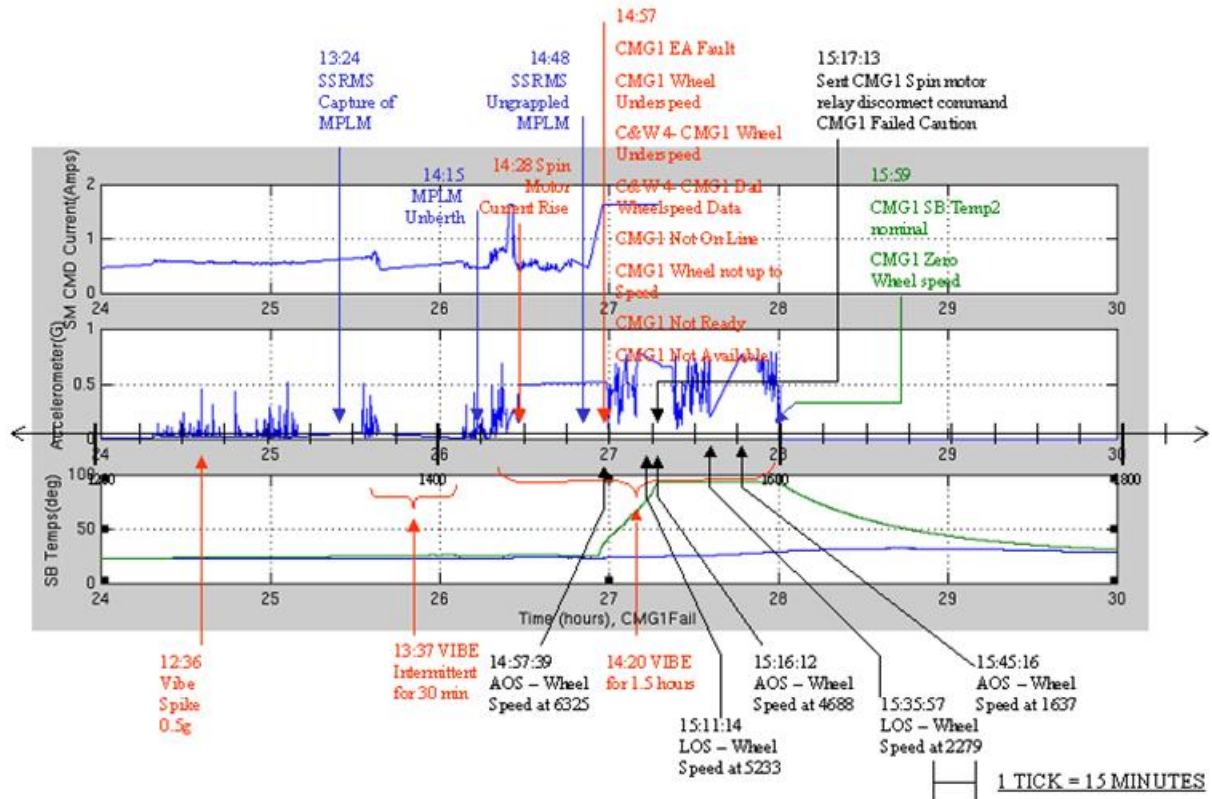


Figure 7. Hard Failure and Shutdown GMT 159/2002/12:00-18:00

CMG3 “Soft” Failure

CMG3 operated continuously at 691 rad/s (6600 rpm) from its activation on February 12, 2001 until the unbalance sensor level reached the criteria (0.2 g) for removal from the active steering law on Day 272, September 29, 2006. This occurred as the CMGs were being pre-positioned for Momentum Management startup in the XVV flight attitude. CMG3 was kept out of the steering law pending further analysis. Several times the unbalance sensor levels reached 0.2 g while the CMG was operational but not used to actively control the ISS. On Day 283, October 10, 2006, the unit was shut down because the unbalance sensor reached the shut down criteria of 0.4 g. Figure 8 shows the performance signatures and events that preceded the shut down of CMG3. CMG3 was returned to L-3 Communications Corporation Space & Navigation (L-3 S&N) on March 11, 2008 for disassembly and a failure investigation.

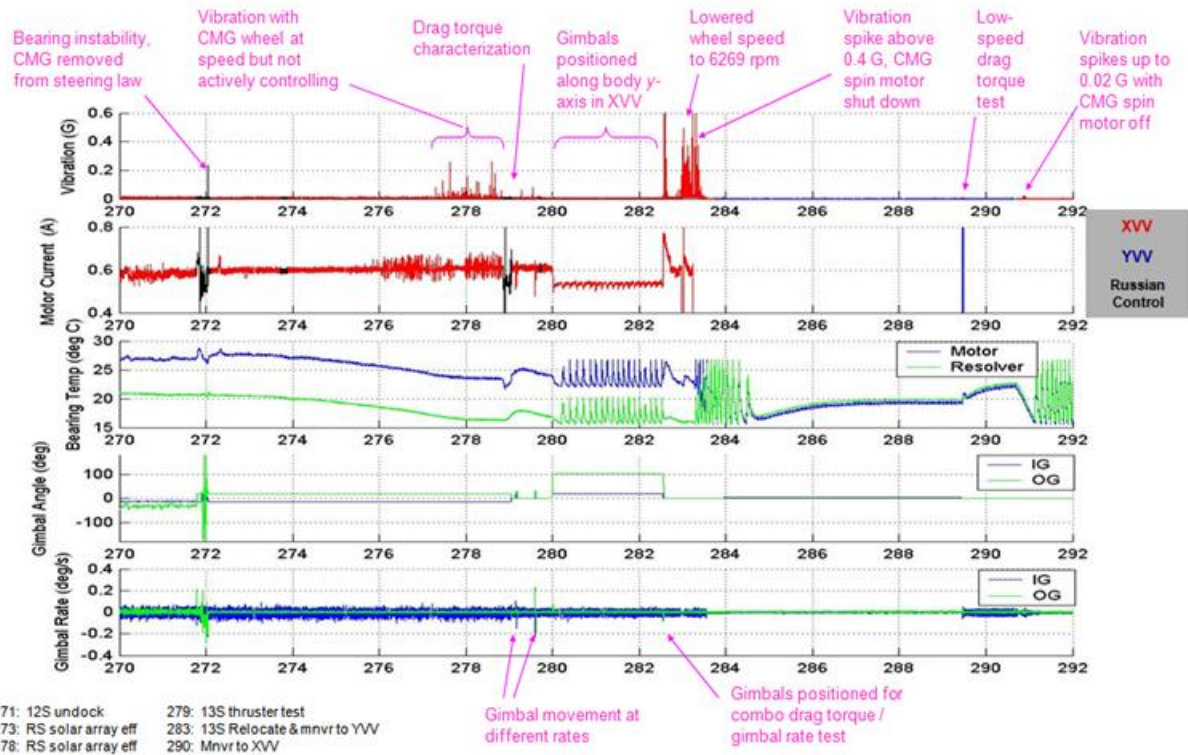


Figure 8. CMG3 Time Line to Shutdown

Forensic Findings

CMG1 Forensic Findings

The failure investigation confirmed that the HR spin bearing of CMG1 suffered a failure after 1.3 years of operation. This spin bearing was severely damaged and the rings were separated. Exposure to high temperature was clearly evident. Verification testing of the active oiler system flowrate could not be performed due to the extensive damage from high temperature. The inner raceway contained a significant amount of smeared metal. A secondary raceway was generated when some of the balls were driven from the manufactured raceway and became wedged between the outer race land and inner race land on the load side of the inner race. Two balls were fused together with severe skidding damage at both the inner and outer race contact locations. The remaining 13 balls were of various size and shape. The inner race was seized to the flywheel shaft and required the machining of two axial slots for removal from the flywheel shaft. The outer raceway also contained smeared metal and was stuck in the bearing housing steel sleeve. The outer race was seized in the bearing cartridge steel sleeve and was also machined out using a similar technique. No damage was done to bore of the steel sleeve during the outer race removal process. The retainer was almost completely destroyed, with only two significant pieces remaining, showing that the cage appeared to split circumferentially down the center line. The two major fragments remaining each had portions of several ball pockets. A smaller segment containing several pads on which the cage is guided by the inner race land was also recovered. There was no obvious evidence that the cage had experienced unusual wear either within the ball pockets or at the pad-land interface.

The SM bearing survived the 72-minute deceleration period. Radial and axial control of the spinning mass was unconstrained by the failed bearing and the spinning flywheel coned about the SM bearing. However, radial constraint is provided by sequential gaps between the rotating mass and the stationary parts, i.e.,

the stator support labyrinth seal/flywheel shaft air gap. These features allow for a controlled fail safe deceleration.

The SM side bearing (non-failed side) was in good condition. Adequate lubrication was noted in the ball race contact zone and at the retainer pad and inner race land interface. The balls were bright with some wear tracks that are considered consistent with operation time. Except for one uneven wear track on the outer race, the wear tracks on both races are considered nominal for the operational time. A ring of degraded lubricant was noted on the inner race land, which is abnormal for the accumulated operating time. The retainer was not damaged and did not contain any evidence of unstable operation or distress. Inspection verified the location of the SM bearing wear tracks were consistent with CMG1's lifetime load conditions. Additionally, testing of the active oiler system verified that the lubricant flow was consistent with the presence of fresh oil in the bearing.

As the investigation continued, the evidence supported that a compromised bearing preload led to the failure. The following findings are evidence that the spin bearing preload system was compromised:

1. Some "fretting" type marks were observed on the steel sleeve of the SM bearing cartridge steel sleeve. The fretting marks were 180 degrees apart from the area on inboard section to the area on the outboard section, an indication of bore misalignment. If these conditions occurred before the failure, either during on earth acceptance testing or during operation, this misalignment would have affected the preload system. In addition, a particular mark coined a "galled fret" was observed on the CMG1 HR steel sleeve. This galled fret may have specifically been the one that prevented the outer race to slide properly which would compromise preload and initiate ball skidding.

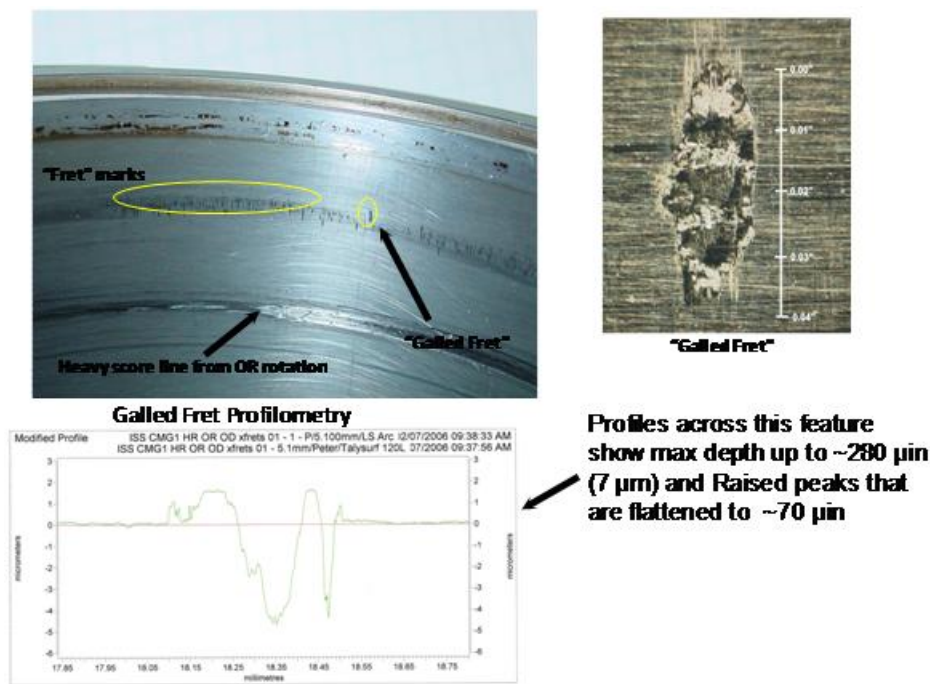


Figure 9. HR Side Bearing Housing Steel Sleeve

2. Some scoring (record grooving) on both the Spin Motor and Hall Resolver side preload nuts has been observed. This condition inhibited the spring action to react properly during the load and release cycle during axial motion of the flywheel. Preload was reduced to cause ball skid.



Figure 10. Pre-Load “Record Grooving”

3. Assembly evaluations also identified a built in misalignment caused by the inner gimbal covers distorting the inner gimbal structure and altering the precision bearing bore alignment. This bore misalignment exacerbated the wear observed on the steel sleeves of the Bearing Housings.

CMG3 Forensic Findings

The most notable observation was the excellent condition of both Inner Gimbal spin bearings. In general, the HR side spin bearing was in good condition. An abundant amount of lubrication was noted in the ball race contact zone and at the retainer pad and inner race land interface. The balls were bright with some wear tracks, i.e., frosted bands, composed of repeated dents most likely caused by hard particles embedded in the raceway. The inner race was not significantly worn. It contained glazed bands but not beyond the original surface finish. The retainer was not damaged. It contained very light deposits around the ball pocket. Some amount of de-wetting was noted on the inner and outer raceways, but not on the balls. Gas Chromatography/Mass Spectroscopy (GC/MS) analysis of the lubricant by The Aerospace Corporation showed good correlation to unused KG80 oil. However, long chain fatty acids and plasticizers contaminants were identified. The burnishing and slight deposition of the darkened lubricant, more on the fore and aft portions of the pocket than on the sides, indicates this bearing may have operated with periods of mild retainer instability. The failure investigation team consensus is that this bearing was in good shape with wear commensurate with its 5.8-year life and *not* a contributor to the observed anomalous accelerometer signature.

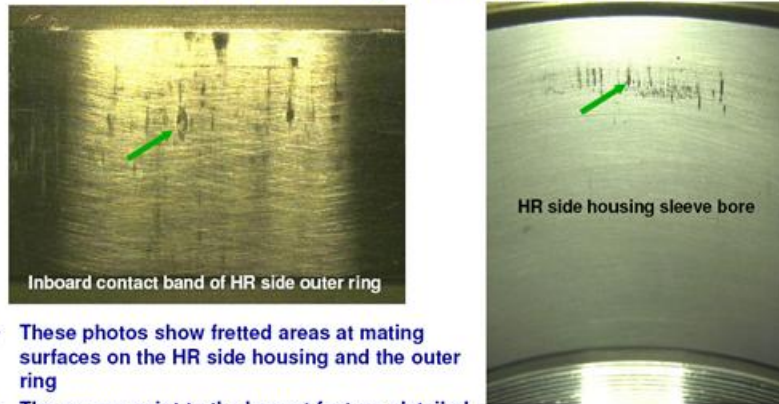
Initial visual observation classified the SM side bearing in comparatively worse condition than the HR side bearing but still acceptable. An abundance of lubrication was noted in the ball race contact zone and at the retainer pad and inner race land interface. The balls were bright, with wear tracks and the oil was beaded as droplets (evidence of dewetting). Some wear tracks are composed of metallic wear debris and some grooves due to mild surface distress. Some patches of the balls are rich in sulfur. Other bands are composed of repeated dents most likely caused by hard particles embedded in the raceway. The inner race contained a significant wear track and glazed bands due to mild surface distress. The retainer was not damaged. Deposition of darkened lubricant was observed on the fore and aft portions of the pockets. Only two of the inboard and outboard quadrants contained minor accumulations of slightly degraded lubricant. The Aerospace Corporation GC/MS Analysis of the lubricant showed good correlation to unused KG80 oil however “contaminants” like long chain hydrocarbons, long chain fatty acids and plasticizers were more predominant in this bearing. The failure investigation team consensus is that this bearing is in worse condition than the HR bearing, but still acceptable, it contained more wear but still commensurate with its 5.8-year life. It had higher concentrations of contaminants and more areas of dewetting, including the balls. It is believed that this wear was accumulated over the life of the unit and not

just in its last days of operation. Additionally, testing of the active oiler systems verified that the lubricant flow was consistent with the presence of fresh oil in the both bearings.

Evidence to further support the CMG1 failure conclusions and provide support that the bearing preload was reduced to cause the unbalance monitor to reach the “take action criteria” for the CMG3 soft failure are:

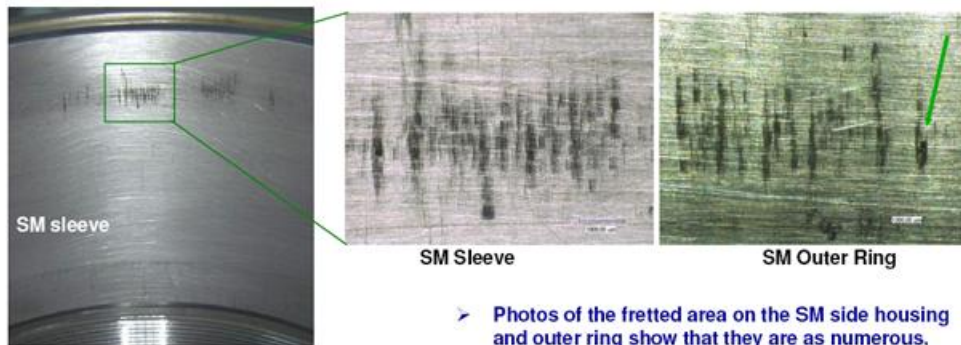
1. Similar “fretting” type marks were observed on the steel sleeve of the bearing cartridge steel sleeves (Figure 11). The fretting marks were near 180 degrees apart from the area on inboard section to the area on the outboard section, an indication of bearing bore misalignment. If these conditions occurred before the failure, either during on earth acceptance testing or during operation, this misalignment would have affected the preload system.

HR Side Outer Ring / Housing Interface

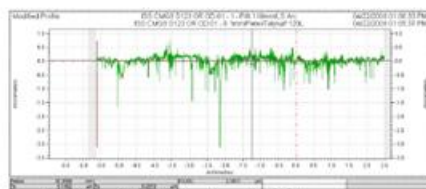


- These photos show fretted areas at mating surfaces on the HR side housing and the outer ring
- The arrows point to the largest feature, detailed on the next chart
- There were generally fewer frets here than on CMG1 and ADP
- There was some evidence of wear marks 180 degrees apart from these on the outboard end of the bore, but this was not as distinct as in CMG1 and qual unit

SM Side Outer Ring / Housing Interface



- Photos of the fretted area on the SM side housing and outer ring show that they are as numerous, but not as severe as on the HR side housing
- The profile shown here was scanned across the corresponding surface of the outer ring inboard contact band
- This profile confirms that the wear is not as severe, but it shows a persistent mildly abrasive contact



Profile of the SM outer ring frets

Figure 11. Typical Cartridge Fretting

- Some scoring (record grooving) on both the Spin Motor and Hall Resolver side preload nuts has been observed (Figure 12). This condition inhibited the spring action to react properly during the load and release cycle during axial motion of the flywheel. Preload was reduced to cause low preload and ball skid.

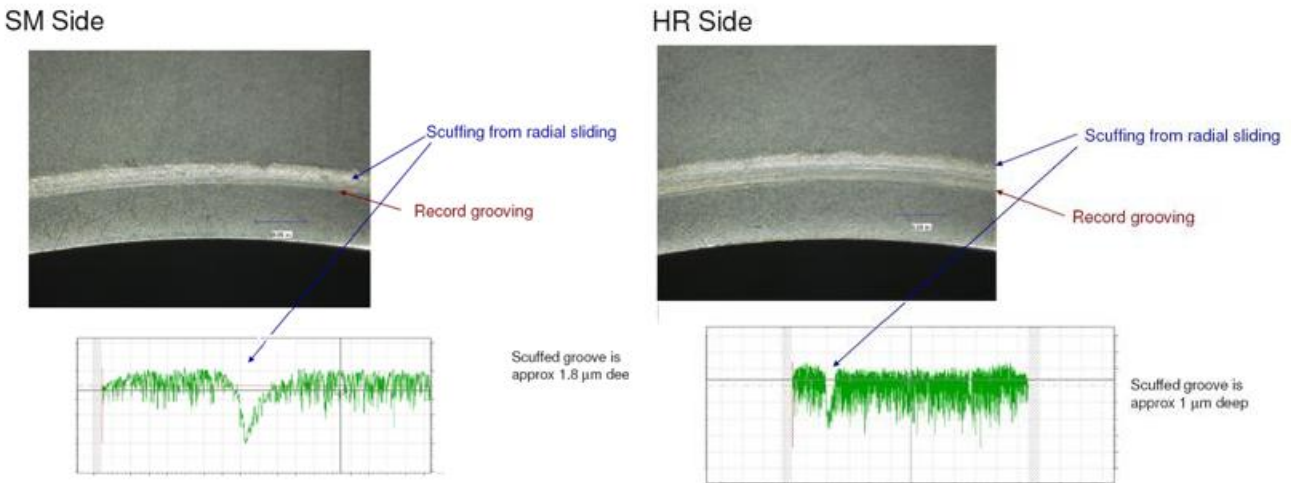


Figure 12. Typical Preload Nut Record Grooving

- Assembly evaluations also identified a built in misalignment caused by the inner gimbal covers distorting the inner gimbal structure and altering the precision bearing bore alignment. This bore misalignment exacerbated the wear observed on the steel sleeves of the Bearing Housings. Similar distortion characteristics to the CMG1 covers were confirmed on CMG3.

CMG1 and CMG3 Most Probable Causes

After a thorough review of the forensic findings and the on-orbit telemetry the failure investigation teams concluded the most probable causes for the CMG1 bearing failure and CMG3 excessive unbalance were:

- Fretting/galling at the bearing Outside Diameter (OD)/Steel Sleeve interface inhibited free motion of bearing preload mechanism, this reduced bearing preload to a threshold level to initiate ball skid which ultimately caused failure.
- Scoring (record grooving) on the Spin Motor and Hall Resolver side preload nuts adversely affected the bearing preload and bore alignment also contributing to a compromised preload that initiated ball skid.
- Bearing misalignment introduced by the inner gimbal covers exacerbates the wear conditions at the preload nut and sleeve interfaces.
- Additionally, research conducted during the CMG Root Cause Investigations showed that the adverse mechanical conditions described above were exacerbated by spin bearing radial loads induced by highest allowable gimbal rates. Operational limits were put in place to control both gimbal angular velocity and acceleration to restrict the amount of radial loading imparted to the bearings.

Design Improvements

The failure investigation, consisting of test, disassembly, evaluation and analysis of CMG1 and CMG3, identified the wear characteristics at the bearing outer race/bearing housing steel sleeve interface, scoring of the preload and inner gimbal cover induced gimbal distortion. These conditions adversely lower the bearing preload to the point where ball skid can occur. This can cause a bearing failure as in CMG1,

or increase vibration to the “take action” criteria as observed during CMG3 on-orbit operations. These observations led to the following redesigns;

1. Change the sleeve material to a harder dissimilar metal than the bearing outer race to prevent fretting and galling
2. Add Rheolube grease to the bearing/steel sleeve interface to improve long term lubrication, reduce wear/galling/fretting, and improve sliding
3. Change the preload nut material from A286 to harder 52100 to prevent wear/record grooving
4. Add flats to the Belleville preload spring to reduce contact stresses and prevent wear/record grooving of the preload nut
5. Improve the inner gimbal cover/inner gimbal interface to reduce gimbal distortion and maintain bearing bore alignment
6. Improve the cleaning process of bearing housing sleeves to minimize/eliminate hard particles that may have contributed to the repetitive marks in the bearing raceway and that may have lodged between the outer race and steel sleeve resulting in locked outer races

The design improvements identified from these investigations were successfully demonstrated in a re-design verification test program and have been implemented in the rebuild of CMG1 and CMG3 to minimize the most probable failure mechanisms and increase the life of the spare CMGs. These CMGs will be stored on the Space Station as “ready to use” spares.

Conclusions

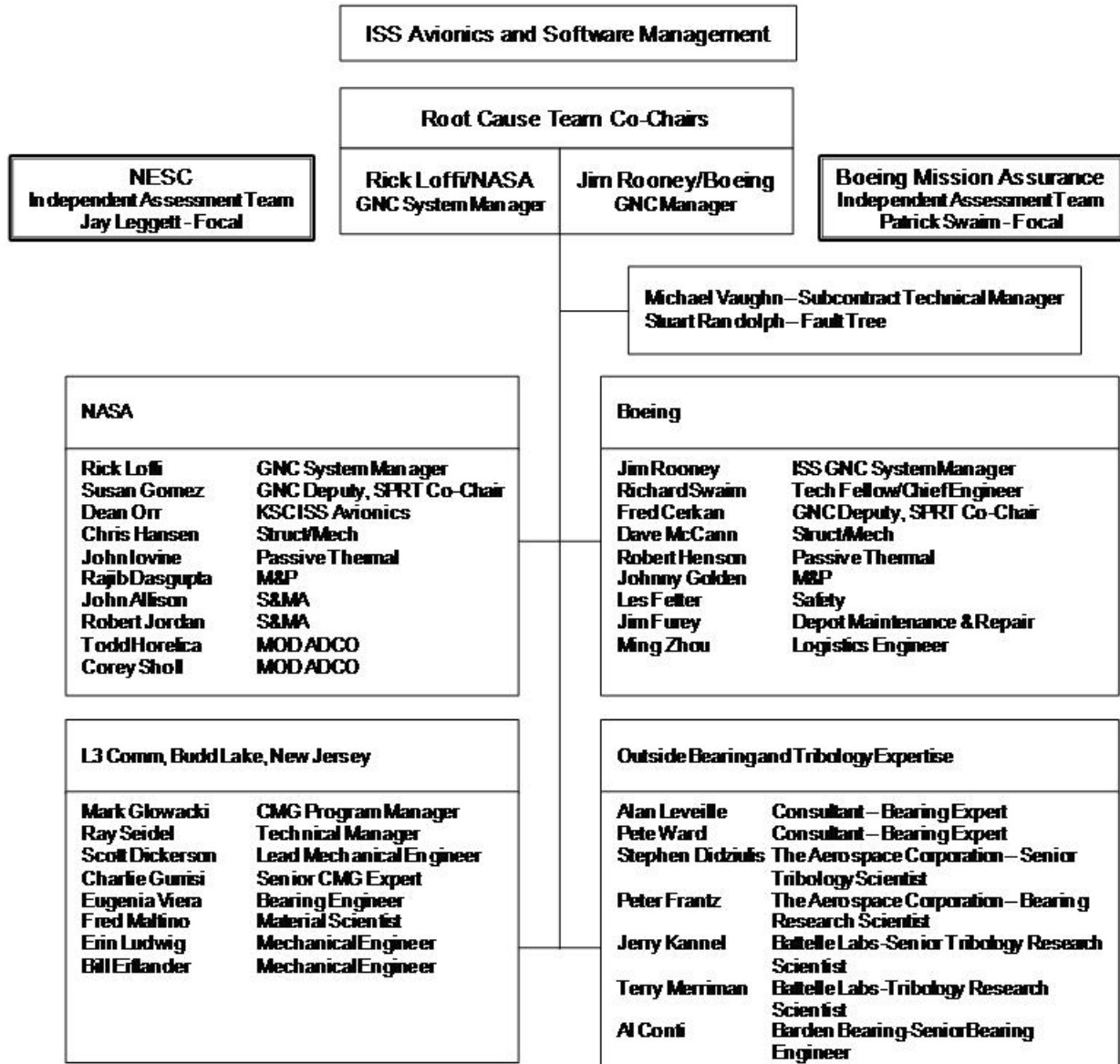
Determining the cause for failure was the primary focus of the investigation teams. The same teams were utilized to develop modifications to eliminate the design susceptibilities. From these two CMG failures, valuable engineering and programmatic lessons learned surfaced to improve future space programs. The lessons learned from these failures are:

1. Sliding fits should be properly designed and lubricated to minimize wear and galling/fretting over the life the device. This can be accomplished through proper selection of materials at the interface. In general, the use of dissimilar metals at sliding interfaces will reduce the likelihood of galling/fretting. Galling/fretting/wear tests should be performed in the design phase to optimize the sliding fit interface.
2. Ensure all structure distortions are totally analyzed in the design phase. Do not underestimate the importance of thermal-stress analysis.
3. Ensure a cleaning validation and verification process are present for the parts in the critical sliding fit applications. Sliding fits can deteriorate quickly if hard particulate residue remains at critical fits from manufacturing operations.
4. As part of the qualification program a disassembly evaluation should be planned. The Space Station CMG program did not include a disassembly of the qualification unit; acceptance was based on performance after environmental exposures. A disassembly and evaluation of the qualification unit may have identified these susceptibilities at the sliding interfaces.
5. New designs based on heritage are a good starting point; however, incorporation of present day technology should not be discouraged. A thorough risk analysis should be performed before a deviation from a heritage design is accepted. Evaluation tests using “design of experiments” must be performed in the development phase to demonstrate the innovative configuration provides a low risk improvement over heritage.

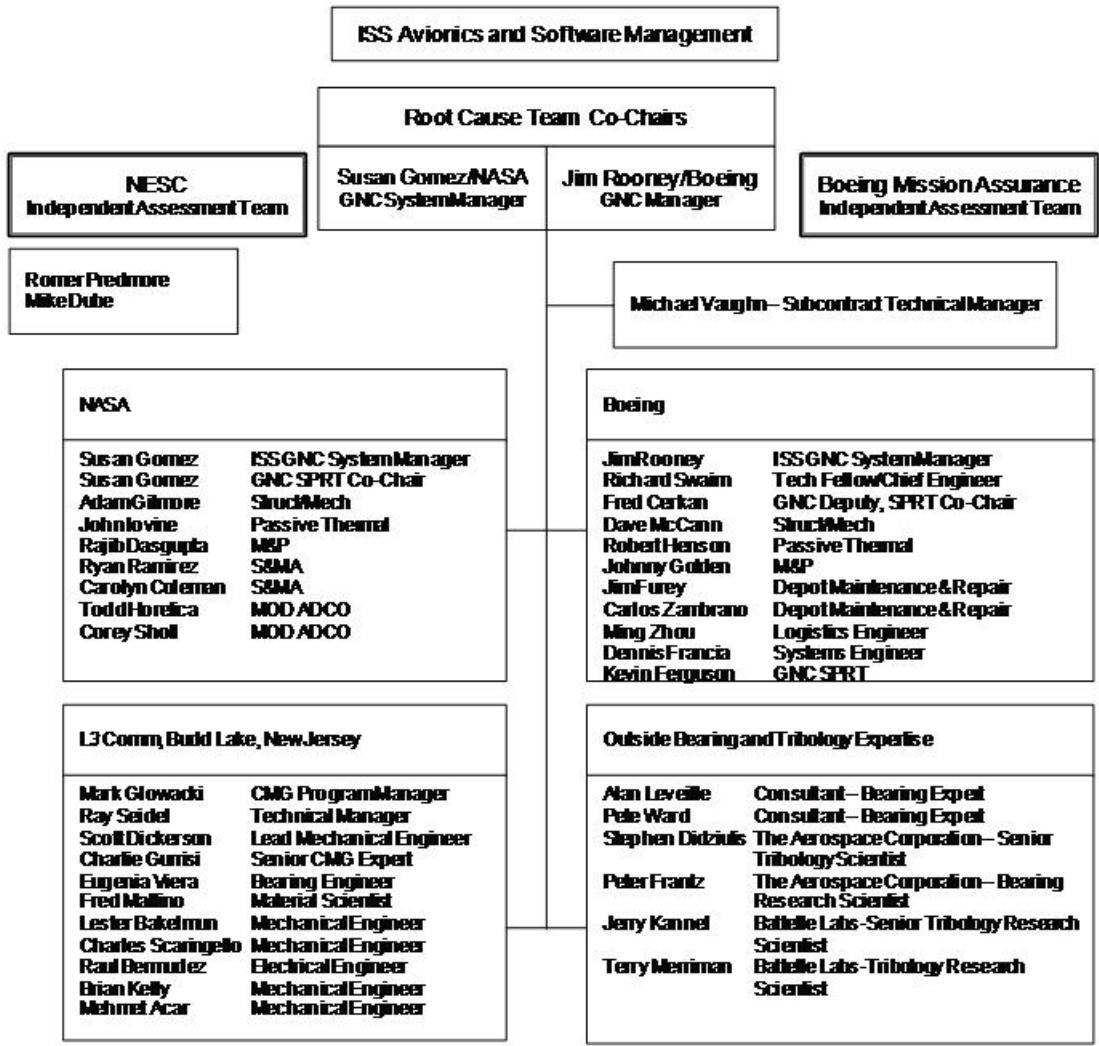
The ISS, an orbiting laboratory, is providing a learning opportunity not only for the planned scientific experiments but also for spacecraft design and operation within the International Aerospace Community. The lessons learned from the CMG failures are only a few of the many that have been identified during the assembly and operational phases of the ISS.

Acknowledgements

The authors and co-authors of this paper express their gratitude to the failure investigation teams. The collaborative efforts of NASA, Boeing, NESC, Battelle, The Aerospace Corporation, L-3 S&N, and independent consultants resulted in comprehensive investigations that resulted in identifying the most probable cause for both anomalies. Accolades were expressed by Boeing and NASA upper management many times for the team work, leadership and efficiency of the teams identified below:



CMG1 Failure Investigation Team



CMG3 Failure Investigation Team

References

- ¹ L-3 S&N CMG Sell Sheet L3SN_24_0603.qxd. "Cleared by Department of Defense/DFOISR for Public Release under 02-S-0862 on February 27, 2002"
- ² Burt, Richard "AAS 03-072 "Failure analysis of International Space Station Control Moment Gyro" 26th Annual AAS Guidance and Control Conference, Breckenridge, Colorado.
- ³ Kennel H.F. "Steering Law for Parallel Mounted Double-Gimbaled Control Moment Gyros – Revision A" NASA TM-82390 dated January 1981



International Space Station Powered Bolt Nut Anomaly and Failure Analysis Summary

Daniel E. Sievers* and Harry K. Warden*

Abstract

A key mechanism used in the on-orbit assembly of the International Space Station (ISS) pressurized elements is the Common Berthing Mechanism. The mechanism that effects the structural connection of the Common Berthing Mechanism halves is the Powered Bolt Assembly. There are sixteen Powered Bolt Assemblies per Common Berthing Mechanism. The Common Berthing Mechanism has a bolt which engages a self aligning Powered Bolt Nut (PBN) on the mating interface (Figure 1). The Powered Bolt Assemblies are preloaded to approximately 84.5 kN (19000 lb) prior to pressurization of the CBM. The PBNs mentioned below, manufactured in 2009, will be used on ISS future missions. An on orbit functional failure of this hardware would be unacceptable and in some instances catastrophic due to the failure of modules to mate and seal the atmosphere, risking loss of crew and ISS functions. The manufacturing processes that create the PBNs need to be strictly controlled. Functional (torque vs. tension) acceptance test failures will be the result of processes not being strictly followed. Without the proper knowledge of thread tolerances, fabrication techniques, and dry film lubricant application processes, PBNs will be, and have been manufactured improperly. The knowledge gained from acceptance test failures and the resolution of those failures, thread fabrication techniques and thread dry film lubrication processes can be applied to many aerospace mechanisms to enhance their performance. Test data and manufactured PBN thread geometry will be discussed for both failed and successfully accepted PBNs.

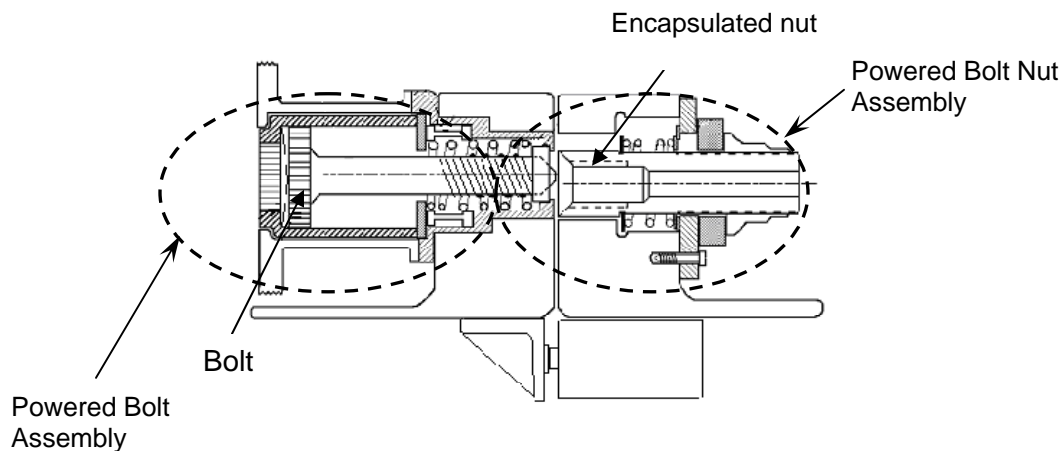


Figure 1: ACBM Powered Bolt as mated to CBM Nut.

* The Boeing Company, Huntsville, AL

Introduction

Boeing was contracted to deliver flight qualified PBNs for use on the ISS. Prior to the current contract, PBNs had not been manufactured since the original ISS contract with NASA in the mid 1990s. Recently, PBNs were fabricated in 2007 and delivered to Boeing in Huntsville Alabama for acceptance testing. Acceptance testing resulted in a PBN functional failure rate of 34%. Due to the complexity of the issue, a tiger team consisting of different engineering facets was established to determine the failure mode and to introduce corrective actions. The Assembly and Acceptance test-bed was investigated for possible causes of failure. These investigations proved the Assembly and Acceptance test-bed were not the cause of the failures. PBN build records and destructive testing of failed PBNs were also investigated for possible causes of failure. Through destructive testing and evaluation, and review of previous build records, the failure mode was identified to be a combination of out of tolerance thread dimensions, out of tolerance thread surface conditions, and improper application of dry film lubricant. Following the root cause investigation, improved process controls were implemented and a new lot of 113 PBNs were fabricated in 2009. These PBNs were acceptance tested and displayed a 0% functional acceptance test failure rate due to thread dimensions and lubrication issues; validating the implemented process controls to be appropriate. The 96 PBNs manufactured in 2007 were scrapped.

Thread Fabrication

Internal thread geometry of an encapsulated nut is difficult to inspect following machining, leaving the thread geometry acceptability to rely primarily on the fabrication processes used during manufacturing. The PBNs are kept to a tolerance of 23 μm (0.0009 in) on the internal thread pitch diameter dimensions to ensure proper bolt to nut clearances after the application of lubricant. It is difficult to maintain these thread dimensions because the nut must be machined and then lapped to ensure surface finish requirements. The PBNs are made of cold worked Nitronic 60, a difficult austenitic alloy to machine because of its susceptibility to internal stresses caused by cold working. If the machinist does not take the proper precautions during machining, these internal stresses will cause the metal to distort during the machining process. These distortions, which may cause mating issues later during acceptance, will be grounds for rejection of the hardware.

The machinist must ensure adequate and uniform lapping over all the internal threads with a hand tool specially made for the PBN thread dimensions to ensure burrs are removed and the required 0.41 μm (16 μin) finish is obtained. The lapping process for the 2009 PBNs consists of machining a bolt to proper dimensions and covering it with lapping compound. When choosing a hand tool to lap the nuts and remove burrs left from machining, the hand tool material must be softer than the nut base material. This is to ensure the burrs will be removed and the base metal will not be damaged by galling with the hand tool. The best way to ensure an adequate finish is to fully engage the softer material tool with lapping compound multiple times to wear down any burrs left from machining. This process was implemented for the 2009 PBNs to smooth out burrs and meet required finishing while opening the nut pitch diameter before the application of lubricant. Figure 2 is a surface finish error (burr) that occurred due to inadequate machining and lapping of the 2007 PBNs. This error may seem minuscule, but when requiring the Powered Bolt to autonomously attach two pressurized elements of the ISS together, a small burr will quickly break through the thin dry film lubricant and cause galling of the Powered Bolt Assembly. The PBNs fabricated in 2007 were polished with a lathe and polishing sponge. The lathe and sponge method is unable to polish in the grooves of the PBN threads; therefore this method will not meet the thread call out and finish of the specified PBN drawing. This process not only leaves room for potential burrs but also does not evenly open the thread pitch. Using a lathe and sponge technique could also damage the threads of the nut if the machinist calculates dimensions wrong or a sizable previously made burr gets caught on the lathe. The PBNs fabricated in 2009 were correctly dimensioned and lapped to open the pitch diameter in order to meet the PBN drawing specifications.

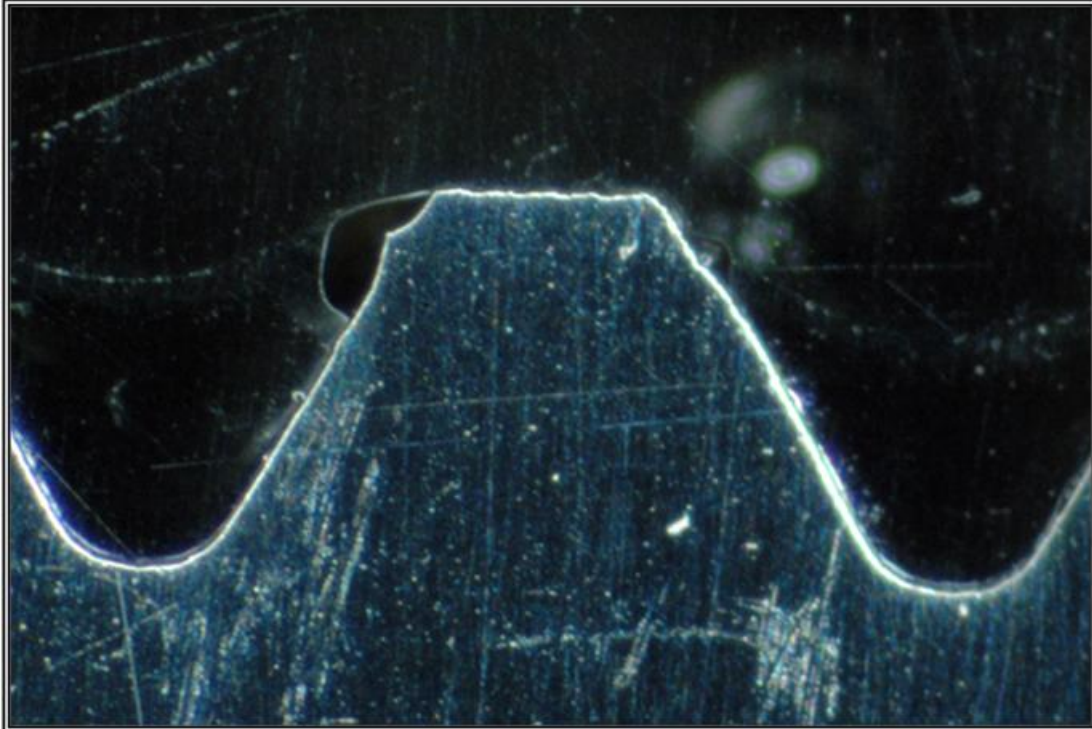


Figure 2: Surface Finish error, burr; 500x magnification

During this anomaly investigation, it was found that a PBN thread dimension call-out was incorrect. The depth of threads called out exceeded the thread area of the encapsulated nut. Only 15 to 16 threads were able to be machined into the PBN barrel given the amount of depth allotted for the threads. However, the thread dimension call-out stated 18 threads should be machined into the nut barrel. This was discovered when running a go/no-go gauge in the PBNs before lubrication to check for correct thread dimensions. The gage would only go 15 to 16 turns depending on the PBN. Repercussions of this incorrect thread dimension not being found would have been seen during the lubrication process while running a thread cutting tap into the nut in order to clear cured lubricant out of each thread groove. The cutting tap would have passed the last thread of the PBN barrel and cut into the base metal at the bottom. Shavings of the base metal could later be caught between the threads of the PBN and Powered Bolt during mating. This extra metal between threads could cause failures due to higher torque limits and damaged lubrication. With this information being discovered before acceptance testing, the correct amount of turns was able to be used during the PBN lubricant tapping process described in the next section. Since a thread cutting tap was never used on PBNs before, there were no shavings of loose base metal and no failures of this type in the past. This incorrect call-out was never noticed during mating of the PBN with the Powered Bolt because the Powered Bolt only enters the PBN with 14 turns.

Lubrication

Dry film lubricants are used in space applications and specifically with the Powered Bolt Nuts for their thermal stability, low abrasivity and low shear strength. Dry Film Lubrication of the PBNs is another important aspect of manufacturing which ensures a smooth running system with no galling issues and consistent torque-tension characteristics of the mechanism. Each PBN should have values above 90.4 N-m (800 in-lb) throughout cycles 2 through 24 of acceptance testing. Unacceptable test data from the PBNs manufactured in 2007 can be seen in Figure 3. If the PBNs are not fabricated or lubricated correctly, testing torque limits above 90.4 N-m (800 in-lb) will be seen during cycles 2 through 24 of acceptance testing resulting in a failed acceptance test. The Acceptance test for the PBNs is a very rigorous test. A Powered Bolt is cycled into a PBN 28 times under a normal operating load. Cycles 0 and

1 are at ambient pressure and temperature. Cycles 2 through 21 are under vacuum at ambient temperature. Cycle 22 is under vacuum and at cryogenic temperatures. Cycle 23 is under vacuum and at hot temperatures. Cycle 24 is at vacuum at ambient temperatures. To finish the test, Cycles 25 through 28 are at ambient temperature and pressure. Figure 4 shows complete acceptance test data of all of the 2009 PBNs. The 2009 Acceptance test data shows more consistent torque-tension behavior of the correctly fabricated PBNs compared to the failed 2007 PBNs.

The lubrication process for an encapsulated nut is very difficult due to its confined area. Most machinery is unable to enter the nut barrel and spray lubricant evenly over all threaded areas. The common process for applying dry film lubricant to small diameter internal threads is to use a spray gun with a long nozzle. The lubrication thickness and uniformity are dependent on several variables; fan speed, speed of the nozzle through the threads, nozzle pressure, agitation rate of lubrication slurry, and nut temperature. If any of the variables are miscalculated or misused, the nut will be processed with agglomerations of the lubricant or areas without lubricant. PBNs may contain both agglomerations of lubricant and areas of no lubricant simultaneously. Each of these defects is hard to detect without proper equipment and knowledge. A borescope is commonly used to look at the internal threads of nuts, but without the knowledge of what to look for, these defects can go undetected.

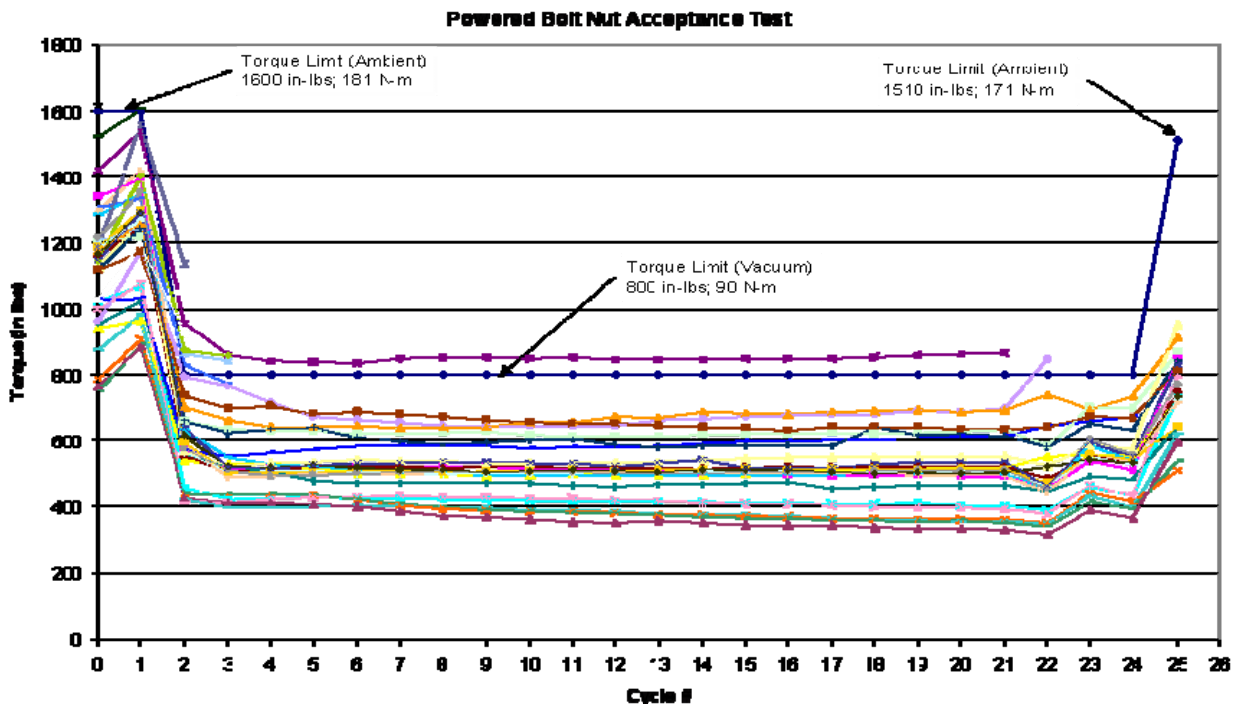


Figure 3: Acceptance test data from failed PBN lot of 2007

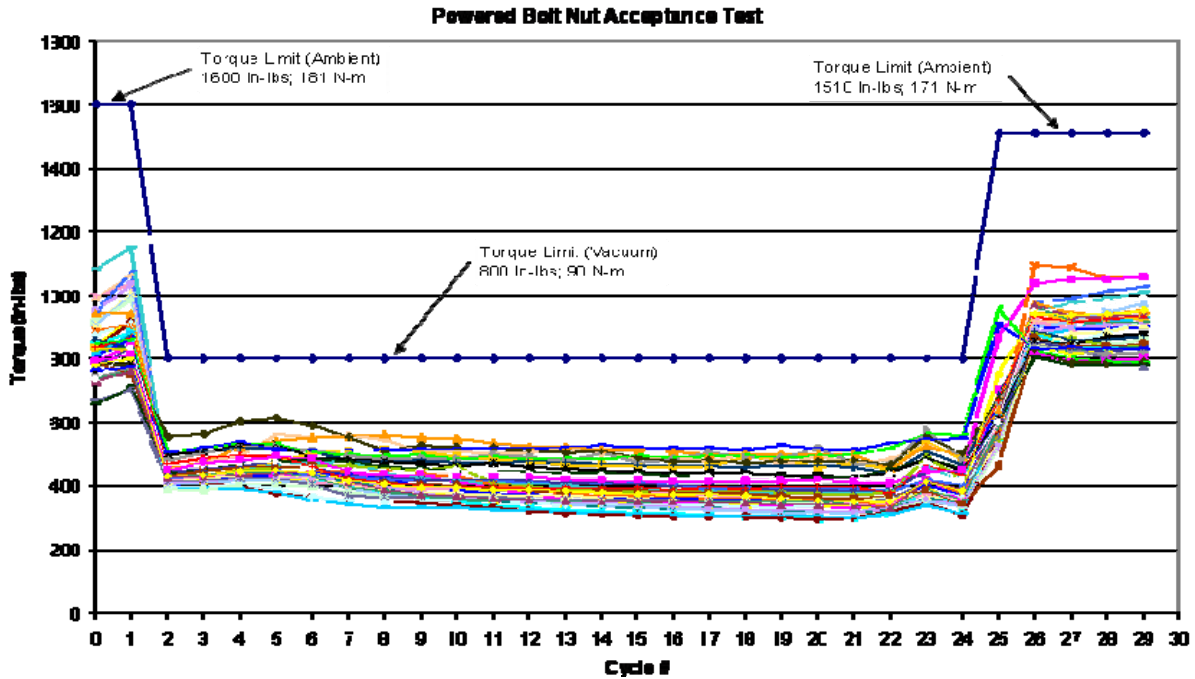


Figure 4: Acceptance test data from passed PBN lot of 2009

Dry film lubricant, which is applied to internal threads using common practices, has an unpredictable thickness. Thickness is almost impossible and usually too expensive to measure in an indestructible manner. If the lubricant is too thick, this will cause high torque limits during acceptance testing leading to failure of the nuts. Thickness of the PBN lubricant was also a reason for failure for some of the previously built PBNs. A way to defer from dry film lubricant being too thick is to use a thread cutting tap. On previously built PBNs, a roll forming tap or a specially manufactured forming tap was used. Both the roll forming tap and specially manufactured forming tap were not sufficient enough to cut through the cured ceramic base coat of the lubricant; this problem will be similar for most ceramic-based dry film lubricants. During this process, the roll forming tap became stuck in the nut barrel on various PBNs and had to be cycled multiple times into the nut. Much force had to be applied to the tap to smooth and cut out lubricant. This process increases the risk of damaging the lubricant or the threads of the PBN. A thread cutting tap should only be used on the fully cured ceramic base coat of the lubricant. Dry film lubricants may be applied in multiple coats and a thread cutting tap should not be used on the top coat. The thread cutting tap will strip the top coat off the base coat and the lubrication properties of the top coat and the lubrication system will be lost.

When deciding on a thread cutting tap, the end thickness of the lube must be taken into consideration. Adding the end thickness of the lubricant and subtracting the top coat not yet applied to the nut pitch diameter will ensure the thread cutting tap only clears out the unneeded base coat of the lubricant and leaves an even and smooth base coat on the threads. Figure 5 is an agglomeration of ceramic particles after curing of the lubricant and before using the thread cutting tap. Another benefit of using a thread cutting tap is cutting out debris which may come loose later during acceptance testing. This loose debris gets caught between the threads and causes torque spike anomalies in acceptance test data. This debris can also lead to false failures. Spraying the top coat of lubricant over a loose base coat will cause a loss of both top coat and base coat as debris during testing. Losing the top coat and base coat in areas will cause the lubrication system to function improperly, leading to higher torque readings and possibly galling. For each PBN, the thread cutting tap was used only one time to mitigate cutting into too much lubricant or causing damage to the lubricant. Using a thread cutting tap on dry film lubricant is not an easy process and difficult to do by hand. The PBNs were placed in a vice while a hand tool was used to gain

cutting torque in order to cut through the cured ceramic base coat. After the correct thickness of the base coat was obtained through proper tapping of the nut, the top coat of the lubricant system was applied. The variables stated earlier in this section are now controlled to ensure a consistent uniform lubrication throughout production.

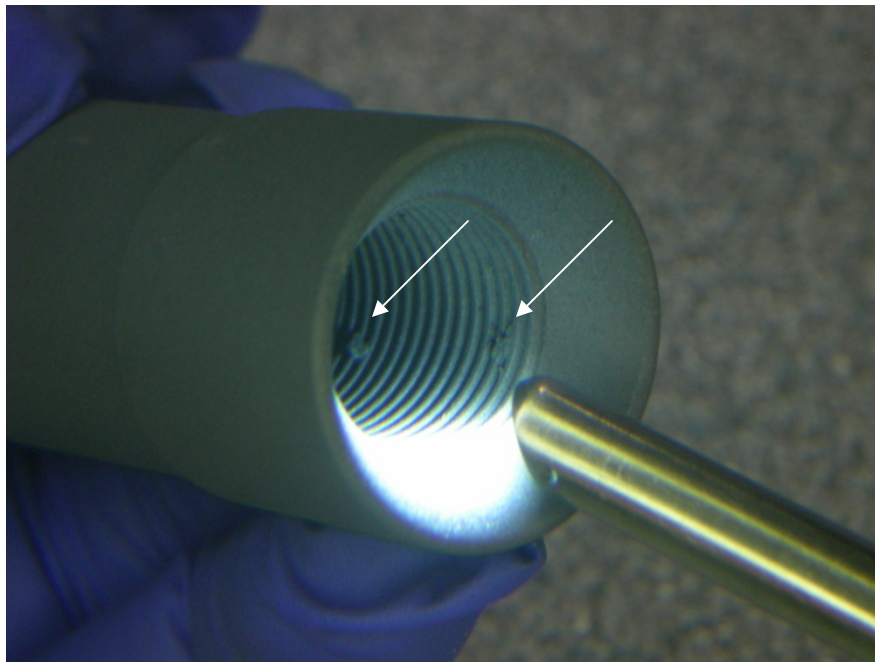


Figure 5: Agglomerations of base coat ceramic of Dry Film Lubricant

If dry film lubricants are applied in a liquid form, the substrate must be heated to ensure proper evaporation of the carrier liquids (commonly known as flashing). If proper flash is not reached, the carrier liquid will migrate with the lubricating particles and pool at its potential energy equilibrium. This pooling will cause uneven lubrication. A result of uneven lubrication can be seen in the case of the Powered Bolt Nuts acceptance test failures. The coefficient of friction was not met during these tests and high torque limits were reached, leading to failure. The dry film lubricant used in this process, Vitro-lube NPI-1220C, is a resin bonded ceramic coating, therefore if the lubricant is not properly flashed, an amber coloration can be seen in resin rich areas (Figure 6). This specific dry film lubricant was chosen because of its thermal vacuum stability and because of its ability to perform reliably under the high load rates of the Powered Bolt assembly; 1.03 MPa of contact stress. Vitro-lube NPI-1220C was also selected due to its superior wear life as compared to other dry film lubricants. This specific dry film lubricant is made up of two parts; a ceramic base coat and a resin top coat. Some dry film lubricants are not resin bonded and the resin rich areas in Figure 6 will not be seen. Areas of high ceramic content can also be seen if Vitro-lube NPI-1220C is not flashed properly; these areas form where the majority of the ceramic base coat pool during lubricant application. Ceramic pooling of a failed PBN can be seen in Figure 7. This result of improper flashing of dry film lubricant can be used as a guide for non-resin bonded lubricants. When using a non-resin bonded lubricant the surface characteristics will be different between base metal and dry film lubricant.

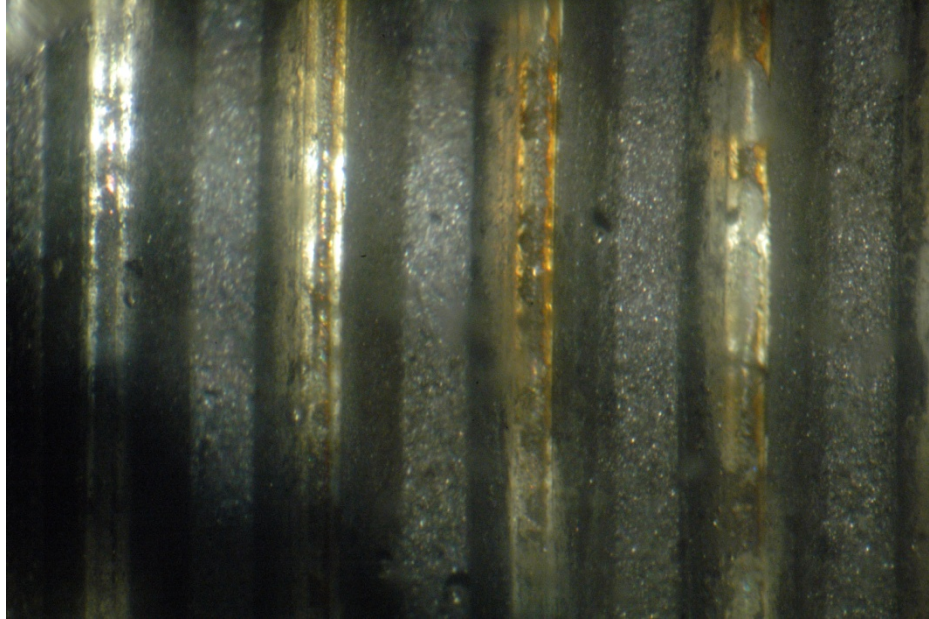


Figure 6: Amber coloration of resin binder; 50x magnification

Oxidation protection given to the substrate ceramic by the phenolic resin was a main factor in choosing resin bonded dry film lubricant for the powered bolt nuts. In the case of PBNs, Molybdenum disulfide (MoS_2) will not oxidize to Molybdenum trioxide (MoO_3), a poor lubricating material, in air due to the use of the top coat resin. A downfall to using MoS_2 over other dry film lubricants is it will fail due to high coefficients of friction when testing in high humid atmospheres under high loads. MoS_2 will oxidize to MoO_3 in high humid atmospheres under high loads. Most non resin-bonded dry film lubricants will slowly oxidize in air environments, such as storage warehouses, leading to early failures of the lubricant.

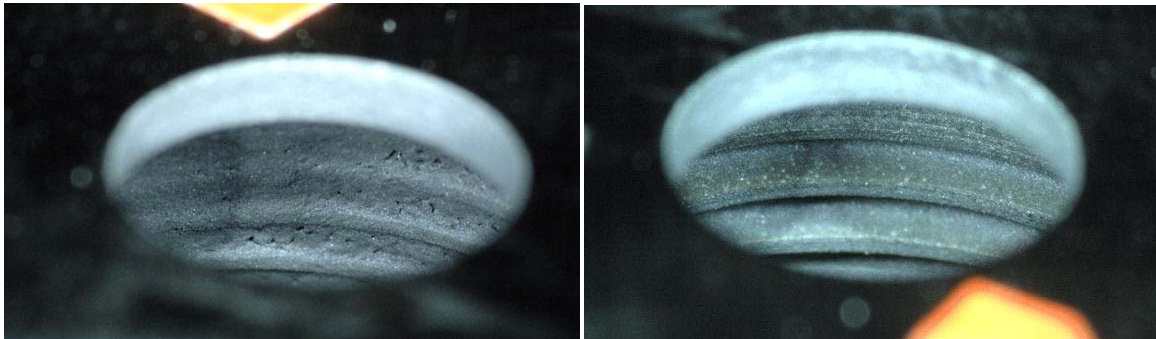


Figure 7: Two 180° views of a failed PBN; 50x magnification

A way of analyzing lubricant for composition is using an Energy Dispersive Spectrometer (EDS). This equipment will show if lubricant is missing from the threads. The EDS indicated that the ceramic base coat was applied to the threads before the resin top coat. Figure 8 shows EDS images of a PBN which failed acceptance testing. Spectrum 1 is of a non-amber colored area and Spectrum 2 is of an amber colored area. The chemistry shows the absence of the Molybdenum disulfide and Antimony which make up the ceramic base coat of Vitro-lube NPI-1220C. This absence of ceramic base coat is a direct cause of not preheating the PBNs before lubrication.

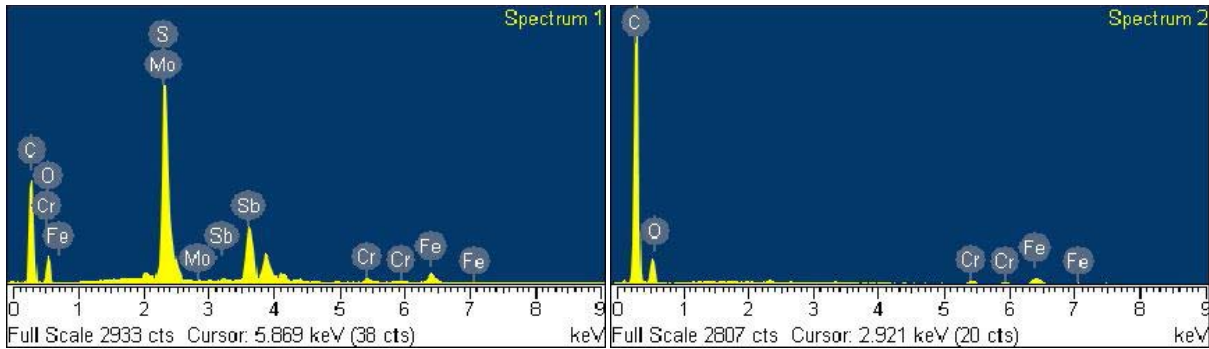


Figure 8: Differences in coating chemistry of PBN

Depending on a substrate's thickness and material type, the temperature of the substrate itself may differ in order to properly flash the carrier liquid. The flash temperature will also differ for lubricants depending on the carrier liquid used. The 2009 batch of PBNs was preheated in an oven/furnace for a specified amount of time at a temperature predetermined based on the PBNs material thickness and the carrier liquid (in this case isopropyl alcohol). A thermocouple was attached to the internal threads of the PBN while in the oven to evaluate the surface temperature where the flashing of the lubricant would take place. During production, the PBNs were taken out of the oven and prepared for lubrication; wheeled to station, set-up properly, etc... Depending on the technician, some of the PBNs would not be lubricated for 10 minutes, losing their flash temperature. It was realized that the PBNs needed to retain flash temperatures during production. To retain this temperature, mitigating risk of improper lubrication, a 3-minute time limit was placed on the PBNs to be out of the oven before being lubricated. Some dry film lubricants, for example Vitro-lube NPI-1220C, are applied in multiple coatings. To ensure proper flashing throughout all coatings, mechanisms must have an out of oven time limit placed upon them to retain their flash temperature during lubrication. This added preheat process to the lubrication method of the PBNs ensured proper flashing of the dry film lubricant leading to even lubrication of the nut threads and less production variation. At completion of the lubrication process, the PBNs exhibited dark spots throughout the nut. Further analysis of these dark spots showed it to be excess top coat. This excess top coat was deemed acceptable because it was not thick enough to cause mating problems and the excess top coat will not cause a lack of lubrication of the system. During acceptance testing this excess top coat will be burnished into the ceramic base coat as is the rest of the top coat.

Conclusions

For future manufacturing of PBNs and other Aerospace mechanisms that have dry film lubrication similar to the Powered Bolt Mechanism, proper processes must be established to ensure a reliable part is produced. These process enhancements will minimize part-to-part variation and acceptance test failures while avoiding added costs and delays in delivering a final product to the customer.

Key process enhancements discovered during this manufacturing anomaly resolution include:

Thread Fabrication

- When lapping a surface, a method that is capable of obtaining the desired surface finish in every thread, groove, etc, must be determined and controlled. In this case, manual thread lapping with a “softer” tool and lapping compound, lapped multiple times worked well to wear down any burrs left from machining.
- Polishing with a lathe and sponge method was eliminated.
- Use of a go/no-go gauge before lubrication to check for correct thread dimensions was implemented.

Lubrication

- To maintain consistent lubrication thickness a thread cutting technique was implemented over a thread rolling tap. Consideration of final lubricant dimensions is a key aspect of choosing a cutting tap.
- A preheating process was implemented to obtain proper flash temperature. Due to the migrating capabilities of dry film lubricants that are applied on to substrates as liquids, it is beneficial to preheat all mechanisms to defer and risk of lubricant pooling or lack of lubricant in less energy potential areas.
- Imposing an out of oven time limit during the lubrication process to keep the mechanisms at flash temperature.

All of these process enhancements placed upon dry film lubricated aerospace mechanisms will ensure proper system operation of equipment, minimize the risk of failure, and minimize product variation during production.

Acknowledgements

The authors of this document would like to thank the employees of NASA Marshall Space Flight Center for their support during this anomaly resolution, especially Phil Hall, and the employees of Boeing for their support and information especially Chuck Dombey. We would also like to thank Mark Haley of National Process Industries and Fletcher Byrd of American Mechanical and Electrical Services.

The International Space Station Solar Alpha Rotary Joint Anomaly Investigation

Elliot P. Harik*, Justin McFatter*, Daniel J. Sweeney**, Carlos F. Enriquez*,
Deneen M. Taylor** and David S. McCann*

Abstract

The Solar Alpha Rotary Joint (SARJ) is a single-axis pointing mechanism used to orient the solar power generating arrays relative to the sun for the International Space Station (ISS). Approximately 83 days after its on-orbit installation, one of the two SARJ mechanisms aboard the ISS began to exhibit high drive motor current draw. Increased structural vibrations near the joint were also observed. Subsequent inspections via Extravehicular Activity (EVA) discovered that the nitrided case-hardened steel bearing race on the outboard side of the joint had extensive damage to one of its three rolling surfaces. A far-reaching investigation of the anomaly was undertaken. The investigation included metallurgical inspections, coupon tests, traction kinematics tests, detailed bearing measurements, and thermal and structural analyses. The results of the investigation showed that the anomaly had most probably been caused by high bearing edge stresses that resulted from inadequate lubrication of the rolling contact. The profile of the roller bearings and the metallurgical properties of the race ring were also found to be significant contributing factors. To mitigate the impact of the damage, astronauts cleaned and lubricated the race ring surface with grease. This corrective action led to significantly improved performance of the mechanism both in terms of drive motor current and induced structural vibration.

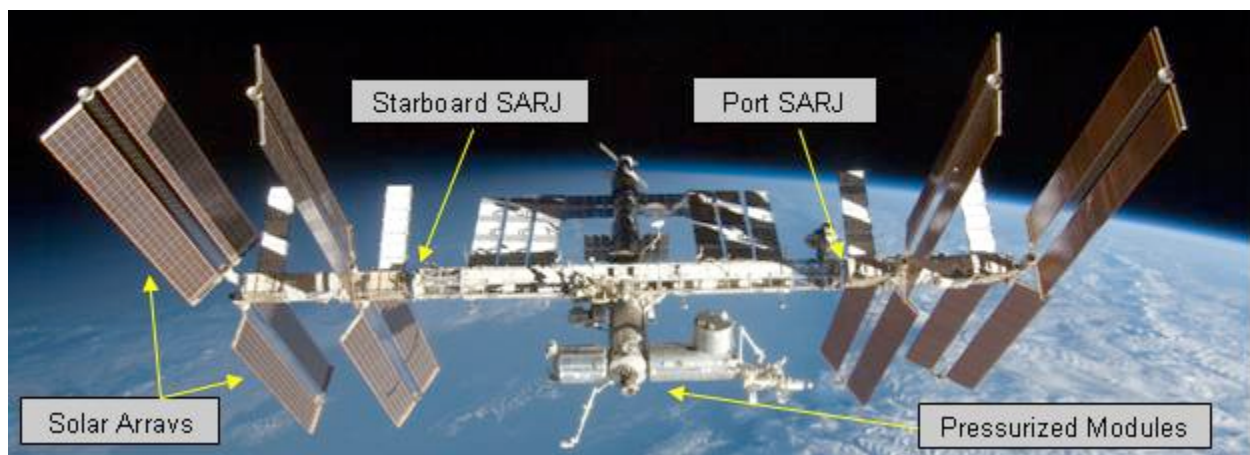


Figure 1. International Space Station as of August 2009

Introduction

International Space Station Overview

The International Space Station (ISS) is a research facility currently being assembled in low Earth orbit. The ISS project is a multi-national effort led by the United States, with partners from Russia, Canada, the European Union, Japan, and others. Construction of the ISS began in 1998 and is scheduled to be complete by 2011 with operations continuing until 2015. The ISS is the largest artificial satellite in Earth

* The Boeing Company, Houston, TX

** NASA Johnson Space Center, Houston, TX

orbit, larger than any previous space station. It was designed as an orbital scientific platform and is intended to operate continuously while supporting a crew of six in pressurized modules. The ISS offers an advantage over spacecraft such as NASA's Space Shuttle because it is a long-term platform in the space environment, allowing scientific experimentation as well as long-duration studies on the human crews that operate them. Long-term expedition crews conduct science daily (approximately 160 man-hours per week), across a wide variety of fields, including human research, life sciences, physical sciences, and Earth observation, as well as education and technology demonstrations. The power required to support the scientific and life sustaining functions of the ISS is provided by arrays of solar panels.

The ISS has a backbone or set of trusses that house several ISS systems. These trusses are joined to a set of pressurized modules that house the crewmembers living and working aboard the ISS. Figure 1 shows the ISS after assembly mission 17A by the Space Shuttle. The pressurized modules are located along the center of the truss structure, extending forward and aft. The power generating solar arrays are located on the port and starboard sides of the truss structure outboard of the SARJs. The location of each Solar Alpha Rotary Joint (SARJ) is indicated in Figure 1.

Solar Alpha Rotary Joint Overview

The SARJ is a single-axis pointing mechanism that allows orbital-rate sun-tracking rotation of the outboard trusses and solar arrays of the ISS. The SARJ completes one full rotation per orbit of the ISS, approximately every 90 minutes. Figure 2 shows a drawing of the SARJ with the major components labeled. The SARJ is capable of transferring 60 kW of electrical power, spare low power (300 W), and data channels across the rotary joint. The total weight of the SARJ is 1161 kg (2561 lb). Two SARJ mechanisms are installed onboard the ISS - Port (activated December 2006) and Starboard (activated June 2007). The SARJ serves as the structural joint between the ISS inboard and outboard truss elements via twelve Trundle Bearing Assemblies (TBA). The trundle bearings straddle between an inboard and outboard triangular cross-section race rings. The race rings are approximately 3.2 meters (10.5 ft) in diameter. TBAs are nominally mounted to the stationary inboard ring while their rollers track against the three surfaces of the outboard race ring.

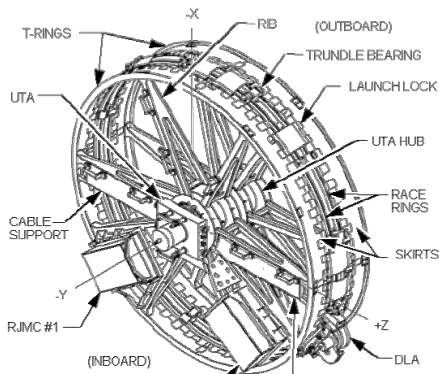


Figure 2. SARJ Overview

These rollers are highly pre-loaded against the race ring to allow them to react ISS structural loads. The bearing race is made of a 15-5PH stainless steel forging with a nitride hardened case. TBAs are designed for individual on-orbit replacement to protect the mechanism against a roller bearing failure. The SARJ is driven by one of two redundant Drive Lock Assemblies (DLAs) that interface with an integral bull gear on the race ring via a motor-driven pinion. Each DLA is controlled by a Rotary Joint Motor Controller (RJMC) which, in conjunction with processors in the ISS computing infrastructure, performs closed loop control of the joint's motion. SARJ system health and status data is relayed by the processors to the ground in the ISS telemetry stream.

Trundle Bearing Assembly Overview

The TBA contains three roller bearing assemblies: two identical upper rollers and a lower, slightly wider, roller. A picture of a TBA is shown in Figure 3. The roller assemblies consist of an internal double row tapered roller bearing whose cup is shrunk fit inside of an outer roller. The outer roller is the physical interface with the SARJ bearing race. The outer roller is made of 440C and is lubricated with 1250-2250 angstroms of gold applied via an ion deposition process. The gold plating on the rollers serves as the sole lubrication scheme for the roller/race interface (the internal tapered roller bearings have a grease lubricant). At the time of the SARJ preliminary design it was believed that the mechanism would be exposed to the atomic oxygen present in the low Earth orbit environment. The final design included thermal shrouds around the entire circumference of the mechanism, but these were not part of the baselined design at the time the lubrication system was being selected. Due to the long life requirement

(30 years) and the assumed exposure of the mechanism to atomic oxygen, lubricant selection criteria of the day [1] led designers to select a metallic film lubricant.

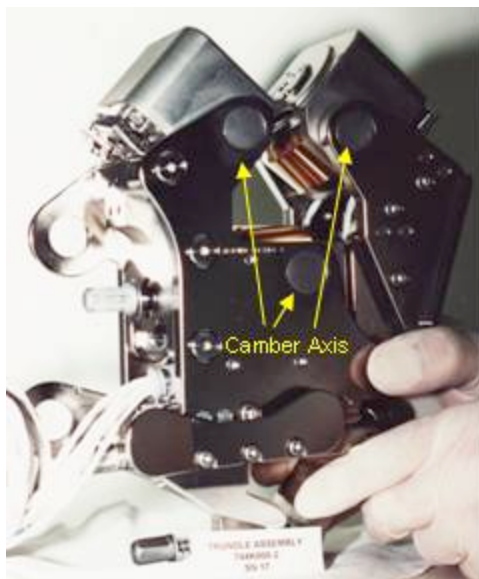


Figure 3. Trundle Bearing Assembly

The roller assembly is fitted into the trundle bearing via a camber pivot axis. This fitting is free to rotate approximately three degrees to allow for proper alignment of the outer roller with the bearing race under mechanical and/or thermal deflections. This rotational axis of the roller assembly leaves the roller susceptible to an overturning moment caused by thrust loads at the roller/race interface. This effect is discussed in detail below. The design intent was that the solid film lubricant on the rollers would mitigate these thrust loads.

On Orbit Anomaly Investigation

Approximately eleven weeks after the Starboard SARJ was activated on-orbit, the mechanism began exhibiting anomalous operational data. For the following two months, engineers on the ground reviewed on-orbit telemetry and worked with the ISS operators and ISS crew to determine the most likely cause of the anomalous signature through a series of on-orbit tests. Eventually, an inspection of the mechanism during an EVA found that the bearing race was damaged and covered in debris.

Initial Anomaly Investigation

The SARJ software provides continuous status on most of the system's performance parameters. These parameters include, but are not limited to, position, speed, motor current draw, target tracking accuracy, and hardware temperatures. This telemetry is reviewed continuously to ensure the health and effective operation of the mechanism. The first indication of anomalous behavior came from unexpected changes in the Starboard SARJ telemetry. In early September 2007, the ISS operations team raised a concern that the difference between the commanded and actual velocity of the SARJ was increasing. The SARJ controller software uses the difference between commanded and actual velocity to determine how much current to provide to the mechanism's drive motor. The change in velocity profile prompted a detailed review of the SARJ operational data. From this review, engineers determined that subtle changes in SARJ performance could be noted starting on September 1st. Figure 4 shows the onset of the anomalous data signature. There are two pieces of telemetry shown. The first is the joint position and the second is the commanded velocity of the mechanism. The three plots depict ten minutes periods of time from three consecutive orbits. Two observations can be made from these data: (1) the irregular data signature initially occurred at a specific angular position of the joint, and (2) the magnitude of the irregularity is

increasing with time. The frequency of the data spikes increased with time such that after a few days the commanded velocity at all SARJ angles was off nominal.

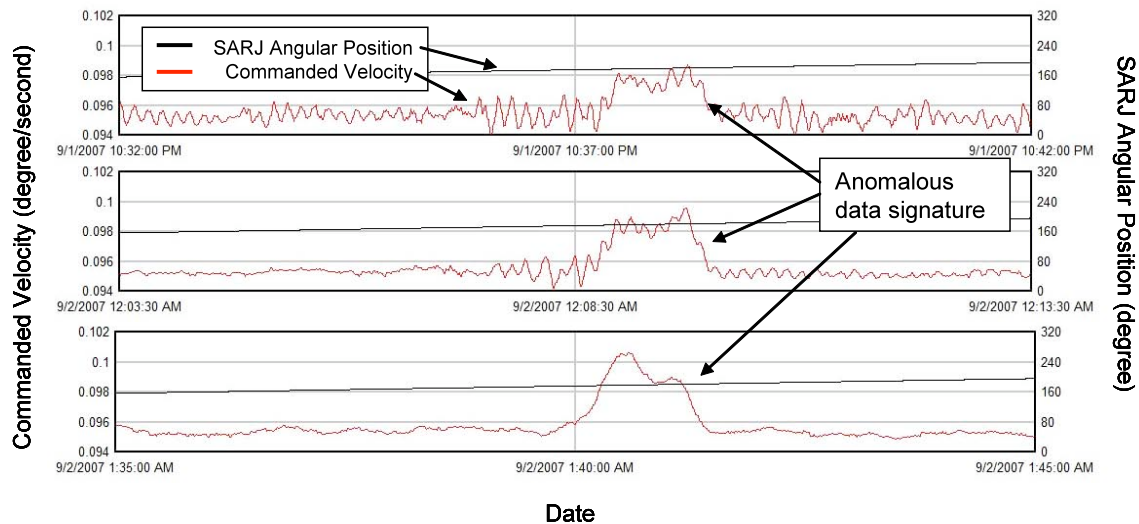


Figure 4. Anomalous Data Signature from the SARJ Controller

This anomalous signature appeared similar to a signature encountered previously on the Port SARJ. The Port SARJ data signature was caused by a problem with the SARJ controller software. With that in mind, the controller and manager software for the system were reset. The intent was to clear out memory buffers and re-initialize controller variables that could be accumulating and leading to the anomalous data signature. The software resets did not lead to any change in the anomalous signature. The SARJ controller did not appear to be the primary cause of the anomaly.

Efforts to exonerate additional components of the system were attempted by switching logical command strings. The SARJ controller architecture utilizes two fully redundant command strings. Each string is composed of a multiplexer/de-multiplexer (MDM) where the SARJ controller software is housed, a RJMC where the velocity control loop and motor power source is located, and a DLA which interfaces with the driven gear of the SARJ and houses the drive motor. Changing commanded strings did not have an appreciable effect on the anomalous data signature. This action demonstrated that the hardware from each drive string was not solely responsible for the data signature.

After clearing the software, MDMs, RJMCs, and DLAs, the primary focus of the investigation turned to the controller logic. While specific anomalies in the software had been ruled out, it was postulated that the controller might be over correcting for slight changes in mechanism performance. If this were the case, then controller parameters could be modified to optimize system performance. A thorough review of the controller logic did not produce any evidence that the anomalous signature could be a controller effect.

Five weeks into the anomaly investigation engineers had eliminated a number of likely causes for the anomaly but still did not understand the root cause. Then a significant change in the drive motor current, approaching system limits, led engineers to the conclusion that the problem was most likely mechanical in nature. An increase in joint drag appeared to be the cause of the anomaly.

Joint Drag Changes During the Anomaly Investigation

The drive motor current is directly related to the torque required to overcome internal drag and applied load in order to rotate the joint. Assuming a benign loading environment, the SARJ torque is a direct measure of the friction in the joint. The relationship between torque and drive motor current is shown in Equation 1 (torque constant and SARJ gear ratios can be assumed to be constants).

$$\text{SARJ Torque} = \text{Drive Motor Current} \bullet (\text{Torque Constant} \bullet \text{SARJ Gear Ratio}) \quad (\text{Eq. 1})$$

Prior to the anomaly peak motor currents of 0.25 ampere were nominal. This corresponds to joint drag of approximately 790 N·m (590 ft·lbf). During the initial investigation, the peak currents increased to levels as high as 0.60 ampere, or 1910 N·m (1410 ft·lbf) of joint drag. The system capacity is 1.4 amperes. While the increase in drag was over 100% of the nominal value, it was still well within system capacity with a torque margin of 1.33. The drive current readings remained steady for two weeks at the increased level. The system experienced another drastic increase in drive motor current in the first week of October. The multiple changes in drive motor current throughout the course of the investigation are shown in Figure 5. After the 3rd step change drive motor currents were over 1.2 amperes, or 3810 N·m (2810 ft·lbf) of joint drag. In a one week period, the torque margin for the mechanism had decreased from 1.33 to 0.17. There was a risk that with another step change in required current there would be an unrecoverable stall of the mechanism.

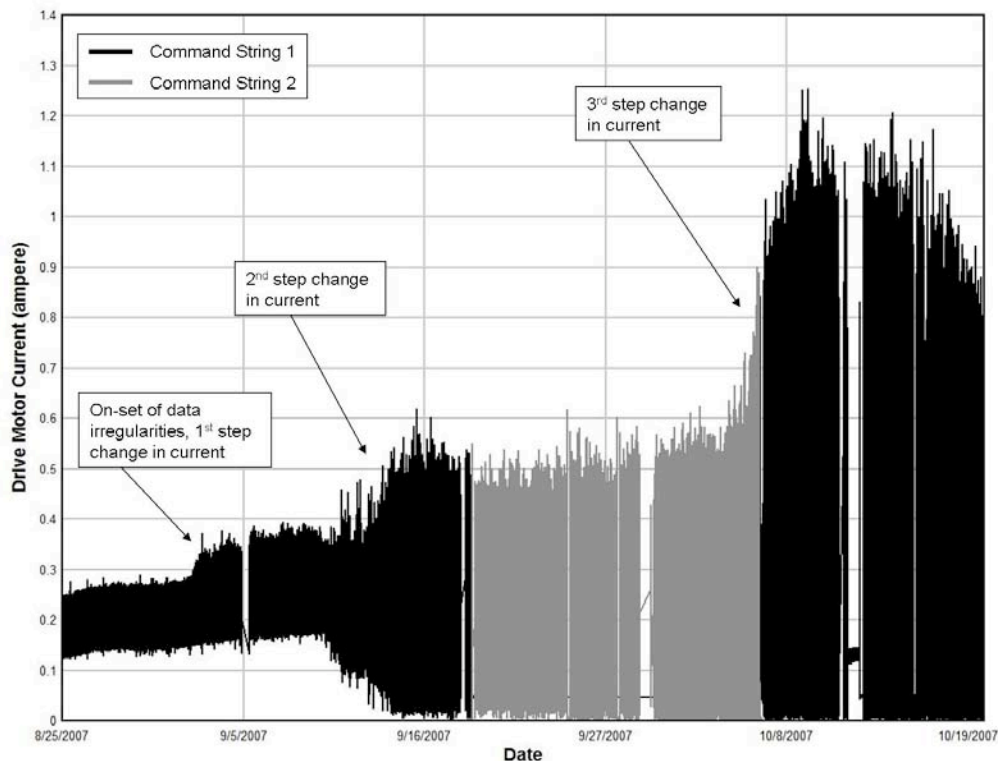


Figure 5. Starboard SARJ Drive Motor Current Changes during the Course of the Anomaly Investigation

In order to fully characterize the joint drag, an on-orbit test was executed. The objectives of the test were to take the controller software out of the loop and directly measure joint drag for all angular positions of the joint. The test objectives were accomplished by operating the mechanism in a mode of operations called “Torque as Stepper” (TAS), which does not utilize the controller loop. In TAS mode, the operator keys in a level of commanded current. The procedure for the test had the operators iteratively step up the amount of current requested until the mechanism began rotating. This was done in 30 degree increments so as to cover all angular positions of the joint. The TAS test confirmed conclusively that the controller was not contributing to the current spikes and that the high drag condition existed across the entire circumference of the joint, although some areas were worse than others. During the test, drag levels ranged between 2380 N·m (1760 ft·lbf) and 2860 N·m (2110 ft·lbf).

The anomaly investigation team was confident that increased joint drag was the source of the data anomalies, however, the source of the drag was unknown. An EVA task was planned on the upcoming Space Shuttle mission to investigate the nature and source of the suspected mechanical drag.

Extra Vehicular Activity and Mechanism Inspection

The goal of the EVA inspection was to look for a “smoking gun” that could have led to the off-nominal data trends. Specifically, the crew was asked to inspect the thermal covers shrouding the joint (Multi Layer Insulation, or MLI, covers) and the bolts that serve as the structural attachment between the MLI covers and the SARJ. This inspection would have revealed any evidence of a micro-meteoroid strike or of some interference between the MLI covers and the rotating half of the SARJ mechanism. Additionally, the crew was asked to inspect the launch restraint fittings to determine if there was any interference with the MLI covers. If time permitted, the crew was also asked to remove a MLI cover to inspect the bearing races and TBAs.

Nothing off nominal was noted during the external survey. The crew had sufficient time to remove a MLI cover for additional inspection. Upon removing the cover the astronaut immediately noticed that there were fine metal shavings across the outboard bearing race surface. Additionally the astronaut noted that the TBA roller housing was acting as a magnet and collecting metal shavings. Samples of the debris collecting around the TBA housing were gathered and returned to ground for analysis (results discussed below). A characteristic picture of the condition of the mechanism can be seen in Figure 6. The outboard race ring, and specifically the outer canted surface, appeared discolored and mottled and there was debris on much of the surrounding hardware.

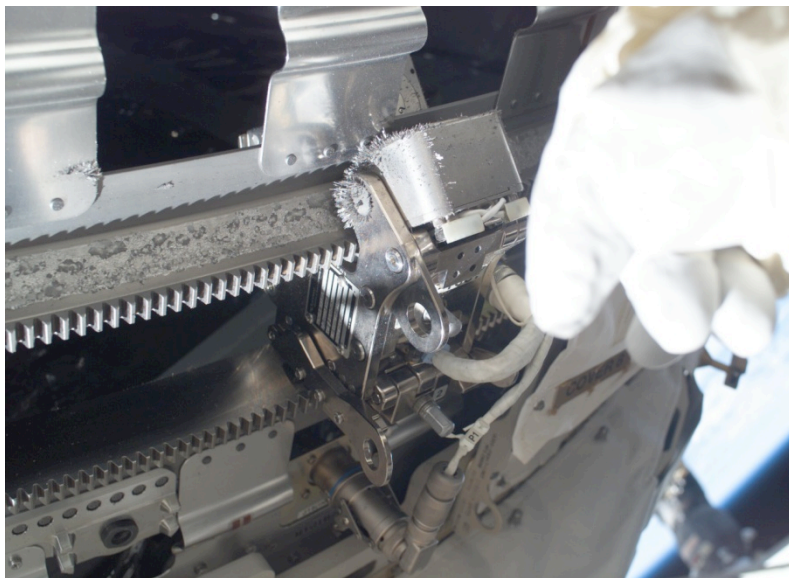


Figure 6. Astronaut Inspecting the Starboard SARJ During an Extra Vehicular Activity

The root cause of the damaged bearing race was not immediately known. It was clear, however, that the mechanism was mechanically damaged and operating in a significantly degraded condition. There was concern that continued operation could exacerbate the problem. Also, the vibrations caused by rotating the joint had become severe enough that accelerated hardware fatigue was a concern. The anomaly investigation team recommended that operation of the Starboard SARJ be halted immediately until the root cause of the anomaly was known.

After seeing the damage on the Starboard SARJ, engineers requested an inspection of the Port SARJ. It appeared to be operating as expected based on telemetry review. The inspection would provide a point of comparison to the Starboard SARJ as well as a baseline image of the mechanism. The Port SARJ

inspection was executed on the following EVA. The astronaut determined that the Port SARJ race rings looked pristine. The inspection confirmed that the damage was confined to the Starboard SARJ. Figure 7 shows a picture of the mechanism taken during the inspection. There is no apparent damage or debris accumulating around the bearing race surfaces or the TBA.



Figure 7. Astronaut Inspection of the Port SARJ During an Extra Vehicular Activity

Lessons Learned

The source of the anomalous data signature was determined less than eight weeks after its genesis. During this period of time the mechanism continued to operate and damage to the bearing race propagated around the entire circumference of the ring. It is possible that if the source of the anomaly had not been discovered, the damage would have progressed further (affecting one of the undamaged bearing surfaces). In hindsight, the anomaly investigation deserves further scrutiny to assess which diagnostic approaches were most effective, and whether any improvements could have been made to the anomaly investigation process or the health monitoring system.

The best data came from a hands-on visual inspection of the suspect mechanism. For many spaceflight mechanisms, this is not feasible, or comes at an extremely high cost. On-orbit testing also provided an effective means of exonerating specific components as well as characterizing the mechanism performance. A systemic review of all possible contributing factors and appropriate test strategies should be developed immediately after an anomaly is identified.

Additional instrumentation on the mechanism would have aided in diagnosing the anomaly. Strain gauges and accelerometers mounted directly to the TBAs would have been extremely useful. There are strain gauges on the SARJ system but none that measure local deflections at the bearing housings. The SARJ system is susceptible to high tractive forces (addressed in detail in the proceeding sections) which would have been picked up on locally mounted strain gauges. There are accelerometers on the ISS truss but these are not part of the SARJ monitoring and diagnostic system. Ground development testing indicated that the SARJ system was susceptible to debris generation. Accelerometers would provide an indication that debris in excess of expectations was present. A failure modes analysis should lead to the most effective instrumentation and monitoring criteria for a mechanism. Given the susceptibility to debris generation and sensitivity to tractive forces additional instrumentation would have been appropriate for the SARJ.

More consideration early on should have been given to halting operation of the mechanism until the anomalous data signature was better understood. Cessation of nominal operations was not seriously considered until just prior to the EVA inspection because the changes in operating conditions did not represent an immediate threat to successful operation. The system was still effectively tracking the sun with ample torque margin. Instead of focusing on overall system capabilities, it would have been more useful to focus on relative changes in the operational performance. For example, a change in drive motor current from 0.25 to 0.50 ampere represents a change of only 17% in terms of overall torque margin. However, it also reflects a 100% increase in joint drag. This jump in required current should have caused significant enough concern to stop operating the mechanism. Changes relative to previous operational data, or data from the rest of the hardware fleet, are more indicative of hardware issues than changes relative to overall system capability.

Anomaly Root Cause Investigation

A team was formed immediately after the EVA inspection of the Starboard SARJ revealed significant damage to the bearing surface. The team was made up of individuals from NASA Johnson Space Center (JSC), Kennedy Space Center (KSC), Marshall Space Flight Center (MSFC), Glenn Research Center (GRC), Goddard Space Flight Center (GSFC), NASA Engineering and Safety Center (NESAC), The Boeing Company, Lockheed Martin Space Systems Company (LMSSC), ATK, and Purdue University. The team's charge was to determine the root cause of the anomaly, determine a corrective action for the damaged mechanism, and determine appropriate recurrence controls for the undamaged (Port) SARJ.

The debris samples taken during the EVA inspections were analyzed in detail by Boeing Houston and NASA JSC and KSC materials and process teams [2]. The analysis yielded several key findings. First, the debris was primarily composed of the case material. Second, the debris thickness showed that the damage did not extend into the core material. And third, the morphology of the debris indicated that the damage was initiated via subsurface spalling. It was not immediately clear to the anomaly investigation team what conditions would generate sufficient stresses to cause the premature case spalling observed.

The anomaly team created a fault tree to aid in the search for the root cause of the damage and to focus in the areas that were critical for investigation. The focus areas were software, hardware, and operations. The fault tree yielded over 350 events that were studied individually. The fault tree events were closed by providing analysis, testing, simulation, or a combination of these. The closure process for the fault tree required that events be combined in a worst-case fashion. A review of fault tree events led to the identification of a set of critical variables for this anomaly. The critical variables were determined to be roller misalignment, lubrication selection and roller/race ring friction, bearing material properties, and applied loading. The team evaluated the interdependencies between the critical variables to determine the most probable root cause of the anomaly.

TBA Roller Misalignment

The TBA roller design causes a pushing action on the roller as the SARJ rotates. This design does not auto correct for roller misalignments as a castoring, or pulling, design would [3]. Misalignment is inherent to any design and manufacturing process. The trundle bearings used match drilled assembly procedures to minimize tolerance build-up and associated roller misalignment. Actual misalignment was not measured on individual units as part of hardware acceptance. After the anomaly had occurred, roller misalignments were measured at MSFC using a coordinate measuring machine as part of the root cause investigation [4]. The measurements showed that the trundle bearing misalignments were all within tolerances (± 1 degree). Nevertheless, coupled with high friction, the misalignments were large enough to generate detrimental thrust loads on the roller bearings.

Lubrication Selection and Roller/Race Ring Friction

Gold lubrication was the design choice to mitigate the frictional loads caused by these misalignments in both the TBA and DLA rollers. Test data obtained as part of the SARJ Anomaly (discussed in further detail below) show that a gold film on the trundle bearing rollers could maintain a coefficient of friction of

approximately 0.2 between the TBA rollers and race ring [5]. Nominally, a coefficient of friction of 0.2 ensures that the SARJ system maintains dynamic stability, which allows the race ring to react loads distributed along the full contact patch of the trundle bearing rollers. However, an instability arises when the ratio of thrust load to normal load rises above a critical value of 0.4. At this level of friction, an overturning moment caused by small misalignments in the roller, and subsequent thrust forces, cause the trundle bearing roller to tilt about its camber axis. The roller tilt causes a decrease in the roller race contact and an associated increase in stress at the contact. Test data determined that friction levels in excess of 0.4 are expected if no lubricant exists in the bearing contact, provided that sufficient roller misalignments are present [5].

Bearing Material Properties and Susceptibility to Spallation

The anomaly team postulated that increased friction between the roller/race interface could cause a stress field with the maximum shear stresses at the nitride case/15-5PH core interface. The team also determined that the solid film gold lubricant was not properly adhered to the rollers [6]. Without the gold

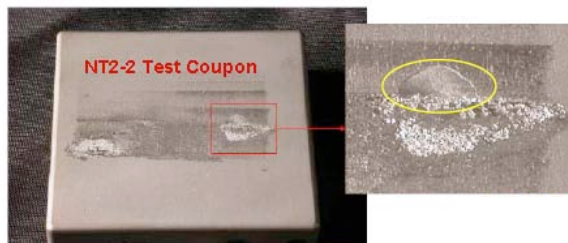


Figure 8. Trundle Test Rig Coupon Showing Fingernail Type Spalling [7]

lubricant in place, the system becomes susceptible to increased shear and normal stresses. The high shear stresses at the case/core interface could lead to subsurface initiated spalling of the case material. Multiple tests were performed over several months in an attempt to reproduce this failure mechanism. Tests performed at the LMSSC facilities in Sunnyvale on a Trundle Roller Rig were successful in recreating the spalling effect observed on-orbit [7]. The test rig loaded a 440C roller against a nitrided 15-5PH coupon. The roller was then rolled in a reciprocating

motion along the coupon's surface. Figure 8 above shows a test coupon from the rig. The inset in the figure shows an example of a "fingernail" type spall. Spalls of this type were also noted in on-orbit inspection photos.

Applied Loading

The Trundle Test Rig confirmed that subsurface spalling could be induced in the SARJ bearing materials given sufficiently high stress conditions. Additional work was required to validate that the TBA roller kinematics were capable of generating the high stresses required given the expected loading conditions.

A dynamic simulation was developed to perform analysis of the SARJ trundle bearings. The purpose of this simulation was to quantify the loads between each of the trundle bearing rollers and the race ring. The simulation included the race ring deformation caused by the thermal environment, the stiffness of the trundle bearing itself, and the stiffness of the inboard and outboard trusses of the ISS. It also included the structural flexibility of the ISS trusses. The simulations were used to perform parametric studies in support of the closure of the SARJ Fault Tree events. The simulation used traction data obtained from NASA GRC testing for the contact between the race ring and the TBA rollers both with and without gold coating. The simulation was used to estimate the loads at the roller to race ring interface and to illustrate the kinematic behavior of the TBA rollers. The development and results of this simulation are discussed below

Analysis of Roller Edge Loading

The effect of small angular misalignments on rolling traction forces has been studied by a number of investigators, as summarized by K.L. Johnson in [8]. Solutions to the governing equations of rolling have been developed in closed form for a few geometries, and powerful numerical methods have been developed to address the problem for more general application. These methods are important for the present investigation because the angular misalignment of the trundle bearing rollers can lead to dramatic changes in the loads and stresses on the race ring surfaces.

The mistrack or “toe” angle of a TBA roller is the misalignment of the roller due to rotation about an axis normal to the race ring surface. The existence of some small mistracking angle is inherent in the hardware build process. The metrology laboratory at MSFC performed detailed measurements of the mistrack angle of the Starboard SARJ TBA rollers after they had been returned from orbit. Mistracking between the roller and race creates a friction force on the roller in the thrust direction, denoted Q in Figure 9. This yields a moment about the camber axis, which is reacted by the normal load between the roller and race. As the magnitude of the thrust friction increases, the load distribution on the roller becomes unevenly distributed to react the induced moment. The distance d in Figure 9 denotes the lateral distance from the camber axis to the center of normal pressure of the contact. In stable tilting, the distance d increases with increasing camber tilt, offsetting the camber moment generated by an increasing thrust friction Q . However, after a certain camber angle threshold is reached, d begins to decrease with increasing camber angle, causing the roller to enter into unstable tilting. The analysis and inspection of the Starboard SARJ TBAs shows that the outer canted rollers remained in the regime of stable tilting during the time when the race ring was being damaged.

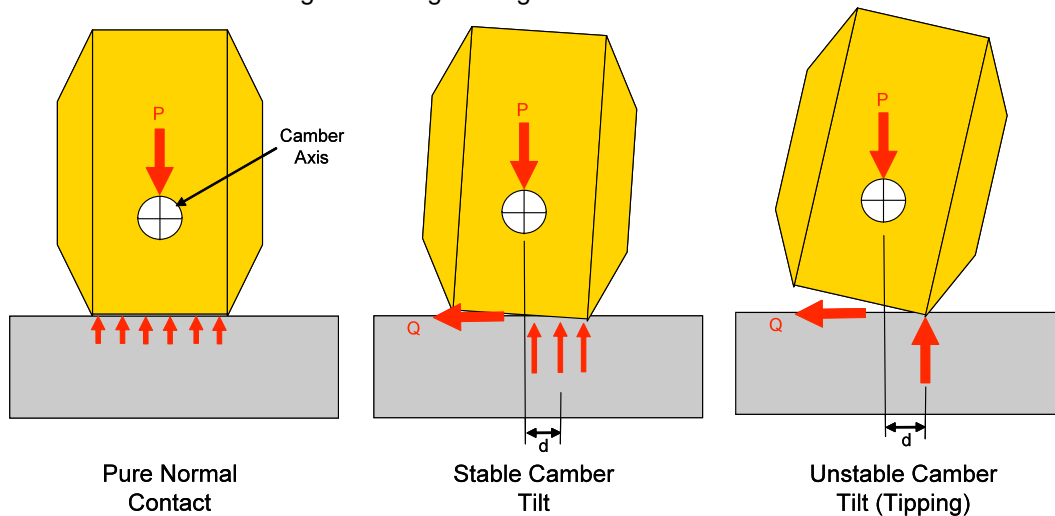


Figure 9. Trundle Bearing Roller Stability

In order to investigate the effect of roller mistracking on the contact forces, a numerical boundary element analysis tool was developed by researchers at Purdue University and Boeing. This tool was rigorously validated against closed form solutions and also shows excellent agreement with the traction results obtained through testing at Glenn Research Center (GRC) [5]. GRC was able to quantify the friction-mistracking relationship in a Vacuum Roller Rig (VRR). The VRR replicates the flight-like rolling interface and materials in a vacuum environment. A comparison between traction curves developed by test at GRC and via analysis is shown in Figure 10. One will note that the analytical results closely match the test data. It is also worth noting that the VRR rollers do not have identical degrees of freedom to the TBA rollers and therefore the TBA rollers must be addressed by a modified thrust curve (discussed below, see Figure 13).

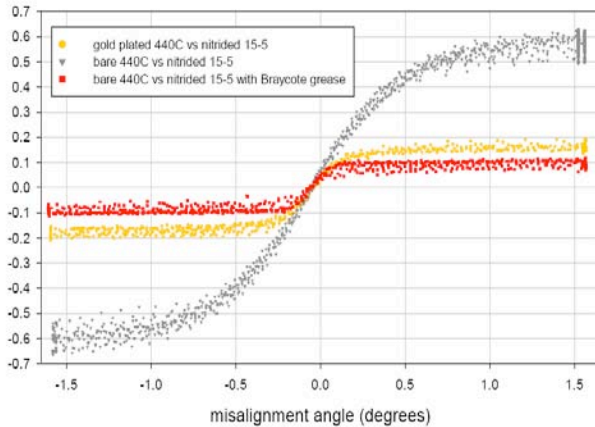


Figure 10. Comparison of Thrust Curves from Analytical Results and VRR Test Data [5]

Figure 11 shows the transverse shear traction distribution on the GRC test rollers for a representative misalignment case. The plot on the left shows that the contact area is divided into regions of stick and slip. The stick region, shown in green, is located at the leading edge of the contact. As the unstressed material of the test rollers enters into the contact patch, the shear deflections and tractions between the two rollers build until the shear tractions reach the limiting value of friction defined by the coefficient of sliding friction, μ , times the normal pressure. As material moves through the trailing end of the contact, slipping occurs between contacting points on the rollers, and the shear tractions remain at the limiting value of friction.

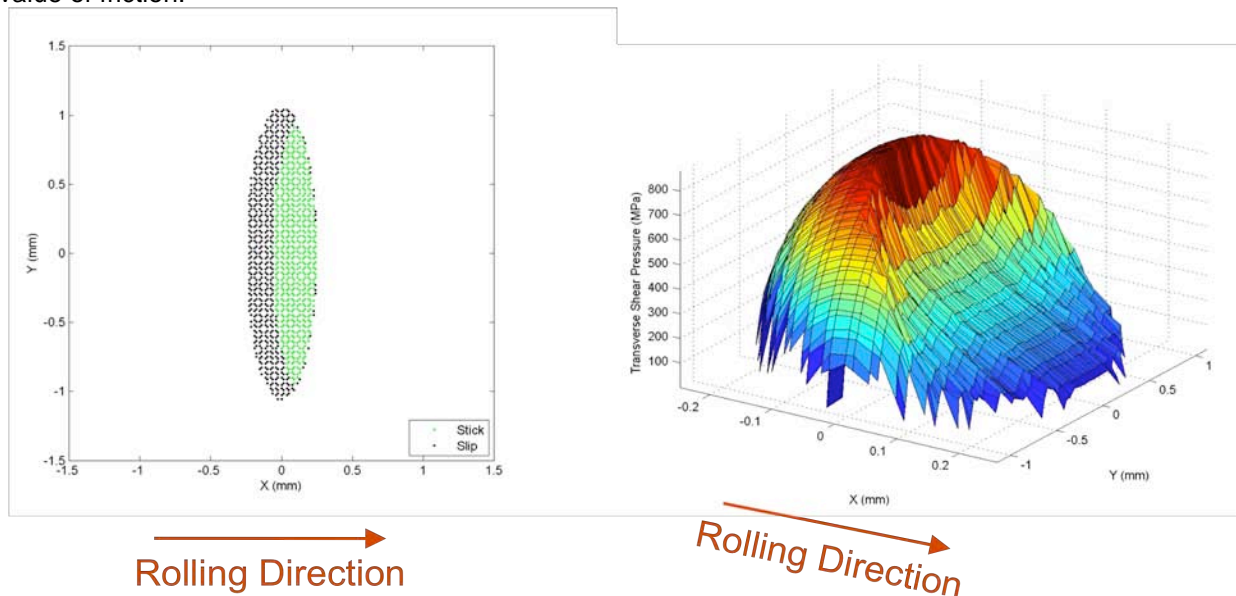


Figure 11. Shear Traction Distribution for GRC Test Rollers, $Q/P = 0.4$

For increasing mistrack angles, the stick region gradually decreases in size until the total thrust load equals μ times the normal load, at which point the entire contact region is in slip. For small mistrack angles such as those observed on the Starboard SARJ TBAs, the rollers remain in partial sliding, and the total frictional force is less than the limiting value of sliding friction.

The tractive phenomena in the flight TBA rollers are analogous to those in the GRC test rollers, with the exception that the TBA rollers have an additional camber degree of freedom. The flight TBA rollers also have a flat profile that transitions to a 1.5-mm (0.060-in) blend radius at the edges of the contact. As a

result, the size and shape of the contact patch for a TBA roller vary dramatically depending on the thrust loading and camber angle of the roller. The contact patch dimensions are plotted in the left portion of Figure 12 for increasing values of thrust load. This plot shows that as the TBA roller tilts on edge due to the thrust loads, the area in contact with the race ring is reduced. The right portion of Figure 12 shows that the average normal contact pressure increases dramatically as a result of the reduced contact area.

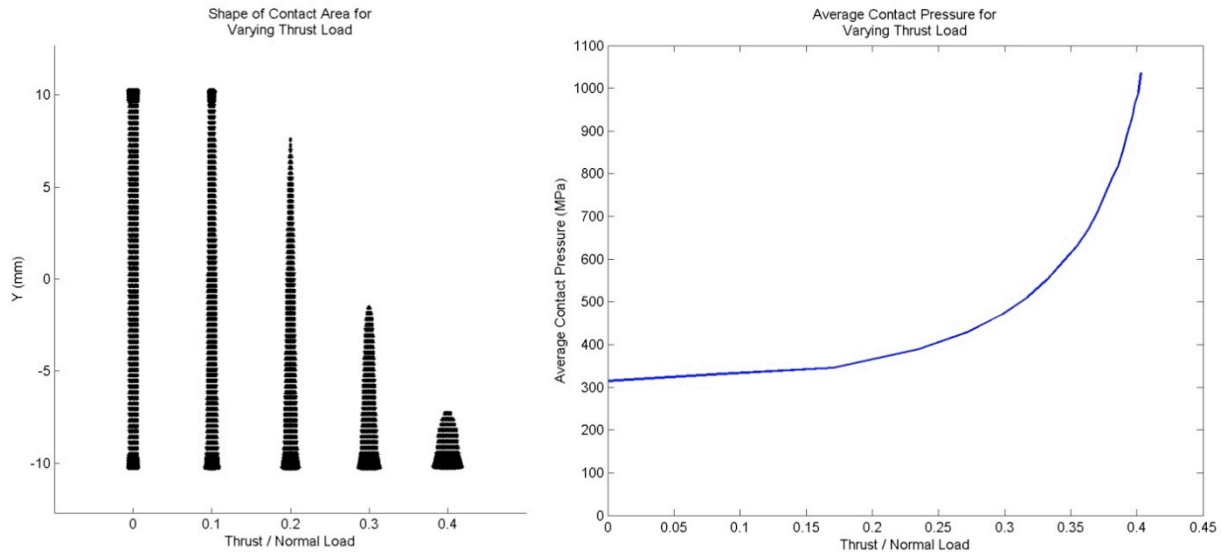


Figure 12. Contact Patch Dimensions and Average Contact Pressure for TBA Roller

In the study of rolling contact mechanics, the relationship between the transverse rolling creep (related to the mistrack angle) and the traction ratio Q/P is known as the traction curve. The analysis of the SARJ TBA rollers found that the shape of the contact patch caused by cambering has an influence on the traction curve for the roller. This effect is such that as a TBA roller begins to tip about its camber axis, the frictional loads are less severe than they would otherwise be, thereby mitigating the tipping phenomenon. The blue dotted line in Figure 13 shows the traction curve for the flight TBA roller if the camber axis were fixed at 0° . The red dotted line shows the traction curve if the camber axis were fixed at 2° . In the actual TBA, where the camber axis is free to rotate, the traction curve follows the 0° fixed camber curve for small mistrack angles. However, for larger mistrack angles the changing geometry of the contact patch causes the thrust friction loads to be less severe than in the fixed camber case, as shown by the solid black line in the figure. Despite this phenomenon, thrust loads as high as 0.4 times the normal load can be generated with mistrack angles less than 0.5° .

Detailed measurements and tolerance analysis of the Starboard SARJ TBAs identified an approximate worst case mistrack angle of 0.36° . The normal and shear pressure distributions at the contact are shown in Figure 14 for that mistrack case. As a result of camber tilting, only about one quarter of the width of the roller is in contact with the race ring surface. The resulting stresses at the interface between the race ring case material and the parent material were found to exceed the yield strength of the parent material.

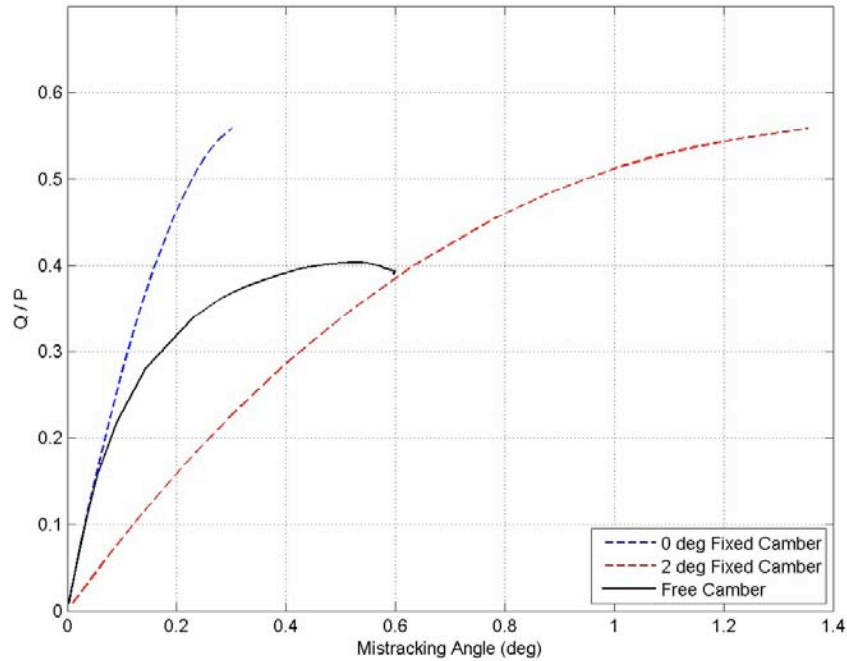
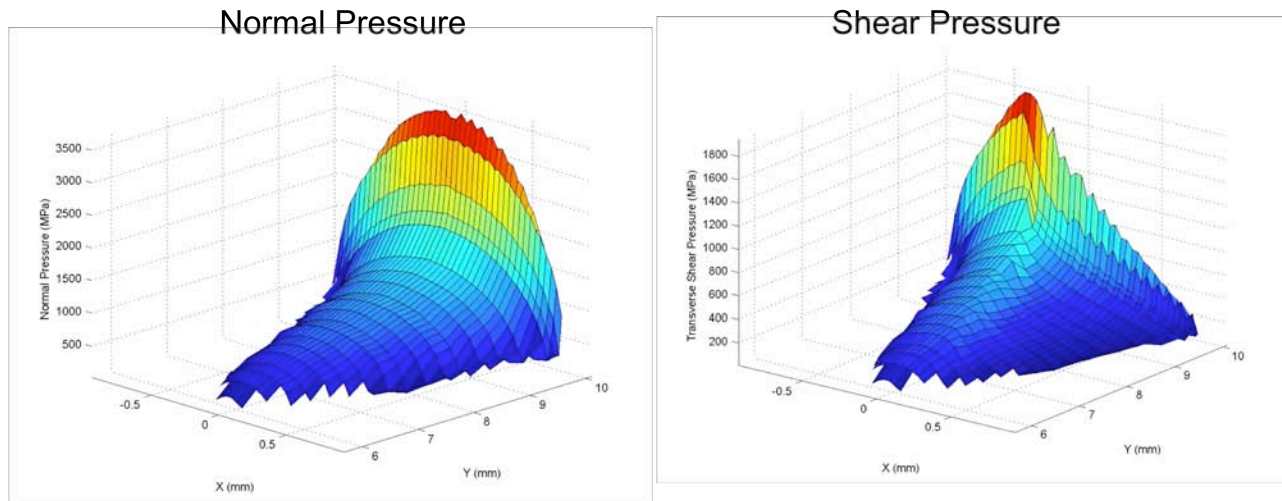


Figure 13. Traction Curves for Outer Canted TBA Roller



Max Normal Pressure: 3.67 GPa
 Total Normal Load: 3.66 kN

Max Shear Pressure: 2.83 GPa
 Total Shear Load: 1.41 kN

Figure 14. Distribution of Normal and Shear Pressure for 0.36° Mistracking, TBA Outer Canted Roller

In addition to concentrating the contact pressures at the roller edges, frictional thrust loads due to mistracking also have the effect of increasing or decreasing the normal loads on adjacent rollers. Depending on the specific combination of roller mistrack angles and the direction of SARJ rotation, it is possible for the race ring's triangular cross-section to be wedged in between two of the TBA rollers. This wedging action is analogous to a positive feedback loop. Frictional loads on the Datum A and outer canted rollers lead to increased normal loads on those rollers, which in turn allow the contacts to generate

higher frictional loads. Photographs of the damaged race ring surface taken by the on-orbit crew support the hypothesis that the initiation of damage occurred under these wedging conditions.

Contact Stress for Flat and Crowned TBA Rollers

The root cause team further found that the bearing edge stresses were exacerbated by the flat, uncrowned profile of the TBA rollers. The roller geometry made the system sensitive to non-Hertzian effects, which gave rise to high pressure points at the edges of the rollers during the initial run-in period of the mechanism. These high pressure points are visible in the contact stress profile of the TBA rollers shown in the left side of Figure 15. Part of the recurrence control plan for the SARJ is to modify the rollers on any spare TBAs to include logarithmically crowned rollers. The logarithmic roller profile is a shape that has been mathematically optimized to eliminate the high pressure points that ordinarily occur at the edges of cylindrical roller bearings.

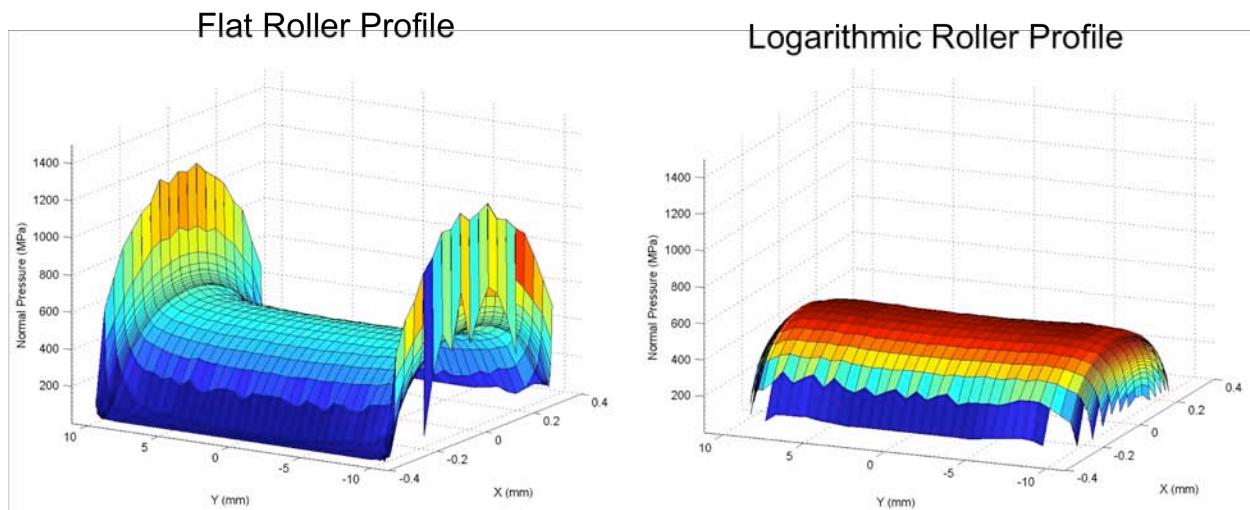


Figure 15. Normal Contact Stress Distribution for TBA Roller, P = 4.36 kN (980 lb)

Root Cause Investigation Conclusions

On-orbit video photographic, visual evidence, and debris samples analyses indicate that the SARJ race ring nitrided layer spalled from the base 15-5 PH steel. The spalling occurred over a period of two and one half months after the Starboard SARJ on-orbit activation. The first signs that the spalling was taking place were manifested through telemetry data that indicated the average operating current of the SARJ was rising from nominal values of 0.15 amp to as high as 0.8 amp.

During this time, the Structural Dynamic Measurement Data System of the ISS was indicating vibrations that were anomalous. These vibrations were later confirmed to be linked to the degrading condition of the SARJ race ring surface. As the race ring surface became progressively rougher over time as a result of the spalling, the vibrations the ISS was sustaining while the Starboard SARJ was rotating were a concern to the structural life of the Space Station. These vibrations were inducing load cycles on ISS hardware that were high enough to be counted in the nominal ISS loads spectrum for structural fatigue.

Testing and analysis indicate that the SARJ race ring surface damage was caused by tractive forces (normal and shear) applied to the race ring surface by the TBA and DLA rollers. Severe loading cases are observed with mistracking angles smaller than the as-measured TBA mistracking angles. Mistracking loads are sensitive to roller edge loading, multiple roller mistracking, direction of mistracking and race ring rotation direction. Analysis indicates that worst loads occur on the gear side of outer canted surface and Datum A surface.

Testing shows that gold, as a solid lubricant, is capable of maintaining a low coefficient of friction (0.2) for mistracking angles higher than the maximum conservatively predicted angle for the TBAs [4,5]. Testing reproduced several visible features of the on-orbit damage [7]. Testing also shows loss of gold adhesion [6]. Using the same roller material as the SARJ TBA, the ion-sputtering process used for the starboard SARJ rollers was re-created and the gold finish was tested. The tests exonerated the gold plating process. However, aging humidity tests indicated that, in time, the gold film would delaminate from the parent material due to corrosive growth on the substrate.

Metallographic analysis was performed to compare the imperfections between the race rings used for the starboard SARJ and the port SARJ. The data indicate that the defect concentrations in the starboard ring nitrided case are approximately six times that of the port nitrided case. The difference in the nitride case defect concentrations makes the starboard SARJ race ring more susceptible to damage initiation and damage propagation caused by high loading. It also may explain the survivability performance of the port SARJ race rings [10].

Anomaly Most Probably Root Cause

The kinematics of the TBA and DLA mechanisms require that the roller thrust loads (related to friction coefficient and mistracking angle) be controlled to ensure stable roller line contact with the race ring surfaces. Inadequate lubrication of the roller/race ring interface combined with roller mistracking angles within specification resulted in thrust loads high enough to cause at least some of the TBA or DLA rollers to edge load as the SARJ rotated. When a roller is edge loaded, the preload on that roller is concentrated on a reduced contact area resulting in high contact stresses and shear stresses in the race ring case and core. These stresses exceed the allowable bearing strength capability of the race ring case and core leading to brittle fracture and spalling of the nitrided layer from the starboard SARJ race ring.

Lessons Learned

As part of the root cause investigation, the build paper was reviewed. Unlike the Port SARJ which was tested in vacuum, the Starboard SARJ was not due to cost considerations. A complex mechanism such as the SARJ cannot be analyzed for break-in performance. Instrumented vacuum testing, particularly for the break-in period, might have yielded indications that the as-built mechanism was not operating nominally. Since the degradation of the Starboard SARJ took place over a short period, during accelerated testing the current increase would have been evident in a very short period of time.

The build-paper investigation also indicates that the testing decisions made for the Starboard SARJ did not accurately account for the friction differences between an ambient and vacuum test environment. The root cause investigation highlighted the sensitivity of the SARJ to small changes in friction. The SARJ Structural Test Article was tested at ambient to verify drive pinion life. The test was not intended to verify system life. However, since the entire system was utilized during the test, successful completion of the test gave a false sense of security regarding system-level life. Recent testing indicates that the vacuum coefficient of friction between 15-5 PH nitrided steel and 440C steel roller is approximately 0.6 [5]. It is now understood that operating the SARJ with coefficients of friction greater than 0.3 increases the risk of roller tilting and resulting damage to the race ring surface.

The root cause investigation also highlighted the importance of correlating testing with analysis and dynamic simulations. Cost-effective and cost-saving simulations can aid the mechanism designer in the understanding of the mechanism performance prior to its fielding. Moreover, mechanism testing should have as a stated objective the correlation of the critical variables of the mechanisms performance. This process can increase the chances of finding phenomena that may be time consuming to test without prior knowledge. The lesson learned here is two-fold and inextricable. A complex mechanism should not be flown into space without testing, nor should it be flown only having been tested. Analysis must be integral to the testing but should not be used in lieu of testing. There are many conditions for mechanism failure that could be understood in a reasonable and cost-effective basis only by analysis.

The damage sustained by the starboard SARJ highlights the importance of sound design and verification practices in the development of complex rotating space machinery. The non-Hertzian contact mechanics of the roller bearing to race ring interface proved to be a crucial detail of the system. Special attention should be given to such effects in the design of bearing systems. The SARJ exhibited high vulnerability to damage during the initial run-in phase of the mechanism's life. The risks incurred during this period can be mitigated through the use of adequate lubrication, crowned rollers, detailed screening of the nitriding process, the implementation of a pre-flight run-in period, and a thorough understanding of the differences between ambient and vacuum performance. The addition of these elements to the design, verification and operational plans for the SARJ forms the basis for the continued successful use of the mechanism in flight.

On-Orbit Implementation of a Corrective Action

Operations of the Starboard SARJ were severely restricted as soon as the damage was observed. The reduction in operation protected the ISS structure against the vibrations caused by SARJ rotations and against a stall of the mechanism. If the SARJ were to experience an unrecoverable stall, the operational impacts to the ISS would be significant enough to affect future missions and utilization of the station. These potential operational impacts to the ISS warranted corrective action.

The SARJ recovery team concluded that it was a reasonable action to remove debris, to the extent possible, from the damaged race ring and to add grease lubricant to all three bearing surfaces of the race ring. Debris removal was intended to decrease drive motor currents and improve torque margin. The intent of the lubricant was to improve the lubricity between the roller/race interface in order to maintain a coefficient of friction below the critical roller tipping value; the improved lubricity, in turn, would protect the remaining undamaged surface from experiencing degradation. Braycote 602EF[®] was chosen because the base oil has the lowest vapor pressure of all available space greases. It also has molybdenum disulfide which is an excellent lubricant for sliding and capable of handling high loads.

Procedure Development

A preliminary cleaning and lubrication method was developed with inputs from the EVA tools and crew training teams. This method was successfully executed on a small section of race ring during an on-orbit test on the ISS 1J mission. Armed with the lessons learned from the cleaning trials, the team decided to clean and lubricate the entire damaged race ring during the STS-126/ULF2 mission. The team also decided to remove and replace all of the TBAs during ULF2. A significant amount of debris had accumulated on the TBAs, so their replacement would result in additional removal of debris from the joint. This also allowed for the return the original TBAs for inspection to assist in the root cause investigation.

The cleaning and lubrication trials showed that the best method to clean the SARJ was to wet the surface with an EVA wipe pre-lubricated with Braycote 602EF[®] and then scrape the surface with a scraper tool. Lubricating the surface prior to scraping proved to be the best method to contain the loose debris particles and prevent them from being liberated and dispersed throughout the rest of the mechanism while scraping. The final application of lubricant to the surfaces after cleaning was done using a grease gun. The inner race ring surface is not visible to the crew so a unique lubrication tool, called the J-Hook nozzle, was developed by the JSC EVA tool team to allow the crew to lubricate that surface. Photos of the tools used are shown in Figure 16.

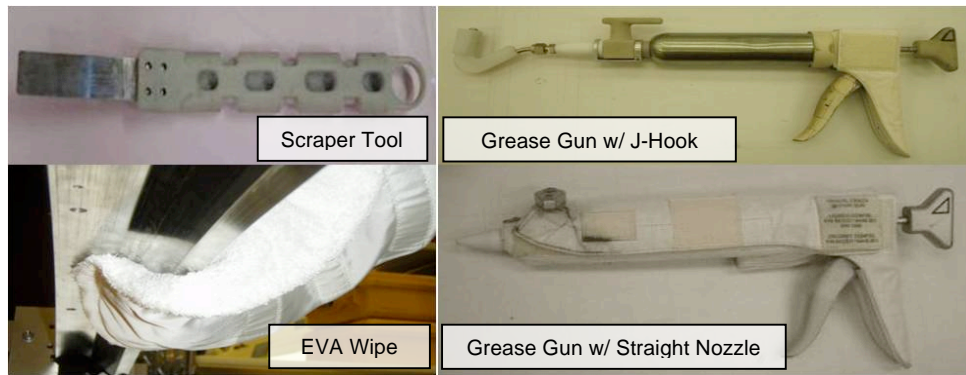


Figure 16. Tools used in SARJ Clean and Lube Operations

While the cleaning methods were developed based upon the on orbit trials, the method to lubricate the cleaned race ring was developed on the ground. A 60-degree section of race ring was used to determine the pattern and quantity of grease to be applied. Based on testing and crew input, it was decided that the best way to apply lubrication to the race ring was to place a single bead of grease down the middle of the roller track. The outer 45 and datum -A- surfaces were lubricated in this manner. The inner 45 race surface was lubricated using the J-Hook nozzle. The J-Hook was designed so the grease would be smeared along the width of the race ring surface and would encompass the roller track of the TBA and DLA rollers. The final grease configuration required residual grease dams on either side of the roller track after the TBA roller had passed over and spread the grease. These repositories of grease on the sides of the track serve as a source of oil that will constantly re-wet the roller track and provide lubrication during subsequent SARJ operations.

Lab tests were also run where grease was added to a race ring surface contaminated with metallic particles similar to the debris retrieved from the SARJ on orbit. These tests showed that the hydrodynamic force generated by the roller passing over the grease was enough to push a majority of the debris out of the roller track. As a result, the addition of lubricant to the damaged race ring serves a dual purpose as a cleaning fluid for any debris left on the SARJ after the cleaning operation. The clean and lubrication operations were successfully completed during ULF2. Figure 17 shows the final application method and grease configuration.

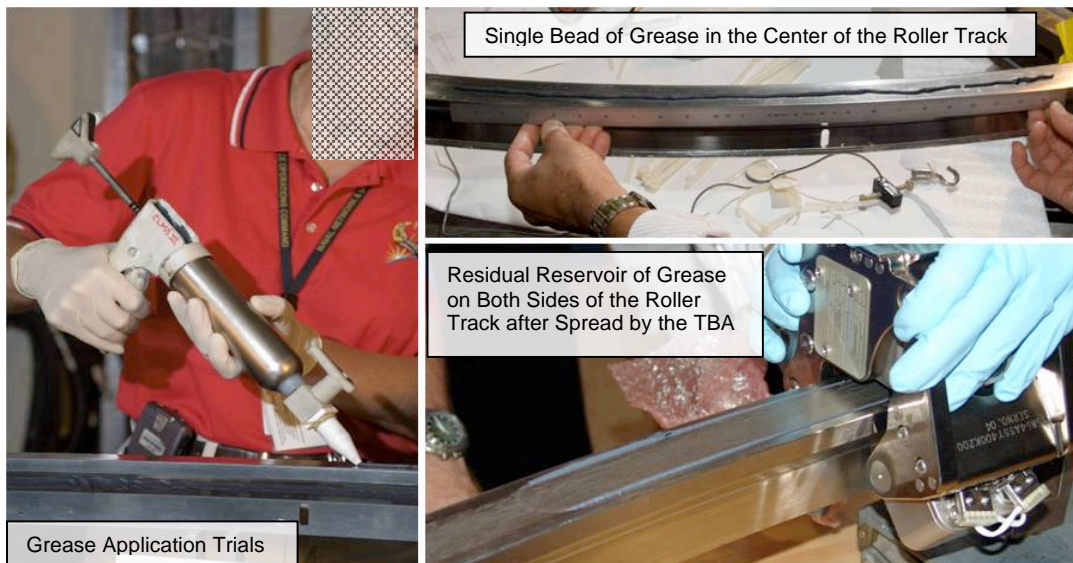


Figure 17. Final Grease Application Methods

Results of Corrective Action

Following the successful cleaning and lubrication of the starboard SARJ, the joint was rotated and the motor drive current was monitored. The motor current decreased immediately from a pre-cleaning and lubrication average of 0.242 ampere to 0.174 ampere. The more critical benefit was the significant reduction in the maximum current levels. The large swing in motor drive current observed prior to the clean and lube operations was mitigated significantly, resulting in a reduction in the maximum current from 0.870 ampere to 0.384 ampere. These results demonstrate that the clean and lube operations were successful in increasing the stall margin in the SARJ which, in turn, maintains operational flexibility of the ISS. These post lube data also compare well with the performance of the starboard SARJ telemetry prior to the anomaly when the SARJ had an average motor current of 0.153 ampere and a maximum of 0.221 ampere. Data plots showing the motor current prior to the clean and lube operations (data taken during the 10A mission), during ULF2 just after the clean and lube operations, and data taken during ULF2 stage operations are shown in Figure 18.

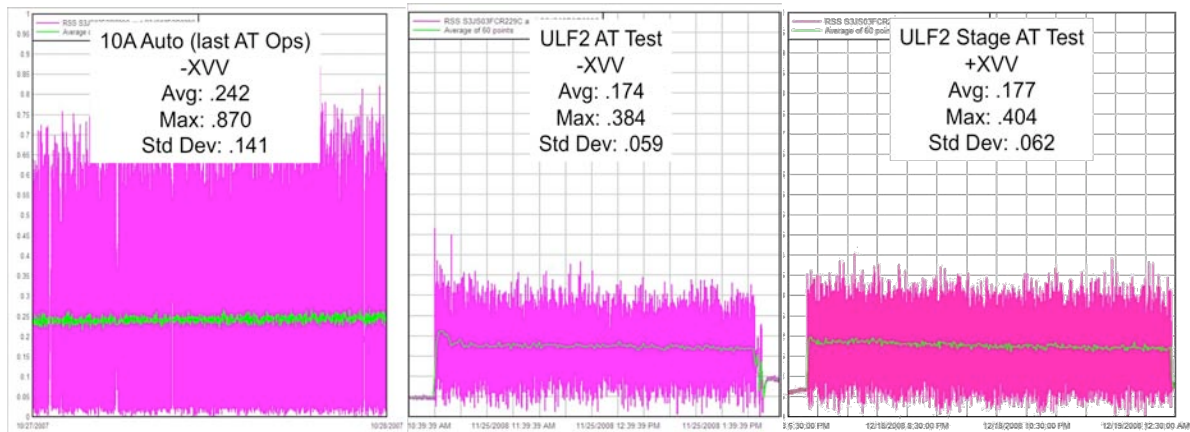


Figure 18. Starboard SARJ Motor Drive Current Comparison Pre and Post Clean & Lubrication

The port SARJ was also lubricated with Braycote 602EF[®] during Flight ULF2 using the same procedures and tools as were developed for the starboard SARJ. The lubricant was intended to protect the mechanism against damage by the same mechanism as was experienced by the starboard SARJ. Pre and post lubrication data for the port SARJ shows a 20% decrease in average drive motor current, shown in Figure 19. This drop is significant as it indicates that the mechanism pre lubrication was operating in a regime of higher roller/race friction than post lubrication and was therefore more susceptible to damage initiation prior to the application of the grease lubricant.

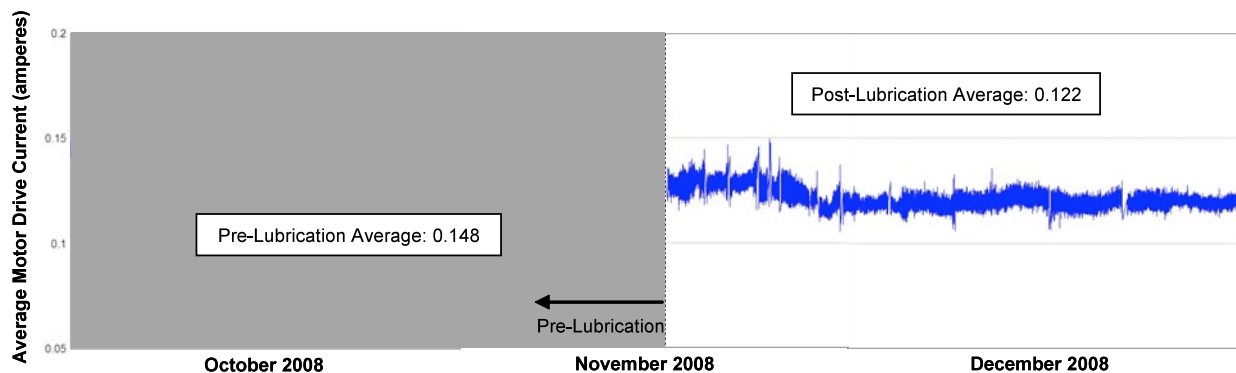


Figure 19. Port SARJ Average Motor Drive Current Comparison Pre and Post Clean & Lubrication

As noted earlier, anomalous structural vibrations were one of the first hints of a problem with the SARJ. The surface of the race ring had degraded significantly and it was not anticipated that the clean and

lubrication tasks would have a significant impact on the vibrations observed on ISS. The accelerometer data after ULF2 showed that the peak accelerations had been reduced significantly. Data plots showing pre and post ULF2 accelerometer data are displayed in Figure 20 and show the dramatic decrease in vibrations to the ISS due to SARJ rotation.

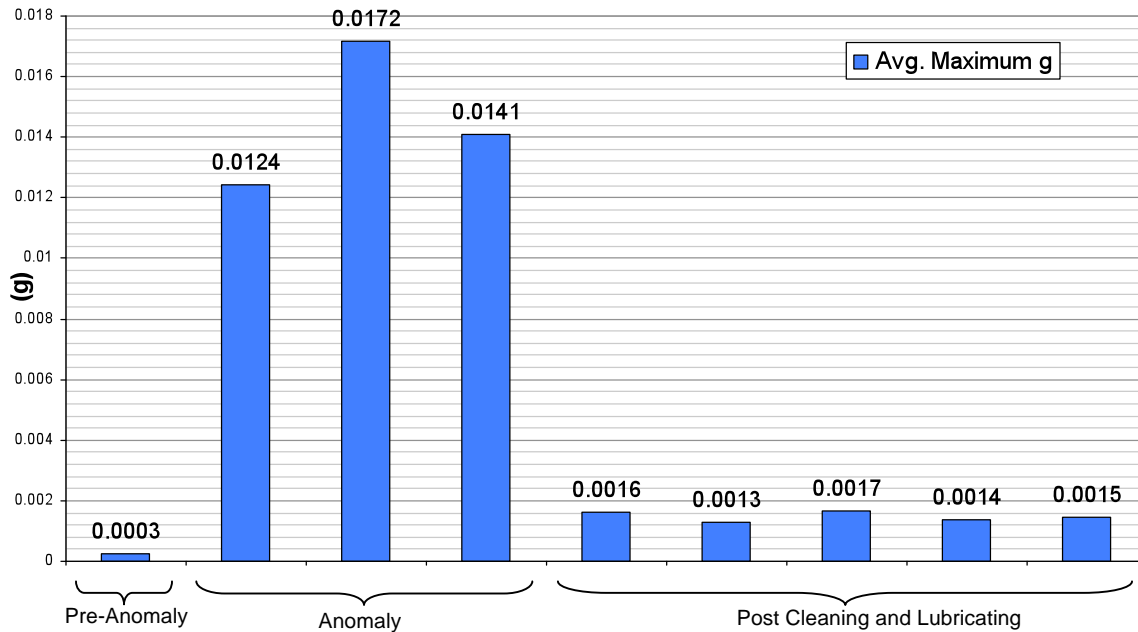


Figure 20. ISS Acceleration Data Pre and Post ULF2 [g]

Lessons Learned

The dramatically improved performance of the SARJ mechanism due to the cleaning and addition of grease to a damaged and contaminated race ring is an important finding for space systems mechanism design. Most directly, these observations can be applied to the design of mechanisms that will, by nature of their intended use, be exposed to high levels of contamination (e.g., mechanisms on lunar or Martian based systems). It is recommended that designers consider adding the capability of re-lubrication and/or cleaning of bearing systems, especially those which be exposed to high debris filled environments.

Conclusions

Anomalous performance of the Starboard SARJ was noted shortly after the mechanism was activated on-orbit. An inspection found that there was debris covering the bearing race of the rotating mechanism. An anomaly team was immediately formed to investigate the issue. Through a series of tests, analysis, and simulations the team determined that the most likely cause of the damage was high friction at the bearing/race ring contact coupled with a susceptibility of the bearing mechanism to an overturning moment on the bearing rollers. Dynamic analysis simulating the contact conditions of the SARJ mechanism, both lubricated and un-lubricated, confirmed that in the un-lubricated condition sufficient stresses occur to damage the race ring. Grease lubricant was applied to the mechanism in order to mitigate the existing damage as well as prevent further damage. Additionally, astronauts removed the debris noted during previous inspections. These actions proved effective as overall joint drag significantly decreased as did structural vibrations caused by operating the mechanism.

The SARJ anomaly investigation and recovery provides several lessons learned both in the arena of diagnosing on-orbit anomalies and in complex aerospace mechanism design and verification. Mechanism design should incorporate proven and verifiable features whenever possible. Features that do not lend

themselves readily to analysis cannot easily undergo the rigorous verification process that aerospace mechanisms demand; for example the TBA roller profile gives rise to non-Hertzian contact effects, which requires advanced analytical methodology in order to recover the stresses. The acceptance program for complex mechanisms should include a run-in period during which the mechanism is operated in the flight environment. This run-in period should be used to correlate analytical models of the mechanism as well as provide a baseline of expected performance for the mechanism while on-orbit. Test correlated and verified models can be used to determine system level sensitivities and potential design problems. Additionally, understanding the sensitivities of the system will allow for the most effective use of instrumentation and monitoring techniques of the mechanism while on orbit. A baseline performance characterization provides ground operators an effective means for gauging the severity of changes in performance after activation. Finally, mechanisms that operate in an environment susceptible to debris contamination should consider inclusion of re-lubrication and cleaning capabilities. These lessons should be utilized by architects of future aerospace mechanisms to yield more robust systems.

References

1. Leger, L. J. & Dufrane, K. (1987). "Space Station Lubrication Considerations." *21st Aerospace Mechanisms Symposium Proceedings*. NASA-CP-2470.
2. Wright, M. C., Salazar, T., Kim, H., Tucker, B., Lubas, D., Marciniak, P., McDanel, S. (2008, February). "International Space Station (ISS) Starboard Solar Alpha Rotary Joint (SARJ) Expedition 16 EVA 13 and 14 Debris Analysis." KSC Engineering Directorate, Materials Science Division.
3. Favero, J., Frazier, B., Nielsen, P. (1998, October). "SARJ Dynamic Simulation Analysis and Results." The Boeing Company. A03-J092-PN-M-9801474.
4. Moore, L.E. "DRAFT SARJ Anomaly Report for Review – STATUS." Message to Carlos Enriquez. 13 July 2009. E-mail attachment.
5. Krantz, T., DellaCorte, C., Dube, M. (2010). Experimental Investigation of Forces Produced by Misaligned Rollers. *40th Aerospace Mechanisms Symposium Proceedings*. **Manuscript in preparation.**
6. Enriquez, C.F. (2009, September). *International Space Station Solar Alpha Rotary Joint Anomaly Report*. The Boeing Company, International Space Station Program. D684-13412-01.
7. Loewenthal, Stu, Scotty Allen, and John Golden. "Solar Alpha Rotary Joint Anomaly Test Findings: Mechanism Perspective." *Aging Aircraft 2009*. (2009): Print.
8. Johnson, K.L. (2003). *Contact Mechanics*. Cambridge, United Kingdom: Cambridge University Press.
9. Laible, M. (2009). "SSARJ Autotrack Test 5 Results." The Boeing Company, Houston, Loads and Dynamics.
10. Martinez, J.E. "SARJ DIGS % Area Calculations." Message to Dr. John Goldon. 01 December 2009. Email attachment.

Test Validation of the Repair to the Space Station Solar Alpha Rotary Joint

Curtis Allmon*, Will Wilkinson* and Stu Loewenthal*

Abstract

The Solar Array Alpha Joint Lubrication Interval Test (SARJ LITE) test rig was built as a method to evaluate the performance of the grease repair on the Starboard SARJ of the International Space Station (ISS). The on-orbit SARJ was temporarily parked after receiving significant damage on one of its race ring surfaces as a result of inadequate lubrication (high dry contact friction) and unaccounted for roller traction kinematics. In a scaled down rig, flight-like roller bearings were preloaded and cycled on a nitrided 15-5 race surface. Grease was added to the track and with instrumentation monitoring performance, trending data will be extracted and used to determine lubrication intervals for both Port and Starboard ISS SARJ's. The grease lubrication was found to be effective in eliminating the high friction that contributed to the on-orbit race damage.

Introduction

The ISS is powered by eight solar arrays that track the sun for optimum power generation. Each Solar Array is mounted to a Beta Joint that provides a degree of rotational freedom and, further inboard, a cluster of four arrays is mounted to SARJ, one starboard and one portside, providing an additional degree of rotational freedom (see Figure 1). The Alpha and Beta joints by design provide continual year round tracking of the sun. This paper covers the ground testing used to determine lubrication intervals for the Space Station SARJ's. Included is an overview of the SARJ, a description of the on-orbit anomaly that led to the greasing of the SARJ, a thorough description of the test rig used to determine the intervals for relubrication, and a summary of the performance to date, and the plan forward.

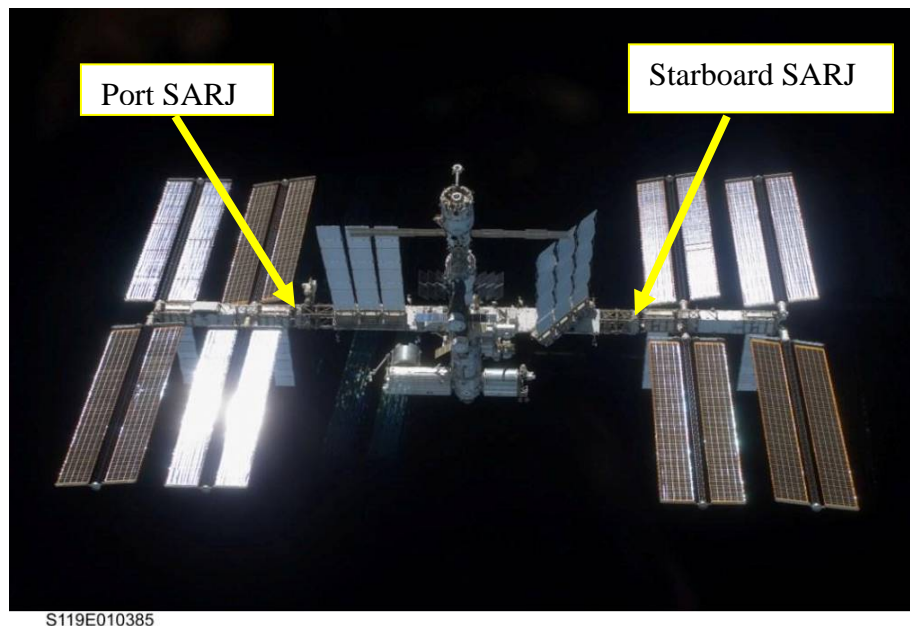


Figure 1: Space Station on-orbit

* Lockheed Martin Space Systems Company, Sunnyvale, CA

Background

The Space Station utilizes two SARJ's, a Port and a Starboard, whose primary purpose is to rotate the outer most truss segments and allow the solar arrays to track the sun. Sun tracking is achieved through rotation of two orthogonal joints, the Alpha and the Beta. The loss of a SARJ would mean significantly reduced rotation of the solar arrays as the Beta joint would then be the only joint left; power harnessing would be significantly reduced.

Each SARJ consists of 12 trundles, 2 race rings, and 2 drive motors called DLA's (Drive Lock Assembly). The trundles are the bearing assemblies that allow one race ring to rotate relative to the other. The DLA is the motor that drives the ring using a pinion gear that engages the race rings bull gear. In primary operation, the trundles and DLA's are mounted to the inboard side and the outboard race ring is driven. In its redundant mode, or outboard operations, the trundles and DLA's are flipped and mounted to the outboard side and the inboard race ring is driven. The redundant mode of operation is only used if there is a failure or issue with the inboard mode of operation.

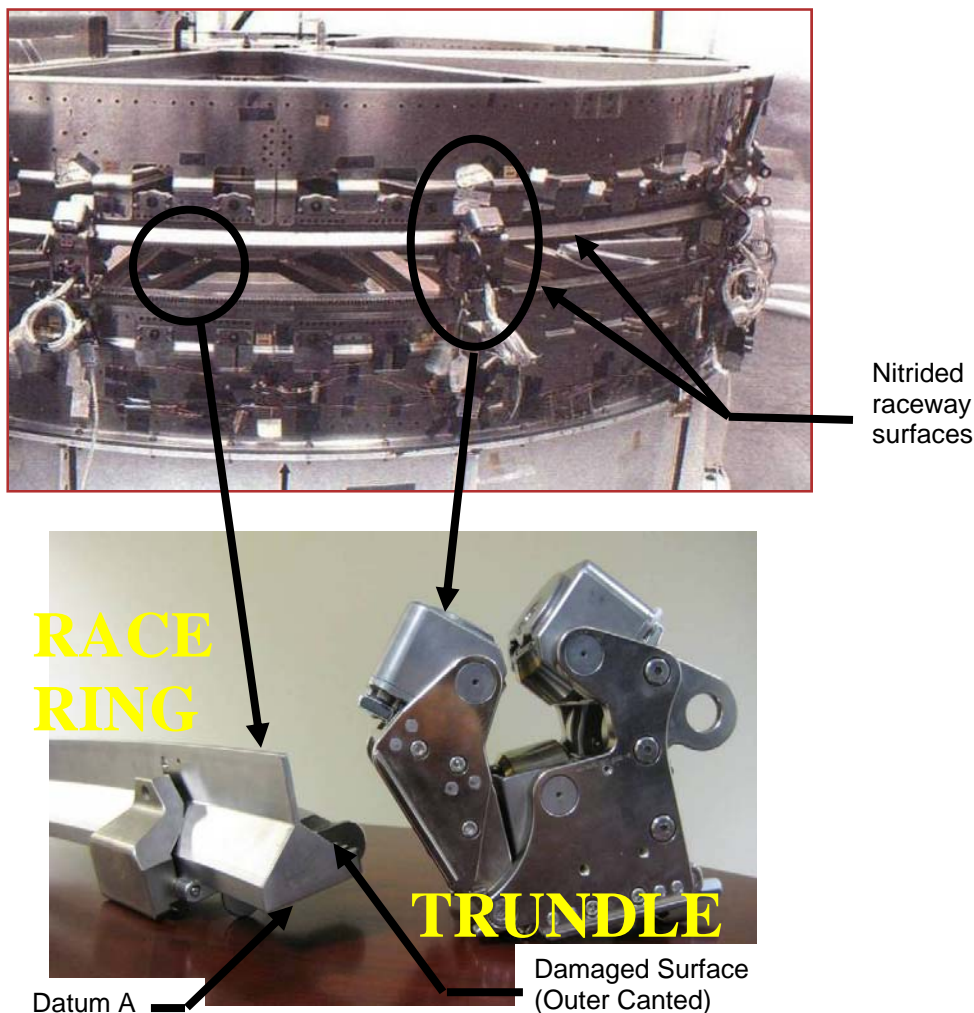


Figure 2: SARJ with blowup of a trundle and a race ring segment

Each trundle bearing assembly consists of three rollers that are made of 440C with an ion-plated gold coating. The DLA assembly consists of two trundle-like bearing configurations called followers, which also each consist of three 440C gold-coated rollers. The rollers between the trundle and the followers differ in

several minor respects such as contact width and edge radius. Although the follower rollers have a slightly larger overall width, their contact width is slightly less due to their larger radius. Both the trundles and the followers have a datum A roller that rides on the bottom surface of the race ring (see Figure 2) that is different than the other two rollers. The datum A roller is wider and also has a different taper angle. Its corresponding surface on the race ring was also different than the other two surfaces as it was ground and the other two surfaces were not.

In the fall of 2007, an increase in the drive current was observed on the Starboard SARJ. After further monitoring, it was decided to park the joint in order to prevent any further damage. The Starboard SARJ had only been operating for approximately 5 months compared to the Port SARJ, which had been operating nominally for approximately 14 months. Shortly thereafter, an EVA ensued, which included an inspection of the ring. It was then discovered that a significant amount of damage had been done to the outer 45 deg canted race surface with debris being observed in high quantity on much of the adjacent hardware all around the race ring.

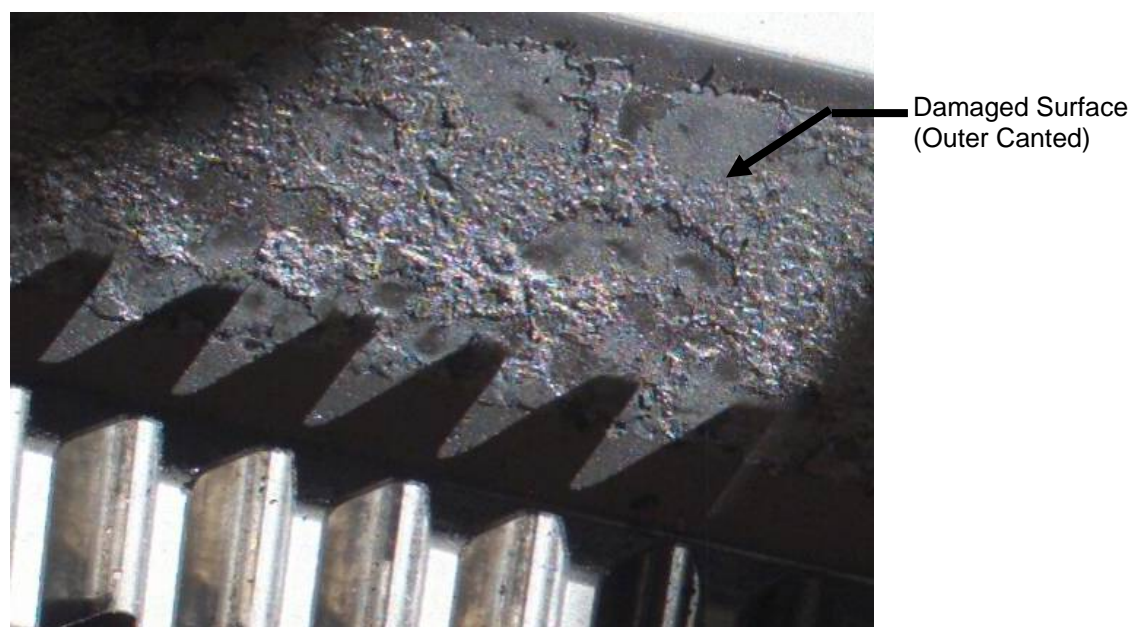


Figure 3: Damaged on-orbit SARJ race ring

A root cause investigation was then initiated. A fault tree was built with all conceivable possibilities of cause being included. Each item was closely reviewed and rated on likelihood based on results from data review, analysis, test, and on-orbit inspection. It was determined that roller mistracking coupled with high surface friction from dry roller contact was the root cause of the failure. The high contact stress due to roller edge loading as a result of mistracking caused the roller to spall the nitride case. Mistracking is the result of the rollers being slightly misaligned (<0.5 deg) relative to the race as shown in Figure 4. A side friction force is generated at the roller/race contact since the rollers are slipping slightly as they roll. The side force creates a tipping moment about the camber pivot axis. This in turn causes the roller edge to dig into the race as illustrated in Figure 4. The details of the failure investigation are discussed in a companion paper (Reference 1).

A subsequent EVA inspection of the Port SARJ revealed traces of grease on the race surfaces. It was discovered that the trundle bearings had most likely leaked out a sufficient amount of grease to adequately lubricate the ring surfaces and prevent the rollers from edge loading and causing the damage to the race surface. A review of the differences between the Port and Starboard SARJ's had revealed that

the Starboard SARJ never had a thermal vac test performed, which may have created the environment for the Port SARJ trundles to leak some grease.

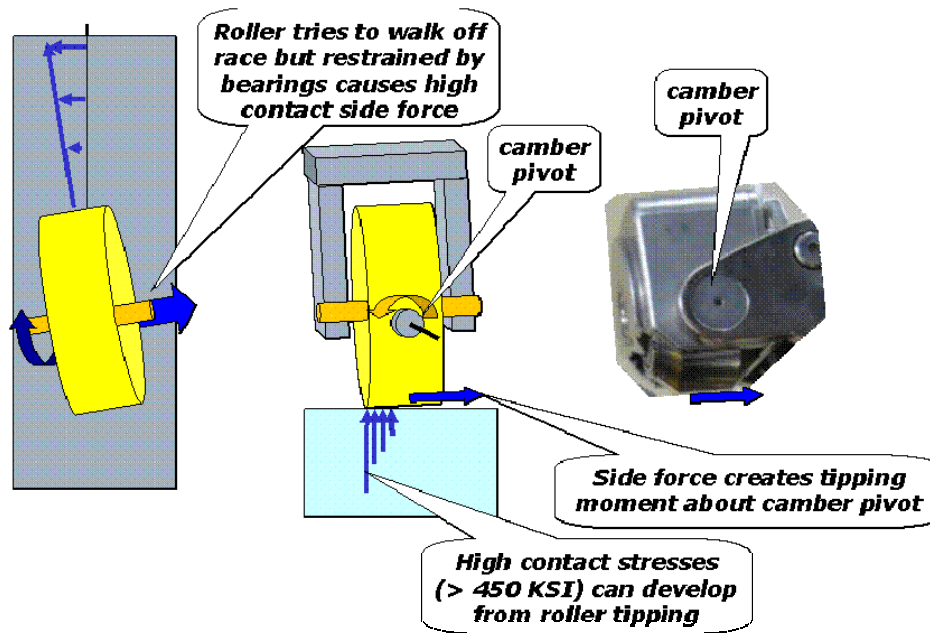


Figure 4- Mechanics of mistracking causing tipping and edge loading

As part of the recovery effort, both the Port and Starboard SARJ's were greased using Braycote 602 during mission STS-126 Nov 2008. Since then, the Port SARJ has been under continuous operation with nominal performance while the Starboard SARJ remains parked except for an occasional test run for evaluation. Several questions remained unanswered including: a) at what rate would the damaged ring continue to degrade after greasing during normal auto-tracking (continuous operation), and b) at what time intervals would relubrication operations be needed for both joints? Furthermore, how long could the relubricated damaged ring last before a transition to outboard operations be required?

Rig Design

These unanswered questions led to the need for some additional ground testing. It was decided that a high-fidelity test rig dubbed the SARJ LITE (Lubrication Interval Test) would be created to determine lubrication life on the SARJ. This was accomplished by building a scaled-down version of the flight SARJ that simulated flight trundle bearing kinematics such as mistracking along with flight roller and race geometries/materials.

Its purpose was threefold. First, to use the rig to damage the test plate to generate flight-like race damage. Secondly, to test for ring durability by making sure running on the damaged surface doesn't lead to catastrophic breaks in the ring; and thirdly, to determine grease relubrication intervals that would reveal how often an EVA is needed to relubricate the rings. The SARJ LITE data in addition to data from other component test rigs are being used to steer decisions for future Space Station operations.

In the on-orbit configuration, 12 sets of trundle rollers and 2 sets of DLA follower rollers ride on the race ring surface. With the race ring diameter being nearly 10 feet (3 m), it was decided that a full-scale test rig would not be feasible so a smaller size was chosen to be compatible with a thermal chamber but the spacing between trundle rollers would be maintained. The DLA follower rollers were left out due to their significantly reduced preload that lessened the likelihood of their contribution to ring damage. A configuration of three equally spaced rollers was chosen for the rig. It was additionally decided that since

each trundle assembly has two different roller types, a wide and a narrow, two different race tracks would be utilized to run simultaneous tests, one for the wide and one for the narrow. The rig was setup so each track and preload system was independent of the other and could be run by itself or in parallel with the other. The preload system initially used a stack of Bellville washers to achieve the desired preload (roughly 13.3 kN (3,000 lb)). After analysis of the roller support structures (called spiders) however, it was determined that the spiders had sufficient compliance and were soft enough to act as the Bellville stack themselves, so the Bellville washers were taken out of the design. Instead of modeling the trundle assembly, which includes a cluster of three rollers, the test rig simply used a single test roller backed with a support roller (see Figure 5). The preload was to be set with an individual preload bolt for each test setup, evenly distributing the load between the three rollers.

Roller geometry was maintained close to flight with the exception of the taper angle, which was increased to accommodate the reduced size of the test plate. The camber axis was also included in the test trundle design. The camber axis was intended to allow the roller to tilt, which causes the roller to lay flat against the race ring. However, it was this very camber feature that ended up contributing to the race damage by allowing the roller to tip and initiate the damage to the ring. A feature was added to the rig design to lock the roller housing at a particular camber angle. The roller was then maintained with edge loading for extended periods during attempts at damaging the race in a flight-like manner.

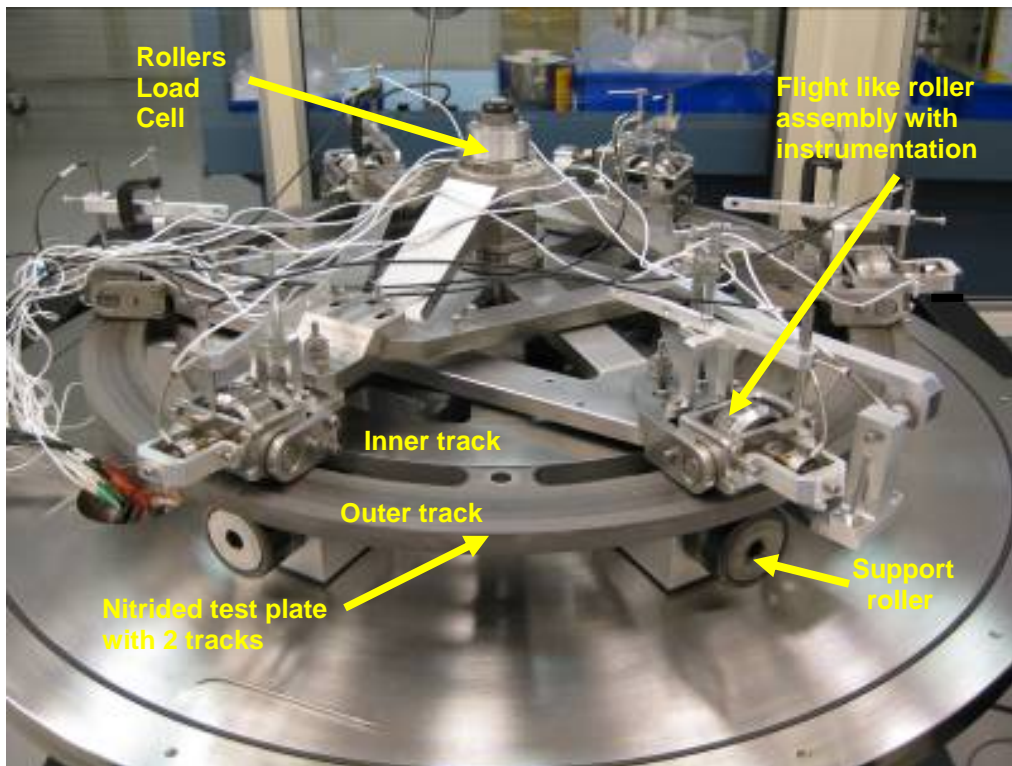


Figure 5- SARJ LITE Rig (vacuum chamber cover not shown)

Adjustment of the mistracking angle was another feature built into the rig (see Figure 6). The mistracking element was important because it played into the root cause. Some of the rollers from actual on orbit trundles were measured and found to have a certain amount of mistracking built into them due to tolerancing buildup. This data was used to aid the final setting for the lube life test. Additionally, since the rig would be used to cause initial damage to the plate, a roller adjusted to a high mistrack angle could quicken the damage runs. The mistracking was set using a known zero, which was achieved using instrumentation that defined a perfect alignment of the roller relative to the track. An LVDT as shown in

Figure 6 was used to aid in defining the motion required to obtain a particular mistrack angle. Once the angle was achieved, the three fasteners holding the bearing mount to the spider were tightened. This process was performed on each bearing assembly.

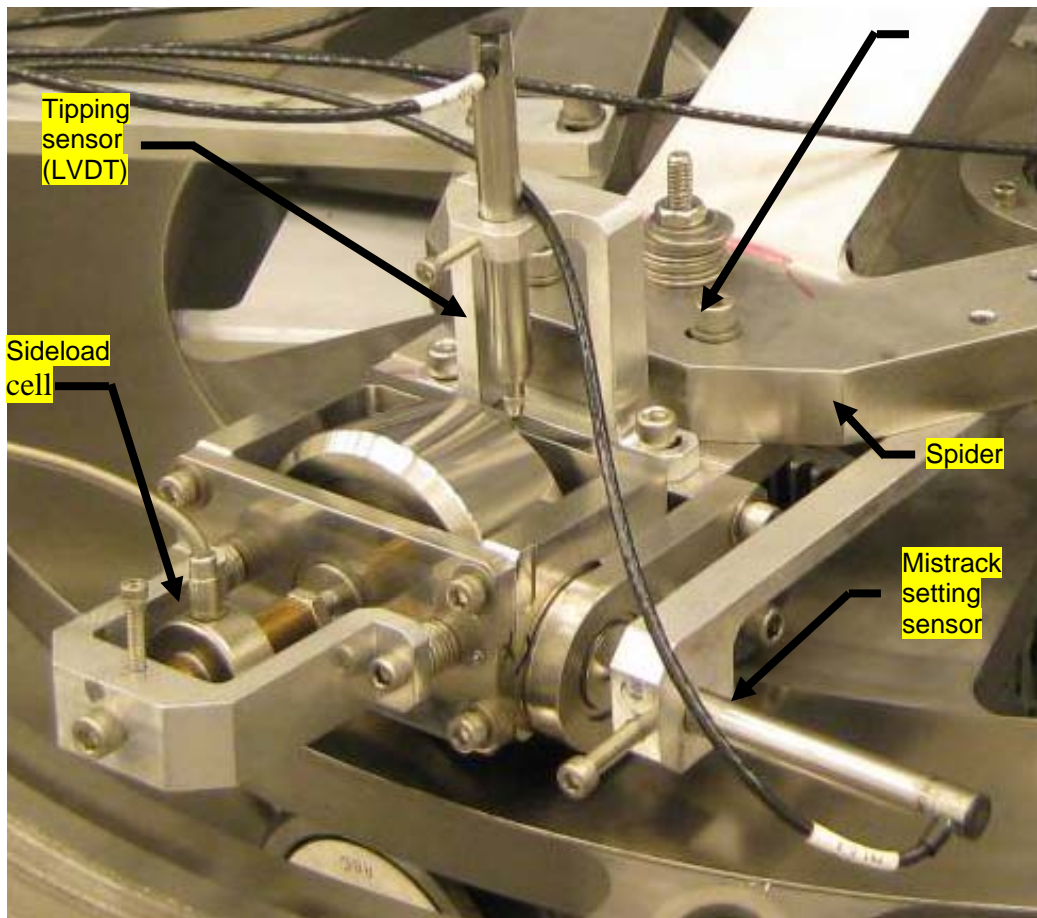


Figure 6: Test roller with its respective instrumentation

Pre-Test Damage Phase

The first task was to damage the outer track to simulate the damage condition of the on-orbit Starboard race. This race had significant pitting both across the track and along the entire circumference. The nitrided layer was broken through and only islands, remains of the surface, were left with the majority of the nitride case turned into debris (see Figure 3). It was originally thought that the rig could be used to damage the test plate using hardened rollers and purposely mistrack them to high angles to induce tipping, or even to pin them to maintain an extreme tipped state. The damage runs were made initially with only the three outer track rollers engaged so the entire inner spider, including its rollers, was disengaged. Difficulty was encountered when attempting to spall the test plate. The rig was then reconfigured (see Figure 5) with extensions added to the inner spider, which allowed all six bearing assemblies to run on the outer track and double the number of stress cycles the ring would see. This helped speed up the damage but the damage was confined to a narrow region (see Figure 7).

It was suspected that the roller tipping was too high (see Figure 8) to propagate the damage across the track. So the tipping angle was reduced to get more roller contact across the width of the track. Early results looked promising as some additional spalling was observed, but over time roller and track wear

became the dominating factor (see Figure 7). Wear simply produces debris that eventually becomes pancake-like in appearance. It differed from the on-orbit pitting and spalling observed. The 440C rollers would wear at the tips (see Figure 9) where the contact was made and become dull and a trough would gradually form on the track.

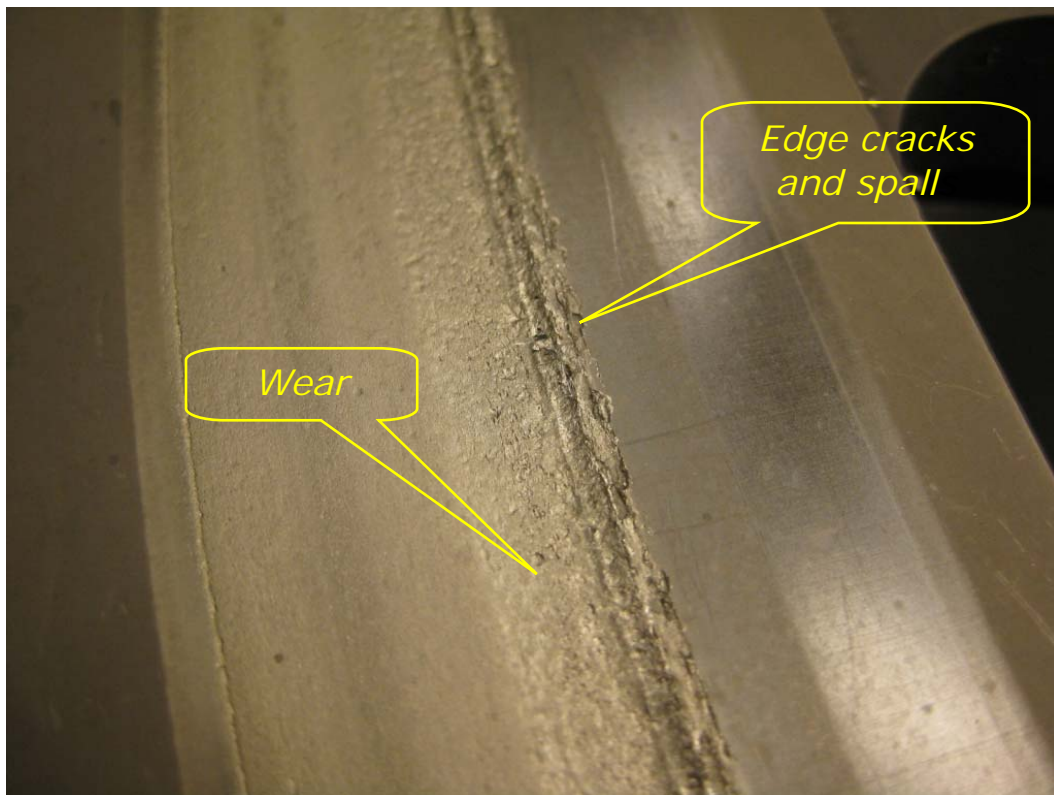


Figure 7: Example of damage generated on outer track

Additional attempts were made using alternate tip angles, mistrack angles, and preloads, with mostly wear being created. Harder tool steel rollers were also implemented but they also began to wear and lose their edge over time.

It seemed that no matter what the configuration was, the result was more of the same. It was later determined using a comparison of samples that the on-orbit case hardened nitride layer had more subsurface defects (porosity, etc.) than that of the test plate. Although the test plate was nitrided at the same vendor as the flight race rings, its superior metallurgical structure made it less susceptible to damage. This was perhaps the key factor for our inability to damage the test plate.

Other techniques for damaging the race had been pursued and some looked promising. These methods included EDM'ing, etching, pressing pins, and use of a friction stir welder. The friction stir welder at JSC used a single roller on a linear path and could cause damage on a single chord. Sixteen chords would cover the entire plate. The initial damage was done with a mistracked and tipped roller. The stir welder would then be radially offset inward for more damage passes and the process of shifting inward repeated until a strip of nearly 5 cm (2 in) was produced (see Figure 10). Once the damage runs were complete, the plate was shipped to Sunnyvale and mounted onto the test rig.

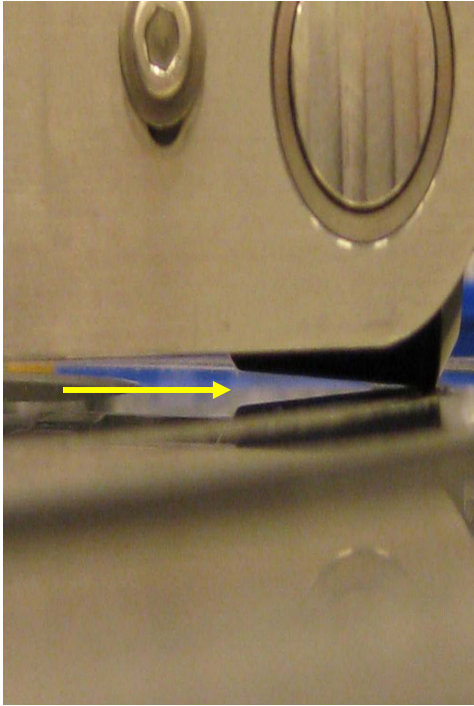


Figure 8: Tipped roller

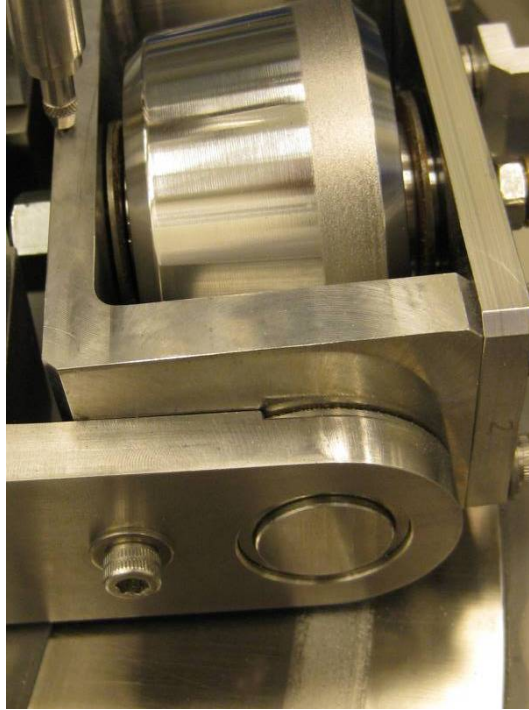


Figure 9: Roller and track wear

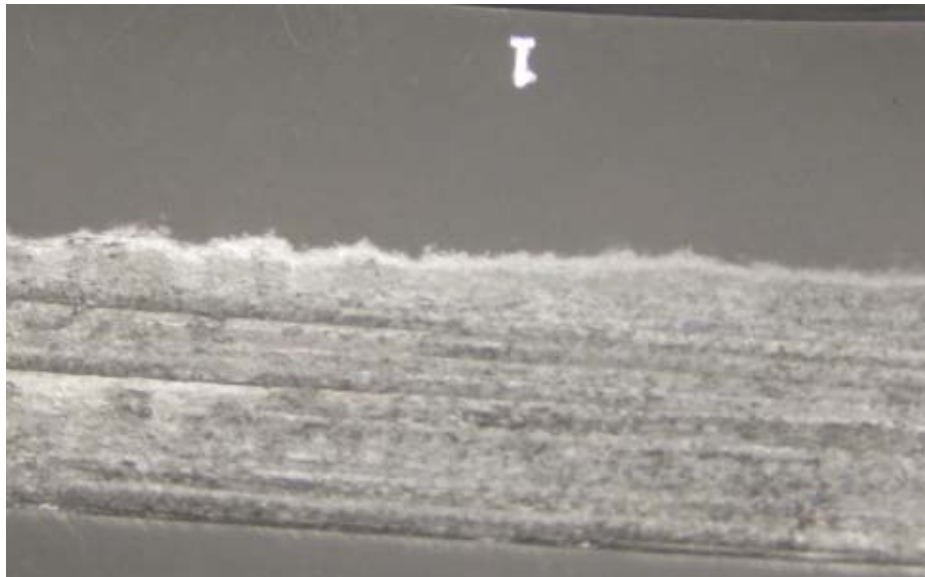


Figure 10: Damaged Outer track before test start

Test Results

Ring Durability

The first task was to determine if the damaged flight race could suffer a structural failure if continued on-orbit operation was resumed. It was decided to run the previously damage test plate dry to bound the problem. This was in line with the test philosophy of doing ring durability testing prior to the main test for lubrication life.

The ring durability test was started with the rollers set at flight-like mistrack angles based on measurements made on flight trundles at NASA MSFC. LVDT's were set up on the rollers to monitor tipping and the load cells in line with the roller axis were set up to monitor sideload. Unfortunately, due to the sensitivity of the load cell and the higher drag in the bushings through which the bearing shaft rides, the exact friction values couldn't be extracted from the data. The load cell data however, was still very useful for monitoring trending of the sideload of each roller. With the preload set at a flight-like value, roughly 4 kN (900 lb) per roller, the test was started.

Initial testing was performed with no lubrication in order to characterize the track dry. It was also performed at ambient pressure to create a baseline to which data could be compared to during the transition to vacuum. The sideload values were high relative to the later runs with grease. Also, edge loading was observed upon examination of the tracks but no tipping was evident. It was decided to limit the amount of dry running to preserve the Datum A track so as to ensure a flight-like surface for the lubricated portion of the test. The surface was run on just long enough to obtain some wear but not long enough to cause damage since the on-orbit datum showed minimal signs of damage.

After approximately 16 equivalent flight months of testing, the previously damaged outer track showed no significant structural degradation other than generation of additional surface wear debris and a deeper groove under the edge of the tipped roller. The test results showed that structural damage even at the high stresses associated with tipped rollers and dry running would not jeopardize the structural integrity of the SARJ.

Lubrication

Grease was then added to the track using a grease gun similar to the on-orbit gun and in similar quantity. A single bead of the Braycote 602 flight grease was added to the center of the track around the entire circumference. The test was restarted at ambient pressure for more data and then the lid was put on the fixture and the chamber taken to vacuum. The grease effect on the track was an immediate reduction of close to 50% of the sideload as expected. After a short period of time, the grease was pushed out of the way and the sideload increased and then stabilized (see sideload drop at 6000 revs in Figure 11).

Another important variable was the test speed. The test speed needed to be fast enough to perform the test in a reasonable time frame but slow enough to ensure a flight-like test environment. Running too fast could cause the track to starve itself of grease and that is exactly what was observed during initial grease runs.

As shown in Figure 11, the sideload friction levels climbed back to the pre-grease levels after only a few thousands revs at 1 rpm. This test speed is approximately 20X faster than flight. Based on previous SARJ coupon testing, it was known that speed affected grease performance so it was clear that the speed would have to be reduced in order to allow the grease to produce a flight-like affect. The test rate was then lowered to 0.4 rpm at roughly 17000 plate revs. The sideloads then started to drop. The track was then re-greased and the sideload dropped even more as expected. They remained reasonably stable until at about 21000 revs when an operator error inadvertently switched the test speed back to 1 rpm. Figure 11 shows that the sideloads continued climbed again until about 29000 revs when the speed was reduced back to 0.4 rpm which lowered the sideload once more. Clearly there was a direct connection between surface speed and grease effectiveness. The explanation for this is that the grease needs

sufficient time to flow back into the contact between roller passes after being pushed to the side (see Figure 12). The time required is a function of the length of travel, which is significant for our test rollers being relatively wide. This grease flow phenomenon is relatively well documented, e.g., see Reference 1. Further observations allowed determination of the 0.4 rpm to be the threshold at which the lube life test should be performed. It provided an approximate 8 to 1 test acceleration factor, which was tolerable as 3 years of on-orbit data could be gathered in just over 4 months.

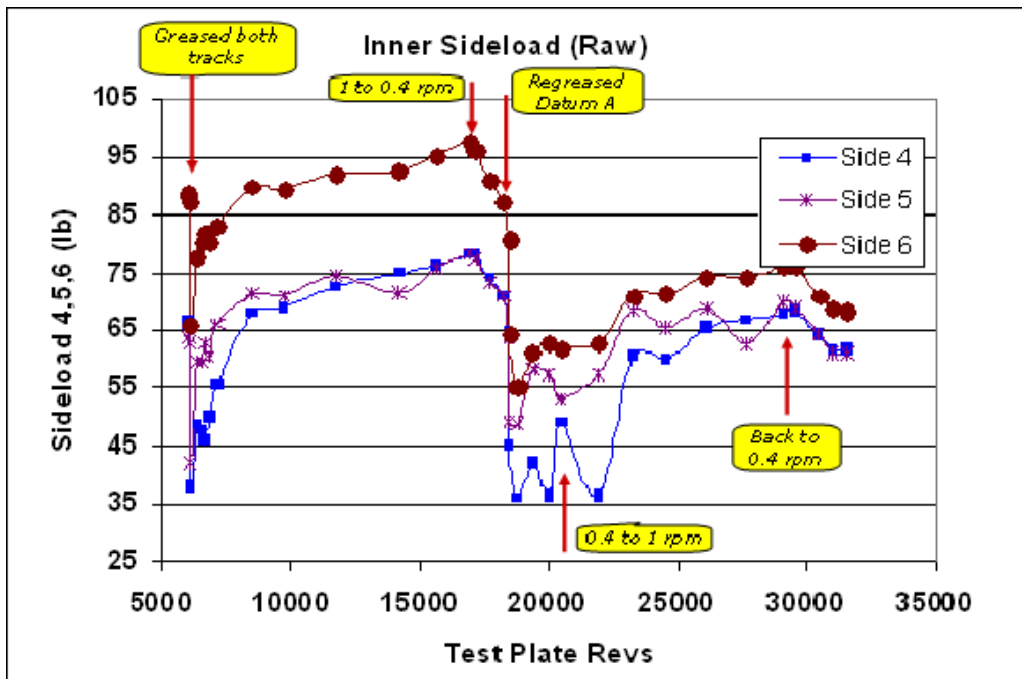


Figure 11: Datum A sideload friction data showing the benefit of grease and low test speed

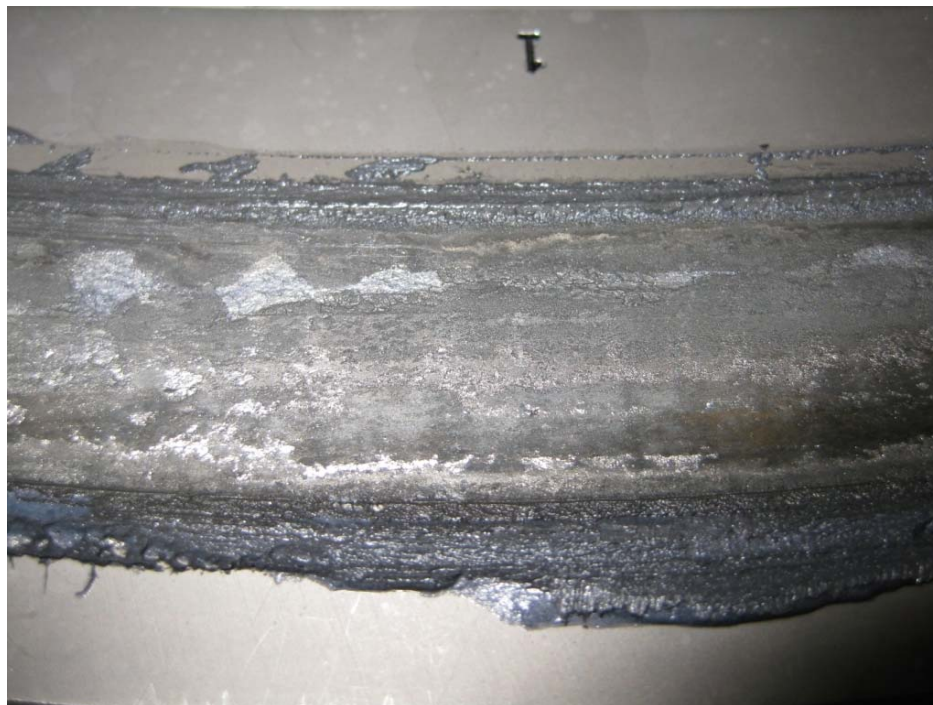


Figure 12: Damaged Outer track with grease

Lubrication Interval

The goal of the lubrication interval portion of the test was to determine how long the SARJ could run without needing a resupply of grease. Each relube would mean an additional EVA, which is added risk and cost to the Space Station program. Data for sideload, tipping, drag torque, temperature and preload was gathered and plotted against time. The sideload friction data (as shown in Figure 13) provided the most relevant feedback to aid in determining the need to relubricate as an increase would indicate a drying track. As shown, the sideload curve remains flat with no sign of any significant trend increases after 125,000 total revs on the damaged outer track and nearly 95,000 revs on the Datum A track at the time of this writing. This is equivalent to about 3.5 years on-orbit since the last greasing. The local up and down variations in side load appearing in Figure 13 closely follows the temperature of the load cell mounting structure, which is also plotted. Apparently, the differential thermal expansion of the mounting structure alters the load cell reading since the load cell is so stiff.

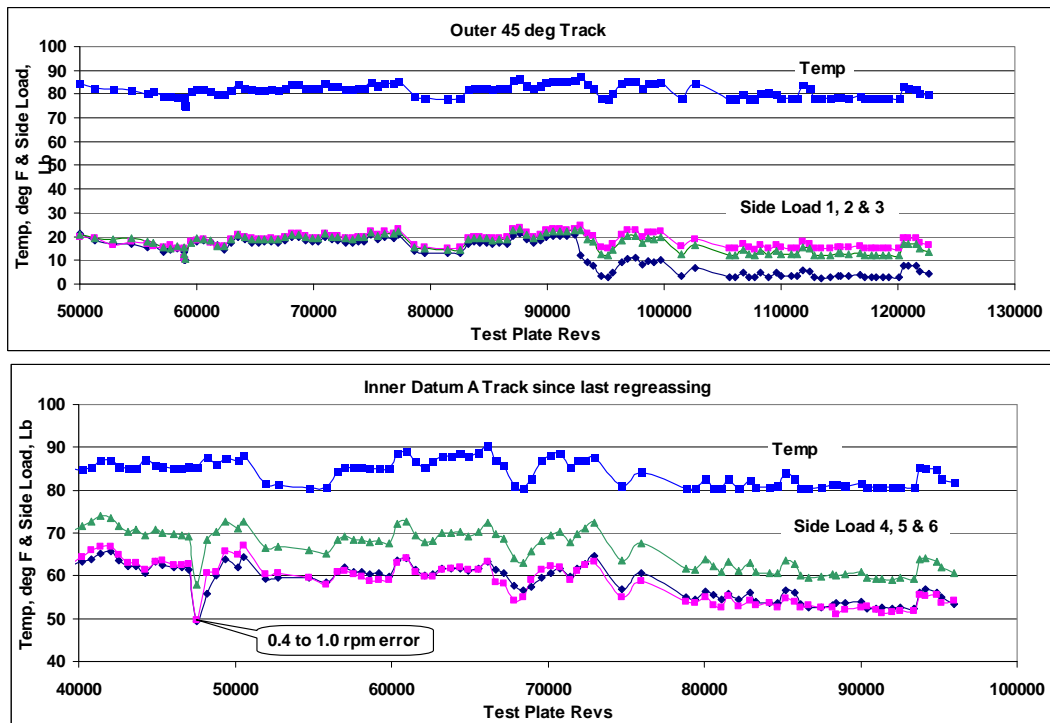


Figure 13: Sideload vs. test plate revs

Roller tipping angle and roller drag are also indicators of increased friction and the lubricant drying out. As shown in Figure 14, the tipping LVDT curve and drag torque curve for the outer track is also relatively flat over time. This indicates that the grease is still effective. However, the drag on the inner track seems to be increasing (more negative) slightly at this point and will continue to be monitored.

This is consistent with intermediate visual inspections of the tracks where the outer track remains relatively well greased throughout its entirety. The voids and pits in the damaged outer track were filled with the grease as the rollers plowed through the track, thus creating a reservoir and perhaps allowing the roller to track interface to remain somewhat wetted (see Figure 12). On the other hand, the inner track looked relatively dry as the grease had been pushed out of the way, leaving only a thin film of oil that would be sufficient enough to keep the roller interface wet. The inner track does show a propensity to dry out faster than the outer track.

This portion of the test is still young and as it progresses, data will continue to be collected and monitored for shifts and changes. The outer track has passed the 3.5 year on-orbit mark since the last lubrication and the inner track is closing in on three years. Testing will likely continue to mid 2010.

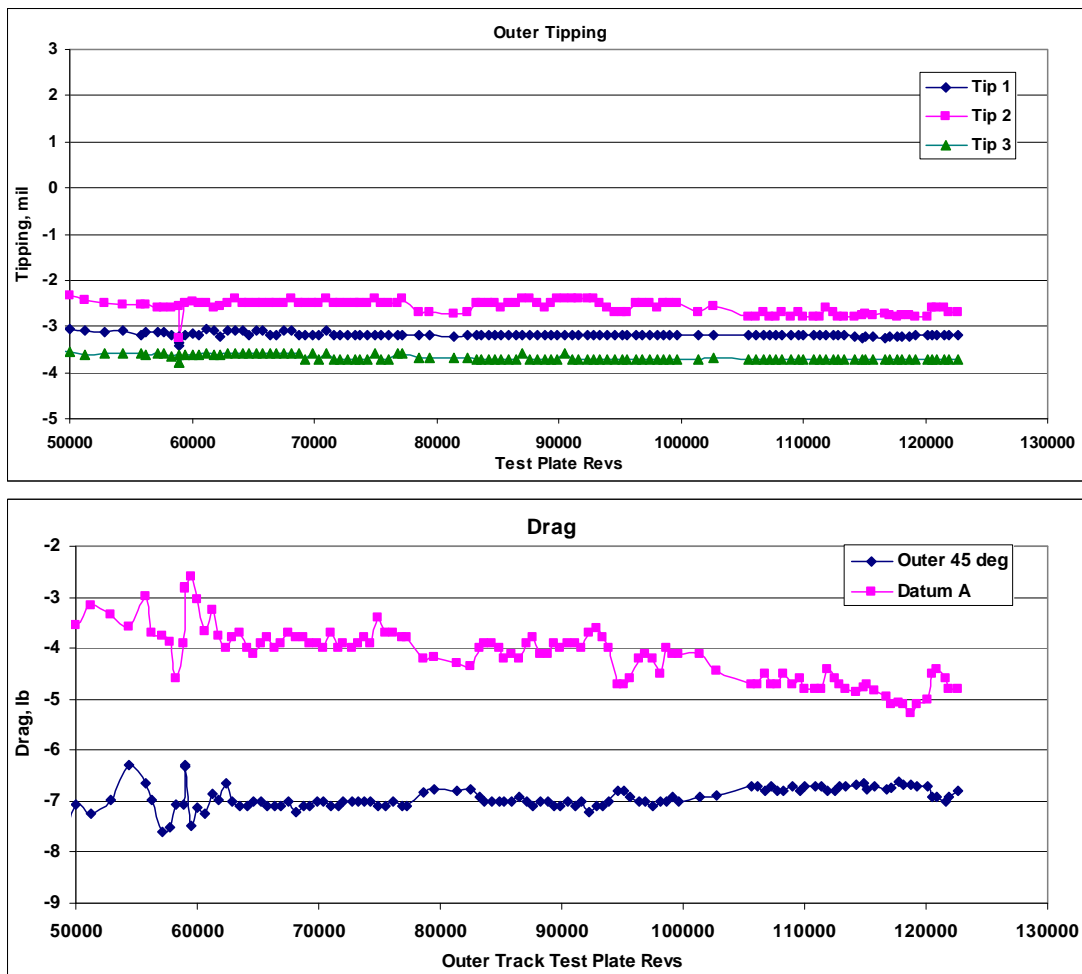


Figure 14: Tipping & drag vs. revs

Conclusion

A test rig was developed that closely simulates the roller/race contact conditions of the SARJ trundle rollers. The test plate was artificially damaged to represent the on-orbit damage race. The test results show that grease lubrication is an effective way of combating the high friction that led to roller tipping and high edge contact stress that led to the on-orbit failure. On-orbit relubrication intervals in excess of 3 years are reasonable based on the data generated to date. The authors would like to acknowledge the contribution from the experts at Boeing, NASA, NESAC, and ATK in the design and formulation of test requirements for the SARJ LITE rig.

References

1. Harik, E.; Sweeney, D.; Enriquez, C., and McFatter, J.; "Diagnosing On-Orbit Failures International Space Station (ISS) Solar Alpha Rotary Joint (SARJ) Bearing Failure," 40th AMS Proceedings (to be published), 2010
2. Cann, P. M., "Starvation and Reflow in a Grease-Lubricated Elastohydrodynamic Contact," *Tribology Transactions*, vol 39, no. 3 (1996), 698 - 704.

Experimental Investigation of Forces Produced by Misaligned Steel Rollers

Timothy Krantz^{*}, Christopher DellaCorte^{*} and Michael Dube^{**}

Abstract

The International Space Station Solar Alpha Rotary Joint (SARJ) uses a roller-based mechanism for positioning of the solar arrays. The forces and moments that develop at the roller interfaces are influenced by the design including the kinematic constraints and the lubrication condition. To help understand the SARJ operation, a set of dedicated experiments were completed using roller pairs. Of primary interest was to measure the axial force directed along the axis of rotation of the roller as a function of shaft misalignment. The conditions studied included dry and clean surfaces; one surface plated by a gold film, and greased surfaces. For the case of a bare 440C roller against a nitrided 15-5 roller without lubrication, the axial force can be as great as 0.4 times the normal load for a shaft angle of 0.5 degree. Such a magnitude of force on a roller in the SARJ mechanism would cause roller tipping and contact pressures much greater than anticipated by the designers. For the case of a bare 440C roller against a nitrided 15-5 roller with grease lubrication, the axial force does not exceed about 0.15 times the normal load even for the largest misalignment angles tested. Gold films provided good lubrication for the short duration testing reported herein. Grease lubrication limited the magnitude of the axial force to even smaller magnitudes than was achieved with the gold films. The experiments demonstrate the critical role of good lubrication for the SARJ mechanism.

Introduction

The International Space Station makes use of a roller-based mechanism for positioning of the solar arrays. The fundamental concept of the roller-based mechanism of the Solar Alpha Rotary Joint is described by Loewenthal and Schuller [1]. A careful study of the SARJ system reveals an interesting and significant interplay of forces at the interface where the rollers of the rotary joint mechanism touches the large rotating ring. It is well established in the literature that forces and moments can develop at the interacting surfaces in rolling and sliding contact [2,3]. The forces and moments that develop are influenced by the details of the design including the kinematic constraints. Proper understanding of the influence of roller misalignment has proven to be important in the development of a roller mechanism used for positioning of a radio astronomy antenna [4,5,6]. The influence of roller misalignment is likewise important for the operation of the SARJ mechanism.

The roller and ring of the SARJ mechanism and the meaning of the term "shaft misalignment" is depicted in schematic form in Figure 1. The SARJ rollers are constrained to rotate about shaft axes that nominally intersect the rotational axis of the ring (Figure 1 [a-b]). Any deviation from perfect alignment of a roller axis and ring axis (Figure 1[c]) will give rise to a force at the contact interface in the direction of the roller shaft axis (termed herein the axial force). The magnitude of the axial force will depend on the magnitude of misalignment, the normal load on the roller, the stiffness of the system, the torque transmitted by the roller, and frictional condition of the contacting surfaces. The SARJ mechanism was built to high precision, and the installed roller shaft angle (misalignment) was within a fraction of a degree to perfect alignment. As will be evident from this study, misalignments of even such small magnitude can produce significant forces that influence the performance of the mechanism.

^{*} NASA Glenn Research Center, Cleveland, OH

^{**} NASA Goddard Space Flight Center, Greenbelt, MD

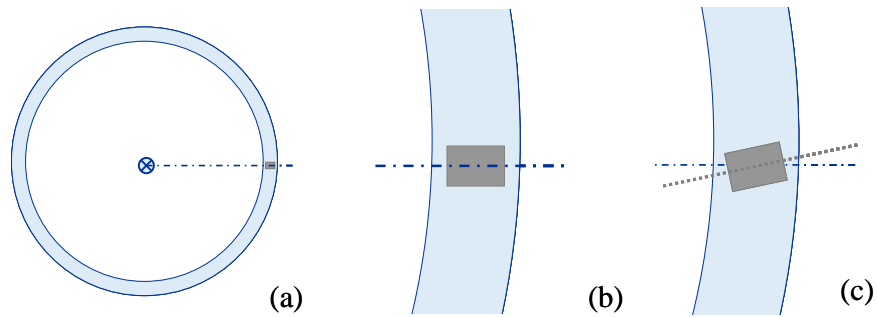


Figure 1 - SARJ ring and roller schematic, top view. (a) Overall view, roller axis aligned with ring axis; (b) close-up view near roller, aligned axis; (c) close-up view near roller, roller axis misaligned (misalignment magnitude greatly exaggerated).

The axial force that develops in response to the misalignment of the axes can have a significant influence on the operating conditions of the SARJ hardware. The axial force and the associated moment that arise from misaligned axes are carried by a pair of tapered roller bearings via the roller shaft to the roller housing. The axial force interacts through a pivot point in the roller housing (Figure 2). In the absence of misalignment, the pivot point allows for uniform contact of the nominally flat roller profile contacting the nominally flat raceway surface. But for the case of misaligned axes, the axial force acts via the pivot point and produces a non-uniform contact pressure across the roller profile. Note from Figure 2 the moments created by the normal load and axial force acting via the pivot point must be balanced for static equilibrium. Thereby, the axial force acts to shift the position of the resultant normal load along the face of the ring and roller contact. The axial force arising from misaligned axes can, if of sufficient magnitude, cause tipping of the roller. Also note that the axial force acting on a roller is carried to the roller shaft via a pair of lightly-preloaded tapered roller bearings. The magnitude of the axial force influences the drag torque of the bearings and thereby influences the torque required to rotate the mechanism.

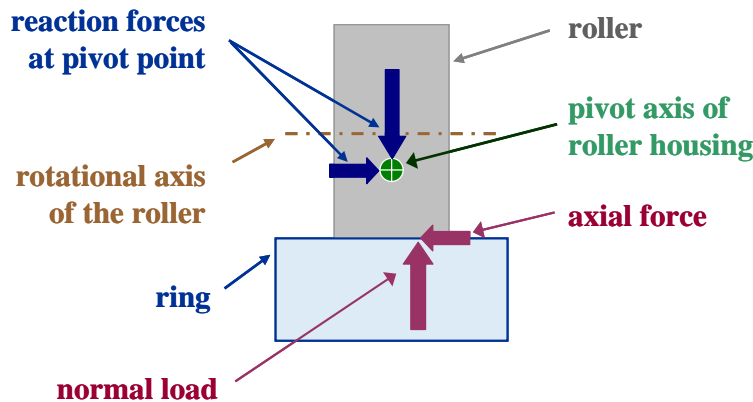


Figure 2 - Schematic of the SARJ roller and ring in contact, front view. Illustrated are the forces imposed by the ring on the roller and the reaction forces at the pivot point in the roller housing.

To help understand the SARJ mechanism operation, a set of dedicated experiments were completed using roller pairs. The purpose of the experiments was to quantify the relationship of the misalignment of roller axes to the resulting forces that develop. The relationship of shaft axis misalignment magnitude to axial force magnitude was determined for the material combination used in the SARJ mechanism for a variety of surface and environment conditions as can influence the friction and, thereby, the behavior of the mechanism.

Apparatus, Specimens, and Procedures

Test Apparatus for Roller Pairs

Testing was done using the NASA Glenn Research Center Vacuum Roller Rig (Figure 3). The rig allows for application and measurement of a load pressing the rollers together while having a purposely misaligned and adjustable shaft angle. The rig is depicted in schematic form in Figure 4. A drive motor provides motion to the driving roller. A magnetic-particle brake attached to the output shaft imposes torque on the driven roller. The rig can be operated with the brake not energized. For such a condition the torque transmitted through the roller pair is only the drag torque of the output shaft (drag of the seals and support bearings). The normal load pressing the rollers together is provided by an air cylinder. The cylinder acts through a gimbal point to rotate the plate that mounts the driving shaft and drive motor. The rotation of the drive motor plate displaces the driving roller toward the driven roller shaft. The pressure to the cylinder, and thereby the load between the contacting rollers, is adjusted by a hand-operated valve (open-loop control). Testing can be done in vacuum or ambient air. Vacuum is provided by a diffusion pump with a liquid nitrogen cold trap. The diffusion pump is assisted by a mechanical vacuum pump. Figure 5 provides a simplified schematic labeled with some of the nomenclature used herein.

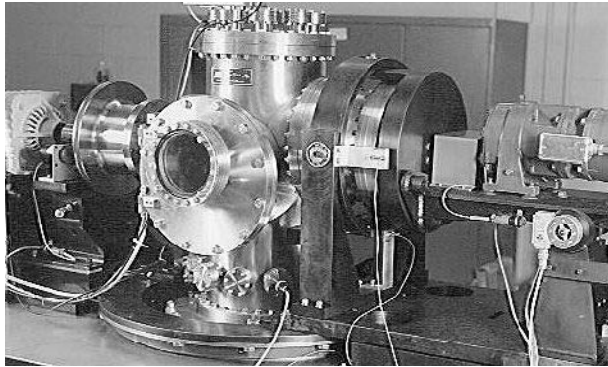


Figure 3 – Vacuum roller rig.

A set of sensors on the test apparatus monitors the test conditions. The outputs of the analog sensors were digitized and stored via a data collection unit at a rate of 0.66 Hz. Each of the sensors and the methods of calibration will be described in turn.

The misalignment of the driving roller shaft and driven roller shaft is depicted in an exaggerated manner in Figure 4(b). The misalignment is measured via a linear variable differential transformer (LVDT). The transducer housing is attached to the bedplate, and the translating, spring-loaded transducer tip contacts against a mechanical stop on the turntable. The mechanical stop is mounted at a known radial distance and tangential orientation from the center of the turntable. Calibrated gage blocks were used to displace the transducer by known amounts, and using the rig geometry the equivalent angular rotation of the turntable was calculated. The preceding steps established the relationship of change in transducer output to the change in relative shaft angle. To establish the aligned condition, a special tooling block was machined to locate the roller-mounting surfaces of the two shafts as parallel. With the shafts aligned by the tooling block, the transducer circuit balance was adjusted to provide an output of zero. The precision of this method for aligning the shafts was limited by the dimensions of the roller mounting surfaces used as the reference planes. From the test rig drawing tolerances and geometry, the alignment procedure using the tooling block to define the zero-degree position has an accuracy of no better than 0.11 degree.

The torque on the output shaft is monitored by a strain-gage type torquemeter of 22 N-m (200 in-lb) torque capacity. Calibration was done in place using deadweights acting on a torque arm of known length.

The load that presses the rollers together is termed herein the “normal load” (Figure 5). The normal load is applied via an air-pressure actuated piston. The air piston acts through a load cell against the drive motor plate that is gimbal-mounted relative to the test chamber (Figure 4(a)). In this way the air cylinder moves the roller on the input shaft in an arc motion toward the test roller. Once the rollers are in contact, additional force commanded from the air cylinder increases the normal load between the test rollers. The force sensed by the load cell located between the gimbaled motor plate and the air piston is a linear combination of two sources, the unbalanced mass relative to the gimbal point and the normal load on the test roller.

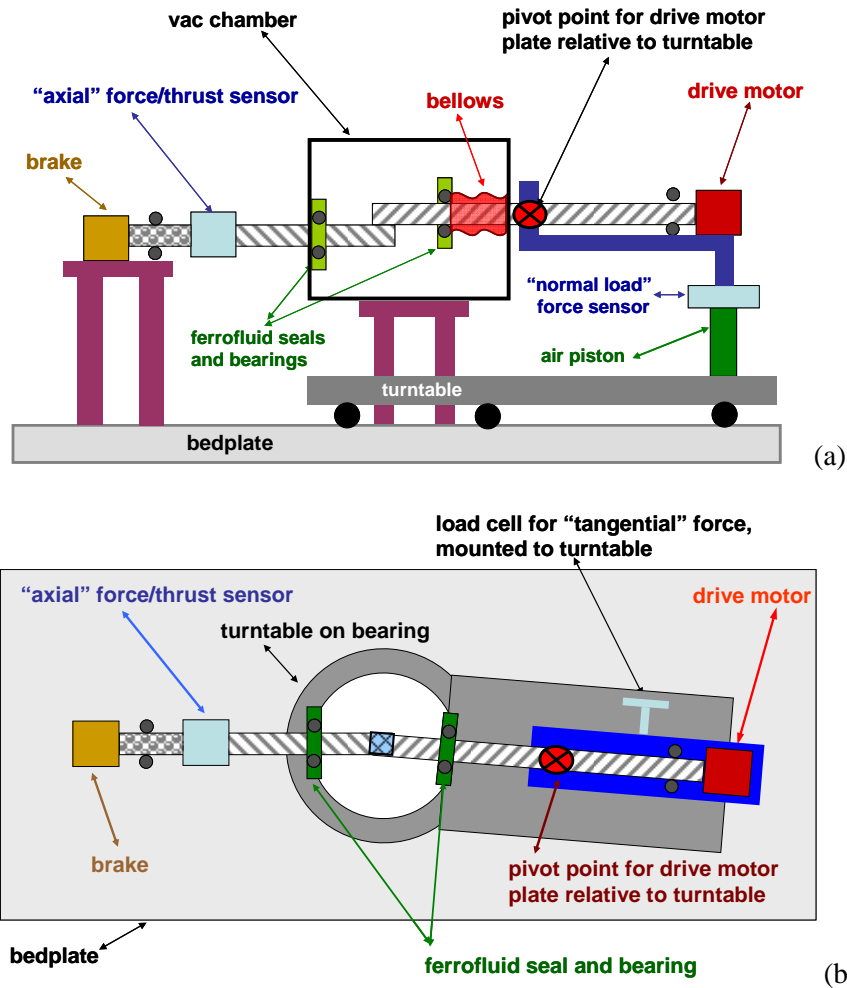


Figure 4 – Schematic views of the vacuum roller rig. (a) Schematic, side view. (b) Schematic, overhead view with shaft misalignment depicted and exaggerated.

The following calibration procedure was used so that the two sources influencing the load cell output during testing could be separated. First the load cell was removed from the rig, calibrated using deadweights, and reinstalled on the test apparatus. Next, a LVDT was used to monitor the displacement of the motor plate. With no test roller installed on the output shaft, the air piston was used to move the motor plate through the full range of motion while recording the output of the calibrated load cell. In this manner the force as sensed at the load cell due to the unbalanced mass of the gimbaled motor plate was determined as a function of the motor plate position. Next, the end of the input shaft where the test roller is mounted was attached by a highly-rigid link to the apparatus frame. The rigid link included a calibrated reference load cell in the load path. The rigid link was carefully positioned to be oriented in the position and direction of the normal load created between the contacting test rollers. By increasing the pressure

on the air-piston actuator, load was created on the rigid link and measured on the reference load cell. This procedure established the relationship of the normal load on the test roller acting through the gimbal point and resulting in a force imparted on the load cell located at the air piston. During testing both the motor table position and load cell force was recorded. From the table position data and calibration data, the force attributed to the unbalanced mass on the gimballed motor plate could be subtracted from the force value recorded by the load cell. The value remaining from the load cell (after the subtraction operation) is due to the normal force between the test rollers, and via the calibration curve the load on the test roller is determined.

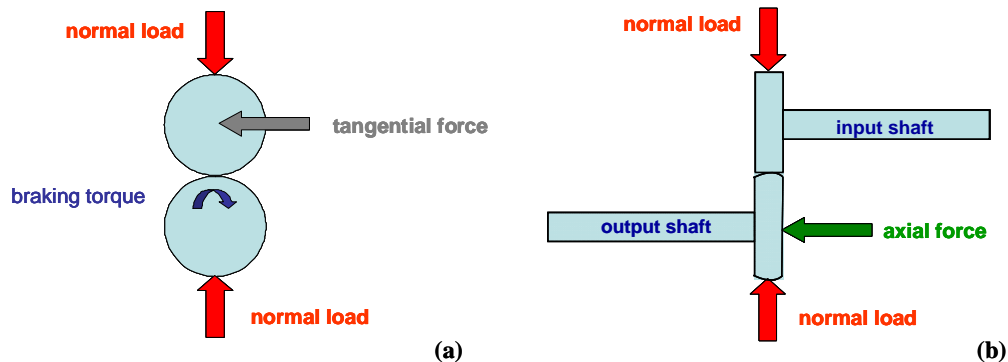


Figure 5 – Simplified schematic view including some of the important sensed data.
(a) Schematic, front view. (b) Schematic, side view.

When rollers operate in a misaligned condition a force will develop in the direction of the shaft axis [2,3,5,6]. In such a condition points on the two rollers in intimate contact and within a “stick” zone of the contact patch are constrained to move in unison. If the points were not in contact the kinematic constraints would provide a slightly different path of motion. The difference in the actual path of motion and that defined by the motion if the points were not in contact gives rise to surface strains and a resultant axial force. A sensor to measure this force is labeled as the “axial force” sensor in Figure 4. The axial force sensor is co-located on the output shaft with the torquemeter sensor. The configuration of the rig did not allow for direct deadweight calibration in place. To calibrate the sensor in place, the following procedure was used. First, a load cell was calibrated via deadweights and then was placed on the free end of the output shaft to act as a reference load cell. A threaded jackscrew acted against the reference load cell and a hard stop in the vacuum chamber. Adjusting the jackscrew length allowed for changing the force imparted on both the reference load cell and, the rig’s axial load cell and to the machine frame. In this manner the same force was applied to both load cells, and the reference cell output used to calibrate the axial load cell sensor in place.

The preceding two paragraphs describe the sensors (and sensor calibrations) to determine two mutually perpendicular forces acting on the driven test roller. A force also acts along a third axis. This is the force directed tangential to the roller diameter and is termed here as the “tangential” force. The tangential force on the input shaft roller acts through a gimbal point (Figure 4(b)). The rotational motion about the gimbal point is restrained by a mechanical link to the turntable structure. There is a load cell load in the load path from said mechanical link to the turntable structure. This sensor was calibrated in place by using a pulley-cable system and dead weights to relate the tangential force applied at the test roller position to the sensor output. During testing, this sensor is also affected by spin moments (Ref. (2)) that can develop in roller contacts. The data from the tangential force sensor was recorded for possible future use, but such data were not of immediate interest and are not reported herein.

Shaft speeds and total number of shaft revolutions were measured using encoders on each shaft. The encoder pulses were counted and recorded via a digital pulse counter. The encoder pulses were also monitored by a frequency converter to provide a convenient shaft speed display to the test operator. The encoders provide 6,000 pulses for each shaft revolution.

The pressure in the chamber was monitored by an ionization gauge at the top of the main test chamber. The typical pressure in the testing chamber during vacuum testing was 5×10^{-6} Torr. Vacuum is provided by a diffusion pump with a liquid nitrogen cold trap. The diffusion pump is assisted by a mechanical vacuum pump. The diffusion pump and cold trap arrangement prevents oil vapors from the mechanical vacuum pump to enter the test chamber so as to maintain the desired tribological test condition.

Test Specimens

The test specimens used for this research had a nominal geometry of 35.6-mm (1.4-inch) outer diameter and a 12.7-mm (0.5-inch) width. The roller on the drive motor (input) shaft was made from 15-5 alloy (matching the SARJ raceway material). The roller on the brake (output) shaft was 440C alloy, matching the SARJ roller material. A set of nitrided 15-5 rollers were manufactured to match the processing parameters of the SARJ ring. An additional set of 15-5 rollers without nitriding were manufactured for research purposes. In the remainder of this document we use the term “un-nitrided” to refer to a 15-5 roller that does not have the nitride surface layer. The profile across the roller width for the 15-5 rollers was nominally flat. The mating 440C rollers used for this project had a crown radius profile across the roller width. For the test apparatus used, at least one of the two rollers must be crowned to have a controlled contact condition. The nominal crown radius of the 440C test rollers for this project was approximately 42 mm (1.65 inch). The 440C rollers had a measured surface hardness via a Rockwell tester of typically 56 HRC. The SARJ mechanism makes use of gold-plated rollers. A subset of the 440C rollers were provided with gold plating. All of the gold-plated test rollers were done in a single batch process. The plating vendor reported the applied gold layer thickness as 2300 angstroms.

A photograph of a pair of rollers installed and undergoing test is provided in Figure 6. The upper roller is a 15-5 roller with a nominally flat profile. The bottom roller is the 440C roller having a crown radius. The localized contact provided by the crowned roller is evident in Figure 6.

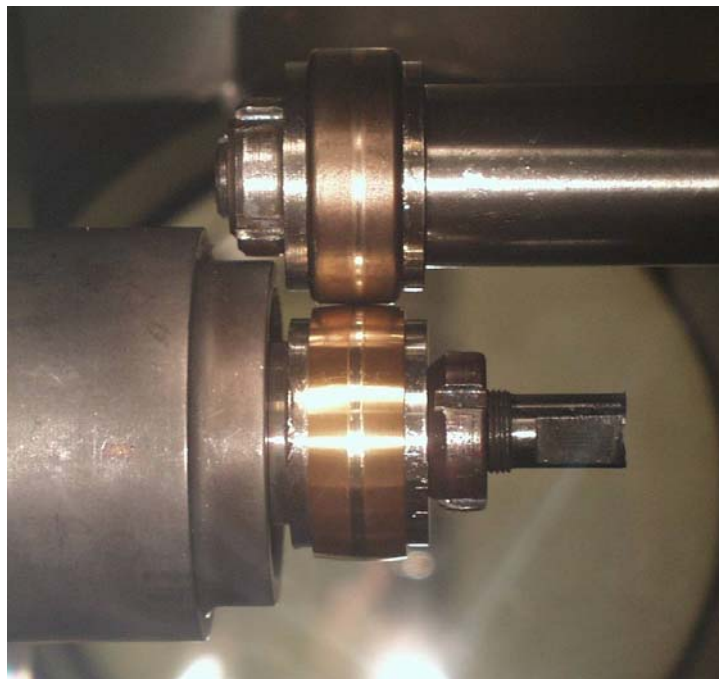


Figure 6 – View of tested rollers in the test apparatus showing localization of the roller contact and crowned profile of the lower roller.

To document the surface condition of the new rollers, rollers were inspected via a stylus profilometer using a diamond-tipped stylus. The data were processed to assess the roughness features. The roughness of a 440C roller was typically 0.14 micrometer roughness-average. The roughness of a nitrided 15-5 roller was typically 0.62 micrometer roughness-average. Plots of the roughness profile for a typical 440C and nitrided 15-5 roller are provided in Figures 7-8 (note the differing automatic scaling used in these two figures).

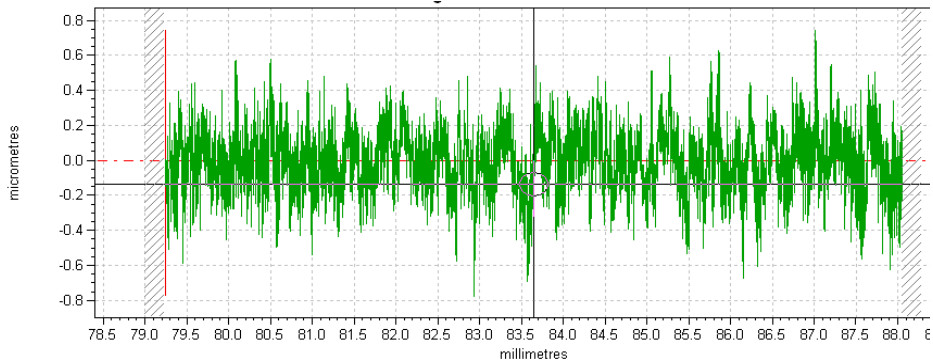


Figure 7 - Typical roughness of a 440C roller.

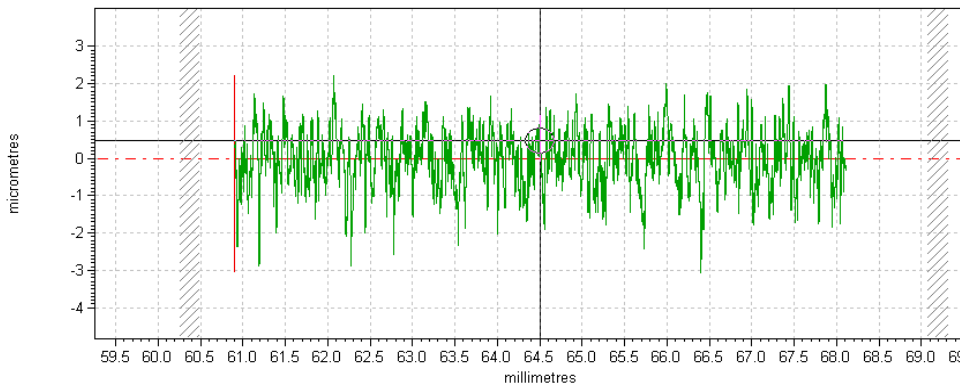


Figure 8 - Typical roughness of a nitrided roller.

Procedure to Install Test Rollers

Test specimens were cleaned and installed using careful procedures to provide a clean test surface. The 15-5 test rollers were cleaned just prior to installation into the rig using de-ionized water and 0.05 micron alumina powder. After appropriate hand scrubbing, the cleaning powder was rinsed with deionized water making sure that the entire roller surface wetted uniformly to confirm complete cleaning of surface oils. The water was removed from the roller using dried pressurized nitrogen. Bare (without gold-plating) 440C specimens were cleaned in the same manner as the 15-5 specimens. The 440C test rollers with gold-plating were vacuum-sealed in plastic bags by the plating vendor, and so cleaning with alumina powder was not needed. The bags remained closed until ready for installation. Test rollers and mounting hardware were handled only with gloved hands and clean tools to complete installation into the test apparatus.

Procedure for Testing Rollers

The first step for testing after installation of the test rollers was to immediately isolate the testing chamber and provide a vacuum, using the mechanical roughing pump, to approximately 50×10^{-3} Torr chamber pressure. This isolation step was done even if test scheduling required some delay between the time of installation of rollers and the time for testing to minimize exposure of the cleaned surfaces to any contaminants that might be present in the atmosphere. Just prior to testing the diffusion pump was energized and the pressure in the testing chamber established to approximately 5×10^{-6} Torr.

Some tests were done to investigate the influence of grease lubrication of the performance of the contacting rollers. For these tests the roller surfaces were lubricated using a space-qualified grease. The base oil of the grease is a stable perfluorinated polyether. The gelling agent is a tetrafluoroethylene telomer. The grease contains molybdenum disulfide. The grease was applied using a syringe. The difference in the mass of the syringe before and after applying the grease was 0.34 gram. The grease was distributed on the rollers by positioning the rollers with only a small gap between them and the shafts were rotated. As the grease became distributed by the shaft rotation the gap between the rollers was slowly reduced in increments. This action proved effective to distribute the grease about the roller circumference, and by visual inspection the distribution of the grease about the roller circumference appeared uniform.

Once rollers were installed and the chamber pressure test condition was established, the next step of the test procedure was to “run-in” the roller surfaces. In general contacting surfaces will quickly “run-in” via wear and deformation of asperity features. The test rig shaft misalignment angle was set to 1.5 degrees and the rollers were brought into contact with approximately 667 N (150 lb) normal force between the rollers. The test rig was operated for at least 1000 shaft revolutions to run-in the test surfaces.

The third step of the test procedure was to smoothly and continuously change the misalignment angle while recording data to investigate the traction capability of the contact. This step was done to establish the relationship of the misalignment angle to the developed axial force. The misalignment angle was changed by hand-turning of a threaded rod to rotate the turntable relative to the rig bedplate. The misalignment angle was swept from a position of approximately 1.5 degrees to a position of -1.5 degrees, and after a short pause the direction reversed and the angle adjusted again in a smooth fashion back to the starting angle of 1.5 degrees. The angle adjustment occurred over a time of approximately three minutes. During these sweeps of the misalignment angle the magnetic-particle brake on the output shaft was not energized, and the recorded torque on the output shaft was in the range 0.8~1.2 N-m (7~11 in-lb). The procedure to adjust the misalignment angle was repeated for 3 values of the normal load, approximately 445, 667, and 890 N (100, 150, and 200 lb).

The preceding paragraphs described the procedure to investigate the behavior of the contact with small torque transmitted by the roller pair. Next, a test was completed to assess the relationship of axial force as a function of the torque transmitted by the rollers for a condition of shaft misalignment of 1.5 degrees. The rollers were the same roller pair as described in the preceding paragraph. The rig was operated at a speed of approximately 15 rpm. The test was done in vacuum of 5×10^{-6} Torr. The normal load between the rollers was 436 N (98 lb). With the test operating, the braking torque on the output shaft was adjusted until the output shaft was at a near stall condition because of the high braking torque. The data was processed to determine the measured axial force as a function of the torque transmitted by the roller pair.

Test Results

Axial Force as a Function of Shaft Misalignment Angle

Data were recorded and processed to determine the axial force created in the direction of the rotational axis of the output shaft as a function of the operating condition. The array of testing that was performed is documented in Table I. Each of the test conditions of Table I were repeated for 3 levels of applied normal load, the targeted loads being 445, 667, and 890 N (100, 150, and 200 lb). A Hertz contact analysis was completed for each of the three targeted load using the calculation method of Hamrock and Brewe [7]. The maximum calculated contact pressures for these loads are 1.55, 1.79, and 1.97 GPa (225,000, 260,000, and 285,000 psi) respectively. The measured loads (as opposed to the targeted test loads) were used for the processing and reporting of data and results.

The axial force that developed in the contact was measured and plotted as a function of the misalignment angle. Figure 9 is a plot of data for the case of un-nitrided 15-5 roller with a 440C roller in a vacuum environment for three levels of normal load. The data has been plotted as a ratio of the measured axial force to the measured normal load as a function of shaft misalignment angle. The data shows that, for

practical engineering purposes of this investigation, the functional relationship of the axial force/normal load ratio to shaft misalignment angle is not strongly influenced by changes in the normal load. To simplify the plotting and discussion of data, the results for the three levels of normal load were treated as a single dataset for the remainder of this report.

Table I – Test Conditions

Roller on input shaft	Roller on output shaft	Grease lubrication?	Chamber condition
un-nitrided 15-5	440C – no plating	no	vacuum
un-nitrided 15-5	440C – no plating	yes	vacuum
nitrided 15-5	440C – no plating	no	vacuum
nitrided 15-5	440C – gold plating	no	vacuum
nitrided 15-5	440C – no plating	yes	vacuum
nitrided 15-5	440C – no plating	no	ambient air

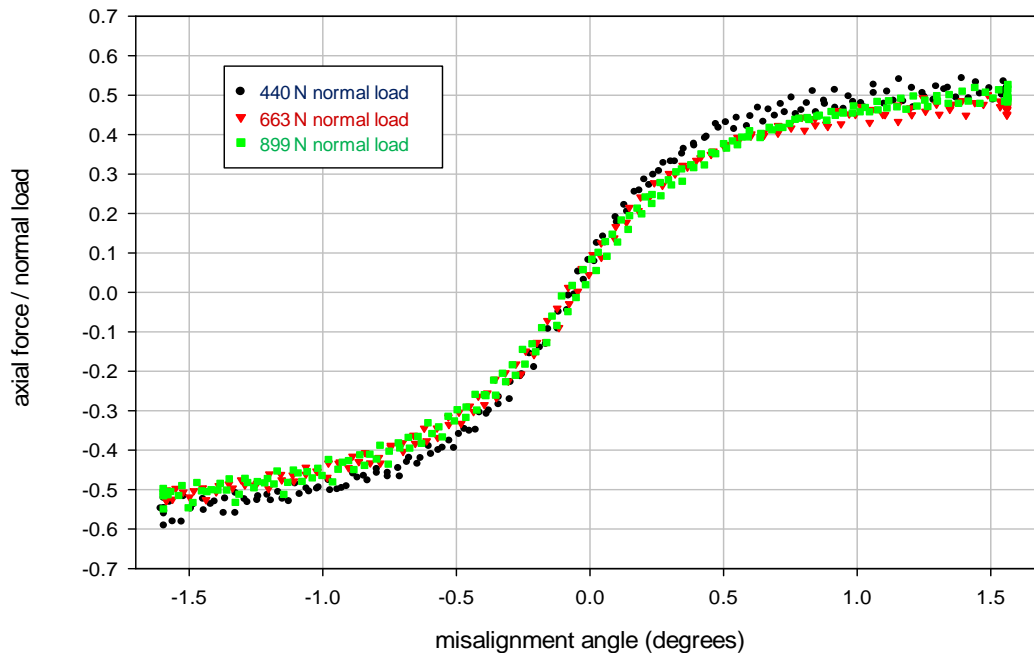


Figure 9 – Ratio of axial load to normal load for three levels of normal load. Test conditions were nitrided 15-5 roller vs. bare 440C (no plating) roller, no grease, in vacuum.

The results of testing at three levels of normal load for the case of a 440C roller mated with a nitrided 15-5 roller and operated in a vacuum are provided in Figure 10. For the case of a bare (un-plated) 440C roller against a nitrided 15-5 roller and without lubrication, the axial force can be as great as 0.4 times the normal load for a shaft angle of 0.5 degree. Experiments and analysis done by others have shown that such a magnitude of force on a SARJ roller would cause roller tipping and contact pressures much greater than anticipated by the designers. However, for the same base materials but provided lubrication via a solid gold film or via grease, the axial force does not exceed about 0.2 times the normal load even for the largest misalignment angles tested. For practical purposes, for the case of lubricated rollers the maximum attainable axial force develops for shaft angles of about 0.5 degree. These test results highlight the critical role of lubrication for the SARJ mechanism.

If the raceway of the SARJ mechanism becomes damaged, it is possible that the un-nitrided substrate will be exposed and will interact with the hardened 440C roller surface. Therefore, it was desired to study the case of un-nitrided material mating with 440C rollers in a vacuum environment. The results of these tests

with the un-nitrided material are provided in Figure 11. The data for nitrided roller is also provided on the chart for comparison. The axial force that develops for the case of un-nitrided vs. 440C with no lubrication is somewhat less than can be obtained for the nitrided surfaces. Still, with no lubrication the axial force can be high, an undesirable condition for the SARJ mechanism. Providing grease lubrication to the un-nitrided 15-5 material greatly reduces the maximum attainable axial force with the value limited to about 10 percent of the applied normal load. Comparing the data for testing with grease (Figures 10 and 11), regardless of the nitrided or un-nitrided condition the functional relationship of axial load to shaft angle is approximately the same, and the axial force is limited to about 15 percent of the normal load.

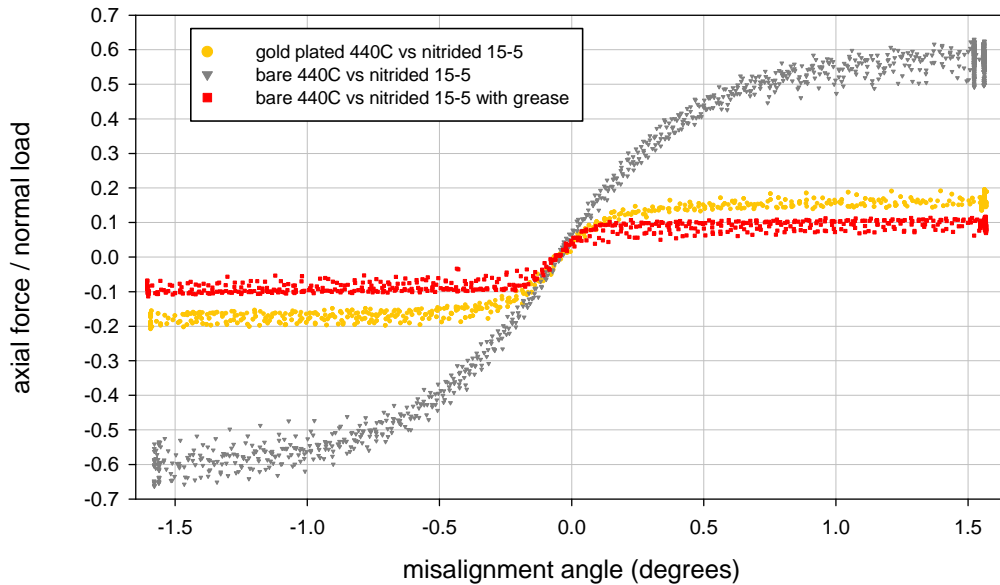


Figure 10 – Axial force as a ratio of the normal load as a function of the shaft misalignment angle when testing nitrided rollers. The data were recorded as three levels of normal load (445, 667, and 890 N) {100, 150, and 200 lb}.

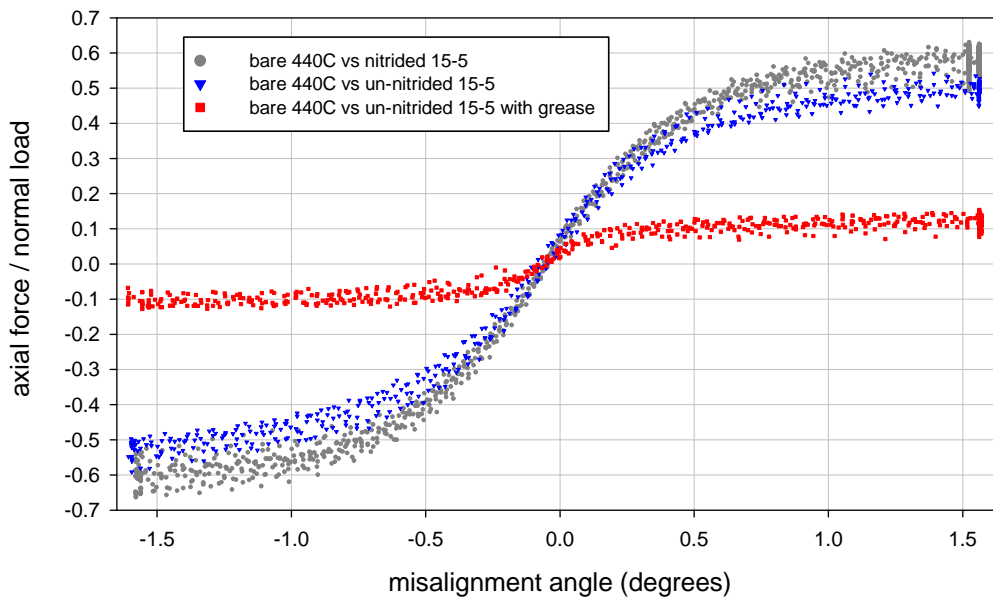


Figure 11 - Axial force as a ratio of the normal load as a function of the shaft misalignment angle when testing un-nitrided rollers. The data were recorded as three levels of normal load (445, 667, and 890 N) {100, 150, and 200 lb}. Data for nitrided rollers from Figure 10 are included for comparison.

Certain testing of the full-scale SARJ mechanism was done in an air environment. To provide some insight about the relative behavior of rollers operating in vacuum or air, a set of tests were conducted in air using a bare 440C roller and a nitrided 15-5 roller with no lubrication. The testing was done for 3 levels of normal load (445, 667, and 890 N), {100, 150, and 200 lb}. The results of the testing are provided in Figure 12. The maximum attainable axial force is slightly less when testing in air as opposed to testing in vacuum. The test was conducted using a pair of rollers that was first exposed to vacuum for testing and then exposed to air for approximately 20 minutes before starting the testing. It is recognized that this lab procedure does not necessarily recreate the surface condition of the SARJ mechanism during full-scale testing. The test data show that high magnitudes of axial force can be created when operating 440C rollers against nitrided 15-5 rollers in air.

The data of Figures 9-12 provide insight about the operation of the SARJ mechanism. Large axial forces can develop even for small magnitudes of shaft misalignment. These axial forces in the case of the SARJ mechanism act via a pivot point in the housing to produce non-uniform contact pressures across the roller width, and if the forces are of sufficient magnitude can cause roller tipping. The experiments and data demonstrate the critical role of good lubrication. The gold films provided good lubrication for the short duration testing done and reported herein. It was noted that the gold did wear away during testing, and by cursory visual inspection the gold appeared to have been removed for the contact path. However, the axial forces remained low indicating good lubrication. Close inspection of the rollers after removal from the rig with the aid of magnification revealed that the gold, while depleted in depth and coverage, was not completely worn away during these tests. The grease lubrication limited the magnitude of the axial forces that could develop to even smaller magnitudes than was achieved with the gold-film lubrication.

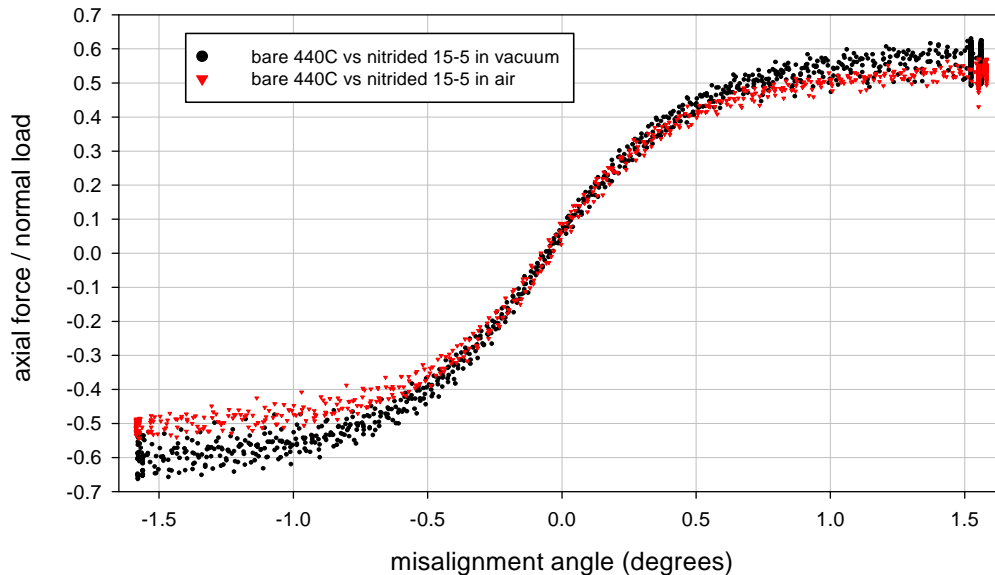


Figure 12 - Axial force as a ratio of the normal load as a function of the shaft misalignment angle when testing nitrided rollers in vacuum and in air. The data were recorded as three levels of normal load (445, 667, and 890 N) {100, 150, and 200 lb}.

Axial Force as a Function of Braking Torque with Shaft Misalignment

The data results presented in the previous section was for the condition of a small amount of torque transmitted by the rollers. To gain additional insight about the behavior of rollers in contact with shaft misalignment, a test was completed to assess the relationship of axial force as a function of the torque transmitted by the rollers for a condition of shaft misalignment of 1.5 degrees. The rollers used for this test were a bare 440C roller and a previously run nitrided 15-5 roller. The rig was operated at a speed of approximately 15 rpm. The test was done in vacuum of 5×10^{-6} Torr. The normal load between the rollers was 434 N (98 lb). With the test operating, the braking torque on the output shaft was steadily increased. The axial force (normalized to the normal load) as a function of the braking torque applied to the output shaft is provided in Figure 13. As the braking torque increased, the axial force decreased as should be expected and will be explained in discussion to follow. The axial force changes in a non-linear fashion with respect to the braking torque on the output shaft. The contacting region between the rollers includes both a stick and slip zones. The transition from stick to slip depends on the total traction force comprised of two orthogonal components, the axial and tangential forces. The application of additional braking torque increase the tangential component of the traction force and thereby alters the contact conditions, with the stick zones decreasing in size and the slip zones increasing in size. This test highlights that the axial force that develops when shafts are misaligned at small angles is largely the result of strains that develop in the stick region of the contact. The total traction force that can be supported by the contact is limited by the frictional condition of the mating surfaces. As was highlighted in the previous section, lubrication limits the total traction capability of the contact and thereby limits the magnitude of the axial force in response to shaft misalignment.

The trends of the data of Figure 13 demonstrate that the axial force to normal load ratio investigated herein, although having a mathematical form matching that of coefficient of friction, is not a direct measure of the coefficient of friction of the contacting surfaces. The friction condition indeed plays a primary role influencing the behavior of the contact. The axial force to normal load ratio is also influenced by the design details and by the operating conditions including the torque transferred by the roller.

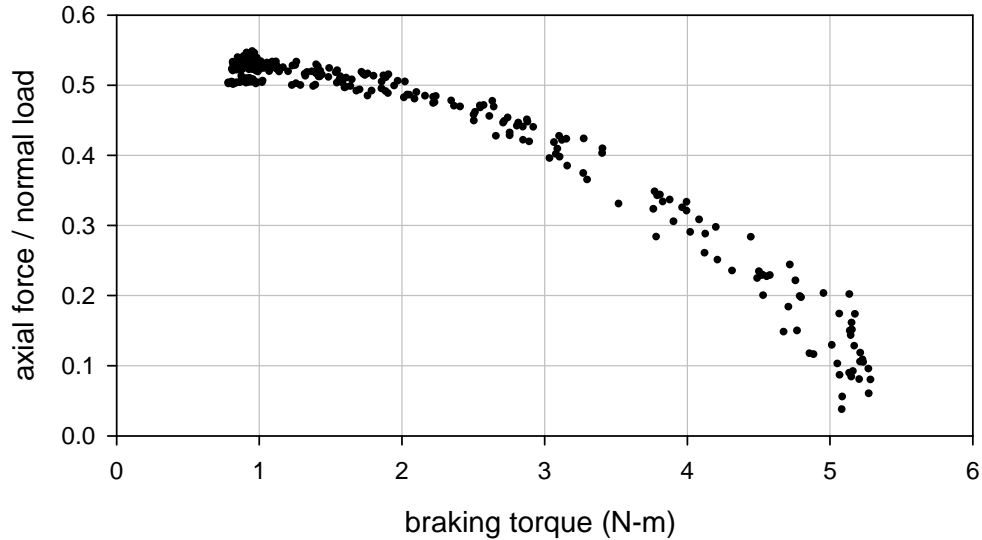


Figure 13 – Axial force as a ratio of the normal load as a function of braking torque applied to the output shaft for a bare 440C roller and a nitrided 15-5 roller operating in vacuum at 15 rpm.

Summary

A set of experiments were done using roller pairs to understand and quantify the forces that can develop for a variety of test conditions. The materials and test conditions were selected to help understand the behavior of the SARJ mechanism. Tests were done using hardened 440C rollers mated with 15-5 rollers, the 15-5 rollers being both in nitrided and bare (not nitrided) condition. Tests were done with no lubrication, solid gold-film lubrication, and grease lubrication. Of great significance to the operation of the SARJ mechanism is the magnitude of the axial force that will develop because of shaft misalignment. The experiments demonstrate the critical role of good lubrication for the SARJ mechanism. The following specific results were obtained:

1. For the case of a bare (un-plated) 440C roller against a nitrided 15-5 roller without lubrication, the axial force can be as great as 0.4 times the normal load for a shaft angle of 0.5 degree. Experiments and analysis done by others have shown that such a magnitude of force on a SARJ roller would cause roller tipping and contact pressures much greater than anticipated by the designers.
2. The axial force for the case of bare (un-plated) 440C vs. un-nitrided 15-5 with no grease is somewhat less than can be obtained using the nitrided 15-5 surfaces. Still, with no lubrication the axial force can be high, an undesirable condition for the SARJ mechanism.
3. For the case of a gold-plated 440C roller against a nitrided 15-5 roller without grease, the axial force does not exceed about 0.2 times the normal load even for the largest misalignment angles tested.
4. For the case of a bare (un-plated) 440C roller against a nitrided 15-5 roller with grease lubrication, the axial force does not exceed about 0.15 times the normal load even for the largest misalignment angles tested.

5. The experiments and data demonstrate the critical role of good lubrication. The gold films provided good lubrication for the short duration testing done and reported herein. Grease lubrication limited the magnitude of the axial force to even smaller magnitudes than was achieved with the gold-film lubrication.
6. For the case of a bare (un-plated) 440C roller against a nitrided 15-5 roller without lubrication, the maximum attainable axial force was slightly less when testing in air as opposed to testing in vacuum.

Acknowledgements

This research was supported by the NASA Engineering Safety Center. The experimental work was done with assistance from Mr. Justin Elchert of Case Western Reserve University as part of the NASA GRC LeRCIP Summer Student Program.

References

-
- ¹. Loewenthal, S. and Schuller, F., "Feasibility study of a discrete bearing/roller drive rotary joint for the Space Station", NASA Technical Memorandum 88800, 1986.
 2. Johnson, K.L., **Contact Mechanics**, Cambridge University Press, 1985.
 3. Kalker, J.J., "Rolling contact phenomena: linear elasticity", Rolling Contact Phenomena CISM Courses and Lectures, Issue: 411, Springer-Verlag, 2000.
 - ⁴. Woody, D. and Lamb, W., "A design for a precision 10-m sub-millimeter antenna", ALMA Memo 241, Mar 1999. <http://www.mma.nrao.edu/memos/html-memos/alma241/memo241a.pdf>, accessed Feb. 26, 2009.
 - ⁵. McGinness, H., "Antenna azimuth bearing model experiment," DSN Progress Report 42-53, July and August 1979, Jet Propulsion Laboratory, Pasadena, Calif., 1979.
 - ⁶. McGinness, H., "Lateral forces induced by a misaligned roller," DSN Progress Report 42-45, March and April 1978, Jet Propulsion Laboratory, Pasadena, Calif., 1978.
 - ⁷. Hamrock, B., and Brewe, D., "Simplified Equation for Stresses and Deformations," ASME J. Lubr. Technol., 105, pp. 171–177, 1983.

Mars Science Laboratory Sample Acquisition, Sample Processing and Handling: Subsystem Design and Test Challenges

Louise Jandura *

Abstract

The Sample Acquisition/Sample Processing and Handling subsystem for the Mars Science Laboratory is a highly-mechanized, Rover-based sampling system that acquires powdered rock and regolith samples from the Martian surface, sorts the samples into fine particles through sieving, and delivers small portions of the powder into two science instruments inside the Rover. SA/SPaH utilizes 17 actuated degrees-of-freedom to perform the functions needed to produce 5 sample pathways in support of the scientific investigation on Mars. Both hardware redundancy and functional redundancy are employed in configuring this sampling system so some functionality is retained even with the loss of a degree-of-freedom. Intentional dynamic environments are created to move sample while vibration isolators attenuate this environment at the sensitive instruments located near the dynamic sources. In addition to the typical flight hardware qualification test program, two additional types of testing are essential for this kind of sampling system: characterization of the intentionally-created dynamic environment and testing of the sample acquisition and processing hardware functions using Mars analog materials in a low pressure environment. The overall subsystem design and configuration are discussed along with some of the challenges, tradeoffs, and lessons learned in the areas of fault tolerance, intentional dynamic environments, and special testing.

Introduction

The Sample Acquisition/Sample Processing and Handling (SA/SPaH) subsystem for the Mars Science Laboratory (MSL) is a Rover-based sampling system capable of operating in the cold temperature, low pressure, reduced gravity environment of Mars (Figure 1). Scheduled to launch in 2011, the Rover carries a suite of ten scientific instruments capable of making remote and *in situ* measurements of the environment and of the rocks and regolith acquired by SA/SPaH. The SA/SPaH acquires rock and regolith samples from the Martian surface, processes them into fine particles through sieving, and delivers small portions of the powder into the two analytical instruments, SAM and Chemin, inside the Rover. SAM analyzes the chemistry relevant for life, including carbon chemistry, and Chemin determines the mineralogy of the delivered powder. The SA/SPaH can acquire powder from rocks at depths of 20 to 50 mm and can also pick up loose regolith with its scoop. The overall scientific goal of the mission is to assess the habitability, both past and present, of the sites visited by the Rover. The duration of the primary mission is one Martian year (approximately two Earth years.)

In order to perform its main functions of examining, acquiring, processing, and delivering samples for scientific investigation on Mars, SA/SPaH consists of a 5 degree-of-freedom, 2-meter-long Robotic Arm which can manipulate the Turret-mounted tools and instruments. The Turret (Figure 2) is approximately 600 millimeters in diameter and contains 5 devices: a powder acquisition Drill, a scooping, sieving, and portioning device called CHIMRA, a Dust Removal Tool (DRT) for clearing the surface of scientific targets, and two contact instruments, APXS and MAHLI, mounted on vibration isolators. APXS, an Alpha Particle X-ray Spectrometer, and MAHLI, an imager, are two of the ten scientific instruments on MSL.

* Jet Propulsion Laboratory, California Institute of Technology, Pasadena, CA

SA/SPaH also contains other hardware that supports the overall sampling investigation (Figures 3 and 4). These include two spare bits for the Drill in individual Bit Boxes, an Organic Check Material (OCM), an Observation Tray, and Inlet Cover mechanisms that are placed over the SAM and Chemin solid sample

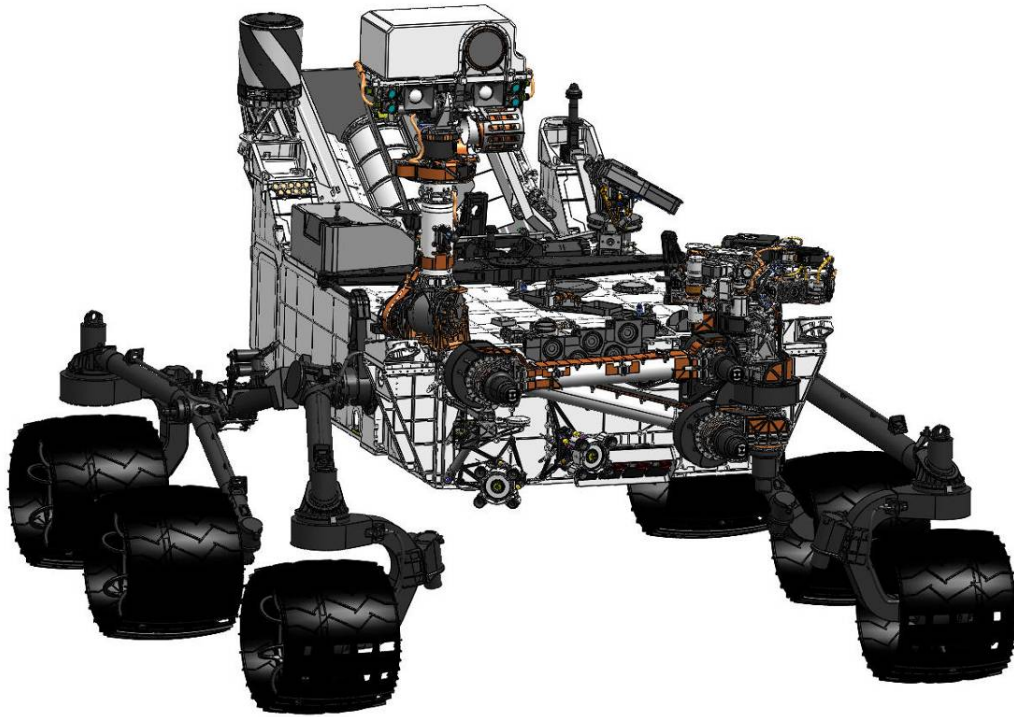


Figure 1. SA/SPaH is mounted on the front of the Rover and is shown in a configuration suitable for driving.

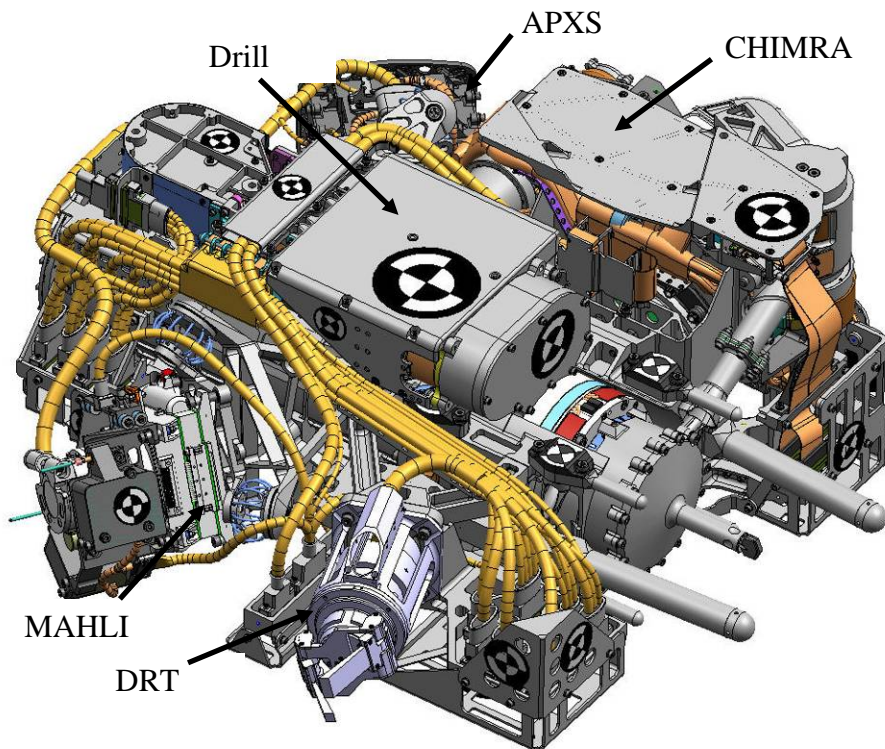


Figure 2. The approximately 600-mm-diameter Turret consists of 5 devices.

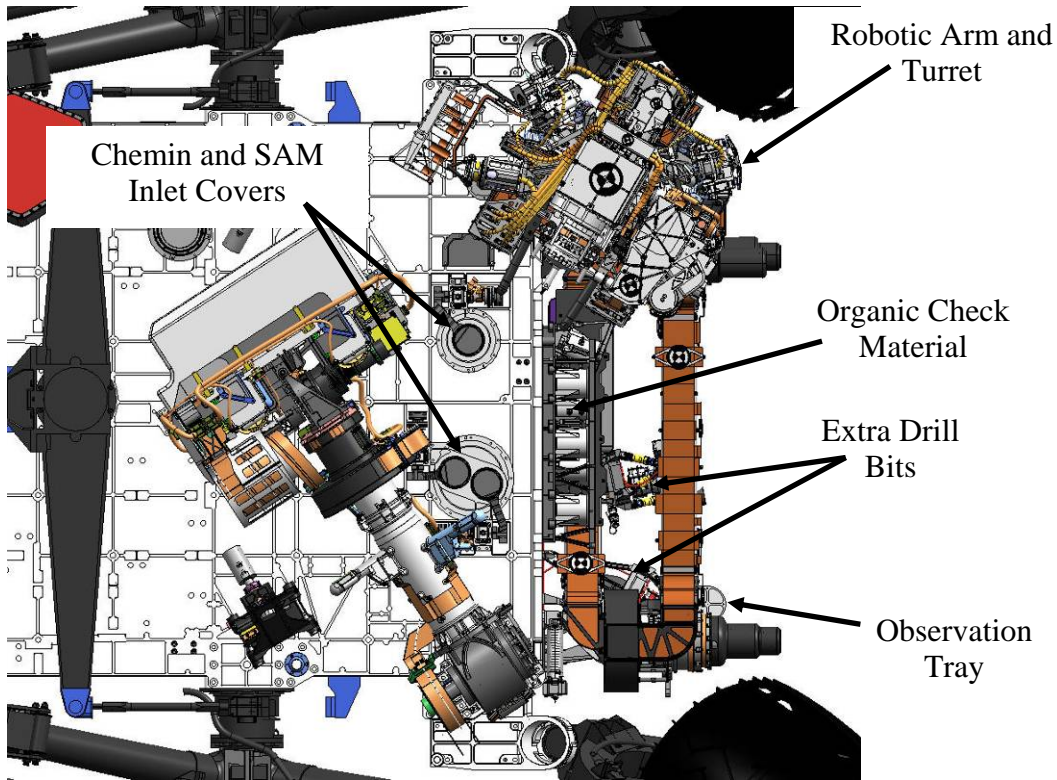


Figure 3. Top View of the stowed SA/SPaH on the Rover

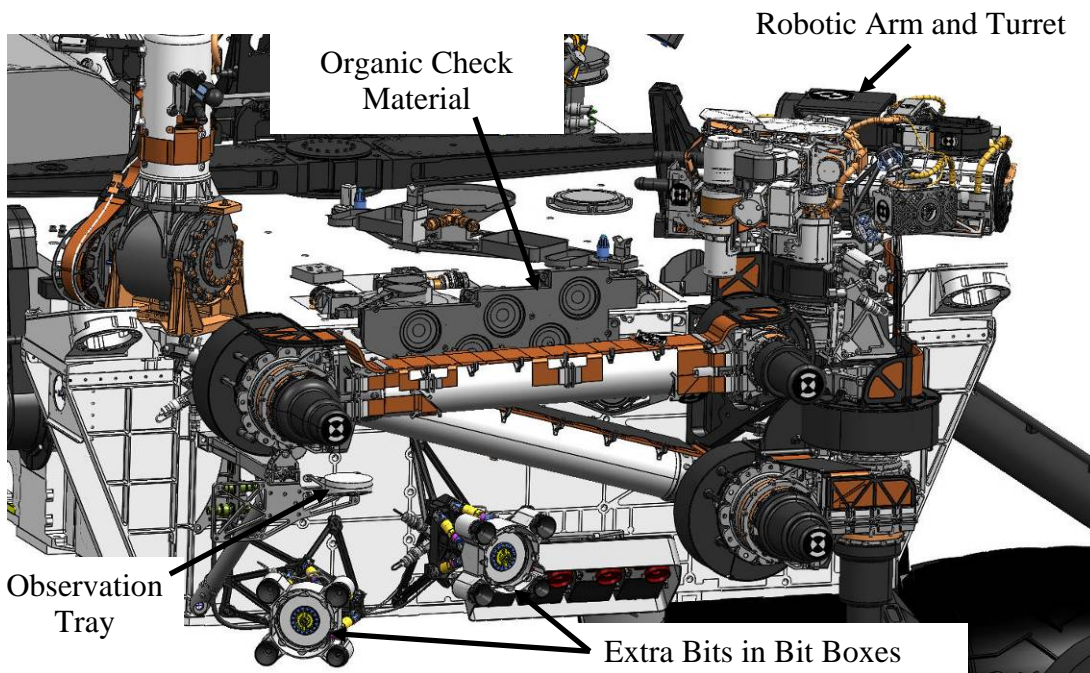


Figure 4. Front View of the stowed SA/SPaH on the Rover

inlet funnels on the Rover deck. The OCM is an inorganic matrix material spiked with a known fluorocarbon calibrant. It is sampled using the Drill and processed with CHIMRA before being deposited in SAM. It is used to assist in the validation of the SAM science results with respect to the detection of organics or the lack thereof. The Observation Tray is a place where sample can be placed for viewing with the APXS or MAHLI. The Inlet Covers are dust covers for the SAM and Chemin funnels.

Subsystem Design and Configuration

The SA/SPaH subsystem is a highly mechanized system with 17 actuated degrees-of-freedom (4 on the Drill, 4 on CHIMRA, 1 on the DRT, 5 on the Robotic Arm, and 3 on the Inlet Covers). Sixteen of the mechanisms are driven by rotary actuators consisting of brushless motors with planetary gearboxes, and encoders as commutation and motor position feedback devices. Drill percussion uses a linear voice coil actuator. Many devices include power-off brakes. The actuators on the Robotic Arm also have output resolvers.

Functionality

These 17 degrees-of-freedom are used in a coordinated fashion to perform the operations used to prepare, acquire, process, and deliver samples, and to support other activities necessary for conducting the scientific investigation on Mars. The required operations are:

- Remove dust from the surface of rocks with the DRT
- Place MAHLI and APXS on rock and regolith targets for *in situ* analysis
- Acquire powdered sample from rock interiors, 20 to 50 mm deep
- Acquire regolith sample from the Martian surface
- Process the sample by sorting into fines less than 150 μm and creating up to 6 portions of volume 45 to 65 mm^3 each
- Process the sample by sorting into fines less than 1 mm and creating a single portion of volume 45 to 130 mm^3
- Deliver the portions of sub-150 μm sample to SAM and Chemin
- Deliver the portion of sub-1 mm sample to SAM
- Deliver the remaining sub-150 μm sample to the Observation Tray
- Use the DRT to clean the Observation Tray
- Place APXS and MAHLI on their respective calibration targets
- Acquire powdered sample from the OCM on the Rover using the Drill
- Acquire a bit from a bit box
- Open and close the Inlet Covers over the SAM and Chemin funnels

The 2-meter-long Robotic Arm places and holds the turret-mounted tools and instruments on both rock and regolith targets in its primary workspace and on Rover-mounted hardware such as the Observation Tray, OCM, and Bit Boxes. The Arm also repositions the Drill and CHIMRA with respect to gravity during their sample processing and sample flow activities. Finally the Arm brings CHIMRA into close proximity with the SAM and Chemin solid sample inlet funnels so that CHIMRA can drop its sample portions into the instruments. Figure 5 illustrates the Arm in representative poses for each of these types of activities. Figure 5a shows operation in the primary workspace. Figure 5b indicates a sample processing activity. In Figure 5c, the Arm positions the Turret near an inlet funnel.

The Turret is formed by attaching the 4 other Turret devices to the Drill. The CHIMRA is connected with a parallel blade flexure, the DRT is connected with a bracket, and both instruments (APXS and MAHLI) have a vibration isolator between it and its mounting bracket connected to the Drill. The Drill is attached to the Arm output plate which is rotated using the Turret actuator of the Arm. It is likely obvious by looking at the Turret in Figure 2 that the task of configuring and packaging the Turret was a very challenging endeavor. The challenge is caused both by the large amount of functionality placed on the Turret and by the number and complexity of the interactions with the Martian surface and the Rover-mounted hardware. Choosing this mounting scheme means that the Drill cannot be removed from the Turret without

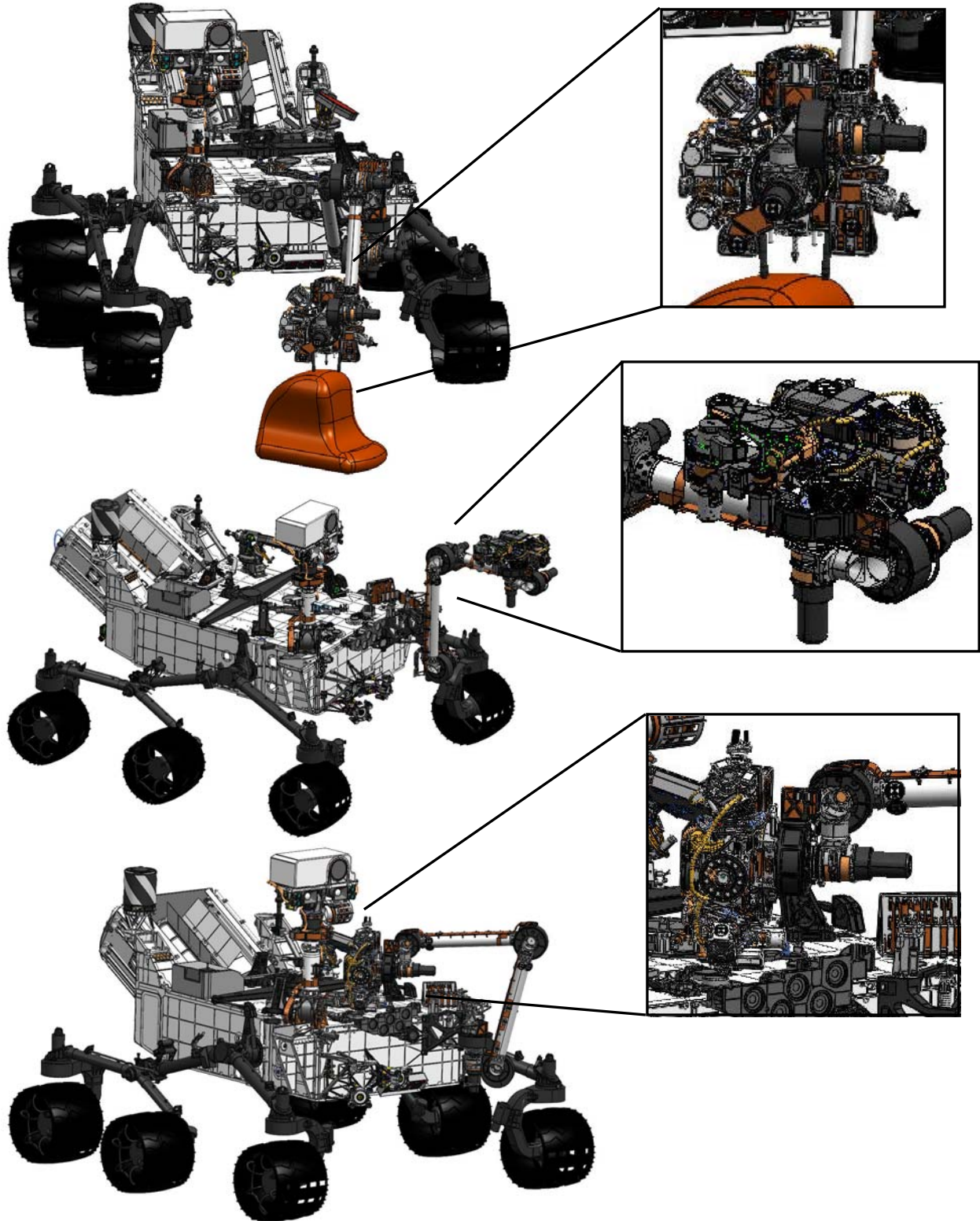


Figure 5. Representative Robotic Arm poses used in sample pathway 1, Drill to sub-150 μm portion: a) Acquiring sample with the Drill, b) Sieving with CHIMRA, c) Depositing a sub-150 μm portion into a SAM Inlet funnel.

disassembly of the entire Turret. Modularity was abandoned in favor of saving the mass and volume of an intermediate mounting structure. Turret mass and volume are both highly constrained resources that had to be committed to early in the design process. Turret mass drives the Arm loads and sizing while Turret volume affects the overall configuration of the subsystem since clearances between the Turret and other hardware had to be considered in both the stowed condition and during operations which put the Turret in close proximity to the Rover.

The Arm exerts large forces between the Drill contact sensor/stabilizer mechanism and the rock surface, stabilizing the Drill against the rock. This keeps the Drill from walking across the rock surface when the cutting bit engages the rock surface. The Arm creates this preload force by placing the Drill against the rock surface using the Drill contact sensor/stabilizer (Figure 5a) and then overdriving the Arm actuators so that the entire system winds up against the overall stiffness of the Arm. The Arm produces >240 N of preload force at its tip in many drilling configurations. The Arm uses the contact sensors on each instrument for placements of APXS and MAHLI. Instrument placements occur with much smaller tip forces (<3.5 N) since neither instrument requires preloading to perform its function.

In SA/SPaH, sample is acquired through either rotary percussive drilling with the Drill on rock targets or by scooping loose regolith with the CHIMRA. The Drill acquires powdered rock samples from up to 50 mm below the rock surface using 3 of its 4 actuated degrees-of-freedom. While the Drill bit is translated into the rock surface, percussion and rotation of the Drill bit also occur to cut and powder the rock material and convey it into the sample collection chamber of the bit assembly. The collected powder travels through the bit using the pathway shown in Figure 6. The fourth degree-of-freedom is used to release the Drill bit assembly from the Drill and to acquire a replacement bit from the front of the Rover. For scooping, the Arm positions the CHIMRA scoop above the loose regolith in an open position. Once positioned, the scoop is closed using its single actuated degree-of-freedom, acquiring material.

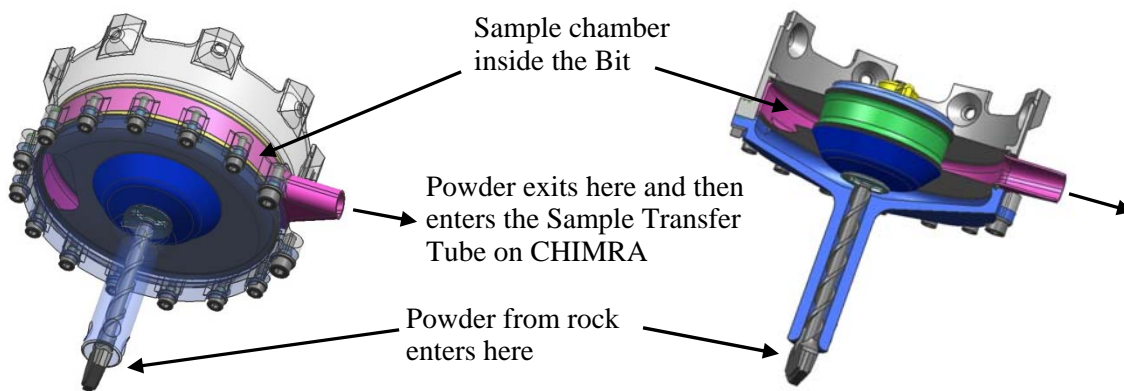


Figure 6. The Drill sample pathway is contained in the Drill Bit. [Reference 1]

Powdered sample from the Drill moves into the CHIMRA for processing using Arm motions to bias the sample flow and Drill percussion to create material motion. All processing of the powdered or scooped samples, which includes sieving and portioning, takes place in the CHIMRA. Various chambers, labyrinths, and sieves within CHIMRA are used to sieve and portion the material. These functions are carried out by rotating the Arm Turret Actuator to align CHIMRA with respect to the gravity vector to bias the sample flow into the desired chamber while producing material motion with a vibration mechanism. Figure 7 depicts the sample pathways used in the CHIMRA to perform its processing functions. The CHIMRA sieves are mounted to mechanisms that impart shock into the sieves to clear and clean them, preventing cross-contamination and clogging throughout the mission life. This is termed thwacking. The intentional dynamic environments created to move sample around are a key feature of the subsystem and device designs. These are percussion in the Drill and vibration in the CHIMRA. Orientation with

respect to gravity is used only to bias the direction of sample movement but nowhere within the subsystem is gravity relied upon as the sole prime mover.

Sample Paths

The functionality described in the previous section supports the following five minimum sample pathways required for the scientific investigation on Mars.

1. Acquire rock sample with the Drill and deliver up to six 45-65 mm³ portions of particles less than 150 μm to SAM and Chemin.
2. Acquire regolith sample with the CHIMRA Scoop and deliver up to six 45-65 mm³ portions of particles less than 150 μm to SAM and Chemin.
3. Deliver the remaining bulk processed sub-150 μm sample (rock or regolith), after portioning to SAM and Chemin, to the Observation Tray.
4. Acquire regolith sample with the CHIMRA Scoop and deliver one 45-130 mm³ portion of particles less than 1 mm to SAM.
5. Acquire OCM sample with the Drill and deliver up to six 45-65 mm³ portions of particles less than 150 μm to SAM and Chemin.

Figure 5 illustrates three representative Robotic Arm poses used during sample pathway 1. In Figure 5a, the Arm has positioned and preloaded the Drill on the target rock. The Drill then uses its translation, percussion, and rotation degrees-of-freedom to powder the rock and auger the powder into a collection chamber in its Drill bit assembly. Sample moves from the Drill bit assembly into CHIMRA through a Sample Transfer Tube connecting the two devices. Particle motion is accomplished by using the Arm to bias the particle flow with respect to gravity and alternately turning on Drill percussion and CHIMRA

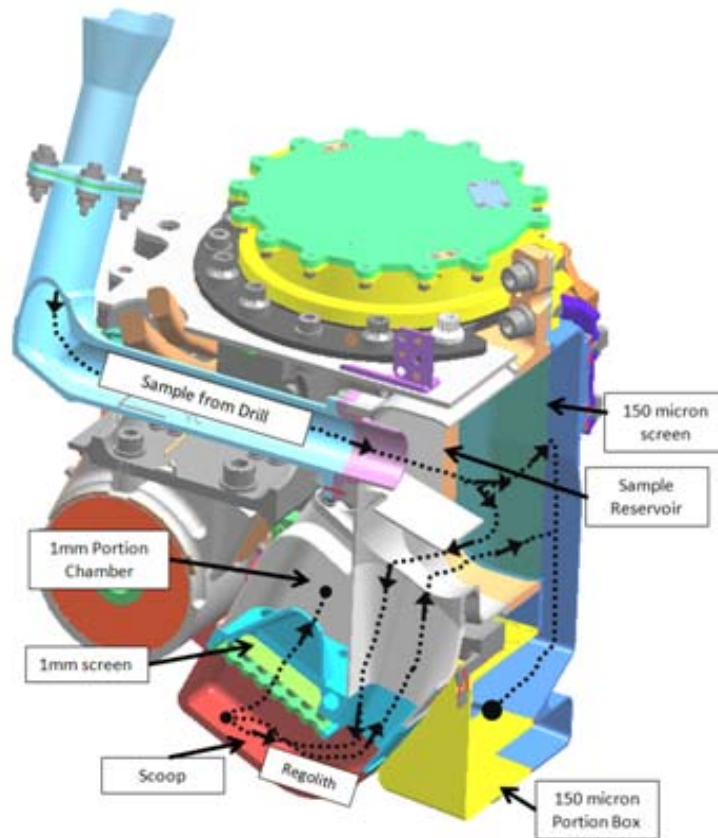


Figure 7. CHIMRA has three required sample pathways: Drill to sub-150 μm portion, Scoop to sub-150 μm portion, and Scoop to sub-1 mm portion. The Drill to sub-1 mm portion pathway is also physically possible. [Reference 2]

vibration until the powder has moved from the Drill to CHIMRA. Once inside CHIMRA, powder moves using Arm repositioning and CHIMRA vibration until the pose in Figure 5b is achieved. In this pose, the powder is above the 150- μm sieve. CHIMRA vibration operates until all particles smaller than 150 μm have passed through the sieve. Arm repositioning and CHIMRA vibration is again used to move the sieved particles into the portioning chamber and to create the 45-65 mm^3 portion. The Arm moves CHIMRA to the position in Figure 5c above one of the SAM inlets. The Inlet Cover door opens, the CHIMRA portion door opens, and vibration moves the portion into the funnel. CHIMRA can create and deliver additional portions to either SAM or Chemin. If none are desired by either instrument, the Arm moves CHIMRA away and the Inlet Cover door closes. At this point a number of different choices are available. The Arm can move CHIMRA into a position where it can be opened up and viewed by the Rover cameras. The remaining sub-150 μm particles can be placed on the Observation Tray for viewing by the APXS or MAHLI or all the remaining material can be discarded onto the ground. After CHIMRA uses vibration and thwacking to clean itself, it is ready to process a different sample.

Fault Tolerance

As described in the previous sections, the 17 actuated degrees-of-freedom in the SA/SPaH subsystem are arranged to provide the required functionality and create the 5 minimum sample paths needed to support the scientific investigation targeted at the acquisition and analysis of rocks and regolith. A mix of hardware redundancy and functional redundancy is used with the components of the sample paths to ensure that in the event of a failure, some of the sample paths remain intact. In addition to the hardware components of the SA/SPaH subsystem (Arm, Drill, CHIMRA, Inlet Covers), consideration must be given to the science instruments the SA/SPaH feeds with sample (SAM, Chemin), and the motor drivers.

The Arm is critical to all aspects of the sampling functionality and all 5 sample paths because it positions and manipulates all the Turret-mounted tools. The failure of any Arm joint severely degrades the subsystem functionality and leaves none of the 5 sample paths viable. Therefore the approach here is to provide hardware redundancy, particularly in the electrical circuits required for Arm use. The Avionics subsystem provides the capability to operate 8 actuators simultaneously across all the Rover functionality (32 actuators total, 17 in the SA/SPaH). Multiplexing of the motor drivers provides the needed operations. Due to the importance of the Arm functionality, the multiplex table has a backup driver available if a primary driver for an Arm joints fails. These redundant drivers for each Arm joint are carried in separate cable paths in both the round wire and the flex cable out to each Arm actuator. Moreover these are carried through multiple lines in the flex cable so in the event of a problem in one of the lines, a degraded torque capability would be available. The windings of the motor are not fully redundant but again these elements are created by multiple physical wires terminated at multiple pins so a degraded torque capability would be available in the event of a problem. Each Arm actuator has a power-off brake that is mechanically engaged when non-powered to lock the motor rotor, preventing rotation. A brake solenoid is energized to release the motor. The brakes have redundant coils, each capable of releasing the brake, energized by separate brake drivers and separately cabled. All actuators with brakes on the Rover are configured with redundant solenoids. The mechanical components of each Arm actuator such as bearings, gears, and shafts are not redundant. The life requirement for the Arm joints is not very large: 6000 output cycles or less, depending on the joint. Ensuring a reliable design is done through life testing of a qualification unit.

Instead of using a hardware redundancy approach, the Drill and CHIMRA taken together are designed to have functional redundancy in the overall ability to acquire, process, and deliver samples to the SAM and Chemin instruments. Multiple sample paths from acquisition to depositing into Instrument Inlets exist and while all paths are not equally important to the science investigation, all provide useful science. Figure 8 illustrates the Drill, CHIMRA, and Inlet Cover functions comprising each of the 5 sample paths and the required degrees-of-freedom to perform each function. Except for CHIMRA Vibe, the failure of a single actuated degree-of-freedom can cause the loss of a function and the loss of one or more sample paths but other sample paths remain viable. Due to its importance in all the CHIMRA functionality, CHIMRA

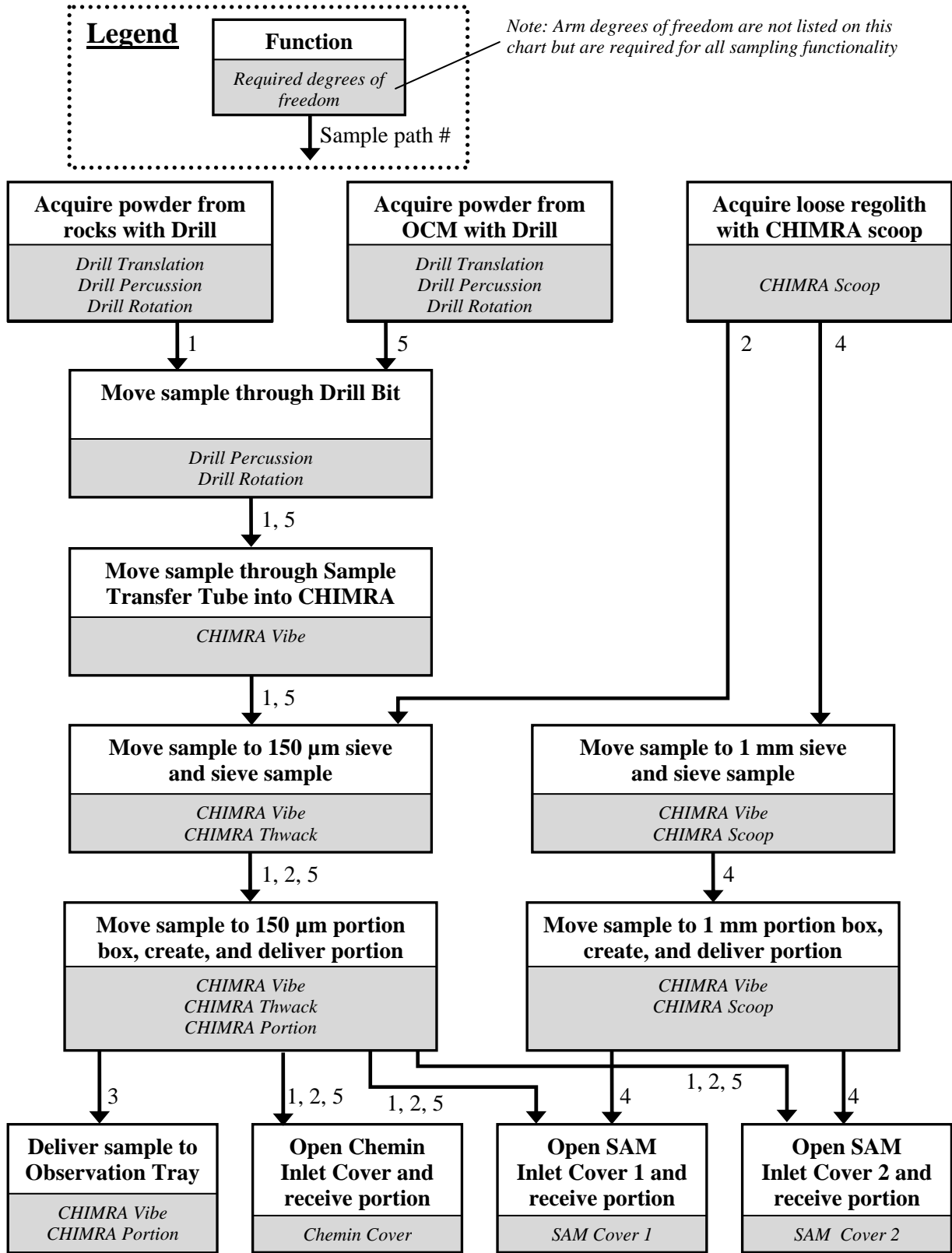


Figure 8. Flowchart of the Drill, CHIMRA, and Inlet Cover functions comprising the 5 sample pathways and the individual degrees of freedom required to perform the function.

Vibe was a likely candidate for hardware redundancy, however there was no place to package a redundant mechanism. Unlike the Arm joints, Vibe requires a high-speed, high-life mechanism so electrical circuit redundancy without mechanical redundancy is not as strong a solution and was not pursued. Instead, Drill percussion may be a viable backup for CHIMRA vibration during these activities. Initial indications from dynamic characterization testing show promise for this possibility but the result will not be definitive until it is demonstrated with sample.

Another failure scenario considered along the sample paths is clogging. This is prevented most effectively through good design practices: large physical paths where particles flow and large margin in the vibration and percussion used to move the particles. The redundant sample paths in CHIMRA allow for some functionality if one path is clogged. CHIMRA can also be opened up and viewed by the Rover cameras which may assist in diagnosing the clog and using dynamic inputs to clear it. However, if the failure to acquire sample with the Drill or to move sample through the Drill is due to clogging of the bit with sample, the bit can be exchanged for a spare bit. Bit release can also be used if the bit is stuck in the ground and cannot be extracted using the large retraction force capability of the Drill translation mechanism.

To enable the effective use of the functional redundancy approach for the Drill and CHIMRA, both the Turret configuration and the subsystem hardware configuration must ensure that the failure of one tool does not preclude the use of the others. More specifically, a CHIMRA scoop or thwack actuator failed in any position cannot prevent the use of the Drill and a Drill feed actuator failed in any position cannot prevent the use of the CHIMRA. In addition these failures cannot prevent the Arm and Turret from returning to its restraint for driving.

Lessons

In a sampling system of this complexity, there is an inherent tradeoff between redundancy of capability (function) and breadth of function when choosing the required sample pathways. The specific choices have consequences for both the kind of scientific investigation that can be conducted and for the engineering implementation so the appropriate balance needs to be achieved through iterative conversations between engineering and science. Moreover, the fault tolerance approach is intimately connected to these choices and needs to be considered at this point in time.

The required sample paths must be determined early in the design phase and specified completely by defining the volume of sample, particle size, processing steps, and sequence of processing. The processing of sample and movement of material are volume intensive activities. Sample paths need to be configured and volume and mass resources allocated to the functions so the detailed mechanical design can begin. Once sample paths are selected, the system rigidizes around them and significant changes are no longer possible. The process here is analogous to configuring a spacecraft.

Dynamic Environments

Both the Drill and the CHIMRA create intentional operational dynamic environments to perform their functions on the rocks and regolith they operate on. Although this approach is a robust way to move sample, there are difficulties and challenges with creating an intentional dynamic environment on the coupled dynamic system of the Arm and Turret. One of the main challenges is to create the dynamic environment in the areas where it is needed (the sample processing and flow areas) while keeping it away from the places it is unwanted (the sensitive Turret-mounted instruments, APXS and MAHLI).

The basic design concept for the Turret regarding operational dynamic environments is to separate the operational frequencies of the Turret-mounted tools, CHIMRA and the Drill, and to provide isolation for the Turret-mounted instruments, APXS and MAHLI. Drill percussion operates at about 32 Hz. The translating components inside the Drill are mounted on springs that act to reduce the kickback force disturbance to the rest of the Turret devices from percussion. CHIMRA vibration is created by rotating an eccentric mass at a constant speed where the speed is chosen to be at the frequency of a CHIMRA mode of vibration. Some adjustment of the CHIMRA frequency can be made by changing the thickness of

the parallel blade flexure. The vibration level is adjusted by changing the amount of the eccentric mass and the mass is chosen to produce between 4 and 10 G at the 150- μm sieve. Development testing showed that 150- μm sieving required the highest level of vibration among all the CHIMRA sample functions. 4 G at the 150- μm sieve provided performance with margin for sieving the most difficult material that was tested. 10 G was used as the design limit. An initial prediction of the CHIMRA vibration mode was about 85 Hz but the range of 70-100 Hz was reserved to account for uncertainties. The Turret design keeps the non-CHIMRA Turret modes out of the 70-100 Hz range to minimize the coupling between CHIMRA modes and other Turret modes through frequency separation. The Instrument Isolators are required to limit the Instrument response at the Instrument mounting interface to: 1) 4 G during steady state operation of the CHIMRA and the Drill, and 2) 6 G during transient operation of the CHIMRA and the Drill (such as startup).

The initial Isolator design concept was composed of six linear compression spring struts in a hexapod arrangement (Figure 9). The isolation performance of this concept can be accurately modeled so the spring stiffness can be chosen analytically and then confirmed by test without numerous iterations, a clear advantage over the final wire rope design. However, this design did not fit within the severe volume constraints on the Turret. Also the part count and mechanical complexity of the spring struts was higher than the wire rope Isolator design.

Our wire rope Isolator design (Figure 9) is based on a commercial product used for disturbance attenuation for equipment mounted on aircraft and in shipping containers. It is a mechanically simple component but it is highly nonlinear and not easily modeled. Testing showed that as the disturbance amplitude increases, the Isolator frequency decreases. Sizing our Isolator design required numerous development test iterations. After the desired loop length was chosen by testing the commercial versions, an Isolator suitable for flight was created using aluminum caps with stainless steel wire rope bonded into holes tailored to provide a good bonded joint. Further development testing determined the appropriate number of wires needed for each Instrument Isolator to meet its performance requirements while minimizing the instances of the Isolator bottoming out during random vibrate testing. Response limiting during random vibrate testing is also being used to prevent this issue.

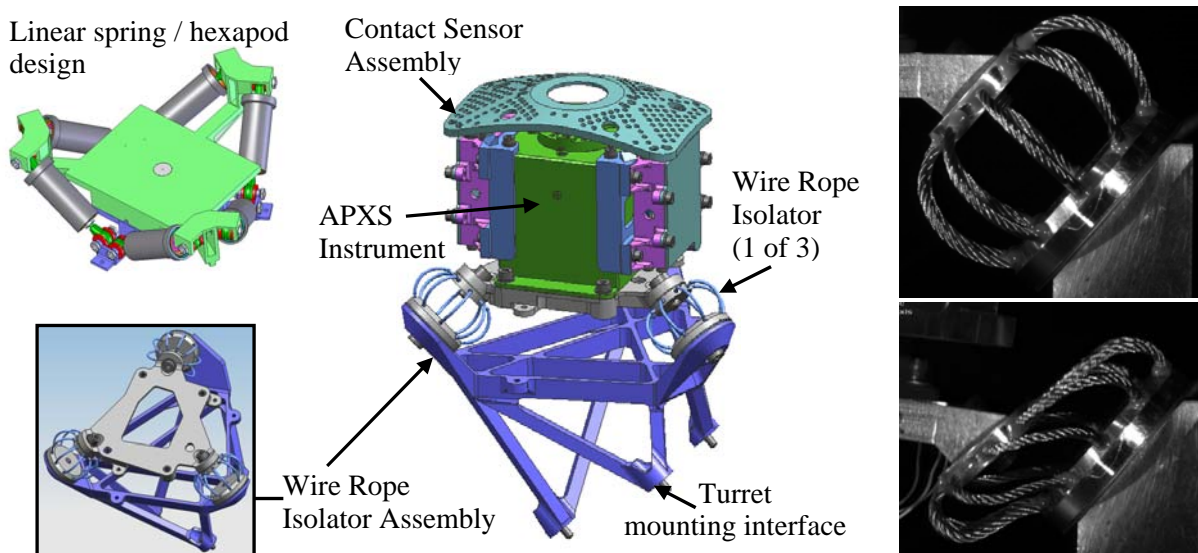


Figure 9. Two Isolator designs were considered before the wire rope design was chosen. The APXS instrument is shown on its wire rope Isolator. One of the wire rope Isolators is shown deforming under the PF level launch environment during an Instrument Isolator development test.

Lessons

When using large intentional operational dynamic environments in a sampling system, anticipate the need for isolation to protect sensitive instruments located near the dynamic sources. Address the need early on in the subsystem configuration studies by either using discrete isolator assemblies (as in SA/SPaH) or by physically separating these instruments from the dynamic sources in the overall configuration.

The wire rope isolator proved to be an effective solution for our space-constrained Turret but at the expense of lots of development test time.

Testing

For many elements of the SA/SPaH design, testing began with development testing on specific functions of sampling to determine and appropriately size the basic elements of the subsystem and the devices within the subsystem. These tests informed our hardware design choices and were used extensively in the areas where new designs were developed such as the Drill, CHIMRA, DRT, Instrument Isolators, and Bit Box. Development testing was the start of our process of risk reduction and subsystem characterization.

All SA/SPaH hardware elements have both an Engineering Model (EM) and a Flight Model (FM). EM units are flight-like but generally see a reduced test program (no random vibrate and limited or no thermal testing) prior to delivery to a system testbed. EM tests for the Drill, CHIMRA, and Arm are targeted at understanding the mechanism performance. In the testbed, this hardware is eventually assembled into a Rover-based SA/SPaH subsystem and operated with flight-like electronics and flight software in an Earth ambient environment, including operations on rocks and regolith. In a few instances (DRT, Instrument Inlet Covers, and Instrument Contact Sensors), EM units see a full test program and serve as Life Test Units prior to testbed delivery. FM units see a full test program designed to prove acceptance for flight.

In addition to the EM and FM units, the Drill, CHIMRA, and Instrument Isolators also have a Qualification Model (QM). QM units are used for mechanism life tests, structural verification, sampling verification and validation (operating on Mars analog rocks and regolith in a low-pressure Mars environment over the temperature range), validation of the contamination control processes, and thermal characterization.

The Drill and CHIMRA in the integrated Turret configuration form a critical portion of the MSL sample chain from acquisition of material until deposition into the analytical instruments. In addition to the typical flight hardware qualification test program, two additional types of testing form an essential part of the test program. The first is the dynamic characterization of the Turret hardware to its self-induced operational dynamic environments of CHIMRA vibration and Drill percussion. The second is the testing of the sample acquisition and processing hardware functions using Mars analog materials in a low-pressure Mars environment over the required temperature range.

The flight-like EM Turret, consisting of the EM Drill, CHIMRA, Instrument Isolators, mounting brackets, and mass models in place of the DRT, APXS, and MAHLI, was assembled on the EM Arm (Figure 10). The Turret and Arm were heavily instrumented with accelerometers to measure the response to CHIMRA vibration and Drill percussion in various Arm poses relevant to the SA/SPaH functions. Locations include the soft side of the MAHLI and APXS Isolators, near each CHIMRA sieve, the Sample Transfer Tube, the Drill aft housing, and some of the Arm joints (a total of 10 3-axis accelerometers).

The purpose of Turret dynamic characterization testing is to determine the response to CHIMRA vibration and Drill percussion at critical locations on the Turret, to find the frequency of the CHIMRA mode, therefore determining the operating speed of CHIMRA vibrate, to select the value of the eccentric mass that produces 4-10 G on the primary sieve, and to confirm that the Isolator requirements are met in the presence of the Drill and CHIMRA operational dynamic environments. Figure 11 shows two of the many poses characterized in the testing. The primary sieve pose is a particularly important one since it sizes

the eccentric mass. Data were taken with the Arm in the sieve pose with the Turret at different angles and the Drill in the surface stow position. The Drill surface stow position aligns the sample exit on the Drill bit with the Sample Transfer Tube. In the nominal operating position (Turret at 180 degrees), the results show the Instrument response meets the 4 G requirement during steady state CHIMRA operation with the steady state response at CHIMRA set near 8 G in the X direction. The CHIMRA response in the Y and Z directions is less than 4 G. No higher response was observed during startup. It is interesting to note that by changing the Turret position, the CHIMRA response can be increased or decreased (over the range of 7 to 10.5 G in the X direction) while still meeting the Instrument requirements. This may prove to be a useful feature if difficulties are encountered during testing or on Mars.

The EM Turret is about to begin testing with Mars analog materials in a low-pressure environment which is called EM Dirty Testing to highlight the fact that rocks and regolith are being processed. Although extensive development testing was done, this is the first testing with Mars analog materials on flight-like hardware in an assembled flight-like configuration.



Figure 10. The assembled EM Turret with the Drill, CHIMRA, and Instrument Isolators installed. Mass models are used for the DRT, APXS, and MAHLI.

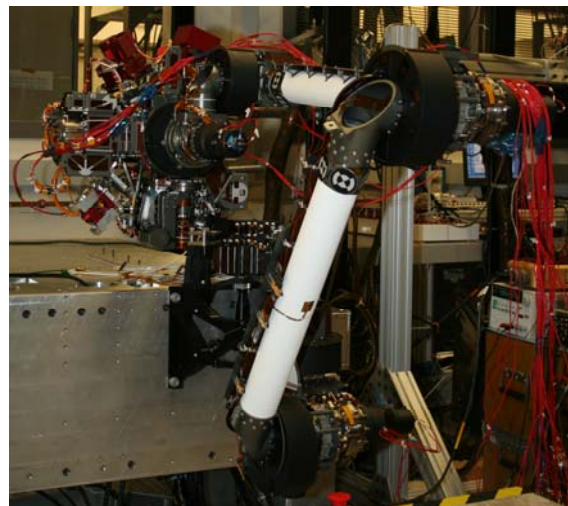


Figure 11. The EM Turret / Robotic Arm during dynamic characterization testing: primary sieve pose with the Turret at 180 degrees (left) and depositing a 150-µm portion (right).

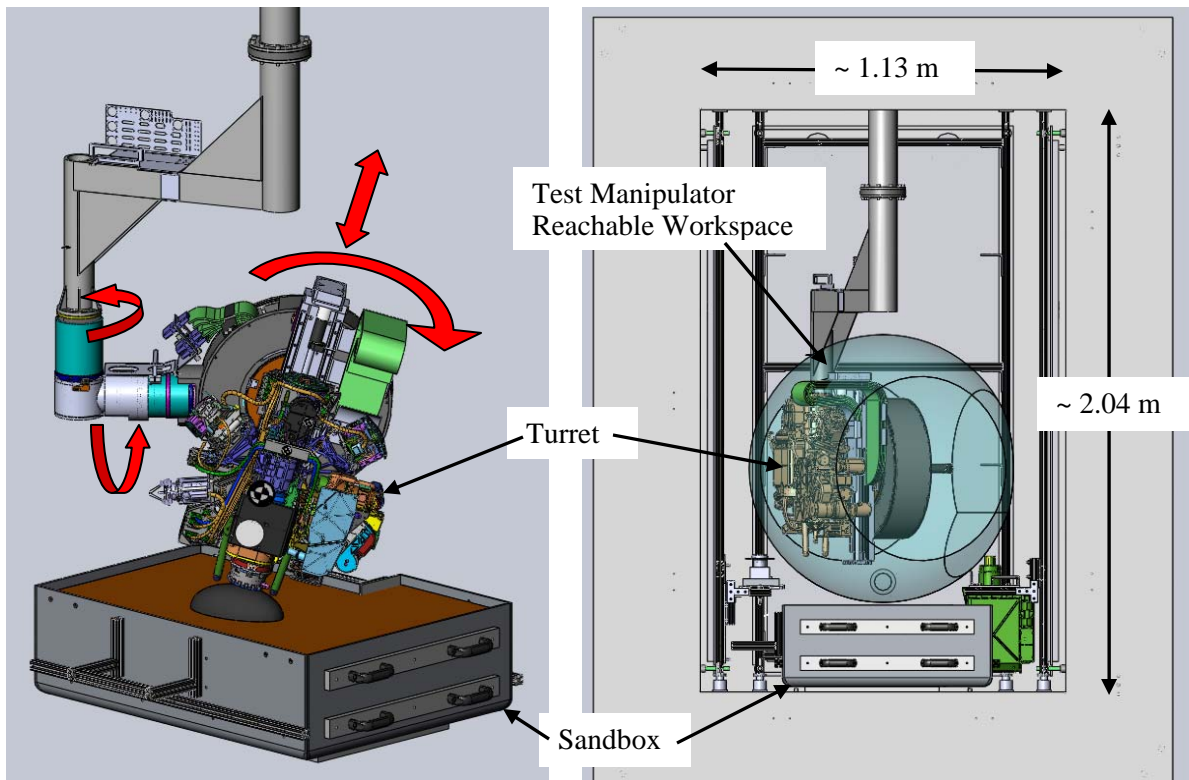


Figure 12. The Turret is shown installed on the test manipulator and drilling a rock in the sandbox (left) and inside the chamber (right).

Figure 12 illustrates the Turret installed on the test manipulator and in the test chamber. The 4 degree-of-freedom test manipulator was developed as a substitute for the Arm during both the EM and QM Dirty Test programs for two reasons. One is that no Arm is available to support these tests since the EM Arm is fully subscribed in the testbed and there is no QM Arm. Two is the test manipulator enables the testing to occur in a chamber that is more manageable in size than the one that would accommodate the Arm. The more manageable size comes at the cost of another dynamic characterization program. Dynamic characterization of the EM Turret instrumented with accelerometers on the test manipulator will be done in the same manner as when it was installed on the Arm. For the sampling functional performance results on the test manipulator to be valid, the Turret response needs to reproduce or be bounded by the Turret response on the Arm so the functional performance can be linked to the operational dynamic environment that the flight configuration produces. Adjustments in the test manipulator after characterization may be required to accomplish this.

Lessons

Characterize the operational dynamic response in hardware configurations other than the nominal ones. Although this time will be difficult to find in the typically oversubscribed test schedule, it can result in ways to alter the behavior of the system that may prove useful when difficulties are encountered both in the Earth-based sampling testing and in service on Mars.

The additional complexity added to the test program when using intentional dynamic environments to process sample cannot be overstated. Care must be taken to ensure that the relevant environment is produced when the hardware test configuration changes.

Conclusions

The MSL SA/SPaH has been designed and implemented, with flight-like EM hardware about to start Dirty Testing and the remaining hardware (QM, FM) soon to follow. Along the way some lessons were learned in subsystem configuration, fault tolerance, intentional dynamic environments, and special testing. Additional lessons are still to come as the EM, QM, and FM test programs are completed.

Acknowledgements

The work described in this paper was performed by the Jet Propulsion Laboratory, California Institute of Technology, under contract with the National Aeronautics and Space Administration.

Creating something like the SA/SPaH and producing it for flight is an enormous undertaking that relies on substantial contributions from far too many people to name effectively. So I will acknowledge a set of JPL people while recognizing that they like me are just the most visible representatives of the group. The hardware cognizant engineers and their teams have worked tirelessly for years to reach this point: Kyle Brown (Bit Box), Brett Kennedy (Robotic Arm), Dave Levine (Turret Configuration, Isolators), Avi Okon (Drill), and Dan Sunshine (CHIMRA). Mark Balzer, Richard Barela, Kevin Burke, Joe Melko, Suparna Mukherjee, Matt Orzewalla, Don Sevilla, Lori Shiraishi, Jeff Umland, and Chris Voorhees have made substantial contributions, also for years. Special thanks go to Dave Putnam of Lockheed Martin, Sunnyvale, who spent a great deal of time with the team when the Drill and CHIMRA mechanisms were in their infancy.

References

1. Okon, Avi B. "Mars Science Laboratory Drill." *Proceedings of the 40th Aerospace Mechanisms Symposium*, (May 2010).
2. Sunshine, Daniel. "Mars Science Laboratory CHIMRA: A Device for Processing Powdered Martian Samples." *Proceedings of the 40th Aerospace Mechanisms Symposium*, (May 2010).

Mars Science Laboratory CHIMRA: A Device for Processing Powdered Martian Samples

Daniel Sunshine*

Abstract

The CHIMRA is an extraterrestrial sample acquisition and processing device for the Mars Science Laboratory that emphasizes robustness and adaptability through design configuration. This work reviews the guidelines utilized to invent the initial CHIMRA and the strategy employed in advancing the design; these principles will be discussed in relation to both the final CHIMRA design and similar future devices. The computational synthesis necessary to mature a boxed-in impact-generating mechanism will be presented alongside a detailed mechanism description. Results from the development testing required to advance the design for a highly-loaded, long-life and high-speed bearing application will be presented. Lessons learned during the assembly and testing of this subsystem as well as results and lessons from the sample-handling development test program will be reviewed.

Introduction

The CHIMRA (Collection and Handling for *In situ* Martian Rock Analysis) is the sample processing device for the Mars Science Laboratory (MSL). Scheduled to launch in the fall of 2011, MSL is the next step in NASA's search for evidence to determine if the red planet's environment was, or still is, suitable for microbial life. To accomplish this goal, MSL houses an advanced suite of scientific instruments that will be able to ascertain whether the local geological environment contains the chemical building blocks of life. In order to feed science samples directly to these instruments, MSL required a state-of-the-art Sample Acquisition / Sample Processing and Handling (SA/SPaH) subsystem able to collect, sort, and deliver acquired samples to instruments in the rover. Utilizing a five degree-of-freedom robotic arm (Figure 1) and a rotary percussive drill that forms the backbone of a five instrument turret (Figure 2) the SA/SPaH subsystem is able to collect powdered rock from depths up to 50 millimeters. This powdered rock is then transferred to the CHIMRA (Figure 3) for processing.

Each of the requirements for an extraterrestrial sample processing device are individually simple, however when combined together, they form a collection of interconnected and dual-purposed device constraints. The sample processing device must both acquire scooped regolith as well as accommodate sample transfer from the drill. The collected regolith or drilled powder must be sorted and separated into either sub-1 millimeter or sub-150 micron particle sizes, reduced to a portion size of 45-65 cubic millimeters for sub-150 micron sample or 45-130 cubic millimeters for sub-1 millimeter sample and delivered to the science instruments on the rover. In addition to these science-driven sampling requirements, a number of self-imposed design constraints were created that are essential to any extraterrestrial sample processing device. These additional design constraints increase the robustness and adaptability of a remotely operated sample processing system. The response to these multi-faceted constraints is an innovative and functionally dense device: the CHIMRA.

* Jet Propulsion Laboratory, California Institute of Technology, Pasadena, CA

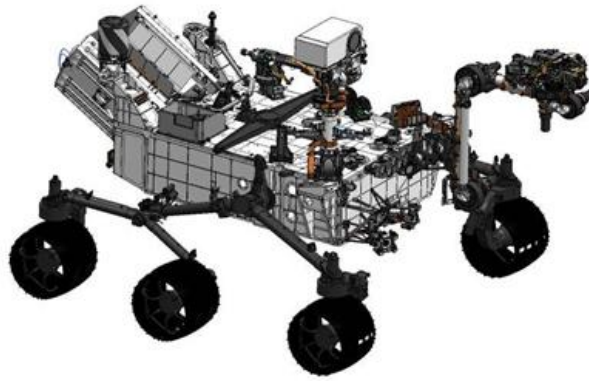


Figure 1. SA/SPaH is a rover-mounted sampling system

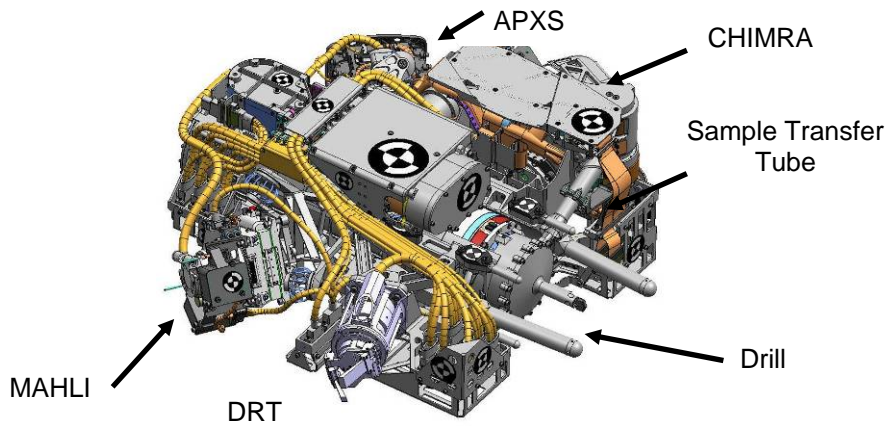


Figure 2. CHIMRA is one of five instruments on the turret

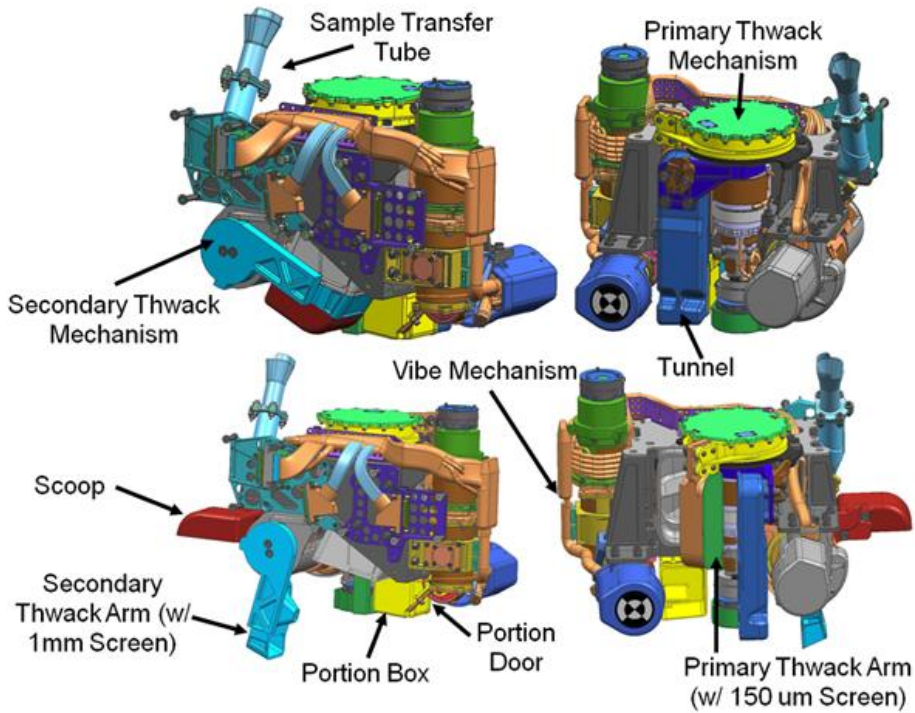


Figure 3. CHIMRA: open and closed configurations

Overview of CHIMRA

The majority of CHIMRA's sample processing functionality is accomplished inherently with the overall design configuration. The internal structure is a labyrinth (Figure 5) that contains two primary passageways used to flow sample into a central processing reservoir from two independent sources: bulk regolith, scooped from the Martian soil by CHIMRA, or powdered sample collected by the drill and transferred via the sample transfer tube. From the central processing reservoir, sample can be diverted through either a 150-micron sieve or a 1-millimeter sieve into two independent portioning chambers. A schematic of the CHIMRA sample processing paths is shown in Figure 4.

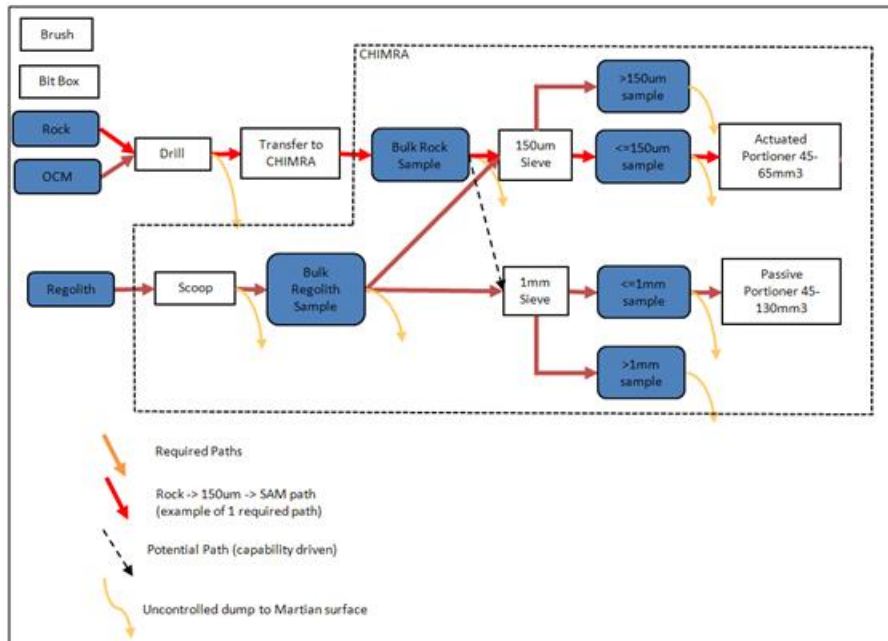


Figure 4. CHIMRA Sample Processing Paths

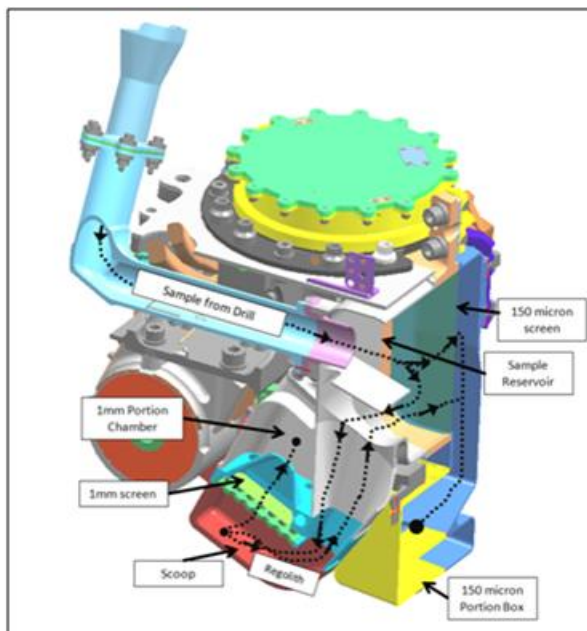


Figure 5. Internal CHIMRA Labyrinths



Figure 6. One-way valves to control flow

In order to create sample flow within its internal passageways, the CHIMRA is vibrated as a whole with a dynamic level of 4-10 G's while it is reoriented with respect to gravity by the Robotic Arm. The dynamic environment is generated by a mechanism that couples the speed of a spinning eccentric mass with the natural frequency of the structure supporting CHIMRA from the turret. This allows the 8-kg CHIMRA to be shaken with a relatively small input force of 150 N. Internal geometric one-way valves (Figure 6) and chamber sizing is used to prevent migration of sample within CHIMRA into unwanted compartments. A combination of dilution cleaning, using chemically understood sample to flush CHIMRA, and forced ejection of clogged particles is used to internally clean CHIMRA between sample processing tasks. Both the 150-micron and 1-millimeter sieves are attached to thwacker mechanisms: a mousetrap mechanism that slams the sieve and frame against a hardstop in order to induce a dynamic impact pulse that ejects clogged particles from the sieve and jolts other internal clogs free.

CHIMRA is composed of four distinct mechanisms, each driven by an actuator: the primary thwack mechanism (PTM), the secondary thwack mechanism (STM), the portion actuator, and the vibration mechanism. Each of the thwack mechanisms performs multiple functions, making configuration of CHIMRA in the required volume achievable by minimizing the number of required actuators. Each actuator in CHIMRA was configured to be supported by a central core structure. This is in contrast to the style of a robotic arm configuration where actuators are supported serially off one another. With a central core configuration, each actuator is only required to move the structure associated with its function. This reduces the output gearbox requirements of a given actuator, lowering the mass and volume required of that device.

The method of creating a sample portion had to both accurately generate a small volume of sample and be robust to the presence of sub-millimeter particle dust. To remove any possibility of an active portion mechanism becoming mechanically clogged or jammed, a passive method of portioning was implemented. Both the 150-micron and 1-millimeter portion chambers contain an open-ended cylinder, or sample tube, that is sized to fill with a specific volume when material is vibrated into it. After bulk sample is brought to the portioning chambers, dynamic excitation and specific rotation of CHIMRA allows gravitational forces to help fill the sample tube, remove excess sample above the tube and eject the sample contained in the cylinder from CHIMRA. The internal geometry that facilitates these actions in the 150 micron portion chamber is illustrated in Figure 7. Once the sample tube is filled, additional vibration levels off the tube and motivates the excess sample to an overflow chamber. The correct portion size is now held in the portion tube while the excess sample is prevented from exiting CHIMRA with the delivered portion. The portion actuator then opens a door at the base of the sample tube and vibration motivates the sample to fall out. After the existing portion is delivered, a new portion can be created by using a 360-degree rotation of the turret to bring the sample in the overflow chamber back above the portion tube. The inclusion of a dedicated portion actuator helps guarantee the ejected sample is less than 150 micron. This is because prior to exiting the sample tube, particles must first pass through the 150-micron screen. A detailed study was conducted on the optimal portion tube geometry to ensure that a consistent portion size is reliably generated and a favorable particle-to-tube-diameter aspect ratio is maintained, thereby minimizing the likelihood of internal arching or tube clogging. The passive method employed by CHIMRA for generating a 150-micron portion provides a consistent portion size without requiring mechanical components that would likely jam when manipulating fine dust particles.

A combination of geometry and internal features allowed a second portioning mechanism to be seamlessly integrated into existing CHIMRA features; this novel configuration removes the need for an additional actuator but sacrifices some portion size consistency. Figure 8 illustrates the features of the scoop and 1-millimeter thwack arm that allow for portion generation. Bulk sample is first sorted by both a four millimeter grate and a 1-millimeter sieve before it is passed through a one-way valve into the 1 millimeter portioning chamber. The purpose of the four millimeter grate is not to sort the sample, but instead to provide structural protection for the fragile 0.05-mm thick, 1-millimeter sieve, in order to ensure that it is not punctured when the scoop is full and closed.

The key element of the STM that allows for portioning functionality is the float between the motion of the secondary thwack arm and the scoop. The secondary thwacker arm is preloaded closed against the scoop. When the scoop is opened the secondary thwack arm will follow the scoop for ten degrees until the STM latch is engaged and the thwack arm restrained. This provides the opportunity to discard all excess sample in the 1-millimeter chamber as well as sample greater than 1 millimeter contained in the scoop. The only sample retained will be what is contained in the portion tube integral to the thwack arm. A bypass valve allows this generated portion to be brought back into the scoop chamber where it can be distributed to the instruments by pouring it out the opened scoop. The sacrifice made by not dedicating an actuator to 1-millimeter portioning is that the generated portion size has the possibility of containing particles that did not pass through the 1-mm screen. Specifically, this is any sample that did not fall out of the scoop at the previous step. This is because the sample distributed to the instruments does not exit CHIMRA from a chamber that can only be accessed by first passing through a screen as is the case with the 150-micron portion design. This shortcoming is mitigated by including a visual inspection step in which the scoop is opened and the sample is visually examined prior to delivery.

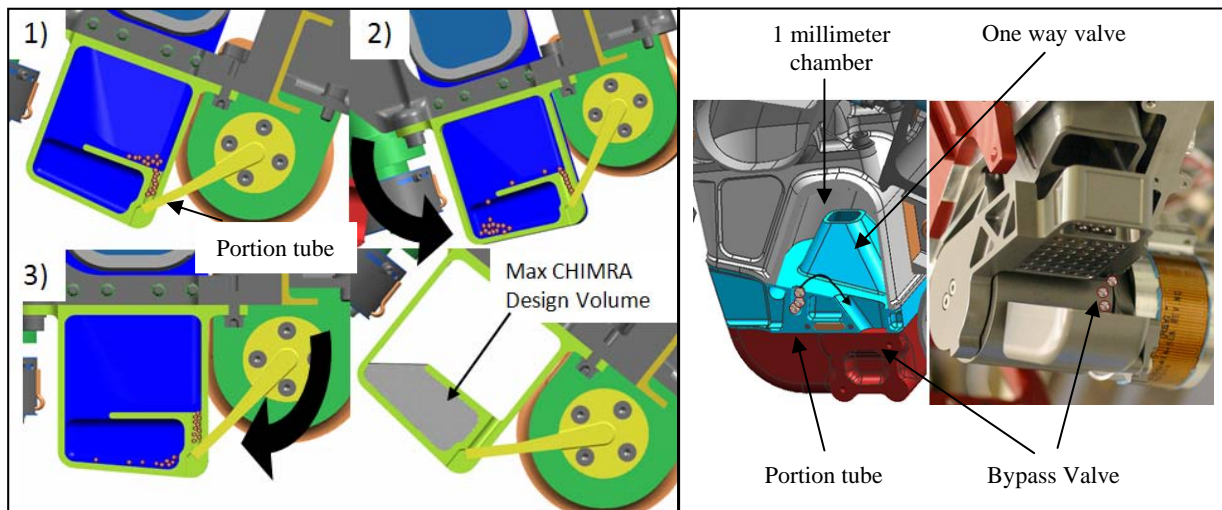


Figure 7. 150-micron Portioning Method

Figure 8. 1-millimeter Portioning Method

Sample Processing Robustness via Design Configuration

With few examples of design heritage to learn from and base the CHIMRA design on, a set of sample handling guidelines was established prior to structuring the CHIMRA layout. This allowed design iterations to be evaluated against predetermined principles that were chosen to maximize the design robustness independent of the implementation constraints. These established guidelines can be broken into two categories: features that minimize the likelihood of internal particle clogging and elements that allow assessment of problems or clogs as they arise. The CHIMRA also required configuration adaptability for sample processing in the case of an actuator failure. These elements established the driving principles behind CHIMRA's sample processing robustness.

While the design features utilized to mitigate clogging are straightforward, the design difficulty for CHIMRA arose when external volume or mass constraints forced compromise between sample processing guidelines and subsystem device requirements. For example, the aspect ratio of a chamber's size to size of a particle passing through that chamber was carefully monitored; the final CHIMRA design strived to maintain a 10:1 aspect ratio. However, this was a compromise from the original 20:1 design philosophy that was eroded as wall thicknesses were increased to meet structural requirements, passageways were reduced to meet subsystem volume allocations, and overall design was changed to

accommodate growing volumes of delivered actuators. Although ultimately reduced, this “order of magnitude” rule of thumb has proven to be successful during development testing of the device. In addition to tracking the aspect ratios of sample passageways, all sample chambers were sized to have at least twice as much internal volume as the maximum sample volume that would be contained, an achievable goal because the sample volume acquired from the drill and the scoop can be controlled and therefore designed around. To avoid unexpected particle behavior in a 3/8 G environment or for a unique rock type, the CHIMRA design intentionally minimizes the frequency of scenarios in which it has to rely on sample to act in a certain manner, such as remaining within one chamber or returning backwards through a screen it had just been sorted through. This latter requirement was stipulated for two reasons: most industry sieves are not symmetric and have a preferred sorting direction and the CHIMRA method of screen unclogging would only unclog sample from a single direction. A common form of clogging found in early testing occurred when an elongated particle would pass through a two-dimensional orifice, change direction and not be able to return through that same entrance. To alleviate this behavior and to ensure that a non-spherical particle does not get trapped within CHIMRA, the exit of any particular chamber was designed to be significantly larger than the entrance. This feature is most notably seen in the exit from the 1-millimeter grate (Figure 9), where a clearing channel was introduced to prevent sample less than 4 millimeter in diameter but greater than 1 millimeter in diameter from becoming stuck between the two screens. Another feature incorporated within CHIMRA was to align the interface between a door and CHIMRA with the rotation axis of the door. This removes the tangential motion between a closing door and CHIMRA which could foreseeably result in a perfectly sized particle creating a Morse taper effect and wedging the door shut.

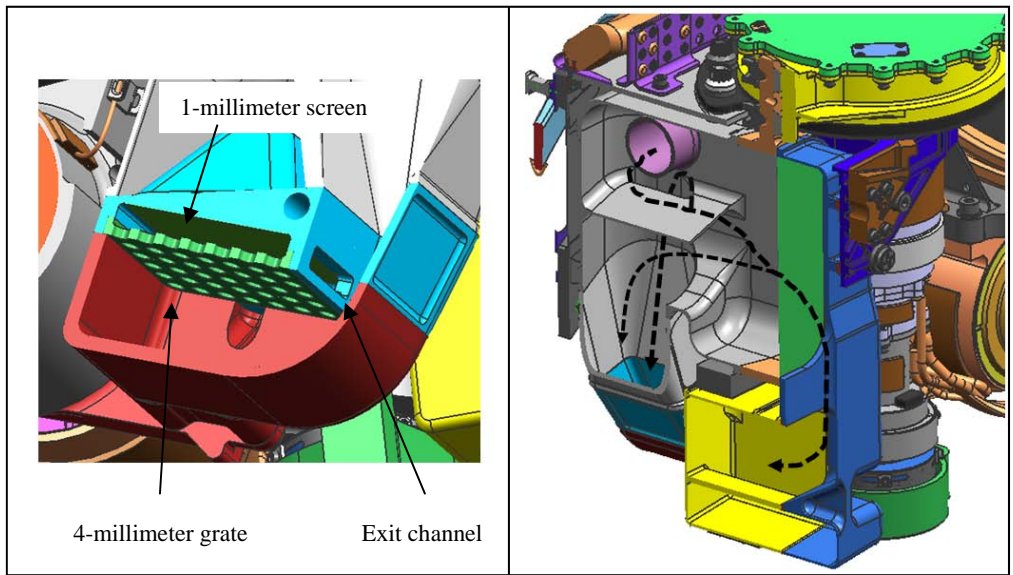


Figure 9. Features to minimize clogging **Figure 10. Sample Diverter Operation**

Of equal importance to anti-clogging features are design elements that allow troubleshooting when performance of the sample processing device begins to degrade. Specifically, the internal layout of CHIMRA allows almost all of the internal surfaces to be visually inspected by an external camera. Additionally, a rover camera can inspect sample prior to delivering portions for instrument ingestion; this provides a checkpoint to give ground operators the option to triage samples that look troublesome for the instruments. CHIMRA minimized the black-box design architecture (sample in/sample out) whenever possible to provide ground operators with maximum opportunity to assess problems as they arise and to adapt operations to prevent repeat incidents. The sample transfer tube that funnels sample from the drill into CHIMRA is the exception to this as it was not possible to include a method of internal visual inspection.

CHIMRA's capacity to adapt to any singular element failure and maintain the ability to process and deliver drilled sample was primarily accomplished through design configuration. If a component of the 150-micron portioning mechanism malfunctions, such as a failed portion actuator or jammed portion tube, the 150-micron sample can be rerouted to the scoop and distributed through the 1-millimeter portioning mechanism. A failure of the scoop or thwack actuator was more problematic to accommodate in design. This is because the internal configuration of CHIMRA that maximizes the internal viewing surfaces results in using both the tunnel and scoop to route sample internally. This meant that an actuator failure in an open configuration could ultimately cause all sample to be lost during processing. To address this, the primary reservoir diverter (Figure 10) was implemented to ensure that sample can still be internally routed to a portioning device without losing the majority of the bulk sample in situations where the tunnel or scoop has failed open. A failed scoop actuator will also not impede sample drop-off to the rover inlets. The relative configuration of the 150-micron portion tube and the scoop swept volume allows CHIMRA to be lowered down to the rover deck to deliver sample even if the scoop actuator is failed open.

It would be naive to assume that CHIMRA potential malfunctions are limited to actuator failures; internal clogging is also a concern. The inclusion of two radically different means of motivating sample within CHIMRA, sinusoidal vibration and high energy impact events, maximizes the likelihood that particles stuck within its cavities can be removed. A notable exception to the self-sufficient redundancy of CHIMRA is a scenario in which the device failure occurs within the vibration mechanism. While the development plan for this scenario was to motivate sample through a portioning chamber by using a thwacking device to vibrate CHIMRA, initial testing suggests that utilizing the drill's percussive voice coil (1) will be more effective in generating internal CHIMRA dynamics.

Although the previously discussed guidelines were already culled from a far greater list that covered implementations more unique to CHIMRA, there are three universal concepts that, above all else, will make CHIMRA a robust and useful tool to the science community for a lifetime on Mars. The first is the ability to view all of the internal areas within CHIMRA to allow ground operators to understand how sample is behaving within CHIMRA and to troubleshoot any problems that arise during mission life. Second, a science sample can be delivered to the rover instruments even in the event of a malfunction. Third, the design configuration allows for multiple methods to motivate sample through CHIMRA. Finally, it is worthwhile to explicitly address the conflict of interest in designing a sample processing stage within a constrained volume. A number of changes can occur during subsystem design maturation: actuator volumes can increase, external volumes can become encroached upon, and structural components or interfaces are increased in size. Each of these changes can be reacted to by shrinking internal passageways; compromising on the features that will ultimately make the device a successful sample processing device. All effort should be made by subsystem configuration engineers to afford the sample processing device a greater volume than is thought to be needed.

Thwack! - Development of the Primary Thwacker Mechanism

The complexity of the PTM and STM does not lie in the mechanism itself as both are essentially simple latch and pawl mechanisms. Instead, the difficulty was in the amalgamation of typical mechanism robustness metrics with the nonstandard and undefined mechanism goals: clearing a screen clogged with an unknown particle type.

Both the PTM (Figure 11) and STM have enough similarities that only the development of the PTM will be discussed in detail. The input to the mechanism is the tunnel base (shown in blue in the cross section). This is the same structure that supports and manipulates the tunnel that facilitates sample movement from the 150 micron screen to the portion box. Contained inside the tunnel base is the latch cartridge and tang assembly. The latch cartridge houses a spring-preloaded Vascomax latch. This latch has redundant rotating surfaces: the latch itself pivots around a pin and the pin is able to rotate independently via the bronze-impregnated, steel-backed bushings that provide the straddling support. The tang assembly is a Vascomax pawl with an internal set of duplexed back-to-back bearings that allow the tang to rotate independently within the tunnel base. The output of the mechanism, shown as yellow in the cross section,

is attached to the 150-micron sieve frame and is supported by a lightly-preloaded, thin-section, back-to-back duplex bearing pair. These two independently rotating elements of the PTM, the tang assembly and mechanism output, are coupled together and attached to a pre-wound spiral spring. In the nominal closed configuration, the thwacker arm is preloaded against CHIMRA. When the tunnel is opened five degrees, the mechanism output and tang assembly are engaged by the latch cartridge fixed inside the tunnel base. Additional rotation of the tunnel base forces the output, sieve frame, and tang assembly to also rotate, lagging five degrees behind the tunnel. This rotation further winds the spring. At the end of the mechanism range of motion, the latch is disengaged from the tang by a non-rotating stop fixed to the static mechanism structure. Once disengaged, the wound spring accelerates the output and sieve frame back into the closed position, generating the inertia impact thwack that is used to eject stuck particles. As the tunnel closes, the latch rides over the backside of the tang, snaps back into the armed state, and resets the mechanism.

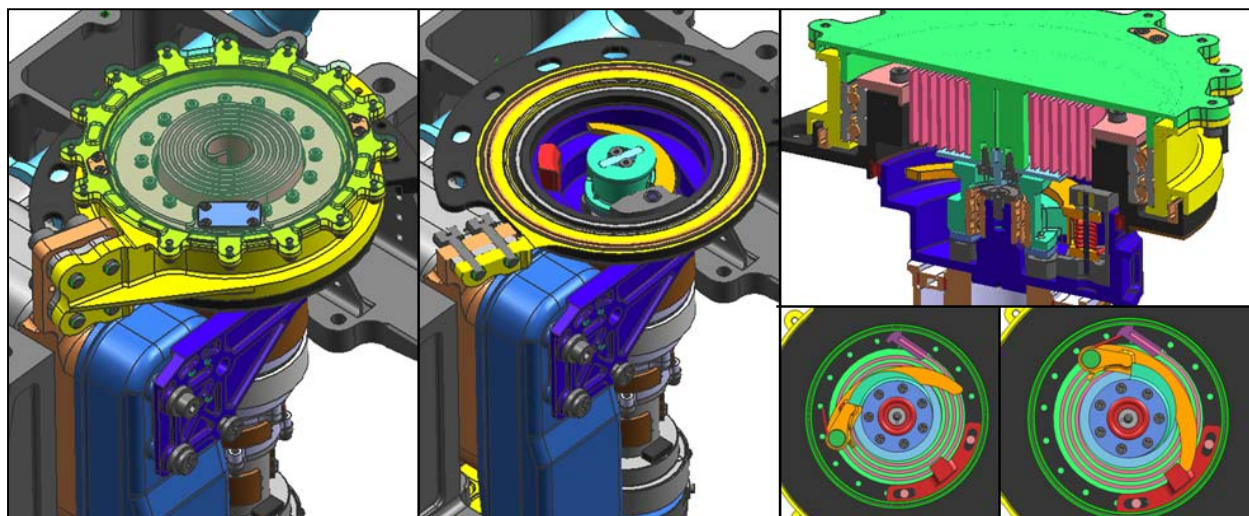


Figure 11. Primary Thwack Mechanism

The primary challenge to overcome in the PTM design was a poor initial test program that resulted in ambiguous functional mechanism requirements. Combining the parameter space of multiple sieve designs, different rock types, and alternating number of thwacks into an efficient development test program meant that only a rudimentary understanding of the phenomena was developed before the design moved on. Additionally, the single life requirement of 500 thwacks made it appear practical to only perform a life test on a single parameter configuration. Therefore, only one full life test was performed early in the CHIMRA life cycle to define the thwack impact speed requirements of the mechanism. This design point was chosen to bludgeon sieve unclogging so that our limited experience was compensated for with a heavily margined impact speed. Early in the CHIMRA design cycle, an impact speed was selected that efficiently unclogged the screen, however left no option to compromise on performance to relax mechanism requirements.

The requirements of the PTM are interconnected in a manner that forced an advanced level of computational design synthesis to meet all functional and traditional mechanism requirements. An inertial dynamic simulator was created in Simulink to allow the spring rate, preload and angular displacement to be modified and simulated. This was used in conjunction with empirical results from targeted cold bearing and seal drag tests to converge upon an acceptable design. While the minimum functional requirements had to be met at the earliest possible thwacker release point, all structural design loads had to account for the last possible release point; this occurs when the spring is at its maximum angular displacement. As the structure was modified to survive these worst case design loads, the rotational inertia of the mechanism increased, forcing the spring energy to increase to maintain the same minimum impact speed. This obviously boosted the impact energy going into the structure and forced additional iterations.

To both maintain the desired thwack impact speed and converge on a structural solution, the range between minimum and maximum release had to be closely controlled.

A computational mechanism simulator was created that modeled the specific mechanism components and forces between them to accurately predict the point of thwack release. Incorporated into this model was a variable range of friction coefficients applied to all sliding surfaces and rotary joints. Because the release angles between the latch and tang depended heavily on the machined final dimensions of the internal mechanism components, a method of inducing variation due to tolerances was incorporated into the mechanism simulator. A standard tolerance stack-up across the mechanism was fed into the simulator to account for how small deviations in part tolerances affected the release point of the mechanism. Finally, the change in mechanism release as a function of component wear at end-of-life was incorporated into the model. The mechanism simulation additionally aided the design because it was able to predict the specific contact angles and surfaces that were frictionally compressed at all moments of the latch release. This allowed internal radii to be dialed in to ensure that local yielding from contact stress did not occur (this was later verified in subcomponent mechanism life test). It was only through this computational design synthesis, which was able to account for frictional dependency, manufacturing tolerances, spring variability and internal component wear, that the range of mechanism release was well understood (Figure 12) and the convergence of a solution that met all functional and traditional requirements of the PTM was possible.

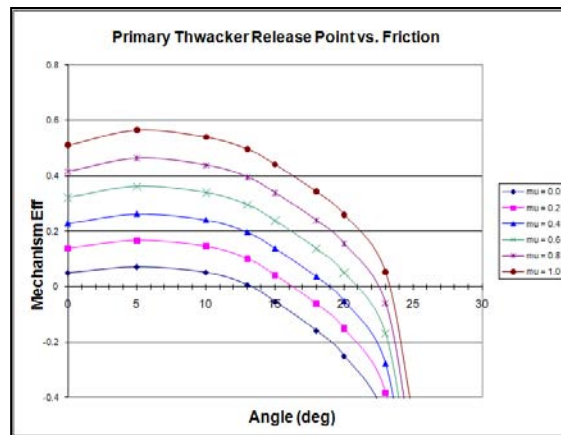


Figure 12. Output of Mechanism Simulator

When assembled and tested, the PTM showed a release point within two-tenths of a degree of where expected and the actual thwack impact speed was predicted within ten percent. During the development and assembly of the PTM, three lessons were learned. 1) Developing a sufficient understanding of the sensitivities in the functional requirements of a mechanism is worth the testing time to find them. This allows changes late in the design phase to be incorporated without re-dialing in the entire mechanism. It was likely that a reduction in the thwack impact speed could have been made and still met unclogging performance metrics, however, the mechanism was unable to capitalize on that possibility due to lack of test data. 2) Mechanisms that have tight requirements on internal alignment should not be split across an interface. As can be seen in the cross section of the mechanism, the upper and lower portions of the mechanism are not explicitly connected. This drove substantial assembly effort to ensure that these two parts were able to be aligned to each other with a high degree of accuracy. 3) The trial-and-error fabrication technique of hand-winding steel springs was not compatible with the high degree of accuracy required for this mechanism. In hindsight, a feature to vary the initial spring preload within the mechanism should have been included. Spring variations had been accounted for in the design by having a settable latch release position, but it would have been far more efficient to modify the initial spring preload when installed in the mechanism.

Good Vibrations: Development of the Vibration Mechanism

The heart and soul of CHIMRA's sample processing ability, the Vibration Mechanism (VM) (Figure 13), is required to generate the dynamic environment CHIMRA uses to flow, sort and portion sample over an operational life of two years and 200 million revolutions. The load generating component of the VM is an eccentric tungsten mass that is supported by two back-to-back, spring-preloaded, angular contact bearings. The motor-side bearing is pressed onto the shaft as well as into the housing; whereas the outboard bearing only contains a press fit on the outer race. The inner race is pressed onto a hollow shaft (green in Figure 13) that slips over the primary shaft of the mechanism. The sliding inner race is then preloaded with a wave spring, reducing the preload sensitivity to assembly tolerances. The central shaft and eccentric mass is driven by the vibration motor through a flexible helical-coupler at speeds between 4000 and 6000 revolutions per minute.

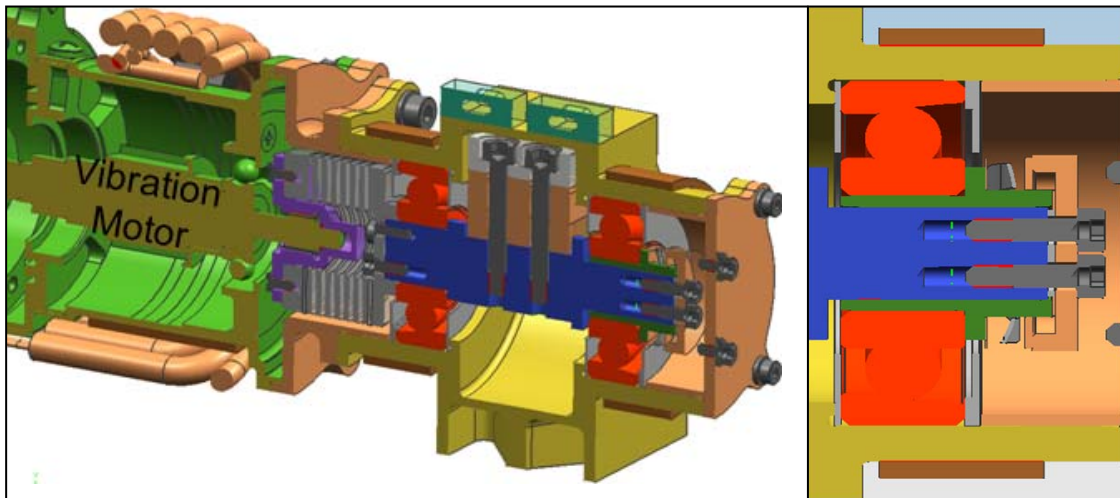


Figure 13. Vibration Mechanism

The torque available from the largest MSL motor was limited when operating at 6000 rotations per minute. This power limitation forced the VM to balance the competing requirements of bearing lubrication drag and long mechanism life. This balance was struck through development testing in the following way. The bearing and lubrication design evolution dictated finding a bearing configuration that produced contact stresses less than 1.38 GPa (200 ksi), converging through test on the maximum lubrication fill factor that afforded acceptable torque margin, and testing the mechanism across the significant life requirements of the device. A development test program was conducted that compared the final lubrication drag across a temperature range of -70 to +70 degrees Celsius for two bearing sizes (10-mm OD and 30-mm OD), two different radial loads (150 and 250 N), three test speeds (4000, 5000 and 6000 rotations per minute) and increasing fill factors working up to 30% fill factor by volume. The bearings were initially greaseplated with Braycote and additional fill factors were generated by inserting a slurry of Braycote grease and Brayco oil. By fabricating and testing three different mechanisms simultaneously, each of the previous variables could be individually varied. When the optimal configuration was found, it was successfully tested past 200 million cycles across a fluctuating temperature profile that represented the flight environment (Figure 14).

A striking result from this testing was that the combination of the parameters unique to this application resulted in visible transitions across three different lubrication regimes: mixed boundary/elastohydrodynamic, purely elastohydrodynamic and hydrodynamic. For discussion purposes, the 10-mm OD bearing did not display significant changes in performance across the parameter design space and therefore the discussion will focus only on the 30-mm OD bearing. In the vibration mechanism, the load generated from the eccentric mass is proportional to the operating speed squared. However,

testing on both the development unit and the flight unit indicated that the recorded lubrication drag was insensitive to changes in the load applied. This was true even if the load was increased from 100 to 250 N. It is therefore assumed that substantial changes in recorded drag at different operating speeds are primarily a result of the change in speed. Figure 15 illustrates how changes in speed and chamber test temperature affect the lubrication drag within the mechanism. Predicted trends of an inverse relationship between lubrication drag and operating speed were observed. This suggests that increased operating speed is driving the lubrication regime of the bearing from an elastohydrodynamic regime to more hydrodynamic than was expected.

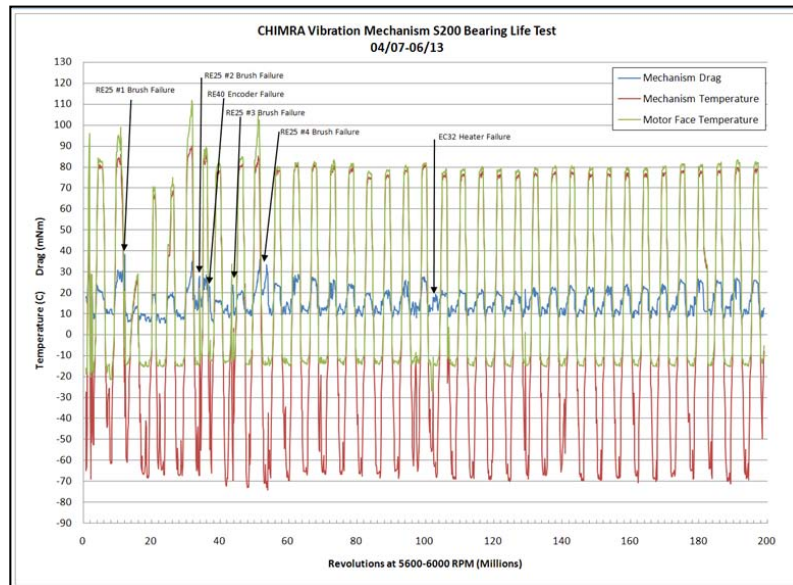


Figure 14. 200-million cycle bearing life test

The transition through different lubrication regimes is also obvious where the expected inverse relation between chamber temperature and lubrication drag was not observed. Specifically, across all three operating speeds, the lubrication drag recorded at -25 degrees Celsius was less than at ambient (20 degrees) and -65 degree Celsius. The low lubrication viscosity at ambient temperatures resulted in a mixed boundary/ elastohydrodynamic operating regime. However, as the temperature decreased to -25 degrees Celsius and viscosity increased accordingly, the regime changed to be pure elastohydrodynamic one and a corresponding lower lubrication drag was recorded. Further decreases in temperature (-65 degrees Celsius) were sufficient to thicken the viscosity to a level where the operating regime of the bearing was hydrodynamic and the corresponding lubrication drag increased beyond that of the elastohydrodynamic regime. This same transition across lubrication regimes was recorded when testing two operating speed across the temperature range on the flight VM (Figure 16) and is consistent with Stribeck Curve Theory (3). A significant increase in drag can be seen when the lubrication fill factor is increased from 15% to 20%. The final parameters selected for the flight configuration were a 30-mm OD bearing with an additional 15% fill factor by volume that is operated at a contact stress of 862 MPa (125 ksi). Once assembled, an infant mortality test was successfully performed that exercised the flight mechanism to 20 million revolutions.

Reflections on Development Testing to Support the Design of a Sample Processing Device

To mature the design of the CHIMRA sample processing system, an extensive suite of development tests were conducted to form a basis of particle flow mechanics. A quick review of the relevant results that the CHIMRA designing principles were based on will provide future designers a more advanced platform to start from when creating a similar design. The results from a series of tests aimed at sample flow across surfaces revealed that both the surface finish and method of surface preparation had a strong effect on

particle retention. All of CHIMRA's sample transfer surfaces are an annealed titanium alloy and hand polished (using a fine grit) to have a smooth surface finish. Both the 150-micron and 1-millimeter screens were 0.05-mm thick and fabricated through a photo-chemical etching process that was compatible with titanium. This temperature compatibility removed a CTE mismatch between the screen and the titanium sieve frame that would result in varying screen tautness across temperature. Sinusoidal vibration was shown to be extremely efficient at motivating particles through chambers similar to CHIMRA as long as the vibration levels were above a floor of 1 G. For the purpose of sorting sample at 150-micron size, it was found that vibration levels of 6 G's or larger in any singular direction motivated sample through the sieve at acceptable rates, however it is important to note that there is an exponential relationship between the sieve throughput by mass and the vibration environment applied. Additionally, having levels around 6G's or greater in two directions motivates sample through a screen substantially better than vibration in only one direction.

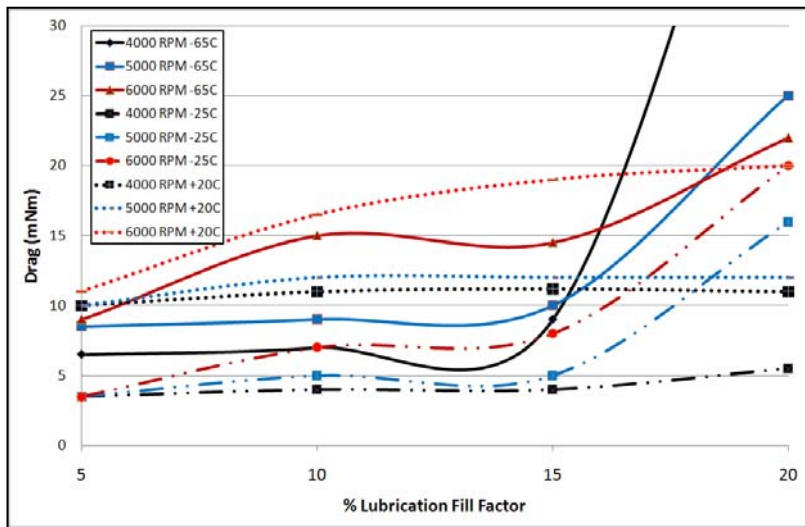


Figure 15. Development Test Unit Drag

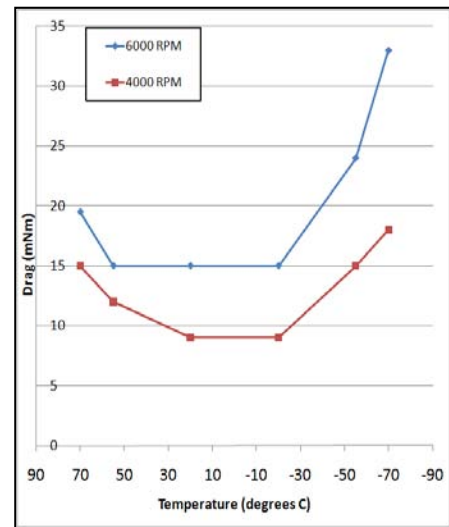


Figure 16. Flight VM Drag

In addition to the specific design points discussed above, global statements from lessons learned during the development testing planning and execution can be made. It is extremely important to conduct all tests where particle interactions between particles or surfaces are being studied in a relevant environment. An important detail to track is the moisture content in the sample and the gas being used to purge the test environment; in fact, because atmospheric moisture can have a drastic effect on the results, test chamber humidity should always be specifically measured and controlled, and sample should be baked out for 24 hours prior to test. A hole in the CHIMRA development test suite that became apparent late in the design was that consecutive runs of alternating relevant samples had never been performed. In fact, these types of tests performed by another instrument on MSL suggest this condition generates the worst electrostatic charge. To allow electrostatic charge to be realistically developed, it is important that all test articles have a similar ground path as the flight unit or be electrostatically isolated to simulate a worst case charge buildup. A final recommendation for similar test programs is to be mindful of how clever a designer gets in attempting to extrapolate results to form conclusions not explicitly tested for. At the time of CHIMRA's design, particle behavior and interactions within a device such as CHIMRA are far from being fully understood and therefore the best way to guarantee a successful design is to explicitly perform tests that mimic the flight application as closely as possible.



Figure 17. CHIMRA Installed on EM Turret

Conclusions

At the time of writing this paper the qualification and flight CHIMRA mechanisms are being assembled. The engineering model CHIMRA has been functionally tested at ambient conditions and integrated at the next higher level of assembly onto the Robotic Arm as part of the Turret (Figure 17). At this integration level, the dynamics of the CHIMRA when driven by the vibration mechanism were recorded in all relevant robotic arm positions. This test data will be leveraged when the engineering model turret is installed in a pressure chamber on a non-flight robotic arm. In this chamber, the end-to-end sample processing capability of CHIMRA will be tested and verified. It is during this test that the true robustness of CHIMRA as a sampling platform will be measured.

Acknowledgements

The work described in this paper was performed by the Jet Propulsion Laboratory, California Institute of Technology, under contract with the National Aeronautics and Space Administration.

The design, fabrication and assembly of the CHIMRA subsystem would not have been possible without the tremendous amount of dedication, hard work and sacrifice made over a two year period by the CHIMRA team: Andrew Bingham, Dave Berdahl, Cambria Hanson, Joel Johnson, Robert Kovac, Kurt Knutson, Matt Orzewalla and James Wincentzen. A heartfelt thanks goes to those who acted as mentors to myself and my team, providing their own time to ensure the success of CHIMRA: Mark Balzer, Kevin Burke, Randy Foechner, Louise Jandura, Joe Melko, Dave Putnam, Lori Shiraishi, Jeff Umland and Chris Voorhees.

References

1. Okon, Avi. "Mars Science Laboratory Drill." *Proceedings of the 40th Aerospace Mechanisms Symposium*, (May 2010).
2. Jandura, Louise. "Mars Science Laboratory Sample Acquisition, Sample Processing and Handling: Subsystem Design and Test Challenges." *Proceedings of the 40th Aerospace Mechanisms Symposium*, (May 2010).
3. Czichos, H. 1978. *Tribology: A systems approach to the science and technology of friction, lubrication and wear*. Amsterdam: Elsevier Scientific Publishing.

Performance of Regolith Feed Systems for Analog Field Tests of In-Situ Resource Utilization Oxygen Production Plants in Mauna Kea, Hawaii

Ivan I. Townsend*, Robert P. Mueller**, James G. Mantovani**, Kris A. Zacny*** and Jack Craft***

Abstract

This paper focuses on practical aspects of mechanical auger and pneumatic regolith conveying system feeding In-Situ Resource Utilization Oxygen production plants. The subsystems of these feedstock delivery systems include an enclosed auger device, pneumatic venturi educator, jet-lift regolith transfer, innovative electro-cyclone gas-particle separation/filtration systems, and compressors capable of dealing with hot hydrogen and/or methane gas re-circulating in the system. Lessons learned from terrestrial laboratory, reduced gravity and field testing on Mauna Kea Volcano in Hawaii during NASA lunar analog field tests will be discussed and practical design tips will be presented.

Introduction

In-Situ Resource Utilization (ISRU) means using local resources on extra-terrestrial bodies to support human and robotic operations on the surface (Cooke 2006, Caruso 2007, Sanders 2008). One method of ISRU is the production of water from the metallic oxides in the lunar regolith by the use of, for example, a carbothermal reaction or a hydrogen reduction process. Electrolysis of the water yields oxygen which can then be used for life support, consumables, and propulsion propellant. Large mass savings are possible in lunar architectures that use ISRU since a large fraction of required oxygen won't have to be transported from the Earth to the moon. In order to make ISRU oxygen production a reality, critical subsystems have to be developed and tested much sooner than non-critical parts. One of the critical systems is a regolith feed system, whose task is to deliver highly abrasive lunar soil feedstock directly into the reactor. The system has to be highly reliable, dust-tolerant, and lightweight and must also be able to dispose of the spent regolith after the reaction process.

This paper will present lessons learned from the design, fabrication and field testing of both auger and pneumatic types of regolith feed systems for hydrogen reduction and carbothermal oxygen production plants that were operated on Mauna Kea Volcano in Hawaii during NASA lunar analog field tests. The volcanic ash called Tephra, which

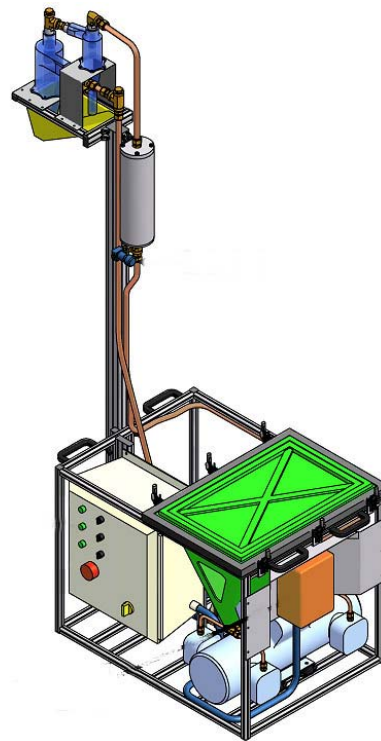


Figure 1. Depiction of the Pneumatic Regolith Feed System for a Carbothermal O₂ Reactor.

* ASRC Aerospace, Kennedy Space Center, FL

** NASA Kennedy Space Center, FL

*** Honeybee Robotics Spacecraft Mechanisms Corporation, New York, NY

is found on the Mauna Kea volcano, is a good mineralogical simulant for lunar regolith. This soil was used as a feedstock for the two types of ISRU reactors to produce the water that could subsequently be electrolyzed to yield oxygen.

Regolith Feed Systems for ISRU Oxygen Production Plants

A regolith feed system needs to provide an efficient and reliable mechanism for regolith transfer in order to serve as an interface between an excavator system that collects raw regolith material, and an ISRU production plant that extracts useful product materials, such as water vapor, from the regolith through a chemical process. Auger and pneumatic regolith conveying systems are two types of regolith feed systems that have been field tested and are described below. Each was tested at the Mauna Kea lunar analog field site; the auger system in November 2008 and the pneumatic system in February 2010.

ROxygen is a NASA ISRU project that is concerned with extracting oxygen from the mineral Ilmenite in the lunar regolith via a hydrogen reduction process in a fluidized-bed reactor system. The ROxygen regolith transfer team identified the flow and transfer characteristics of lunar soil simulant to be a concern for lunar oxygen production efforts. It is important to develop hardware designs that have the ability to flow and transfer a given amount of lunar regolith simulant to a desired vertical height under lunar gravity conditions. The first generation of the project (ROxygen I) tested an inclined auger regolith feed system to transfer material approximately 7 ft (2 m) vertically from the ground and into a solids inlet located at the top of an ISRU reactor chamber. For ROxygen II, a pneumatic method was designed to convey the regolith vertically which avoided exposing any moving parts to abrasive regolith simulant particles. A similar "proof of concept" pneumatic regolith transfer system was built and field tested at Mauna Kea for the Carbothermal ISRU project, in which oxygen is extracted from metal oxide minerals using a carbothermal reduction process that utilizes methane. The pneumatically conveyed granular material is separated from the convey gas using cyclone separator technology.

Auger Regolith Feed System

Description

The National Aeronautics & Space Administration (NASA) In-Situ Resource Utilization (ISRU) program in the Exploration Technology Development Program (ETDP) has designed and built oxygen production plant prototype under the name of ROxygen. The first generation prototype (ROxygen I) was tested in November 2008 on Mauna Kea volcano in the Big Island of Hawaii. The ROxygen I system was a self contained hydrogen reduction reactor payload that was part of the modular Outpost Precursor Testbed for ISRU & Modular Architecture (OPTIMA) system. The goals of the OPTIMA test were to demonstrate: (1) an excavation and regolith delivery to/from ISRU plant, (2) oxygen extraction from regolith at the desired outpost production rate, (3) oxygen storage, and (4) system integration, modularity of modules for swapping, and surface operations.

The ROxygen I regolith simulant feed system was designed to deliver regolith simulant from ground level to the inlet tube located at the top of the ROxygen I reactor cylinder. The reactor was designed with a vertical configuration to allow gravity to feed regolith simulant into and out of the reactor cylinder. In addition, the regolith simulant feed system was required to channel the spent regolith from the outlet of the reactor to a regolith disposal location on the ground for eventual pickup by a spent regolith removal system. The feed system had to be simple, lightweight, reliable, safe and capable of transportation and field assembly. The packaging of the feed system into the overall ROxygen I prototype envelope was a major driver in the generation and selection of various concepts. In order to maintain pressure inside the reactor, the regolith feed system had to be capable of isolating the reactor at the inlet and outlet tubes. Regolith tolerant valves were researched and developed with seals capable of maintaining a desired pressure even after cold and hot regolith had passed through them. Since the energy requirements of an ISRU reactor can be quite large as the regolith heats to a temperature approaching 1000 degrees Celsius, it was highly desirable to incorporate a heat recuperation system into the regolith feed system.

The hot regolith that was ejected from the reactor had to heat the cold regolith in the input hopper prior to introducing it into the reactor for the next batch of oxygen extraction.

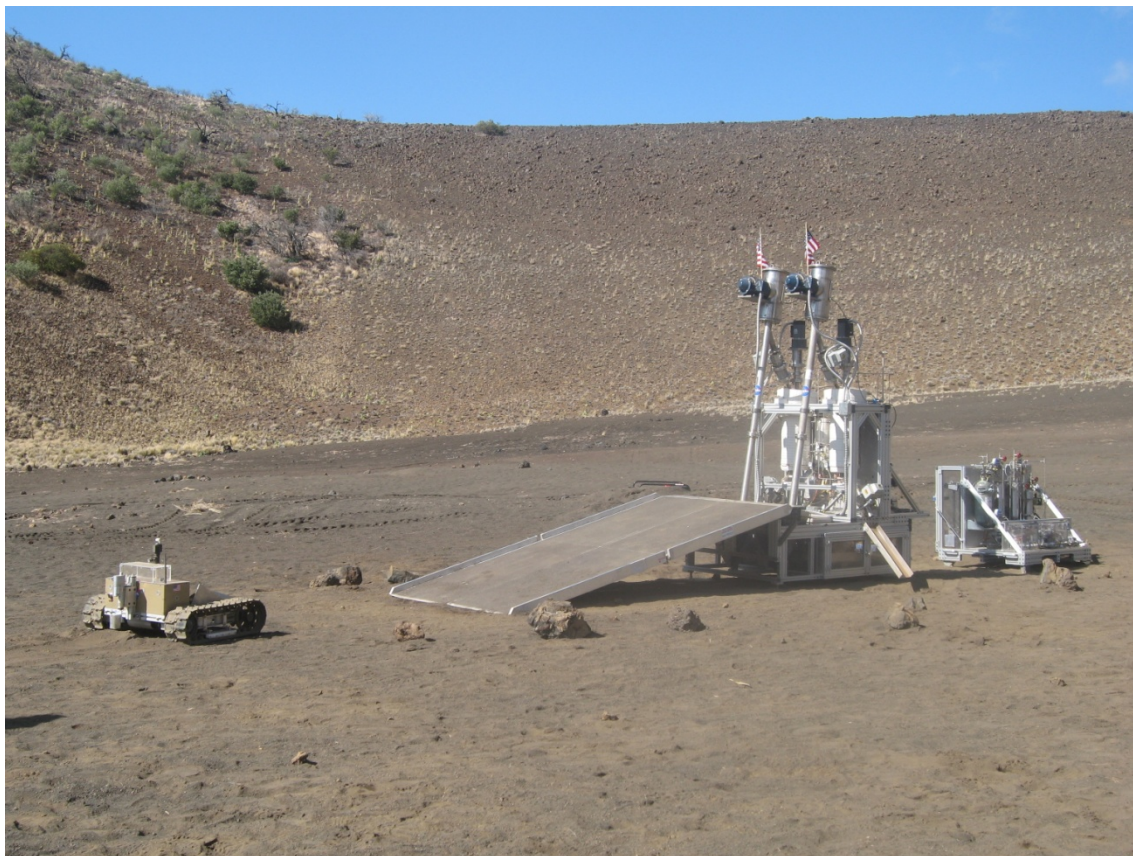


Figure 2: A small excavation rover known as CRATOS is poised to climb up the ramp to deliver about 20 kg of tephra to the input hopper of the ROxygen I demonstration plant. The ROxygen I oxygen production plant was field tested in Nov 2008 on the Mauna Kea Volcano in Hawaii, and used an enclosed, inclined auger as the regolith feed system in a parallel configuration.

Regolith valves for hot regolith are highly specialized and few vendors are capable or willing to tackle this challenge. Gemco Valve Inc. was the only vendor that was willing to design and manufacture the regolith handling valve for the ISRU ROxygen I project (see Fig. 3). Lead times for regolith tolerant valves with metal seals were a challenging aspect of this design. Valves that are designed for terrestrial regolith or abrasive materials handling are not normally designed to operate in a vacuum or to provide a reliable pressure seal. This application called for 20 psi (138 kPa) on one side and near perfect vacuum on the other. Valves that handle regolith transfer application do not typically have an acceptable leak rate. Since hydrogen gas is being used in the reactor, the risk consequence of a leak of hydrogen in an oxygen test environment in Earth's atmosphere would be very high. On the moon, a leak would result in the loss of valuable hydrogen gas. Some aerospace applications require regolith handling valves to be light weight and small diameter. However, regolith handling valves are not typically designed for applications requiring less than 3-inch (7.6-cm) diameter and can be bulky and heavy. Regolith handling valves that operate at temperatures above 800 degrees Celsius are not readily available when required to operate with a vacuum on one side and pressure on the other. Commercially available valve actuators are bulky and not aesthetically pleasing. Metallic seals have difficulty sealing, so an interference fit must be designed which can cause high actuation torque values. Moreover, when the valve gets hot, the metals expand causing an even higher operating torque due to an increased interference fit. The sharp regolith particles contribute further to a degradation of the sealing surfaces.

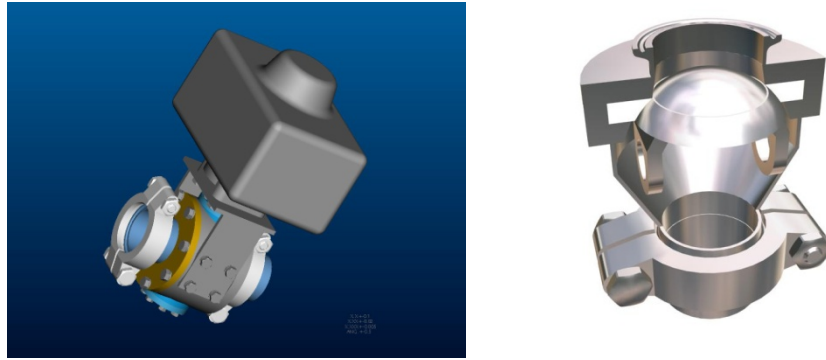


Figure 3: Spherical Disc Valve from Gemco, Inc. having a 5-cm diameter and metal seats.



Figure 4: Hot Tephra (~1000 C) flowing out of Gemco, Inc valve attached to the bottom of the ROxygen I Reactor.

Results and Lessons Learned from the Nov 2008 field test

NASA held an ISRU field test in November 2008 on Mauna Kea, Hawaii at a location called “Wahine” Valley. The valley had the advantage that fine grained Tephra had been washed into the valley basin over time, and there is sparse vegetation with a low organic content to the Tephra. In addition, transportation required good packaging of all hardware, similar to the requirements of space transportation and the environment was extremely dusty which served to provide additional operational challenges.

The ROxygen I hardware was assembled and checked out on site. The testing showed that 10 kg of Tephra could be reliably transferred into the reactor in 470 seconds. Eventually it was determined that 8 kg was the optimal reaction mass and this mass of Tephra was transferred in 408 seconds with smooth

flow out of the hopper and into the auger lift mechanism. The Tephra was also successfully withdrawn from the reactor with gravity feed through the outlet valve. The valves performed well but required adjustment in order to achieve the desired leak rate without having excessive torque on the actuation mechanism.

Multiple reactor operations were performed. The goal was to process three batches with one of the two reactors performing back-to-back tests. The ISRU tests were performed successfully and it was shown that water could indeed be made from Tephra and subsequently electrolyzed to produce oxygen.

Severe dust storms and fluctuating temperatures added to the challenges of the field test and emphasized the fact that the equipment design must be very robust to survive the environmental conditions it will face on the moon which will be much more severe than anything that can be experienced in a field test on Earth.

There were several lessons learned during the design phase, assembly and integration phase of the ROxygen I system, and also during the field testing on Mauna Kea.

The design team was geographically dispersed between Florida, Texas, Ohio, California and New Jersey. Collaborative work was required using Computer Aided Design (CAD) tools and electronic data exchange as well as more traditional methods such as team telecons and white board brainstorming and design sessions. Communication through weekly telecons with frequent CAD file exchange was vital to making this team function effectively.

Lead times for regolith tolerant valves with metal seals were a challenging aspect of this design. Regolith valves are highly specialized and few vendors were capable or willing to tackle this challenge. Lead times as long as 6- 8 months for a custom valve design are typical. The motors on top of the auger tubes were not aesthetically pleasing and increased the volumetric envelope of the ROxygen 1 system substantially. Other designs were subsequently developed during the Phase I concept generation, and the system involving pneumatic conveying of regolith was eventually selected as the regolith feed system for ROxygen II.

During the assembly and integration phase of ROxygen I, the input hopper system was built in a mock up version using polycarbonate sheets for flow visualization. The flow was immediately visible and verifiable. Many hours of analysis were saved by rapid prototyping and experimental testing methods. In addition, an opportunistic reduced gravity flight on the C-9 NASA aircraft at Ellington field proved that the concept would work under 1/6-g conditions using gravity feed albeit with some enhancements to accelerate flow.

It was also discovered that the auger worked well with JSC-1a in the vertical configuration but was inconsistent with Tephra in that orientation. As a result, it was found during the checkout stage of the Mauna Kea field test that the auger system could work reliably with Tephra at an incline angle of 10 deg from the vertical. The auger system is sensitive to particle size and type. Large pebbles tended to jam the auger, so that a size sorting system is needed for auger-based regolith feeding systems. This was achieved during the field test by pre-sieving and final sieving using a mesh screen mounted on the auger opening.

In addition to the Mauna Kea field test, a 2008 reduced gravity flight experiment was performed to study the effect of gravity on the flow of regolith was studied onboard a reduced gravity flight using a mock-up of the ROxygen I hopper (see Fig. 5). The lunar regolith simulants studied were NU-LHT-2M, JSC-1A, and OB-1, and the experiments were conducted at 1/6-g, 1/3-g, 1-g, and 2-g.



Figure 5: Flight experiment in May 2008 to test the flow of regolith simulant inside a hopper under reduced gravity conditions.

Results for NU-LHT-2M Lunar Simulant Testing at 1/6-g using the Hammer Technique

Testing showed that quicker taps with a hammer at approximately 1" amplitude and approximately 4 strikes per second enhanced flow better than slow hard strikes. This hammering technique took 15 parabolas to empty the B-Side hopper for a total time of 300 seconds at 1/6-g.

Results for NU-LHT-2M Lunar Simulant Testing at 1/6-g Using the Front-To-Back Shake Technique

Front to back vigorous shaking worked better than hammering. This shaking technique took 8 parabolas to empty the A-Side for a total time of 160 seconds.

Results for NU-LHT-2M Lunar Simulant Testing at 1/6-g Using the Bounce Technique

Bouncing the entire assembly off the floor of the aircraft worked better than both hammering and shaking with an amplitude of approximately 2" and frequency of approximately 3 bounces per second. A-Side took approximately 97 seconds on average to empty its contents. B-Side took approximately 69 seconds to empty its contents. Testing clearly showed that the bouncing technique was the best flow enhancing technique for this simulant.

Results for JSC-1A Lunar Simulant at 1/6-g

Both Side A and Side B did not flow without employing flow enhancement techniques.

Results for OB-1 Lunar Simulant at 1/6-g Using the Hammer Technique

Side A would flow until the hopper was empty using the Hammer technique in approximately 245 seconds. Side B would flow until the hopper was empty in approximately 133 seconds.

Results for OB-1 Lunar Simulant at 1/6-g Using the Side-To-Side Shake Technique

Side A would flow until the hopper was empty using the side-to-side shake technique in approximately 102 seconds. Side B would flow until the hopper was empty using the Side-To-Side technique in approximately 96 seconds on average. This simulant showed that it would not flow without using flow enhancement techniques and that the Side-To-Side Shake technique allowed the simulant to flow more consistently and faster than the Hammer technique.

Results for OB-1 Lunar Simulant at 1/3-g

Side A simulant flow would randomly stop and require flow enhancing assistance but flowed well during most tests without assistance and displayed an average 38 seconds to empty the hopper. Side B simulant flow would occasionally stop flowing but flowed well for the majority of tests and displayed an average time of 34 seconds to empty the hopper.

Results for OB-1 Lunar Simulant at 1-g

The hopper hourglass assembly has heat transmitting fins on Side A and no fins on Side B. This simulant would begin to flow but would stop and did not flow reliably flow at 1-g from side a without the use of flow enhancing techniques (Suspect the simulant was wet because it flowed better at 1/3-g than at 1-g, we should repeat the 1-g testing). The flow would stop normally after approximately 25 seconds and would not re-start without the use of a flow enhancement technique.

Results for OB-1 Lunar Simulant at 1-g Using the Hammer Technique

Hammering did help the flow characteristics allowing the simulant to flow from the hopper in approximately 41 seconds. Hammering would allow constant simulant flow but the flow would stop if the hammering technique was not maintained. Side B without the heat transfer fins did exhibit simulant flow during most of the tests. The simulant flow would occasionally slow but did not stop allowing the hopper to empty its contents in approximately 25 seconds on average.

Results for OB-1 Lunar Simulant at 2-g

Both Side A and Side B flowed well during 2-g runs and did not require flow enhancement techniques. Side A would empty the hopper in approximately 24 seconds. Side B would empty the hopper in approximately 20 seconds.

Pneumatic Regolith Feed System

Description

A typical pneumatic conveyor system consists of four basic elements: (1) a source of compressed gas, (2) a device for feeding granular material into the gas flow, (3) a conduit for the dusty gas flow, and (4) a gas-solids separation device at the receiving end of the pipeline. An open-loop pneumatic conveyor system does not attempt to recover the convey gas, whereas a closed-loop system does recover the gas.

Industrial types of pneumatic conveyor systems on earth can be open-loop or closed-loop depending, for example, on whether or not the convey gas is inherently valuable or is environmentally hazardous. However, pneumatic conveyor systems that are developed for lunar applications must be closed-loop systems in order to reuse the gas, which represents a scarce and valuable resource on the moon. Although a pneumatic lunar regolith conveyor system that is developed for field testing on earth may be operated as an open-loop prototype, the technology must be developed eventually for a closed-loop system for the planetary exploration. Consequently, the effect of the gravitational environment must be taken into account when developing a planetary regolith pneumatic conveyor system (Liu 1988, Sullivan 1992, Sullivan 1994, Schrunk 1999, Crosby 2008).

Experiments had been performed in earth's gravity at NASA Kennedy Space Center, but results were not known for the lunar gravity environment. A reduced gravity flight (RGF) experiment was led by researchers from NASA KSC and was based on the previous terrestrial experiments, but reconfigured to a portable design. The RGF experiment was conducted over two flight days (13-14 August, 2009) onboard a Zero-G Corporation aircraft that was configured for reduced gravity testing and was prepared for the flight test at the NASA JSC Reduced Gravity Office's facility located at Ellington Field in Houston, Texas.

Pneumatic conveying will prove to be viable for the moon if the transported dusty gas can be filtered sufficiently at the delivery end to allow for recovery of the transport gas for repeated use. Since membrane filters are impractical on the moon due to high maintenance costs, cyclones appear to be the

only maintenance-free alternative for separating pneumatically conveyed lunar regolith particles from the convey gas. Crosby and Agui (Crosby 2008) recently studied the cyclonic filtration of a dilute flow of lunar regolith simulant particles (JSC-1AF) in reduced gravity as a possible means of filtering air inside a habitat. Our study differs from this previous work by focusing on the pneumatic transport of a very dense flow of lunar regolith simulant, and the use of a series array of cyclones to separate the dense dusty gas flow.

Results and Lessons Learned

The objective of the Carbothermal Regolith Feed System was to transfer 5 kg of Hawaiian Tephra from a hopper capable of accepting regolith from an excavator and deposit the regolith into a receiving bin similar in size and height to the Carbothermal Reduction System regolith receiving bin that was tested during the integrated Carbothermal Reduction System Field Test in Hawaii 2010. The Carbothermal Regolith Feed System was designed to lift regolith approximately 2 meters and weigh approximately 52 kg without regolith. A composite hopper was used with a non-sealing lid. The pneumatic feed system for the Carbothermal field test on Mauna Kea in Feb 2010 met all of the requirements and achieved a cyclone particle separation efficiency of 99.7%. The pneumatic feed system delivers approximately 0.63 kg of Hawaiian Tephra per minute. Regolith delivery is fairly linear taking approximately 8 minutes to deliver 5 kg to the receiving bin.

Tephra Transfer Rate

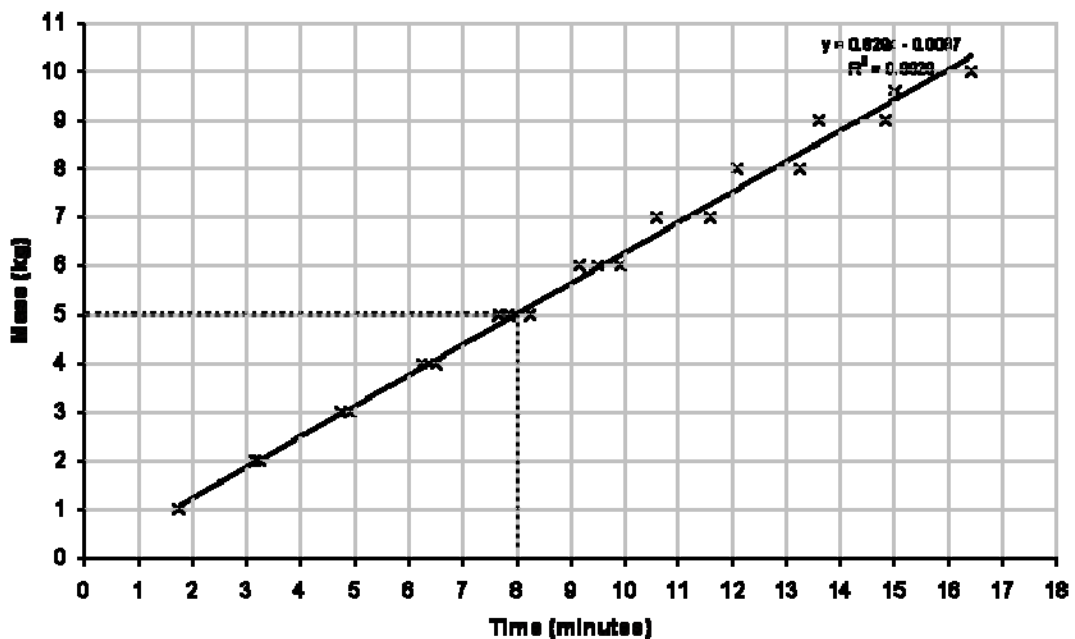


Figure 6: Results from a December 2009 test showing the measured Tephra mass transferred by the Carbothermal Regolith Feed System as a function of time.

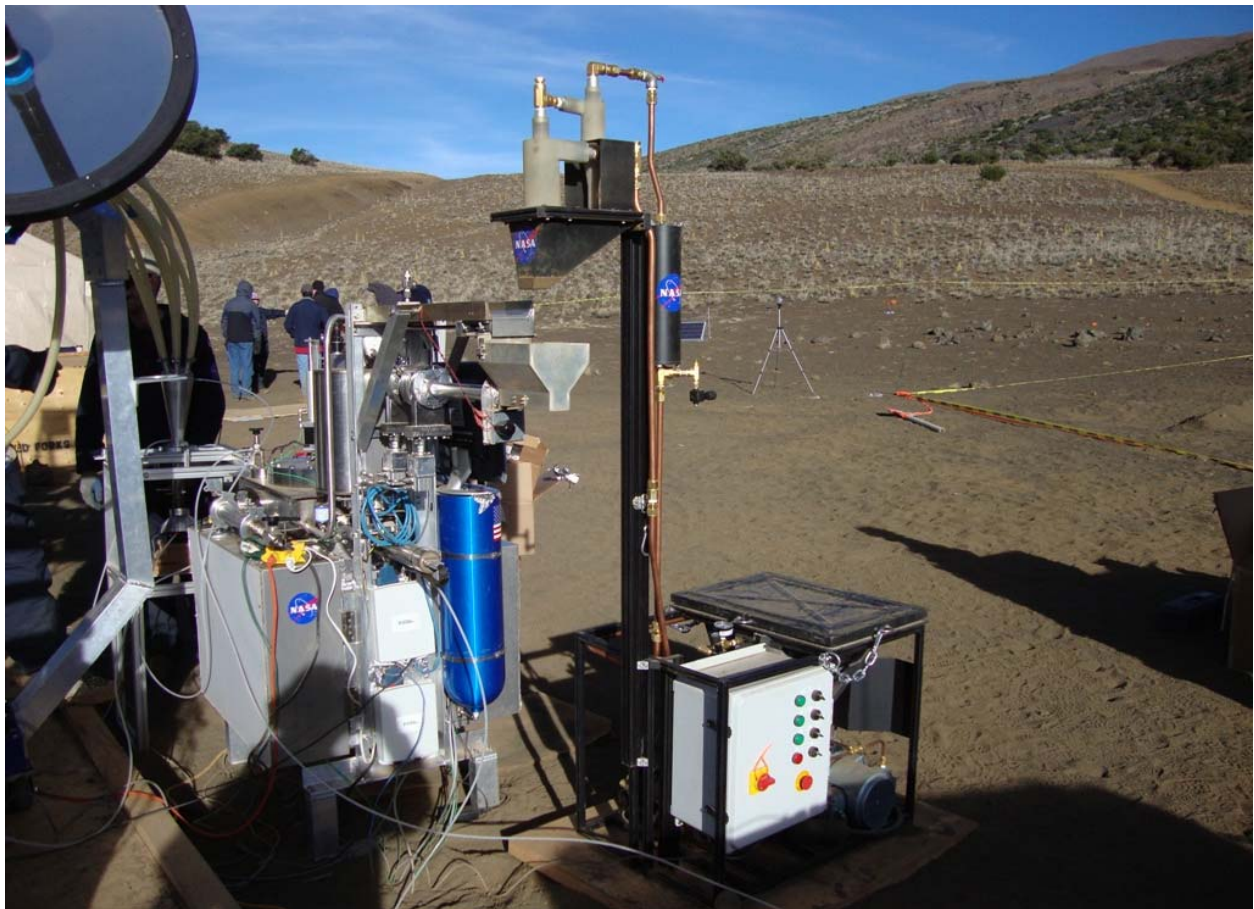


Figure 7: The Pneumatic Feed System “Proof of Concept” Demonstrator for the Carbothermal O₂ Reactor which was developed by NASA KSC and Honeybee Robotics, and demonstrated on Mauna Kea in February 2010.

In the 1-g environment of earth, pneumatic conveying utilizes a small amount of compressed gas to transport a large quantity of granular material. A carefully designed cyclone separator can mechanically separate the mixture of gas and granular material in a highly efficient manner, including micron-sized particles. When the solid particulates in the dusty gas flow collide with each other and with container walls, they can become charged triboelectrically. This effect can be utilized to enhance the particle removal efficiency by applying an electric field to the dusty gas flow inside the cyclone to guide the charged particles towards the wall of the cyclone where they slow down and agglomerate, which makes it easier to collect the particles at the solids outlet port located at the bottom of the cyclone (Dietz 1982). This type of cyclone is called an electrocyclone.

A reduced gravity experiment was performed by JSC researchers in 1992 involving the pneumatic transport of 150-micron-diameter glass beads using a venturi eductor to feed the glass beads into an air flow. They found that choking velocity measurements for vertical particle flow against gravity was noticeably lower at 1/6-g as compared to 1-g (Sullivan 1992, 1994). A lower choking velocity may result in less internal pipe erosion caused by abrasive lunar dust if the dust can be conveyed at a lower velocity. However, the disadvantage with lowering the gas flow rate is that since cyclone separators are designed to operate at a specific input flow rate, a lower flow rate can reduce the gas-solids separation efficiency. Another aspect of our study was to investigate the use of an electrocyclone as a means of maintaining a level of high efficiency for particle removal even if the dusty gas flow velocity is lowered. A high particle

removal efficiency at the receiving end of the pneumatic transfer process is necessary in order to be able to recycle the convey gas for repeated use.



Figure 8: The exhaust from the cyclone separator in the foreground in the right figure was the input for an electro-cyclone (left figure) positioned behind it during the reduced gravity flight pneumatic regolith transfer experiment conducted in August 2009. Reduced gravity flight experiment in Aug 2009, and cyclone separators for gas-solids filtration, including electro-cyclone.

The three main objectives of the terrestrial and reduced gravity flight (RGF) experiments were (1) to demonstrate the feasibility of pneumatically transferring lunar regolith as a dense, dusty gas to an ISRU reactor, (2) to measure our system's typical mass transfer rate for a given lunar regolith simulant that is conveyed pneumatically against gravity as a dusty gas to a fixed vertical height under local gravity conditions (1-g and 1/6-g), and (3) to determine the efficiency of our series cyclone filtration system in removing particles from the exhaust gas flow, including the potential use of an electrocyclone to enhance particle removal efficiency.

The configuration of the experiment is depicted below in Figure 9, and the specific details are as follows:

- The experiment assembly in Figure 9 consists of a polycarbonate secondary containment box with a secondary High Efficiency Particulate Arresting (HEPA) filter, supply and discharge containers for lunar regolith simulant, an eductor for pneumatic conveying, a convey pipe, two cyclone separators connected in series with HEPA filters on the exhaust of the final cyclone, air pressure and flow rate meters, and dust particle counters connected to the dusty gas inlet and the clean gas outlet of the second cyclone. Optional is a high voltage power supply that allows the second cyclone B to act as an electrocyclone if desired.
- Two lunar regolith simulants, known as NU-LHT-2M and Tephra, were studied. One simulant at a time was contained within the experiment assembly shown in Fig. 9. The NU-LHT-2M lunar regolith simulant is based on the chemical composition of NASA averaged Apollo 16 regolith samples. Tephra is a volcanic ash and cinder material from Mauna Kea, Hawaii.

Figure 9 is a schematic of the experiment hardware contained within an aluminum framed housing, and enclosed by sheets of transparent polycarbonate around the sides and by sheets of aluminum at the top and at the base. The housing structure was designed to allow the pneumatic regolith transfer experiment to fly in a safely contained manner onboard an aircraft which conducted a series of parabolic flight paths. During each parabola, the RGF experiment was performed for 25 seconds under simulated lunar gravity conditions after which time the air flow was shut off during a period of time in which the experiment experienced variable gravity conditions including increased gravity. The use of HEPA filters ensured that

particles larger than 0.3 micron would not exit into the ambient atmosphere outside of the pneumatic conveyor system. The polycarbonate sheets allowed for the pneumatic regolith transfer to be visible outside of the box, and also served as a secondary containment in case of dust leakage from the system. A secondary HEPA filter was mounted on the secondary containment box to prevent the filtered air from pressurizing the box. Compressed dry air was used as the convey gas so that the exhaust gas from the cyclones did not have to be vented outside of the aircraft.

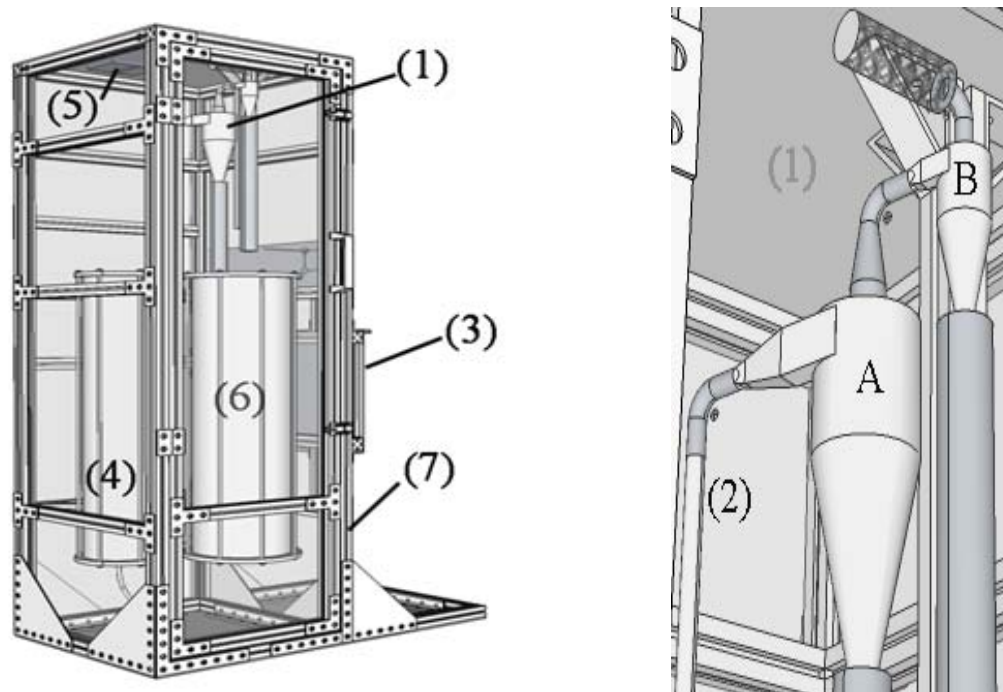


Figure 9. Graphic of the reduced gravity (1/6-g) experiment hardware including a close-up view (right-side graphic) of a series array of cyclones with the upper most having a HEPA filter attached to its exhaust gas outlet. The same setup was also used for ground tests at 1-g. (1) Two cyclone array using a mechanical cyclone (A) and an electrocyclone (B); (2) SS pipe; (3) Interface panel for gas inlet and gauges; (4) Regolith supply container and venturi eductor; (5) HEPA filter on the secondary containment box (7); (6) Regolith discharge container representing an ISRU reactor mockup; and (7) Secondary containment box using aluminum frame and supports, and polycarbonate sheets. Total mass of the flight rig including lunar regolith simulant: 195 kg.

The regolith supply container (transparent acrylic) in Fig. 9 could be filled with 16.5 kg of lunar regolith simulant that was to be transferred to the regolith discharge container (also transparent acrylic), which served as a mockup of an ISRU reactor chamber. Height restrictions onboard the RGF aircraft limited the total transfer height to 1.5 m for conveying the lunar simulants from the bottom of the regolith supply container to the inlet of the first cyclone located above the regolith discharge container.

The gas/solids mixer shown in Fig. 10 is a stainless steel venturi eductor. The eductor pulls granular material out from the center of the bottom plate of the regolith supply container, and it is used to entrain the lunar regolith simulant into the air flow and to convey the dusty gas along a stainless steel pipe to the cyclone separators.

The cyclone body and air exhaust pipe of the two cyclones shown in Fig. 8 were fabricated from stainless steel, and they were joined using a non-metallic cap to electrically insulate the exhaust pipe from the cyclone body when the cyclone (B) is operated as an electrocyclone. Except for the air exhaust pipe of the electrocyclone, which is connected to the high voltage output cable of a high voltage DC power

supply, the cyclone body and all other metal components contained within the secondary containment box are connected to the electrical ground.



Figure 10: An eductor produces a dense flow of dusty gas by creating a partial vacuum via the Venturi effect that entrains lunar regolith feedstock material into a flow of clean dry air.

Figure 11 shows the actual testing of the pneumatic transfer hardware during the reduced gravity flight as Tephra was transferred pneumatically into the Regolith Discharge Container, which served as an ISRU reactor mockup. Although nearly all of the Tephra was transferred during the reduced gravity flight, dust adherence to the walls of the acrylic container prevented an exact determination of the total time needed to complete the pneumatic transfer of Tephra into the discharge container. The same hardware setup was used to conduct the terrestrial testing discussed next. The RGF results are discussed later in further detail.



Figure 11: Photo of the RGF experiment showing Tephra that fell from cyclone A into the Regolith Discharge Container. The Tephra flowed vertically upward along a convey pipe from the eductor located at the bottom of the Supply Container (not visible in photo). The convey pipe had a vertical-to-horizontal transition which connected it to the inlet of cyclone A in Fig. 9. The gas exhaust from cyclone A became the input for the smaller cyclone B, which discharged dust into the blue hose shown in the picture. The exhaust from cyclone B passed through HEPA filter bags before exiting into the transparent containment box, which had a secondary HEPA filter that allowed the filtered air to enter into the aircraft cabin.

Terrestrial Experiments

When compressed dry air was applied to the gas inlet of the venturi eductor, the partial vacuum created by the eductor was found to immediately begin feeding lunar regolith simulant material into the input air flow to the eductor, thus producing a very dense flow of dusty air that exited the eductor along the convey pipe towards the cyclone separators. Tephra, being less dense than NU-LHT-2M and having a different particle size distribution, was found to be relatively easier to convey pneumatically than NU-LHT-2M. Although, the supply container had a flat bottom rather than a funnel shape in order to reduce the overall height of the container, each simulant material was successfully educted from the center of the supply container's base plate. The total amount of material that was transferred from the regolith supply container depended on the magnitude of the air pressure applied to the gas inlet of the eductor, and on the efficiency by which the regolith simulant could be fluidized within the container before being drawn out by the eductor.

The dusty air flow that was produced at the eductor traveled a vertical height of 1.5 m before entering the first cyclone. Most of the granular material collected by the first cyclone exited the solids outlet port at the bottom of the cyclone to be deposited into the regolith discharge container. The dusty exhaust gas that exits from the top of any cyclone contains fine particles having sizes typically no larger than nine times the cut diameter of the cyclone. However, the actual size distribution of the particles contained in the flow between our two series cyclones could not be determined without disturbing the dynamics of the dusty air flow. The exhaust gas from the first cyclone became the input dusty gas flow for the smaller second cyclone, which was designed to have a cut diameter of a one micron or less. However, due to the very dense flow of dusty air (also observed in 1/6-g) entering the second cyclone, it was not possible to operate the second cyclone as an electrocyclone, which only performs effectively on a dilute particle input flow that was not able to be achieved using only two cyclones separators connected in series. Since the regolith feed to the eductor was not being metered during the terrestrial and reduced gravity tests, the continuous dense flow of dusty air overwhelmed the cyclones.

The supply container would typically be filled with 15 – 17 kg of lunar regolith simulant. Each of the lunar regolith simulants, NU-LHT-2M and Tephra, was able to be pneumatically transferred from the center of a flat-bottom regolith supply container. With some fluidization of the simulant in the supply container, it was possible to transfer all but ~1 kg of simulant to the discharge container, which served as a mockup of an ISRU reactor chamber. Depending on the effectiveness of the fluidization of the granular material inside the supply container, typical mass transfer rates of 2 – 4 kg/min were achievable with an unmeted regolith feed to the eductor. Although metering the feed of regolith to the eductor would reduce the mass transfer rate and lengthen the overall transfer time, this would likely result in an improved performance of the cyclone separators in removing particles from the dusty air flow and depositing these particles into the regolith discharge container. These tradeoffs must be considered in designing a pneumatic regolith transfer system for lunar operations.

Reduced Gravity Experiments

A flight rig was constructed at NASA Kennedy Space Center to meet the safety requirements for conducting reduced gravity (1/6-g) tests onboard an aircraft. The aircraft achieves short periods of reduced gravity by flying a series of parabolic flight trajectories. During the parabolic trajectory, the aircraft also experiences periods of increased gravity (~1.8 g) which the experiment must also endure. The RGF pneumatic transfer experiment was initiated immediately after the lunar gravity condition was achieved and was terminated approximately 25 sec later at the end of the reduced gravity experience. Figure 11 shows the pneumatic transfer of Tephra under simulated lunar gravity conditions.

As in the terrestrial tests, it was observed that most of the Tephra transferred from the supply container to the discharge container located beneath the cyclone, but the dense flow overwhelmed the cyclone separators. Insufficient visibility through the secondary containment box prevented the precise determination of the number of parabolas required to transfer the Tephra under 1/6-g conditions. Although the mass transfer rate of Tephra could not be determined, it was observed that approximately

15 kg of Tephra was easily transferred pneumatically from the supply container in less than the ~15 minute duration in simulated lunar gravity.

When the NU-LHT-2M transfer process began under 1/6-g conditions, this granular material was also transferred easily from the supply container to the discharge container despite being more compactable than Tephra. However, after ten parabolas (~250 sec), it was observed that the transfer process had stopped. Although the NU-LHT-2M was assumed to have been sieved, a post analysis showed that a ~0.5-cm-diameter “rock” had become clogged in the eductor’s solids inlet which prevented regolith simulant particles from entering the eductor and being entrained in the air flow. Nevertheless, it was observed that 8.8 kg of NU-LHT-2M could be transferred vertically resulting in a mass transfer rate of 2.1 kg/min. The Tephra mass transfer rate is believed to be probably greater than this value given that Tephra is less dense than NU-LHT-2M.

The efficiency of our particular series cyclone filtration system in separating particles, including the use of an electrocyclone, could not be determined due to the dense flow of dusty air having overwhelmed the cyclones in 1-g and in the 1/6-g environment. The dense flow must be factored into a re-design of the cyclone system and 1/6-g effects must be included in the design parameters. It is likely that different cyclone systems will be required for the terrestrial 1-g system and for the lunar 1/6-g system due to the expected higher mass transfer rate of regolith in 1/6-g (Sullivan 1992, 1994).

A pneumatic alternative to the venturi eductor for transferring regolith is to use the jet-lift method, which was successfully demonstrated at low pressure (Zacny). The jet-lift method selectively excites particles through transfer of gas momentum into the particles in the vicinity of a gas injection head. The resulting dusty gas flow is subsequently transported along a tube containing the particles as the gas attempts to ultimately escape into a low pressure environment. Experimental tests in a vacuum chamber at ~5 torr demonstrated regolith-mass-to-gas-mass transport efficiencies exceeding 1000:1 utilizing this technique.

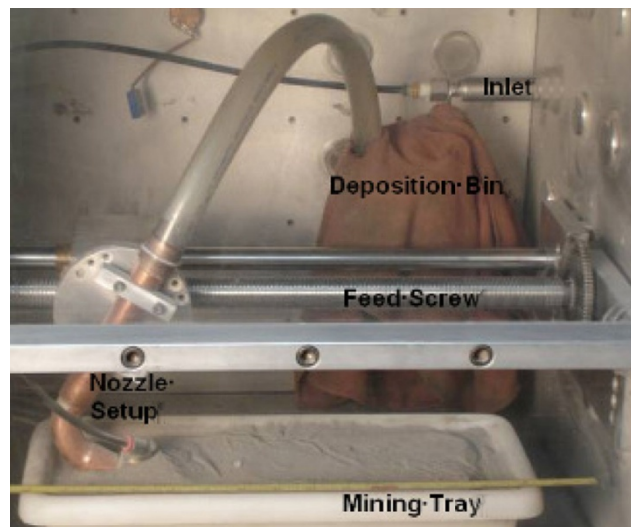


Figure 12: Jet-Lift Regolith Transfer method.

Finally, the compressor requirements for pneumatic regolith transfer are 5 SCFC at 20 psi (138 kPa) of gaseous hydrogen. Since the temperature of the regolith transferred is approximately 700 degrees Celsius, compressors that meet these requirements are highly specialized and few vendors are capable or willing to tackle this challenge. Consequently, the search is continuing for a compressor that is suited to the special conditions imposed on the pneumatic regolith feed system by the ISRU reactor’s working environment.

Conclusions

The OPTIMA tests on Mauna Kea, Hawaii in November of 2008 demonstrated the feasibility of producing oxygen at rates equivalent to 660 kg/year in a Lunar Outpost. The enclosed auger regolith feed system performed well and met all objectives. Batches of 8 kg of tephra were consistently, repeatably and successfully fed from the input hopper to the reactor and then expelled to the surface. High temperatures and abrasive particles were handled well with this system. Lifetime testing is required to determine the wear rates and ultimate system reliability. The system proved to be very robust in limited field testing. Phase II of the ROxygen system design will incorporate the lessons learned and increase the fidelity of the prototype hardware.

As a result of terrestrial and reduced gravity experiments, we have been able to show that the dense-flow pneumatic transfer method is able to successfully convey lunar regolith simulants such as NU-LHT-2M and Tephra to a vertical height of 5 ft (1.5 m), which is not an absolute physical limit but simply a limitation that was imposed by the available vertical space in the reduced gravity aircraft. Although we have shown that it is possible to transfer lunar regolith simulants pneumatically as a dense flow of dusty gas in a simulated lunar gravity environment, it is also important to realize that the reduced gravity aircraft also undergoes periods of increased gravity as high as 1.8 g, which may cause the granular regolith simulant material to become compacted. The degree to which this effect might influence the pneumatic regolith transfer process can be lessened by keeping the simulant in a semi-fluidized state throughout the parabolic flight.

A cyclone separator is an important component of a pneumatic regolith transfer system delivers the regolith to a desired location, and filters the convey gas sufficiently so that the gas can be reused. It may be possible to design a single cyclone to perform gas-solids separation provided that a moderate dense flow of dusty gas is able to yield a sufficient mass transfer rate by metering the regolith feed at the eductor. The exhaust gas from any cyclone separator will contain fine particles that may be detrimental to the mechanical operation of a compressor intended for reusing the gas. In that case, a second cyclone, known as an electrocyclone, may be designed to remove particles that are even smaller than those removed by an ordinary cyclone of the same size.

Overall, the reduced gravity flight experiment and field testing proved that lunar regolith simulant can be effectively conveyed pneumatically in an ISRU oxygen production plant in order to introduce regolith simulant into the reactor; fluidize it within the reactor and hopper feed systems; transfer it from outer reactor annulus zones to an inner reactor cylinder vessel; and subsequently expel it from the reactor for disposal or use in subsequent resource processing (silica, aluminum, titanium, iron, etc.). The results of this experiment were used to influence the design of the ROxygen second generation oxygen production system being developed by the NASA ISRU project, in order to show that it is indeed possible to produce a minimum rate of one metric ton of oxygen per year (of lunar operation) from lunar regolith simulants in a reliable, long life and low maintenance system.

Acknowledgements

The NASA RFS team would like to acknowledge the support of the ETDP, CxP Lunar Surface Systems Office and the ISRU project for funding and directing technology development and systems integration work. In particular we would like to thank the ISRU project manager: Mr. William Larson, the deputy ISRU project manager: Mr. Gerald Sanders, the Director of the Innovative Partnerships Program (IPP), Mr. Douglas Comstock, and the Chief of the Lunar Surface Systems (LSS) Office, Mr. Christopher Culbert.

The reduced gravity experiment was supported by the NASA IPP under a 2009 program known as Facilitated Access to the Space Environment for Technology Development and Training (FAST). NASA IPP also supported the Pacific International Space Center for Exploration Studies (PISCES) analog field tests on Mauna Kea Hawaii in November 2008, as well as the Carbothermal pneumatic feed system attachment that will be tested in January 2010 at the PISCES test site, Mauna Kea, Hawaii.

Outstanding assistance from the Reduced Gravity Office at NASA Johnson Space Center ensured that the experiment would fly safely. The NASA KSC Prototype Development Laboratory contributed substantial manufacturing expertise and effort in order to produce this experimental payload under tight schedule constraints. Ground-based tests at NASA Kennedy Space Center were supported through funding from the NASA KSC CDDF program and from the ROxygen ISRU project under NASA ETDP. Finally, the management of the NASA KSC Surface Systems Office and KSC Engineering and Technology Directorates were very supportive of this advanced technology development effort.

In addition all of our industrial partners mentioned in the paper above, as well as component suppliers that have often provided invaluable advice and support. Most of all the team of dedicated engineers and technicians must be thanked for their commitment and hard work in order to design, fabricate and test these ISRU systems, often in harsh and demanding field test analog site locations with dust storms, extreme temperatures and long test days.

References

- Caruso, J.J., Greer, Lawrence C.; John, Wentworth T.; Spina, Dan C.; Krasowski, Mike J.; Abel, Phillip B.; Prokop, Norman F.; Flatico, Joseph M.; Sacksteder, Kurt R., "Cratos: A Simple Low Power Excavation and Hauling System for Lunar Oxygen Production and General Excavation Tasks," PTMSS Conference, Sudbury, Ontario, Canada, 10-13 Jun. 2007
- Cooke, D. et al, Exploration Strategy and Architecture, Implementing the Vision, 2nd Space Exploration Conference, AIAA, Houston (2006).
- Crosby, Kevin M., Agui, Juan, Pennington, C., Sorenson, E., Martin, E., Fritz, I., and Frye, B. (2008). "Inertial Filtration of Lunar Dust in Reduced Gravity," LPI Contribution No. 1446, p. 43, presented at the Joint Annual Meeting of LEAG-ICEUM-SRR, 28-31 October 2008, Cape Canaveral, Florida.
- Culbert, Chris (2009). "Lunar Surface Systems Project Overview."
NASA, http://www.nasa.gov/exploration/library/lss_systems_concepts_workshop.html.
- Dhodapkar, Shrikant, Jacob, K., and Hu, S. (2006). "Fluid-Solid Transport in Ducts," in "Multiphase Flow Handbook," ed. Clayton T. Crowe, Taylor & Francis, Boca Raton, Florida.
- Dietz, P.W. (1982). "Electrostatically Enhanced Cyclone Separators," Powder Technology 31, 221-226.
- Liu, Henry, and Marrero, T.R. (1988). "Transportation by Pipelines in Space Colonies," in "Engineering, construction, and operations in space", Proceedings of Space 88, Eds. Johnson, S.W., and Wetzel, J.P., 29-31 August 1988, Albuquerque, New Mexico.
- Mills, David, Jones, M.G., and Agarwal, V.K. (2004). "Handbook of Pneumatic Conveying Engineering." Marcel-Decker, New York.
- Pell, Mel, Dunson, J.B., and Knowlton, T.M. (2008). "Gas-Solid Operations and Equipment," Ch. 17 in "Perry's Chemical Engineers' Handbook" (8th Edition), eds. Green, Don W. and Perry, Robert H., McGraw-Hill, New York.
- Sanders, G.; Larson, W., "NASA In-Situ Resource Utilization (ISRU) Development & Field Testing," Presentation to "Hawaii's Aerospace Industry: The Next Frontier", Honolulu, The Hawaii State Capital Auditorium, August 21, 2008
- Schrunk, David G., Sharpe, B.L., Cooper, B.L., and Thangavelu, M. (1999). "The Moon: Resources, Future Development and Colonization," Wiley-Praxis, New York.
- Sullivan, Thomas A., Koenig, E., Knudsen, C.W., and Gibson, M.A. (1992). "Pneumatic Conveying of Materials at Partial Gravity," AIAA 92-1667, presented at the AIAA Space Prog. and Tech. Conf., 24-27 March 1992, Huntsville, Alabama.
- Sullivan, Thomas A., Koenig, E., Knudsen, C.W., and Gibson, M.A. (1994). "Pneumatic Conveying of Materials at Partial Gravity," J. Aerosp. Eng. 7(2), 199-208.
- Zacny, Kris A., Mungas, Greg, Mungas, Chris, Fisher, Dave, and Hedlund, Magnus. "Pneumatic Excavator and Regolith Transport System for Lunar ISRU and Construction", Paper #AIAA 2008-7824, AIAA SPACE 2008 Conference & Exposition, 9 - 11 September 2008, San Diego, California.

Refined Gearbox Design for the Chariot Lunar Rover

Steve Bauman* and David Lewicki*

Abstract

In planning for NASA's return to the moon by the year 2020, the NASA Johnson Space Center (JSC) designed and built a lunar concept vehicle called Chariot. Slightly larger than a pickup truck, it was designed to demonstrate similar utilitarian functions, but with twelve wheels for redundancy, reliability, and reduced surface contact pressure. JSC designed a motor gearbox to drive each of Chariot's six wheel pods. The pods can be independently steered over 360° for maneuverability. This paper describes the design of a second generation, drop-in replacement gearbox. The new design has a lower parts count, and is lighter than the original, which represents a step toward flight hardware.

Introduction

The goal of this work is to demonstrate a gearbox for Chariot that would be closer to what NASA could ultimately send to the moon. With fewer moving parts, it would be smaller, lighter, and have improved reliability. Helicopter gearbox designs, one of our major research areas, share the concerns for reliability and weight reduction that space hardware demands. Therefore, NASA Glenn Research Center was selected to help custom design the Chariot gearbox. As part of this effort, high-performance, aerospace quality gears were designed, specified and fabricated.

Design requirements for the new gearbox were developed to include, very importantly, that the new gearbox make use of identical motors so that direct comparisons could be made quantitatively. Like the original, two gear reduction speeds would be provided, and each would supply nearly the same output gear reduction ratio as the original. The same mounting bolt pattern to the steering box top plate would be specified so that replacement of the original gearbox would be straightforward, with minimal operational downtime. Similarly, the electrical circuits would be compatible, and the exact same electrical wire connectors used.

Description of Chariot

Chariot is slightly larger than a pickup truck and is designed for truck-type utilitarian purposes on the moon (Fig. 1). This includes the ability to carry astronauts and/or substantial loads of equipment or regolith. It can be fitted with a soil-moving blade, and the flat top deck of the vehicle lends itself to custom-configurations for different missions.

Chariot has six identical and independently motor-driven wheel pods, three on each side of the vehicle (Fig. 2). Each pod has a pair of driven wheels, so the vehicle has a total of twelve wheels total. Having numerous wheels and pods creates redundancy to assure reliability, and reduces the ground surface contact pressure. All six pods and wheel pairs can be steered independently, and to any angle (a full 360-degree capability) making the vehicle highly maneuverable. For example, it can travel a straight path or make turns while maintaining the vehicle body at any desired angle relative to the motion (often referred to as crab-motion control). Steering can also be optimized for special duties such as towing another vehicle, or conducting regolith excavating operations.

* NASA Glenn Research Center, Cleveland, OH

Each wheel pair is driven by a differential which is powered by a shaft that extends vertically down through the steering gears from a motor-gearbox mounted on top. This gearbox is the subject of this paper. Furthermore, each pod has its own combination of passive and active suspension. The active part allows for adjusting the chassis height, including lowering it to the ground for easy egress of the astronauts, and easier loading and unloading of cargo.

The vehicle can be operated by an on-board astronaut (Fig. 1), a remote astronaut (possibly while stationed in a lunar habitat), or remotely from earth. Some limited autonomous operation is also likely. The prototype has been demonstrated with an astronaut operation station. A suited astronaut stands on a platform which holds the operator controls, an instrument panel, and a surround railing for astronaut safety. This entire structure, controlled by the astronaut, rotates to provide the full range of visibility that a constraining suit would not otherwise easily allow.



Figure 1. Chariot with Astronaut Operation Pod (Dec-07)



Figure 2. Chariot Wheel Pods

More recently, the Chariot has been outfitted with a pressurized crew cabin that occupies most of the available mounting space. In this configuration, the vehicle is called the Lunar Electric Rover (LER). The cabin allows for shirt-sleeve operation for up to four astronauts, and includes berthing for extended occupations of up to 14 days (Fig. 3, 12, 14). Normal access to the cabin is through a door on one side of

the cabin. Using Chariot's sideways crab motion ability, the cabin door can be 'docked' to a mating door, thus maintaining a pressurized environment.

There are two externally mounted lunar walking suits located on the back side of the cabin. By way of clever "suit ports", an astronaut can enter and occupy either suit from inside the cabin, and become sealed-off and disconnected from the cabin, all with no help. Following the completion of their extraterrestrial activities, the astronaut can return to the cabin using the reverse procedure. This system is intended to minimize the invasive moon regolith from entering the pressurized volume.



Figure 3. LER Starboard Center Wheel Pod with New Gearbox

The Original Gearbox

As already mentioned, one gearbox on each pod drives the differential that turns both wheels. The original gearbox was designed and built around readily purchased off-the-shelf gears, bearings, electric clutches, and shafting. The design utilizes a total of 12 gears, 17 bearings, and 7 different shafts (Fig. 4). The design also incorporates an electric brake that prevents motion when it is de-energized, and an RPM encoder. Two selectable speed ratios are provided. The low speed provides a 16:1 gear reduction for a vehicle speed of about 4.8 km/hr (3 mph), while the high speed provides a 4:1 gear reduction for a vehicle top speed of 19 km/hr (12 mph). The speed selection is accomplished with two electric clutches.

Two concurrently operating electric motors drive the first large gear, both to generate adequate power and for motor redundancy (Fig. 5). The motors used are rated for 300 VDC, and each one draws up to 8 amps to produce 2.1 kW (2.8 hp) at peak efficiency. The resulting gearbox works very well, and is still in use on the LER prototypes today.

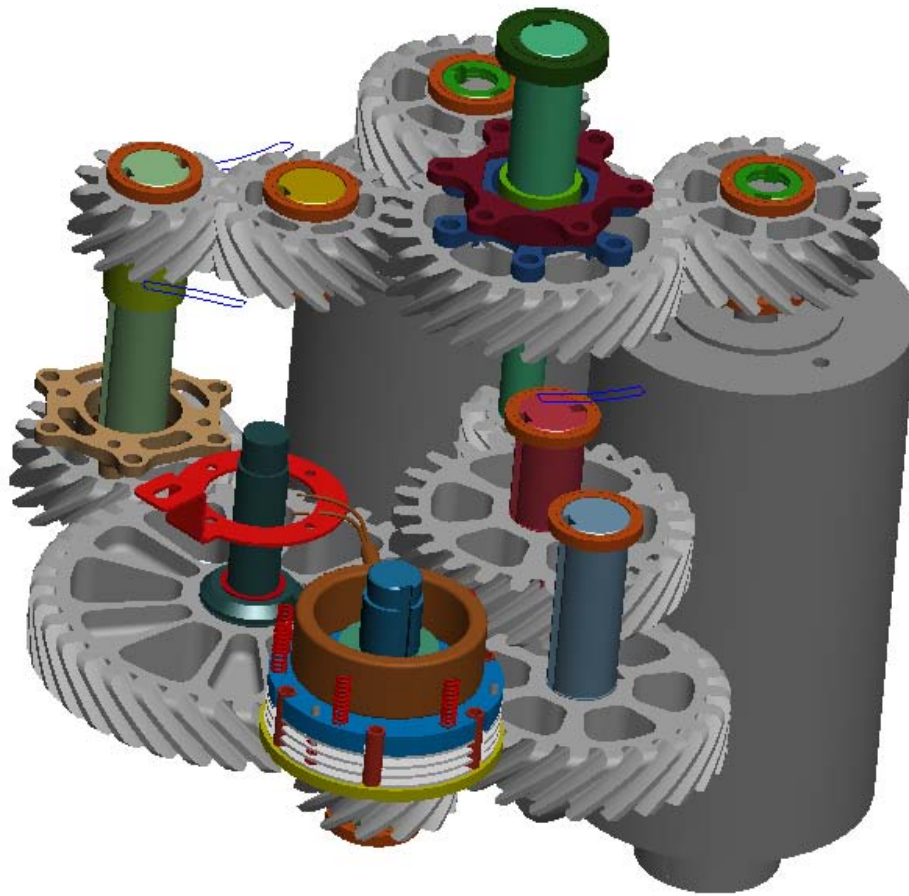


Figure 4. Illustration, Original Gearbox Gear Train

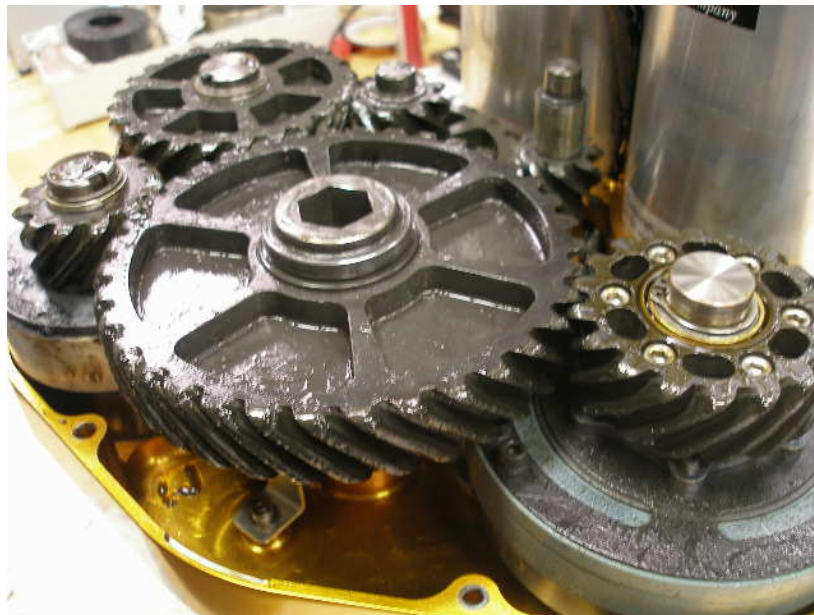


Figure 5. Original Gearbox, Lid Removed

Second Generation Gearbox, Concept

The design goal for the new gearbox was to provide a configuration which would be better suited to send to the moon. By using helicopter-grade gearing, the new design would have fewer gears, and be both smaller and lighter.

Drive Train Design

Reducing the number of gears inherently requires that each meshing gear pair accomplish more of a gear reduction than might be possible or practical when constrained by the use of catalog gears. The original design used off-the-shelf gears to meet the time and budget constraints for the fabrication of the original gearboxes. For the second generation gearbox, after considering many different gearing configurations, the simplest approach that still met the speed range criteria was adopted. Custom-made high-strength gears allowed the use of fewer (7 instead of 12) and lighter gears. Also, the gear train consists of just two parallel axes, resulting in fewer shafts (3 instead of 7) and bearings (13 instead of 17). Two electric clutches, similar to those in the original gearbox, were mounted in series on the same shaft (Fig. 6). This also allows the gear casing profile to be reduced in size, thus contributing to making a more compact and lighter final product.

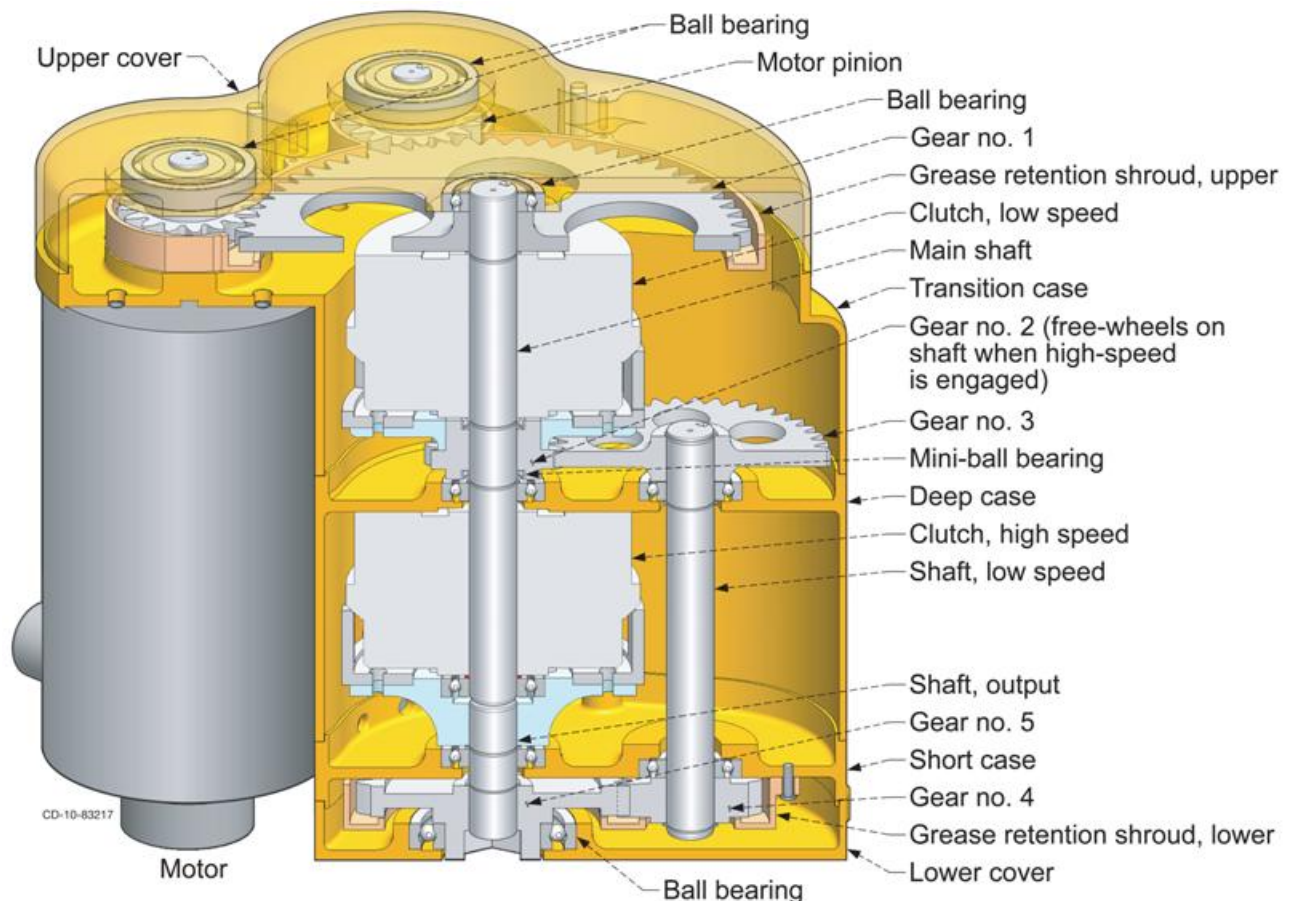


Figure 6. Chariot Gearbox Cross-Section Labeled Illustration

Like the original gearbox, the two motors both mount into their own stub shafts which are supported at both ends by ball bearings, and have integral gear pinions. This allows for the motors to be installed or removed from the assembly without opening the gearbox. Also like the original gearbox, both motors drive the same gear, but in this gearbox design, the gear must be quite large in order to achieve an immediate gear reduction of 3.94. This gear drives the main shaft which extends vertically down and drives both the low and high-speed electric clutches. When high speed is required, the low speed clutch is disengaged and the high-speed clutch is engaged. This causes the main shaft to drive the output shaft, which is located at the end of the main shaft, and gear #5. The output shaft is supported by its own bearings, one on the shaft and the other on gear #5. Gear #5 includes the female hex which is the output of the gearbox. It mates to the existing shaft hex that protrudes above the gearbox mounting plate atop the steering box of the wheel pod. Conversely, when low speed is required, the low-speed clutch is engaged and the high-speed clutch is disengaged. This causes gear #2 on the end of the low-speed clutch to drive the low-speed shaft via gear #3, and gear #4 then drives gear #5 on the output shaft and with an additional 4.1 gear reduction for a total low speed gear reduction of 16.14:1. When in high speed, gear #2 is back-driven by gear #3 and #4 and spins relative to the main shaft on its own mini-ball bearings.

Various gear sizes and pitches were considered until the final design was adopted and the exact gear ratios were established (Fig. 7). Given these, the various low and high output speeds, torques, and power were calculated for each of the motor characteristics of top speed, peak efficiency and peak power. This data was then used to select the electric clutches, mainly based on their torque capability, a maximum of 95 N-m (70 lb-ft). For high speed, this torque represents the gearbox output torque limit because the clutch is acting directly on the output shaft. For low speed, the additional gear speed reduction of 4.1 results in an output torque capability of 389 N-m (287 lb-ft).

Gearing

Gearbox Plane	Gear Pitch	lesser face width (mm)	lesser face width (in)	Gear #	no. of Teeth	Gear #	no. of Teeth	Reduction	low speed reduction
Upper	8	6.4	0.25	0	16	1	63	3.938	2.100 x 1.952 4.100
Center	10	6.6	0.26	2	20	3	42	2.100	
Lower	10	13	0.51	4	21	5	41	1.952	

Output Reduction	
High Speed	3.938 x 4.100
Low Speed	16.144

Motors and Gearing

Motor: Magmotor/SatCon Product no: 730420001

Motor	Torque				Speeds			Power watts		
	One Motor N-m	2 X motor N-m	High Speed N-m	Low Speed N-m	motor rpm	High Speed rpm	Low Speed rpm			
Top speed	0.0 (0.0 lb-ft)	0.0 (0.0 lb-ft)	0.0 (0.0 lb-ft)	0.0 (0.0 lb-ft)	2439	619	151	0 (0 hp)		
max efficient	9.18 (6.77 lb-ft)	18.34 (13.54 lb-ft)	72.3 (53.3 lb-ft)	296.4 (218.6 lb-ft)	2185	555	135	4202 (5.63 hp)		
peak power	28.24 (20.83 lb-ft)	56.5 (41.7 lb-ft)	222.4 (164.0 lb-ft)	911.9 (672.5 lb-ft)	1657	421	103	9805 (13.15 hp)		
stall	88.10 (64.98 lb-ft)	176.2 (130.0 lb-ft)	693.8 (511.7 lb-ft)	2844.6 (2098.0 lb-ft)	0	0	0	0 (0 hp)		
					Approx. motor speed at clutch torque maximums					
Clutch static maximums:					95 (70 lb-ft)	389 (287 lb-ft)	2105.4	535	130	5314.4 (7.127 hp)

Figure 7. Chariot Gearbox – Gear Ratios and Torques, Speeds, Power

The motor speed was approximated being loaded to these torque limits, and this was used to estimate the maximum low and high-speed output RPM and power-out before either clutch would be expected to begin slipping. If a clutch should start to slip, the output power would drop dramatically because the slipping friction of the plates would provide a much lower output torque. This could also damage the clutch because it is not designed to slip for long periods, or to dissipate the resulting heat. Currently, the power to the drive motors of the Chariot control system should not provide enough current to the motors to exceed the clutches' torque rating.

Gears

The gear teeth pitch and face widths were selected based on the anticipated operational loads and speeds. Traditional formulas were used to calculate gear tooth stresses, and to help decide the required gear pitch and face width. The width of the smallest of the two meshing gears at all three gear meshing planes is 1.5 mm (0.06 in) larger, which allows the gears to tolerate some axial misalignment due to dimensional tolerance stack-ups during assembly. The smaller gear was selected to have the larger width in order to keep the overall weight minimized, and to bolster wear duration of the faster turning gear. For example, while the large gear #1 has a face width of only 6.4 mm (0.25 in), which is enough from a gear tooth-strength standpoint, both motor pinions have a face width of 7.9 mm (0.31 in) to ensure that, after final assembly, the entire 6.4-mm (0.25-in) width of gear #1 is engaged. Similarly, gear #2 has a larger face width than gear #3, and gear #4 is larger than gear #5. Also, both gear #1 and #3 are large enough to be lightened-up by the addition of a pattern of holes, again in an attempt to minimize the weight of the final product. The gears are designed to helicopter-grade quality, or an American Gear Manufacturers Association (AGMA) gear tolerance Class 12.

Casing Design

It was a design goal for the case to shroud the gears as tightly as possible to minimize both the size and weight of the final product. It should be noted again that for compatibility, the same motors as used in the original gearbox were also used in the second generation gearbox. Due to time constraints, commercial off-the-shelf clutches were used that were very similar in size and capability to those in the original gearbox. Although the main drive gears were sized and optimized for minimum weight, the overall gearbox size was largely dictated by the size of the motors and clutches. Slightly taller than the original, the new gearbox is not nearly as broad, and is therefore smaller and lighter. Considerable effort went into fine-tuning the gearbox design so that the mounted height of the motors would only be slightly above the mounting plate (Fig. 8).

A stacked-component approach was used in the design of the case. This helped keep the size profile minimized because it allowed the top gear plane, with the two motor pinions and large gear, to be shrouded closely by way of the Top Cover before transitioning to the majority smaller profile required for the main body which encompasses the rest of the gears and both electric clutches (Fig. 6). A total of five parts make up the complete case: The Upper Cover, Transition Case, Deep Case, Short Case, and Lower Cover. Having a multi-part casing also reduced the machining risk on each separate part. The fit between all parts was kept flat (planar) for machining simplicity.

There was no seal designed between the casing interfaces. Like the original gearbox, no oil containment was required because grease lubrication was planned. However, a full perimeter lip was designed into the face-fits between each casing part. This serves to hold the required relative positioning between each of the casing parts for shaft and bearing alignments, and to make assembly easier. It also serves as a partial seal to help keep dirt out, and extraneous grease in. The final wall thicknesses were determined in part through the limited use of finite element analysis. The analysis indicated that the casing thicknesses could have been reduced further, but 3.18-mm (0.125-in) thickness for most of the walls was determined to be the minimum from a standpoint of machining comfort, stiffness, and warpage concerns.



Figure 8. New Gearbox on Bench

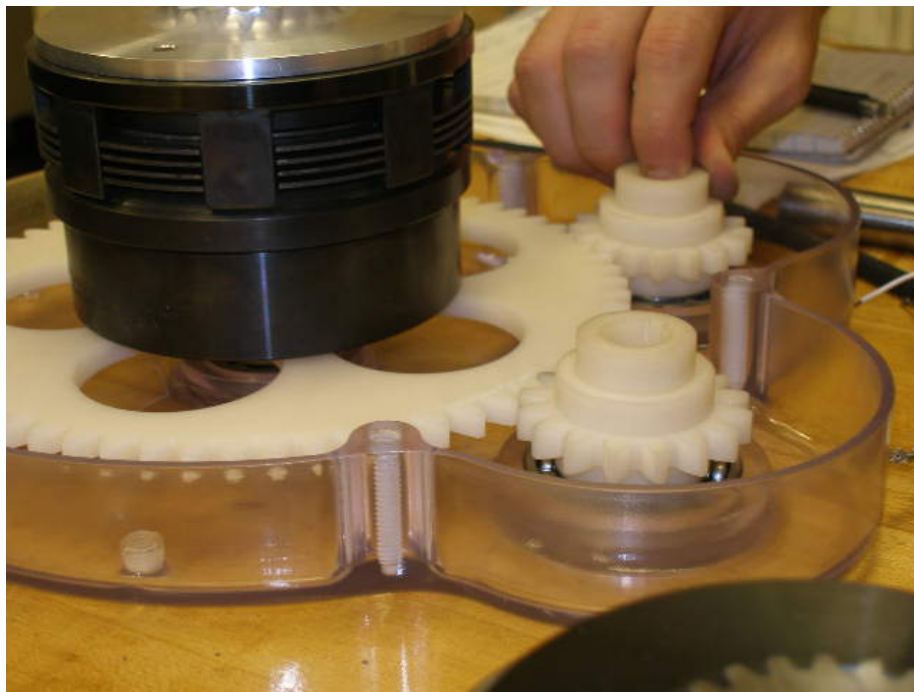


Figure 9. Rapid Prototype Gears in Clear RP Lid

Rapid prototypes (RP) were made of all the casing parts and gears before the design was finalized (Fig. 9) to allow for practicing the assembly sequence. The transparent casing parts were helpful during the trial assemblies. Some important changes to the final case design details resulted, and a detailed assembly procedure was initiated.

Grease Retention Shrouds

Enclosures around the gears were added to help hold the applied grease close to the teeth to extend the re-grease service lengths. Referred to as grease retention shrouds (GRS), similar enclosures have been used in certain commercial products such as heavy-duty hand drills. Of the three gear meshing planes of the design, a GRS was designed for two of them; the upper area where the two motor pinions engage gear #1 (Fig. 10), and at the lower output end where the low speed gear #4 engages with the output gear #5. The center gear plane of gear #2 and #3 was not shrouded because it would have made final assembly difficult, and the space between gear #3 and the housing was prohibitively small.

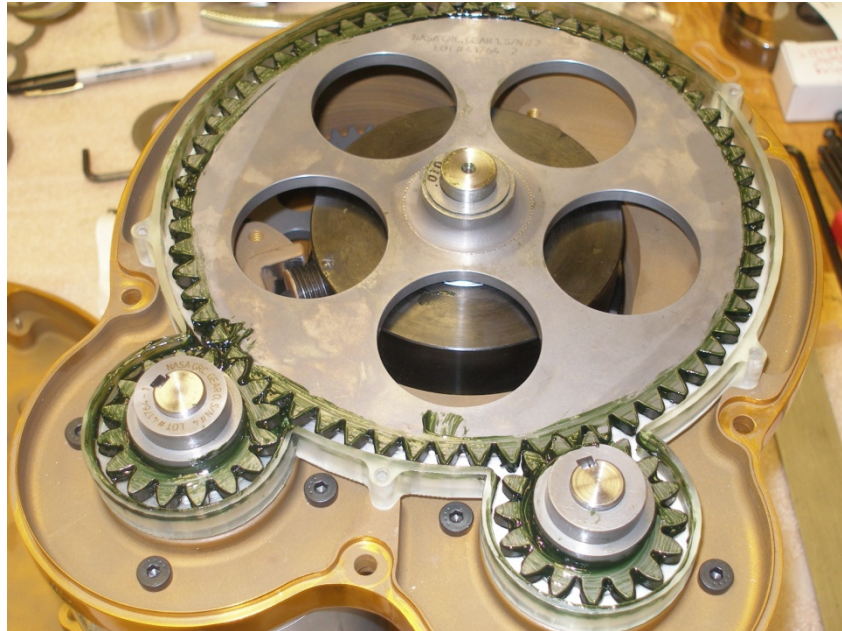


Figure 10. New Gearbox, Motor Pinions and Gear #1, with GRS

For quick and inexpensive fabrication, the GRS's were made by rapid prototyping. Exposure tests were conducted using coupons of three different RP materials and two kinds of grease because of concern whether commonly available RP materials might degrade when in contact with the anticipated hydrocarbon based greases. The results indicated that the material used by a laser stereolithography machine showed excellent property resistance to the grease exposure, therefore, work continued using the same material and process.

The Lower GRS is positioned over gears #4 and #5, and is screwed to the Short Case. This occurs just before the Lower Cover is installed and the lower four case parts are fastened (sandwiched) together by long screws. The Upper GRS was originally designed similarly, to be screwed to the Upper Cover, because this worked well with the topside-down order of assembly that is used. However, as a result of trial practice assemblies with the rapid prototype case, it was demonstrated that there is a great advantage in being able to remove the Upper Cover after the gearbox assembly was otherwise complete.

Removing the Upper Cover is the only way that, after the assembly is otherwise complete, a final check of whether the top gear meshing plane of gear #1 to the motor pinions is adequately centered (usually done by way of adding shaft shims). The Upper Cover is fastened on separately from the other four casing parts, making its post-assembly removal possible. Removal of the Upper Cover also serves as a convenient way to grease the gears initially, and to occasionally inspect the area for grease distribution and gear wear. The motors can even be run with this cover off, although only slowly and unloaded because all three shafts are not properly supported since their secondary support bearings are pressed into the Upper Cover.

With the GRS screwed to the Upper Cover, removing this cover required that the motor pinions and Gear #1 also come off, trapped and pulled by the GRS. While this is theoretically possible, in practice, these gears usually do not remove easily, and since the GRS is not very strong, it could easily break while attempting this. Therefore, instead of using screws, the design was changed so that holes in the GRS would fit onto pins from the case. Because it was desired to either remove the Upper Case and have the GRS remain in place on the Transition Case, or during initial assembly, place the GRS on the Upper Case and add the Transition Case to it, locating pins were provided on both cases (Fig. 11). Supports were designed into both case parts to help hold the GRS in its final trapped position, although a precise final position is actually not required. This approach appeared to work well.



Figure 11. New Gearbox, Lid Removed

Gearbox Fabrication and Assembly

Two functional gearboxes of the same design were fabricated in-house and assembled. One was ultimately adapted and mounted to the Chariot prototype while the other was kept for dynamics testing and modeling. A combination of 6061 and 7075 aluminum alloys were used due to their availability in the required starting stock sizes, and since either one suited the structural needs of the housing. The end result was that the Upper Cover, Transition Case and Deep Case were made of 7075, while the Short Case, Lower Cover, and the later Adapter Spacers were made of 6061.

Three case parts were primarily machined using a CNC 2-axis milling machine, while two were completed on a more sophisticated CNC machine that directly used the solid model data. After all five parts were close to completion, the assembly was placed into a boring machine to accurately locate and precisely precision machine the bearing pockets. Two additional parts were designed to allow the gearbox to easily adapt to Chariot; a new steering-box top plate on which the gearbox mounts, and a spacing plate to raise the mounted height of the new gearbox to accommodate the more shallow mating female hex.

The “Assembly Procedure” that was developed during trial assemblies with the RP casings was used for assembly, but with many changes and a great deal more added detail. One of the main lessons learned during the build was the need to pay attention to how the gears were to be axially aligned. Shaft shims were used to accomplish the aligning, but decisions of how to determine the shim size, what measurements were needed, and in what order to perform all the operations proved to be a challenge. Although the final assembly procedure does capture the process very well, it was more time consuming than originally thought.

Conclusions, Gearbox Mounted to Chariot

The new gearbox was completed and mounted on the center starboard pod of the Chariot, in LER form, for an inaugural drive (Fig. 3, 12-15). Software adjustments within the Chariot main drive controller were required to accommodate the slightly different gear ratio outputs. Also, the motor forward and reverse functions, due to the different gearing, had to be swapped for the High Speed function to work correctly. Beyond these issues, the gearbox appears to have operated well.



Figure 12. Chariot in LER Form, Starboard Center Wheel Pod with New Gearbox



Figure 13. LER Starboard Center Wheel Pod, New Gearbox Close-up



Figure 14. LER with New Gearbox Climbing a Steep Grade

Lessons Learned

1. Document the complete “Design Requirements” early, and revisit them regularly. While the project intent was to supply a smaller, lighter “drop-in replacement” gearbox with all the capabilities of the original, in the casing design process, both the rotary encoder and electric brake were dropped. JSC agreed to allow us to not provide these features, since they use the encoders integral to the motors, and not every gearbox has to have an electric brake.
2. While assembly is one thing, serviceability is quite another. Although it was possible to fully assemble the gearbox as designed, it would be highly beneficial if the Upper Cover could be removed without disassembling most of the unit. This led to an alteration in the way the Upper GRS was secured, allowing removal of just the Upper Cover.
3. Even in high precision work, account for tolerance stack-up by design. For instance, leave room on drive axles for spacing shims. Given the tolerance stack-up of any gearbox assembly, shims may be needed.
4. When possible, build contingency time into the schedule. Even in-house manufacturing shops may miss an estimated completion date, or number of hours to completion, as occurred with the gearbox casing parts. Due to Constellation Program driven priorities, the in-house shop started in August 2008 and was to be complete in October, but was not completed until December.
5. When schedule and budget allow, particularly for “high visibility” activities, minor resources devoted to “quality finish” of a product can be beneficial. Not all viewers appreciate seeing the “engineering details” hanging out. In this case, in order to match the original parts' finish, the original gearbox anodizing vendor was utilized after local vendors proved unable to match the required polished color finish.

Summary

A second generation “drop-in replacement” gearbox was designed and built for the concept vehicle called Chariot. State-of-the-art aerospace gear design and manufacturing practice were taken advantage of to produce optimally light weight gear sets, which were incorporated into a smaller, lighter gearbox with otherwise conventional components. The “lessons learned” in this gearbox build are broadly applicable.

Nickel-Titanium Alloys: Corrosion “Proof” Alloys for Space Bearing, Components and Mechanism Applications

Christopher DellaCorte*

Abstract

An intermetallic nickel-titanium alloy, 60NiTi (60wt%Ni, 40wt%Ti), is shown to be a promising candidate tribological material for space mechanisms. 60NiTi offers a broad combination of physical properties that make it unique among bearing materials. 60NiTi is hard, electrically conductive, highly corrosion resistant, readily machined prior to final heat treatment, and is non-magnetic. Despite its high titanium content, 60NiTi is non-galling even under dry sliding. No other bearing alloy, metallic or ceramic, encompasses all of these attributes. Since 60NiTi contains such a high proportion of titanium and possesses many metallic properties, it was expected to exhibit poor tribological performance typical of titanium alloys, namely galling type behavior and rapid lubricant degradation. In this poster-paper, the oil-lubricated behavior of 60NiTi is studied.

Introduction

Binary Nickel-Titanium (Ni-Ti) alloys are in widespread use in the medical and dental industries in applications where their biocompatibility and unique superelastic or Shape Memory Effect characteristics are readily exploited [1]. The Ni-Ti family of alloys traces their origins to pioneering work of William J. Buehler and his colleagues at the Naval Ordnance Laboratory during the late 1950's [2,3]. The designation NITINOL often used for these alloys is an abbreviation for Nickel-Titanium Naval Ordnance Laboratory. Buehler's early efforts identified both the Nitinol 55 and Nitinol 60 alloys, which contained 55 and 60 weight percent nickel respectively. Nitinol 55 is soft and was found to be easier to mechanically work and form than Nitinol 60 that was prone to excessive work hardening. Several hand tools were fabricated from Nitinol 60 to take advantage of its high hardness, electrical conductivity, non-magnetic behavior and corrosion resistance [4].

Materials for high performance bearings, gears and other mechanical components require a number of specific properties and characteristics. Among these key attributes are high strength and hardness, high thermal conductivity, and the ability to be manufactured to very high levels of precision with regards to final dimensions and surface finish. In addition, excellent corrosion resistance and good tribological properties are often of importance especially for applications in extreme environments. Spaceflight hardware destined to operate in the vacuum of space, beyond the realm of atmospheric corrosion, often must be stored for extended periods before launch, and are subject to bearing and gear corrosion problems. In select applications involving electric machines and sensitive instrumentation, good electrical conductivity and non-magnetic properties can also be highly desirable. Unfortunately, no currently deployed material possesses all of these properties.

Traditional tool steel based bearing materials, such as M50 and 52100 enjoy widespread application due to their high hardness, ease of manufacture and good tribological properties. However, these alloys suffer from corrosion attack if not protected and though electrically conductive they are also highly magnetic. In addition, when used as bearing rolling elements, their high density leads to high centrifugal forces and limited fatigue life. These considerations have driven the search and development of alternate bearing and mechanical component alloys, namely stainless steels and ceramics.

*NASA Glenn Research Center, Cleveland, OH

Stainless steels such as 440C are widely used in the bearing and gear industry where corrosion resistance and high hardness are required. These martensitic stainless steels are reasonably low cost, easy to machine prior to heat treatment and are dimensionally stable. When prepared through vacuum melting processes, they achieve very uniform, fully dense microstructures which lead to fine surface finishes and good fatigue behavior. Despite being referred to as “stainless”, however, the 400 series martensitic steels are prone to corrosion and are more accurately referred to as “corrosion-resistant” alloys rather than stainless. They are also highly magnetic.

Silicon Nitride ceramics, on the other hand, are essentially corrosion proof. They can be polished to very fine surface roughness and are quite wear resistant. Silicon nitride’s low density compared to steels also makes it ideal for ultra high-speed applications because lower centrifugal stresses result. These attributes make silicon nitride the material of choice for high stiffness, high load, and high-speed bearings and for applications that include corrosive conditions and aggressive sliding environments. Such applications include bearings for gas turbine hot sections, cryogenic oxidizer turbopumps and components for diesel engine fuel injection systems. Though non-magnetic, silicon nitride is an electrical insulator. It is also more expensive to manufacture than steels owing to the complexity and cost of the high temperature, high pressure powder metallurgy processing required. Another shortcoming of silicon nitride is the difficulty of fabricating it into bearing raceways and other complex geometries.

Historically, metallic alloys with high concentrations of titanium are poor tribological materials in that they do not respond well to lubrication by organic fluids [5]. For instance, alloys such as Ti-6Al-4V exhibit galling behavior in dynamic contacts even under conditions well lubricated by oils and greases. During contact, titanium readily transfers to the counter-face leading to rough surfaces, high friction and wear. In addition, titanium alloys are recognized as being chemically aggressive causing degradation of many lubricants [6]. When titanium alloys must be used due to other attributes like high specific strength or corrosion resistance, tribological contact is avoided through the use of thick barrier coatings and claddings.

Based upon a wealth of negative experience with titanium alloys in tribological contacts, 60NiTi would appear an unlikely candidate as a bearing material. On the other hand, ceramic materials with high concentrations of titanium can exhibit desirable tribological properties. Titanium carbide (TiC) and Titanium dioxide (TiO₂) are good examples. TiC coatings are often used to improve the surface finish and performance of stainless steel rolling elements in bearings and TiO₂, in the form of rutile, has been put forth as a potential solid lubricant under certain conditions [6, 7]. These ceramic materials, however, are brittle and cannot be used as structural elements. In the present paper, we present evidence that hardened NiTi alloys can be produced that are devoid of shape memory or superelastic behavior and that such alloys display excellent tribological properties under oil-lubricated contact conditions.

Materials and Procedures

The 60NiTi balls evaluated in this work was manufactured via a high temperature proprietary powder metallurgy process roughly similar to that described in the literature [8]. Pre-alloyed 60Ni-Ti powder was HIPed into rough, spherical ball blanks that were then ground, polished, and lapped to produce high quality (Grade 5) bearing balls 0.5 inch (12.5 mm) in diameter. 60NiTi plates were cut from cast and hot rolled plate stock. A multi-step thermal process (heat treatment) was used to enable rough machining of the plates and grinding of the bearing balls in a softened state followed by lapping to a very fine surface finish in a final hardened condition. The finished 60NiTi ball specimens, shown in the photograph in Figure 1, are bright and shiny in appearance and resemble conventional polished steel balls.

The elemental composition of the bearing material, as measured by atomic emission spectroscopy and energy dispersive, semi-quantitative X-ray analysis, were consistent and showed the specimens are nominally 55 atomic percent Nickel with the balance titanium. This translates to 60 weight percent Nickel, 40-weight percent titanium, hence the historical designation of NITINOL 60 or 60NiTi. Density was

measured at 6.71 g/cc and is about 15% lower than 440C stainless steel. Table I displays known and estimated properties of 60NiTi.



Figure 1. Nitinol 60 grade 5 test balls.

Table I. Nominal Comparative properties for conventional bearing alloys and NiTi55 and 60NiTi Nitinol 60 grade 5 test balls.					
Property	NiTi-60	NiTi-55	440C	Si3N4	M-50
Density	6.7 g/cc	6.5 g/cc	7.7 g/cc	3.2 g/cc	8.0 g/cc
Hardness	56-62 Rc	35-40 Rc	58-62 Rc	1300-1500Hv	60-65Rc
Thermal Conductivity W/m-°K	18	9	24	33	~36
Thermal Expansion	~10x10-6/°C	~10x10-6/°C	10x10-6/°C	2.6x10-6	~11 10-6/°C
Magnetic	Non	Non	Magnetic	Non	Magnetic
Corrosion Resistance	Excellent	Excellent	Marginal	Excellent	Poor
Tensile/Flexural Strength	~1000MPa	~900 MPa	1900 MPa	600-1200MPa (Bend Strength)	2500 MPa
Young's Modulus	~114 GPa	~100 GPa	200 GPa	310 GPa	210 GPa
Poisson's Ratio	TBD	~.3	.3	.29	.30
Fracture Toughness	TBD	TBD	22 MPa/√m	5-7 MPa/√m	20-23 MPa/√m
Maximum Use Temp	~400° C	~400° C	~400° C	~1100° C	~400° C
Electrical Resistivity	~80x10-6 Ω-cm	~80x10-6 Ω-cm	~36x10-6 Ω-cm	Insulator	~60x10-6 Ω-cm

*TBD means "to be determined"

Figure 2 shows the cross sectional microstructure of the 60NiTi ball specimens in the final hardened and polished condition. Microhardness measurements indicate values in the range of 58-62 on the Rockwell C scale in the hardened condition. As with most HIPed or sintered powder compacts, the prior particle boundaries are quite evident and are delineated by oxides and other tramp phases. Despite containing only Ni and Ti, Ni-rich NITINOL microstructures can be very complex due to a series of metastable intermetallic phases that could exist depending on thermal history [9]. Analysis of the 60NiTi ball specimens reveals multiple discrete phases (NiTi_n) with NiTi dominating at approximately a 77% volume fraction. The balance is made up from Ni₄Ti₃ at 11%, Ni₃Ti at 10%, and NiTi₂ at 2%.

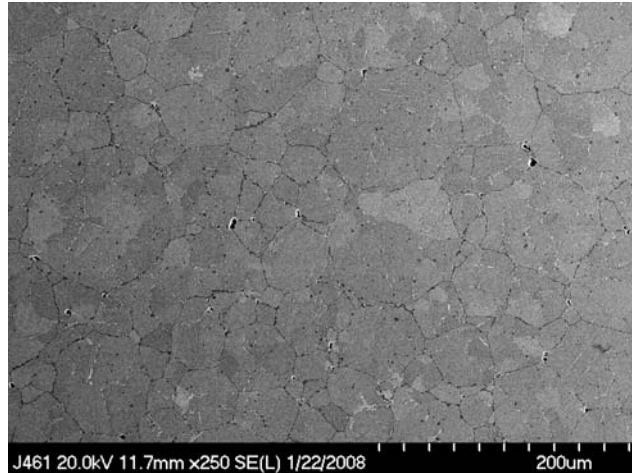


Figure 2. Cross-section electron micrograph of Nitinol 60 ball.

Preliminary differential scanning calorimetry results for the bearing blanks and finished bearings suggest that the 60NiTi bearing blanks may have a slight amount of martensite that could form if cooled below -15°C but in the hardened condition are microstructurally stable down to at least -100 degrees centigrade. This indication is corroborated by our physical measurements of the bearing balls and plates that have been dimensionally stable throughout the processing, handling and research activities undertaken. Buehler also reported excellent stability during the early alloy development [3].

To assess its tribological properties, Spiral Orbit Tribometer (SOT) tests were conducted using a single 60NiTi ball loaded between two rotating disks, lubricated with synthetic oil and tested in a vacuum. In this test, the 60NiTi ball is marginally lubricated with a small quantity (~ 25 micrograms) of oil and undergoes mostly rolling contact interrupted by a scrubbing/sliding event every disk rotation. The SOT is depicted in Figure 3 and described in detail in references 6 and 10. It is basically a thrust bearing with one ball and flat races (plates). One of the plates is stationary and the other rotates to drive the ball into an orbit that is an opening spiral. The ball contacts a "guide plate" at the end of each orbit, which forces the ball back into its initial orbital radius. A piezoelectric force transducer supporting the guide plate senses the frictional force developed on the ball as it slides on the rotating plate during the contact of the ball with the guide plate. During this contact, the coefficient of friction is obtained from this force and the load imposed on the system. The tribometer is housed in a stainless steel chamber that can be evacuated by a turbomolecular pump to $\leq 2 \times 10^{-8}$ Torr. It can be operated either in this vacuum environment or at atmospheric pressure.

The plate specimens were 440C stainless steel or 60NiTi. They were lapped flat and their final polish resulted in an arithmetic mean surface roughness, R_a , < 25 nm (1 min) determined by optical interferometry. The 60NiTi balls were 12.7 mm (.5 in.) diameter, Grade 5. The final surface cleaning procedure for all ball and plate specimens was by lightly rubbing with aqueous slurries of silicon carbide polishing powders, followed by sonication in deionized water. This preparation results in a surface on which water exhibits zero contact angle (spreads) and which exhibits an XPS spectrum a) devoid of impurities other than a small feature due to adventitious carbon.

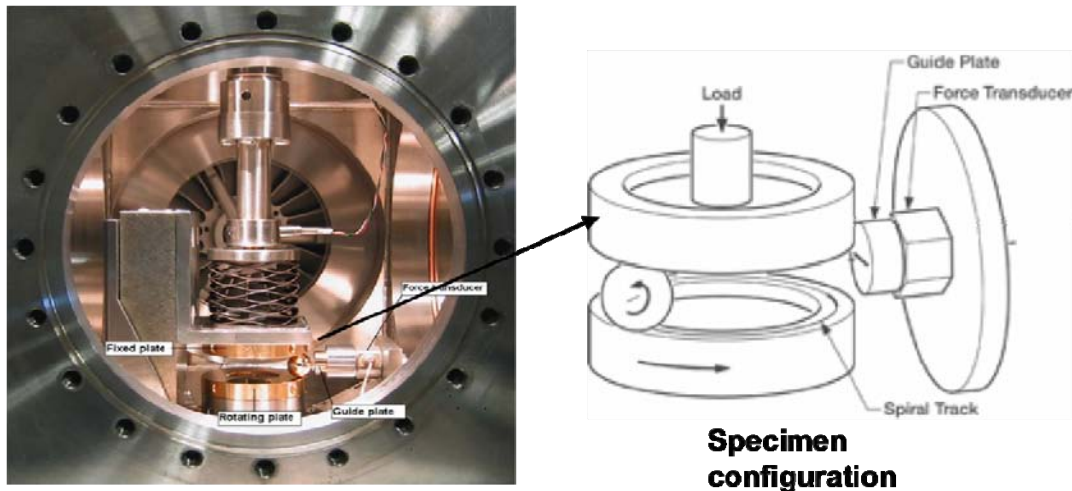


Figure 3. Spiral Orbit Tribometer used to evaluate the relative lubricant life of various alloys under simulated bearing conditions.

The plates were initially clean and only the ball was lubricated. For the present tests in the boundary regime, the ball is first weighed and then lubricated by dripping a dilute solution of the lubricant, ~ 1 mg of lubricant per ml of hexane solvent, onto the ball rotating on a small bench lathe. The ball is reweighed after evaporation of the solvent and the lubricant charge is obtained from the weight difference. About 20 mg (24 nl) of lubricant, a multiply alkylated cyclopentane (MAC) designated by the trade name Pennzane 2001A, were used on each ball. Tests were run here at a system load of 130 N (30 lb), which resulted in a track width of ~0.4 mm and corresponds to a Hertz pressure of 1.06 GPa. The test conditions result in operation in the boundary lubrication regime. Considering the small quantity of lubricant present in the tribosystem, test lifetimes on the order of a few tens of thousands are typical for good tribological materials like 440C and past experience with the SOT indicate its relevance in mimicking the conditions in a space ball bearing application [6].

Results and Discussion

Under these conditions considered representative of precision bearings, performance (life and friction) was comparable to that observed with 440C bearing balls. Figure 4 shows friction for tests of 60NiTi balls running against 440C plates (left graph) and Nitinol 60 plates (right graph) in the SOT. Typical lubricant lifetimes were approximately 30,000-60,000 revolutions indicating a slow lubricant consumption rate. In one test using both 60NiTi plates and ball, the rig was permitted to run well beyond the complete consumption of lubricant. In that case, friction climbed to a coefficient of around 0.35 but was stable and no galling tendencies were observed.

In comparison, SOT tests of balls sputter coated with pure, thin titanium films degrade the lubricant, experience high friction and seizure within a few dozen revolutions. Unlike traditional titanium alloys, the 60NiTi alloy performs well and is a good candidate for bearings and mechanical components and is impervious to the corrosion issues facing traditional bearing materials especially during storage before launching.

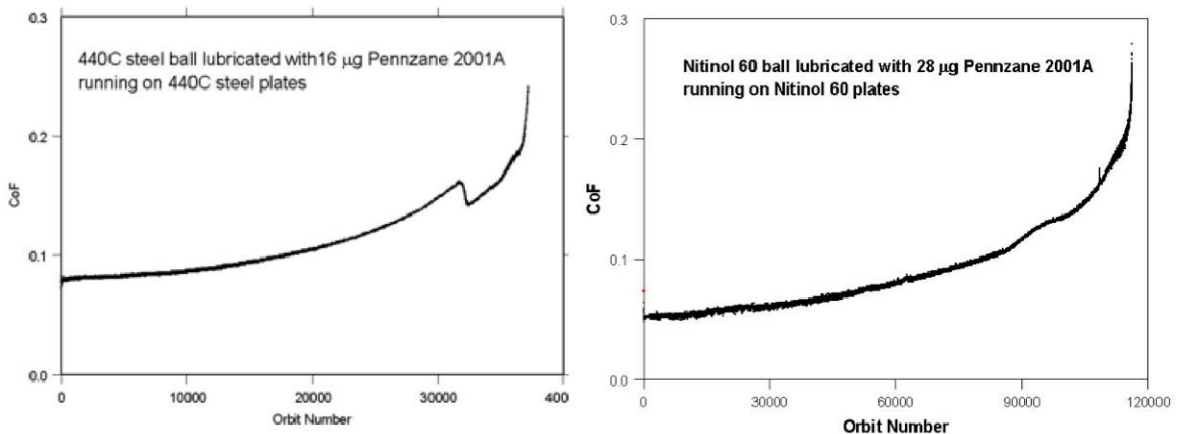


Figure 4. SOT results for Nitinol 60 ball running against 440C (left) and Nitinol 60 plates (right) showing comparable behavior.

Summary

This research effort has identified 60NiTi alloy as a promising candidate material for bearing and mechanical component applications. 60NiTi, when appropriately processed and fabricated, is dimensionally stable, hard, wear resistant, non-galling, and tribochemically benign in the presence of liquid lubricants. This behavior is in stark contrast to conventional alloys that contain such large amounts of the metal titanium. It is believed that the good tribological performance under oil lubrication observed for 60NiTi may extend to the entire NiTi family of alloys since they all share similar phase constituents and basic atomic level bonding. The tribochemistry of 60NiTi and its metallurgical relatives is under further study.

The identification of a viable bearing material that is non-magnetic, electrically conductive, hardenable, displays favorable tribochemistry and is non-corrosive is a major research finding. No other bearing material yet discovered has such a broad combination of properties. While it is clear that near term niche applications such as aerospace bearings and gears exist, many non-obvious applications are also likely to present themselves. These include wear resistant, corrosion proof knives and cutters, electric machine structural and dynamic components, high performance fasteners, valve components and many others.

Clearly, much more research will be required to understand the 60NiTi material and its metallurgical relatives. The relationships between mechanical and physical properties, atomic structure and micro-scale ordering and surface chemical interactions remain to be investigated. Nonetheless, the NiTi metallurgical system clearly has engineering potential well beyond shape memory alloy applications that has only begun to be exploited.

References

1. S.A. Shabalovskaya: "Surface, Corrosion and Biocompatibility Aspects of Nitinol as an Implant Material", *Bio-Medical Materials and Engineering*, volume 12, 2002, 69-109.
2. Buehler, W.J., J.V. Gilfrich, and R.C. Wiley: "Effect of Low-Temperature Phase Changes on the Mechanical Properties of Alloys near Composition TiNi", *Journal of Applied Physics*, volume 34, number 5, May 1963, pages 1475-1477.
3. Bueher, W.J.: "Intermetallic Compound Based Materials for Structural Applications", *Proceedings of the 7th Navy Science Symposium: Solution to NAVY Problems Through Advanced Technology*, May

- 14-16, 1963, U.S. Naval Aviation Medical Center, Pensacola, Florida, volume 1. Office of Naval Research, Arlington, VA, May 1963.
4. W.J. Buehler: "NITINOL Re-Examination", White Oak Laboratory Alumni Association Leaf, Winter 2006, volume VIII, Issue I, www.wolaa.org.
 5. R.W. Roberts and R. S. Owens; Titanium Lubrication, *Nature*, volume 200, October 26, 1963, pages 357-358.
 6. Jones, W.R.Jr., Pepper, S.V., Wheeler, D.R., Jansen, M.J., Nguyen, Q.N., and Schroer, A., "The Effect of Stress and TiC Coated Balls on the Lifetime of a Perfluoropolyether Using a Vacuum Rolling Contact Tribometer", *Tribology Transactions*, volume 43(2000), 4, 685-688.
 7. M.N. Gardos, H.H. Hong, and W.O. Winer: "The Effect of Anion Vacancies on the Tribological Properties of Rutile (TiO₂-x), Part II: Experimental Evidence", *STLE Tribology Transactions*, volume 33, number 2, April 1990, pp. 209-220.
 8. M.D. McNeese, D.C. Lagoudas, and T.C. Pollock; "Processing of TiNi from Elemental Powders by Hot Isostatic Pressing", *Materials Science and Engineering A280* (2000), pp. 334-348.
 9. K. Otsuka and X. Ren: "Physical metallurgy of Ti-Ni-based shape memory alloys," *Prog. Mater. Sci.*, vol. 50, pp. 511-678, 2005.
 10. W.R. Jones, Jr., S.V. Pepper, M.J. Jansen, Q.N. Nguyen, E.P. Kingsbury, S. H. Loewenthal, and R. E. Predmore: "A New Apparatus to Evaluate Lubricants for Space Applications-The Spiral Orbit Tribometer (SOT), NASA TM-2000-209935.

Gossamer Technology to Deorbit LEO Non-Propulsion Fitted Satellite

C. Dupuy* and O. Le Couls**

Abstract

Since 2004, CNES has decided to apply the end of life Code of Conduct rules to debris mitigation. Originally drawn up by the main European space agencies, it contains basic rules to be applied in space in order to limit the increase of orbital debris. In low Earth orbit, the rule is to limit in-orbit lifetime to 25 years after the end of the operational mission, or else to transfer to a graveyard orbit above 2000 km. In order to follow these instructions, a task force was set up in 2005 to find the best way to implement them on MICROSCOPE and CNES microsatellite family (MYRIADE). This 200-kg spacecraft should be launched in 2014 on a 790-km high circular orbit. Without targeted action, its natural re-entry would occur in 67 years.

Two strategies to reduce this time period were compared: propulsive maneuvers at the end of the mission or the deployment of large surfaces to increase significantly the ballistic coefficient. At the end of the trade off, it was recommended:

- For the non-propulsive system fitted satellites, to use passive aerobraking by deployment of added surface,
- For satellites having propulsive subsystem in baseline for mission purposes, to keep sufficient propellant and implement specific maneuvers.

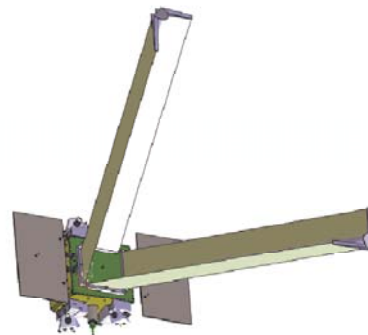
The poster gives an overview of the process that led to the development of a deployable aerobraking wing using a lightweight aluminized Kapton membrane and an inflatable aluminum laminate boom.

- The main requirements
- The trade off among various aerobraking solutions
- The development plan

This technology presents a very attractive potential and it could be a first step in using of inflatable technology on spaces vehicles, before to deal with others more exigent applications.



MICROSCOPE, orbital configuration



MICROSCOPE, deorbit configuration

Figure 1

* Centre National d'Etudes Spatiales, Toulouse France

** EADS Astrium, Saint Médard en Jalles, France

The MICROSCOPE Spacecraft

MICROSCOPE is based on CNES' MYRIADE micro-satellite product line which started in 1998. Its scientific objective is to test the Equivalence Principle with an accuracy of 10⁻¹⁵, about three orders of magnitude better than the accuracy of the present on ground experiments. The space mission exploits the Earth as the gravitational source, the very quiet in orbit environment and the possibility of a very long free fall motion for the integration of the measurement.

The T-SAGE instrument is composed of two differential electrostatic accelerometers (see Figure 2). Each one includes two cylindrical and concentric test masses. The attitude, as well as the atmospheric and thermal drag of the satellite, are actively controlled in such a way that the satellite follows the two test masses in their pure gravitational motion. The test-mass motions, within the highly stable silica instrument frame, are also servo-controlled using very accurate capacitive position sensing and electrostatic actuators. The relative position of the two masses is thus maintained motionless and the fine measurement of the control force leads to the test of the Equivalence Principle with the expected 10⁻¹⁵ accuracy. The mission is obviously extremely sensitive to microperturbations such as structural micro-cracking and fluid motions. It was apparent very early in the design that no liquid propulsion system could be envisaged. The satellite drag compensation and attitude control involves a specific propulsion system. For the first time, FEEP thrusters have been chosen but due to technical problems a cold gas solution is now being investigated. The satellite will be on a sun-synchronous polar orbit at 790-km altitude with an ascending node at 6 h or 18 h. This leads to a nominal orbit where natural re-entry would take place in 67 years (see Figure 3). At 200 kg, MICROSCOPE is heavier than common MYRIADE satellites. Its general architecture also presents several particularities:

- the payload is in the middle of the spacecraft,
- the body is wider (870 x 790 section instead of 600 x 600),
- the solar array is based on two symmetrical single-panel wings instead of the standard MYRIADE two-panel wing solar array.



Figure 2: T-SAGE instrument

De-Orbiting MICROSCOPE: Options and Constraints

The dominant factor of orbit erosion is the atmospheric drag, which depends linearly on the surface to mass ratio (S/m) of a given spacecraft. The deceleration due to drag can be written as:

$\gamma = \frac{1}{2} \rho \mathbf{S/m} C_d \mathbf{V}^2$, where:

- ρ is the local atmospheric density,
- C_d is the coefficient of drag, in practice between 2 and 3, assumed to be equal to 2.6 in the rest of this study,
- \mathbf{V} is the orbital velocity.

The surface \mathbf{S} is the cross section perpendicular to the velocity vector (see figure 5). After the end of its operational life, the attitude of the satellite will not be controlled. Since for most of the decay phase (above 650 km) there is no obvious natural self-pointing, we consider that all altitudes would be equally

likely. The **average apparent surface** of MICROSCOPE is evaluated at 2.7 m^2 . With a mass of 200 kg, this leads to :

$$S/m = 0.0135 \text{ m}^2/\text{kg}.$$

With the DTM94 atmospheric model, using the Codior software, which is a semi-analytical tool for long term extrapolations developed by SERGA for CNES for sun-synchronous or low orbits, we find that MICROSCOPE's natural re-entry would occur 67 years after decommissioning (see Figure 3), which is assumed to take place on January 1 2017.

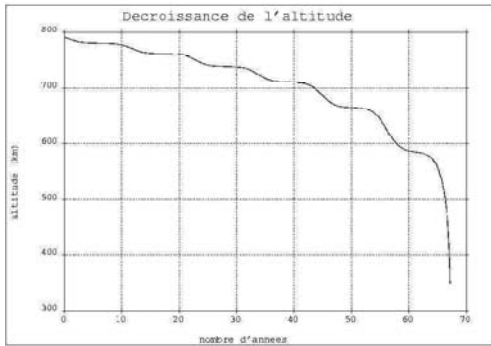


Figure 3: MICROSCOPE's orbital decay without special maneuver

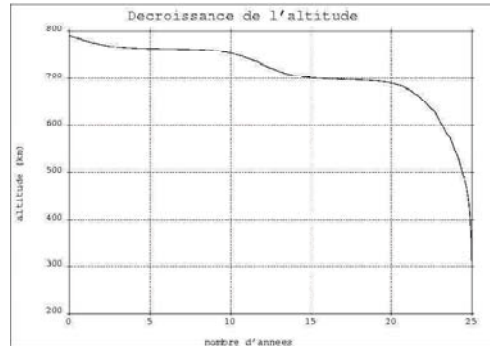


Figure 4: MICROSCOPE's orbital decay with 6-m^2 drag area

Since MICROSCOPE is below 800 km, the Code of Conduct option to transfer it to a graveyard orbit higher than 2000 km at the end of its life does not seem feasible within the mass and volume allowed for the spacecraft. We will therefore focus our efforts on ensuring that re-entry will occur in less than 25 years after the mission's end. Considering its relatively small mass, uncontrolled re-entry is acceptable. Two main strategies were identified:

- "Drag raise": increase of natural orbit erosion so that orbital decay from the original orbit will take less than 25 years,
- "Propulsion": maneuver to go down to an orbit where life-time is less than 25 years.

The only option that has been studied in detail for "drag raise" increase, is to deploy surfaces around the spacecraft to raise natural aerodynamic drag. Other concepts could have been involved (deployment of tethers to use magnetic forces for braking), but they were quickly dismissed as impractical for a small satellite. Figure 4 shows that the required 25 years re-entry would occur if the S/m is set to $0.03 \text{ m}^2/\text{kg}$, which calls for a mean drag area of 6 m^2 . This result corresponds to a beginning of de-orbiting at the start of 2017. This means an addition of 3.3 m^2 of drag surface to the operational configuration of MICROSCOPE.

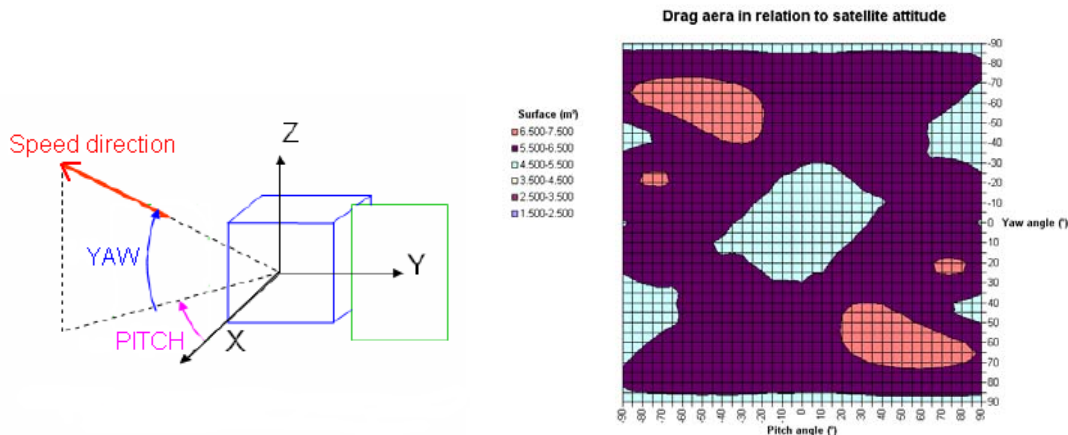
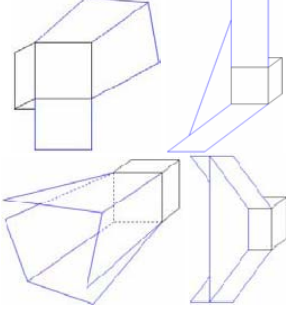
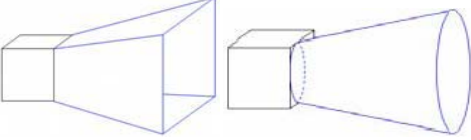


Figure 5: Drag area calculation

Drag Raise: Review of Concepts

To begin with, a target shape for the deployed surfaces was selected. The ideal system would create additional drag homogeneously over all possible attitudes of the spacecraft. In theory, one may try to approach the shape of a sphere.

 <p style="text-align: center;">Sphere Diameter ≥ 2.7 m</p>	<ul style="list-style-type: none"> ☹ Volume > 10 000 liters ☹ Deployed total area > 23 m² ☹ Mass budget > 30 kg ☹ Yoke necessary to link with satellite
 <p style="text-align: center;">Dihedral</p>	<ul style="list-style-type: none"> ☺ easier to accommodate and complement the surface provided by satellite & solar array panels ☺ Mass < 15 kg ☺ Dihedron could be done with serial of flat panel arrangement or with boom associated with deployed membrane film.
 <p style="text-align: center;">Cone</p>	<ul style="list-style-type: none"> ☺ Same advantages than dihedron arrangement ☹ Difficult to provide a perfect cone shape without discontinuities ☹ Not necessary for uncontrolled re-entry

→The dihedral shape was finally chosen!

To build the wings, two families of technologies were quickly identified. The first is based on low weight flat panels. Because of the restrictions on volume in packed configuration, only 2 wings of 3 panels (0,5 m² each) can be accommodated. This only leads to a total mean drag area of 4 m², 2. m² short of the 6. m² target.

Based on sandwich panels with carbon fiber sheets, the total mass of this package including holding and deployment devices has been evaluated at 6 kg. Even though de-orbiting with this system would take around 40 years without margin from the nominal orbit, we disregarded it for the more innovative second solution family.

The second family of technologies is based on unfolded Aluminum / Kapton membranes with deployable structures. Figure 6 describes various concepts that were assessed for deployment.

Technological trade off

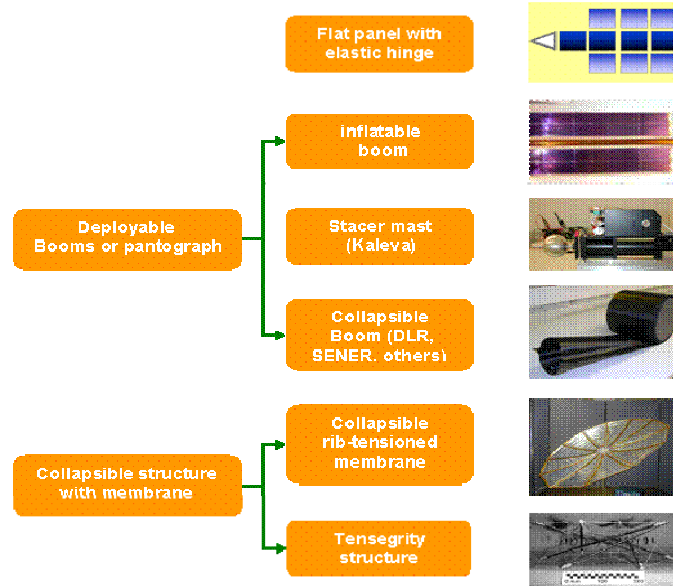


Figure 6: Technological trade off

- **Tensegrity** structures, made from cables and struts to which a state of pre-stress is imposed that imparts tension to all cables. This solution was assessed to be complicated for this type of application, and not easily accessible.
- **Deployable masts** based on multi-coil Stacer tube, such as those used on Demeter. Here, the fact that the mast rotates through deployment is unfavorable.
- **Doubly curved membrane stiffened** by thin-walled collapsible ribs such as the Collapsible Rib Tensioned Surface (CRTS) reflector developed by ESA. Here the packaging and the demonstration that micro-cracking would not happen during the mission, seemed difficult.
- **Bi-stable masts** such as those originally developed by DLR for solar sails, made of two laminated flexible -shaped sheets bonded at the edges to form a tubular shape. The main disadvantage is in their significant mass for a limited (compared to solar sail) area such as in this application,
- **Inflatable mast** made of aluminum laminate. This is the solution that was finally selected because of its light weight and its efficient packaging especially in term of volume. It is presented in more detail. The total mass of two inflatable wings offering 3.7 m² of drag area is 12 kg.

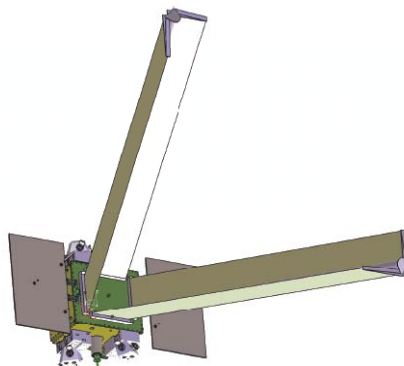


Figure 7: wings with inflatable mast

De-Orbiting Wing Technology

The de-orbiting configuration is shown in Figure 7. Two 5-m-long wings made of aluminized Kapton membrane (100 g/m² density) have been deployed by a central inflatable mast. The actual total mean drag surface becomes 6.7 m².

The total provisional mass, with margin, of a two-wing package is 12 kg (5 kg per wing and 2 kg for the inflation system), including thermal control. The materials have been selected for their endurance to ultraviolet exposition, and to atomic oxygen aggression. They can also cope with high temperatures which are expected when the membrane is in full sun.

IDEAS General Architecture

The IDEAS system is composed of several sub-systems (see Figure 8), each of them ensuring one or several specific functions.

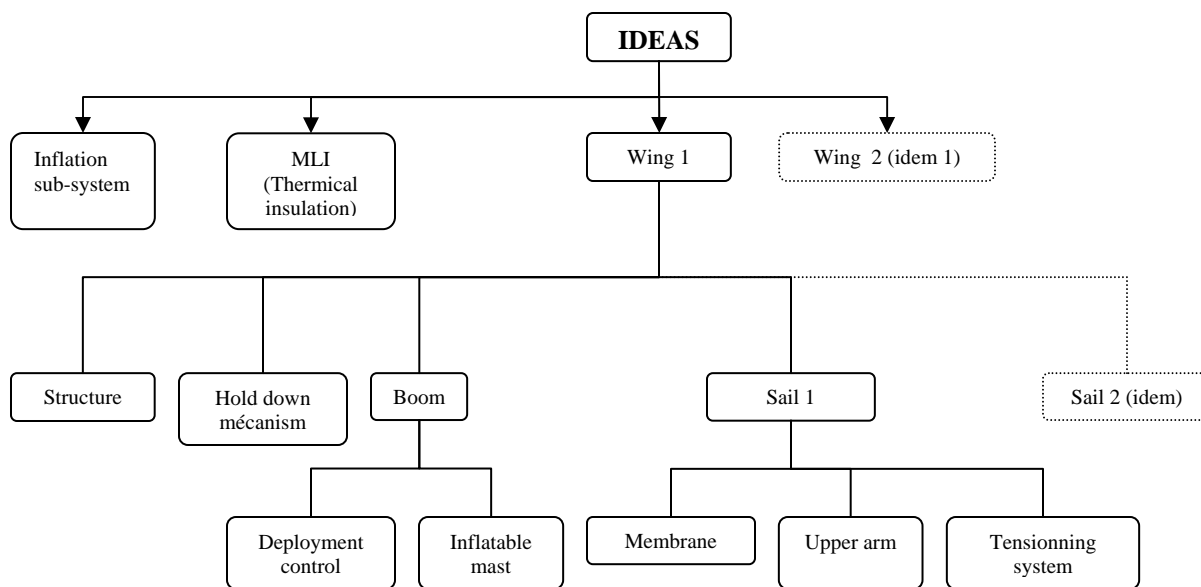


Figure 8: Product tree

The hold down sub-system function is to maintain IDEAS in folded configuration and to ensure the unlocking before deployment. The inflation sub-system function is to ensure the boom deployment and rigidization. It is also ensuring the venting of the boom in folded configuration during launcher phase, and in deployed configuration after rigidization. The MLI (Multi Layer Insulation) sub-system function is to ensure the thermal protection of IDEAS system from the external environment, in stowed configuration. The wing's function is to ensure the deployment of the aerobraking surfaces for IDEAS operating life. The two wings have the same definition and are composed of one boom and two membranes. The boom is ensuring the deployment and the rigidization to maintain the wing in deployed configuration (with inflation sub-system), and the two membranes are ensuring the aerobraking function.

The inflated boom of the selected technological solution has to be rigidized after deployment to ensure a correct mechanical behavior of the deployed surface without maintaining pressure. Several solutions have been analysed:

- solvent evaporation
- Sub-Tg
- thermal polymerisation
- photochemical polymerization
- metallic laminate yielding

The criteria considered are power need, long in-orbit storage consequences (premature rigidization risk) and feasibility complexity. The retained solution is the metallic laminate yielding.

Presentation of the Laminate Technology

The principle of folding, deployment and rigidization of the IDEAS boom is described in the following illustration.

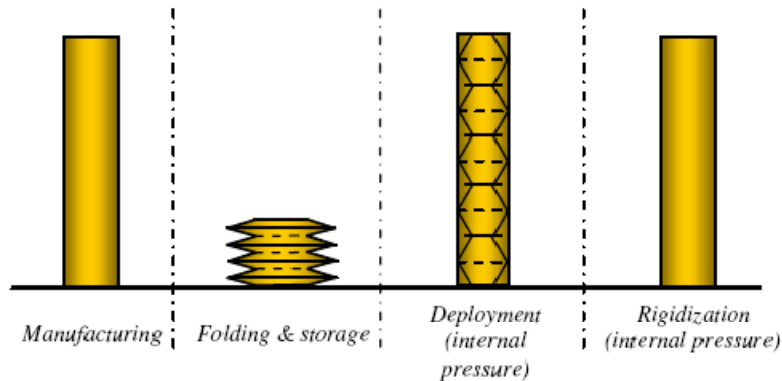


Figure 9: Boom folding, deployment and rigidization concept

The rigidization process chosen, “metallic laminate yielding”, consists of applying to the boom material a sufficient deformation - applied by internal pressure – to suppress geometrical defect created by yielding of the material during folding. Once the defects are suppressed, the mechanical behavior of the boom is ensured by its own stiffness. The boom material used to ensure this function is polyimide/aluminum/polyimide laminate.

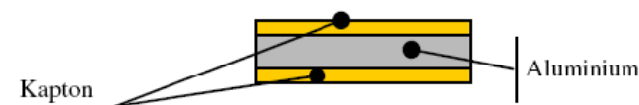


Figure 10: Laminate definition

The aluminum layer ensures the mechanical behavior after rigidization. The Kapton internal layer ensures the protection of the aluminum layer from internal mechanical “aggressions” and the tightness during boom inflation. The kapton external layer ensures the protection of the aluminum layer from external mechanical “aggressions” and has a thermal protection function. The main advantages of this solution are the good material stability during storage phases and the use of the same source of energy as for the deployment (no electrical power is necessary to rigidize).

Laminate aluminum boom technology is useful to in orbit low-stress-loaded structures. For the IDEAS wings at altitude up to 320 km, aerodynamics pressure is estimated below $0.42 \text{ E}^{-3} \text{ Pa}$. This is negligible face to dynamics load due to uncontrolled effect. Spin speed could reach $10 \text{ }^\circ/\text{s}$.

A test campaign has been performed, and demonstrates the good behavior of 1-meter long boom, after deployment and rigidization (2). For a 4,6-meter long boom with 160-mm diameter, the maximum flexure load is 6 Nm and maximum compression load 60 N.



Figure 11: 3-meter wing breadboard

Conclusion

The choice of the passive aerobraking to respect the IADC code of conduct, is validated, for the Myriade microsatellite family without propulsion system. The development of this equipment is linked to the MICROSCOPE project. The deorbiting progress with deployable aerobraking appendage is under CNES patent (3).

In 2007, inflatable aluminum laminate boom and deployable membrane have been tested in microgravity environment during a 0g flight test campaign. A 3-meter wing breadboard has been manufactured and tested on ground by Astrium Space Transportation.

Technological solution for deployment and rigidization are chosen and validations are well advanced. Currently the project is ending of the preliminary design phase and the PDR review is scheduled for the beginning of 2011. The achievement of the de-orbiting sub-system development is foreseen end of 2013, with the delivery of the flight model for MICROSCOPE satellite.

IDEAS project is, more than the development of a product dedicated to MICROSCOPE, the development of a concept and its associated technology that can have other potential others space applications.

References

1. 2007Aluminum laminate technology for micro-satellite Deorbiting aerobrake system“ – O. LE COULS, D. LACOUR (EADS Astrium), C. DUPUY (CNES) – 3rd European Workshop on Inflatable Space Structures, ESTEC, October 12th 2006
2. The innovative deorbiting aerobrake system “IDEAS”: The gossamer technology for Micro-satellite deorbiting – 10th European Conference on Spacecraft Structures, Materials & Mechanical Testing, Berlin 10-13 September
3. Satellite airbrake device Patent n° WO2007096428

Preliminary Assessment of Seals for Dust Mitigation of Mechanical Components for Lunar Surface Systems

Irebert R. Delgado* and Michael J. Handschuh**

Abstract

Component tests were conducted on spring-loaded Teflon seals to determine their performance in keeping lunar simulant out of mechanical component gearbox, motor, and bearing housings. Baseline tests were run in a dry-room without simulant for 10,000 cycles to determine wear effects of the seal against either anodized aluminum or stainless steel shafts. Repeat tests were conducted using lunar simulants JSC-1A and LHT-2M. Finally, tests were conducted with and without simulant in vacuum at ambient temperature. Preliminary results indicate minimal seal and shaft wear through 10,000 cycles, and more importantly, no simulant was observed to pass through the seal-shaft interface. Future endurance tests are planned at relevant NASA Lunar Surface System architecture shaft sizes and operating conditions.

Introduction and Background

NASA's Constellation program currently calls for an eventual return to the moon. During the Apollo Missions astronauts sited multiple problems with lunar dust. This included accelerated visor wear, false instrumentation readings, seal failures, abrasion of materials and degradation of mechanisms. Lunar dust has been characterized to be very abrasive with sharp angular features and ranging in diameter from tens to hundreds of micrometers.¹ With NASA's current plans for an extended stay on the lunar surface, dust mitigation of gearbox, motor, and bearing housings is especially critical. One technology currently under development is a spring-loaded Teflon seal which could potentially be used for dust mitigation of mechanical housings. These types of seals have seen use as dust mitigation components in the Mars Exploration Rover Instrumentation Deployment Device as shown in Figure 1. The device is responsible for the deployment, placement, and control of various measurement devices including a Mossbauer Spectrometer, Alpha Particle X-ray Spectrometer, Microscopic Imager, and Rock Abrasion Tool.² The Rover uses canted, spring-preloaded sliding Teflon seals manufactured by Bal Seal[®] to keep small dust particles out of the rover mechanisms.³ Because of the Rover's continued successful long-term operation on the Martian surface, baseline experiments were run on this type of dust seal using lunar simulant to determine their potential performance on mitigating dust in lunar mechanisms.

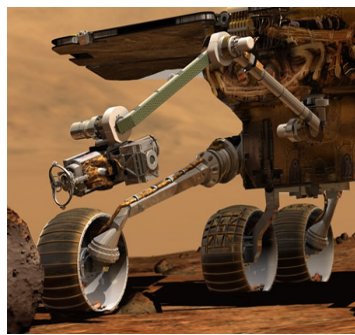


Figure 1 Mars Exploration Rover Instrumentation Deployment Device.



Figure 2 Bal-Seal Cross-Section

* NASA Glenn Research Center, Cleveland, OH

** Ohio State University, Columbus, OH

Discussion

Experimental Procedure

A series of rotating shaft tests were run against spring-loaded Teflon seals to determine their performance in preventing lunar simulant from passing through the seal-shaft interface. Baseline tests without simulant were run in ambient dry-room conditions to determine wear of the Teflon seal against both stainless steel and anodized aluminum shafts. Then, these tests were repeated using lunar simulants JSC-1A and LHT-2M. Finally, these tests were repeated in vacuum. Shaft rotation was constant at 20 RPM per lunar rover technology demonstrator requirements. The number of cycles was limited to 10,000 to determine initial feasibility of the seals. Note that with NASA's planned extended operations on the lunar surface, the seals are expected to last for millions of cycles. Thus, endurance tests on these seals are planned for design validation. Table 1 shows the matrix of tests completed for this feasibility study. In addition, a secondary study on the initial wear rate of the seal was performed for 0.375-in (9.52-mm), 0.75-in (19.0-mm), and 1.5-in (38-mm) diameter seals where the seals were weighed after 1000, 3000, and 10,000 cycles.

The simulants JSC-1A and LHT-2M were synthetically manufactured such that their physical and chemical properties, as well as composition, simulate lunar regolith. JSC-1A simulates lunar regolith found in the mare, or dark regions of the lunar surface while LHT-2M simulates lunar regolith found in the highland, or light regions of the lunar surface.⁴

Table 1 Bal-Seal Test Matrix

Seal ID	Seal Diameter mm (in)	Atm	Shaft	Shaft ID	Simulant
A22, A23	9.52 (0.375)	Dry Room	anodized Al	SA22, SA23	none
B7, B20	19 (0.75)	Dry Room	anodized Al	SB7, B20	none
C17, C18	38 (1.5)	Dry Room	anodized Al	SC17, SC18	none
B12	19 (0.75)	Dry Room	stainless steel	T6	none
A12	9.52 (0.375)	Dry Room	anodized Al	SA51	JSC-1A
B10	19 (0.75)	Dry Room	anodized Al	SB10	JSC-1A
C6	38 (1.5)	Dry Room	anodized Al	SC51	JSC-1A
B13	19 (0.75)	Dry Room	stainless steel	T8	JSC-1A
A17	9.52 (0.375)	Dry Room	anodized Al	SA55	LHT-2M
A18	9.52 (0.375)	Dry Room	stainless steel	S-10	LHT-2M
A13	9.52 (0.375)	4x10 ⁻⁷ torr	anodized Al	SA52	none
B11	19 (0.75)	4x10 ⁻⁷ torr	anodized Al	SB51	none
A15	0.375	3x10 ⁻⁷ torr	anodized Al	SA53	JSC-1A
A16	0.375	4x10 ⁻⁷ torr	anodized Al	SA54	LHT-2M

Test Article Description

An example of the spring-loaded Teflon seal, manufactured by Bal Seal, is shown in Figure 2. The seal is composed of a PTFE - Polytetrafluoroethylene ring with a U-shaped cross-section. A stainless steel canted coil-spring is inserted into the U-shaped cross-section thereby energizing the seal.⁵ Seal sizes of 0.375-in (9.52-mm), 0.75-in (19.0-mm), and 1.5-in (38-mm) inner diameter were selected to test against either stainless steel or anodized aluminum shafts of the same diameter.

Test Equipment Description

The test set-up is composed of a test stand, motor, seal housing, seal, and shaft as shown in Figure 3. The assembly is arranged in a vertical orientation to allow lunar simulant to enter the seal-shaft interface through the top of the assembly. The top of the seal housing is designed with a coned interior to funnel simulant towards the seal-shaft interface.

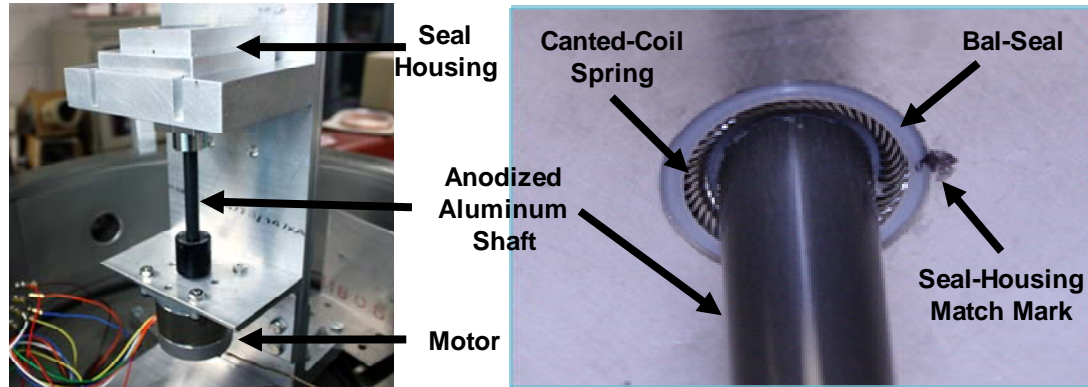


Figure 3 Rotary seal rig test set-up and view of underside of seal within seal holder.

Procedure

Prior to testing, the seals were first cleaned with Alconox, rinsed with ethanol alcohol and dried to remove any residual oils or other residue. Pre-test photos were taken of the seals and weight and inner-diameter measurements were recorded. Pre-test photos were taken of the shafts as well, and their surface roughness profiles were recorded. Shaft roughness averaged $0.102 \pm 0.013 \mu\text{m}$ ($4.020 \pm 0.514 \mu\text{in}$) for the stainless steel shafts and $0.145 \pm 0.019 \mu\text{m}$ ($5.691 \pm 0.758 \mu\text{in}$) for the anodized aluminum shafts. A representative profilometer plot of the surface roughness measured around the shaft circumference is shown in Figure 4.

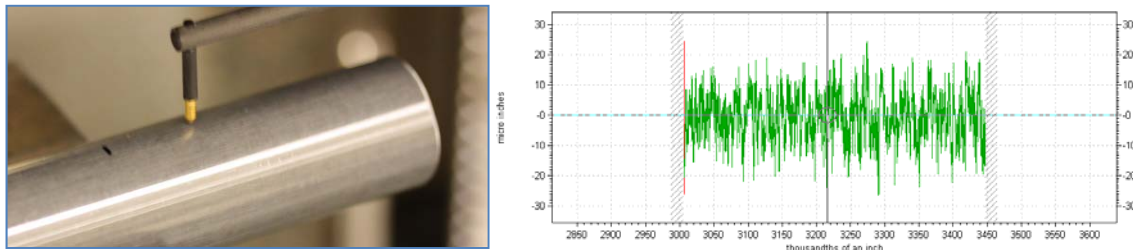


Figure 4 Profilometer stylus measuring anodized aluminum shaft surface and sample shaft roughness profile.

Prior to installation, the seal and shaft were allowed to sit in the dry-room overnight to remove any residual moisture. The seal was then installed in the seal holder with a slight interference fit and oriented with the U-shaped channel opening of the seal facing downward. Note that simulant would be introduced at the top of the rotary seal rig. The seal was match-marked with respect to its orientation in the seal holder to determine if the seal rotated during testing. The top and bottom pieces next to the seal holder were installed using socket head cap screws, SHCS. Attention was given to ensure that no misalignment occurred when tightening the SHCS that bolt the three pieces of the seal holder together. The assembled seal holder was placed on the seal cartridge holder of the rotary seal rig, Figure 3. Depending upon the test seal size, the appropriately sized coupling adapter was used to mate the test shaft to the motor. The test shaft was carefully inserted into the top opening of the seal cartridge and gently pushed downward until seated inside the coupling adapter. After securing the shaft to the coupling, match-marks were made on the shaft and coupling adapter to determine if any slippage occurred during testing. For baseline tests with no lunar simulant added the motor was run for 10,000 cycles. For tests with either JSC-1A or LHT-

2M, approximately 20 ml of simulant was added to the top of the seal cartridge prior to test start-up. In addition, a secondary platform was attached to the shaft just below the seal cartridge holder to contain any simulant that may pass through the seal-shaft interface.

After testing was completed, the seal cartridge along with the shaft were removed from the rotary seal rig. Observations were made as to the amount of seal and shaft wear. Post-test analyses included shaft profilometry, seal weight loss, and microscopic examination of both seal and shaft surfaces. For tests with lunar simulant, any simulant remaining at the top of the seal cartridge was removed prior to disassembly and examination of the test seal and shaft. More importantly, observations were made to determine if simulant had passed through the seal-shaft interface. The seal cartridge was disassembled starting from the bottom of the cartridge to determine the extent to which simulant had passed through the seal-shaft interface, if any.

For tests in vacuum, a vacuum-rated motor was used in place of the dry-room motor. The rotary seal rig was placed within a bell jar capable of 10^{-7} Torr, Figure 5. The chamber was then pumped down overnight until approximately 4×10^{-7} Torr was reached. Tests were also run at 10,000 cycles and 20 RPM. Disassembly and examination procedures of both the test seal and shaft were identical to dry-room post-test procedures.

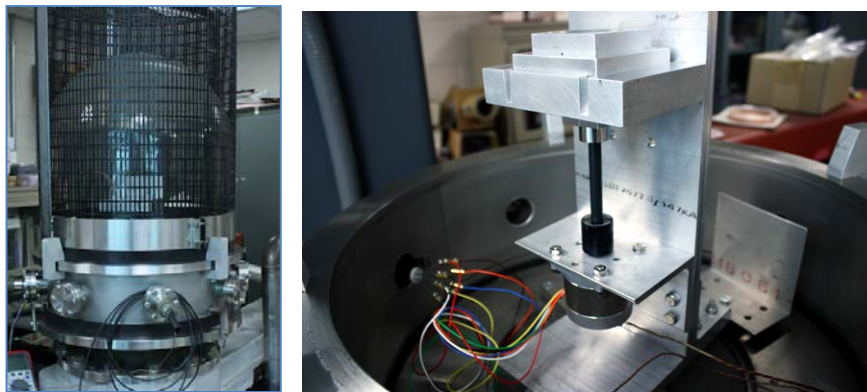


Figure 5 Bell Jar vacuum chamber containing rotary seal rig test set-up.

Results and Discussion

For all tests run in the dry-room or in vacuum with either JSC-1A or LHT-2M, no simulant was observed to pass through the seal-shaft interface, as shown in Figures 6a and 6b. Note that only Teflon flakes were observed on the downstream side of the seal-shaft interface. This is indicative of some seal wear as will be quantified later in the discussion. Also note that the simulant was observed to go no further than approximately half-way down the inner diameter of the Bal-Seal.

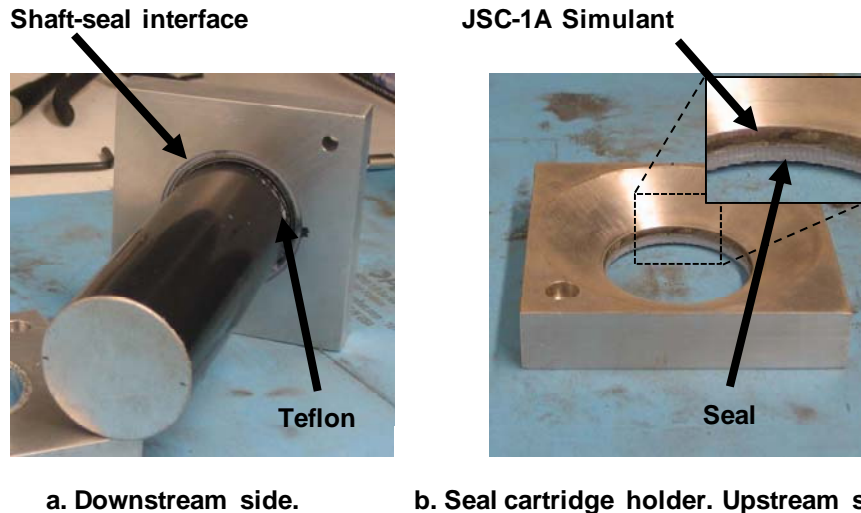


Figure 6 Typical seal-shaft observations for tests run with either JSC-1A or LHT-2M.

Table 2 shows results of Bal-Seal tests through 10,000 cycles. In general, seal weight loss was greater for increasingly larger seal diameters due to a larger contact area and increased surface speed due to increased circumference. For example, for dry-room tests run without simulant, the average seal weight loss ranged from 0.11 to 0.33% for the 9.5-mm (0.375-in) diameter seals, from 0.07% to 0.66% for the 19-mm (0.75 in) diameter seals and from 2.63 to 3.0% for the 38-mm (1.5 in) diameter seals. Post-test roughness profiles for dry-room test shafts run without simulant (Tests A22, A23, B7, B20, C17, C18) were inconclusive ranging from -7.34% (smoother surface) to +2.72% (rougher surface). In comparison, these same tests run with JSC-1A (Tests A12, B10, C6, A17) showed a more definitive roughness change of +15% (rougher surface) on average. Preliminary tests in vacuum show minimal seal weight loss through 10,000 cycles. In fact seal weight loss was identical at -0.11% for the 9.5-mm (0.375-in) diameter seal tested without and with JSC-1A (Tests A13 and A15, respectively). Seal weight loss was doubled at -0.22% for the same sized seal tested with LHT-2M (Test A16). Although the vacuum test results are encouraging, repeat tests are necessary to validate these results. Unfortunately, a malfunction in the vacuum motor occurred after these 4 tests. Thus further testing was postponed. Post-test surface roughness profiles for the vacuum tested seals were again inconclusive with results ranging from -13.87% (smoother surface) to +6.90% (rougher surface). Preliminary tests of Bal-Seals against stainless steel shafts show seal weight losses comparable to the anodized aluminum shafts. However, the large change in surface roughness for shaft S-10 does not appear to be consistent with the -0.11% seal weight loss of Seal ID A18. In fact, this inconsistency between seal weight loss and change in shaft surface roughness is apparent for a large portion of the test results. Further analysis in data and procedures is necessary to reconcile these differences in surface roughness with seal weight loss. Supplementary testing was performed to determine cycles versus wear for three seal sizes. Results are shown in Figure 7. As expected, the larger contact surface area of the 38-mm (1.5 in) seals incurred more wear through 10,000 cycles than the 19-mm (0.75 in) or 9.5-mm (0.375-in) seals. Further long-term testing is necessary to determine if the seal wear rate remains constant, increases, or possibly stabilizes to some final seal weight loss. Note that these tests were run at constant speed and that future tests may involve start-stop cycles, ramp-up and ramp-down in speed, etc. Finally, infrared microscopy has confirmed the presence of Teflon being transferred to the anodized aluminum shaft surface. The presence of Teflon on the rotating surface provides additional lubrication between the shaft and seal which could potentially increasing seal-shaft life. Further tests are needed to assess the performance of this lubricating layer through extended operations.

Table 2 Wear results for Bal-Seal Tests through 10,000 Cycles

Seal ID	Environ.	Seal Diameter mm (in)	%Wt Change	Simulant	Shaft	Shaft ID	%ΔRa
A22	Dry Room	9.52 (0.375)	-0.24	none	Anod. Al	SA22	2.16
A23	Dry Room	9.52 (0.375)	-0.33	none	Anod. Al	SA23	-1.25
B7	Dry Room	19 (0.75)	-0.61	none	Anod. Al	SB7	-5.2
B20	Dry Room	19 (0.75)	-0.87	none	Anod. Al	SB20	-7.34
C17	Dry Room	38 (1.5)	-3.00	none	Anod. Al	SC17	0.04
C18	Dry Room	38 (1.5)	-2.63	none	Anod. Al	SC18	2.72
B12	Dry Room	19 (0.75)	-0.13	none	SS	T6	5.32
A12	Dry Room	9.52 (0.375)	-0.27	JSC-1A	Anod. Al	SA51	12.14
B10	Dry Room	19 (0.75)	-0.54	JSC-1A	Anod. Al	SB10	13.73
C6	Dry Room	38 (1.5)	-1.46	JSC-1A	Anod. Al	SC51	19.55
B13	Dry Room	19 (0.75)	-0.66	JSC-1A	SS	T8	-0.39
A17	Dry Room	9.52 (0.375)	-0.17	LHT-2M	Anod. Al	SA55	14.81
A18	Dry Room	9.52 (0.375)	-0.11	LHT-2M	SS	S-10	30.48
A13	4x10 ⁻⁷ torr	9.52 (0.375)	-0.11	none	Anod. Al	SA52	-13.87
B11	4x10 ⁻⁷ torr	19 (0.75)	-0.07	none	Anod. Al	SB51	5.70
A15	3x10 ⁻⁷ torr	9.52 (0.375)	-0.11	JSC-1A	Anod. Al	SA53	-8.03
A16	4x10 ⁻⁷ torr	9.52 (0.375)	-0.22	LHT-2M	Anod. Al	SA54	6.90

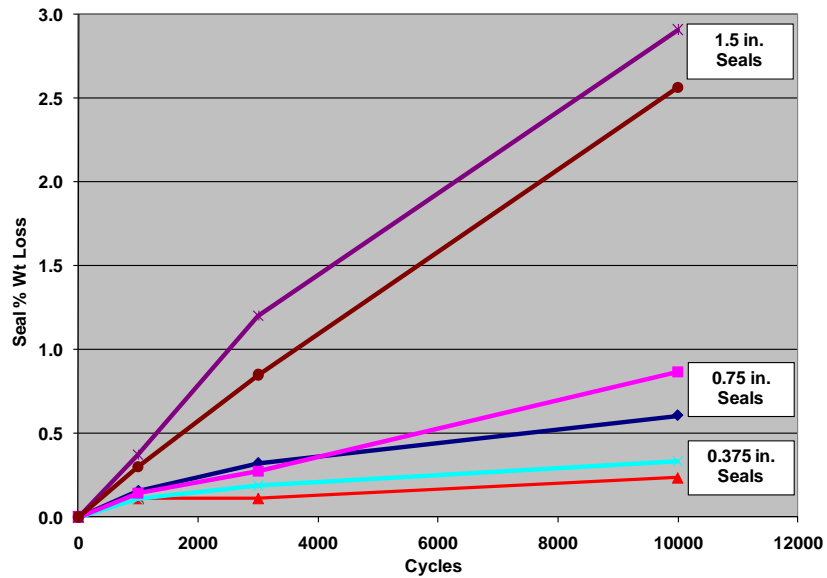


Figure 7 Seal percent weight loss versus cycles.

Conclusions and Recommendations

Seals of three different diameters were tested: 9.5 mm, 19 mm, and 38 mm (0.375 in., 0.75 in., and 1.5 in). Tests were conducted at 20 RPM up to 10,000 cycles in dry-room and vacuum conditions using lunar simulants JSC-1A and LHT-2M. For the tests conducted:

- No simulant was observed to pass through the seal-shaft interface.
- A minimal amount of wear was observed on both seal and shaft. Seal weight loss was minimal with only Teflon 'flakes' observed on the downstream side of the seal.
- Shaft profilometry generally show a slight deterioration in shaft surface roughness with simulant use. Inconsistencies between surface roughness and seal weight loss require further analysis.
- Infrared microscopic analysis of the anodized aluminum shaft surface has revealed the presence of Teflon which is beneficial as a lubricant between the seal and shaft during operation.

Based on these results, further tests are planned including effects of temperature and extended cycles in vacuum. Efforts are also underway to integrate the seal tests with NASA Lunar Surface Systems architectures.

Acknowledgements

The authors wish to acknowledge Dr. Paula Dempsey, Dr. James Gaier, Dr. Ken Street, and Daniel Valco for their guidance in testing and analyses of the seals. We also acknowledge Mr. Mark Hyatt of the Exploration Technology Development Program for his support of this study. Finally we also acknowledge Ed Sechkar, Scott Panko, and Frank Lam for design, assembly, fabrication of the rotary seal test rig hardware, and programming of the vacuum motor controller.

References

1. Gaier, James R., "The Effects of Lunar Dust on EVA Systems During the Apollo Missions." NASA/TM—2005-213610
2. Baumgartner, Eric T., et.al., "The Mars Exploration Rover Instrument Positioning System." Proceedings of the 2005 IEEE Aerospace Conference, Big Sky, MT, March 2005.
3. Harrington, B.D and Voorhees, C.: The Challenges of Designing the Rocker-Bogie suspension for the Mars Exploration Rover. Proceedings of the 37th Aerospace Mechanisms Symposium, May 19-21, 2004, Johnson Space Center, Houston, Texas.
4. Sibille, L, Carpenter, P., et.al., "Lunar Regolith Simulant Materials: Recommendations for Standardization, Production, and Usage." NASA/TP—2006-214605
5. Reciprocating Seal Catalog DM-6, Bal Seal Engineering

Development of the Tri-ATHLETE Lunar Vehicle Prototype

Matt Heverly*, Jaret Matthews*, Matt Frost* and Chris McQuin*

Abstract

The Tri-ATHLETE vehicle is the second generation of a wheel-on-limb vehicle being developed to support the return of humans to the lunar surface. This paper describes the design, assembly, and test of the Tri-ATHLETE robotic system with a specific emphasis on the limb joint actuators. The design and implementation of the structural components is discussed, and a novel and low cost approach to approximating flight-like cabling is also presented. The paper concludes with a discussion of the “second system effect” and other lessons learned as well as results from a three week long field trial of the vehicle in the Arizona desert.

Introduction

In order to establish a continual human presence on the Moon we must develop assisting infrastructure that can carry cargo as well as provide mobility to the astronauts for exploration and the development of a central, but not necessarily fixed, lunar base. The Tri-ATHLETE vehicle system is a new form of two cooperative robotic vehicles that can act individually or physically connect together through a structural pallet to transport and manipulate cargo.

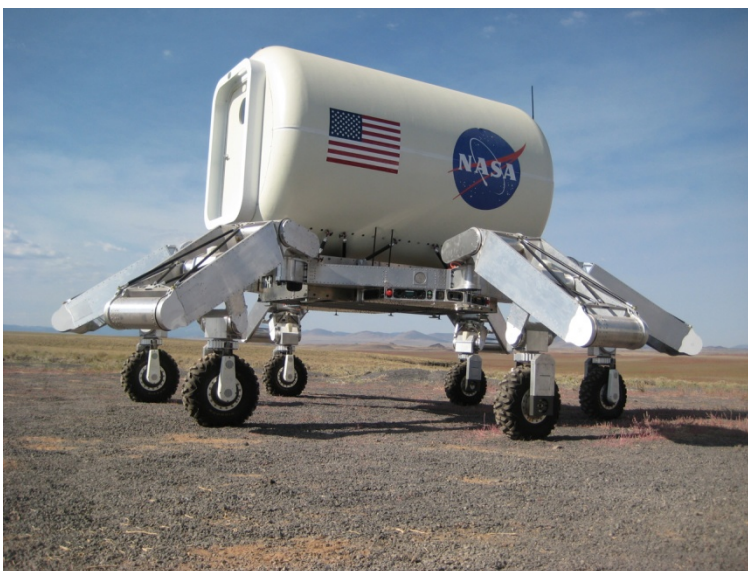


Figure 1. The second generation ATHLETE rover

The basis of the ATHLETE (**A**ll **T**errain **H**ex **L**imed **E**xtra **T**errestrial **E**xplorer) robot is the wheel-on-limb vehicle concept. This hybrid mobility platform enables the vehicle to traverse at high speeds across benign terrain, as well as enabling walking, by locking the wheels and using them as feet, on extreme terrain. This vehicle architecture also allows for manipulation since the vehicle is stable on three or more wheels. Non-adjacent limbs can be lifted and used to interact with the environment. A tool mechanism at

* Jet Propulsion Laboratory, California Institute of Technology, Pasadena, CA

Proceedings of the 40th Aerospace Mechanisms Symposium, NASA Kennedy Space Center, May 12-14, 2010

the end of the limb, attached to the wheel hub, allows for interchangeable tools, such as a gripper or an auger, to be used for manipulation. This unique vehicle design allows for significant weight savings over a traditional planetary roving vehicle that must have large wheels to allow for low ground pressure as well as high torque wheel actuators since the vehicle cannot walk in extremely soft or steep terrain.

The ATHLETE project started in March of 2005 [1, 2]. The first generation vehicle was completed in October of that same year. This 1000-kg, 2-m tall vehicle was developed rapidly with the intent of providing a hardware platform to aid in the development of the robotic system's software. This software development vehicle ended up performing five field tests in natural terrain throughout the United States. These field tests enabled the team to test the vehicle's capabilities such as traversability over soft terrain, walking, repelling, and manipulation in unstructured environments. From this first prototype several new capabilities were discovered and several vehicle deficiencies were revealed.

In October of 2008 the design of the second-generation vehicle was initiated. The intent of the second vehicle was to maintain all the functionality of the first generation, as well as add the capability of generic cargo transport and offloading from a lunar lander. This new requirement led to the development of two, cooperative three legged vehicles know as Tri-ATHLETES. These vehicles can function independently to traverse without cargo, but can also combine on either side of a structural pallet, using a generic hook and pin interface, to form a single six legged system with one Tri-ATHLETE vehicle acting as the master and the second vehicle as the slave. The pallet can be loaded with any type of cargo; Figure 1 shows a mock habitat as the payload. Once docked, the vehicle can transport the cargo to the desired location. The Tri-ATHLETES can then undock, as shown in Figure 2, leaving the pallet and payload behind, and drive to a new location as two, three legged robots to combine with a new pallet and payload for transport.



Figure 2. Two Tri-ATHLETE vehicles prior to docking to the mobile habitat / pallet

The requirement of cargo offloading from the deck of a 3.2m tall lander, shown in Figure 3, drove to an additional joint over the original six degree of freedom ATHLETE limb. Because of the extreme height of the lander deck compared to the limb length necessary for walking and manipulation, the seventh degree of freedom is implemented as a thigh pitch joint that simply acts to change the length of the limb from a long configuration for high cargo offloading to a more compact configuration. The resulting kinematic configuration is a yaw – pitch – pitch – pitch – roll – pitch – roll arrangement shown in Figure 4. While this is less than ideal from a workspace optimization perspective, it allows for the upper thigh to extend and then fold upon itself creating the desired long and compact configurations.

The second generation ATHLETE system stands 4.1 m at full height and is approximately half scale of the conceived flight vehicle. This will allow for payload retrieval from the top of a 6.4-m tall Altair Lunar

Lander as outlined in the Constellation Lunar architecture [3]. This also allows for a 3.5-m diameter x 8-m long cylindrical habitat that is potentially suitable as long duration living quarters for multiple crew members on the lunar surface [4]. While the ATHLETE vehicle concept is highly scalable, the current ½ scale was chosen due to practical limitations of transporting reasonable payloads in Earth gravity. Each Tri-ATHLETE has a mass of 720 kg and the two Tri-ATHLETES combine to have a payload capacity of 500 kg. For the lunar environment, the payload / vehicle mass fraction would increase drastically allowing the mass of the entire ATHLETE mobility system to be between 15 – 20% of the payload mass that it transports.



Figure 3. ATHLETE vehicle standing 4-m tall, shown crawling off of a ½ scale lunar lander mockup

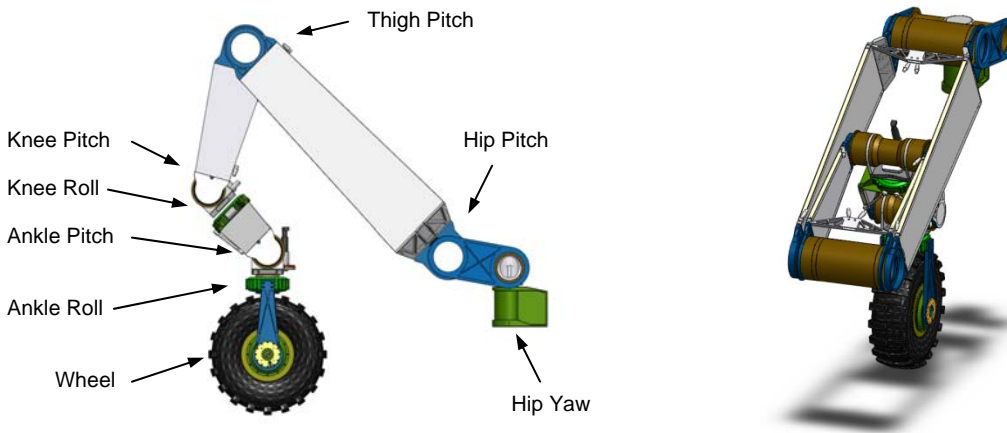


Figure 4. Layout of Tri-ATHLETE limb

Joint Details

The two, three legged Tri-ATHLETE vehicles are identical to each other. The limbs of the Tri-ATHLETE vehicle are also all identical, making six copies of each joint. Of the seven joints in each limb there are only two truly unique joint designs (yaw/pitch, and roll). While each joint has a unique gear ratio and torque capability, the basic joint designs are all the same. Every joint has a brushless DC motor with a power-off holding brake and an incremental encoder. There is a low power motor that is used in the Hip Yaw, Knee Roll, Ankle Pitch, and Ankle Roll Joints and a high power motor used in the Hip Pitch, Thigh Pitch, and Knee Pitch joints. Having only two unique motors minimizes the different interfaces necessary and allows for a significant amount of interchangeability between joints. Each motor has a planetary

gearbox with a ratio ranging between 40:1 and 81:1, depending upon the joint configuration. The output gear of each joint is a CSG style harmonic drive. This motor / brake / planetary / harmonic actuator configuration allows for zero backlash at the output of the joint and gives high torque capability in a relatively low mass configuration. This also allows for the use of a relatively small brake attached to the motor shaft that can hold a substantial output torque due to the large gear reduction. Figure 5 shows a representative joint (Hip Pitch) in the Tri-ATHLETE system. The joint is configured such that the motor / planetary body and the flexspline of the harmonic drive are stationary with respect to the previous joint in the kinematic chain. The wave generator of the harmonic is connected to output of the planetary gearbox using an involute spline. The Oldham coupling that is standard in the harmonic component set is discarded to reduce mass. The involute spline coupler bolts directly to a custom six bolt pattern in the wave generator. While this configuration saves mass over the use of the Oldham coupler, tight positional tolerances and alignment features are required to ensure proper concentricity between the planetary output shaft and the rotational axis of the harmonic. No-load current measurements of the joint assembly are no larger than no-load current of the motor / planetary alone indicating that the combination of the interface and the tolerances on the indicating features is sufficient to align the mechanism without binding. A non-standard bearing was required in the output of the planetary gearbox to handle the thrust loads generated by the harmonic wave generator. The circular spline of the harmonic is the output of the actuator and is connected to a thin walled output tube. This tube houses the outer race of a pair of thin section radial bearings that are spread across the entire length of the actuator give large moment carrying capability. The structure of the output of the joint is configured as a yoke, giving large side load capability, connecting to each side of the output tube. The yoke structure then connects to each side of the next joint in the kinematic chain.

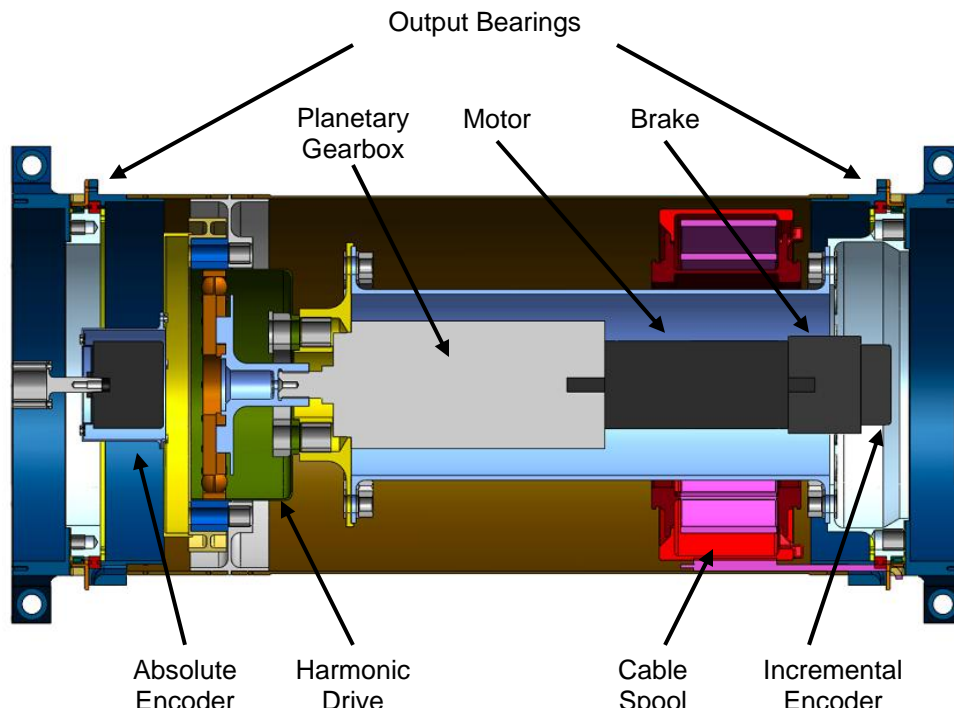


Figure 5. Cross section of the Hip Pitch joint actuator

The output torque capability of each joint is based upon the ratchet torque of the harmonic. This value is used as the design load for all the structural components in the joint. The machined parts are designed with a 1.5 Factor of Safety on yield strength and a 2.0 Factor of Safety on ultimate strength above the harmonic ratchet torque. In this way, the harmonic acts as a mechanical fuse. Loads larger than the rated ratchet torque will cause a non-catastrophic ratchet event. This reduces the future torque carrying

capability of the joint, but it does not result in complete joint failure. If a structural component were to fail, then an overload event would cause complete loss of the joint instead of simply reduced capability.

Table 1 below summarizes the capabilities and overall gear ratios of each of the joints. The speed of each joint is based upon the desire to actively servo the limbs over undulating terrain with slopes up to 10° while keeping the pallet level at the nominal driving speed of the vehicle, 3 kph.

Table 1. Summary of Joint Gear Ratio and Capability

Joint	Overall Gear Ratio	Harmonic Drive	Ratchet Torque	No-Load Speed
Hip Yaw	6,591 : 1	CSG-40-80	3.600 Nm	0.16 rad/s
Hip Pitch	-6,480 : 1	CSG-58-80	10,000 Nm	0.11 rad/s
Thigh Pitch	-6,480 : 1	CSG-58-80	10,000 Nm	0.11 rad/s
Knee Pitch	-3,240 : 1	CSG-40-80	3.600 Nm	0.22 rad/s
Knee Roll	3,514 : 1	CSG-32-50	1,200 Nm	0.30 rad/s
Ankle Pitch	6,591 : 1	CSG-32-80	1,800 Nm	0.16 rad/s
Ankle Roll	3,514 : 1	CSG-32-50	1,200 Nm	0.30 rad/s

The joint is sealed using a two layer seal. The outer seal is a Nomex felt to protect from large size particles. These felt seals have a rectangular cross section with a height / width aspect ratio between 1.25 and 2.0, where height is measured parallel to the rotation axis. The seal is compressed axially between 7% and 16% of its nominal height and rides on hard anodized aluminum surfaces. This amount of compression provides for good sealing, but contributes to significant drag torque. The highly compressed seals were also forced out of their designed grooves since the hoop strength of the seal is extremely low. Axial compression between 5% - 10% is sufficient for the felt seal design and in practice the seal should be captured or bonded in place to prevent radial expansion of the felt material. The inner seal is a spring loaded Teflon lip seal that also rides on a hard anodized surface. This seal prevents small particles from entering the joint and will remain in contact through thermal expansion and contraction with very little change in lip sealing force due to the radial expanding spring. This same method of double seal has been used successfully in high dust environment missions such as the Mars Exploration Rovers [5].

Joint Sensing and Control

The overall coordination of the joints is done by the main computer, which is housed in the rover body. This computer transmits via point commands to each motor controller over a CAN network bus at 8 Hz. The motor controller is housed locally at each motor and controls the motion of the joint using a position control loop at 2.7 kHz. Joint position via points are updated during motion and are fed from the main CPU to the local controllers. The motor controllers then update the position setpoint and smoothly transition to the new motion profile.

Each joint has both an incremental encoder on the motor input as well as a 12-bit absolute encoder on the joint output. The motion of each joint motor is controlled via the incremental encoder, and the limb kinematics is determined from the high precision output encoder. Using these two position sensing devices, the mechanical windup of the joint can be determined. This measurement combined with a characterization of the torsional stiffness of the joint gives the torque experienced at each joint. Using the joint torques and the vehicle's kinematic pose, the robot can determine the ground contact force of each limb and can autonomously make adjustments to correctly distribute the vehicle load over all the limbs [6].

Structural Details

Most of the Tri-ATHLETE components are made from 7075-T6 aluminum. Due to the large thermal extremes of the lunar environment this material is likely not appropriate for a flight system, but the low cost, low mass, high strength combination led to its use in the prototype vehicle. 7075-T6 is approximately 1.8X as strong as 6061-T6, but can be up to three times the raw material cost. Due to the complexity and machining time of many of the Tri-ATHLETE parts, the use of 7075-T6 added approximately 20-25% to the total cost per part. Given the added strength to weight ratio of 7075-T6 this trade was an economical way to keep the total mass down.

To further reduce cost and mass, bonded and rivet joints are used whenever possible. These joints act similar to monolithic parts in their strength and weight characteristics, but without the high cost associated with machining large complicated geometries. The output tubes of all the joints are manufactured with bonded and riveted end fittings as well as a bonded and riveted interface that bolts to the circular spline of the harmonic. Hysol EA 9394 adhesive is used as a liquid shim between concentric features. Radial rivets are then used to join the parts. In analysis, it is assumed that the rivets take the entire load while the adhesive contributes no shear strength, only transmitting compressive load. The body of the rover is made from a similar riveted structure. Custom structural ribs are joined to an aluminum sheet metal skin using a combination of blind as well as solid aluminum rivets. This allows the body, shown in Figure 6, to be a closed box structure, which gives a high strength-to-weight and stiffness-to-weight ratio.

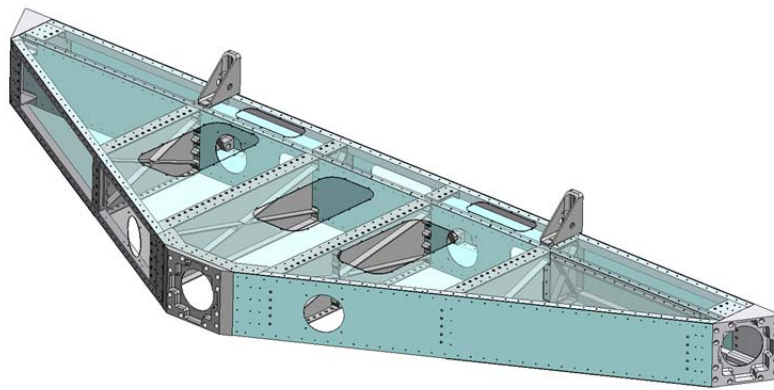


Figure 6. ATHLETE rover chassis, implemented as a riveted box structure

With the exception of the riveted tubes and the riveted body frame, all structural interfaces are implemented using a bolted joint in friction. This allows for interchangeable components without the need for matched and pinned joints. Each structural joint was analyzed using a clamping force equal to the bolt preload multiplied by the number of bolts with an assumed coefficient of friction of 0.2. The bolt preload is based upon the minimum load of either the bolt or the internal threads. For the bolt, the maximum load is 50% of the fastener ultimate tensile strength using the tensile stress area. For the internal threads, if an insert is used, the preload capability is 50% of the pullout load for inserts. If the bolt threads directly into a tapped hole, then the maximum preload is 57% of the load capability of the tapped hole. The application torque is then

$$T=KPD. \quad (1)$$

where P is the preload, D is the nominal diameter and K is the nut factor which depends on the lubrication and surface finish. The nut factor that was used was based on tension versus torque testing performed at JPL using Solithane applied to the threads. In the ATHLETE vehicle Loctite 243 was used instead of Solithane, but it was considered an equivalent lubricant for fastener installation and a similar fastener staking method once it had cured. For all critical fasteners, 1200 MPa (180 ksi) steel black oxide socket head cap screws were used. For non-structural fasteners, such as external covers, stainless steel fasteners were used. This makes for easy identification of fasteners that require precision assembly with a torque wrench.

Avionics Packaging

Each Tri-ATHLETE contains an identical set of avionics, which are packaged in a “drop tray” that can be easily lowered down from the main rover chassis shown in Figure 7. Central to the drop tray, and dominating its design considerations, is a set of four Valence Technologies lithium iron magnesium phosphate batteries wired in series. The resulting 78-kg pack has a voltage of 51.2 V and a capacity of 130 Ah. The batteries are capable of providing 300 A max current for 30 seconds. The batteries are charged by a pair of 1 kW / 60 V power supplies whose outputs are toggled by a battery management system (also from Valence) that monitors the battery health and state of charge. The drop tray also houses a 4U cPCI card cage that contains four XCalibur1000 800-MHz PowerPC computers from Extreme Engineering. These computers were chosen because of the existence of a space flight qualified computer with comparable capabilities. One of the four computers is devoted to controlling the rover’s motion and communicating with ground systems while the other three computers are each devoted to stereo vision processing for four of the twelve camera pairs on the rover. Seven of these camera pairs are housed in the drop tray along with a 1-W wireless router and other navigation/attitude control sensors (MEMS IMU, GPS, and high resolution tilt sensor).

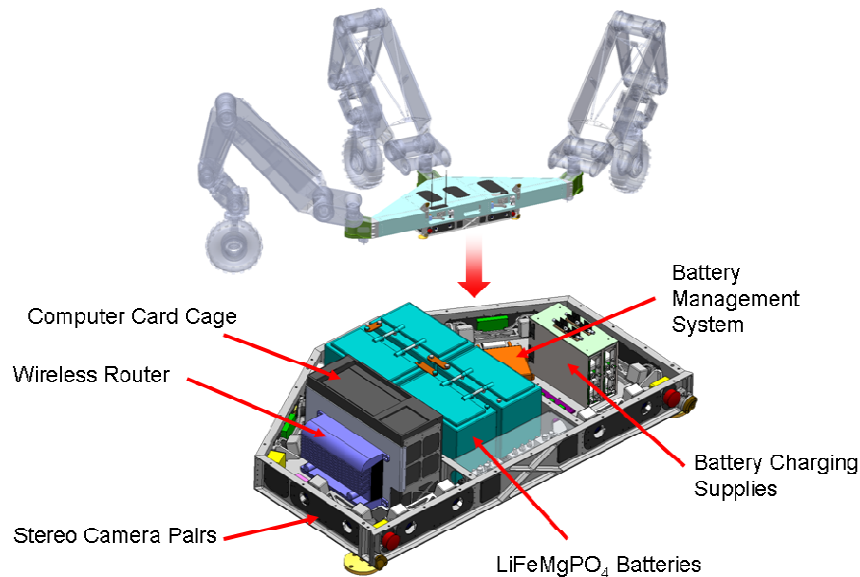


Figure 7. Rover avionics, housed in a drop tray that can be lowered from the main chassis

With the exception of the leg cabling harness and distributed motor controllers, the drop tray contains nearly all of the rover’s avionics and associated wiring. This proved to be of great convenience and represents a significant advancement over the previous chassis design. The ability to remove the avionics in this monolithic way allowed for easy assembly, maintenance, and repair operations. In addition, the drop tray provided a method for bench top testing all the major systems before they were fully integrated into the rover.

Cabling Design

A major innovation in the Tri-ATHLETE vehicle over the original ATHLETE is the implementation of the cable harness. The original vehicle used a round wire harness that was entirely external to the limb. This created several “chopping” points where the cable could be cut by structural links passing over each other. For the second generation of the robot, the cable harness is completely internal to the limb structure. This is implemented using essentially a round wire harness imbedded in a flat silicone extrusion. This technique, developed by Cicoil™, allows for the use of any combination of round wires, packaged in a flexible, flat ribbon arrangement. The harness is routed down along the limb and an

internal cable spool is used to create a clock spring configuration with the cable that allows for the ± 180 degree range of motion at each joint.

The cable harness is broken in to seven segments, where each segment terminates at the joint motor controller. Multiple cable segments allows for the ability to quickly sever the limb at any joint. This is extremely useful for both debugging and repair. A custom board connects the appropriate power line from the harness to the motor / controller and interfaces the controller to the CAN communications bus that runs down the entire length of the limb. The cable itself consists of a 60V DC power bus, a 12-V DC auxiliary power line, CAN bus, and a CAT6 Ethernet line to transmit video from a camera at the limb end effector. Since the required current for all joint motors can be as large as 100 A, the power bus is implemented using 15 twisted and shielded 22-gauge wire pairs, connected to the main power system in parallel. These power lines are configured such that 5 pairs provide power the upper most actuators in the kinematic chain (Hip Yaw, Hip Pitch, & Thigh Pitch). The next five pairs of the 60-V bus power the actuators in the lower portion of the limb (Knee Pitch, Knee Roll, Ankle Pitch, & Ankle Roll). The last five pairs power the wheel motor, which can consume 30 A continuous and 60 A peak current. In this way, the power axes can be stripped away from the main harness as the cable progresses down the limb, incrementally shrinking the width of the cable. A cross section of the cable harness is shown in Figure 8.

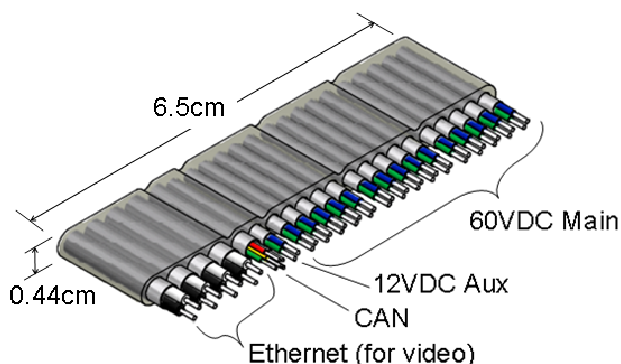


Figure 8. Leg Harness Cross Section

Wheel Design

The Tri-ATHLETE team is also collaborating with Michelin on the development of a non-pneumatic compliant wheel design that is appropriate for the lunar environment. This 71-cm diameter by 23-cm wide wheel is sized to support both the Tri-ATHLETE and NASA JSC Chariot rovers (2500-N nominal load, 4500-N max load, 10-kph top speed) and efficiently carries load by using Michelin Tweel® derived mechanics [7]. One advantage of this approach is that the wheel's effective contact pressure is largely independent of load and uniform across the ground contact area. A low and uniform ground contact pressure greatly contributes to the overall mobility performance of Tri-ATHLETE. In addition, this wheel design, which contains no elastomers, exhibits low energy loss from obstacle impacts and allows for a tunable vertical stiffness that is independent of contact pressure. These features are important because the wheel system is the only additional source of passive compliance beyond actuator windup and deflection of the major structural members on Tri-ATHLETE.

The most recent design iteration, shown in Figure 9, of the so-called Michelin Lunar Wheel is comprised of a proprietary composite that has a specific elastic strength (elastic strength/density) that is 4.7 times that of 7075-T6 aluminum and 7.2 times that of 36NiCrMo16 steel. This material was chosen primarily because of its excellent cryogenic resilience such that the wheel may remain flexible at the lower end of the lunar surface temperature regime (40K, -233.15°C). Paradoxically the mechanical properties of the

composite (flex fatigue, compression and tensile modulus) improve at cryogenic temperatures. This has enabled JPL and Michelin to demonstrate driving the wheel more than 5000 km under load while being fully immersed in liquid nitrogen. With a mass of only 15 kg, this wheel has a load carrying multiplier (load capability/wheel mass), which is three times that achieved by the original Apollo Lunar Rover wheel.



Figure 9. Michelin Lunar Wheel Impacting a 10-cm Tall Rock

Lessons Learned

The Tri-ATHLETE robot is the second generation of ATHLETE vehicles. The first vehicle was completed in 7 months from concept to fully functional robot. The vehicle was then tested for three years and its shortcomings became evident. In the design of the second generation ATHLETE vehicle, the development team tried to solve all of the problems with the first vehicle and add substantial functionality, which in turn added significant complexity, cost, and schedule over the development of the first vehicle. From the onset of the re-design effort the team was very aware of “the second system effect” but was unable to avoid it [8]. Continually trying to solve every problem led to a significant slip in the schedule and a significant increase in the scope of the project. What started as the re-design of only two joints to increase the load carrying capability of the vehicle, quickly escalated to a complete re-design with significantly more complex end-of-year milestones. In hindsight it would have been easier to break the re-design of the vehicle in to smaller incremental developments so that new innovations could be tested and refined instead of one large re-design effort.

Tri-ATHLETE is a research project with a team of four mechanical design engineers. This is a relatively small project, but large enough to necessitate consistent guidelines and requirements across the team. This was implemented using clear load cases, structural margin philosophy, and design procedures. The load case was clearly defined as a two-leg iron cross, which is the vehicle supporting itself on two opposing limbs completely outstretched. This sets the load capabilities of each of the pitch joint actuators and associate structure. Similar pose derived requirements size the necessary capabilities for the yaw and roll joints. The mass of components was reduced to the extent possible while still meeting the functional and structural requirements. A guideline of \$1000/kg was used to evaluate the merit of light-weighting features, meaning special machining operations would be employed simply to remove mass from custom designed parts if the incremental cost of that particular machining operation per unit of mass removed was below \$1000/kg. Even with a small team, these clear guidelines established at the beginning of the project kept the entire team designing to the same requirements and reduced the amount of time spent debating the proper balance of capability, complexity, and cost.

In contrast with the implementation of rigorous structural guidelines, much looser rules were used when designing the cable routing. Schedule allowed for the testing of the cable spool clock springs that were used inside the joints because of rapid prototyped cable trays, but it did not allow for an entire joint to be

assembled before setting the cable segment length. As a result, motor controller mounting locations were only approximated and the true cable path was not defined. At the time of procurement of the cables, the length was only roughly approximated and 45 cm (18 inches) was added to either end of the cable as margin. This ultimately resulted in significantly more cable than was necessary and posed a significant challenge of packaging excess and unplanned cable. If more time were invested initially in the definition and modeling of the cable routing, then less margin for uncertainty would be necessary. While accurately modeling cabling is difficult it ultimately saves significant time and effort in the long run.

Conclusions

In September of 2009, the vehicle was tested for three weeks at the Black Point lava flow near Flagstaff, AZ. This test demonstrated an initial set of capabilities for the vehicle, including demonstrating the offloading of cargo from a 3.2-m tall mock lander, walking over obstacles over 1-m tall, excavating soil using a backhoe tool attachment, and accumulating more than 6km of total traverse distance. This field test also highlighted the shortcomings and exposed some of the complexities of the system. Future refinements will deal with problems of electrical noise in the actuators, power system upgrades, and limited bandwidth from simultaneously commanding and coordinating 48 actuators and 24 cameras on each Tri-ATHLETE vehicle. All of these shortcomings, however, can be overcome and the Tri-ATHLETE system has proven to provide a unique capability of cargo handling and transportation, as well as tool use and payload manipulation that fits well within the current lunar architecture.

Acknowledgements

The authors would like to thank the entire ATHELTE team, the staff of Michelin Recherche et technique S.A. for the design and construction of the Michelin Lunar Wheel, and the NASA Human-Robot Systems (HRS) project, part of the Exploration Technology Development Program (ETDP), for funding this work. The work described in this paper was performed by the Jet Propulsion Laboratory, California Institute of Technology, under contract with the National Aeronautics and Space Administration. Copyright 2009 California Institute of Technology. Government sponsorship acknowledged.

References

1. Wilcox, B.H. "ATHLETE: A Cargo and Habitat Transporter for the Moon", Proceeding of the 2009 IEEE Aerospace Conference, Big Sky, Montana, USA, March 7-14, 2009.
2. Heverly, M., Matthews, J. "A Wheel-on-limb rover for lunar operation," in Proceedings of the 9th International Symposium on Artificial Intelligence, Robotics and Automation in Space (ISAIRAS), February 25-29, 2008.
3. Carroll, Michael. The Seventh Landing: Going Back to the Moon, This Time to Stay. pg 82 Springer New York. 2009.
4. Toups, L., Kennedy, K.J., et al, "Constellation Architecture Team-Lunar Habitation Concepts", Proceedings of the AIAA Space 2008 Conference & Exposition, San Diego, California, September 9-11, 2008.
5. Krishnan, S. Voorhees, C., "The use of harmonic drives on NASA's Mars Exploration Rover," Harmonic Drive International Symposium 2001 Nagano, Japan November 20-21, 2001.
6. Collins, C. "Stiffness Modeling and Force Distribution for the All-Terrain Hex-Limbed Extra-Terrestrial Explorer (ATHLETE)", Proc. ASME 2007 International Design Engineering Technical Conferences & Computers and Information in Engineering Conference, Las Vegas, Nevada, USA, September 4 – 7, 2007.
7. Rhyne, Timothy B. and Cron, Steven M. "Development of a Non-Pneumatic Wheel," presented at the 24th Annual Meeting and Conference on Tire Science and Technology, Tire Society, Akron, Ohio, USA. September 20-21, 2005.
8. Brooks, Fred. The Mythical Man Month. Addison-Wesley, 1995

An Approach to Designing Passive Self-Leveling Landing Gear with Application to the Lunar Lander

Troy B. Rippere* and Gloria J. Wiens*

Abstract

Once the lunar lander has touched down on the moon problems can occur if the crew module is not level. To mitigate, compliant landing gear provide a solution that would allow the module to be leveled once it has landed on some ground slope. The work presented here uses compliant joints, or flexures, for each leg of the module and optimizes the mechanics of these flexures such that the module can be passively leveled over a range of landing slopes. Preliminary results suggest that for landing on a slope of up to 12 deg the effective slope of the module can be reduced to a maximum of 2.5 deg.

Introduction

During the next lunar mission one of the challenges that will be faced is the possibility of landing on a slope of up to twelve degrees. Among other potential issues caused by landing on a slope, such as difficulties while offloading cargo, is the concern of “fly-out” problems during ascent from the lunar surface. By considering the lunar module and its four deployable legs as a single spatial mechanism, the legs can be designed in a novel manner with the objective of passive self-leveling in mind.

Additionally, to avoid issues associated with lubricating joints this problem can be approached using compliant joints, or flexures, which are thin members that provide the relative rotation between two adjacent rigid members through bending. Previous work has shown how flexures can be approximated as linear torsion springs with stiffness k [1]. From this, a variety of techniques can be applied to find appropriate flexure stiffness of each joint so that the combination of the weight of the lunar lander and the resistance to deflection from the flexures will effectively reduce the relative angle of the module with respect to the horizontal plane over the range of potential ground slopes.

Background

It should be noted that the approaches presented here model the module with four identical equally spaced legs. Furthermore, each leg is designed to have a joint connecting it to the module, a joint connecting it to the landing pad at the bottom of the leg, and a third joint spaced somewhere between the first and second joints.

Assumptions

For these analyses, the following initial assumptions were made:

1. The landing area of the lunar surface can be modeled as a plane. In other words, there are no craters or boulders that would affect a single leg.
2. There is a uniform probability of landing on any ground slope between zero and twelve degrees.
3. There is a uniform probability of landing at any twist angle. Here twist angle is defined as rotation of the module in the ground plane. A 0 deg twist angle means that the line between one set of two opposing pads is orthogonal to the local gravity field, or that those two pads are level. A 45 deg twist angle means that line between two adjacent pads is orthogonal to the local gravity field, or that they are level. It follows that the other set of two adjacent pads will also be level with respect to each other.

* University of Florida, Gainesville, FL

4. Upon landing, the landing pads will remain fixed relative to one another as they were in the undeflected configuration; landing impact will not affect the placement of individual pads on the ground.

Leg Numbering System

Figure 1 and Figure 2 show the leg numbering system that is used to describe joint orientations.

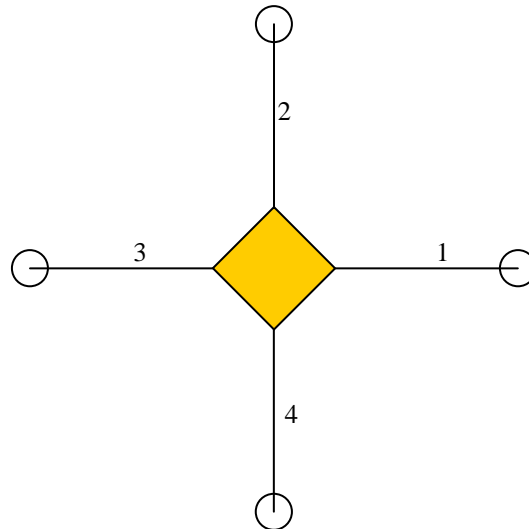


Figure 1. Top view of module with legs numbered

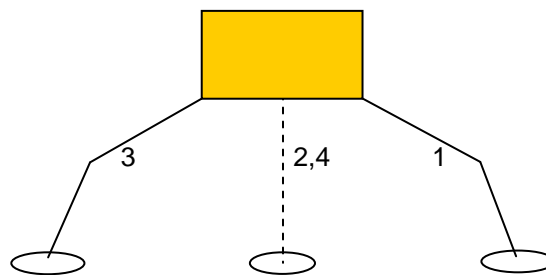


Figure 2. Front view of module with legs numbered

Joints

As mentioned previously, each leg will have a joint that connects the leg to the module. For the analyses presented here these joints will be flexures whose bending axes are perpendicular to the plane formed by that leg and the opposing leg when the landing gear is in its undeflected configuration. For example, in Figure 2 the flexure axes of legs 1 and 3 will be out of the page while the flexure axes of legs 2 and 4 will be parallel to the page. For each leg, this flexure will be called flexure f .

Additionally, the joints that connect the legs to the landing pads will be spherical joints and thus will not have any resistance to rotation.

Next, the joint in the middle of each leg will be the flexure equivalent of a universal joint with perpendicular axes. This is accomplished by having two flexures serially connected as depicted in Figure 1. One of the bending axes will be parallel to the bending axis of the joint which connects the leg to the module while the other axis will be in the plane formed by that leg and the opposing leg. For each leg, the

flexure with the bending axis parallel to that leg's bending axis of flexure f will be called flexure d while the serially connected flexure will be called flexure e .

Because it has been shown that flexures can be modeled as linear torsion springs, subsequent modeling will assume that the flexures are traditional revolute or universal joints with torsion springs to resist rotation about the bending axes. For the model of each analysis, it is assumed that the bending axes of flexures d and e both pass through the same point.

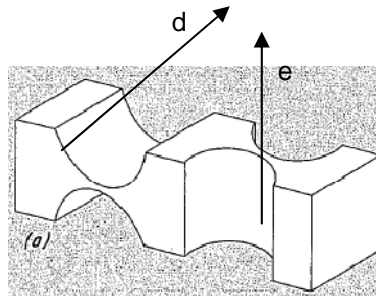


Figure 1. Universal flexure created by serially connecting two flexures [2]

Analysis

Two-Dimensional Analysis

The first analysis performed was a two-dimensional analysis in which the plane that was analyzed was that which is formed by two opposing legs in the undeflected configuration. The active flexures for the planar analysis of legs 1 and 3 are shown in Figure 4. It can be seen that legs 2 and 4 together form a single middle leg that has one flexure. Additionally, to account for the change in length of legs 2 and 4 projected onto the plane due to the out of plane motion, the middle leg is of variable length. This variable length is depicted in Figure 4 by a double headed arrow.

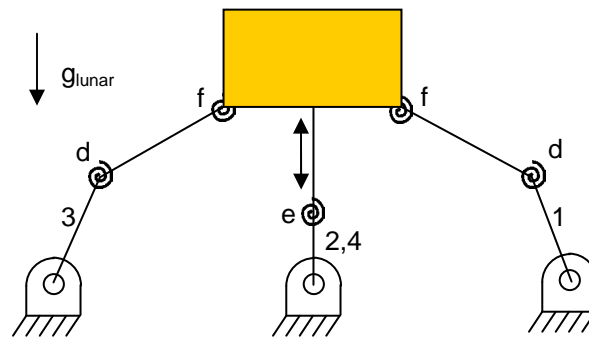


Figure 2. Joints and links for planar analysis

The three spring stiffnesses will be determined as follows:

1. Give an initial guess of spring constants for flexures d , e , and f .
2. For a given ground slope find the angle of each joint as described below.
3. Using static balancing equations find the required lunar weight of the module such that the combination of the weight of the vehicle and the resistance to bending in the springs will put the module in static equilibrium. For a given set of spring stiffnesses there exists one unique solution of required weight that will hold the module in static equilibrium at the desired level configuration.
4. Repeat steps 2 and 3 for n steps of ground slope between 0 deg and 12 deg.
5. Calculate the average required weight from the n steps in step 4.
6. Use forward divided differences with steps 4 and 5 to estimate the gradient of average required weight with respect to the stiffness of each spring.

- Use steepest descent to find the set of stiffnesses (d , e , f) that minimizes the difference between the calculated average required weight and the known lunar weight of the module using the estimate of the gradient from step 6 for each iteration.

This planar mechanism has seven bodies (including the ground) and eight revolute joints resulting in two degrees of freedom. Addition of the variable length of the middle leg gives a total of three degrees of freedom.

Because the mechanism has three degrees of freedom, three choices regarding its configuration must be made. The first choice, which should be the most obvious, is that the module be level with respect to the local gravity field. The second choice is the length on the adjustable leg which will account for any ground slope going into the page. Lastly, the angle of flexure d on the uphill leg is assumed to be constant at an angle of 180 deg. This assumption remains valid for any configuration that would otherwise try to extend the angle beyond 180 deg if the leg is designed with a mechanical stop preventing a greater angle. An example of a configuration after these three choices is shown in Figure 5.

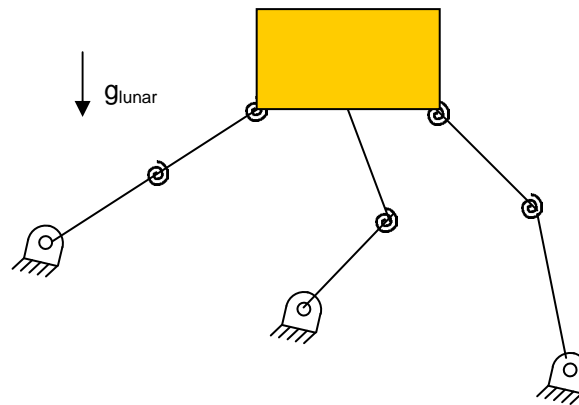


Figure 5. Configuration of leveled module

Three-Dimensional Analysis

The second analysis performed was a three-dimensional analysis. This analysis looks at the mechanism as a whole instead of just a projected plane while also providing a slightly different approach to finding the optimized spring stiffnesses.

This approach is as follows:

- Give an initial guess of spring constants.
- For a given ground slope and twist angle find the mechanism configuration as described below.
- Using static balancing equations find the required lunar weight of the module such that the combination of the weight of the vehicle and the resistance to bending in the springs will put the module in static equilibrium. For a given set of spring stiffnesses there exists one unique solution of required weight that will hold the module in static equilibrium at the desired level configuration.
- Use forward divided differences with step 3 to calculate the gradient of required weight with respect to the stiffness of each spring. While there exists a unique solution of required weight for a set of spring constants, for the inverse problem when given the required weight there exists a plane of solutions for the set of spring stiffnesses. The calculated gradient is the normal vector to all of the planes of solutions for any given required weight.
- Calculate the point that is closest to the initial guess of spring constants and on the plane of solutions when the required weight is equated to the given weight of the module.
- Using the point found in step 5 and the normal vector, calculate the equation of the plane.
- Repeat steps 2 through 6 for m steps of twist angle between 0 and 45 deg. Because of symmetry any twist angle can be modeled by a twist angle between 0 deg and 45 deg.
- Repeat step 7 for n steps of ground slope between 0 deg and 12 deg.

9. Using linear least squares, find the point that minimizes the L^2 -norm of the vector of the distance between this point and each plane found in step 8. This point is defined to be the set of optimum spring stiffnesses.

This spatial mechanism has ten bodies (including the ground), four spherical joints, four universal joints, and four revolute joints. This gives six degrees of freedom, which means that the module itself can be positioned and oriented in any manner within its workspace.

Similar to the planar analysis, it is first necessary to find the angles of each joint to then find the optimum spring stiffnesses. Also similar to the planar analysis, the orientation is assumed to be level. This reduces the degrees of freedom by two because the module must be level about two orthogonal horizontal axes. The third choice of configuration is that the module is at some assumed height which is below its undeflected height on a level surface. Essentially this is saying that on a level surface, the weight of the module would cause some sort of deflection in the joints and would sink by some amount. This analysis assumes that the height of the module will be at 90% of its undeflected height.

After these two constraints on orientation and one constraint on position, three degrees of freedom still remain. It is assumed that the preferred leveled equilibrium configuration of the module will be one which minimizes the deflections in the flexures, where here minimization is defined as minimization of the L^2 -norm of the vector of the twelve flexure deflections. Using the Matlab `fmincon` function, these remaining degrees of freedom, two of which are position in the horizontal plane and the third is the rotation in the horizontal plane, can be found which minimize the deflections.

Results and Conclusions

For both the two-dimensional and 3-dimensional analysis, the flexure has the dimensions as depicted in Figure 6. The stiffness for flexure can be approximated in terms of its geometric dimensions as follows:

$$k \approx \frac{2Eb t^{5/2}}{9\pi R^{1/2}} \quad (1)$$

Two-Dimensional Analysis

The optimum spring stiffnesses as determined by the first analysis were found to be:

$$\begin{bmatrix} k_d \\ k_e \\ k_f \end{bmatrix} = \begin{bmatrix} 3.841 \times 10^3 \\ 5.562 \times 10^4 \\ 5.840 \times 10^4 \end{bmatrix} \frac{N \cdot m}{rad} \quad (2)$$

From this and the spring stiffness approximation of equation (1), the dimensions of the flexures as shown in Figure 6 are on the order of:

$$\begin{bmatrix} b \\ t \\ R \end{bmatrix} = \begin{bmatrix} 0.1 \\ 0.01 \\ 0.5 \end{bmatrix} m \quad (3)$$

Using these spring stiffnesses and the given weight of the module a static analysis was performed for a range of ground slopes between 0 deg and 12 deg. The maximum angle of the module in this range was 2.5 deg at a ground slope of 12 deg.

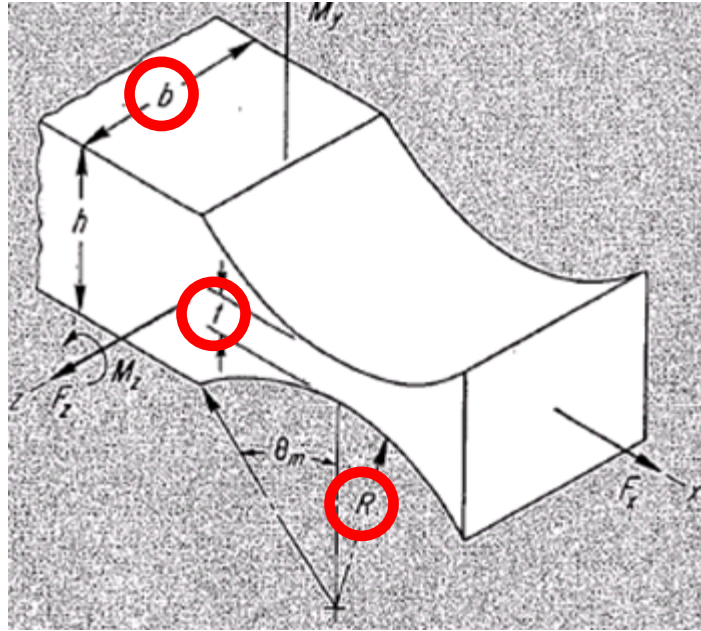


Figure 3. Flexure dimensions [2]

Three-Dimensional Analysis

The optimum spring stiffnesses as determined by the second analysis were found to be:

$$\begin{bmatrix} k_d \\ k_e \\ k_f \end{bmatrix} = \begin{bmatrix} 1.077 \\ 1.811 \\ 2.162 \end{bmatrix} \times 10^5 \frac{N \cdot m}{rad} \quad (4)$$

From this and the spring stiffness approximation of equation (1), the dimensions of the flexures as shown in Figure 6. Flexure dimensions are on the order of:

$$\begin{bmatrix} b \\ t \\ R \end{bmatrix} = \begin{bmatrix} 0.2 \\ 0.01 \\ 0.05 \end{bmatrix} m \quad (5)$$

The static analysis that was performed for the calculated spring stiffnesses for the two-dimensional analysis has not yet been performed for the three-dimensional analysis. This will be completed in future work.

Comparing the results of the two analyses it is seen that the optimum stiffness as found by the two-dimensional analysis is only about one-fourth as that obtained from the three-dimensional analysis. This discrepancy is likely due to the different assumptions of the two analyses, specifically the length of the adjustable leg and the fixed angle of the uphill leg in the two-dimensional analysis. Additionally, because of the assumption that the bending axes of flexures *d* and *e* pass through the same point, it follows that the flexure radius *R* must be small because the flexures are actually serially connected. Because of this, the three-dimensional analysis might prove more accurate because of this much smaller dimension.

Future Work

In addition to the three-dimensional static analysis for the calculated spring stiffnesses there are a few other tasks that can improve the robustness of this method. These include calculating and minimizing the stresses in the flexures and taking into account the change in module weight once the payload has been unloaded. Additionally, minimizing the effect of single-leg disturbances, such as one leg landing on a boulder or in a small crater or being displaced by landing impact, would increase the robustness. Also, for more insight into the actual bending mechanics, a finite-element analysis might prove more accurate than the linear spring approximation. Lastly, looking at different flexure shapes, as described in [3], might provide a better flexure system.

Acknowledgments

The research of this paper was funded by the NASA Graduate Student Researchers Program and the University of Florida Alumni Fellowship Program.

References

1. Howell, L. L. *Compliant Mechanisms*. New York: John Wiley & Sons, ©2001.
2. Paros, J. M. and L. Weisbord. "How to Design Flexure Hinges." *Machine Design* (November 1965), pp. 151-157.
3. Lobontiu, N. *Compliant Mechanisms: Design of Flexure Hinges*. Boca Raton: CRC Press, ©2003.

Design and Manufacture of a Highly Reliable, Miniaturized and Low Mass Shutter Mechanism

M. Manhart*, T. Zeh*, G. Preißler*, A. Hurni*, G. Peter+, I. Walter+, J. Helbert+,
K. Multhaup** and H. Hiesinger**

Abstract

This paper describes the development, manufacturing and testing of a lightweight shutter mechanism made of titanium for the MERTIS Instrument. MERTIS is a thermal infrared imaging spectrometer onboard ESA's future BepiColombo mission to Mercury. The mechanism is built as a parallelogram arrangement of flexible hinges, actuated by a voice coil. In a first test run, it was shown that the selected EDM processing led to the generation of titanium oxides and an oxygen-enriched surface layer on the substrate (so called α -case layer). In the revised version of the shutter, it was possible to manufacture the complex geometry by micro-milling and an adjacent pickling procedure. The adequacy of this approach was verified by lifetime and vibration testing.

Introduction and Requirements

The MERTIS instrument is a thermal infrared imaging spectrometer onboard ESA's future BepiColombo mission to Mercury. For the spectrometric data acquisition, a calibration signal that contains information about the instrument background radiation is required. This is performed by periodical acquisitions while the targets scene (i.e., planet radiation) is blocked. Therefore, a mechanical shutter is required to block the optical path from the planet view of the instrument.

The main requirements for the shutter mechanism are specified in Table 1.

Table 1: Shutter main requirements

	Requirement
Mass	25 g
Max. dimensions	20 x 40 x 5 mm ³
Max. Frequency	10 Hz
Duty cycle	1:10
Lifetime test	100 x 10 ⁶ cycles
Fail safe position	Shutter-blade in open position
Aperture	1.5 mm x 8 mm

* Kayser-Threde GmbH, Munich, Germany

+ Deutsches Zentrum für Luft- und Raumfahrt (DLR), Berlin, Germany

** Institut für Planetologie, Westfälische Wilhelms-Universität, Münster, Germany

Shutter Design

In an extensive study, all major shutter driving principles have been investigated for their use in MERTIS: rotary DC motors, linear piezo actuators/motors, piezo bender actuators, and linear voice coil actuators (VCA).

An important criterion was that the majority of possible failures shall lead to a defined fail safe position (i.e., shutter-blade open). Therefore, the voice coil actuator with a moving magnet and a stationary double coil (HELMHOLTZ alignment) was selected. It is simple to design a VCA mechanism where the inactive or standby shutter-blade position is open.

Figure 1 shows the assembled shutter. Flexible hinges that enable frictionless, linear guiding were selected to achieve the demanding lifetime requirements. The shutter consists of a parallelogram assembly with two flexible hinges that enables a nearly linear 1.5-mm movement of the rocker with its shutter-blade. Furthermore, the VCA with its moving magnet, the stationary double coil and a magnetic sensor (GMR) for a position feedback signal for the control electronics are shown.

A number of dramatic failures of flexible hinges systems during vibration test have been reported. For random vibration, the high Q-factors at resonance together with high mid-frequency PSD levels can lead to high loads on the flexible hinges [1]. Furthermore, a sufficient stability against transverse loads has to be guaranteed. Two measures have been taken in order to prevent damage during vibration tests or during satellite launch:

- a snubber that acts as a mechanical limiter against unwanted high displacements of the rocker,
- reduction of the moving mass to the smallest possible amount in order to limit the kinetic energy of the rocker.

It was possible to reduce the moving mass of the rocker to 0.3 gram. The design process was supported by rigorous analysis, including detailed FEM and stress analysis of the flexible hinges.

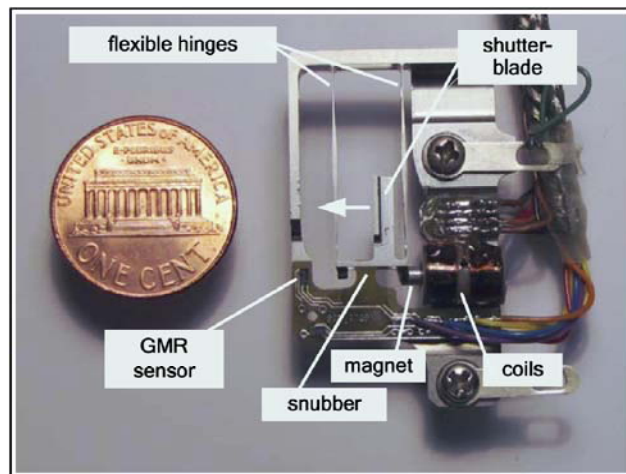


Figure 1: Complete integrated shutter mechanism with milled titanium structure (EM, Engineering Model). The arrow near the shutter-blade indicates the displacement direction for the 1.5-mm movement.

Material Selection and Manufacturing Aspects

A large variety of materials is available for flexible hinges. Properties like material density, Young's modulus, endurance strength, thermal conductivity and manufacturability have to be considered carefully for each application. For MERTIS, different materials like copper-beryllium alloys (e.g., CuBe₂), martensitic steels, and titanium alloys have been traded. The combination of high fatigue strength and low density made titanium Ti6Al4V the material of choice. The maximum Von Mises stress in the shutter structure is 132 MPa, which is well below the limit of 350 MPa at 0.5×10^9 cycles for Ti6Al4V [2].

The dominant design driver for the hardware realization was the manufacturability of the 80- μ m-thick titanium hinges with a reproducible quality. Basically, there are two possible ways for the implementation:

- A setup where separate components and materials like hinges, shutter-blade and support structure are assembled together.
- An integral, monolithic approach where hinges, shutter-blade and support structure are manufactured in a single process and from a single piece of raw material.

The chosen integral, monolithic design offers the important advantage that deformations due to different coefficients of thermal expansion can be avoided and that no adjustment is required after the manufacturing. However, taking into account the required flexible hinge thickness of 80 μ m (result of the FEM-Simulation), the challenge for the hardware manufacture becomes apparent.

Indeed, the manufacturing of the very thin monolithic structure with the sophisticated mounting of the rocker caused most of the difficulties.

In a first run, the structure was manufactured by wire-cut EDM (Electrical Discharge Machining). The result was not satisfying due to the heat induced surface changes during the machining. One influence was visible as annealing colors on the titanium structure. Furthermore, the high affinity of titanium to oxygen in combination with high local EDM-processing temperature resulted in the formation of titanium oxides and an oxygen-enriched surface layer on the substrate (so called α -case layer, see Figure 3). The presence of such a layer promotes crack formation under loading conditions.

The resulting spring constant of the flexible hinges varied by more than factor 2 (see table in Figure 2).

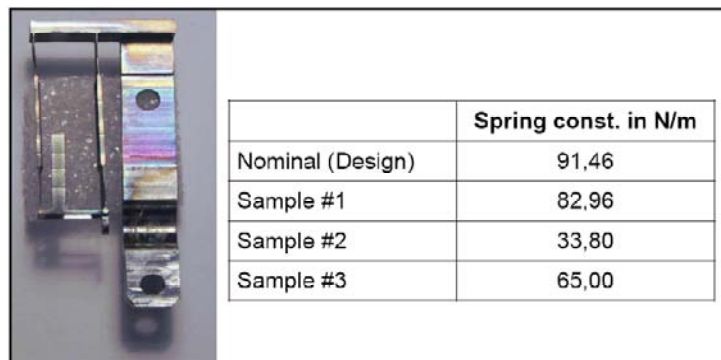


Figure 2: EDM-processed shutter sample structure (left) and variation of the spring constants of three EDM-machined samples (right).

Due to the strong variation of the spring constants, the EDM-process has to be judged as being not practical for the MERTIS shutter. The negative (thermal) influence of EDM machining on the fatigue behavior of Ti-alloys has been observed by several other authors. An antiquated, but still excellent overview is given in MIL-HDBK-697A [3].

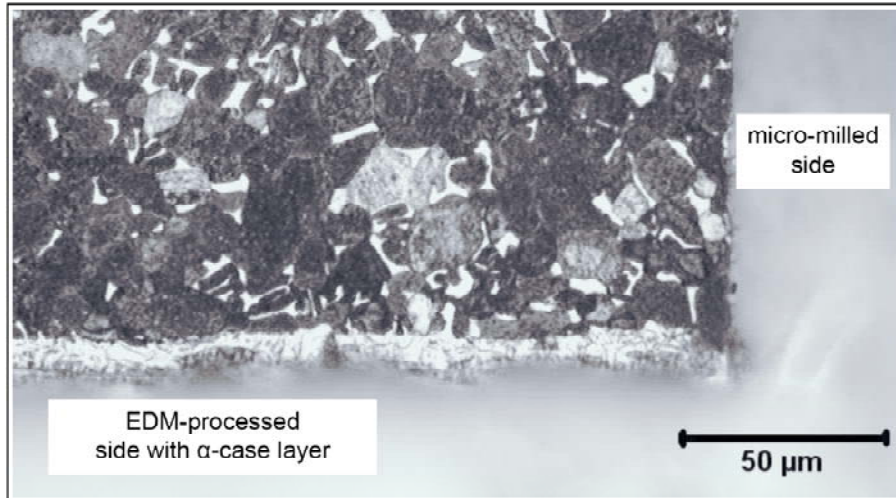


Figure 3: Micrograph of the Micro-milled (right) and EDM-processed (below) shutter structure.

A new manufacturing approach was selected and the shutter mechanical part was optimized for micro-milling instead of EDM machining. Through the application of dedicated cutting parameters, the generation of heat in the device was effectively reduced. Due to a lower the power consumption the spring constant was designed to 39 N/m.



Figure 4: Micro-milled and passivated shutter structure.

Despite the demanding and sensitive manufacturing tolerances, the spring characteristics of the micro-machined shutters had a variance below ± 1 N/m, which indicates a good reproducibility.

An unwanted result of the micro-milling process is the generation of burrs that are formed on the material edges. These burrs have shall be removed for fracture prevention, fatigue resistance, or the danger of flaking particulates. The burrs were eliminated by chemical deburring, i.e., an acid pickling procedure. Besides deburring, the pickling process was also used to tune the spring constants to their nominal values. The final step was a metallographic analysis and microscopic inspection of the structure and especially the surface.

The chemicals which have been used for pickling are free of nitrate, produce no hydrogen when applied (prevents hydrogen embrittlement), and the material removal is about several $\mu\text{m}/\text{min}$. The process works

at ambient temperature and leaves a smooth silvery, passivated surface finish on the shutter structure (see Figure 2).

Table 2: Variation of the spring constants of four, micro-milled and chemical processed shutter samples. The final, nominal values is 39 N/m ± 8 N/m.

	Initial spring const. after micro-mach.	After pickling process
Sample #4	76.8 N/m	36.1 N/m
Sample #5	76.0 N/m	37.6 N/m
Sample #6	77.04 N/m	37.97 N/m
Sample #7	75.95 N/m	36.24 N/m

The assembled mechanism (as shown in Figure 1) is currently in life testing and further environmental tests. Tale 3 summarizes the actual performance of the shutter engineering model.

Table 3: Intermediate results of the shutter development.

	Requirement	Result for the EM
Mass	25 g	13 g
Max. dimensions	20 x 40 x 5 mm ³	20 x 38 x 4 mm ³
Max. Frequency	10 Hz	130 Hz
Duty cycle	1:10	compliant
Lifetime test	100 x 10 ⁶ cycles	in progress
Fail safe position	Shutter-blade in open position	compliant
Aperture	1.5 mm x 8 mm	compliant

Vibration and Lifetime Testing

Extensive mechanical load tests have been performed. The selected maximum load level of 53 g RMS was about 150% above the nominal load.

The test criteria were:

- no deformation on the flexible hinges or structure,
- no performance degradation and
- no failures in microscopic inspection.

The shutter EM showed neither degradation nor any other failure after the mechanical load test.

After the vibration test, accelerated life testing is currently in work to verify the lifetime performance of the shutter. Currently over 90 million cycles have been processed without any change of the initial shutter parameters.

Summary and Lessons Learned

The initially used procedure of EDM machining of the thin flexible shutter hinges was not the appropriate technology. It was shown that the unfavorable oxidation affinity of titanium, which is accompanied by a variation of the structural properties, lead to arbitrary results and a low surface quality.

With a revised version of the shutter, it was possible to manufacture the complex geometry by micro-machining and an adjacent pickling procedure. The variation of the spring constant was below ± 1 N/m. The realization as a monolithic structure offers further potential for miniaturization. In general, the usage of titanium offers advantages due to the low mass, high specific stiffness (ratio of the specific strength and the Young's Modulus) and high fatigue strength.

Acknowledgements

MERTIS is a joint project of the Institut für Planetologie (IfP) at the Westfälische Wilhelms-Universität (WWU) Münster and two institutes of the German Aerospace Center (DLR) in Berlin-Adlershof, as well as several industrial partners, including Kayser-Threde GmbH München. The MERTIS instrument, funded by the Federal Government of Germany through the German Space Agency, is part of the scientific payload of the BepiColombo mission to Mercury. This mission is developed by the European Space Agency (ESA) in close collaboration with Japan.

References

- [1] S.D. Lewis et al.: *SPACE MECHANISM DEVELOPMENT LESSONS TO BE LEARNED – AN INDEPENDENT VIEW*. In: Proceedings of the 9th European Space Mechanisms and Tribology Symposium, 19-21 September 2001, Liège, Belgium.
- [2] Theodore Nicholas: *High Cycle Fatigue: A Mechanics of Materials Perspective*. Elsevier Science; ISBN-10: 0080446914, September 27, 2006
- [3] MIL-HDBK-697A (NOTICE 1), *TITANIUM AND TITANIUM ALLOYS*, 1 JUNE 1974

Miniaturized Single-Shot Valve and its Application to the ExoMars Pasteur Payload

Pierre Muller*, Hartmut Henkel* and Sabine Klinkner*

Abstract

Hermetically sealing a gas tank and opening it into tubing under telecommand control is a function required in various space instruments. There are a number of space valves that are power saving, withstand vibration, and do not contaminate the gas. But none of them combines these features with low mass and the ability to withstand temperatures of 130°C during the sterilization process mandatory for planetary missions.

In this paper, a novel miniature valve is presented, which is particularly adapted to space applications. It is electrically actuated, utilizing a bimetallic snap-disc that pierces a metallic membrane by a needle pin, thereby opening the valve. The design of this single-shot valve is such that it allows it to withstand a temperature of 130°C and a pressure of 50 bars. The valve is also lightweight (6.62 g) and it requires only 9 W to operate.

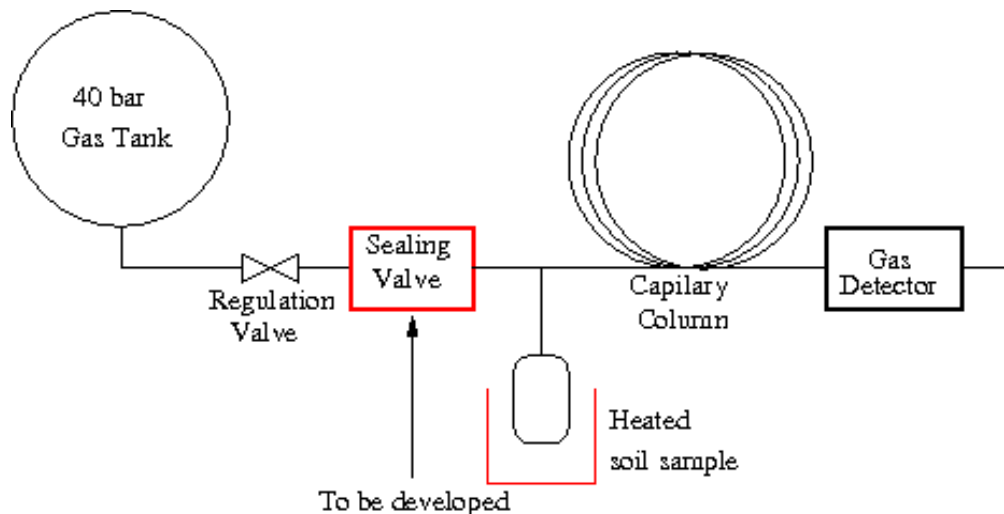


Figure 1. Schematic of a gas chromatograph (MOMA design).

Introduction

How to hermetically seal a high pressure tank and remotely open it in a reliable manner? This technical question arose within the development of the gas chromatograph of the Martian Organic Molecular Analyzer (MOMA), a space instrument part of the ExoMars Pasteur Payload. Onboard is a gas tank, since gas is needed to carry the substances in the chromatographic columns. After assessing the existing valves, the conclusion was drawn that none of these valves was perfectly adapted to the purpose described above.

* von Hoerner & Sulger GmbH, Schwetzingen, Germany

Therefore other solutions were considered. A self-opening valve consists of two main elements: the sealing element, and an actuator. All combinations of existing sealing elements and actuator were listed, and it appeared that sealing valves is a field that requires more exploration. Who has ever built a sealing valve with a piezoelectric actuator? To the current knowledge this has never been done. This seems also the case for a valve working with a bimetallic snap-disc.

This paper first explains the motivation of this development, in particular the function the valve has to fulfill in the MOMA gas chromatograph. After this, the basic design and the refined design of the valve are developed. Finally, the valve was tested and the design reviewed.

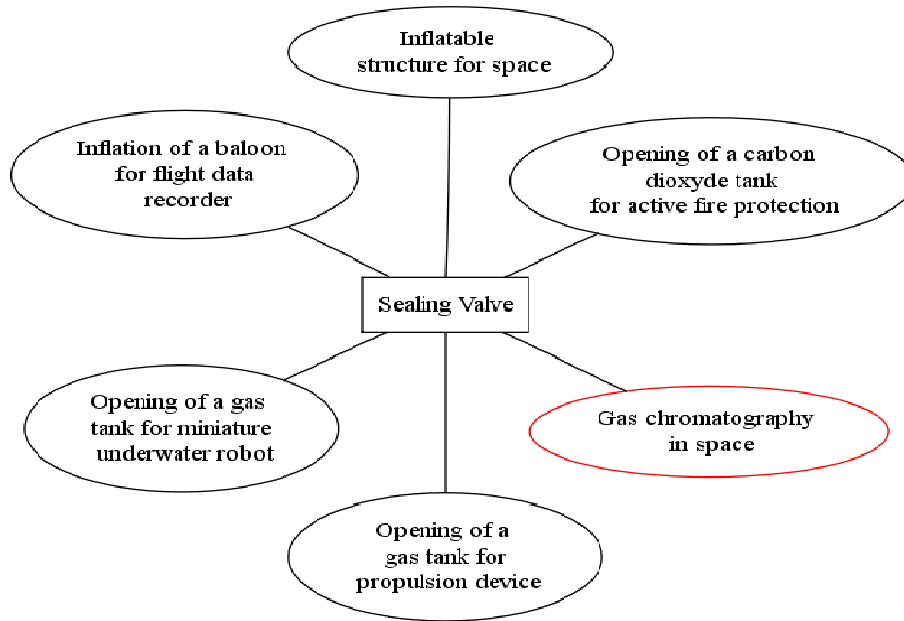


Figure 2. Diagram of the applications of the valve.

Purpose

MOMA is a project of the Max Planck Institute for Solar System Research and the Laboratoire Atmospheres, Milieux, Observations Spatiales. The MOMA objective is the analysis of the Martian soil composition during the ExoMars mission. It consists mainly of a gas chromatograph and a laser spectrometer. The gas chromatograph uses helium to carry the evolved gases from the heated soil sample to the capillary columns, as shown in Figure 1. The speed of the gas flow is regulated by a thermal regulation valve in which the flow is controlled by a sapphire ball compressed to the aperture to a higher or lower level. The compression of the ball is determined by the thermal expansion of the body of the regulation valve, which is heated by a resistor. In this continuous process the regulation valve opens as its temperature is increased. Here a key problem appears, as the entire instrument is heated up during the sterilization process required by the committee on space research for missions to the Martian surface: If no other device is hermetically closing the gas tank during sterilization, it would lose its contents. The main focus of the development presented here is to have a valve that truly hermetically seals the tank, before it is opened by breaking the seal. The initial hermeticity is the key point to select a single-shot valve principle.

The projected valve has to be very lightweight (maximum 10 g), as the mass budget of the scientific instrument is very limited. The flow rate does not need to be very large, as the typical flow rate of helium

in gas chromatography using capillary columns does not exceed 50 ml/min. However the other specifications are quite harsh: the valve has to withstand the gas tank pressure of 50 bar, and a temperature of 130°C (temperature of the sterilization process) should not modify its behavior.

A further purpose of this work is to propose a smaller and more rugged alternative to the existing valves that provide hermetic sealing at pressures in the range of 50 bar. Such valves can have a wide range of applications. Indeed, it can be used in the space industry for deployment of inflatable structures, for opening of a gas tank for an electrostatic ion thruster or other space experiments with gas. On the ground, it can be used for opening a CO₂ tank for active fire protection. A gas tank of an underwater robot could also be opened to bring it at the surface.

Existing Sealing Valves

Having an overview of existing valves was a very helpful step of this work. The focus was placed on single-shot valves, for the reason that it seemed the only reliable way to keep a tank hermetically sealed years after filling. The first encountered single-shot valve was the solenoid valve from the company Industria, France. This valve was already on board the Aerosol Collector Pyrolyzer (a GC-MS) for Huygens, and isolates the gas tank of the COSAC instrument, part of the ESA cometary mission Rosetta. It consists of a quite bulky solenoid actuator and of a thin membrane that obstructs the gas flow and can withstand pressures up to 50 bar. When it is electrically powered, the solenoid displaces a pin that pierces the membrane.

Very original other means to pierce a metallic foil to open a tank were found for space. In the Thermal Evolved Gas Analyzer on-board with the Phoenix Mars mission, the gas tanks are opened with a foil punctured by a wax actuator [1]. Here the device is not suited for the application because typical fusion temperatures of wax are below 130°C. Often used in the space industry is the Pyrovalve, manufactured by Conax, Florida [2]. It has been used for instance in the Titan and Delta II NASA missions. Here, the gas flow is blocked by a ram that is moved downwards by an explosive initiator placed on a tube above. The data sheet claims that the valve does not contaminate the gas and that the operating pressure reaches 647 bar. The reasons why it is not suitable for the application is the maximum storage temperature of only 60°C and its bulky construction.

The Space Science and Technology Department, Rutherford Appleton Laboratory has designed a one-time opening valve for the carrier gas tank of the Ptolemy instrument, a gas chromatograph coupled with a ion trap mass spectrometer built for the Rosetta mission [3]. Using this valve, the tank is normally sealed by a hollow and frangible pillar. A shape memory alloy (SMA, here Nitinol) actuator, having the ability to bend when heated over a certain temperature, is placed near this pillar. To release the gas, a heater outside of the housing elevates the temperature of the nitinol actuator, which bends and breaks the seal. The pressure of the Ptolemy tank is similar to the one of MOMA, and the valve is effective more than 15 years after filling. But also here the low actuation temperature of 76°C prohibits its use for MOMA.

Interesting is also the concept of an alternative to the Pyrovalve [4] which utilizes three burst discs (diaphragms specially designed to burst at a precise pressure difference) to form two chambers. The left chamber is pressurized at the tank initial pressure, while the right chamber is pressurized at the external pressure. A heater is able to elevate the temperature and thus the pressure inside the left chamber. This causes the discs to burst in the succession middle-left-right. This system has apparently not yet been realized.

A further project, launched by NASA aims at finding an alternative to the Pyrovalve. The principle is close to the one of the Ptolemy valve: the actuator is a SMA tube that can be heated from the outside. As the SMA is heated, it recovers its expanded shape, and the evolving force breaks a titanium tube responsible for the gas-tightness. Here the actuation temperature is linked to the used alloy nitinol, and is therefore approximately the same as for the Ptolemy valve. For this reason it cannot be used in MOMA.

On some one-time opening valves, the sealing element is neither broken nor pierced, but melted. The Angström Space Technology Centre has developed a valve made from two silicon discs or wafers forming a filter and a heater [5]. The gas path is obstructed by an indium solder (melting point 156.6°C), that can withstand 100 bar pressure and is melted within 10 s requiring power of 13 W. The silicon element weighs only 0.4 g, but the housing weight amounts to 140 g. The Jet Propulsion Laboratory has also built the micro-machined isolation valve, opening when a doped silicon membrane melts (less than 30 mJ are needed). The Pyrex housing has a burst pressure of about 200 bar. A disadvantage of these valves is that parts from the solder can be released into the carrier gas, although both valve types integrate a filter that captures the larger particles. Another thermally actuated valve using paraffin as seal was developed, but it can be excluded for the MOMA instrument because of the low actuation temperature.

Basic Design

Looking at all these valves increased the motivation to build a new valve. Also, the basics of a sealing valve were retained: it is always a combination of a sealing element and of an actuator. The sealing element can be a frangible pillar, a shaft, a meltable element or a metallic membrane. All possibilities of sealing element are used in single-shot valves. However not all possible actuators have been tried for such an application. Particularly interesting are actuators that are activated by a temperature change. Good examples are the regulation valve of MOMA, the valve with a wax actuator, or the valve with a shape memory alloy. Indeed it only requires a heater, which is a very simple and rugged way to transmit energy. Moreover, the heater can be placed outside the body of the valve, which avoids complications with cables fed through the body of the valve. The only problem with thermal actuation is that the activation temperature has to be above 130°C, temperature of the sterilization process, with a sufficient margin. Ideally, there should exist an activation temperature point, and the actuation should not take place progressively. Which thermal actuator has a well defined actuation temperature? Shape memory alloys are very interesting, and materials that recover their shape at temperature over 150°C were searched. The Company Dynalloy could provide high temperature SMA made of NiTiPt with a recovery temperature of 300°C. But high temperature SMA is still a field of research, and these are very costly elements, only available in the form of wires. A rugged design needs an actuator with a longer heritage. A longer heritage and also high working temperature is given by snap-discs. These are made of two layers of metals foils with different thermal expansion coefficients and bend at a determined temperature. This actuator was favored because it is very easy to fit inside a housing, very light, and does not produce any out-gassing, like thermal actuators based on phase change.

Having chosen the actuator, the sealing element remained to be selected. Also here, the criterion was the reliability. Therefore it was looked for a component that has a broad use and that benefits from wide knowledge. An attractive device on which the design could be based on is called burst disc. It is basically a thin disc of gas-tight material that ruptures at a certain pressure difference between the two sections it separates. These discs are widely used to protect against over-pressures. Similar to the solenoid valve from Industria, a membrane could be punctured by a pin attached to the actuator. The first test showed that the force and the displacement yielded by the bimetallic snap-disc were sufficient to clearly pierce a membrane similar to a burst disc calibrated at 150 bar. The next step was to design the body of the valve with heater, tubes, and adequate pin attached to the snap-disc.

Refined Design

In order to ensure a high reliability, some important design parameters have to be selected carefully. For example the pin has to be fixed in a manner that it cannot accidentally touch the membrane, the membrane and the housing have to be so thick that they withstand the high pressure.

First of all, a housing made of stainless steel was chosen, to be weld-compatible with the 1/16" (1.6 mm) outer diameter tubes used in gas chromatography. As basic shape, a cylinder was chosen, to just fit the dimension of a commercial snap-disc that is 12.7 mm. From the beginning, a configuration was found,

where the snap-disc does not block the flow of gas: the inlet tube and the outlet tubes will be placed at the same side of the housing, the inlet (high pressures) at the side and the outlet with the membrane at the center (See Figure 3). This has also the advantage to let one side free for the placement of the heater. A heater with a diameter 12.7 mm from the manufacturer Minco could be found. It is an ohmic heater that is very thin and lightweight that can heat up to a temperature of 200°C. The cover material of the heater is made of Kapton .Because of its low out-gassing rate and because it remains stable in the temperature range of -273°C to +400 °C, Kapton is a material that is often used in the space industry. The heater has a hole in the middle so that it can be reliably fixed via a screw and a custom-made washer. As shown in Figure 3, the pin is also attached via a hole in the middle of the snap-disc and a washer. The parts are soldered together with a 300°C melting temperature solder. The pin is gold plated and the washer is made of brass, so it can be soldered without any problem.

The snap-disc itself is held in place by the two main parts of the housing that form the volume for the snap-disc where it cannot touch the membrane when it is not actuating. It was also verified by CAD that the pin enters in the membrane with a reasonable margin. The snap-disc is not fully fixed to the body of the valve, but has a little play to let it bend correctly, this also providing thermal expansion. The snap-disc does not separate the inside of the valve into two chambers; a little drilling is in the housing equalizes the pressures. Hence it is ensured that gas pressure cannot activate the snap-disc.

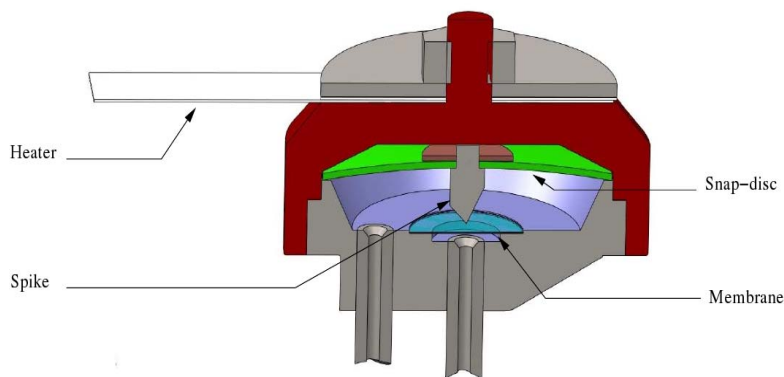


Figure 3. 3D view of the inside of the valve.

The thickness of the housing was determined with a finite element analysis program. The behavior of the housing under a pressure of 50 bars was simulated. Resulting from the analysis, the housing was reinforced at the fixing points of the tubes. This resulted in a mechanical factor of safety using the von Mises yield criterion of 3.34.

All welds were carried out using Nd:YAG Laser technique. The process for welding the membrane to the housing needed some iteration to come to a gas-tight result, but now the process is well determined. Once the valve had been manufactured, the overall gas tightness could be verified, and also that the valve opens when electrically powered.

Design Verification

Testing a single-shot device is a critical issue, because repeatability has to be tested over many valves, and therefore has to be carried out carefully.

A helium leak detector was used to test separately the gas-tightness of the welds for mounting the membrane within the housing. No leak could be detected after one hour at 30 bar inner pressure. The valves were tested in an oven at 130°C and it was observed that the valves were afterwards still gas-tight. The opening test was also successful: in average after 90 s of powering the valve at 9 W, the valve at 30

bar on the inlet opens and bubbles become visible if the outlet is put in water. A test with an open valve was also carried out, in order to observe the hole created by the pin after actuation.

Nevertheless, the valve is still not formally space qualified; this would imply a program with testing of a large amount of valves, including thermal cycling and vibration test.

Conclusion

Bimetallic thermal actuation is a very simple, rugged and widely used principle. However, its use is mainly confined in thermal switches where the force needed is not large. In some application where a small, simple actuator, preferably without harness, is required, a standard snap-disc can be a good choice.

Even though single-shot devices have drawbacks concerning their testing, they provide a considerable advantage concerning their reliability. In the specific case of MOMA where a perfectly hermetical device is required, it is safer to choose a sealing element based on single-shot operation.

The valve built (see Figure 4) has the advantage over the previously foreseen solenoid valve to be lighter by a factor of ten. Space qualification was taken into account from the beginning of the design task, and testing showed high reliability of the device.

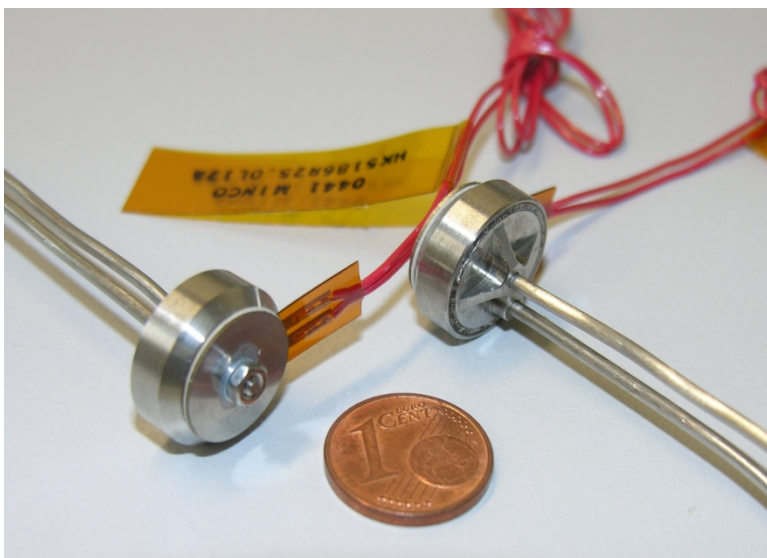


Figure 4. Photo of the manufactured valves.

References

1. http://planetary.chem.tufts.edu/Phoenix/thermal_evolved_gas_analyzer.htm
2. <http://www.conaxfl.com/Aerospace/1832205.htm>
3. Edeson, Ruben, Martin Whalley, Barry Kent, Simon Canfer and Eric Sawyer. "SMA gas release mechanism for the Rosetta Lander's Ptolemy instrument", *Acta Astronautica*, Volume 58, Issue 11, June 2006, pages 576-582.
4. http://www.techbriefs.com/index.php?option=com_staticxt&staticfile=/Briefs/Mar00/MS22726.html
5. Bejhed, Johan, Pelle Rangsten and Johan Kaohler. "Demonstration of a single use microsystem valve for high gas pressure applications", *Journal of Micromechanics and Microengineering*, February 2007

MoS₂-Filled PEEK Composite as a Self-Lubricating Material for Aerospace Applications

Géraldine Theiler* and Thomas Gradt*

Abstract

At BAM, several projects were conducted in the past years dealing with the tribological properties of friction couples at cryogenic temperature and in vacuum environment. Promising candidates for vacuum application are MoS₂-filled PEEK/PTFE composites, which showed a friction coefficient as low as 0.03 in high vacuum. To complete the tribological profile of these composites, further tests were performed in ultra-high vacuum (UHV) at room temperature. In this paper, friction and stick slip behavior, as well as outgassing characteristics during the test are presented.

Introduction

Ultra-high vacuum, a wide temperature range, presence of atomic oxygen, and limited applicability of liquid lubricants, make open space an extremely hostile environment for tribologically stressed components in satellites. In most of these systems, self-lubricating materials must be employed. These include lamellar solids, soft metals, and polymers. Solid lubricants usually are applied as thin film (sputtering), bonded film (with organic binder), or mixed in a polymer matrix (Polyimide and PTFE) [1]. MoS₂ is the most widely used solid lubricant in vacuum environment and has been successfully used in space applications for many years. In vacuum, MoS₂ films exhibit extremely low friction, but in the presence of humid air, friction and wear rate increase significantly.

Since many space mechanisms must be ground tested before launch, sometimes in atmospheric air, there has been much research performed to improve the performance of MoS₂ under atmospheric conditions [2]. One method is the co-deposition of MoS₂ with metal [2] or DLC [3]. Good performance was obtained with WC/DLC/WS₂ coatings in vacuum and air [4]. Another approach is to optimize MoS₂-filled polymer composites.

At BAM, the tribological behavior of MoS₂-filled PEEK composites was investigated in the temperature range between -80°C and +160°C in high vacuum [5, 6]. Particularly in the lower temperature range and at higher loads, the composites showed high wear resistance and friction coefficients as low as PVD coatings. To complete the tribological profile of these composites, further tests were performed in ultra-high vacuum at lower sliding speed. In this paper, friction and stick slip behavior, as well as outgassing characteristics during tests are presented.

Experimental

Tests were performed with a pin-on-flat configuration in oscillating sliding at room temperature in a UHV tribometer [Fig. 1]. The spherical polymer pins used in these experiments were made of PEEK composite filled with 10% by volume carbon fibers, 10% by volume PTFE and 10% by volume MoS₂. The counterface material was X5CrNi1810 steel (similar to AISI 304), with a roughness $R_a \cong 0.2 \mu\text{m}$. Test parameters are summarized in Table 1.

* Federal Institute for Materials Research and Testing (BAM), Berlin, Germany

During the friction experiment, a mass spectrometer was used to measure the outgassing of the materials. After the experiments, SEM and EDX were performed at the surface of the samples as well as XPS analyses.

Technical data - UHV Tribometer:

Sliding mode: reciprocating
 Load: 5 mN to 5 N
 Stroke: 3 mm
 Frequency: ca. 0.5 – 1.5 Hz
 Temperature: Room temperature
 Residual pressure: 10^{-10} - 10^{-4} hPa

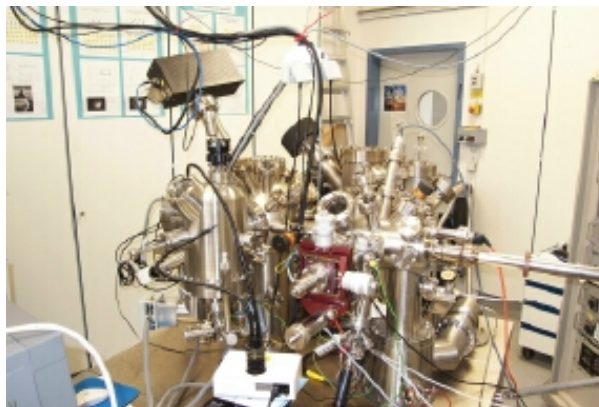


Figure 1. Ultra high vacuum tribometer (UHVT)

Table 1. Test parameters in UHV

residual pressure (hPa)	stroke (mm)	velocity (m/s)	Load (N)	cycles
10^{-9}	3	0.01	5; 10	500

Results

Figure 2 indicates an average friction coefficient of 0.12 – 0.15 with a maximum at 0.25 and accompanied by stick-slip behavior under these conditions. The influence of load on the friction coefficient is not as significant in UHV as in high vacuum (Fig. 3), but the values are somewhat smaller at 10 N than at 5 N. The relatively higher friction coefficient in UHV at $v = 0.01$ m/s compared to the one obtained in high vacuum at $v = 0.1$ m/s could be due to the lower sliding velocity or to the fact that the end of the running-in phase in UHV was not yet achieved.

SEM images of the friction surface of the pin and flat after the experiment in UHV at 5 N are presented in Figure 4. EDX analyses of the steel flat indicate that polymer was transferred to it, especially in the grooves present on the surface (Fig. 5). Since the F-map could not be distinguished from the Fe one (of the flat), it is not shown here. MoS_2 is homogeneously transferred, but does not form a closed transfer film on the steel flat. In this case, the very low friction coefficient obtained by MoS_2 film at higher sliding speed in high vacuum cannot be reached.

Furthermore, EDX analyses of the polymer pin indicate a MoS_2 rich surface, intermittent due to carbon fibres (Fig. 6). The analyses revealed also that some Fe has been transferred from the steel to the polymer pin. In addition, XPS analyses were performed after the experiment in UHV. Figure 7 shows the measured binding energy with the corresponding components. Beside MoS_2 , the formation of molybdenum oxides was observed, which could be formed with the oxide layer of the steel disc. The presence of molybdenum oxides could also explain the higher coefficient of friction, as reported in [7].

A preliminary measurement was performed to characterize the outgassing during the friction experiment. Figure 8 indicates that the outgassing increases during sliding, especially for hydrogen and nitrogen compounds. Indeed, due to frictional heat, desorbed hydrogen and trapped gas are released during the test.

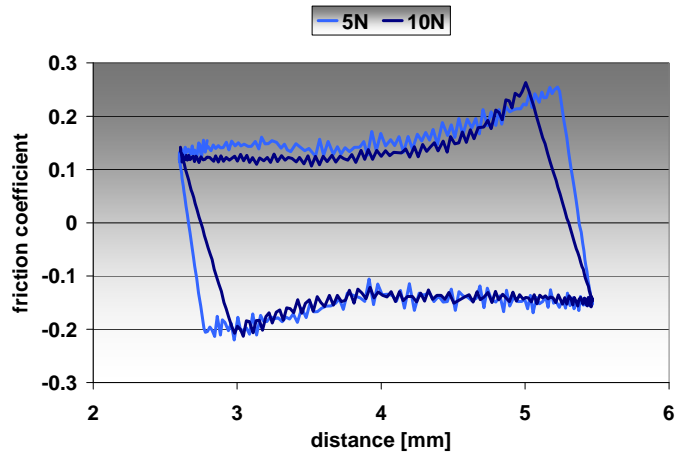


Figure 2. Friction behavior in oscillating motion in ultra-high vacuum

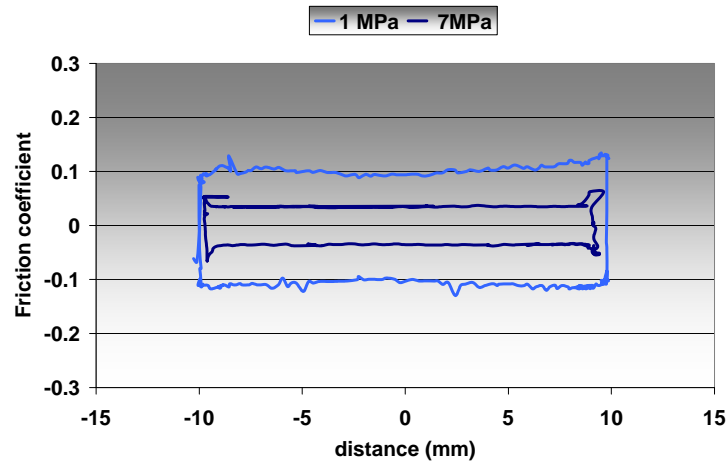


Figure 3. Friction behavior in oscillating motion in high vacuum

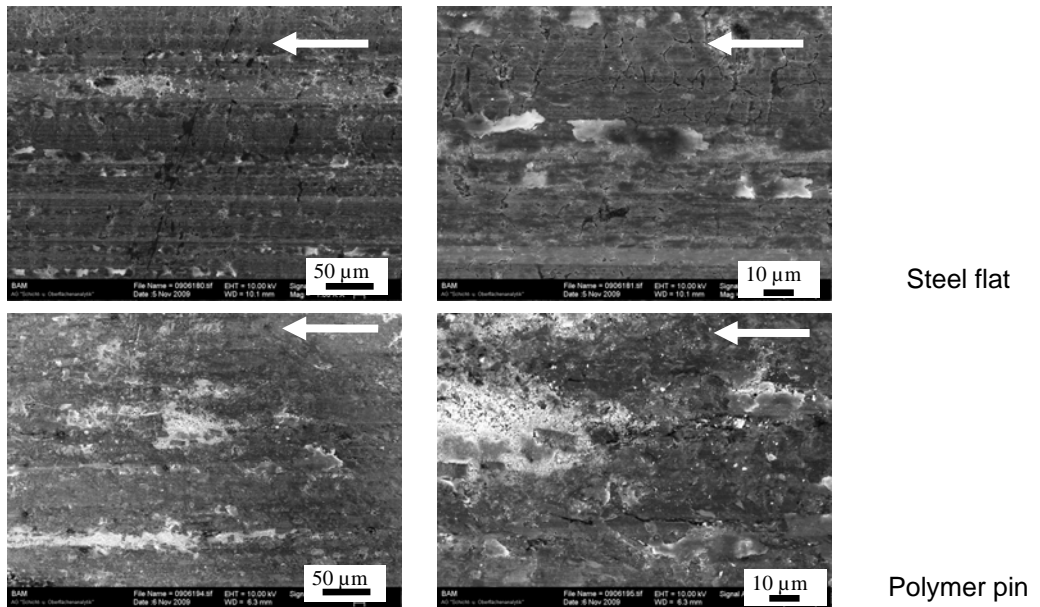


Figure 4. SEM Analyses after the test in UHV at

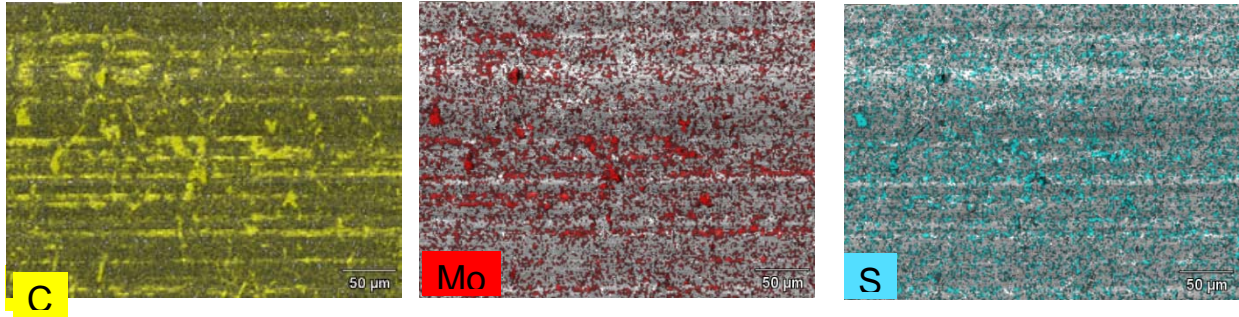


Figure 5. EDX Analyses of the polymer transfer on the steel counterface after the test in UHV at room temperature, 5 N

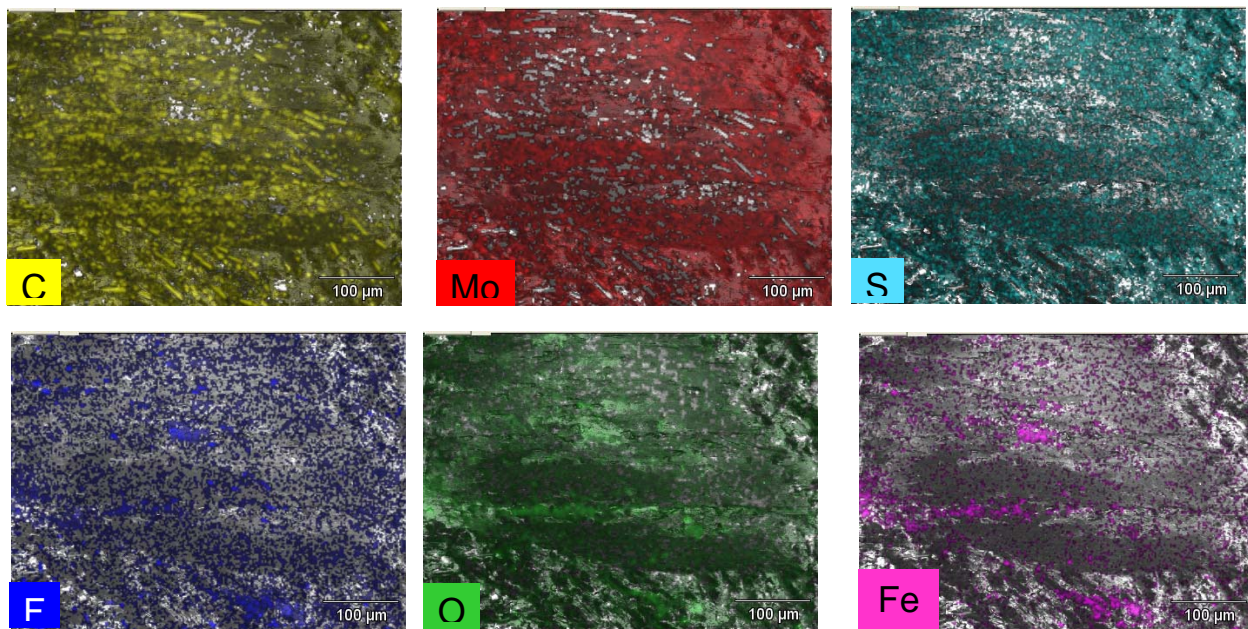


Figure 6. EDX Analyses of the polymer pin after the test in UHV at room temperature, 5 N

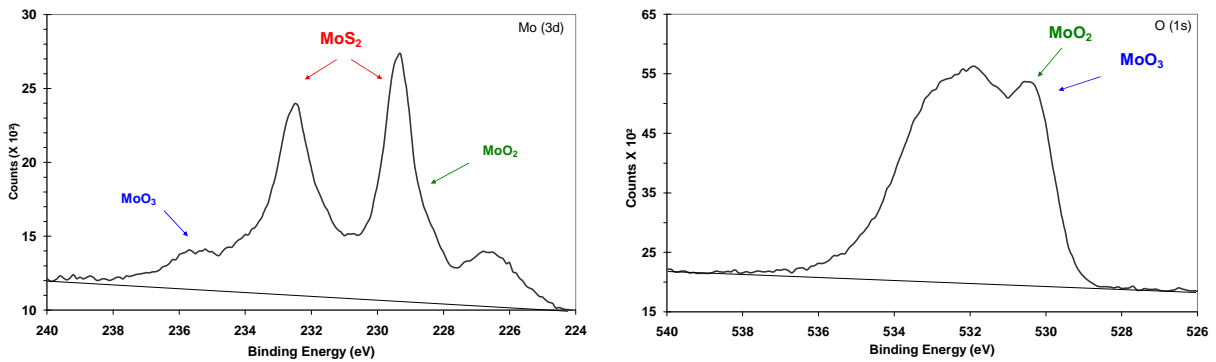


Figure 7. Mo(3d) and O(1s) spectra after the test in UHV at room temperature, 5 N

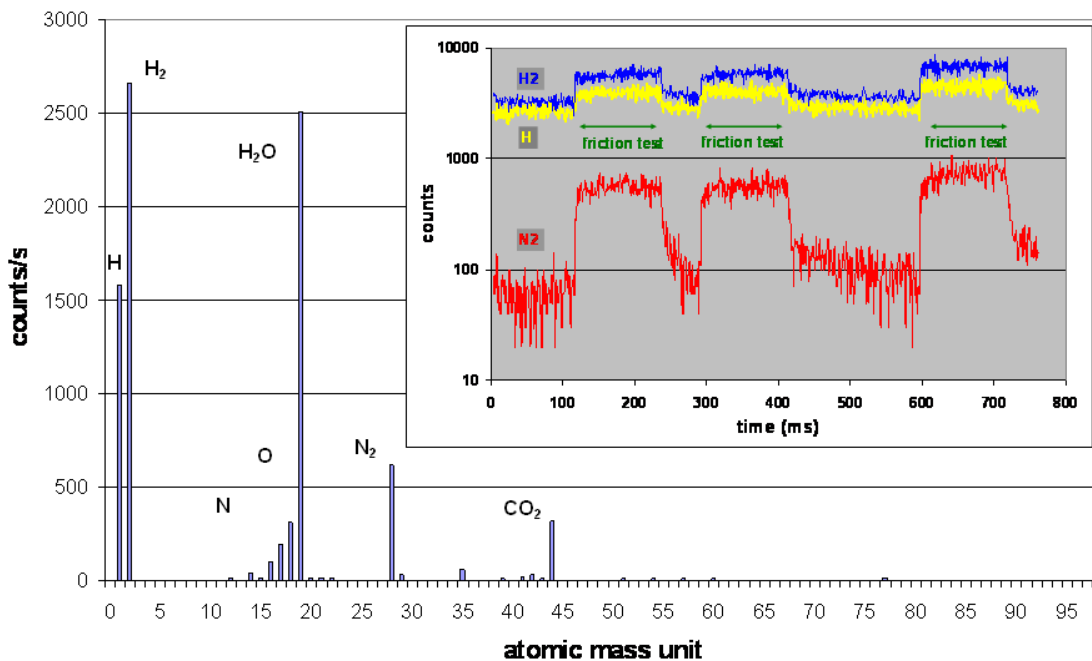


Figure 8. Mass spectroscopy during friction test in UHV

Conclusion

This subsidiary study gives additional information concerning the tribological behavior of MoS₂-filled PEEK in vacuum environment. The outstanding performance of this composite found in high vacuum at $v = 0.1$ m/s [5, 6] is limited in UHV at low sliding speed ($v = 0.01$ m/s), where some static friction as well as increased outgassing are observed. However, since the sliding velocity is an influencing factor on the tribological behavior of polymer composite, further tests in UHV should be performed at higher speed and during a longer period of time to verify the potential of these PEEK composites.

References

- [1] Jones, Jr., W. R., and M. Jansen. "Space Tribology." NASA report TM-2000-209924
- [2] Jones, Jr., W. R., and M. Jansen. "Tribology for Space Application." *Proc. IMechE Vol. 222 Part J. Journal of Engineering Tribology* (2008)
- [3] Noshito, J., S. Watanabe, T. Sakurai, and S. Miyake. "Friction properties of co-sputtered sulphide/DLC solid lubricating films." *Surface Coating Technol.* 200 (2006) 5849-5854.
- [4] Voievodin, A., J.P. Oneill and J.S. Zabinski. "Nanocomposite tribological coatings for aerospace applications." *Surf. Coat. Technol.* 116-119 (1999), p. 36.
- [5] Theiler, G., and T. Gradt. "Influence of the Temperature on the Tribological Behaviour of PEEK Composites in Vacuum Environment." *Artikel: Journal of physics/ Conference series* 100(2008) 072040, 1-4; IOP Publ.ISSN 1742-6588, 1742-6596
- [6] Theiler, G., and T. Gradt T. "Tribological Behaviour of PEEK Composites in Vacuum Environment." *12th European Space Mechanisms and Tribology Symposium (ESMAT 2007)*, September 19-21 2007, Liverpool, UK (Proceedings) 2007, 1-5; Hrsg.: European Space Agency (ESA)
- [7] Martin, J.M., Th. Le Mogne, C. Grossiord, and Th. Palermo. "Adsorption and friction in the UHV tribometer." *Tribology Letters* 3 (1997) 87-94

Evolution of the IBDM Structural Latch Development into a Generic Simplified Design

K. De Vriendt*, H. Dittmer*, D. Vrancken*, P. Urmston** and O. Gracia**

Abstract

This paper presents the evolution in the development of the structural latch for the International Berthing Docking Mechanism (IBDM, see Figure 1). It reports on the lessons learned since completion of the test program on the engineering development unit of the first generation latching system in 2007. The initial latch design has been through a second generation concept in 2008, and now evolved into a third generation of this mechanism. Functional and structural testing on the latest latch hardware has recently been completed with good results.

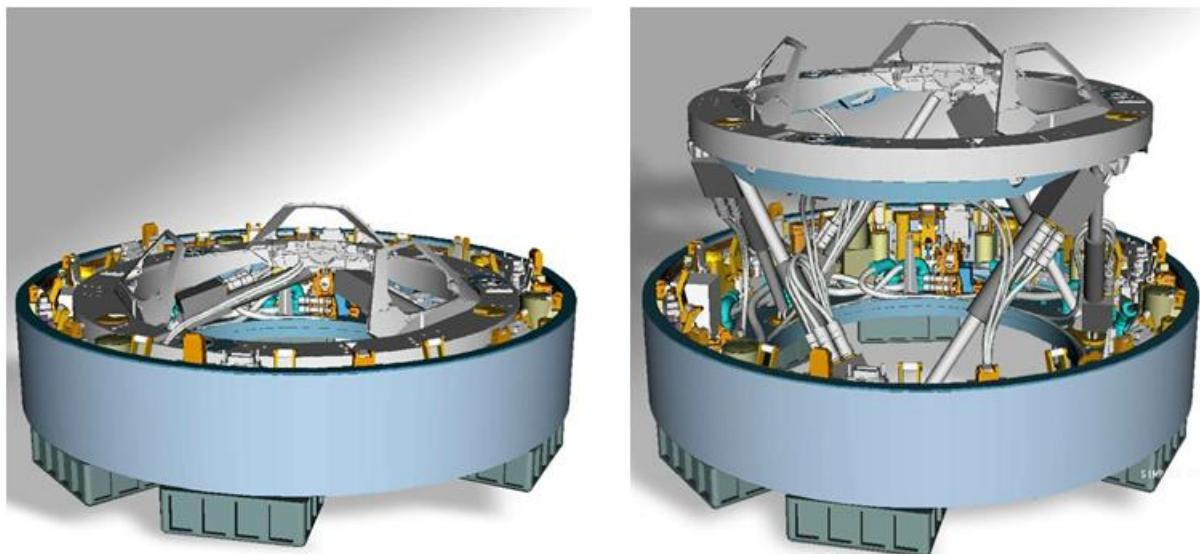


Figure 1 The IBDM equipped with the first generation latching system

General Objective

The IBDM latching system will provide the structural connection between two mated space vehicles after berthing or docking. The mechanism guarantees that the interface seals become compressed to form a leak-tight pressure system that creates a passageway for the astronauts.

The First Generation Latching System

Introduction

The initial latch design was driven by the requirements of the NASA X-38/CRV spacecraft, being the envisaged 7-crew astronaut rescue vehicle for the ISS. This implied that the mechanism had to be single fault tolerant for docking (no catastrophic hazard when in LEO) and dual fault tolerant for undocking (i.e., release).

* Verhaert Space, Kruikebe, Belgium

** ESA/ESTeC, Noordwijk, The Netherlands

Description of the first generation latching system

The general architecture of the latching system (Figure 2) consists of twelve latches and an equal number of latch tabs per IBDM. All are mounted on the inside of the IBDM tunnel wall and are oriented in a radial direction. The androgynous concept of the IBDM enables each latch to mate with a corresponding latch tab on the side of a mating vehicle. The latches can be driven via two independent ring gears that take care of the synchronization between all latches. Each ring gear is individually actuated by a redundant electro-motor.



Figure 2 The Latch (left) and Latch Tab (right) of the first generation latching system

The latch mechanism kinematics are a combination of two 4-bar linkages. The latch has a roller interface for landing onto the hook of a latch tab. The redundancy in the latch release is accomplished by a primary and a secondary drive, plus a pyrotechnic solution. Additionally, a pyro-release capability can also be implemented into the latch tab. The latch tabs each hold a load-limiting device that becomes geometrically positioned in line with the load path of the latch in order to have a minimal hysteresis in the load-limiter operation.

High design loads, the complexity of the design, and the small available volume within the IBDM tunnel have pushed the design of the latch mechanism to the limits. Even with the use of super alloys (MP35N, Custom-455) and the selection of a customized bushing, only minimal positive structural margins of safety could be accomplished.

Shortcomings of the first generation latching system

During the functional testing of the mechanism several anomalies were observed. These are the major findings:

- In the nominal situation (i.e., as required), the kinematics of the latch are designed to follow a vertical trajectory in the final phase of latching (i.e., the roller of the latch approaching the hook of the latch tab, see Figure 3), limiting any transverse loads on the latch mechanism. However, during functional testing, the trajectory showed a motion of the roller towards the edge of the latch tab hook. This happened due to flexibility of the secondary drive elements of the latch that created a bigger than expected deflection of the latch linkages involved.
Test conclusion: the design concept of the latching system appeared not to be safe against inadvertent release of the mechanism (i.e., the latch roller snapping of the latch tab). Therefore, this latching system is no reliable device for a structural connection.
- In order to minimize the primary drive torque to close the latch, the diameter of the free rotating pins had to be reduced. Therefore, custom-sized commercial parts were needed. These were dry-lubricated bushings with a larger L/D ratio than nominal (off-the-shelf) units. It was discovered that the assumptions made for the strength verification of standard parts are not valid for the dimensions of the customized bushings. This was not anticipated by the parts supplier. The load bearing capability of the custom-sized bushings appeared to be lower than the load capability of

standard bushings with the net result that the load capability of the latch/latch tab combination was lower than anticipated.

Test conclusion: Pin and bushing failures have been observed at a significantly lower load level compared to the values predicted by analysis.

- From a very early stage of the development, factors of safety were introduced on the applied loads. Due to the non-linear behavior of the latching system due to the presence of a load-limiter in the latch tab, the structural margin of safety on the resulting stresses are low.

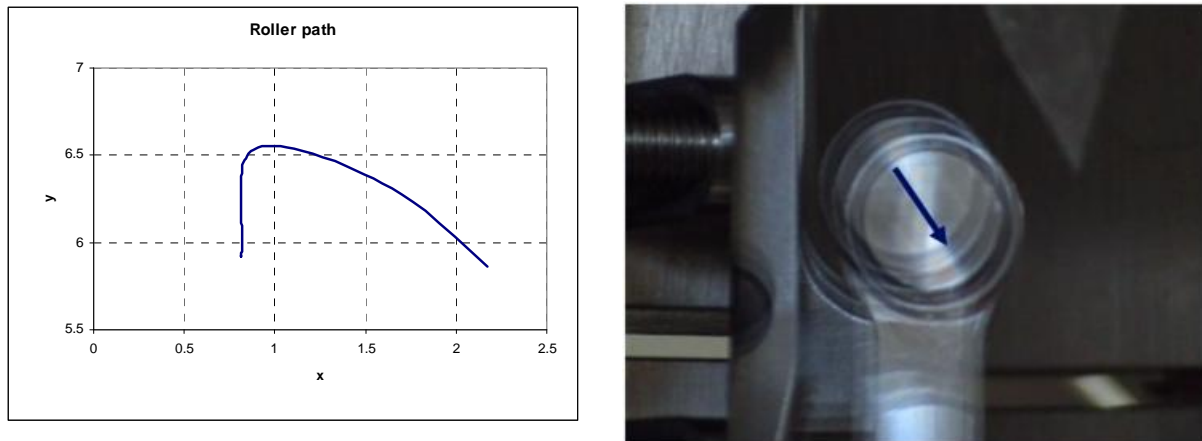


Figure 3 Theoretical (left) versus measured (right) trajectory of the Latch onto the Latch Tab

Lessons learned from the first generation latching system

A thorough investigation of the observed anomalies resulted in a number of valuable lessons learned:

- The shape of the latch tab hook has to be properly controlled by careful factoring of the relative stiffness of the latch and the tunnel, the mounting tolerances and differential thermal expansion. Additionally, positive locking of the latch must be incorporated to prevent the roller interface at all times to snap off the latch tab at (excessive) load increase.
- Avoid as much as possible dual use for both the primary and the secondary drive of single linkage joints.
- Due to the exceptional characteristics of the space environment and the limitations in mass and envelope imposed to any space equipment, the design of structural elements, in particular pins and bushings, cannot be done based on suppliers or textbook generic formulas. Careful estimations of stresses and deformations have to be carried out by FEM, even for simple geometries. Material allowables must be determined by test. Breadboarding and testing of function critical or highly stress elements must be always carried out and results correlated with the FEM models.
- The optimal dimensional relations (i.e., small L/D ratio) for the structural strength of the bushing should be maintained as much as possible. Non-linear contact analysis showed that bushings with a large L/D ratio show a big variation in the stresses in the bushing liner, while this is much less for bushings with a small L/D.
- Suppliers of COTS equipment may only have limited knowledge of their products, usually only around the qualification range of the first product that used the element. It is not always an option to design space mechanisms so they comply with the known environment of these COTS parts, therefore, supplier's calculations and analysis methods have to be carefully assessed and verified by test under the foreseen environment and conditions early in the project when corrective actions or alternative designs can be considered.
- Apply the structural factor of safety on the resulting stresses instead of on the applied loads.

The Second Generation Latching System

Introduction

After cancellation of the X-38 program by NASA, ESA decided to independently pursue the IBDM development – comprising the further optimization of the latching system – for implementation of this docking mechanism into their Space Exploration plans. The second generation latch did therefore take into account the above-mentioned lessons learned, while establishing even more severe requirements for the Exploration purposes. For example, the latching system not only had to be dual fault tolerant for undocking, but also had to become dual fault tolerant for docking.

The size of the second generation latch was enlarged with respect to the first generation latch to assess the feasibility of an increased IBDM tunnel diameter (to also allow for ISPR-racks to pass through the tunnel instead of astronauts only). The second generation latch did focus on the optimization of the primary drive and did therefore not consider the design of a secondary release mechanism in order to fulfil the dual fault tolerance requirement. However, the new overall design concept introduces a redundant release function by the possibility to operate the latching system on the other vehicle side.

Design improvements for the second generation latching system

In order to comply with the more stringent requirements, the following design modifications with respect to the first generation latching system have been incorporated:

- Modification of the overall design concept, in which:
 - the combination of latch and latch tab became replaced by the generic hook-on-hook principle. Therefore each latch will mate with an identical counterpart on the other vehicle side, resolving the necessity for the IBDM to carry the mass of unutilized elements that are imposed for androgyny (i.e., the latch tabs on a passive IBDM).
 - the common drive train has been replaced by an independent motor plus gearbox for each latch.
- Latches have moved from the inside of the tunnel wall to the outside and are oriented in a tangential direction.
- A compliance element has been integrated into the design of the latch itself. Therefore, two mated IBDMs feature double of the latch compliance.
- Inherent positive locking of the latch is incorporated.
- A (primary) drive kinematics has been accomplished that is no longer dominated by the diameter of the pins in the joints. Therefore, the bushings can now be correctly sized (i.e., increased) to the latch load. For reasons of completeness, it has to be mentioned that as a negative consequence, friction losses due to a bigger pin diameter are now a little higher compared to the first generation latch design, resulting in a lower overall mechanical efficiency.
- Conservative factors of safety (1.25 for yield and 1.5 for ultimate) have been taken on the design load stress.

The second generation latch contains a primary drive with linkage kinematics similar to the previous latch design (i.e., a combination of two 4-bar linkages). In analogy to the first generation latch, this results in a vertical trajectory for the operated hook when it approaches its mating counterpart at the final phase of latching.

Lessons learned from the second generation latching system

Hardware has been built and has been subjected to stringent functional and structural tests (Figure 4). The following lessons learned are recorded:

- The hook-on-hook concept does guarantee a stable structural connection.
- The number of moving parts in the latch drive chain has to be (further) reduced as much as possible. Any moving part increases the risk of jamming the mechanism and more joints in the latch leads to lower transmission efficiency. A longer drive train through many linkages results in more difficult control in the synchronization of the release of all latches.

- The load path from the interface load to the load-limiter has to be decreased as much as possible, in order to avoid hysteresis in the load-limiter operation.



Figure 4 Functional and structural testing of the second generation latching system

The (Present) Third Generation Latching System

Introduction

The latest latch design is derived from the second generation latch. It maintains the hook-on-hook concept, but the kinematics are restricted to a single 4-bar linkage. The size of the latch is reduced back to that of the first generation latch (i.e., the size of the latch/latch tab, intended for an IBDM tunnel diameter that allows astronaut passage only).

Per IBDM, 12 latches are attached in a tangential direction to the outside of the tunnel wall (Figure 5). Each latch has its proper motor, gearbox and adjustable compliance element. The motor and the gearbox are developed as an integrated actuator unit. Dual failure tolerance has been established for both docking and undocking, and inherent positive locking of the mechanism provides the guarantee against inadvertent release.

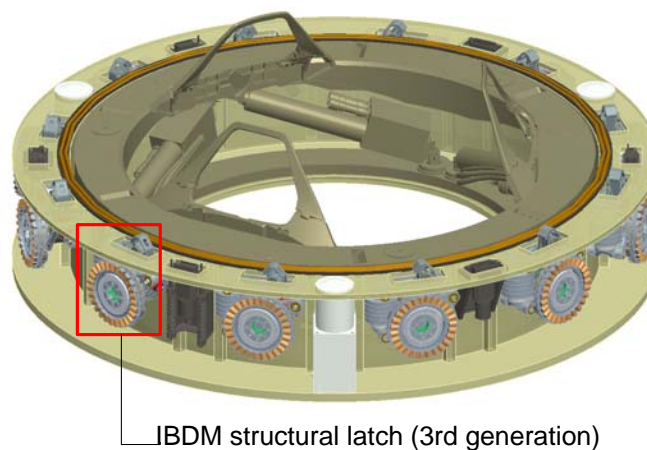


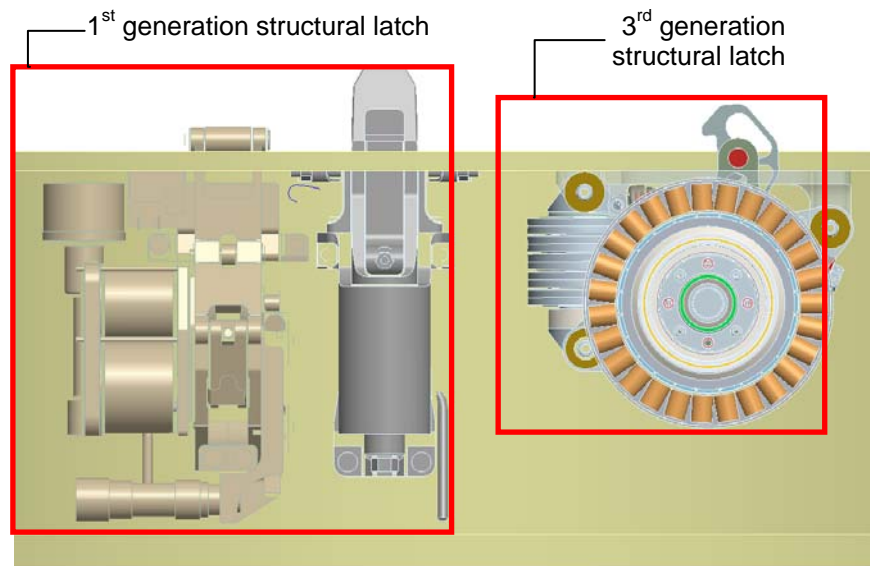
Figure 5 The IBDM with the third generation latching system

Design improvements for the third generation latching system

- The load capability has been significantly increased while the overall mass of the latching system could be slightly reduced (with respect to the latch/latch tab concept, see Figure 6). At the same time, even more standard materials have been applied, like Al 7075 for the latch housing.
- A substantial improvement in mechanical efficiency and reliability could be realized through a simplified design that reduced the number of linkages in the load path of the latch primary drive to a minimum. The short drive train to the latch hook also leads to accurate control in the synchronization of the release of all latches.
- The latch design includes a secondary release mechanism, which:
 - accomplishes the dual fault tolerance requirement.
 - takes into account the Limited Life Item policy for pyrotechnics (i.e., the pyrotechnic release capability being provided on the visiting vehicle only).

The latch secondary drive consists out of tilting the latch hook by rupturing the hold-down bolt. Rupturing the bolt can be done with a Frangibolt actuator or with a rich cut bolt (pyrotechnic).

- The joints in the direct load path of the latch are now equipped with roller bearings instead of bushings, resulting in an increased drive efficiency.
- The load path from the interface load to the load limiter has been shortened, resulting in minimal hysteresis in the load limiter operation.



- | | |
|------------------------------------|------------------------------------|
| ▪ Design load: 34 kN (7640 lbf) | ▪ Design load: 57 kN (12800 lbf) |
| ▪ Single fault tolerant | ▪ Dual fault tolerant |
| ▪ Mechanical drive efficiency: 66% | ▪ Mechanical drive efficiency: 80% |
| | ▪ Reduced mounting envelope |

Figure 6 Comparison of 1st generation structural latch vs. 3rd generation structural latch

Design verification tests on the third generation latching system

Two prototype hardware models are built and they have recently been functionally and structurally tested. By test, a few less-favorable consequences of this generic simplified latch design have been verified for their potential impact on the functionality of the latch.

The investigated points of concern of the present latch design were the following:

- Due to the latch primary drive kinematics consisting out of a single 4-bar linkage, the latch hook will no longer land on its mating counterpart in a straight vertical trajectory. Instead, the hook now has to slide off the mated hook for release. Despite the fact that the latch hooks have been Niflor-coated, friction between the contact surfaces has been increased compared to the separation scenario with a roller interface (being used in the first generation latching system).
- Release capability tests with the push-off force¹ have been executed. The push-off force being applied to the latch is the worst-case condition of two side-by-side latch failures out of all 12 latches.
Test conclusion: all tests did demonstrate the capability of the hooks to release without a problem.
- A preloaded compression spring to the side of the latch hook has to force the hook to close when rotating the latch crank to the closed position.
Test conclusion: test did show that this functionality was also working fine while an LVDT attached to the other side of the latch hook monitors the movement of the hook.

Conclusion

Testing of the latest latch system has demonstrated the capability to design a stable structural connection device that is made dual fault tolerant for both docking and undocking of the IBDM. Design optimization of the mechanism has been realized through analysis and validation of three concept generations. This was accomplished by consistently taken into account the numerous lessons learned that have been gathered along the way. It resulted in a generic simplified design of the IBDM latching system that features an optimized mechanical drive efficiency², mass efficiency³ and reliability⁴.

¹ A push-off force is being exerted on the latch by an energized separation system that must provide the IBDM with a prescribed delta-velocity in case of an expedited departure.

² Mechanical drive efficiency being expressed as the ratio between the required drive torque without and with friction losses in the linkages.

³ Mass efficiency being expressed as the ratio for the load capability versus the mass of the latching system.

⁴ Reliability being expressed as the inverse of the amount of moving parts per drive (considering each moving part as a potential single point of failure).

Development of the Upgraded DC Brush Gear Motor for Spacebus Platforms

Robert H. Berning III* and Olivier Viout**

Abstract

The obsolescence of materials and processes used in the manufacture of traditional DC brush gear motors has necessitated the development of an upgraded DC brush gear motor (UBGM). The current traditional DC brush gear motor (BGM) design was evaluated using Six-Sigma process to identify potential design and production process improvements. The development effort resulted in a qualified UBGM design which improved manufacturability and reduced production costs. Using Six-Sigma processes and incorporating lessons learned during the development process also improved motor performance for UBGM making it a more viable option for future use as a deployment mechanism in space flight applications.

Introduction

DC brush gear motors have been used for several years in various spaceflight applications because of their many favorable design features. They are extremely efficient at converting electrical energy into mechanical energy using only simple control electronics. Existing qualified DC brush gear motors for space flight applications however, use some obsolete materials and processes in their design and construction. The intent of this development was to review the existing BGM design using the Six-Sigma process to identify potential design improvements and to select replacements for the obsolete materials and processes. This paper documents the development and qualification of a UBGM for use as a solar array deployment mechanism on the Spacebus satellite platform that maximizes motor performance, lowers overall drag, and optimizes manufacturability.

The BGM has to operate in hostile environmental conditions during test and flight. The proper selection of materials is critical. Factors that must be considered include:

1. Operate in ambient air, up to 55% relative humidity.
2. Survive random vibration (32.3 G rms)
3. Survive in vacuum (1.0×10^{-5} torr)
4. Operate in vacuum (1.0×10^{-5} torr) from -50°C to $+80^{\circ}\text{C}$.
5. Survive in vacuum (1.0×10^{-5} torr) from -50°C to $+125^{\circ}\text{C}$.

Background

The qualified BGM shown in Figure 1 consisted of a DC brush motor and a multi-stage planetary gear train. The design used brush material that was since discontinued, some obsolete materials, and employed non-forgiving process-driven steps that resulted in high manufacturing costs. The redesign addresses materials and processes, manufacturing changes, and test tooling improvements that are necessary for future successful production of the new upgraded DC brush gear motors.

* Moog Chatsworth Operations, Chatsworth, CA USA

** Thales Alenia Space, Cannes la Bocca Cedex, France

Purpose of Redesign:

1. Enhanced producibility
2. Improved functional performance characteristics
3. Reduced delivery schedules
4. Increased robustness



Figure 1. Existing BGM

Development

The existing BGM design was analyzed and a 3D CAD model was created in Unigraphics. Prior failures and manufacturing problems were reviewed for areas of improvement. A Six-Sigma product assurance process was conducted. Trade studies were performed on major assemblies and a detailed tolerance analysis was completed to identify potential interferences.

A Six-Sigma process improvement team was established. Process walk-throughs were completed on six assemblies and three piece parts from the existing manufacturing and build cycles. Personnel were interviewed and fabrication, assembly and test processes of the existing BGM units were observed. Forty eight items for improvement were identified. Trade studies were initiated on all subassemblies and major components. Design and manufacturing process changes were completed to address all identified issues. The following major areas of potential improvement were identified:

Process Improvements

- Commutator soldering and inspection
- Armature paint integrity
- Armature insulation

Performance Improvements

- Optimized motor speed and motor torque
- Predictable gear head drag

A gear head trade study was completed to develop a consistently producible design with predictable gear drag over the required temperature range. Review of the existing gear head design and a detailed tolerance analysis showed a potential interference at cold temperatures, high drag in the first & second stage bushings, a material combination prone to galling (same gear material used on mating gear teeth) and a high sensitivity to gear center distance shift. The following trade study criteria were selected for gear head design improvement:

- Provide similar gear ratio
- Non-binding operation at extreme temperatures
- Manageable internal loss
- Robust design
- Non-galling material combinations

Three different gear head concepts were selected for design and testing: a completely redesigned gear head (option #1), a harmonic drive gear head (option #2), and a modified existing gear head using radial ball bearings (option #3). Engineering models of all options were fabricated and tested. The redesigned gear head had higher and inconsistent drag over the required temperature range. The harmonic drive gear head exhibited significantly higher drag at ambient temperatures, so no further testing was required. The modified gear head using radial ball bearings (option #3) was ultimately selected based on its low and consistent drag over the required temperature range. Table 1 lists gear head drag of engineering models over the required temperature range. The modified gear head does not exhibit interference over the required temperature range, has reduced drag in the first and second stages, has no galling material combinations and uses a one piece ring gear to minimize sensitivity to gear center distance shift.

Table 1. Gear Head Drag

	Description	Gear Drag @ 450 RPM (N-cm)			Gear Drag @ 450 RPM (in-oz)		
		-50°C	+23°C	+80°C	-50°C	+23°C	+80°C
SN042	Existing Design	0.22	0.06	0.07	0.31	0.09	0.10
Option #1	Redesign	1.78	0.60	0.44	2.52	0.85	0.63
Option #2	Harmonic drive		3.53			5.00	
Option #3	Radial Bearing	0.16	0.01	0.02	0.23	0.02	0.03

A new brush material was identified and selected at the conclusion of the motor trade study. Detailed review of the existing motor design revealed inefficient processes, high brush drag and use of discontinued brush material.

The brush assembly consists of a carbon composite brush, shunt wire, cap, and spring. Eight different brush materials were considered and four were selected for testing. All brushes were tested for motor performance, resistance, drag, spring force, brush wear, commutator wear, smearing, debris, and manufacturing yield. Brush material option #2 and #3 were eliminated due to low motor torque. Brush material option #1 was selected due to poor performance of option #4 in vacuum. Table 2 lists development brush performance. The selected brush material is softer than the existing brush material, resulting in higher motor torque, lower brush drag and less commutator wear.

Table 1. Brush Performance

Brush Material	Motor Torque N-cm (in-oz)	Brush							Commutator	
		Wear in Atmosphere	Wear in Vacuum	Drag N-cm (in-oz)	Debris	Smearing	Resistance (Ω)	Yield	Wear	
1	1.77 (2.50)	Good	Good	0.29 (0.41)	Moderate	None	0.13	Good	Excellent	
2	1.20 (1.70)	N/A	N/A	0.23 (0.33)	N/A	N/A	0.21	Good	N/A	
3	0.85 (1.20)	N/A	N/A	0.25 (0.35)	N/A	N/A	0.20	Good	N/A	
4	1.77 (2.50)	Good	Poor	0.41 (0.58)	Moderate	None	0.16	Excellent	Excellent	
Existing	1.77 (2.50)	Excellent	Excellent	0.46 (0.65)	Light	Light	0.56	Good	Good	

The motor trade study considered all assemblies and machined parts. The producibility of existing motor is poor due to the need for frequent rework resulting in high production costs. Stack fabrication, coating, and attachment methodology were upgraded to current Moog procedures. All uncontrollable and unnecessary processes were replaced or eliminated. For instance, existing BGM commutators are machined after final armature assembly putting the completed armature at risk. UBGM commutator processing was moved to the piece part level to lower the risk to hardware. The soldering process was updated to the current standard. Table 3 shows increased motor torque with new brush materials and design and manufacturing changes.

Table 2 Motor Performance

Motor Torque (N-cm/ in-oz)					
Unit	Brush Material #1	Brush Material #2	Brush Material #3	Brush Material #4	Existing
SN 0042	1.8 (2.5)	1.2 (1.7)	0.85 (1.2)	1.8 (2.5)	1.6 (2.2)
EM0001	2.4 (3.4)	N/A	N/A	2.3 (3.3)	1.9 (2.7)

The overall development of the upgraded brush gear motor was successful. All issues discovered during the Six-Sigma process were addressed. After development was completed a qualification unit shown in Figure 2 was fabricated to production paper work, using production processes and tooling. The unit was subjected to qualification testing which included vibration, thermal vacuum exposures and life tests. The qualification unit successfully passed all qualification and life tests with no findings.



Figure 2. UBGM

Lessons Learned

While the upgraded brush motor development and qualification was successful, but the methodology in some areas could have been improved. The following paragraphs document the major lessons learned during development and qualification.

Understand derived requirements

A firm understanding of the requirements (actual and derived) is needed prior to development. At the onset of the development process, the gear head bushings were identified as a cause of BGM performance problems. A total redesign of the gear head was started, with heritage design practices, processes, and software utilized in the new gear head. Gear design parameters were optimized to allow for greater allowable tolerances and used compatible material combinations to reduce galling and thermal expansion issues. Optimization of the gear head for producibility adversely affected performance, however.

Since the BGM motor torque output is relatively low, it is sensitive to drag torque. Valuable time was spent on developing a new gear head that had a gear drag greater than the motor could produce. If the BGM gear drag data had been available, it would have been realized that there was little chance to design a new gear head with significantly lower drag.

Understand test capabilities

At the start of development it was determined we would test all gear heads before they were integrated into the BGM. It was assumed we would use our standard test setup, tooling and test equipment. During initial gear drag testing it was discovered that minor misalignment caused major shifts in the drag torque measurement. Thermal expansion of the tooling was enough to double or triple drag torque measurements. A standardized process was developed to consistently adjust the alignment before each test.

Verify performance at every environment

During testing it was observed that brush drag and wear were different in vacuum than at ambient pressure. The leading brush material was eliminated after vacuum testing. Almost no wear was observed during ambient and initial vacuum testing, but during extended vacuum testing the brush was completely worn away.

Work with suppliers to understand procured part requirements

One brush manufacturer's brush shunt wire broke significantly more than the others. The brush shunt attachment had to be redesigned to address yield issues. The initial design used an eyelet to keep the solder from wicking down the shunt wire, their internal requirement. The eyelet damaged the wire strands causing them to fail. The eyelet was removed and a braided shunt wire was used. The redesigned brushes were installed into the engineering model for functional and vibration testing. The redesigned brushes successfully completed testing without any broken shunt wires.

The issues involved with the lessons learned were not catastrophic, but each one of them could have had serious consequences. The upgraded brush gear motor was successful because the issues were handled early enough to meet program schedule dates.

Summary and Discussion

After development was completed a qualification unit was fabricated to production paper work, using production processes and tooling. The unit was subjected to qualification testing which included vibration, thermal vacuum exposures and life tests. The qualification unit successfully passed all qualification and life tests with no findings. After qualification and life testing the unit was disassembled and cleaned. All parts were inspected and showed minimal wear and no signs of damage.

New brush material meets all design requirements and brush wear was consistent with wear observed during engineering testing. An estimated brush loss of 17% of brush usable material was observed.

Table 3. Brush Wear

				
New Brush	A1	A2	B1	B2
Percent Reduction	~14%	~14%	~14%	~17%

Table 4. UBGM vs BGM Performance Comparison

Test Description	Units	UBGM						BGM					
		-50°C		+23°C		+80°C		-50°C		+23°C		+80°C	
		Max	Min	Max	Min								
Drag torque Tooling Only (Dynamic torque @ 450 RPM)	N-cm (in-oz)	0.15 (0.21)		0.06 (0.09)		0.04 (0.05)		0.15 (0.21)		0.06 (0.09)		0.04 (0.05)	
Drag torque Tooling only (torque to start)	N-cm (in-oz)	0.18 (0.25)		0.06 (0.08)		0.05 (0.07)		0.18 (0.25)		0.06 (0.08)		0.05 (0.07)	
Drag torque GearBox (Dynamic torque @ 450 RPM)	N-cm (in-oz)	0.31 (0.44)		0.08 (0.11)		0.06 (0.08)		0.37 (0.52)		0.13 (0.18)		0.11 (0.15)	
Drag torque GearBox (Torque to start)	N-cm (in-oz)	0.18 (0.26)		0.06 (0.08)		0.04 (0.06)		0.18 (0.26)		0.07 (0.10)		0.06 (0.08)	
Tool Drag Removed													
Drag torque GearBox (Dynamic torque @ 450 RPM)	N-cm (in-oz)	0.16 (0.23)		0.01 (0.02)		0.02 (0.03)		0.22 (0.31)		0.06 (0.09)		0.07 (0.10)	
Drag torque GearBox (Torque to start)	N-cm (in-oz)	0.01 (0.02)		0.00 (0.00)		0.00 (0.00)		0.01 (0.02)		0.01 (0.02)		0.007 (0.01)	

Test Description	Units	UBGM						BGM					
		-50°C		+23°C		+80°C		-50°C		+23°C		+80°C	
		Max	Min	Max	Min								
Drag torque Motor (Dynamic torque @ 450 RPM)	N-cm (in-oz)	0.99 (1.40)		0.99 (1.40)		0.99 (1.40)		0.85 (1.20)		0.81 (1.15)		0.78 (1.10)	
Drag torque GearBox (Dynamic torque @ 450 RPM)	N-cm (in-oz)	0.16 (0.23)		0.01 (0.02)		0.02 (0.03)		0.22 (0.31)		0.06 (0.09)		0.07 (0.10)	
Drag torque Motor (Torque to start)	N-cm (in-oz)	1.31 (1.85)		1.31 (1.85)		1.31 (1.85)		2.8 (4.0)		2.8 (4.0)		2.8 (4.0)	
Drag torque GearBox (Torque to start)	N-cm (in-oz)	0.01 (0.02)		0.00 (0.00)		0.00 (0.00)		0.01 (0.02)		0.01 (0.02)		0.007 (0.01)	
No load speed (Motor with 6.0 V)	rpm	588	571	549	505	572	563	440	405	480	455	515	470
No load current (Motor with 6.0V)	amps	0.081	0.080	0.077	0.072	0.065	0.062	0.100	0.095	0.098	0.095	0.078	0.075
Time to rotate 90 degrees (Motor and GearBox with 6.6 V)	sec	78.5	75.5	82	76.75	78.75	74.25	68.00	65.00			74.00	72.00
No load speed (Motor and GearBox with 6.6 V)	rpm	0.19	0.20	0.18	0.20	0.19	0.20	0.221	0.231			0.203	0.208
No load current (Motor and GearBox with 6.6 V)	amps	0.101	0.099	0.093	0.084	0.084	0.078	0.080	0.070			0.086	0.083
Stall Torque (Motor with 6.0 V)	N-cm	3.2	3.2	2.4	2.3	2.0	1.9	2.1	1.6	1.2	0.78	1.1	0.78
	(in-oz)	(4.5)	(4.5)	(3.4)	(3.3)	(2.9)	(2.7)	(3.0)	(2.2)	(1.7)	(1.1)	(1.6)	(1.1)
Stall Torque (Motor and GearBox with 6.6 V)	N-m	48.0	47.5	50.6	49.5	48.0	47.5	36.2	33.9	29.0	28.8	33.1	29.9
	(in-lb)	(425)	(420)	(448)	(438)	(425)	(420)	(320)	(300)	(257)	(255)	(293)	(265)

Tested at 6.0 V

Successful qualification was a direct result of the trade study development. The Six-Sigma process and trade study identified the driving requirements. DC brush gear motor performance was improved resulting in approximately 11 N-m (100 in-lb) torque increase at the output. The upgraded gear head assembly is a robust design with lower drag, non-binding operation at all temperatures, and non-galling material combinations. The risk of damage to hardware during assembly was lowered due to design simplification. The new qualified DC brush gear motor is a robust design capable of handling all environmental conditions with consistent predictable performance.

Static Load Distribution in Ball Bearings

Mário Ricci*

Abstract

A numerical procedure for computing the internal loading distribution in statically loaded, single-row, angular-contact ball bearings when subjected to a known combined radial and thrust load is presented. The combined radial and thrust load must be applied in order to avoid tilting between inner and outer rings. The numerical procedure requires the iterative solution of $Z + 2$ simultaneous nonlinear equations – where Z is the number of the balls – to yield an exact solution for axial and radial deflections, and contact angles. Numerical results for a 218 angular-contact ball bearing have been compared with those from the literature and show significant differences in the magnitudes of the ball loads, contact angles, and the extent of the loading zone.

Introduction

Ball and roller bearings, generically called *rolling bearings*, are commonly used machine elements. They are employed to permit rotary motions of, or about, shafts in simple commercial devices and also used in complex engineering mechanisms.

This work is devoted to the study of the internal loading distribution in statically loaded single-row angular-contact ball bearings. Several researchers have studied the subject [1] [2] [3] [4]. The methods developed by them to calculate distribution of load among the balls and rollers of rolling bearings can be used in most bearing applications because rotational speeds are usually slow to moderate. Under these speed conditions, the effects of rolling element centrifugal forces and gyroscopic moments are negligible. At high speeds of rotation, these body forces become significant, tending to alter contact angles and clearance. Thus, they can affect the static load distribution to a great extent.

Harris [5] described methods for internal loading distribution in statically loaded bearings addressing pure radial; pure thrust (centric and eccentric loads), and combined radial and thrust load. These methods use radial and thrust integrals introduced in [2] and those initially due to [3] for ball bearings under combined radial, thrust, and moment load.

There are many works describing the parameters variation models under static loads but few demonstrate such variations in practice, even under simple static loadings. The author believes that the lack of practical examples is mainly due to the inherent difficulties of the numerical procedures that, in general, deal with the resolution of various non-linear algebraic equations that must be solved simultaneously.

In an attempt to cover this gap, studies are being developed in parallel [6] [7]. In this work, a numerical procedure is described for an internal load distribution computation in statically loaded, single-row, angular-contact ball bearings when subjected to a known external combined radial and thrust load. The novelty of the method is in the choice of the set of the nonlinear equations, which must be solved simultaneously. The author did not find in the literature the solution of this problem using the same set of equations.

* National Institute for Space Research, São José dos Campos, São Paulo State, Brazil

Static Load Distribution under Combined Radial and Thrust Load in Ball Bearings

It is possible to consider how the bearing load is distributed among the rolling elements having defined in other works analytical expressions for geometry of bearings and for contact stress and deformations for a given ball or roller-raceway contact (point or line loading) in terms of load. In this section, a specific load distribution consisting of a combined radial and thrust load must be applied to the inner ring of a statically loaded ball bearing so that no tilt is allowed between inner and outer rings.

Let a ball bearing with a number of balls, Z , symmetrically distributed about a pitch circle according to Figure 1, to be subjected to a combined radial and thrust load, so that a *relative axial displacement*, δ_a , and a *relative radial displacement*, δ_r , between the inner and outer ring raceways may be expected. Let $\psi = 0$ to be the angular position of the maximum loaded ball.

Figure 2 shows the initial and final curvature centers positions at angular position ψ , before and after loading, considering the centers of curvature of the raceway grooves fixed with respect to the corresponding raceway. If δ_a and δ_r are known, the contact angle at angular position ψ , after the combined load has been applied, is given by

$$\beta(\psi) = \cos^{-1} \left(\frac{A \cos \beta_f + \delta_r \cos \psi}{A + \delta_n} \right), \quad (1)$$

where A is the distance between raceway groove curvature centers for the unloaded bearing, β_f is the free-contact angle, and δ_n is the total normal deflection at the contacts.

Also, from Figure 2,

$$\delta_a = (A + \delta_n) \sin \beta - A \sin \beta_f, \quad (2)$$

and we can arrive in the expression for the extent of the *loading zone*, that is given by

$$\psi_l = \cos^{-1} \left\{ \frac{A}{\delta_r} \left[\cos \left(\sin^{-1} \left(\frac{\delta_a + A \sin \beta_f}{A} \right) \right) - \cos \beta_f \right] \right\}. \quad (3)$$

From (1), the total normal approach between two raceways at angular position ψ , after the combined load has been applied, can be written as

$$\delta_n(\psi) = A \left(\frac{\cos \beta_f}{\cos \beta} - 1 \right) + \frac{\delta_r \cos \psi}{\cos \beta}. \quad (4)$$

From Figure 2 and (4) it can be determined that s , the distance between the centers of the curvature of the inner and outer ring raceway grooves at any rolling element position ψ , is given by

$$s(\psi) = A + \delta_n = A \frac{\cos \beta_f}{\cos \beta} + \frac{\delta_r \cos \psi}{\cos \beta}. \quad (5)$$

From (2) and (5) yields, for $\psi = \psi_j$,

$$\delta_a - \delta_r \tan \beta_j \cos \psi_j - A \frac{\sin(\beta_j - \beta_f)}{\cos \beta_j} = 0, \quad j = 1, \dots, Z. \quad (6)$$

From the load-deflection relationship for ball bearings and (4) yields, for $\psi = \psi_j$,

$$Q_j = K_{nj} \left[A \left(\frac{\cos \beta_f}{\cos \beta_j} - 1 \right) + \frac{\delta_r \cos \psi_j}{\cos \beta_j} \right]^{3/2}, \quad j = 1, \dots, Z. \quad (7)$$

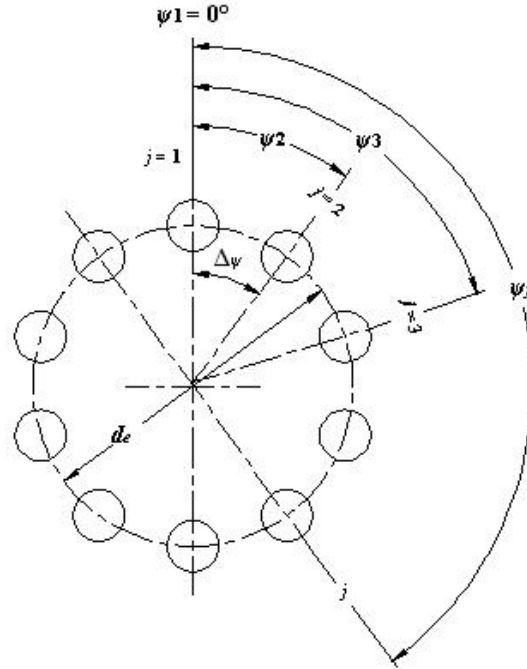


Figure 1. Ball angular positions in the radial plane that is perpendicular to the bearing's axis of rotation, $\Delta\psi = 2\pi/Z$, $\psi_j = 2\pi/Z(j-1)$

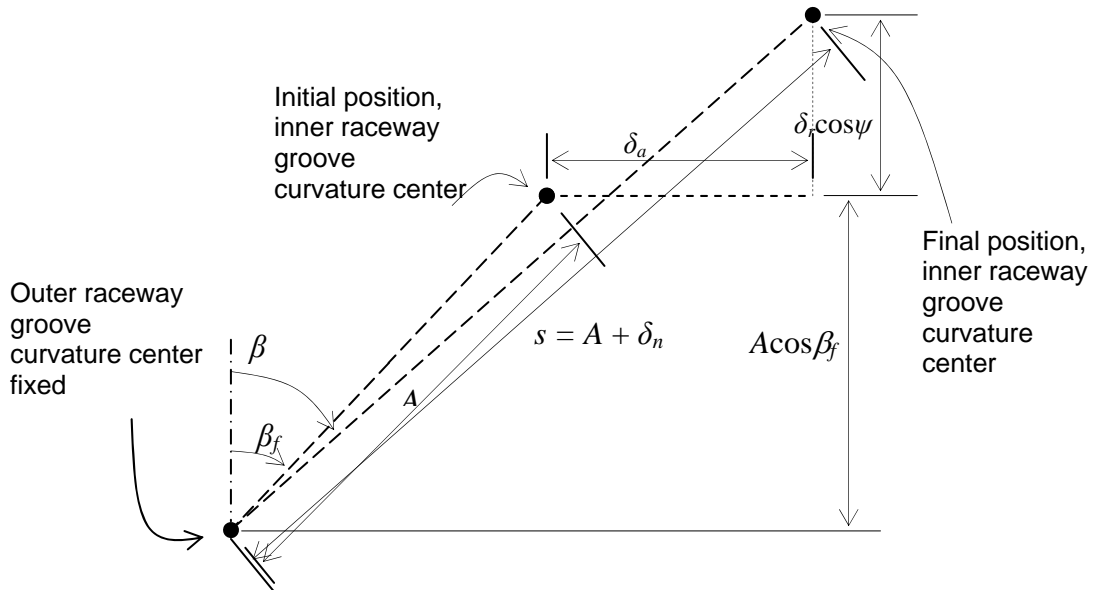


Figure 2. Initial and final curvature centers positions at angular position ψ , with and without applied load

If a thrust load, F_a , and a radial load, F_r , are applied then, for static equilibrium to exist

$$F_a = \sum_{j=1}^Z Q_j \sin \beta_j, \quad (8)$$

$$F_r = \sum_{j=1}^Z Q_j \cos \beta_j \cos \psi_j. \quad (9)$$

Additionally, each of the normal ball load components produces a moment about of the inner ring center of mass in the plane that passes through the bearing rotation axis and contains the external radial load (moments about the other two perpendicular planes are self-equilibrating). For static equilibrium, the thrust load, F_a , and/or the radial load, F_r , must exert a moment, M , about the inner ring center of mass that must be equal to the sum of the moments of each rolling element load, that is,

$$M = - \sum_{j=1}^Z Q_j \sin \beta_j [(R_i + \delta_r \cos \psi_j) \cos \psi_j - \delta_r], \quad (10)$$

where

$$R_i = d_e / 2 + (f_i - 0.5)D \cos \beta_f$$

expresses the locus of the centers of the inner ring raceway groove curvature radii.

Substitution of (7) into (8) yields

$$F_a - \sum_{j=1}^Z K_{nj} \sin \beta_j \left(A \left(\frac{\cos \beta_f}{\cos \beta_j} - 1 \right) + \frac{\delta_r \cos \psi_j}{\cos \beta_j} \right)^{3/2} = 0 \quad (11)$$

Similarly,

$$F_r - \sum_{j=1}^Z K_{nj} \cos \psi_j \cos \beta_j \left(A \left(\frac{\cos \beta_f}{\cos \beta_j} - 1 \right) + \frac{\delta_r \cos \psi_j}{\cos \beta_j} \right)^{3/2} = 0 \quad (12)$$

Equations (6), (11) and (12) are $Z + 2$ simultaneous nonlinear equations with unknowns δ_a , δ_r , and β_j , $j = 1, \dots, Z$. Since K_{nj} are functions of final contact angle, β_j , the equations must be solved iteratively to yield an exact solution for δ_a , δ_r and β_j .

Numerical results

A numerical method (the Newton-Raphson method) was chosen to solve the simultaneous nonlinear equations (6), (11) and (12). To show an application of the theory developed in this work, a numerical example is presented. I have chosen the 218 angular-contact ball bearing that was also used by [5]. Thus, the results generated here can be compared to a certain degree with the Harris results.

Figures 3 - 5 show some parameters as functions of the applied thrust load under a radial load of 17,800 N. We can observe a substantial difference between results found in this work and those found by Harris, for a thrust load of 17,800 N.

Figure 3 shows the normal ball loads, Q . Harris found the following ball load magnitudes: 6571; 5765; 3670; and 1200 N, for the balls located at angular positions: $|\psi| = 0; 22.5^\circ; 45^\circ; \text{ and } 67.5^\circ$, respectively, and found zero ball load magnitudes for the balls located at angular positions $|\psi| \geq 90^\circ$ (p. 262). This work found the following ball loads magnitudes: 5997; 5395; 3807; 1820; and 239 N, for the balls located at angular positions: $|\psi| = 0; 22.5^\circ; 45^\circ; 67.5^\circ; \text{ and } 90^\circ$, respectively, and found zero ball load magnitudes for the balls located at angular positions $|\psi| > 90^\circ$.

This means that Harris calculation has overestimated (or underestimated) the normal ball loads for balls located at angular positions satisfying $|\psi| < 45^\circ$ ($|\psi| \geq 45^\circ$); representing an error of 9.56% in the determination of maximum normal ball load and errors of 6.86%, -3.59%, -34.06% and -100% in the determination of normal ball load for the eight balls immediately about the most heavily loaded ball, respectively.

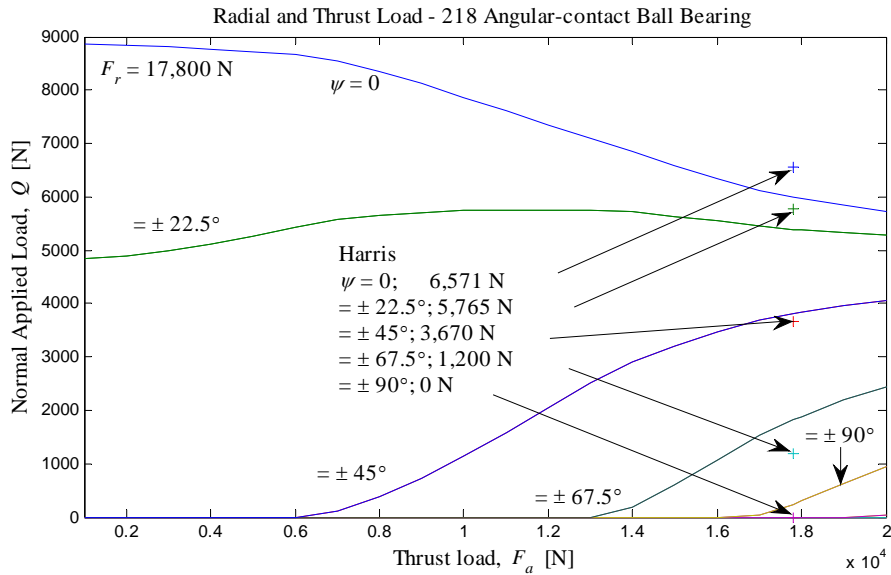


Figure 3. Normal ball load, Q , for 17,800 N radial load, as a function of the thrust load, F_a .

Figure 4 shows the contact angle, β . While Harris assumed a contact angle magnitude of 40° for all balls (p. 260), contact angles ranging from 38.2° to 42.7° were found in this work, while ψ were varied from $\psi = 0^\circ$ to $\pm 180^\circ$, respectively. This represents errors between 4.71% and -6.28% in the contact angles determination, meaning that Harris assumption has overestimated (underestimated) the contact angles for balls located at angular positions satisfying $|\psi| < 90^\circ$ ($|\psi| \geq 90^\circ$).

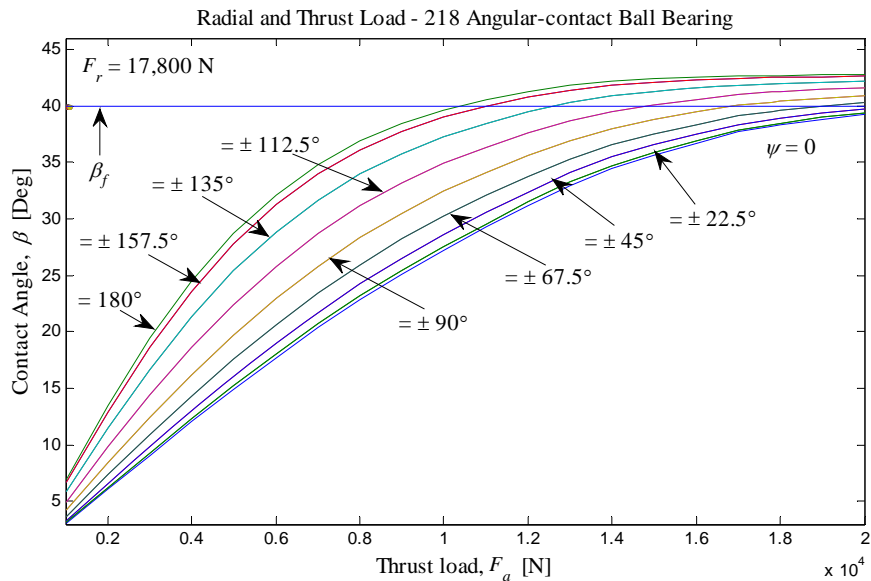


Figure 4. Contact angle, β , for 17,800 N radial load, as a function of the thrust load, F_a .

Figure 5 shows the loading zone, ψ_j . While Harris found a loading zone of 84.84° (p. 262), this work found a loading zone of 97.74° . This represents an error of -13.2% in the loading angle, meaning that the Harris calculation has underestimated the effect of the loading.

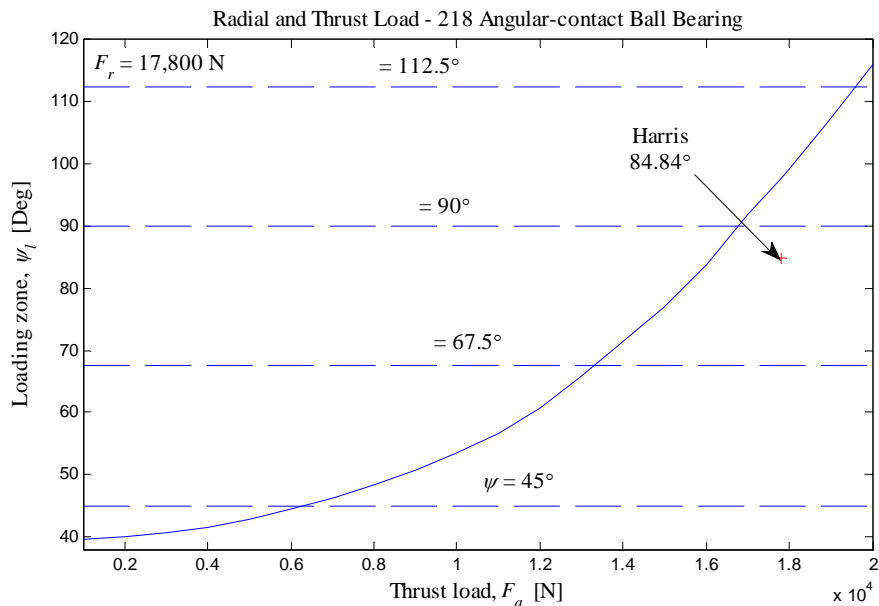


Figure 5. Contact zone, ψ_j , for 17,800 N radial load, as a function of the thrust load, F_a .

Conclusion

A numerical procedure for computing the internal loading distribution in statically loaded, single-row, angular-contact ball bearings when subjected to a known combined radial and thrust load has been presented. The combined radial and thrust load must be applied in order to avoid tilting between inner and outer rings. The procedure requires the iterative solution of $Z + 2$ simultaneous nonlinear equations with unknowns δ_a , δ_r , and β_j , $j = 1, \dots, Z$. Numerical results for a 218 angular-contact ball bearing have been compared with those from the literature and show significant differences in the magnitudes of the ball loads, contact angles, and extent of the loading zone.

References

1. Stribeck, R. "Ball Bearings for Various Loads." *Trans. ASME*, 29 (1907), 420-463.
2. Sjövall, H. "The Load Distribution within Ball and Roller Bearings under Given External Radial and Axial Load." *Teknisk Tidskrift, Mekanik*, häfte 9 (1933), 97-102. (<http://runeberg.org/tektid/1933m/0099.html>)
3. Jones, A. *Analysis of Stresses and Deflections*. Bristol: New Departure Engineering Data, ©1946.
4. Rumbarger, J. "Thrust Bearings with Eccentric Loads." *Machine Design* (15 February 1962).
5. Harris, T. *Rolling Bearing Analysis*. 4th Ed., New York: John Wiley & Sons, Inc., ©2001.
6. Ricci, M. C., "Ball bearings subjected to a variable eccentric thrust load." *DINCON'09 Proceedings of the 8th Brazilian Conference on Dynamics, Control and Applications*, (May 2009). ISBN: 978-85-86883-45-3.
7. Ricci, M. C. "Internal loading distribution in statically loaded ball bearings subjected to a combined radial, thrust, and moment load." *Proceedings of the 60th International Astronautical Congress*, (October 2009). ISSN 1995-6258.

BESST: A Miniature, Modular Radiometer

Robert Warden*, William Good* and Erik Baldwin-Stevens*

Abstract

A new radiometer assembly has been developed that incorporates modular design principles in order to provide flexibility and versatility. The assembly, shown in Figure 1, is made up of six modules plus a central cubical frame. A small thermal imaging detector is used to determine the temperature of remote objects. To improve the accuracy of the temperature reading, frequent calibration is required. The detector must view known temperature targets before viewing the remote object. Calibration is achieved by using a motorized fold mirror to select the desired scene the detector views. The motor steps the fold mirror through several positions, which allows the detector to view the calibration targets or the remote object. The details, features, and benefits of the radiometer are described in this paper.

Introduction

The availability of small, low-cost infrared detectors has enabled the development of small, low-cost thermal imaging instruments. The radiometer, which is the subject of this paper, uses this technology to remotely detect the surface temperature of large bodies of water. Knowledge of the surface temperature of the ocean is an important factor in weather prediction. Currently, the temperature is recorded by large instruments onboard ocean going ships. These instruments are very accurate but are also large and heavy. The temperature readings are limited to the path of the ship so relatively few data points are available for weather forecasting models. Achieving the high accuracy desired requires frequent and regular calibration. This is challenging for the instrument design and usually requires increased volume, mass, and complexity.

The Ball Experimental Sea Surface Temperature (BESST) radiometer was designed and built by Ball Aerospace as a small, modular, light-weight and low-power sensor for sea surface temperature (SST) studies from an Unmanned Aerial Vehicle (UAV). BESST has been demonstrated on a conventional Twin Otter airplane and is part of several NASA proposals. It incorporates a commercial detector to sense the infrared radiation from the surface of the water and features two on-board calibration targets in addition to the ability to view the sky for background readings. BESST uses a combination of windows and filters to improve accuracy by minimizing the effect of water vapor and aerosols in the atmosphere. Special absorptive or reflective paints and treatments are used on the various surfaces, as needed. The resulting measurements of the absolute sea surface temperature are accurate to within 0.3°C.

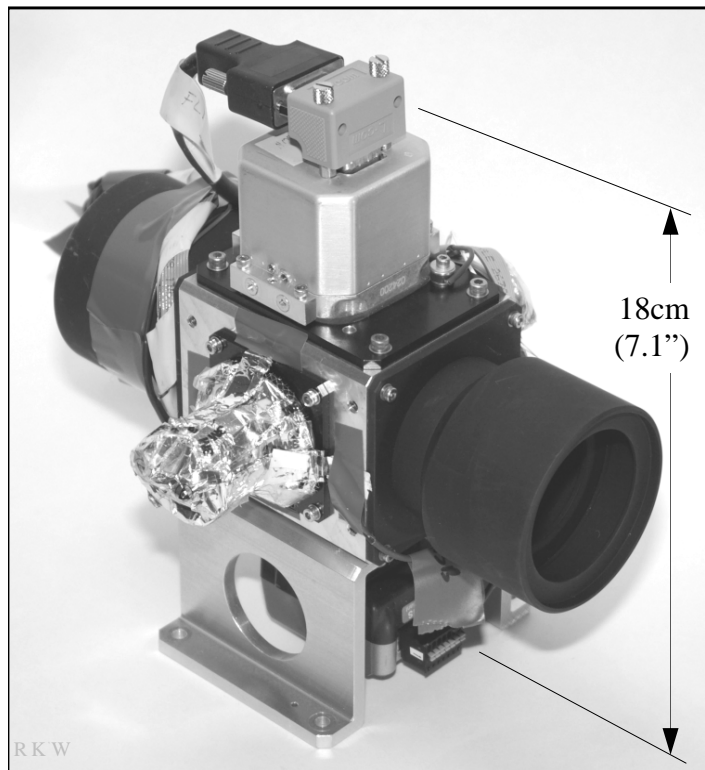


Figure 1. BESST Radiometer

* Ball Aerospace & Technologies, Boulder, CO

Background

Accurate readings of Sea Surface Temperature (SST) are crucial to modeling water-energy cycles, which are used for weather prediction and understanding climate change. Satellite measurements cover broad areas but must be calibrated with actual surface measurements of the water temperature. Current NASA satellites such as the Moderate Resolution Imaging Spectroradiometer (MODIS) and Advanced Very High Resolution Radiometer (AVHRR) operated by NOAA, provide SST measurements with a spatial resolution of one kilometer and a precision of 0.1°C. These satellite SST sensors are calibrated with ship-borne SST instruments that provide a few single point measurements. The ship-board instruments are very expensive to build, operate, and deploy.

The BESST modular radiometer offers an alternative for calibration and validation of on-orbit SST instruments. This alternative uses a small, lightweight radiometer integrated to an Unmanned Aerial Vehicle or conventional aircraft to provide highly accurate, high-resolution SST data for frequent, lower-cost validation of satellite data. The BESST radiometer system has a precision of 0.1°C and can be flown quickly over a large area providing a more complete calibration/validation of image data from the orbiting satellite than is available from ship-borne instruments.

In addition to calibration and validation of satellite measurements, the BESST radiometer can perform studies not previously possible with current SST instruments. BESST can perform high spatial resolution mapping of single satellite pixels to look for small-scale variability in infrared SST patterns. This is particularly important near coastal areas and where rivers empty into coastal waters and form estuaries critical to near-shore activities. Understanding small-scale variability will provide insight and may help close the air-sea heat budget. Figure 2 shows the small-scale variability present within satellite pixel data. Data from the MODIS satellite, large square pixels, is shown with 2 strips of data from a BESST airborne measurement overlaid. The BESST plot clearly shows temperature variability within that region that can significantly affect ocean and climate models.

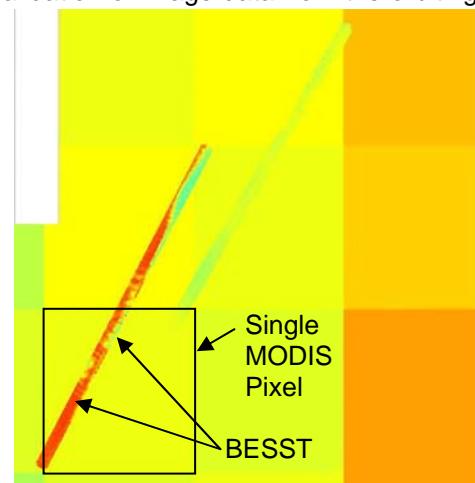


Figure 2: BESST data showing fine structure within MODIS single pixels

Another possible application for the BESST radiometer is the study of diurnal warming. Variability of SST on sub-day time scales is often dominated by the diurnal solar warm layer phenomenon. This warm layer is stronger in lighter winds and solar forcing. In light winds (<2 m/s) it can exceed 2 percent. The depth is inversely proportional to the strength.

There are a number of ways to account for the warm layer in relating SST to the actual subsurface temperature structure. Fairall et al. (1996a) present a simple 1-D model integrated into the COARE bulk flux model (Fairall et al., 1996b, 2003). More recently, Zeng and Beljaars (2005) developed a similar scheme that has been implemented at European Centre for Medium-Range Weather Forecasts (ECMWF) (Brunke et al., 2008). The Fairall scheme was developed and optimized for tropical applications and does not include physics to deal with turning of the near-surface currents by the Coriolis force. Thus, the timing and magnitude of this warm layer at mid-latitudes may not be well-described by the model.

To date, studies of diurnal warming in the SST measurements have been limited to multi-day measurements indicating amplitude change over time. The BESST radiometer can be deployed over a region for full 2D spatial mapping of the diurnal signal at a specific time making it a unique tool for the SST community. Diurnal warming has been recently identified by a NASA study group on SST as the primary uncertainty in satellite SST measurements, and this unique capability of the BESST to study this

temporal/spatial variability greatly increases its importance in being able to augment the ship-based surface temperature measurements.

Design Development

The accuracy of the temperature reading relies on frequent calibration, which involves having the detector look at known temperature sources before looking at the remote object. The initial design requirement was very simple: place a black-body target in front of the optical path in order to calibrate the detector. The initial configuration was to have some sort of flip mechanism to move a black-body target in and out of the detector field of view. It was then determined that two calibration targets should be used: one for the warm black-body and another for ambient temperature. To accommodate two calibration sources, a three position flip mechanism was proposed.

The final design requirement was that a second scene select was needed to look at the sky. It was apparent that in order to get a second sky view, either the detector had to move or a fold mirror was needed to reflect the image through a second baffle tube. The development of the design is shown graphically in Figure 3. Note that each double-ended arrow represents a separate mechanism.

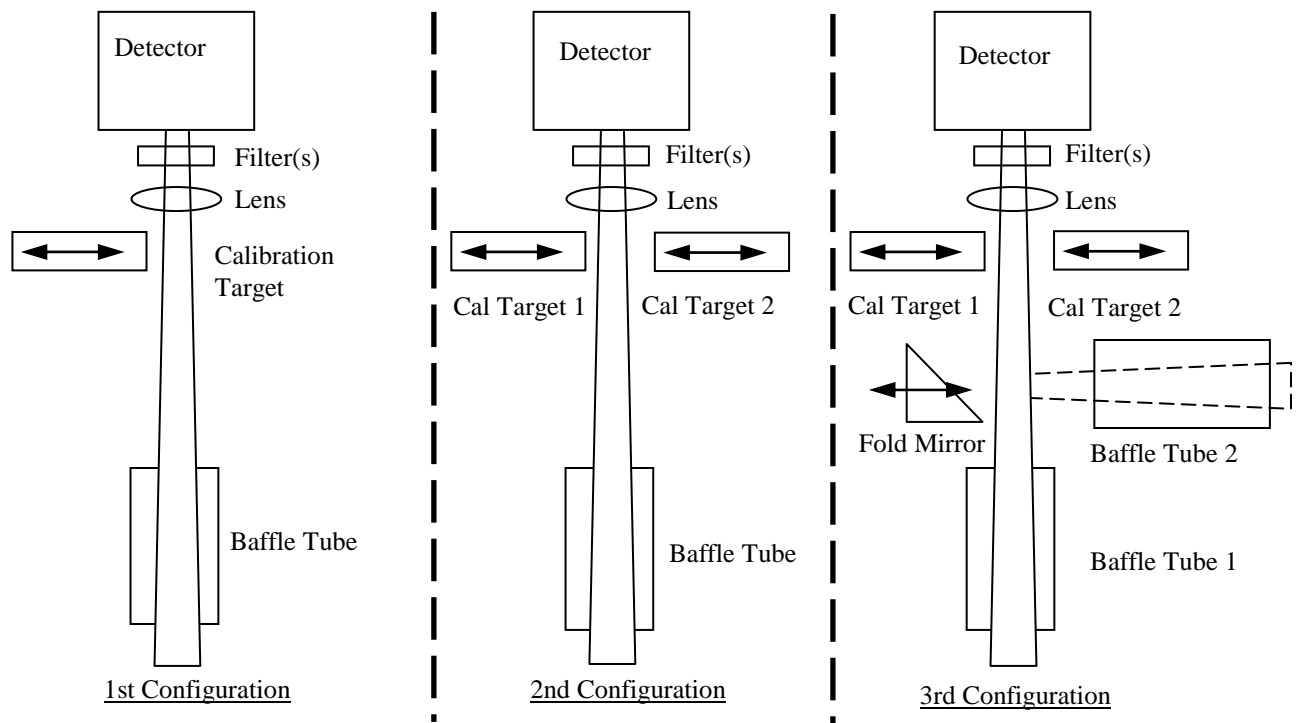


Figure 3. Design Iteration Showing Increasing Complexity

The key design breakthrough was realizing that if a fold mirror was acceptable for one scene, it could be acceptable for all scenes. By rotating the fold mirror as shown in Figure 4, the detector could easily be exposed to different scenes. It is also a benefit to have the fold mirror always in place so that the only variable is the scene.

The design iteration went as shown in Figure 3 with the development progressing at a sketch level before detailed design work was started. A set of well defined concepts and parameters were evaluated before the design work started. The final configuration is the best compromise between optics, thermal, cost and schedule.

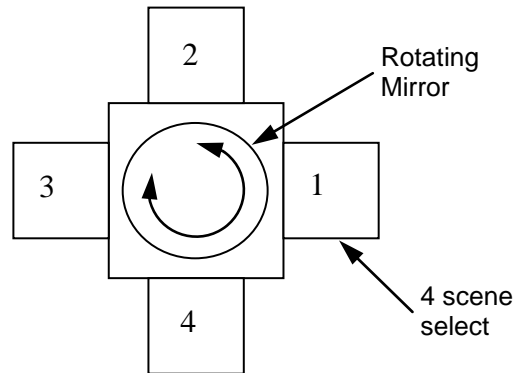


Figure 4. Final Single-Mechanism Configuration

Operation

The basic principal of the design is to have the motor/fold-mirror opposite the detector assembly as shown in Figures 5 and 6. The motor rotation axis is directly in-line with the center of the detector. In this way, the optical path reflects off the fold mirror and can be directed by rotating the fold mirror. The optical path always reflects off the mirror so that the only difference to the detector is the actual scene. In addition, the optical stop is built into the turret, so the stop rotates with the mirror.

On-board calibration is done by alternating the observed scene from the ocean and two temperature-monitored black-body references, the common "two-point" method in radiometers with one heated and the other at ambient instrument temperature. An absolute calibration of these reference blackbodies is performed in the laboratory prior to deployment. A third "sky" port is also available to measure sky radiance to extract its reflection from the ocean temperature measurement. The use of microbolometers eliminates the need for cryogenic fluids, greatly simplifying flight requirements.

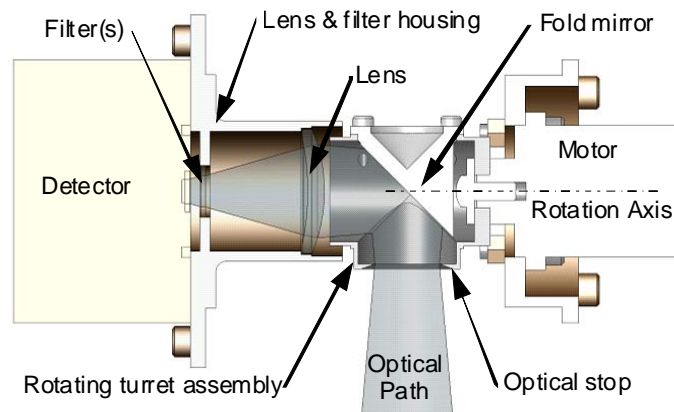


Figure 5. Detector, Mirror & Motor

For calibration, the mechanical design has three desirable features. First, the tight fit between the mirror housing and the lens housing keeps stray light off of the calibration sources. Second, the angle of incidence of the mirror is equal for the calibration sources and the scene. Third, the area of the mirror used is the same for both the calibration sources and the scene.

Description

The six modules that go into the assembly are shown in Figure 7. The central cubical frame is universally symmetric so that any module can mount to any face. The detector module is mounted opposite the motor module previously shown in Figure 5. The motor rotates to position the turret and fold mirror to one of four quadrants. These faces can accommodate either a calibration target or a baffle tube. Light (or heat) from any one of the four faces can then be directed to the detector. The calibration and baffle modules typically mounted on these faces are discussed later in the paper.

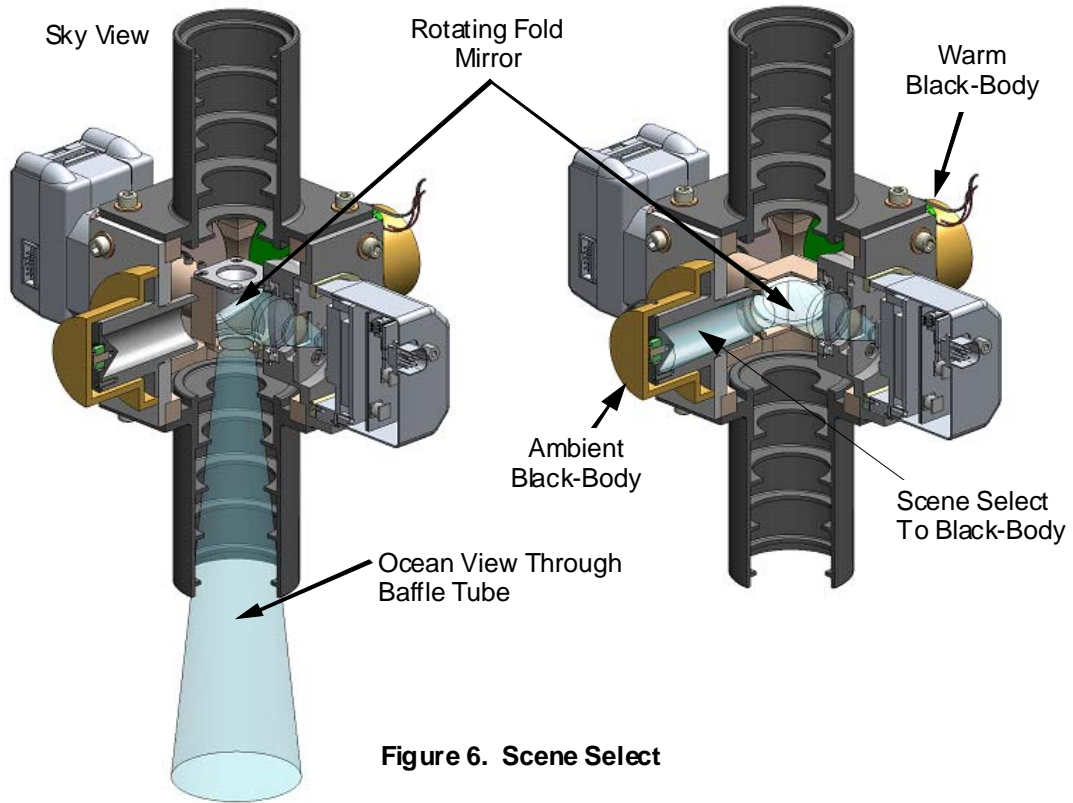


Figure 6. Scene Select

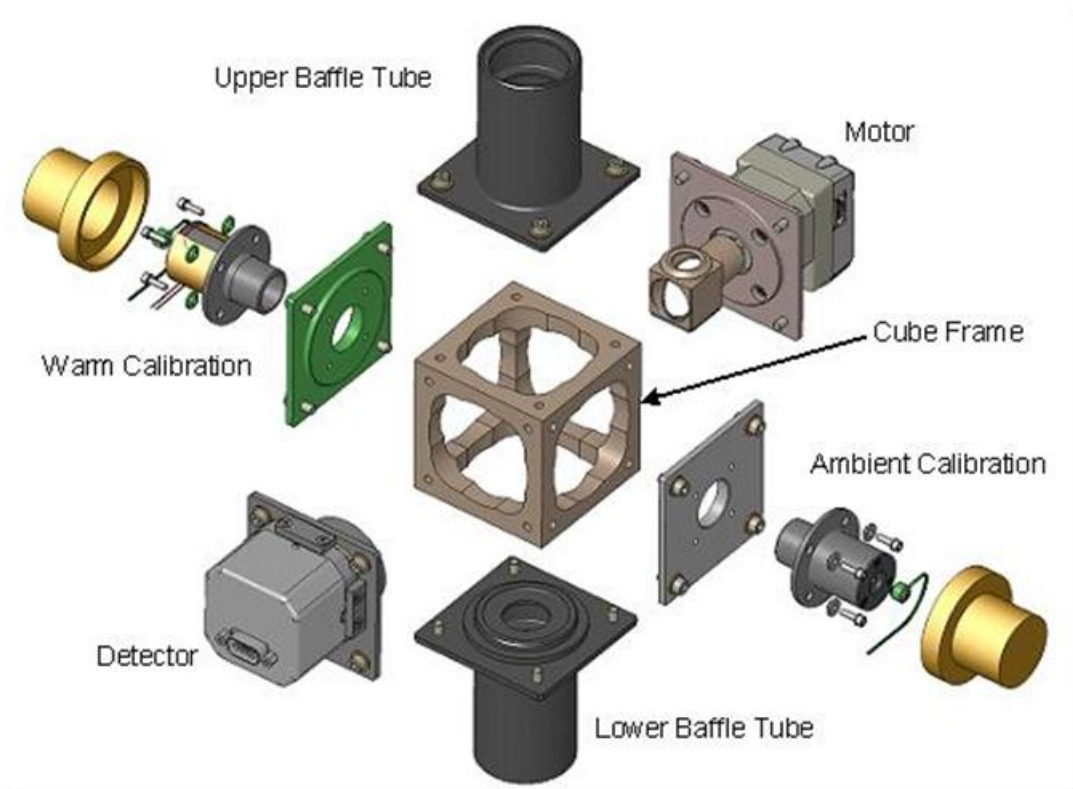


Figure 7. Modules & Frame

Mounting

The BESST instrument can be mounted on any of the six faces as shown in Figure 8 by using a custom bracket to interface with the airborne or terrestrial vehicle. The bracket can also provide additional thermal isolation from the vehicle. The lightest-weight option is to have the support vehicle provide a mounting interface.

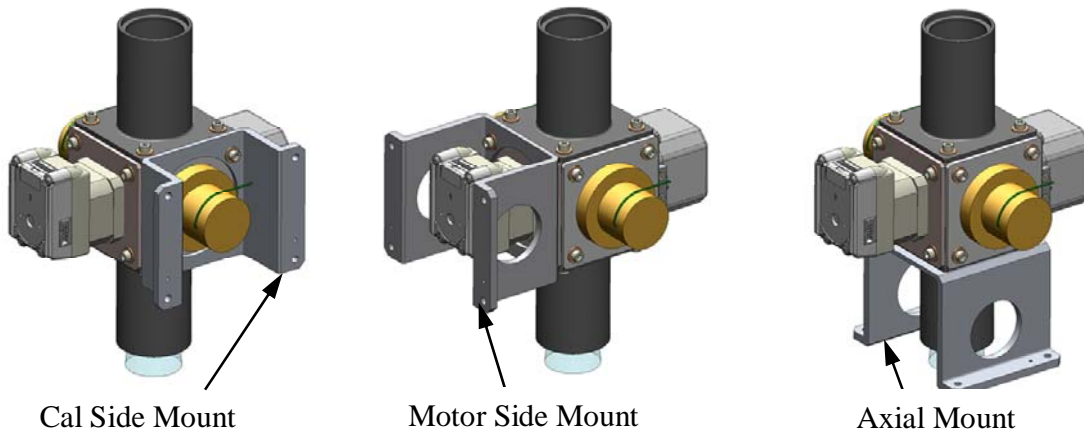


Figure 8. Mounting Options

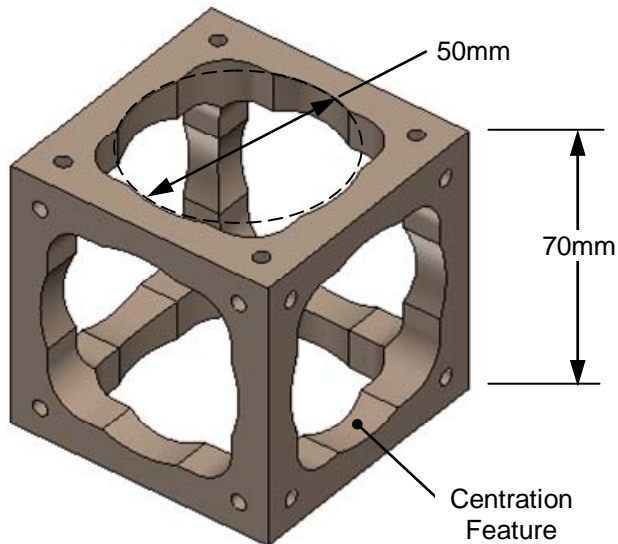


Figure 9. Cube Frame

of the cube. Modules can be replaced or rearranged while maintaining alignment. The focal length is unaffected by rearranging the modules because the distance from the face to the center of the cube is the same for each location.

Detector Module

The detector module consists of the detector as well as any lenses or filters required for the desired operation (Figure 10). A single housing is used to position the optical components so that this module can be aligned and verified as a stand-alone unit. The detector module has a total mass of 225 grams of which the detector assembly is 125 grams.

Cubical Frame

The central structure or chassis for the assembly is a simple hollow cube as shown in Figure 9. Each side is 70-mm long and each face has four tapped holes with which to attach the modules. The six faces are machined out of a single piece of aluminum so that the cube is lightweight but structurally sound. The mass of the aluminum cube is only 180 grams. The cube could be scaled up to accommodate a larger optical path.

Each face also has a diametral centration feature in the form of a close tolerance bore. Each module has a corresponding lip that fits into the bore. As the modules are attached to a given face, they are automatically aligned to the center

Two different detectors have been mounted to the radiometer. The original detector was made by Raytheon and the second detector was made by FLIR. Both are un-cooled microbolometers with a 324 X 256 array with a pixel size of 38 microns.

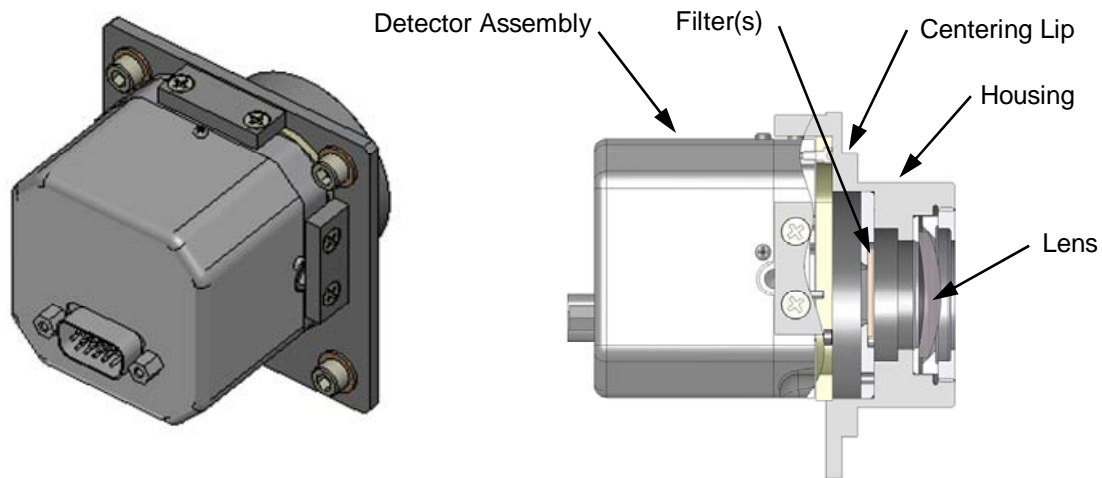


Figure 10. Detector Module

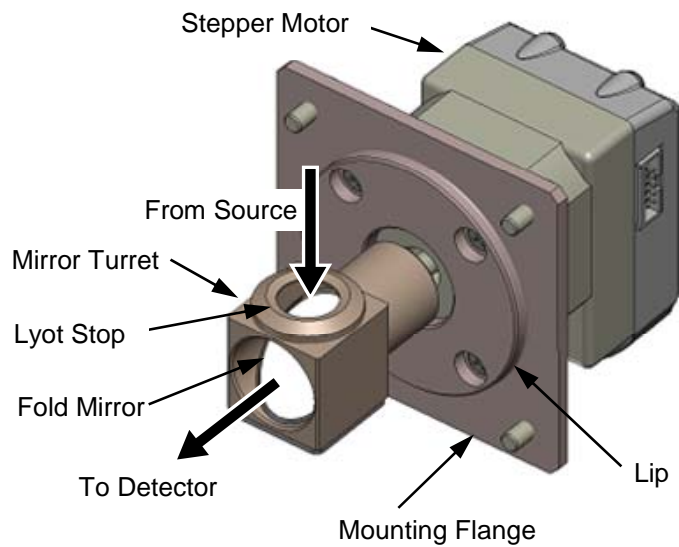


Figure 11. Drive Module

Motor Module

The key to the performance of the radiometer is the ability to easily calibrate the detector. This involves having the detector look at objects that have a known temperature in order to calibrate the output.

The motor module (Figure 11) supports a 45-degree fold mirror that directs the source of light to the detector. The fold mirror is mounted in a rotating turret and the entrance to the turret is the Lyot stop for the optical path.

The only load on the motor is from the turret and fold mirror, which are cantilevered off of the output shaft of the motor. The total offset load is only 33 grams. The total mass for the entire motor module is 380 grams; however, this includes a gearhead and control electronics.



Figure 12. MDrive 17 Motor and controller (300 grams)

Motor Details

The MDrive 17 motor/controller was selected for this program because it is a readily available commercial unit that comes with an integrated controller. At 300 grams, it is reasonably light-weight and the long shaft was convenient for attaching the turret and fold mirror. The unit also comes with a canned software package that loads easily onto a computer. Simple commands can be issued to rotate the mirror to the required quadrant. If step counts are lost, the unit can be commanded to find its home position in order to reset the zero degree location.

An even lighter-weight motor was desired to further reduce the weight of the system. When Sanyo Denki announced a new line of pancake stepper motors that are only 11-mm thick, the program purchased both the 42-mm version and the 50-mm version, as shown in Table 1. Although the new motors were very small and light, the output shaft was found to be too short. A longer version of the 42-mm motor is available with a longer shaft but it is the same weight as the original unit.

Table 2. Alternate motors considered

			
42mm pancake motor (70 grams)	42mm cube motor (240 grams)	50 mm pancake motor (90 grams)	MForce Controller (74 grams)

Overall mass and complexity could be reduced by using a simple 4-position motor; however, a commercial unit does not currently exist. The ideal motor would be a 90° stepper motor that could be rotated 90° with a single switch command. A detent at each quadrant position might be needed to assure repeatability if the natural cogging of the motor is not accurate enough.

Baffle Module

The baffle tube is constructed from a single piece as shown in Figure 13. The purpose of the baffle is to reduce the amount of stray light getting to the detector for the Earth and sky view scenes. The inside of the baffle is painted with a black absorptive paint. Baffle fins are placed so that undesired light is directed to the black surface after one bounce. The total mass for each baffle is 110 grams.

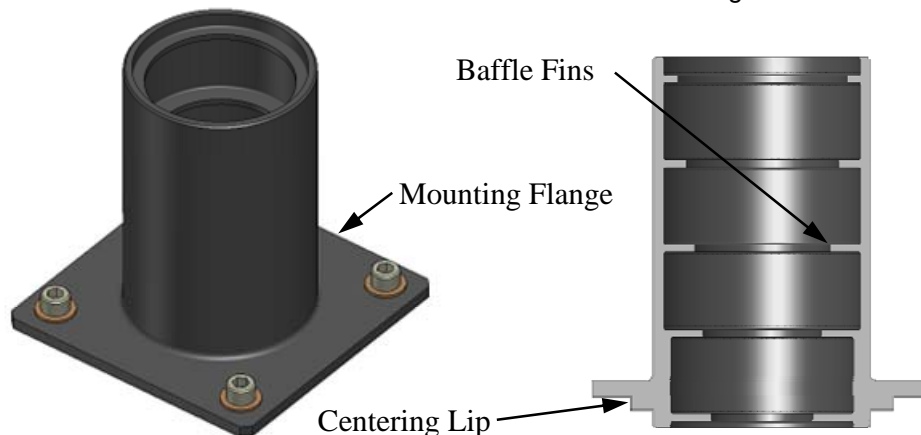


Figure 13. One Piece Baffle Tube

Calibration Module

The calibration target consists of an aluminum tube with a conical end that forms a black-body calibration source. The inside is painted with a black absorptive paint so that when the detector views the target, it sees an accurately defined and uniform temperature. The Calibration Module shown in Figure 14 can be built up in one of two configurations depending on the calibration temperature required. For warm calibration, a fiberglass mounting flange is used so that the black-body target is thermally isolated from the rest of the system. A strip heater, attached to the outside of the aluminum tube, heats the tube to a predefined temperature and a temperature sensor reports the temperature.

Using an aluminum mounting flange and no external heater, the temperature of the target is the same as the temperature of the cube, detector and baffles. No heater is used but a temperature sensor is mounted to the black-body to report the temperature of the assembly. The black-body and temperature sensor are covered by a "hat" made up of Multi-Layer Insulation (MLI). The wires from the temperature sensor and strip heater exit through a small hole in the MLI cover. The mass of the calibration module with the fiberglass mounting flange is 95 grams and the module with the aluminum plate is 110 grams.

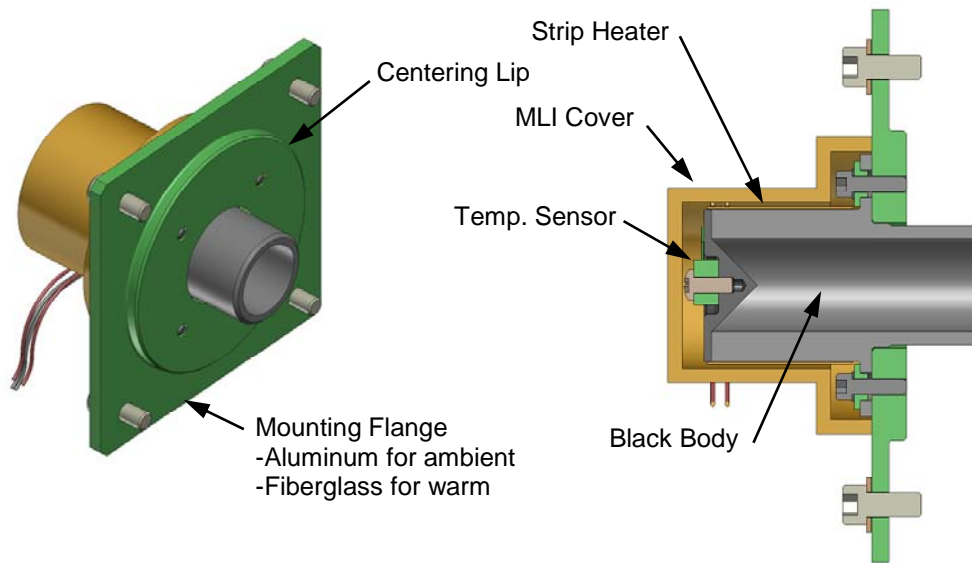


Figure 14. Calibration Modules

Mass

The total mass of the BESST instrument shown in Table 2 is for the radiometer and mechanism only and does not include the electrical cables, computer or battery required for the entire system. Reasonable dimensions and tolerances were used for this development unit. Additional mass savings could be achieved using more complicated machining.

The heaviest component on the list is the motor. For this application, the motor also includes a gearhead and control electronics. A much simpler and lighter motor could be procured but the selected unit was inexpensive, easy to interface with and easy to control.

Table 2. Mass Summary

Module	Mass (grams)
Cube Frame	180
Motor	380
Detector	225
Baffle	110
Baffle	110
Cal Source	95
Cal Source	110
Mounting Bracket	150
Total	1.36 kg (3 lb)

Alternate configurations

Several different configurations are possible as shown in Figure 15. Using the existing central cube, the baffle tubes and calibration targets can be moved around to accommodate the desired mission. The central cube can be replaced with a hexagonal housing to provide additional target viewing options.

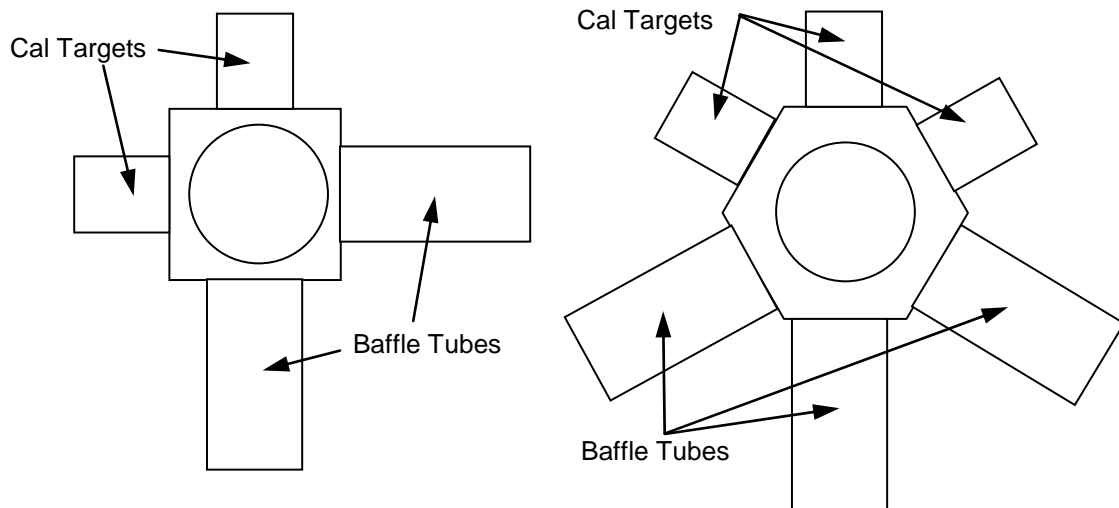


Figure 15. Alternate Configurations

The resulting assembly is a compact sensor approximately the size of a 20-cm cube as shown in Figure 16. Not included in this volume are the mounting brackets, electrical cables, computer and batteries. Also, extended baffle tubes may be needed for specific scene viewing.

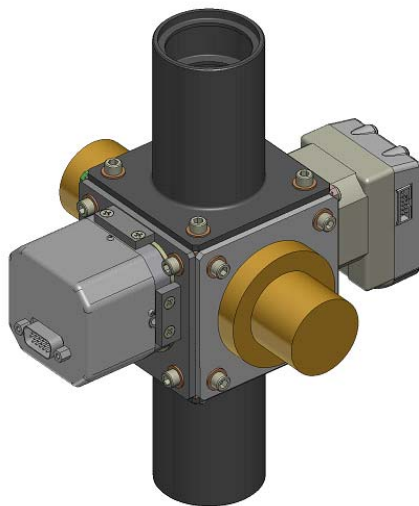


Figure 16. Overall assembly

Flight Performance

The first “flight” of the BESST instrument was actually a field test at a local Colorado lake. The instrument was cantilevered off the side of a small dock as shown in Figure 17. This test simulated the important parts of the system by having a view of the water as well as a view of the sky.



Figure 17. Field Testing

Electronics

The block diagram of the electronics for BESST is shown in Figure 18. The Airborne Computer commands the motor position and records the data from the detector. The motor is commanded to rotate the central fold mirror to view the four scenes: water, sky, warm black-body, and ambient black-body. The detector captures images of each scene through the sequence and the black-body readings are used to provide a highly accurate calibration of the scene measurement. The sequence is automated through the software to collect data over a region of interest.

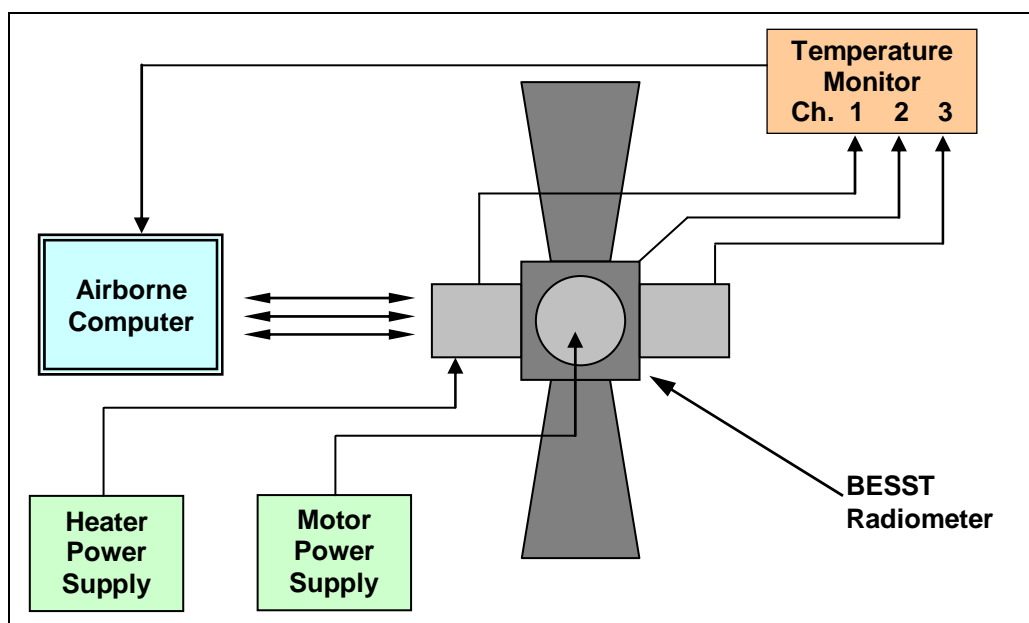


Figure 18: BESST electronics block diagram

Test Results

The BESST radiometer demonstrated excellent performance in a test flight over Salt Lake, Utah. Flying at low altitude, it provided some of the highest resolution water surface temperature measurements yet achieved, as shown in Figures 19 and 20. Each pixel represents roughly 10 meters. The resulting detail uncovers significant spatial variability, with 1 to 2°C warm and cold pools on the order of 50 to 100 meters across.

Predicted noise levels on the order of 0.1°C have been achieved, and the instrument is sensitive to water temperature changes on this level. While absolute accuracy of the measurements cannot be verified for the test flight over Salt Lake, lab testing with controlled, uniform blackbodies has shown the instrument to be accurate to better than 0.3°C. Repeated flight passes have an RMS variability of 0.1°C.

Additionally, the orbiting Moderate Resolution Imaging Spectroradiometer (MODIS) passed over Salt Lake on the day of the test flight, collecting 1-km-resolution surface temperature data. The newly developed radiometer compares well to MODIS, with an average resolved surface temperature difference of roughly 0.9°C.

Much of this difference may be attributed to the disparity in resolution between the radiometer and MODIS. Considering the small-scale surface temperature variation seen during the test flight and the small fraction of each MODIS pixel that was sampled (roughly 7%), this data is not expected to directly represent the average temperature over a 1-km² area measured by MODIS. The measurements match MODIS to within the level of spatial variation observed, confirming the accuracy of the instrument.

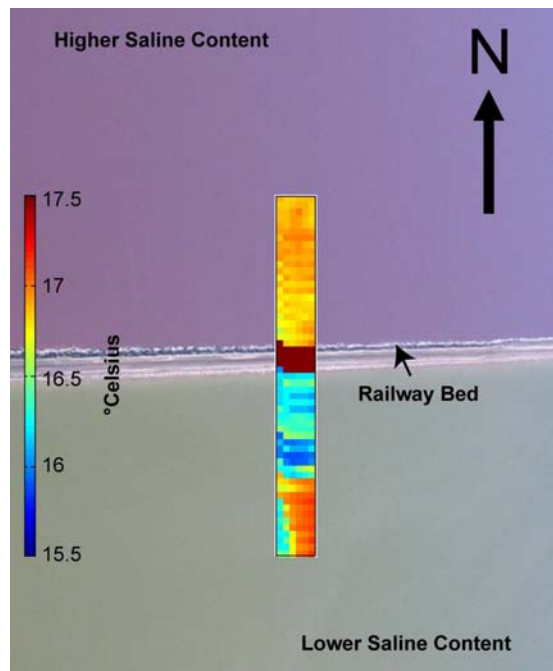


Figure 20. One data transect across a railroad with water on either side

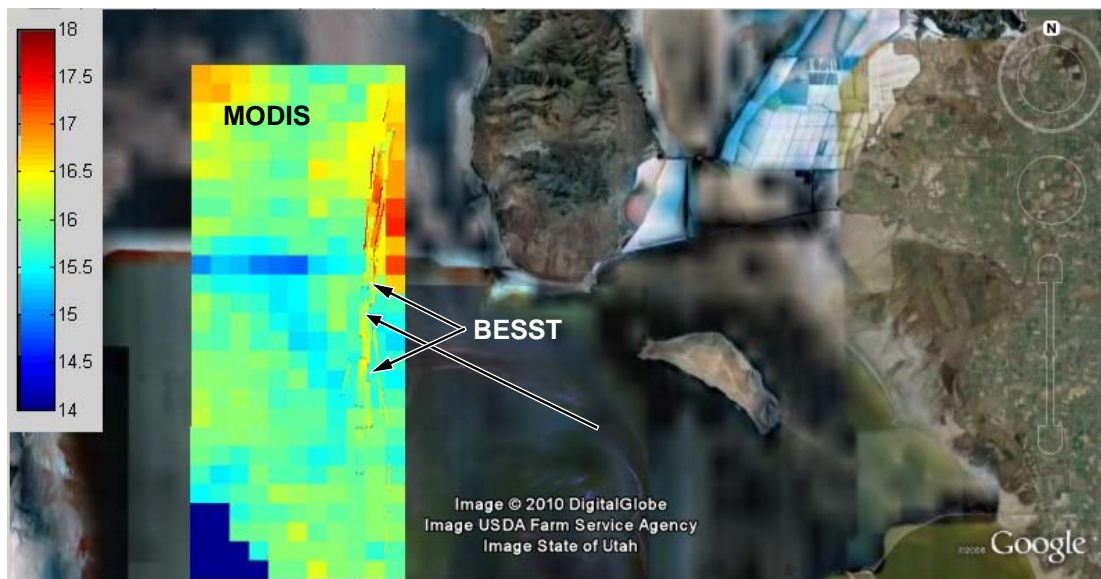


Figure 19. Google Earth overlay showing BESST radiometer data (narrow strips) and MODIS data (large pixels) over Salt Lake, Utah.

Applications

The Modular Radiometer can be used in several applications and environments. It was originally designed to fly on a UAV such as the Aerosonde shown in Figure 22. In this application, sea surface temperatures could be measured over long strips of ocean. The assembly is small and light enough to be compatible with this type of aircraft.

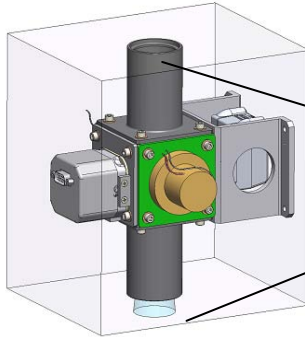


Figure 21. Twin Otter

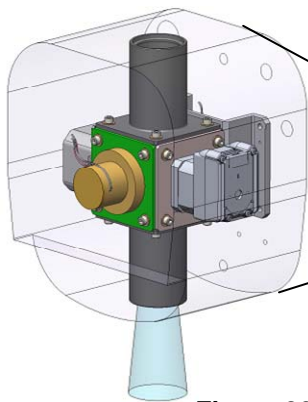


Figure 22. Modular Radiometer on board UAV

To demonstrate capability, however, it was re-configured with a different mounting bracket to fly on a Twin Otter, which is a plane commonly used to test prototype instruments (Figure 21). For this application, the unit was mounted to a central structure and controlled using a laptop computer. Aircraft inverters were available for power to the unit and computer.

With a space-qualified motor, detector and electronics, the Modular Radiometer could be mounted to a satellite to provide remote radiometric sensing capabilities (Figure 23).

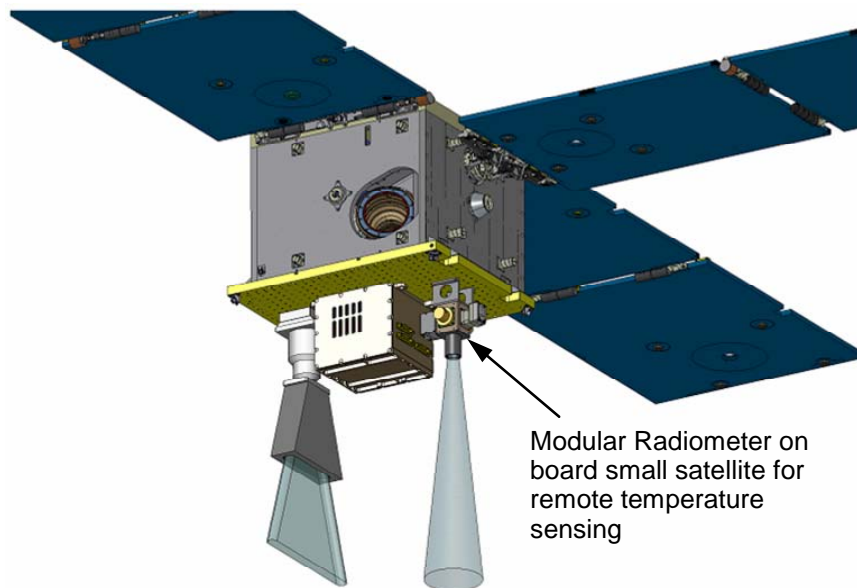


Figure 23. Mounted on Satellite

Lessons Learned

Much of the development of the BESST instrument went very well but there were some specific lessons that were learned that may be of use to the reader:

Communication

Always communicate the status and requirements of a program to all relevant disciplines. If the requirements are not known, make assumptions and communicate those assumptions to the team. For this program, mass was not an actual requirement other than to enable the instrument to be flown on a UAV or satellite at some later date. Consequently, a reasonable effort was made to make the parts lightweight. The mass of each component as well as the entire assembly was calculated regularly and distributed to the team members. Likewise, the voltage and current needed for the motor and heaters were also researched and reported. The systems engineers could then work with these values to anticipate any problems.

Documentation

Maintaining a centralized location for documenting changes to the design and layout of the system was crucial to the success of the instrument. In a development environment, the conceptual layout changes discussed herein impacted all areas of the system and needed to be well understood by each engineer on the project. Turnover of personnel during the lifetime of a project makes documentation even more important.

Detector

In the interest of making the cost per unit of the BESST instrument as low as possible while maintaining calibration accuracy, the original Raytheon Vision Systems bolometer was replaced with a FLIR bolometer which has a larger detector area. The initial unit was designed for the smaller Raytheon Vision Systems detector so that the initial baffle tubes were clipping the edges of the new light path. It was fairly easy to replace the original baffles with two new baffles tubes because of the modularity of the design as shown in Figure 24. The lesson learned is that it is advantageous to provide accommodations for potential detector upgrades or modifications.

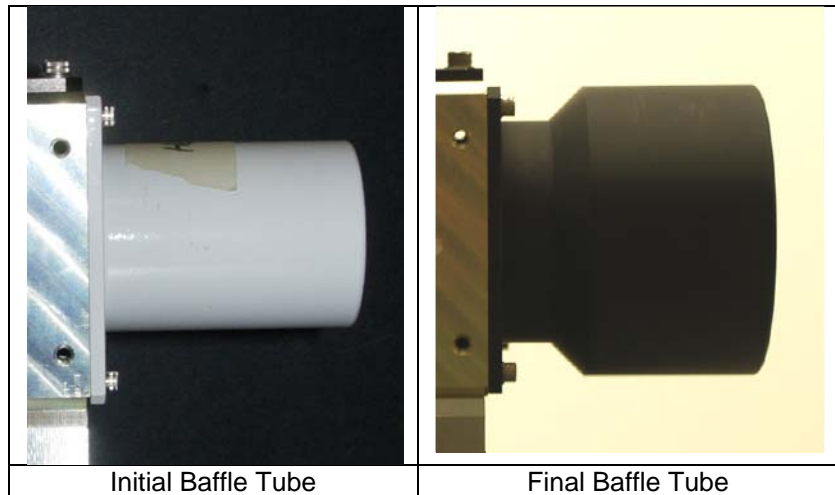


Figure 24. Baffle Tubes

The lesson learned is that it is advantageous to provide accommodations for potential detector upgrades or modifications.

Motor

At the beginning of the program, it was envisioned that a small, simple motor could be procured that would rotate the fold mirror to the four positions. It was thought that a rotary solenoid or a four-pole motor could be used. A detent of some sort might be necessary to hold the mirror in position at the quadrant, but a command to move the motor 90 degrees should be very simple.

In practice, such a device could not be found. Motor vendors were willing to develop a custom motor for this program but the cost was too great for a development effort. The motor that was eventually used is compact and heavy although easy to command. The lesson learned from this is that a motor as a single design component can still be very complicated and difficult to obtain.

Conclusion

The radiometric performance of the BESST instrument meets the science requirements for SST studies for a much lower cost and with better spatial resolution. The accuracy of the microbolometer temperature readings are 0.09°C and the accuracy of the overall instrument is 0.3°C for individual pixels. The temperature accuracy and spatial resolution can be traded off: more pixels can be averaged to achieve better accuracy, but at the cost of lower spatial resolution. This is done during post-processing of the data and will be explored further as part of continued scientific demonstrations.

Laboratory and flight testing of the BESST radiometer have shown it to be a valuable complement to ship-borne SST instruments. In addition to performing calibration / validation activities for satellite SST sensors, BESST can perform measurements with higher spatial resolution and repeat area coverage than currently available instruments. The lightweight, modular design is responsible for these advantages as it allows the instrument to be deployed on a UAV platform in a configuration suitable to each mission.

Acknowledgements

The authors wish to acknowledge the help and support of Ray Demara, Paula Wamsley, Shelley Petroy and the Airborne Initiative group at Ball Aerospace. Also the hard work of numerous engineers, technicians and interns including Paul Kaptchen, Raymund To, Tony Lin and James Lasnik as well as Brian Johnson, Michele Kuester, Jennifer Turner-Valle, Kartik Ghorakavi and Julie Sandberg. A special thanks to Dr. William Emery of the University of Colorado for scientific guidance with respect to SST measurements and requirements.

References

- Brunke, M.A., X.B. Zeng, V. Misra, and A. Beljaars, 2008: Integration of a prognostic sea surface skin temperature scheme into weather and climate models. *J. Geophys. Res.*, 113, D21117.
- Fairall, C.W., E.F. Bradley, D.P. Rogers, J.B. Edson, and G.S. Young, 1996: Bulk parameterization of air-sea fluxes for TOGA COARE. *J. Geophys. Res.*, 101, 3747-3767.
- Fairall, E.F. Bradley, J.S. Godfrey, J.B. Edson, G.S. Young, and G.A. Wick, 1996: Cool skin and warm layer effects on the sea surface temperature. *J. Geophys. Res.*, 101, 1295-1308.
- Fairall, C. W., E. F. Bradley, J. E. Hare, A. A. Grachev, and J. B. Edson, 2003: Bulk parameterization of air-sea fluxes: Updates and verification for the COARE algorithm. *J. Clim.*, 16, 571-591.
- Zeng, X.B., and A. Beljaars, 2005: A prognostic scheme of sea surface skin temperature for modeling and data assimilation. *Geophys. Res. Lett.*, 32, L14605.

Development of an Actuator for Ambient to Cryo Application

Karen Menzel*, Hans Jürgen Jung* and Jörg Schmidt**

Abstract

During the qualification campaign of the NIRSpec Instrument Mechanism, the actuator could not achieve the expected life time which was extended during the development phase. The initial design could not be adapted to the requested number of revolutions during that phase.

Consequently the actuator needed to be modified such that the function of the mechanism would not be endangered and thus the overall function of the NIRSpec instrument. The modification included the change of the overall actuator design - internal dimensions, tolerances, materials, lubrication and assembly process - while keeping the interface to the mechanism, mass, and function.

The lessons learned from the inspection of the failed actuator have been implemented in order to ensure the development and qualification success. The initially available time for this activity was in the range of 6 months to meet the overall program schedule.

Introduction

The actuator consists of a three-stage gearbox flanged to a stepper motor. A lever connected to the actuator by an eccentric mechanism moves the upper sled of the Refocusing Mechanism Assembly (RMA), an optical NIRSpec subunit carrying highly sensitive mirrors (see Figure 1).

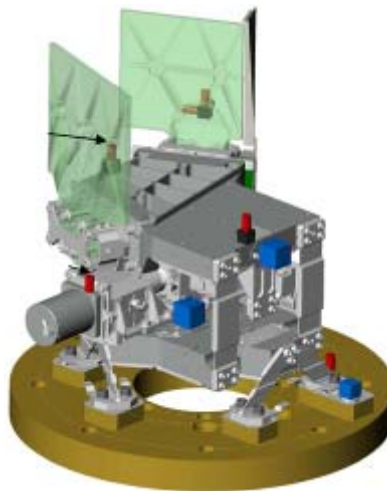


Figure 1: Refocusing Mechanism Assembly

The high non-operational temperature range of 296K as well as the low operational temperature of 30K requires a special design considering the great thermal expansions between 27K and 323K as well as a proper material selection that deals with the change of mechanical properties at cryogenic temperatures. Both the new material concept and the molybdenum disulfide (MoS_2) lubrication coating confronted the engineers with unexpected effects

* EADS Astrium GmbH Satellites, Friedrichshafen, Germany

** PHYTRON-Elektronik GmbH, Gröbenzell, Germany

In order to keep the development risk (both technical and regarding the schedule) low, two different breadboard models and one Qualification Model have been built and tested; two Flight Models and one Flight Spare will be delivered to the customer.

Key Equipment Design and Performance Requirements

The Refocusing Mechanism of the NIRSpec instrument provides the focusing function of the instrument by means of two corner mirrors changing the optical path length by movement of the mirrors.

Three titanium blades guide the RMA upper sled, which is driven by an eccentric drive requiring a maximum torque of about 0.55 Nm. Considering ECSS margins, the actuator has to generate a worst case torque of 1.21 Nm at ambient and 1.4 Nm at 30K driven with a rated current of 120 mA. This is realized by a stepper motor attached to a planetary gear with a gear ratio of 184:1 distributed to 3 stages.

The most important requirement is the large operational temperature range from 30K to 323K. The observations at the first actuator demonstrate the high importance of both the selection of a proper dry lubrication as well as a CTE-consistent design ensuring constant tolerances within the operational temperatures for both the bearings and gears.

According to the expected in-orbit cycles as well as the Flight Model test campaign, the Qualification Model has to be loaded in different cycles from the Midstroke Position resulting in a total of about 400,000 motor revolutions (including ECSS margins) without significant performance reduction. As learned from the first actuator, special attention has to be paid to the metal-to-metal contact due to coating wear between sliding parts after life time that has to be prevented in any case. Therefore, a redundant lubrication design should be considered, especially taking into account the RMA being a Single Failure Object; that means a breakdown of the subunit results in the inability to re-focus the NIRSpec instrument.

The actuator's operation in an environment close to contamination critical optical equipment rules out lubrication systems with particulate or molecular contamination but requires solid lubrication.

Initial Design of First Actuator and Lessons Learned

The first RMA actuator consisted of a material mix of six different sorts of steel with an estimated coefficient of thermal expansion (CTE) at 30K varying between 7.5×10^{-6} 1/K (ball bearings) and 15×10^{-6} 1/K (gearbox housing). This design was based on the experiences in gearbox development for usual applications – every single material has its specific strength playing on the individual function. But this cryogenic application cannot be called usual and different strategies have to be pursued.

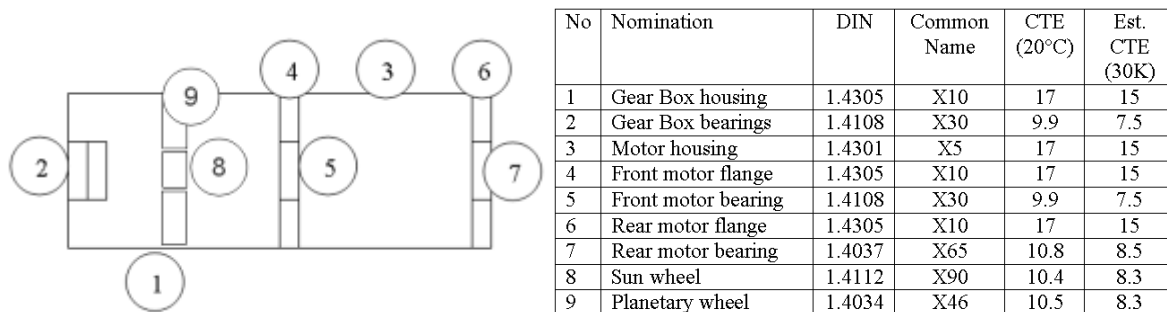


Figure 2: Material concept of first actuator

The shrinking at cryo is likely to have caused increased friction and therefore affected the life-time significantly. The lubricant used, Diconite, showed significant signs of abrasion after life test (about 330,000 motor revolutions) resulting in metal-to-metal contact as well as a major increase in necessary current; according to ECSS, a clear failure of life test.



Figure 3: Lubrication failure of first actuator after life test¹

Motor current measurements during the life test demonstrated that the actuator lubrication would have survived the nominal life time but due to life time extension, the results as described above have been obtained.

Similar actuators have been successfully used in ground-based cryo applications, but in areas where an exchange of a failed actuator can be performed at any time.

Design of the New Actuator

Figure 4 represents the new actuator in cross section, the main design was kept in general but the rear motor bearing was substituted by larger duplex bearings. The rotor axial pre-load spring was moved from the front duplex to the rear bearing. Ideally the front duplex bearings of the motor should have been arranged in 0-orientation to allow a limited rotation of the rotor axis (iso-static support conditions). Due to assembly constraints, an X-arrangement had to be selected in combination with an increased play of the rotor axis rear bearing. The planetary gear with three stages still has a gear ratio of 184:1.

¹ Visible corrosion results from the exposure of the blank metal to air after disassembly of the actuator.

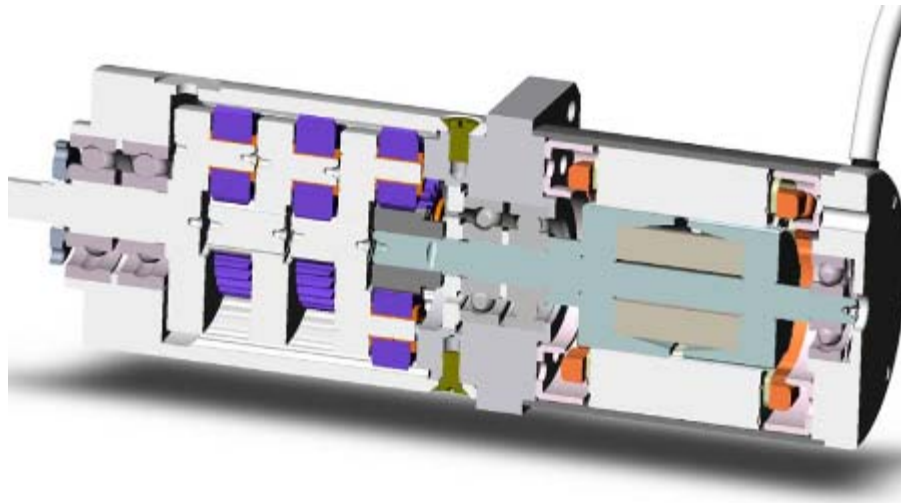


Figure 4: New Design RMA Actuator

The material concept was changed significantly to a CTE-consistent design as increased friction and raised bearing loads are supposed to be at least part of the reason for the first actuator's failure.

As Figure 5 illustrates, all motor and gearbox parts except the screws are manufactured of either hardened Cronidur® (X30) or titanium, the higher CTE of the screws only results in behavior comparable to extension bolts, and the machining of well known material for these critical functional components minimizes risks.

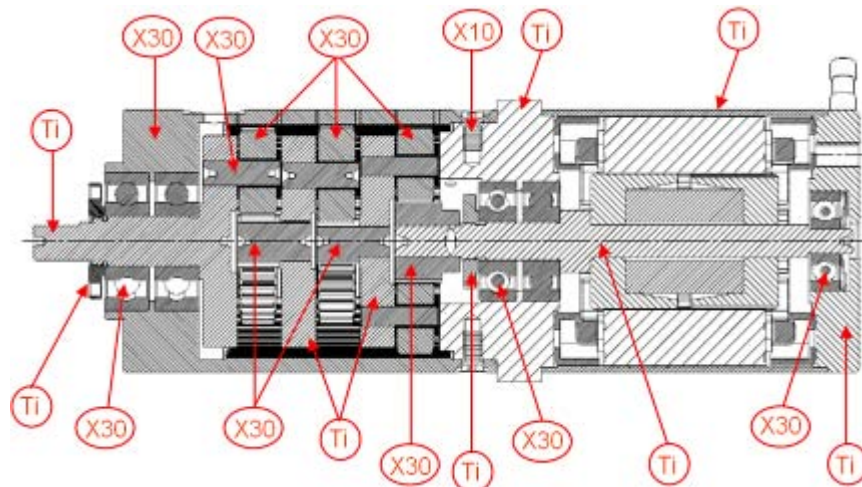


Figure 5: New Material Concept

Coating for Solid Lubrication

After the failure of the Diconite coating during life test, a solid lubricant concept had to be selected that is well known for space applications due to the short time frame of development. Sputtered molybdenum disulphide (MoS_2) seemed to be the most suitable lubricant as it has proven its reliability in numerous space applications. In order to have a backup solution during the development program, a lead lubricated breadboard model was set up, tested and compared to the MoS_2 -coated model before starting the Qualification program - this development approach is explained later on.

Plain Bearing Bushings

Sputtered MoS₂ is well known as a solid lubricant for ball bearings where the predominant relative movement is a combination of sliding and rolling friction. However, this experience cannot be found in a gearbox lubrication application. The planetary wheels are rotating around the pins pressed into the planet carriers. This journal bearing was one of the critical areas where the Dicronite coating wore off. Therefore a redundancy was requested for this function. Plain bearing bushings made of plastics have been found to fulfill this requirement for increased safety against abrasion. In case of local lubrication failure these bushings fulfill journal bearing functions and prevent direct metal to metal contact.

The bushings were tolerance such that they shrink onto the planet axis in cryo in order to gain a defined sliding surface. That requires a small low-temperature embrittlement at temperatures down to -246°C, relatively low CTE and good sliding properties in cryo, all not self-evident for organic plastics.

Different materials have been considered to be implemented in this application:

- Vespel SP1 / Vespel SP3. Vespel is a well known plastic material used in space applications; type SP3 is self-lubricating by containing small particles of MoS₂ while SP1 represents the unfilled material.
- Copper Metal Matrix Composite (Cu-MMC). The self-lubricated Cu-MMC has been developed by Austrian Research Centers for use in tribological sliding contacts under vacuum. It is based on copper matrix with inclusions of solid-lubricant particles and one of its highest advantages compared to plastics is its low CTE.
- Victrex PEEK 450G is supposed to be applicable in particular for cryogenic applications
- Torlon 4203 PAI stands out due to its high ductility – even at cryogenic temperatures
- Sintimid 15M / 30M is a sintered polyimide designed for cryogenic applications and filled with either 15% MoS₂ or 30%, respectively.
- PGM-HT contains of PTFE filled with glass fibers (15%) and MoS₂ particles (5%) and is often used for ball bearing cages

Bushings have been manufactured of all the materials as well as sliding samples for friction coefficient comparison. Friction tests under ambient in combination with MoS₂ powder should give a first impression of the tribological behavior. While Vespel SP1, Victrex and Torlon showed a good machinability, Sintimid, Cu-MMC and Vespel SP3 were very brittle during manufacturing (the higher the filling percentage or the bigger the particles, the worse was the machinability) and some of the bushings broke during machining. It turned out that filled material is not suitable for this application as the marginal wall thickness and the particle size are in the same range.

The bushings were assembled onto the planet axes and exposed to a liquid nitrogen dip test. Sintimid bushings cracked or indeed broke during the test and therefore failed, Victrex material was undamaged in principle but showed slight white marks after removal of the bushings that are suspected to be material degradations.

Based on the experiences with Vespel in an Astrium space application, this material has been selected for the FM1 model but Torlon has been considered to be implemented in one of the breadboard models in order to allocate a backup solution.

Development Concept and Success-Oriented Approach

A success-oriented approach has been chosen due to programmatic reasons: the FM1 was produced and tested with the design described above without the qualification program having started yet. In order to gain confidence, two breadboard models, so called Pre-Qualification Models, have been set up. As every stage of the planetary gear has three (1st stage four, respectively) planet axes that are equally loaded, different bushings could be assembled and their behavior during life test can be compared.

Pre-QM1 is MoS₂ lubricated and contains bushings of Vespel SP1, Torlon and planet axes without bushings according to Figure 6. Pre-QM2 is lead lubricated with bushings of lead bronze assembled or no bushings, respectively (Figure 7). If no bushing is assembled on one of the planet axes, a distance ring is necessary to prevent the appropriate planet gear from moving along the axis.

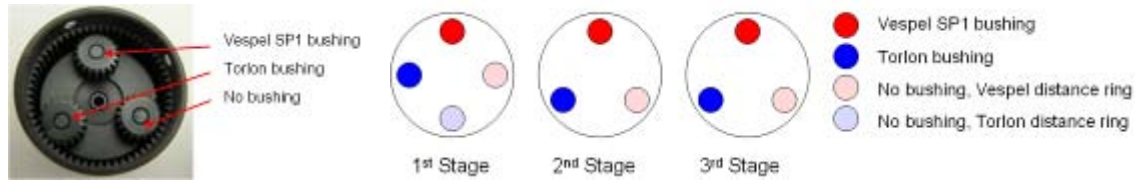


Figure 6: Pre-QM1 design (MoS₂ lubricated)

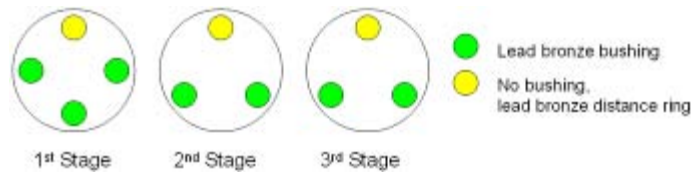


Figure 7: Pre-QM2 design (Lead lubricated)

These breadboard models have been manufactured first and the FM1 production has been started during their test campaign as displayed in Figure 8. Indeed the FM1 has been assembled into the subunit at a time the actuator has not been fully qualified – as the Pre-QM1 and FM1 are not assembled completely identical and the Pre-QM life test was in some ways simplified but equivalent at the best.

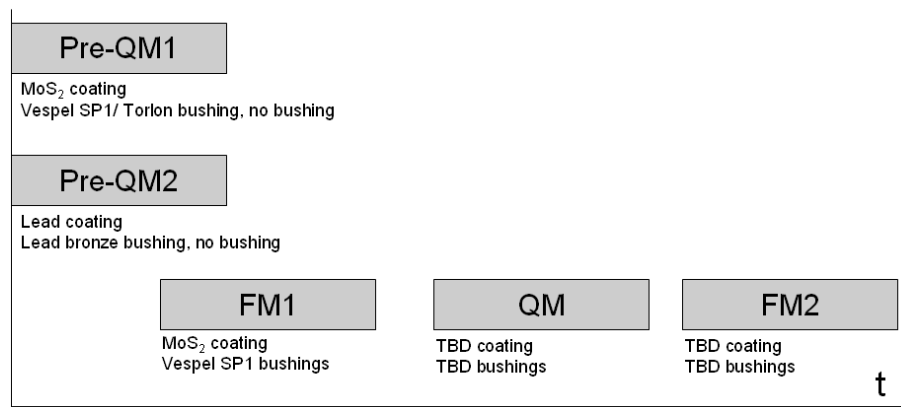


Figure 8: Development concept and success oriented approach

Life Test Pre-QMs

As the Pre-QMs had to be life tested without being integrated into the RMA, an equivalent test set-up had to be designed in order to load the actuators correctly.

Springs connected to a disc (Figure 9) load the actuators with the torque corresponding to the load the real blades are generating in the RMA mechanism. Figure 9 illustrates that the maximum torque at 120° from launch position and the load represented by the spring set-up is very accurate.

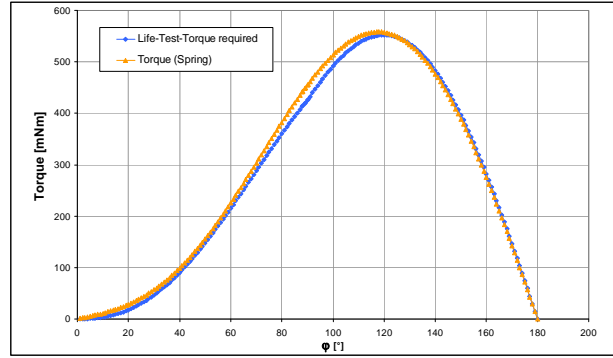
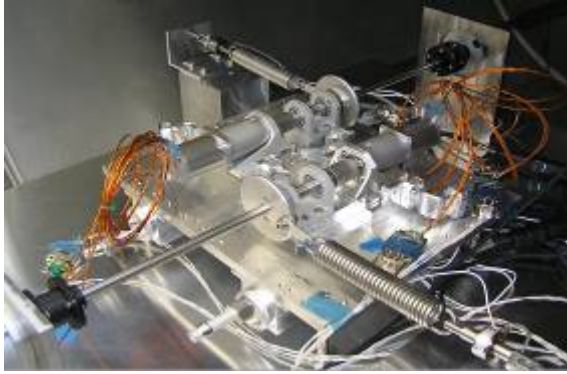


Figure 9: Pre-QM Life Test (left), Load application during life test by spring assembly (right)

The cryogenic temperature during Pre-QM life test was not 30K (liquid helium) but 80K (liquid nitrogen) due to facility reasons. This temperature is justified by the fact that neither the shrinking nor the change in material properties between these two temperatures is high compared to their absolute values.

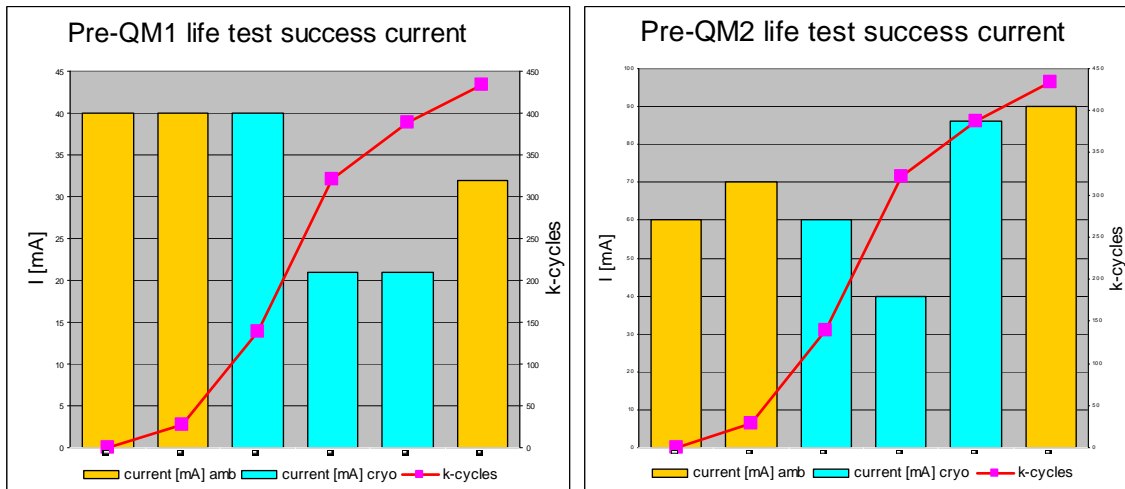


Figure 10: Results of Pre-QM life test

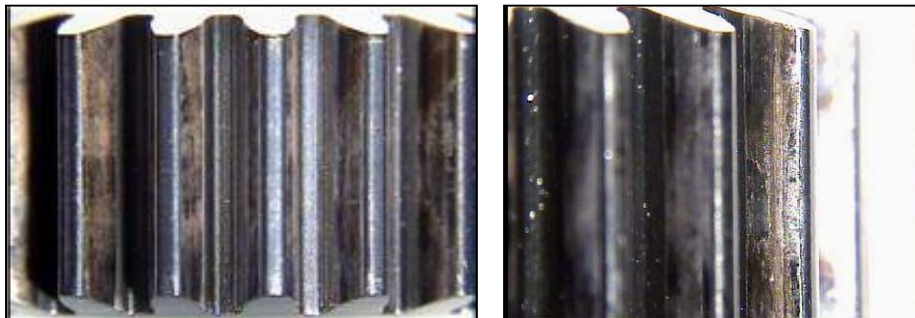


Figure 11: MoS₂ Gearbox inspection after life test

The expected life time of the RMA actuator is about 400,000 motor revolutions including ECSS margins. As Figure 10 illustrates, in the case of Pre-QM1 the so called success current - indicating the friction - does decrease during life time up to the end of life test at about 430,000 motor revolutions. The MoS₂ coating seems to be properly run in at this time. Lead coated Pre-QM2 showed some degradation starting between 320,000 and 380,000 motor revolutions, but is still within the ECSS success criteria at end of

life. The detailed visual inspection of the bushings (Figure 12 and Figure 13) did not show significant differences in abrasion on bushings made of Vespel SP1 and Torlon.



Figure 12: Pre-QM1 Vespel SP1 Bushing and Distance Washer after life test



Figure 13: Pre-QM1 Torlon Bushing and Distance Washer after life test

These test results provide high confidence in the selected material combination. Flakes of coating have been delaminated during vibration (this issue is explained later in detail) from gear teeth on planets, suns and hollow wheel. This damage did not affect the gear-box's performance, the surfaces look smooth and properly run in after life test (Figure 11) and XRF measurement at ESTL revealed a remaining MoS_2 layer of at least 0.14 microns.

The visual inspection of the lead-coated Pre-QM2 gearbox revealed as well a good condition with no evidence of metallic wear of the steel surfaces. XRF measurements confirmed that lead remained on the gear teeth but that in several areas it was extremely thin. Examination of the thickness values show that in all but one case the minimum thickness was less than $0.1 \mu\text{m}$, being as low as $0.03 \mu\text{m}$ in one case. However, it should be stressed that very little lead is required – particularly on polished steel surfaces - to provide effective lubrication.



Figure 14: Lead-coated gearbox and lead-bronze bushing after life test

As with the MoS_2 -lubricated gears, the wear of the lead coatings was uneven across the teeth. This is illustrated in Figure 15 for a planetary gear from Stage 3 where it can be seen that the lead coating in the center of the tooth is virtually unworn whereas elsewhere wear of the lubricant has clearly taken place.

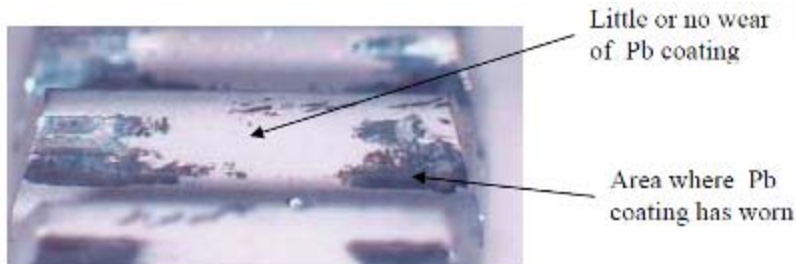


Figure 15: Uneven distribution of remaining lead coating on the planet teeth

It was also apparent that lead had transferred during tooth-to-tooth contact leaving patches where the thickness of the lead was greater than the thickness of the coating as initially applied. This effect accounts for the relatively large patch width (>2 mm) occasionally observed. It should be noted that lead transfers more efficiently than MoS₂ – a fact consistent with the observation that no anomalously high coating thicknesses were observed for the MoS₂-lubricated gears.

Technical Difficulties and Challenges

Planet carriers and gearbox housing

The initial approach was a design containing some parts made of unhardened Cronidur®, namely the planet carriers and the gearbox housing. It is impossible to shrink-fit hardened pins onto hardened carriers and the risk of deformation due to hardening of the hollow wheel (→ ovalization) was supposed to be too high. But Cronidur® is not corrosion-resistant in the unhardened condition and therefore a substitution of the material or heat treatment had to be considered.



Figure 16: Failed pressing trial results

To replace the Cronidur® the planet carriers have been manufactured from titanium and extensive trials have been performed in order to identify the necessary oversize for press fit to transmit the required torque loading to the sun wheel on the one hand but not to exceed the ultimate strain of about 7% of titanium (Figure 16 and Figure 17). In the case of the gearbox housing, a material substitution has been widely discussed with many experts but the number of materials in the same CTE range of Cronidur® is very limited.



Figure 17: Passed pressing trial results with 40 μm oversize

Using titanium for the gearbox housing is out of the question as the gear supplier is not able to cut the internal gear from titanium. The steel 17-4PH has been considered to be an alternative but due to its sensitivity against stress corrosion cracking its usage would have required advanced fatigue analyses.

Sticking to the previous concepts still offers two opportunities: harden the entire gearbox housing (Figure 18 right) or manufacture a hollow wheel ring from Cronidur[®] (Figure 18 left), harden it and assemble it in an integrated design to a titanium housing (Figure 18 middle). Both methods have been tested; entire gearbox and hollow wheel ring have been hardened and 3D-measured afterwards with the following result: the hollow wheel was ovalized but the gearbox stayed stable!



Figure 18: Hollow wheel ring and integrated design vs. gearbox housing completely made of Cronidur[®]

Influence of surface quality on coating adhesion

As indicated previously, both Pre-QM1 and FM1 showed signs of coating delamination on the gear teeth of planets, sun wheel and gearbox housing after vibration test, which was detected during subsequent inspection (Figure 19). This finding raised two main questions:

1. Does a remaining layer of MoS₂ still exist on the gear teeth and is therefore the lubrication sufficient?
2. How can the generated particles be prevented from emerging from the gearbox and possibly contaminating optical equipment on the instrument?



Figure 19: Coating damage after vibration

Investigations at ESTL revealed a minimum MoS₂ layer of 0.14-micron thickness existing on the affected surfaces and the successful Pre-QM1 life tests supports the confidence in the coating quality. But nevertheless an investigation has been started in order to find out whether the chosen pre-treatment electropolishing and the defined surface roughness represent indeed the ideal parameters.

Samples have been manufactured with varying surface qualities between 0.1 micron and 0.5 micron as well as electropolished / not electropolished. The deflating conclusion of the pin-on-disc test following the

coating process: the surface roughness does not influence the quality of the coating adhesion significantly but the electropolishing treatment reduces the endurable revolutions in pin-to-disc test down to 20 to 30% of the un-electropolished samples.

Influence of proper run-in on friction / torque

Molybdenum disulphide is to an extremely high degree hygroscopic. While exposed to ambient atmosphere / humidity it absorbs water and binds it molecularly. Thereby the coating changes its microscopic structure and friction increases. This process is not completely reversible by drying MoS₂ in vacuum but mechanical pressure by performing a run-in has to be applied in order to get over this initial peak torque in the gearbox and ball bearings. However, evacuating throughout the weekend resulted in better torque value instead of evacuating only overnight; a proper run-in even increased the torque margins.

This effect is not unknown in the technical world but it turned out that many experts are of very different opinion how to deal with an MoS₂-coated actuator and that good communication with all suppliers was necessary in order to sensitize every employee to this issue.

Conclusions and Lessons Learned

The first flight model with the MoS₂ dry lubrication and Vespel SP1 bushing has successfully been implemented into the Flight Model RMA. The RMA has performed its acceptance program and is currently mounted onto the NIRSpec optical bench. Though the full qualification program at the end of 2009 is not yet finished we are confident of having supplied an actuator that will safely provide the required functionality throughout the lifetime of the NIRSpec instrument.

During the very short time frame of the execution of this development program (7 months), we have learned a lot both about development programmatic as well as about material and lubrication technologies. Some key lessons learned shall be outlined here - some of them not really new

Programmatic lesson learned:

1. Do not change too many technical parameters at the same time; it may be impossible to identify the reason for both improvement and deterioration!
2. Postponing tests and planning to combine them with other tests due to programmatic reasons can become a shortsighted decision. Both technical and programmatic reasons might eliminate the possibility to perform the particular test at a later time. Certain measurement results can be generated only at one specific time and once this time frame is closed, the opportunity for measurement might be missed forever.
3. Ensure that your suppliers are fully aware about the full story and their contribution to the development success. This is a key success factor to ensure that the suppliers provide their utmost technical capabilities and are extremely flexible on necessary modification which are normal in such a development program. Access to the supplier's expertise can only be acquired if they feel as part of the team and do understand what the final application of their contributed part is. As an example Gysin (gear box) should be mentioned as they succeeded to provide a gear teeth surface quality far beyond their standard industrial needs by proper setting of the standard machinery.
4. A success-oriented approach initially has the charm that it could save time and money but always contains a high risk of failure with doubling the cost at the end as the work has to be done twice. We must confess that we had good luck that the selected combination of materials for the FM1 was the right choice as this combination was found to be the best as result of the pre-QM life test. In many other development programs similar results could not be achieved.

Technical lessons learned:

1. MoS₂ lubrication might be seen as a state of the art dry lubrication. We learned that the processes applied to the materials prior to coating do have a relevant influence on the sputtering process. Even the sequence of processes seems to be of importance. The initial loss of sections of dry lubricant on

the gear wheels as observed after vibration testing (see Figure 19) is still not understood and shall be further investigated (see last chapter "Outlook").

2. When we initially saw those areas of lubrication loss on the gear wheels (see Figure 11) we were sure that this was the end of the story. Thanks to ESTL, who had great confidence in their sputtering process and was confident according to measurements performed to still have sufficient MoS₂ on the teeth to survive the life test, we decided to continue. The life test was a success. Those observed areas increased but the residual MoS₂ layer survived. It is the intention to continue the life test on the pre-QM (see last chapter "Outlook")
3. Witness samples for process control for any kind of surface layer generation should be of the same material and should have been exposed to the same processes and sequence of processes as the units to be treated. In some cases where geometry has also an impact on the surface treatment, the witness sample should have also a similar geometry.
4. Keeping MoS₂ surfaces either in a dry environment or ideally in vacuum or in constant N₂ atmosphere is state of the art knowledge to prevent moisture absorption of the MoS₂. Permanent purging of mechanism elements like bearings is one of the methods applied if the outer environment is not adequate. In the vicinity of optical surfaces at temperatures below those of the mechanism (cold traps), purging or even open venting holes might allow particles from the MoS₂ to escape from the mechanism and to pollute the optical surfaces. As seen from the life test, particle generation cannot be avoided. Consequently the purging process, purging direction and venting hole definition needs to be properly planned at the beginning of the project to prevent pollution effects.

Outlook

In a very short time frame of 7 months a dry-lubricated actuator for ambient and cryo application was developed with a complete new combination of materials. Though the development was a success, some questions are still open and shall be further investigated.

As outlined in the lessons learned, the material treatment process does have an important impact on the sputtering process success. The observed partial loss of lubricant on the gear wheels is still not understood. From the pin-on-disc test results, we do have clear indications that the electro-polishing is of negative influence but the physical or chemical nature of such an effect is still not completely understood. Other effects like the order of hardening and polishing might be also of influence. These effects need to be assessed also for different standard gear box or bearing materials. Astrium wants to initiate a program with ESA, ESTL and further technical surface coating experts to further investigate this issue.

Though we did initially lose some lubricant on the gear surfaces, they survived the life test and it would be of interest to determine the final life of such surfaces in the gear box. So Astrium will continue the life test on the pre-qualification models (both the MoS₂ and the lead lubricated ones). Life test stop criteria will be a certain current threshold (still TBD) which would be equivalent to a certain increase of the friction torque of the unit (e.g., 50%). A dedicated inspection program of the units will follow the life test and results shall be reported at the next ESMATS to be held at Astrium premises in Friedrichshafen in September 2011.

Acknowledgment

Astrium would like to thank their partners in this development program for their utmost efforts they provided in terms of technical quality, adherence to the very tight schedule and their expertise support at any phase of this project.

- Phytron GmbH - motor development and the overall assembly and functional testing
- Gysin AG - gear box components
- GRW - bearing manufacturing and Cronidur[®] hardening
- ESR - MoS₂ and lead lubrication

Development and Acceptance Testing of the Dual Wheel Mechanism for the Tunable Filter Imager Cryogenic Instrument on the JWST

Martin Leckie* and Zakir Ahmad

Abstract

The James Webb Space Telescope (JWST) will carry four scientific instruments, one of which is the Tunable Filter Imager (TFI), which is an instrument within the Fine Guidance Sensor. The Dual Wheel (DW) mechanism is being designed, built and tested by COM DEV Ltd. under contract from the Canadian Space Agency. The DW mechanism includes a pupil wheel (PW) holding seven coronagraphic masks and two calibration elements and a filter wheel (FW) holding nine blocking filters.

The DW mechanism must operate at both room temperature and at 35K. Successful operation at 35K comprises positioning each optical element with the required repeatability, for several thousand occasions over the five year mission.

The paper discusses the results of testing geared motors and bearings at the cryogenic temperature. In particular bearing retainer design and PGM-HT material, the effects of temperature gradients across bearings and the problems associated with cooling mechanisms down to cryogenic temperatures. The results of additional bearing tests are described that were employed to investigate an abnormally high initial torque experienced at cryogenic temperatures. The findings of these tests, was that the bearing retainer and the ball/race system could be adversely affected by the large temperature change from room temperature to cryogenic temperature and also the temperature gradient across the bearing. The DW mechanism is now performing successfully at both room temperature and at cryogenic temperature. The life testing of the mechanism is expected to be completed in the first quarter of 2010.

Introduction

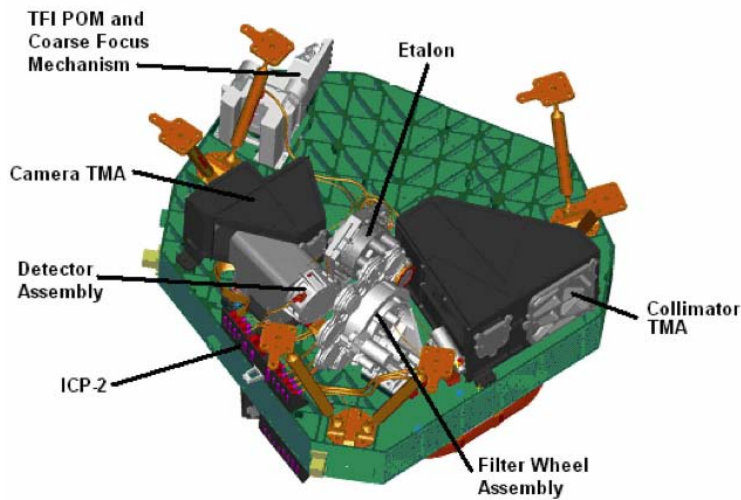
The TFI, which includes the DW mechanism, is shown in Figure 1 (labelled "Filter Wheel Assembly"). The TFI has been designed to provide infra-red narrow band imaging in the 1.5 to 5 micrometer wavelength range. In order to make these observations, it has stringent temperature requirements. The TFI temperature is approximately 35K for JWST science observations.

The role of the DW mechanism is to place optical elements into the optical path, in any combination of corona graphic mask and blocking filter. The optical elements must be placed accurately and in a highly repeatable manner.

The paper discusses the following topics. First, the design of the DW is described in some detail so that the function of each component is clarified for the reader. Secondly, the test results of component parts and the DW assembly are described in more detail.

The geared motor test results are described first and the bearing tests second. The bearing tests revealed an abnormally high start up torque, at cryogenic temperatures, which led to an in depth investigation of this issue.

* COM DEV Ltd., Cambridge, Ontario, Canada



TFI Side

Figure 1. Fine Guidance Sensor – TFI Side

The high initial start up torque at 35K of the bearings was attributed to three causes. The first cause was mitigated by a retainer design change. The second and third causes have been investigated and understood, such that confidence in the flight design is high. The results of the investigation are presented, together with the lessons learned from the problem. Finally, the results of the flight model testing are discussed.

Design Description

A general arrangement of the DW mechanism is shown in Figure 2. The main components are the pupil and filter wheels, bearings, gears, static hub, motor/resolver support plate and the support bracket. The DW mechanism also includes geared stepper motors, resolvers and variable reluctance sensors. A cross section of the DW mechanism is shown in Figure 3. Each wheel (approximately 280-mm diameter) rotates on a duplex pair of angular contact preloaded bearings.

A stepper motor is used to drive each wheel, through a reduction gear train. The stepper motor has been geared down to enable the positional accuracy requirements for each optical element to be met. A resolver provides feedback to confirm that each wheel is in the correct position. Flight software uses the resolver reading to calculate a position adjustment to bring the wheels to the correct position.

All moving parts are lubricated with MoS₂ dry lubricant to be compatible with the cryogenic temperature requirements. The wheels (the bearing housing) and the hub (the bearing shaft) were machined from titanium Ti-6Al-4V. The selection of titanium alloy was dictated by a requirement for low mass and also to closely match the coefficient of thermal expansion (CTE) of the 440C stainless steel bearings.

The bearings were manufactured by ADR of France, with the MoS₂ dry lubricants and the PGM-HT retainer added by ESR Technology in the UK. The bearings are located at the center of gravity of each wheel in order to reduce the bending moments acting on the bearings during launch. The bearing size, ball diameter, and preload are designed to balance the critical requirements – high enough preload to meet the stiffness requirement, but still low enough to allow low running torques and stresses.

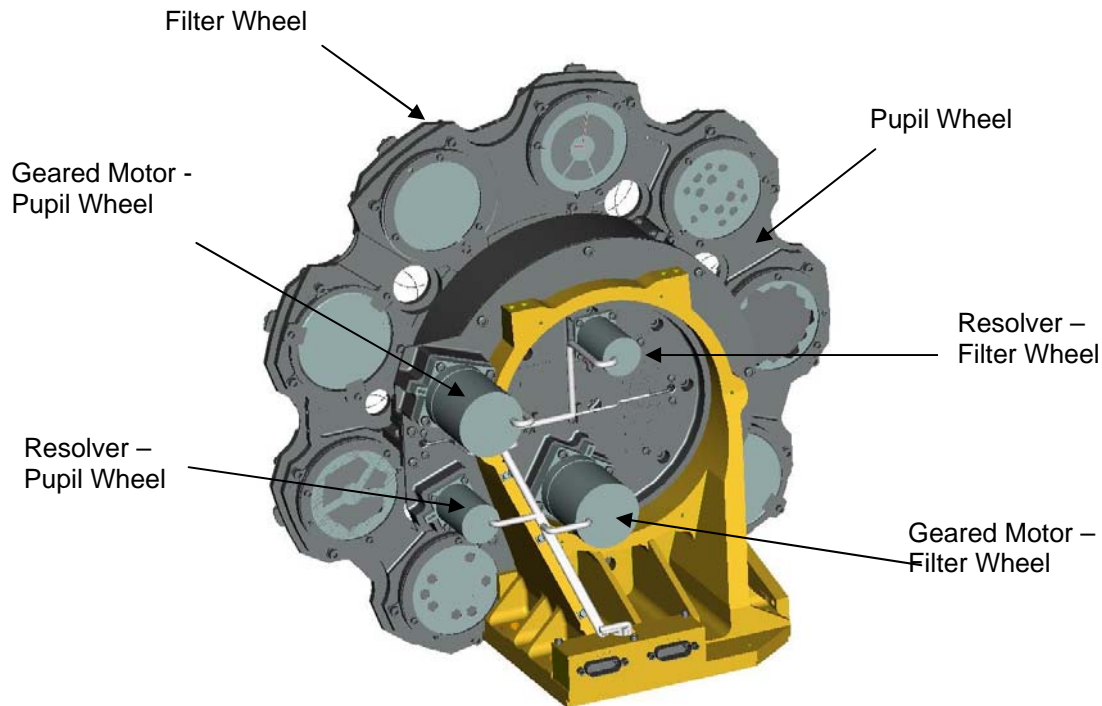


Figure 2. Dual Wheel Mechanism – General Arrangement

Each bearing is secured in place with clamping nuts. Each nut includes a flexure, which is preloaded by the action of torquing the nuts into place. The flexures maintain the preload on the bearings, despite the slight difference in the coefficient of thermal expansion between the 440C bearings and titanium housings. The PW bearing installation is shown in detail in Figure 4. The FW bearing installation is similar.

The bearing “fits” to the wheel and hub are sized so that a line on line to a clearance fit is obtained at the mechanism operating temperature range of 35K. The selection of a small clearance fit at the cryogenic temperature, necessitates that an interference fit between the bearings and shafts exist at room temperature, at the outer diameter. The use of a clearance fit at the cryogenic temperatures is to eliminate bearing race distortion, which could cause variations in bearing preload. The bearing fits were verified using a bread board model (BBM) filter wheel mechanism, tested at 35K. The BBM also served to determine bearing torque at 35 K and to determine a suitable baseline for the motor drive current.

The PW and the FW wheel are each rotated via a pinion and ring gear. The pinion gears are made from stainless steel 13-8 PH and the ring gears are made from stainless steel 17-4 PH. Both gears are lubricated with MoS₂ dry lubricant. The gear tooth size was evaluated using AGMA standards for tooth contact stress and tooth bending stress.

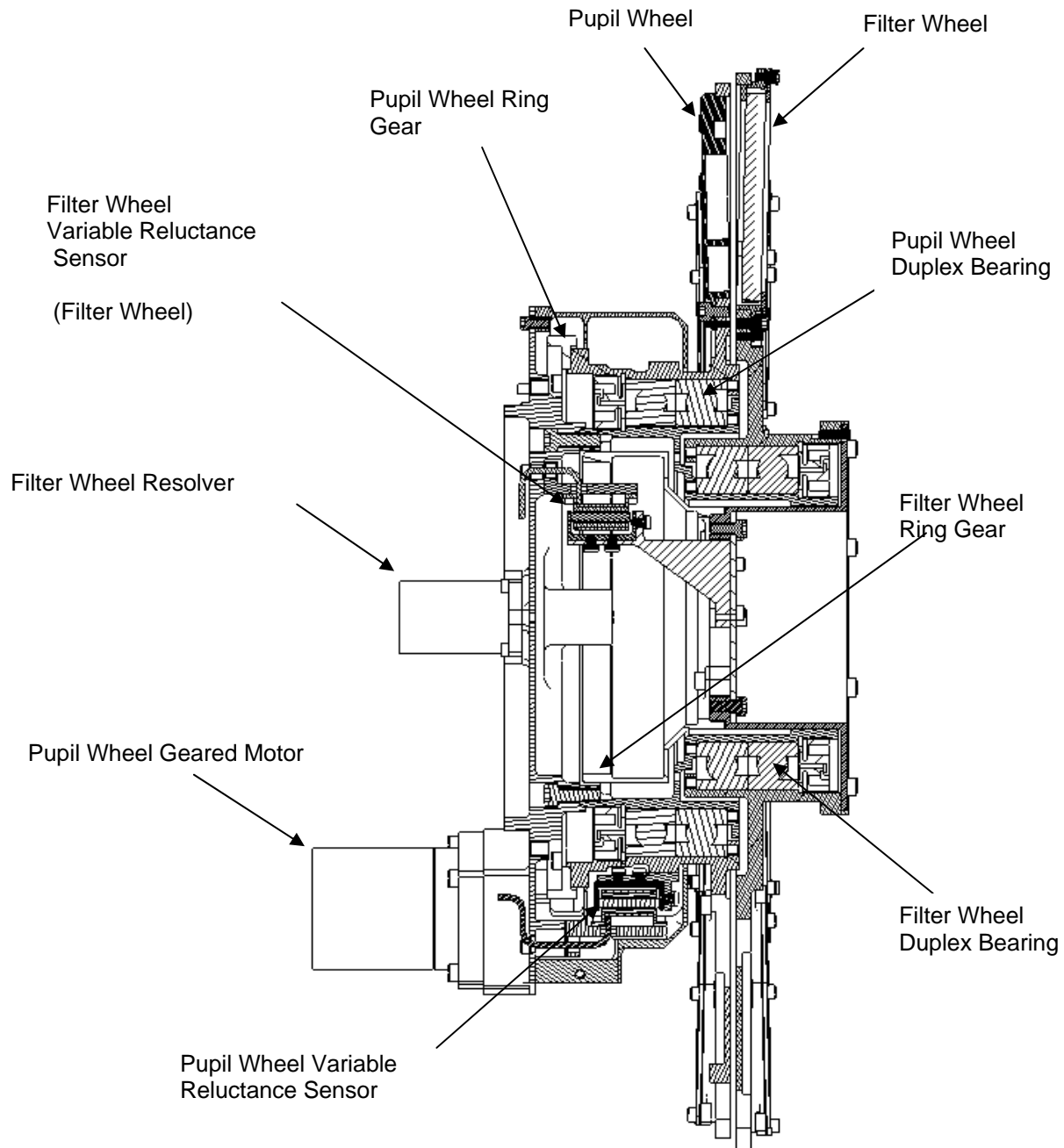


Figure 3. Dual Wheel Mechanism – Cross Section

The gear ratios were selected to give the desired size of granularity of movement of the PW and FW wheel and to reduce same tooth encounters between the pinion gear teeth and the ring gear teeth.

Each wheel is driven by a geared motor. The geared motor drives a pinion gear, which meshes with each ring gear. The geared motor was procured from CDA Intercorp and is comprised of an 8 pole, 3 phase stepper motor, having a 15° step angle and a planetary gear stage having a ratio of 9.6:1. The geared motor bearings and planetary gears were lubricated with Ball Aerospace MoS₂ lubricant.

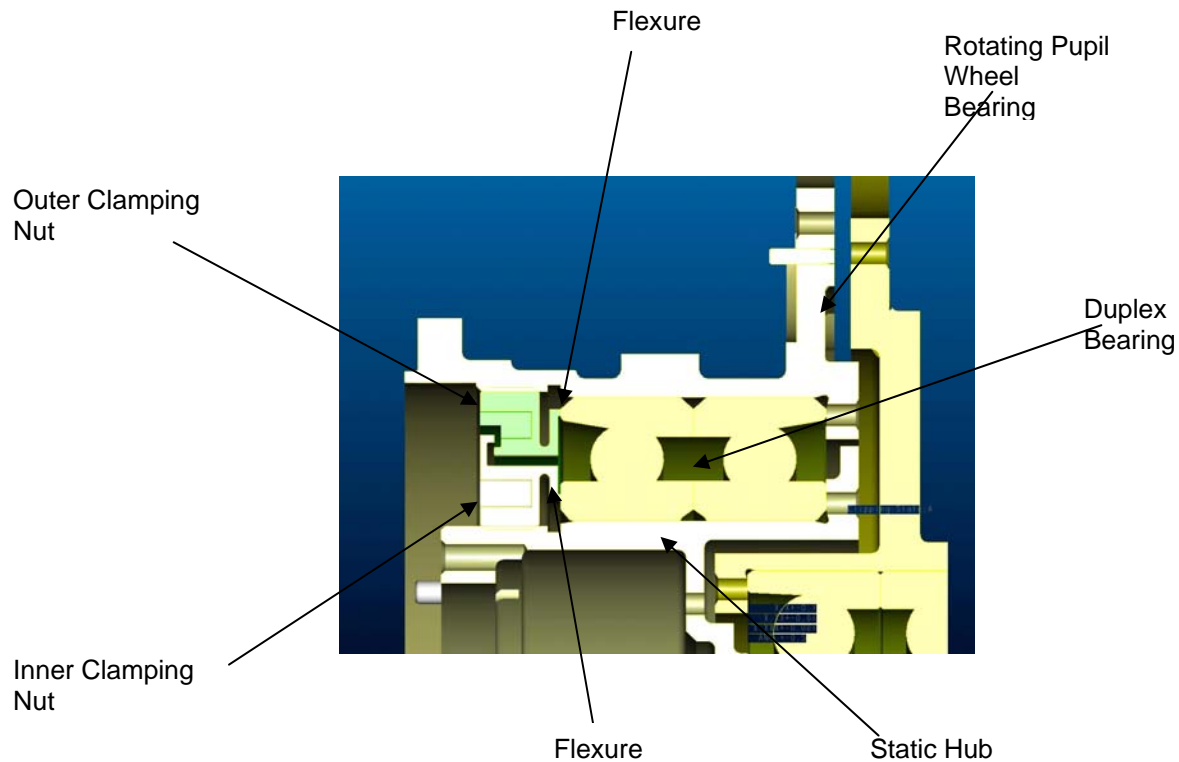


Figure 4. Pupil Wheel Bearing Installation

The geared motors support wheel rotational speeds of 1.5 RPM. The geared motor sizing was based on providing sufficient torque margin when taking into account the resistive torques, due to accelerating the rotational inertia of the wheels and the resistive torque of the bearings. The appropriate factors were applied to the resistive torques, in order to calculate torque margins. The specified output torque of the geared motor was based upon previous measured performance of geared motors completed by CDA Intercorp and the estimate of the resistive torques was based upon measurements of the BBM filter wheel bearing at cryogenic temperatures.

The DW mechanism design has to meet the positioning and repeatability requirement having considered the contributing errors. These errors include the variation in stepper motor step angle, geared motor backlash error, resolver error, ring / pinion gear backlash, tooth pitch variation, thermal distortion and component machining tolerances. Having analyzed the errors, the granularity of wheel motion (and hence gear ratios) were sized to be smaller than the required accuracy.

A resolver position sensor provides feedback to confirm that the wheel is in the proper position. An anti-backlash gear is used on the resolver output pinion to increase the accuracy of this gear train. Since the resolver is geared up by a factor of 9, the resolver turns 9 times for every rotation of the wheel. The resolver provides an absolute read-out, but pending a loss of memory due to a fault condition, the resolver would be unable to determine which 1/9th of a segment the wheel would be in. A reference signal is therefore provided to indicate a home position. The reference signal is provided by a variable reluctance sensor (VR sensor).

Geared Motor Testing – Lessons Learned

The actuation to rotate each wheel is provided by a geared motor. The geared motor is a combination of a three phase stepper motor (step size of 15 deg.) and a single stage planetary gear. The geared motor for the PW is shown in Figure 5.

The geared motor testing was first completed at room temperature. It was important to establish a baseline of the motor performance at room temperature before testing at cryogenic temperatures.

Any issues with the geared motor would have to be found before introducing the motor drive electronics. The motor drive electronics are a COM DEV design. The drive electronics cater to room temperature and cryogenic operation of the motor. This is achieved through a continuous real time measurement of motor winding resistance and a subsequent adjustment of voltage (through time modulation techniques).

The first round of room temperature testing yielded a pull in torque value of 17 N-cm versus a specified requirement of 23 N-cm. This was thought to be a simple shortfall in motor performance and certainly not a design problem. It was decided to proceed to cryogenic temperature testing. The testing at cryogenic temperatures was carried out in a cryogenic chamber together with a feed thru shaft out of the chamber coupled to a torque measurement machine.

The first test at 35K did not result in full rotation of the motor. The motor exhibited some stalling and an investigation was started through the material review board process. Considering the observations, the motor performance appeared normal at room temperature, but the performance at 35K was abnormal. The cause was immediately thought to be a deficiency in the motor and that the cryogenic environment must be causing more friction in the motor bearings and planetary gears.



Figure 5. Geared Motor – Pupil Wheel

The geared motor vendor (CDA Intercorp) was requested to use their own design of drive electronics with the geared motor tested again at cryogenic temperature. The material review board chose the motor “no load response rate” as the most appropriate data to obtain at cryogenic temperature. The “no load response rate” is the maximum speed that the motor can rotate at, in a stable manner, without any load. The “no load response rate” provides a good indication of the health of the geared motor. Higher friction in the geared motor would lead to clear change in the “no load response rate”.

At 35K with the vendor drive electronics, the geared motor was able to rotate at the same “no load response rate” that was obtained at room temperature. This finding proved that the geared motor was not suffering from increased friction at cryogenic temperatures. It was therefore concluded that in some way

the drive electronics were not providing the correct pulses to the motor. The fact that the motor had provided full rotation and a pull in torque value of at least 75% of the specified requirement, at room temperature, seemed to indicate that all was well with the drive electronics.

The first review of the drive electronics test data showed that the current, voltage and power being delivered to the motor at 35K were indeed correct. We expected that these parameters would in some way, be out of specification.

A more detailed and thorough review of the drive electronic motor pulses revealed a problem in the stepping sequence. The stepper motor operates using a six step sequence of closed and open circuits for the three windings. The sequence is provided to the motor by virtue of programming of an FPGA in the drive electronics. It was found that the sequence in the FPGA was actually making the motor step from position 1 to position 3 to position 5 and then to position 1 again. This did cause the motor to rotate, but with diminished torque and half the power. This caused the anomalous behavior at cryogenic temperature and the below specification pull in torque at room temperature. When the sequence was corrected and the motor was tested again at 35K, motor performance was excellent.

Several new technologies had been put into one test, dominated by a new motor design, and its new drive electronics; all operating at the cryogenic temperature environment. This fact made it very difficult to determine the root cause of the issue. The anomalous behavior was incorrectly attributed to the geared motor because the assumption that the drive electronics were correct had been established at room temperature. A month later the problem had been traced back to the stepping sequence in the drive electronics. Also, all of the motor test data gathered at ambient and cryogenic temperature had to be repeated. The lesson learned was that a test should not try to combine too many new technologies in the first test. A check of all items that could affect motor performance should be completed before assigning a cause to a problem.

Thanks go to our vendor, CDA Intercorp, for their timely assistance in trouble shooting this problem. In this case, it was very beneficial to have a "reference" set of drive electronics to expedite testing at the cryogenic temperatures.

Ball Bearing Testing

The PW and the FW wheel bearings are critical items for the dual wheel mechanism. For each mechanism, the torque ratio would in large part be determined by the torque exhibited by these bearings at cryogenic temperatures. An extensive test program was devised to determine bearing performance at cryogenic temperatures.

The design parameters of each bearing are shown in Table 1. A single bearing for the PW and the duplex pair bearing for the PW installed in the PW machining is shown in Figure 6.

It was decided early in the program that the initial bearing tests would be carried out with the bearings already installed in the wheel and hub assembly. It was originally thought to be highly desirable to test the bearings in their actual flight configuration and that "bearing only" tests would be un-necessary. This philosophy would later prove to be overly optimistic.

Table 1: Bearing Design Parameters

BEARING	I.D. (mm)	O.D. (mm)	RACE WIDTH (mm)	BALL DIAMETER (mm)	BALL COMPLEMENT	CONTACT PRESSURE ANGLE	PRELOAD (N)	RETAINER MATERIAL
Filter Wheel	65	90	13	7.94	25	25	712	PGM-HT
Pupil Wheel	100	125	13	7.14	34	25	712	PGM-HT

The cryogenic chamber test set up for the wheel / hub assembly is shown in Figure 7. Note that the cryogenic chamber has a cold plate surface, to which the device under test (DUT) is directly attached.

Each wheel/hub assembly was run-in for 100 revolutions CW and 100 revolutions CCW at room temperature. The torque of the bearings was then measured. Each bearing torque at room temperature was in the range of 8 to 12 N-cm. This was certainly acceptable and proved that the bearings had been successfully installed into the wheels. The next set of torque tests would be carried out at cryogenic temperature.

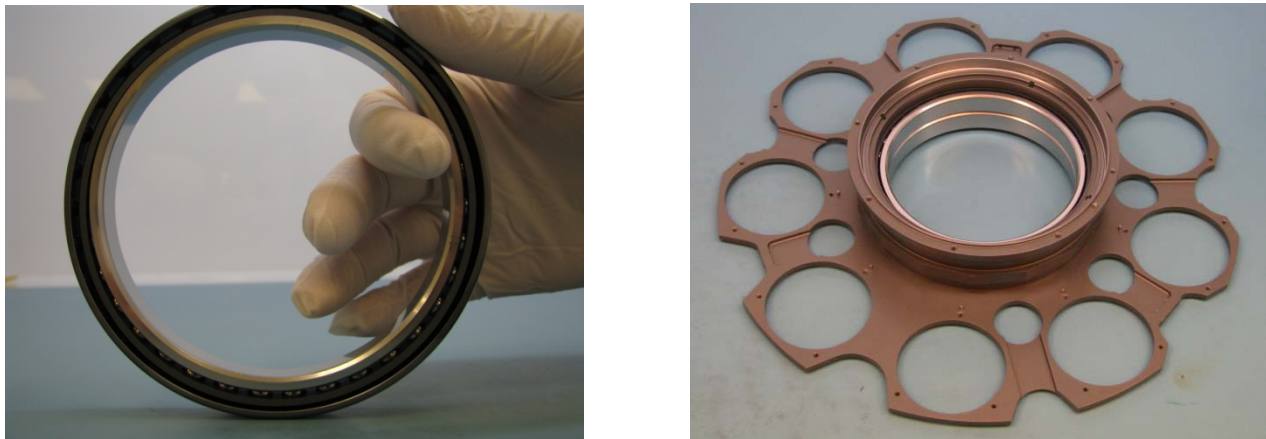


Figure 6. Single Pupil Wheel Bearing & Duplex Pair installed in Pupil Wheel Machining

The wheel/hub assembly was installed in the cryogenic chamber. The chamber was purged with dry N₂ gas for a period of 2 hours (this was the standard purging used for all cryogenic tests) and then a vacuum was drawn in the chamber. The DUT was then cooled down to 32K and a record was maintained of the wheel and hub temperature. It was noted that the wheels cooled at a much slower rate than the hub, leading to a 100K temperature gradient across the bearings.

The PW bearing (cryogenic) torque was measured first. The initial torque measurement was carried out with a hand held torque meter. The initial torque measurement was abnormally high at 202 N-cm. This result was unexpected and indicated that a problem with the bearing was occurring. An investigation of the problem was started and it was decided to continue rotation of the bearing to further characterize the problem. After 4 revolutions, the torque had dropped from 56 to 46 N-cm. After a further 100 revolutions the torque had reduced to 20 N-cm. After a total of 200 revolutions the torque had reduced to 6 N-cm.

The FW bearing (cryogenic) exhibited a similar problem, with an initial torque measurement of 196 N-cm. The behavior when further rotated was similar to the PW bearing, with the torque reducing to an acceptable value of 5 N-cm over the first 100 revolutions.

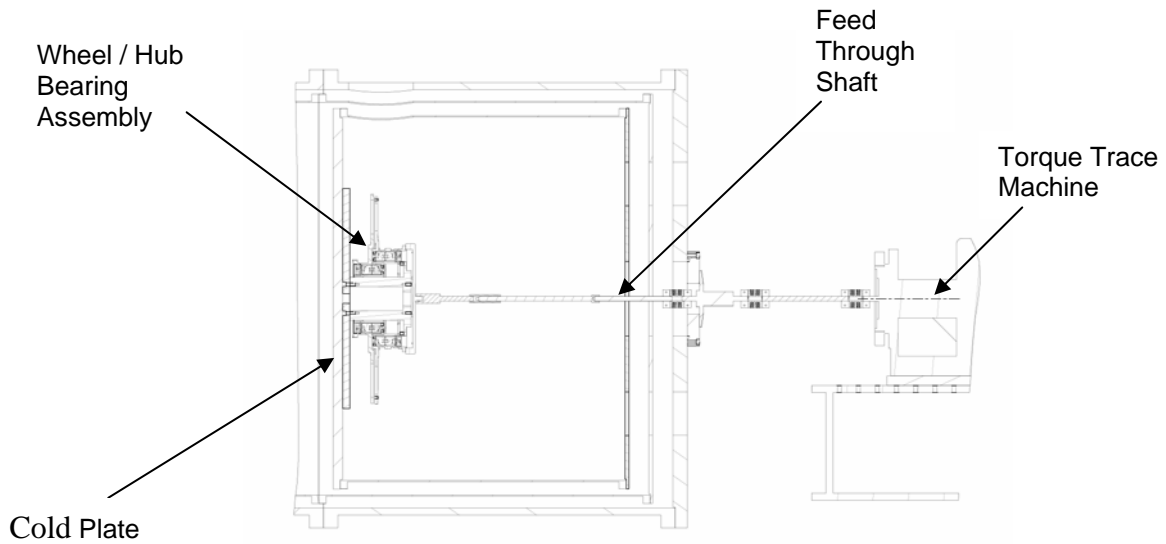


Figure 7. Wheel / Hub Assembly in the Cryogenic Chamber

The bearings were being impeded by something when initially rotated. Over the first four revolutions the torque reduced but was still very high. Eventually an acceptable value of torque (approx. 5 N-cm) was achieved on both bearings after 200 revolutions. The fact that the bearing torque at cryogenic temperature was similar to the ambient torque, after 200 revolutions was encouraging because it implied that the bearings were not permanently distorted by the wheel and hub at 35K. If they were permanently distorted, it did not seem credible that they would ever run well. It was decided to disassemble the wheel/hub assembly, to the extent possible, to make a visual inspection of the bearings. The visual inspection revealed particles of material in the form of flakes and small threads in the vicinity of the retainer and the races. The particle contamination in the bearing is shown in Figure 8.

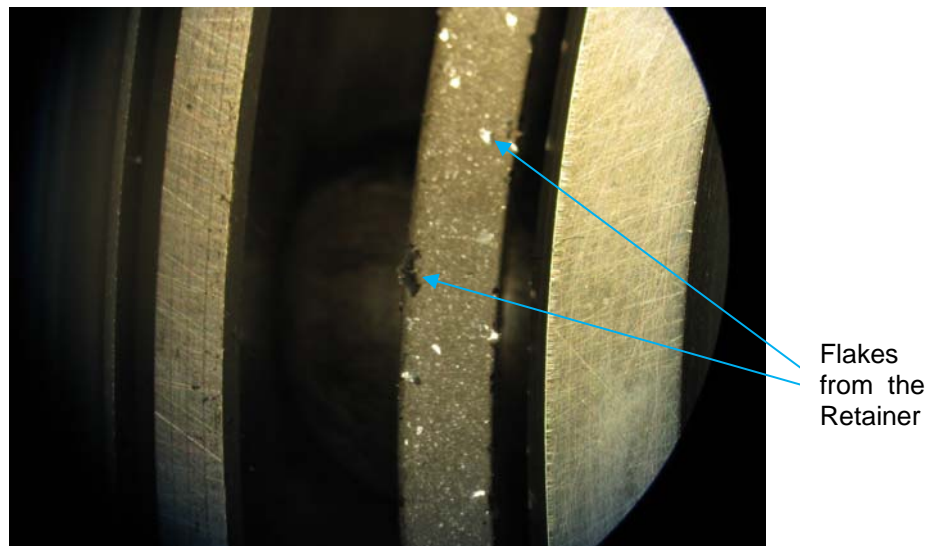


Figure 8. Wheel / Hub Assembly in the Cryogenic Chamber

The particles were identified (by chemical analysis) to be MoS₂ and PGM-HT. Therefore, it was concluded that the retainer was implicated in the problem. The retainer design was reviewed and a dimensional shrinkage analysis of the retainer and race was undertaken.

The retainer design for these bearings had to address two modes of operation. The first, being a floating retainer at room temperature and second, an inner race riding retainer at cryogenic temperature. The extreme temperature change, combined with the large CTE value of PGM-HT, means that the retainer would have only a small clearance from the inner race at cryogenic temperature.

Differential thermal contraction between the cages and the bearing races must be taken into account in the design since operational range is 295K – 35K, hence for this design the validity of CTE data is critical. When the retainer was originally designed, the CTE values used for calculating clearances at 35K was $52 \times 10^{-6} \text{ K}^{-1}$ for PGM-HT and $8 \times 10^{-6} \text{ K}^{-1}$ for 440C [1] over the temperature range of 295K – 35K. A review of more recent test data (provided by ESR Technology) revealed that the CTE of PGM-HT could vary from $80 \times 10^{-6} \text{ K}^{-1}$ at 295K to $60 \times 10^{-6} \text{ K}^{-1}$ at 125 K. No data existed below 125K, so CTE values for the temperature range of 125K to 35K were extrapolated from the most recent data.

The larger values of CTE were used in a dimensional shrinkage analysis of the retainer and the bearing inner race. The results of the analysis showed an interference condition could occur between the retainer and the inner race at approximately 90K for the PW bearing and 60K for the FW bearing.

It was decided to confirm the findings of the analysis by test. The PW bearing was tested again at cryogenic temperature, with torque measurements made at 50, 70, 90 and 100K. The test revealed that below 80K, torque was greater than 50 N-cm. When above 100K, torque was only 10 N-cm. This test confirmed our supposition that an interference was occurring and it was decided to re-make new retainers with a larger inside diameter. The new CTE value was used for the new retainer design. Thanks go to our vendor, ESR Technology for their timely assistance with this issue.

With all bearings having a revised larger retainer installed, the test philosophy of the program was revised. Both the PW bearing and the FW bearing would be tested at the bearing level, at cryogenic temperature. A bearing test fixture was designed by ESR Technology and COM DEV. A novel feature was the addition of a “window” so that a direct view of the retainer could be seen at cryogenic temperature. Temperature sensors were also added to directly monitor inner and outer race temperatures.

The first cryogenic test of a bearing (with the new retainer) gave us a surprise. The bearing still exhibited a high torque when initially rotated at cryogenic temperature (approx. 50 N-cm) but a lower value than that seen before. The bearing recovered quickly to a normal value (10 N-cm) when rotated two revolutions. The good news was that the retainer could be seen to have the design clearance of approximately 0.4 mm from the inner race at cryogenic temperature. The fixture “window” and the clearance are shown in Figure 9.

The post test inspection of the bearing showed no flakes and particles had come off the retainer. The conclusion of the test was that there was still a problem with the bearing, but not necessarily related to the retainer interference issue. A solution to the problem had not yet been found, but the initial torque of 50 N-cm could easily be accommodated by the driving torque available for the geared motor. As a precaution, it was decided to torque test all bearings at 35K. The tests revealed that all bearings had a higher than normal torque when initially rotated at cryogenic temperature. However, bearings having the lowest values of initial torque (≤ 50 N-cm) were selected for flight and the life test program.

The investigation team was re-convened to establish a root cause for the problem. All evidence from the tests to date was reviewed and it was decided to further investigate the effects of the large thermal gradient, which was occurring across the bearing during the cool down. It was already known at this time that the cool down of the DW mechanism over a period of 6 days or less would invite the large thermal gradient across the bearing to occur and therefore may cause the high initial torque at cryogenic temperature to occur in the DW mechanism. A further series of pupil wheel bearing tests were carried out to further characterize the problem and investigate possible mitigation strategies.

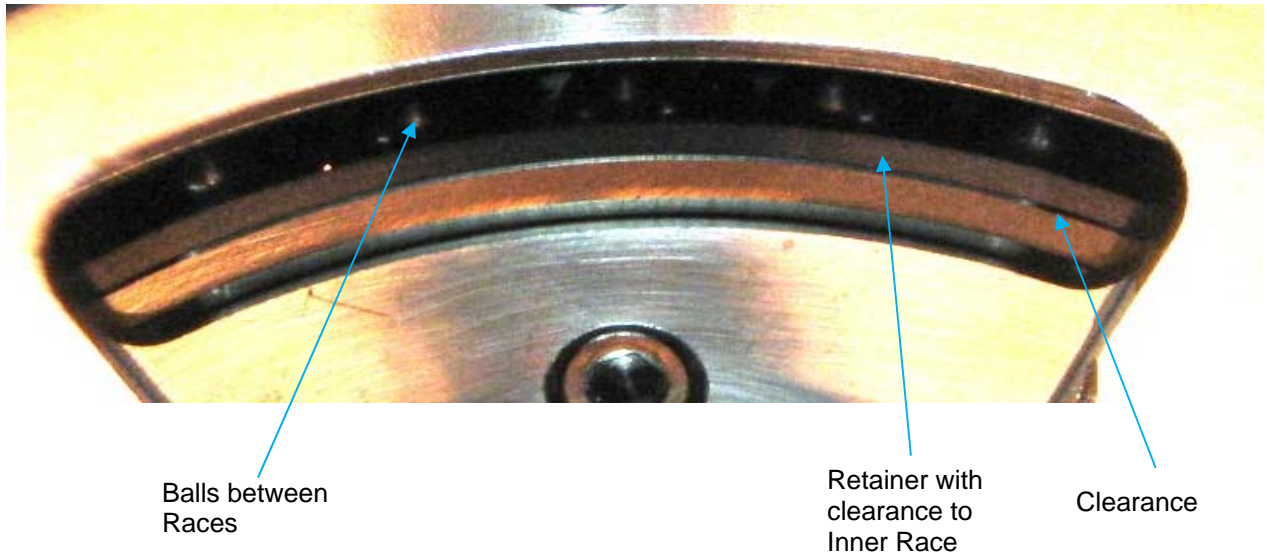


Figure 9. Pupil Wheel Bearing Test at 35K viewed through Test Fixture Window

Bearing Test 1 Objective: To quantify the temperature gradient across the bearing when preload is lost. Pupil wheel bearing was torque tested with various temperature gradients across the bearing. **Result:** Preload was lost when temperature gradient exceeded 5K. This result agreed with analytical prediction. Preload is lost because outer race is temporarily too large to maintain contact with the balls.

Bearing Test 2: Objective: To measure the bearing initial torque at 35K, having periodically rotated the bearing from 150K down to the operating temperature. The purpose of the test was to see if a mitigating strategy could be implemented during the cooling down of the bearing. **Result:** The rotating of the bearing during the cool down (temperature gradient > 5K) did not eliminate the high initial torque when rotated at 35K. Rotating the bearing with no preload on the ball / race system was in-effective.

Bearing Test 3: Objective: To measure the bearing initial torque at 35K, having maintained the temperature gradient across the inner and outer races at less than 5K. In essence, the bearing would be cooled in an iso-thermal manner. Providing an iso-thermal cool down of the bearing could be achieved, the preload between the balls and the races would be maintained during the entire cool down from 295K to 35K. **Result:** The temperature gradient across the bearing was maintained during the entire cool down at 4K or less. Therefore, it was assumed that the preload had been maintained on the bearing. However, a high initial torque of 80 N-cm occurred, but it was observed that the torque reduced down to 10 N-cm in only 10 degrees of bearing rotation. This rapid drop in torque had not been observed on any previous bearing test. It was concluded that the iso-thermal cool down had resulted in better bearing behavior at 35K, but the retainer itself could not be eliminated as a possible contributor to the high initial torque.

In parallel with the individual bearing tests the flight wheel / hub assembly (bearings having the enlarged retainer) was torque tested at 35K. The results of the pupil wheel bearing test was an initial torque of 167 N-cm. Dropping to 31 N-cm after 270 degrees of bearing rotation. The torque trace of the next three and a half revolutions is shown in Figure 10. The torque value drops from 27 N-cm to 13 N-cm in non-linear manner with respect to the rotation angle. Over the next 50 revolutions the torque reduced to an acceptable low value of only 7 N-cm.

The wheel / hub assembly still showed a high initial torque at 35K, despite the use of the larger diameter retainer. A review of the temperature data during the cool down revealed that the bearing had experienced a very high temperature gradient across the races (at one point the wheel being 100K warmer than the hub). This large temperature gradient led to a loss of bearing preload and when the

preload is lost the balls and the retainer could “fall” in the presence of 1G loads into non-optimal locations. These non-optimal locations would be “locked in” when the balls and races re-register, when all bearing components reach 35K. It is theorized that over the first four revolutions the balls are being put back into optimal locations by the act of rotating the bearing.

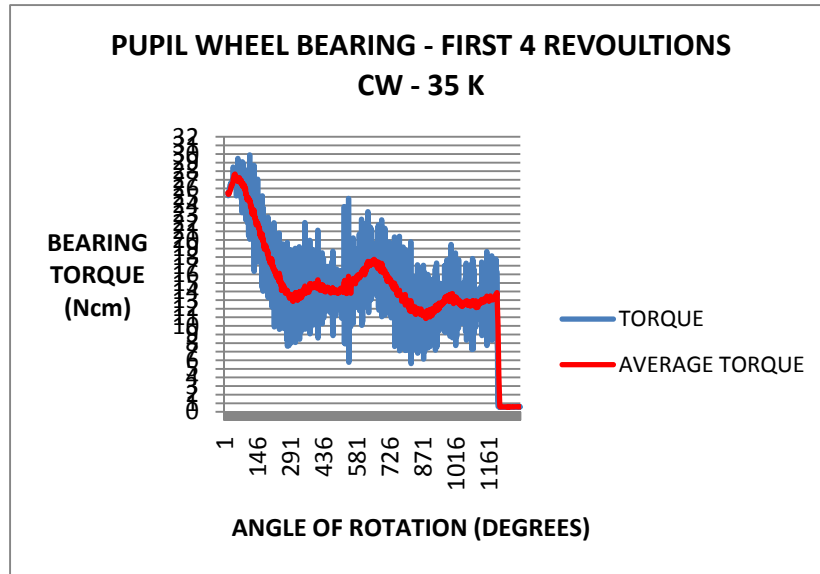


Figure 10. Wheel / Hub Assembly Torque Test at 35 K

The test also proved that the bearing high initial torque could not be due to frozen moisture in the MoS₂. The reason for this conclusion is that a high torque (if due to this phenomena) should clear itself in a single rotation of each ball relative to the races. But the bearing took four rotations to recover. It was not considered plausible that frozen moisture in the MoS₂ could affect the bearing for this many rotations.

Dual Wheel Mechanism Flight Model Tests

It was decided to proceed with the assembly of the DW flight model. Initially, both wheels were tested at room temperature, to establish a clear baseline for performance before testing at 35K. The minimum current for successful operation of each wheel was established at room temperature and then a torque ratio was calculated, based on the maximum motor drive current available. The torque ratios at room temperature were 4.4 for the PW and 4.1 for the FW. After vibration tests were completed, the torque ratios were unchanged. Vibration tests were deemed to be successful.



Figure 11. Dual Wheel Mechanism Flight Model

The first cryogenic temperature test at 35K was completed and the results were satisfactory in terms of overcoming the high torque of the bearings when initially turned at 35K. The torque ratio available to initiate rotation of the wheels (some missed steps permitted), at 35K, was 5.0 for the PW and 3.0 for the FW. The torque ratio is defined as the maximum motor current available divided by the minimum motor current required to simply achieve wheel rotation.

After a run in of the bearings (25 revolutions of each bearing) the torque ratio at the start of science operations (no missed motor steps permitted) at the beginning of life of the mechanism was 2.75 for the PW and 1.83 for the FW. The difference in the torque ratio values was attributed to the fact that the PW geared motor demonstrated a higher pull in torque (31 N-cm) at 35K than the FW geared motor (22 N-cm).

The temperature gradient measured across the bearings (during the cool down) was only 30K. A much lower value than that measured during the cool down of "bearing only" tests. This was attributed to the larger thermal inertia of the all up DW mechanism assembly. It was learnt that each different configuration of hardware cooled to 35K produced very different thermal gradients within the assembly.

The repeatability of positioning each optical element was demonstrated at 35K. The repeatability of the FW was ± 0.133 mm and the PW was ± 0.183 mm, versus a requirement for each wheel of ± 0.2 mm.

Conclusions and Lessons Learned

Item (1) – The bearing retainer suffered an interference condition with the inner race at the cryogenic temperature. This was attributed to an inappropriate CTE design value for the PGM-HT material. The interference was eliminated by enlarging the inside diameter of the retainer. Visual evidence of adequate clearance was obtained by adding a window to the bearing test fixture. It is recommended that precise knowledge of the CTE value of non-metallic retainers be used for designs intended for cryogenic applications.

Item (2) - A non-metallic bearing retainer may be in a non-optimal location when a bearing is initially rotated at cryogenic temperature. This causes a higher than normal torque. This may be caused by the relatively large dimensional change of the retainer cooling down to the cryogenic temperature. The retainer being under a 1G load and being offset from an ideal location may magnify this problem. This problem was rectified by a 10 degree rotation of the bearing provided the bearing was cooled in an isothermal manner. A metallic retainer may eliminate this problem.

Item (3) – When a bearing is cooled in such a way that a large thermal gradient occurs across the bearing, the bearing preload is lost. The loss of preload allows the ball and race system to be in a non-optimal location during the bearing cool down. Also, it is possible that the 1G load pulls the balls and the retainer off center. The balls re-register with the races in a non-optimal location when the preload is re-applied at the cryogenic temperature. The non-optimal location of the balls causes a higher than normal torque when initially rotated at cryogenic temperature. This problem can be rectified by up to four rotations of the bearing. It is recommended that mechanisms be cooled in an isothermal manner. The requirement to cool isothermally is problematic if accelerated cool downs are required for supporting ground tests.

Item (4) – The mechanism level tests cool the DW mechanism in six days. This invites item (3) to occur. Item (2) will always occur even if the mechanism is cooled isothermally over a long period of time.

Item (5) – Bearings behave in a normal manner after items (2) and (3) have been overcome. Tests confirmed that a mechanism torque ratio of greater than 3.0 was available to overcome the problem from items (2) and (3).

Item (6) – The JWST mission cool down is over a several week period. COM DEV expect item (2) to occur in the mission, but not item (3) to occur. However, it was decided to use the accelerated six day cool down as the basis for qualification. Future ground based testing at the instrument level will also have to cool down in six days. This is more severe than the mission itself but now serves as the environment for qualification.

The bearing anomalies described could not be eliminated from the design. However, a successful test campaign of the flight model ultimately lead to establishing acceptable torque ratios to overcome the anomalies.

The authors wish to express their gratitude to COM DEV and Canadian Space Agency management and to COM DEV technical and test personnel for their considerable support in tackling the complex design, build and test campaign for the DW mechanism.

References

1. National Institute for Standards and Technology, 325 Broadway, Boulder, Colorado

Xatcobeo: Small Mechanisms for CubeSat Satellites – Antenna and Solar Array Deployment

Jose Miguel Encinas Plaza^{*}, Jose Antonio Vilán Vilán⁺, Fernando Aguado Agelet⁺, Javier Barandiarán Mancheño^{*}, Miguel López Estévez⁺, Cesar Martínez Fernández^{*} and Fany Sarmiento Ares^{*}

Abstract

The Xatcobeo project, which includes the mechanisms dealt with here, is principally a university project to design and construct a CubeSat 1U-type satellite. This work describes the design and operational features of the system for antenna storage and deployment, and the design and simulations of the solar array deployment system. It explains the various problems faced and solutions adopted, with a view to providing valid data for any other applications that could find them useful, be they of a similar nature or not.

Introduction

Xatcobeo is an educational joint project between University of Vigo and INTA (Spain National Institute for Aerospace Technology), which has been selected to be launched on the maiden flight of Vega. The space segment of the Xatcobeo project is mainly formed by a mechanical structure that complies with the CubeSat 1U standard. Into this structure, five subsystems are going to be implemented: a power subsystem, an on board computer, a Telecommand Tracking and Control system for communications, a solar Panel Deployment Mechanism (PDM), a software reconfigurable radio, and a sensor for measuring the total amount of ionizing radiation in the space.

Mechanisms

Two different deployment mechanisms are included in the satellite:

- An antenna (four monopoles) deployment
- A solar array deployment.

Antenna Retention and Deployment Mechanism for a CubeSat 1U Picosatellite

The CubeSat concept makes small-scale satellite launches viable on a low budget. Dimensions are limited to a 100 x 100 x 100 mm cube and mass to 1 kg, which means all built-in components must weigh and measure as little as possible. These limitations have been borne in mind from the outset when designing the mechanism offering storage capacity and deployment for antennas. The mechanism must fit a casing measuring 82.6 x 98 mm on the front and with a thickness of 6.5 mm. To fully explain the design needs and solutions chosen, the main problems and solutions are given below.

Problems

The problems can be divided into a series of more or less independent sections:

- General configuration.

The design must leave clear as much of the face where it is installed as possible, insulate the antenna connection from the metal of the satellite, and respect the geometry for the antenna position, which will come out at an angle of 45 degrees to the adjacent edge.

^{*} Instituto Nacional de Técnica Aeroespacial (INTA), Madrid, Spain

⁺ University of Vigo, Lagoas Marcosende, Spain

- **Materials selection.**
The material must withstand the various types of radiation present in the working environment and avoid potential risks from electrostatic discharges produced by an atmosphere with a high ion density. In addition, it must withstand the temperature changes occurring when its orbit passes in and out of sunlight, which range from 243 to 293K, and the maximum temperature during launch of 353K.
- **Dimension and mass limits.**
The mechanism must be as light as possible so that other elements can be included on the satellite. The aim is for everything to be under 20 g. Furthermore, it must not protrude more than 6.5 mm from the outer face of the shielding.
- **Mechanical strength.**
The mechanism must guarantee its structural integrity and the retention of the antennas under the effects of knocks and vibrations.

Adopted solutions

All the solutions proposed for each of the above problems are briefly outlined below:

- The mechanism would be built in to a single piece that would act as a support for all the others, which we will call the sub-chassis from here on.
- The sub-chassis would be made of a polymeric material to insulate the antenna electrically; this would later be covered by a layer of dissipative paint.
- The sub-chassis was designed in a continuous ring shape with a C profile, so that the interior space was available for other elements such as solar panels, cameras and so on.
- The chosen polymer was polyamide as this brings together the many features needed for sub-chassis operation such as acceptable resistance to radiation and ultraviolet radiation and great dimensional stability against exterior temperature changes.
- To solve the weight problem, in addition to the material chosen for the sub-chassis, it was decided that the attachment elements should be high strength material in order to reduce size. Finally, titanium Gr5 (Ti6Al4V) M2 nuts and bolts were chosen.
- A surrounding sheet of polyvinyl acetate was chosen for the retention system, a tough and dissipative polymer to avoid static interaction with the antenna.
- This sheet shares its attachment to the sub-chassis with one of the antenna and acts as a retainer for the antenna whilst they need to be folded, as it envelops them on their outer part and keeps them within the continuous C-shaped profile described above.
- The triggering system chosen was a 0.125-W electrical resistance with a ceramic body instead of a Nichrome wire.

Antenna Deployment Mechanism Introduction

One of the advantages and capabilities of a satellite is the ability to collect data in an environment that is difficult for people to access. However, it must be able to communicate that data to areas where humans do have access, i.e., it must have an antenna to send and receive data. These antennas cannot be sent into space already deployed, as this would take up too much room on costly space flights. This is where the deployment mechanism comes into play as it allows them to be folded during the journey and deployed once the satellite is in orbit. The deployment mechanism is, therefore, one that is designed to integrate antenna storage before deployment plus the deployment system and its corresponding burner circuit, all with the smallest size and weight possible.

To achieve such integration, a modular design was proposed that would allow all the mechanisms to be fitted to a single piece, thus saving weight and space, and keeping things simple. The base for this modular attachment system was called the sub-chassis, as the satellite itself was regarded as the prime chassis. The antenna, the retention mechanism and the burner circuit are attached to it and it also acts as

a profile guide for the antenna whilst they are folded. The deployment mechanism operation is analyzed below and the features of the elements that make it up are described.

Sub-chassis

As explained, the sub-chassis is the piece upon which all the necessary elements are attached for deployment mechanism operation.

General requirements and design process

Antenna design basic requirements:

- Each antenna must be located in the center of the edge of the +X face of the CubeSat.
- The exit angle must be 45° ($\pi/4$ rad) with respect to the adjacent edge of each antenna.

A plaque with solar panels to power CubeSat was also expected to be installed on the +X face, so the part used to hold the antenna had to leave as much space as possible for the installation of these panels. Being the largest part in the system meant weight had to be kept down to a minimum to give as much margin as possible to other elements.

In order to save mass, system design began as a set of independent parts, four for antenna attachment and another four as guides to give the folded antenna curvature and keep them within the available envelope. However, the large number of attachment elements needed for this set-up made it unviable. The approach was changed and a continuous profile was designed for attaching the antenna and guiding them in their folded path. The profile moved as far out from the shielding as possible so that the greatest number of solar panels could be installed in the free interior space. The piece to which the antenna was attached was called the sub-chassis.

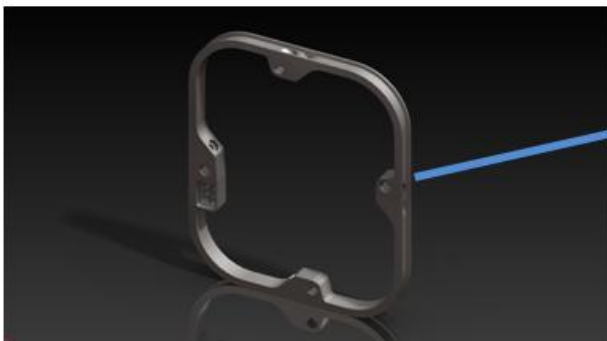


Figure 1. Sub-chassis

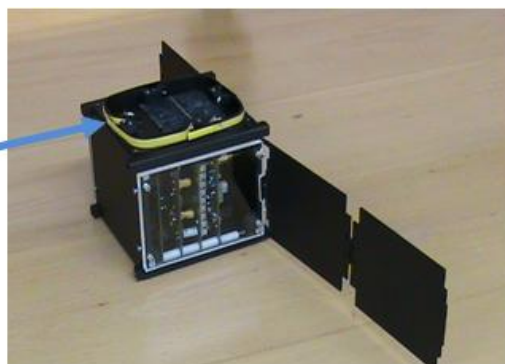


Figure 2. Mechanism built into the Project Xatcobeo prototype

Materials selection

The antenna had to be insulated from the metal of the satellite in order to avoid short circuits when touching the shielding faces. There were two options:

- Make the sub-chassis from metal and include a dielectric piece at the antenna contact areas to insulate them from the rest of the metallic parts.
- Make the sub-chassis entirely from polymeric material.

The first option was seen to have complications with the metal-dielectric interface fitting and there was a risk of contact between the antenna and any other part of the metal sub-chassis, so the sub-chassis made entirely of polymeric material was therefore chosen as safer in terms of antenna insulation.

The material has to fulfill a long list of requirements:

- It had to work correctly at temperatures ranging from 243K, reached when passing through the Earth's shadow, to 353K, reached during launch.
- It needed dimensional stability so that dilations and contractions did not cause tension at the mechanical interfaces of the attachments. At the same time, if the material over-contracted at minimum temperature, this could squeeze the antenna and prevent them from full or partial deployment.
- It needed acceptable resistance to radiation and ultraviolet radiation, both of which are present in the satellite's working environment. According to research in the literature, the e-beam radiation effect on the polyamide would be to increase its elastic limit and decrease its elongation, neither of which poses a problem for proper operation. As for UV radiation, the metallic-based paint cover used to dissipate static charges would notably increase resistance to this type of radiation.
- It had to be extremely light. The final sub-chassis weight is 5 or 6 grams and the attachment elements another 5 grams, which, when added to the weight of the antenna, the electrical resistance, the thermoplastic envelope sheet, the switch and storage thread, meant the whole mechanism weighs in at less than 12 grams.
- Over-fragility had to be avoided to prevent vibration problems during launch.
- It had to be as dissipative as possible so as not to become electrostatically charged when passing through orbital areas with high ion densities and so avoid the risk of experiencing electrostatic discharge that could affect the sub-chassis itself or other elements of the mechanism. To improve dissipation, the sub-chassis would be covered by zinc- or silver-based dissipative paint, except in areas of antenna contact. In this way, dissipation is increased in ionized environments and there is also increased resistance to ultraviolet radiation and, to a lesser extent, to nuclear radiation.
- Last, but not least in importance, it had to be simple, and if possible, cheap to make.

It was finally decided to make the sub-chassis from polyamide (PA6, PA66) using a selective laser sintering process to obtain parts designed by CAD without losing the initial properties of the polyamide produced. This material was able to acceptably fulfill the above requirements.

Antenna Attachment

As described, the antenna had to be located in the center of each shielding edge and have a deployment angle of 45° to this edge. It was thus decided to design a hole in the sub-chassis going through the whole piece, from the outside of its profile to the opposing side. This drill hole is located in the central area of the edge and as close as possible to the sub-chassis attachment to the shielding as this gave the whole assembly more rigidity. Figure 3 shows the location of the entry hole for the antenna attachment bolt from the outside of the profile to facilitate assembly. Figure 4 is a cut away showing the antenna attachment and the area in which it is located. It can be seen how the antenna attachment is adjacent to the sub-chassis attachment to the shielding (yellow piece), as this is the most rigid area of the whole assembly.

With regards to the approach used for attachment, a hole was made at the base of the antenna, through which the attachment bolt was introduced. This bolt served as the axle for the washer, the antenna itself, and the conducting wire in contact with the antenna. The conducting wire transmits signals both from the antenna to the satellite and vice versa. On the other side of the attachment bolt is a nut, also M2, which is inserted into the sub-chassis and whose function is to keep the whole assembly of antenna, connection cable and washer together, as once the bolt is tightened the assembly will be kept fixed by the tension between the nut and the sub-chassis it is embedded in.

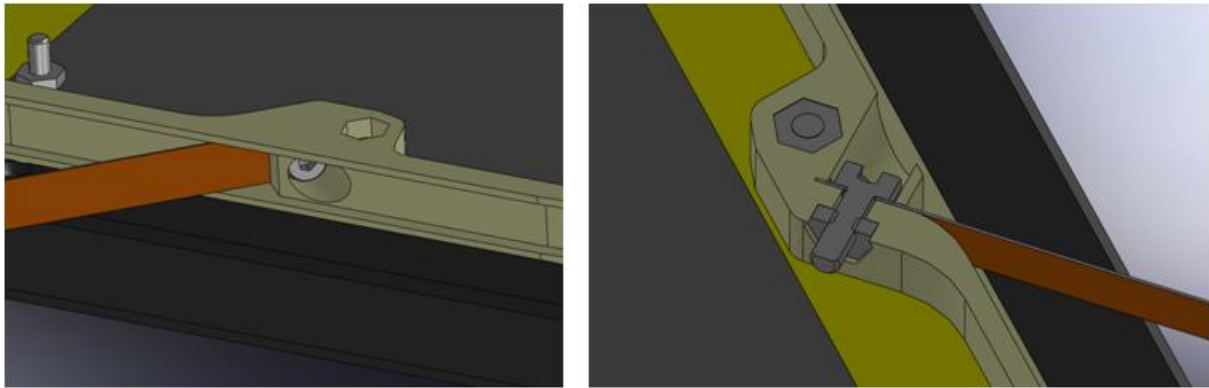


Figure 3. Drill hole and antenna attachment. Figure 4. Method and location of attachment.

Antenna Retention

The retention mechanism keeps the antenna folded from the time the satellite is finally assembled and ready for launch to the moment when the antenna controller indicates they must deploy. It needs to be able to cope with vibrations produced on rocket launch and the temperature changes from assembly to deployment, i.e., dilatations produced by heat variation must not put the system's retention capability at risk nor, obviously, cause damage to the material that would lead to structural breakage or weakening, which would harm the project's aims.

Each antenna, or monopole, is located in the center of the edge of the shielding for the +X face of the CubeSat, coming out at a 45° angle. Each one is 170-mm long, whereas the continuous profile of the sub-chassis is 325 mm in perimeter. This means that no antenna goes right around the profile or any of the others completely. This led to a problem, as it involved 4 retention points, one for each antenna. This meant, furthermore, guiding 4 nylon threads towards the area where the burner element is located, or four burner elements and four burner circuits. The latter was rejected as four circuits and burners would increase overall weight too much, so a way was sought to deploy the four antennas using a single circuit and burner element.

The idea to take a thread from the end of each antenna towards the burning area did not seem the most ideal because of the amount of thread needed to cover the distance and the risk of threads getting crossed. Furthermore, pivots had to be introduced to redirect the threads to an area where the burner element would not interrupt the solar panel positions. That is, the most suitable configuration was sought to ensure that the retention thread was as short as possible and that a single thread was enough to hold all the antennas at the same time, thus requiring only one burning point. This removed the need to place additional burning points and so kept weight down.

Thus the final retention system consisted of an enveloping sheet of thermoplastic material, fixed at a single point to the sub-chassis, which was 425-mm long and so allowed four antennas to be enclosed, once they had been folded, and keep them retained against the continuous profile of the sub-chassis. A perforation was made at the same point on all the antenna for the retention thread to pass through from the outside to the inside of the profile, where the burning element was located.

Attachment system

For the sheet to function properly, it needed to be joined to the sub-chassis. When enclosing the folded antenna, the traction tangential to the sub-chassis profile applied to the enveloping sheet would be turned into pressure on the antenna and so achieve a force at every point along them and keep them folded. The

sheet is attached to the sub-chassis at one of the antenna attachments, which avoids the addition of a new nut and bolt and so keeps weight down.

Operation and explanation of the retention method

The retention system is based on the enclosing sheet's ability to generate pressure on the folded antenna. Given that the sheet shares an attachment with one antenna, it will come out over this and then go a complete turn, around the profile until all the antennas are covered. A traction force is applied to the sheet tangent to the line of the profile, which turns into pressure on the antenna and keeps them pressed in against the sub-chassis profile. Once the sheet has enough force for it alone to keep the antenna folded, it can be tied by the retention thread, which will keep it closed until triggered. This thread is joined to the enveloping sheet using a double knot, one on the internal side of the sheet and one on its external side, to prevent it coming loose after deployment has taken place.

Materials selection criteria

The enveloping sheet needed a material that was flexible but also resistant to traction and that, furthermore, had good dissipation properties for electrostatic energy to avoid build ups that could discharge onto any of the antenna and have unwanted effects. A sheet of polyvinyl acetate was chosen.

Deployment mechanism and burner circuit

Deployment

Antenna deployment was produced by releasing the pressure they were under by burning the nylon thread keeping the enclosing sheet up against them. Once released, the recovery of the elastic force retained in them would place them in the correct position for sending and receiving data. If the antennas are not rigid enough they will take more time to stabilize the oscillation produced during deployment. It could even be the case that insufficient rigidity would leave them in an incomplete curved position due to the rotation of the orbiting satellite of roughly 1 rpm (0.00265 rad/s), which would greatly decrease their properties. To solve this problem, a steel was sought that enabled work in the cold without becoming too hard and that could absorb large amounts of energy without suffering plastic deformation, that is, with a large elastic limit, which led to a steel alloy with chrome and nickel being chosen.

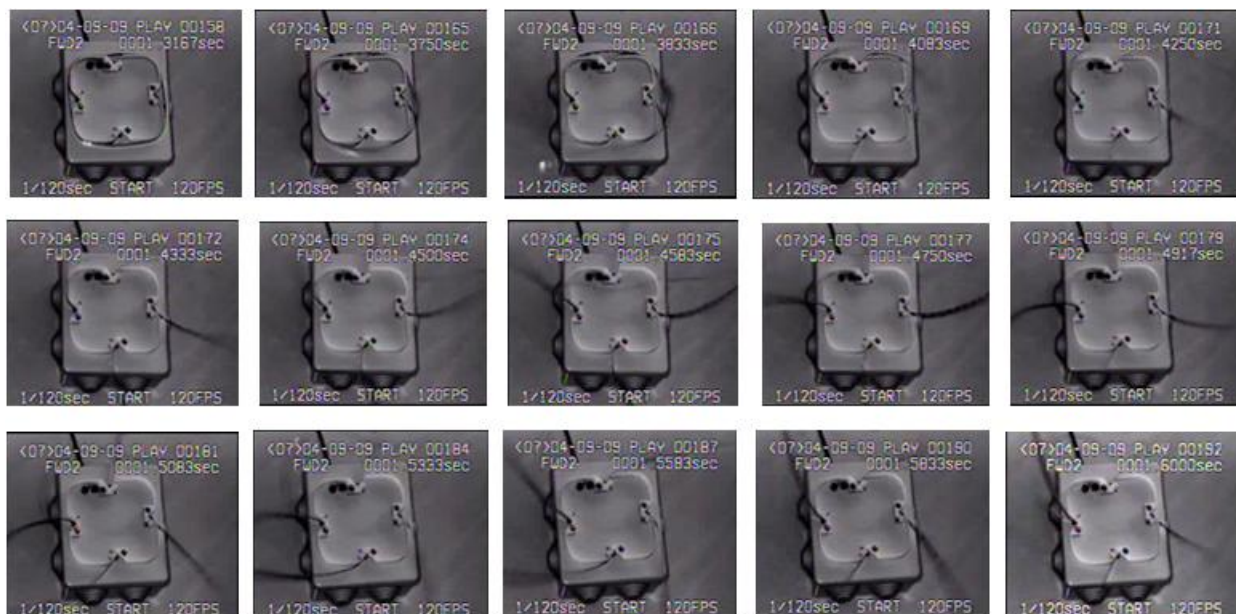


Figure 5. High speed recording of antenna deployment

However, tests carried out on a 5-mm-wide flat metal band, showed that this configuration was not totally valid: it responded well to folding but was too limp during deployment and, once deployed, took too long to stabilize and lost position when even slightly acted upon.

We found the solution to this problem by giving the metal strip a curvature, in such a way that it was slightly arched in a plane perpendicular to the direction of the antenna. This modification reduced deployment stabilization time by 55% and notably improved resistance to losing its position through external activity.

However, it was observed that when tightening the bolt on the convex part against a flat plane (the sub-chassis), the antenna was deformed and its angle out from the shielding edge was no longer 45° but approximately 60° . To solve this problem it was decided to change the flat surface of the sub-chassis for one with the same curvature as the concave part of the antenna and use a washer with a flat side (in contact with the bolt) and a curved one (in contact with the antenna) in order to avoid deformation and so maintain the outward angle of 45° .

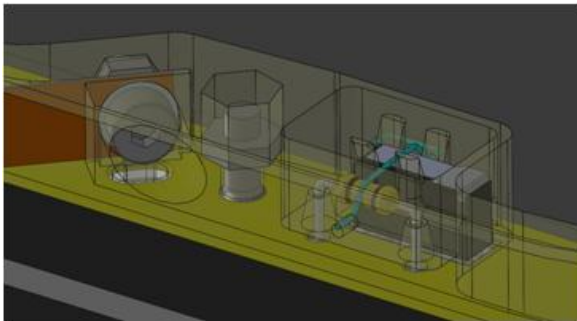


Figure 6. Antenna attachment area

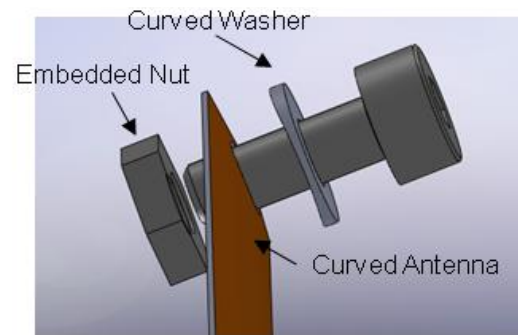


Figure 7. Antenna attachment elements

Burner circuit

The burner circuit is the set of elements that break the thread keeping the antenna folded at the moment of deployment. It is made up of a ceramic resistance and a power circuit to the battery and includes a switch to check deployment, which is triggered by the storage thread. Both the electrical resistance and the deployment switch are housed in a receptacle specially located to get them nearer to the area where the antennas are tied with the retention thread. This minimizes thread length and so prevents possible knots or unwanted tangles.

A 9- Ω , 0.125-W ceramic bodied resistance is used. One idea was to use Nichrome wire but this had the problem of heating its whole volume, which could damage the polymeric sub-chassis, whereas the ceramic electrical resistance focuses the heat source much more, which, moreover, favors retention thread burning.

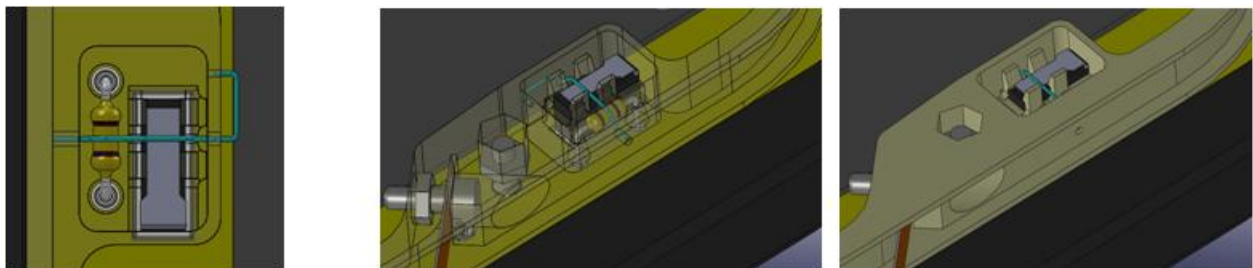


Figure 8, Figure 9 and Figure 10. Receptacle where the Burner circuit is housed.

Dozens of tests were carried out on the burner circuit in the presence of air and at room temperature, and the result was always the same: the resistance burned the 0.25-mm nylon thread in roughly 2 seconds. Tests were also carried out in a climate chamber to simulate the temperature variations experienced in orbit, and the mechanism has shown the same efficacy as at room temperature, having worked at both the minimum and the maximum temperature.

Panel Deployment Mechanism (PDM)

CubeSat missions run into the problem of obtaining more power but having little space allowable to locate solar cells. So starts the look for more power, and to achieve that, more solar panels are needed, and thus small deployment systems. The design of a solar panel deployment mechanism for Xatcobeo is mainly based upon the following goals:

- To ensure a packed maximum envelope of 6.5 mm from the structure in stowed configuration.
- To allow an easy integration in the structure of Xatcobeo. It is intended to pack with the lateral shear panel of Xatcobeo to integrate it as a single unit.
- To minimize mass of deployable parts.

The toughest requirement for solar array deployment in Xatcobeo mission is the necessity to fit all the system in an envelope of 6.5 mm from lateral plate of satellite to avoid interference with the satellite deployer. With this limitation it is possible to fit:

- One lateral aluminum shear panel, one board fixed to that panel holding solar cells, and one movable panel with cells in both faces over a 1.6-mm board.
- One lateral aluminum shear panel, one board fixed to that panel holding solar cells, and two movable panels with cells in both faces over 0.8-mm boards.

Both options have been used in Xatcobeo PDM design.

Solar Array Deployment for Xatcobeo

PDM is a mechanism consisting of two sets of deployable solar panels. In the first one, only one panel is deployed (PDM1) and the second is a double unfolding (PDM2).

Both share the first deployment system, and in the double an extra mechanism is added to allow the unfolding of an extra panel. Due to mass restrictions (to allow higher life span to this satellite mission is necessary to give extra protection against radiation environment and increase the lateral shielding plates) the double deployment system is only used to validate the mechanism concept and instead of boards with solar arrays, two aluminum frames are used.

The primary mechanism (Figure 11 and Figure 12), involves a two-spring system in one axis with a travel limit. The deployable board is fixed to an aluminum hinge by three bolts. This hinge is mounted in the lateral shear plate of structure of Xatcobeo by a system composed by two lugs and shaft. The lugs are mechanized in an enlarged area of that aluminum shear panel. At both ends of the shaft, two steel springs are located. Those springs are the actuators of the rotation movement. There are two mechanical limits (physically stops the opening rotation); first one fixed to the shear plate ensuring the correct maximum angle during deployment (90°), second one is a steel flat spring which fixes the panel in the final position reducing vibration problems (the rotating shaft has a slot on its end, during the rotation the folded part of the spring slips over the shaft till it matches with the slot and the movement stops).

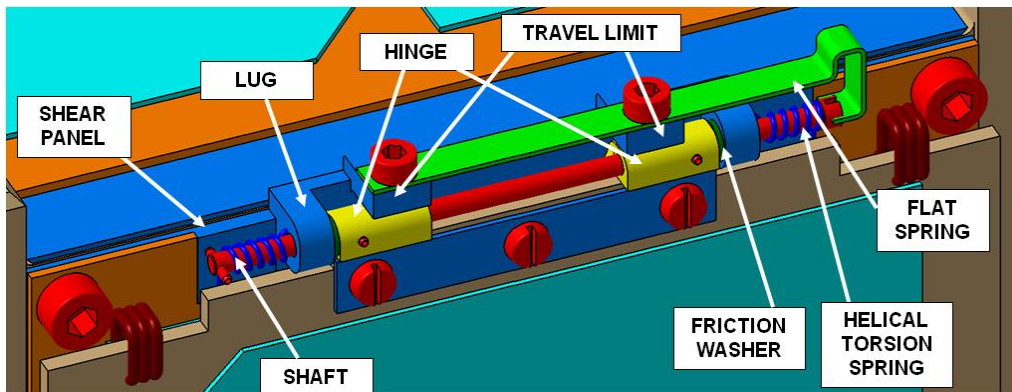


Figure 11. First mechanism detail

In the double deployment (Figure 12) case, two frames (for mass reduction requirements) are deployed successively. The first mechanism is the same described above, and an extra mechanism is added with a harder envelope limitation. The mechanism that unfolds the extra panel consists of two aluminum hinges, each one glued to one side frame. All the parts are assembled by a shaft with two steel rotation springs, and blocked in both sides.

Both deployable systems are fixed in stowed configuration by a nylon yarn. This nylon wire attaches the assembly formed by the movable panels, and the lateral shear panel of structure. So each PDM with its corresponding shear panel can be integrated in the Xatcobeo structure as an individual assembly. To start the movement of the mechanism there are two pyroelectric elements that cut the nylon yarn setting free the panel when commanded. Using two pyroelectric elements, a redundant configuration could be achieved. When the yarn is cut, all the rotation springs are free to start the deployment of the system.

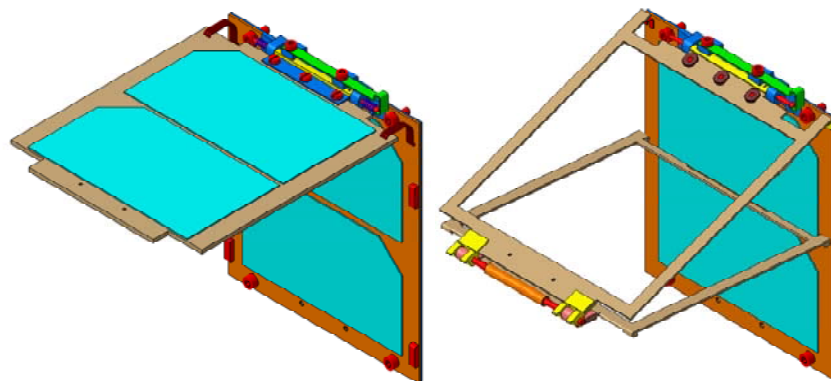


Figure 12. PDM1/PDM2 design

Two main requirements are issued for PDM: it shall deploy only once and shall send the result of the deployment action. To detect the deployment in the single system, power telemetries are used, and in the double a contact switch is designed.

Flat spring blocking system

One of the new advances in this design is the introduction of a flat spring to block the first deployment. It prevents micro vibrations induced movements in a space environment and serves at the same time as the helical springs as an additional blocking system. The blocking induced by this system consists in

fitting the tip of the flat spring into a 1-mm depth slot machined in rotating shaft head. The tip of the flat spring produces a friction force on the head of the shaft, acting as a damping for the rotating movement. The lateral force induced in the shaft is derived from a MSC/Nastran non linear static analysis of the flat spring using different thicknesses and materials. The values obtained are listed in Table 1. From the analysis, a vertical movement above the equilibrium position is observed when the tip of the spring is out of the slot, so this implies to make a thicker slot in shaft head. Other option to be taken into account is to manufacture the shaft head as a half cylinder instead of a slotted cylinder.

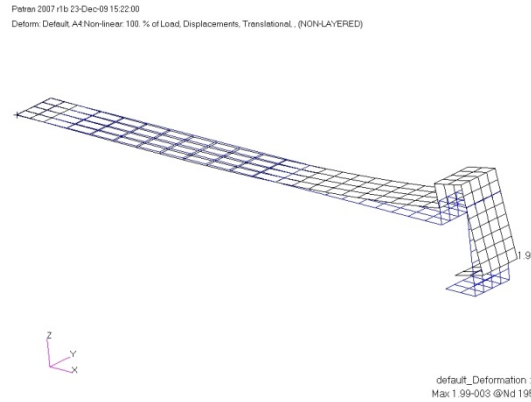


Figure 13. Deformation of flat spring

Table 1. Lateral force for different spring thickness and materials

Spring material	Thickness (mm)	Force (N)
Steel	0.3	1.813
Steel	0.4	7.29
Steel	0.5	13.57
Al	0.4	1.319
Al	0.5	3.525

Lubrication and materials selection

Being a one-shot mechanism avoids lubrication, with the only matter of use different materials in contact areas, and also a test campaign to minimize single failures. The damping of the rotation movement is achieved by: friction between metallic parts in the lug (Al) and shaft (steel) assembly; lateral contacts of plastic washers with principal hinge and lugs; and by friction between tip of flat spring and head of rotating shaft. The damping of the movement that requires friction goes against the requirement of reducing heat transfer amount between deployed parts and main body of the satellite. So the material of the friction washer will be one that allows friction but with low thermal conductivity. And in the lug – shaft area, the design tolerances will be adjusted to attain low contact area.

Simulation

A set of simulations have been run to dimension the springs and select the values for the springs that will be used in flight model. The kinematic and dynamic simulations have been developed using MSC/Adams program.

PDM 1 simulation

In the first simulation, the model is mounted with different sets of helical torsion springs and different flat springs looking for the lower impact force in the mechanical limits. Prior to the simulation, the model needs to be calibrated to define the characteristics of the movable parts and the contacts presented in it.

The mobile part consists of four solar cells, a FR4 board in which panels are fixed, the shaft, the hinge, the bolts that fix it to the board and the wiring of the solar arrays. The mass amount considered in the mobile parts is 40 grams.

There are two contacts in the model (Figure 14):

- The first contact between the hinge and the two blocks in the lateral shear panel of the satellite is of impact kind. It's defined by:
 - Stiffness of the contact. The two blocking elements are the same so only one contact has been considered in the calculations to reduce computation time. So the stiffness of that part has been increased to simulate the stiffness of the other blocking element. The stiffness is the one obtained in a beam with flexion load. The value considered is 21185 N / mm
 - Penetration depth: 0.01 mm
- The second contact between the head of the shaft and the flat spring. The contact has first a friction phase and when the plate enters in the slotted area of the head of the shaft it has an impact phase. The characteristics are:
 - Impact phase:
 - Stiffness of the contact. The stiffness is the one obtained in the tip of the flat spring with flexion load. The value considered is 414 N / mm
 - Penetration depth: 0.5 mm
 - Friction phase. It's between the tip of flat spring (steel or aluminum) and the steel head of the shaft. It's defined as a Coulomb friction force.
 - Static friction coefficient: 0.6
 - Dynamic friction coefficient: 0.4

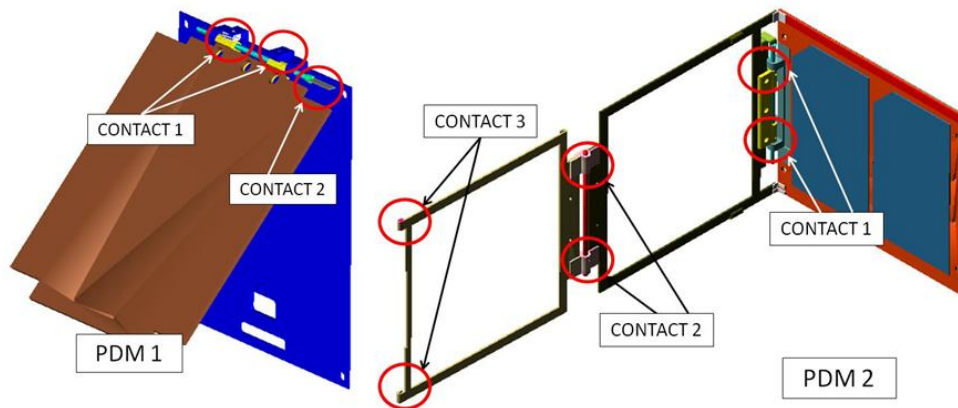


Figure 14. PDM1 / PDM2 Simulation model

The movement is obtained by a revolute joint between the mobile parts and the grounded parts (lateral shear panel of the satellite), located in the shaft axis, and free to rotate around shaft axis.

The parameters that will be used to look for the lower impact force with the analyses are the stiffness coefficient of the torsion spring (one or two acting in parallel) and the lateral force induced in the shaft by the flat spring. The stiffness coefficients of the torsion spring calculated for different wire thickness, spring diameter, number of loops, and number of spring is are listed in Table 2.

Table 2. Stiffness coefficient for helical torsion spring

Wire diameter (mm)	Spring diameter (mm)	Number of turns	Number of springs	Stiffness coefficient (N mm / rad)
0.4	2	5	2	16
0.4	2	5	1	8
0.4	2	10	2	8
0.5	3	10	1	6.51
0.4	2.5	5	1	6.4
0.4	2.5	10	2	6.4
0.4	3	5	1	5.333
0.4	3	10	2	5.333
0.4	2	10	1	4
0.4	2.5	10	1	3.2
0.4	3	10	1	2.667

In the first set of simulations a constant lateral force of 7.29 N is used with different spring stiffness values: 16, 8, 6.4, 5.33, 2.667 N-mm / rad. The results obtained are shown in Figure 15 and Table 2.

Table 2. PDM1 simulation results obtained with spring stiffness variation

Spring stiffness	Force of first impact (N)	First impact time (s)	Number of measurable impacts	End time (s)
16	850	0.12	4	0.6
8	400	0.15	3	0.67
6.4	350	0.17	3	0.69
5.33	300	0.19	3	0.75
2.667	200	0.26	3	0.9

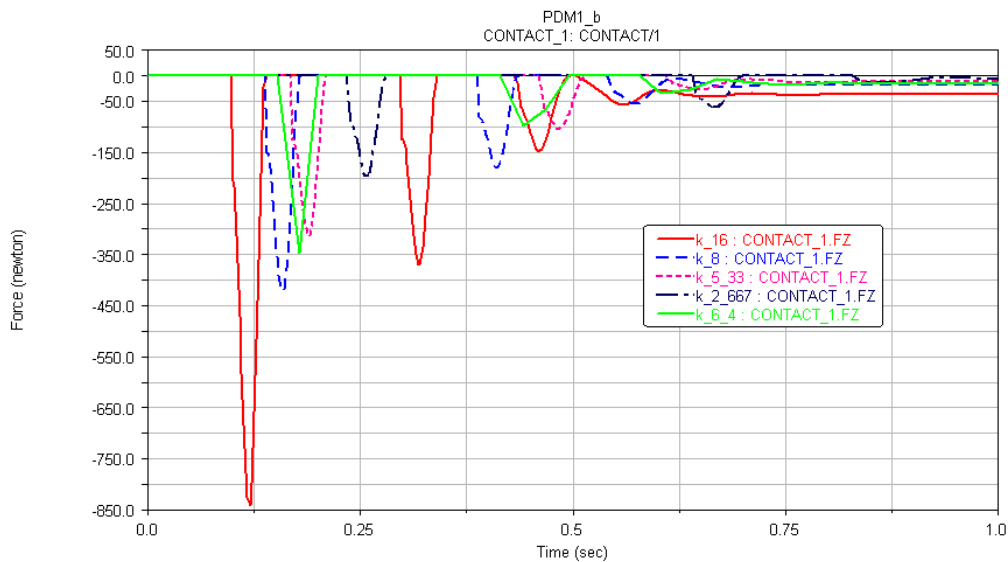


Figure 15. Impact force for different spring stiffness

The end time is taken to be when constant impact force is obtained. Observe that the movement is slower when reducing spring stiffness, and also the impact force decreases.

In the second set of simulations, the stiffness coefficient has been maintained in 6.4 N-mm / rad and the lateral force has changed with the values provided by the use of different spring material and thicknesses. The results obtained are presented in Table 3 and Figure 16.

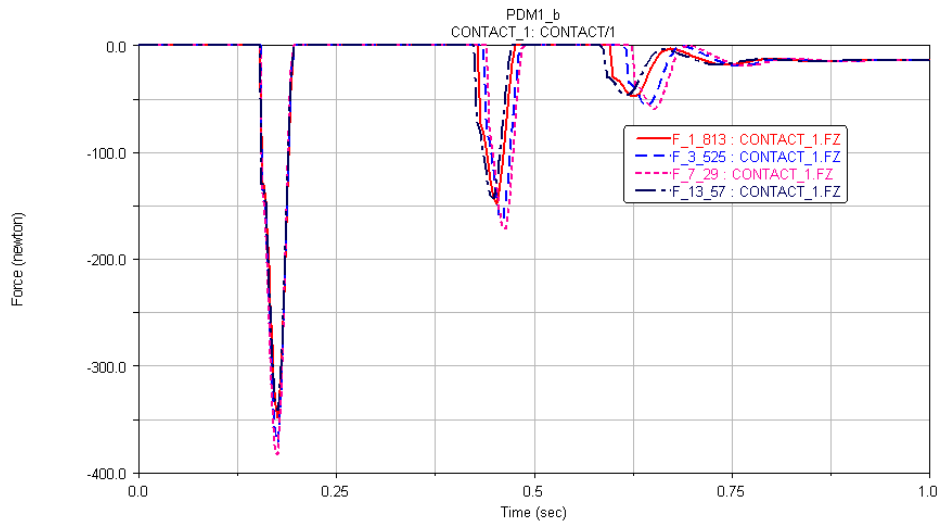


Figure 16. Impact force in for different lateral forces

The lateral force has small influence in impact force. When lateral force is small, impact force can increase, and impact time of last rebounds also increases; but when it's bigger, the friction phase is more important and reduces impact force and impact time, and the flat spring enters in head slot before and helps to finish the movement.

Table 3. PDM1 simulation results obtained with lateral force variation

Lateral force (N)	First impact force (N)	Third impact force (N)	Third impact time (s)
13.57	340	44	0.61
7.29	380	60	0.66
3.525	365	53	0.64
1.813	350	46	0.625

PDM 2 simulation

In the double deployment mechanism, a similar simulation has been held. In this case only the springs have been considered in the optimization of the problem. There are two groups of mobile parts involved in the movement: one group consists of the first frame with its shaft, the principal hinge, and its secondary hinges, with a mass of 8 grams; and the second group is formed by the second frame, its hinges and the secondary shaft, with a mass of 6 grams.

There are three contacts in the mechanism (Figure 14):

- The first contact between the hinge and the two blocks in the lateral shear panel of the satellite is of impact kind. It's the same contact defined for PDM1.
- The second is between the hinges of the two mobile frames. It's also of impact kind and defined by:
 - Stiffness of the contact. The value considered is 1000 N / mm
 - Penetration depth: 0.1 mm

- Third contact between the curved ends of second frame and fixed board over lateral shear panel. It has two phases, one of impact and one of friction. The characteristics are:
 - Impact phase:
 - Stiffness of the contact. The value considered is 10000 N / mm
 - Penetration depth: 0.1 mm
 - Friction phase. It's between the tip of aluminum frame and the FR4 board. It's defined as a Coulomb friction force.
 - Static friction coefficient: 0.3
 - Dynamic friction coefficient: 0.1

Two revolute joints have been included in each rotation shaft to allow movement between mobile parts.

The parameters used during optimization process are the stiffness of principal (k1) and secondary (k2) springs. The results obtained are shown in Table 4.

Table 4. PDM2 simulation results obtained with k1 and k2 spring stiffness variation

k1	k2	Contact 1 Force (N)	Contact 2 Force (N)	End time (s)
16	8	180	670	0.4
8	4	110	340	0.45
6.4	3.2	110	---	0.5
3.2	2.667	102	220	0.55
2.667	2.667	62	---	0.75

As happens with PDM1, when stiffness is reduced the movement is slower and contact force decreases.

Conclusions

Antenna deployment

When this work was begun, the Xatcobeo project management was counting on the possibility of introducing a commercial deployment system weighing more than 100 g. Over time, this cost in weight became unacceptable. So work was started on in-house development with the final aim of dramatically reducing the mass needed for the antenna deployment mechanism. It was decided to use polymeric materials and titanium instead of metals such as aluminum or steel, and the deployment and retention systems were unified around a single support component, which in turn would be the electrical insulation for the antenna. All these decisions had the same aim: reduce weight without compromising the reliability and stability of the mechanism or the assembled whole.

By selecting polyamide 6 as the structural material for the sub-chassis and covering it with zinc- or silver-based dissipative paint, the requirements for the behavior of materials in the working environment were fulfilled.

The choice of attachment elements made of titanium in M2 metric instead of steel in M3 reduced the final weight to just 20% of the initial weight. Furthermore, by making the sub-chassis from polyamide and not aluminum, its mass was reduced by 58.67%.

The final result of development is that the assembly made up of the sub-chassis, attachment elements (bolts, nuts and washers), electrical resistance, switch, heat-stable enclosing sheet and nylon retention thread had a total weight of 12 g.

The reliability shown in the tests; the great lightness of the assembly achieved using low density materials; the large internal space leaving room for solar panels, cameras or other installed devices in the mechanism's installation face; its robustness, which makes it easy to handle and simple to assemble; and its low cost and short manufacture time, thanks to the Selective Laser Sintering rapid prototyping process;

all this, and all that has been explained above means that we have, in conclusion, achieved an ideal mechanism for the storage and deployment of antenna not only for picosatellites such as the CubeSat 1U developed in the Xatcobeo project, but also for other types of picosatellites.

PDM

Small satellites require small mechanisms. But from miniaturization appear new problems such as manufacturing difficulties; in PDM it was to build shafts with the required length, small diameter and the adequate tolerances, which will lead to make shorter broken shafts instead the of full length used now.

A deployment system with a mass of 45 grams using boards of a 1.6-mm thickness was completed, and also it's possible to reach a double deployment with 55 grams using 0.8-mm boards (that in our case is not applicable due to mass restrictions). It's achieved the desired goals of having a system in a 6.5-mm envelope protruding from the satellite and allowing easy integration in such tight dimensions.

A flat spring retention system has been designed to avoid in flight induced micro vibrations and act as an additional blocking system. The flat spring used should be the one that produces the greater lateral force to induce damping in the movement, but not too thick to provoke plastic deformation in the bended area. The selection of springs for PDM1 and PDM2 leads to look for springs with small stiffness: more wire turns, less wire diameter, higher spring diameter and to use only one spring.

References

1. N.K. Pramanik, R.S.Haldar, Y.K.Bhardwaj, S.Sabharwal, U.K.Niyogi, R.K.Khandal, "Radiation processing of Nylon 6 by e-beam for improved properties and performance." *Radiation Physics and Chemistry* 78 (2009) 199–205
2. Clovis Pinto, Leonardo G. Andrade e Silva, "Study of ionizing radiation on the properties of polyamide 6 with fiberglass reinforcement", *Radiation Physics and Chemistry* 76 (2007) 1708–1710
3. Waldir Pedro Ferro, Leonardo Gondim de Andrade e Silva. "Ionizing radiation effect studies on polyamide 6.6 properties" *Radiation Physics and Chemistry* 71 (2004) 267–269
4. A. Toorian, K. Diaz, S.Lee "The CubeSat Approach to Space Access." *IEEE Aerospace Conference Proceedings*, art. no. 4526293
5. M.W.R. Alger, K.D. "A design and development of Pico- and Femto-satellites." *International Journal of Manufacturing Research* 3 (1), pp. 48-79
6. Swartwout, M., Kitts, C., Twiggs, R., Kenny, T., Ray Smith, B., Lu, R., Stattenfield, K., Pranajaya, F. "Mission results for Sapphire, a student-built satellite" *Acta Astronautica* 62 (8-9), pp. 521-538
7. Peter Fortescue, John Stark, Graham Swinerd. "Spacecraft Systems Engineering".
8. Joseph E. Shigley, Charles R. Mischke. "Diseño en ingeniería mecánica"

Concept, Design, and Prototyping of XSAS: A High Power Extendable Solar Array for CubeSat Applications

Patrick Senatore^{*}, Andrew Klesh^{*}, Thomas H. Zurbuchen^{*}, Darren McKague^{*} and James Cutler^{*}

Abstract

CubeSats have proven themselves as a reliable and cost-effective method to perform experiments in space, but they are highly constrained by their specifications and size. One such constraint is the average continuous power, about 5 W, which is available to the typical CubeSat. To improve this constraint, we have developed the eXtendable Solar Array System (XSAS), a deployable solar array prototype in a CubeSat package, which can provide an average 23 W of continuous power. The prototype served as a technology demonstrator for the high risk mechanisms needed to release, deploy, and control the solar array. Aside from this drastic power increase, it is in the integration of each mechanism, their application within the small CubeSat form-factor, and the inherent passive control benefit of the deployed geometry that make XSAS a novel design. In this paper, we discuss the requirements and design process for the XSAS system and mechanical prototype, and provide qualitative and quantitative results from numerical simulations and prototype tests. We also discuss future work, including an upcoming NASA zero-gravity flight campaign, to further improve on XSAS and prepare it for future launch opportunities.

Introduction

As the availability and frequency of CubeSat launches increase, it has become evident the CubeSats can provide opportunities to the scientific community that are either unprecedented or normally reserved for large, complex spacecraft. However, many such missions exceed the typical technical performance or overall constraints of CubeSats, such as their limited power and typical data-rates. In this paper, we present a novel solution to increase the continuous available power on a CubeSat bus from 5 W to 23 W through the use of a small, deployable solar array, which fits within CubeSat volume and mass constraints.

Background

Extendable solar arrays from satellites have been extensively discussed in the literature. By the late 1960's, work was being done to improve upon existing designs for deployable arrays [1] and several patents were in existence [2]. In the early 1980's, flexible solar arrays were under study [3] and more consideration was given to innovative methods of deployment. Also, inflatable arrays were under consideration in the 1990's [4]. Thus by the time CubeSats were conceived in the early part of the century, many types of deployable arrays had been successfully put into practice.

Conforming to a rigid mass and volume standards [5], CubeSats provide a platform for very small (~1 kg, ~10⁻³ m³) and often secondary payloads. The CubeSat standard, the brainchild of Stanford University and the California Polytechnic University, is primarily used by universities, although their value is more broadly recognized by NASA, DOD, and also the traditional aerospace industry. The mass and volume standard enables launching out of a Poly Picosatellite Orbital Deployer (P-POD) or similar deployment mechanism, thus CubeSats substantially simplify the launch integration: The integrator is assured that the P-POD meets certain specifications for launch and the CubeSat has only minimal constraints placed upon it for safety and risk assurance. Since their conception, upwards of 25 CubeSats have been launched with

^{*} University of Michigan, College of Engineering, Ann Arbor, MI

many more waiting for launch opportunities [6] covering many applications, from breakthrough science measurements to technology proving missions.

CubeSats have very important limitations, affecting their breath of use. Most importantly, they have limited power, and must maintain a low mass to conform to the strict CubeSat specifications, which enable their simple integration and thus launch. Several technology developers are now addressing these restrictions through deployables, but their success is very limited after launch [7], [8], and no deployable CubeSat solar array of this type exists.

In this paper, we describe the design, construction, testing, and future considerations for XSAS. We begin with design requirements, carry a design through modeling and prototype testing, continue with a discussion of the design, modeling and testing results of this innovative design, and end the paper with a description of ongoing work, which includes testing in microgravity through NASA's Reduced Gravity Student Opportunities Program.

Design Overview

The XSAS concept is a complete and modular power system composed of two major subsystems: a multi-panel, double-sided, deployable solar array and a power management and storage bus (power bus). While stowed, the solar array and power bus fit within a CubeSat's 1U (10x10x10 cm) and 0.5U (10x10x5 cm) volume respectively. Once released, the array passively deploys in an "accordion style" to increase its surface area. The power bus regulates and stores the energy from the solar array and interfaces directly with the payload through a single universal connection. This makes XSAS a modular plug-and-play "space battery" applicable for small CubeSats. The current design supports 16 stowed solar panels and accommodates payloads of up to 1.5U (10x10x15 cm) completing the maximum 3U (10x10x30 cm) CubeSat size. Figure 1 displays a comparison of a standard CubeSat geometry with an early 14 panel stowed and deployed XSAS integrated 3U CubeSat.

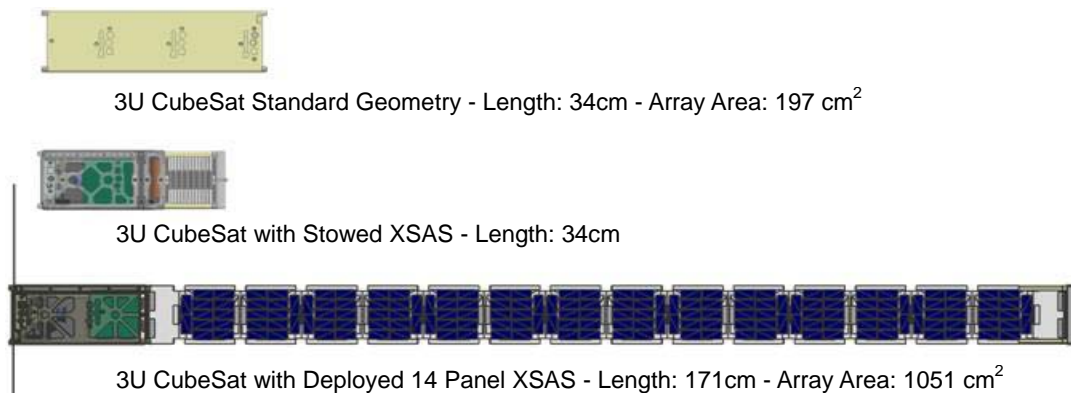


Figure 1. Dimensions of a Standard 3U CubeSat and 3U CubeSat with XSAS

Previous 3U CubeSat were design and flown with a 5.0-kg upper mass limit. However, in August 2009 CalPoly requirements reduced this constraint to 4 kg [5]. As a result, the XSAS design presented in the paper is based on the latter requirement. Table 1 lists the mass budget for each subsystem.

Table 1. XSAS Mass Budget

Components	Mass (kg)
Array*	2.05
Release Mechanism *	0.13
Power Bus*	0.61
Ballast	0.71
Payload	1.50
TOTAL	5.00

* Includes 30% contingency

It will be up to the continued design to modify XSAS for the new mass budget. Based on the Table 1, this could be achieved by incorporating the payload as ballast rather than using empty weight.

Design Requirements

Top level requirements for XSAS are divided into three categories as defined below. While most requirements are vital to the success of this innovative design, some can be modified to satisfy mission specific constraints and needs. This ability to customize the design makes XSAS a truly modular and versatile power system, which is attractive to a variety of researcher groups and industries. Specific qualifications on design, performance, and operation are included within each major category to describe the purpose of each requirement.

CubeSat Interface Constraints

The following list details the top level system requirements, followed by explanations of their application.

- XSAS shall have a stowed and deployed configuration
- Chassis shall include a 0.5U power bus
- Chassis shall include a 1U stowed solar array
- XSAS shall have a maximum mass of 5.0 kg

Due to their standardized geometry and deployment systems, CubeSats have strict requirements on their stowed design. Maximum mass and volume constraints include 5.0 kg and 3U geometry respectively. Therefore, as listed, XSAS is required to be no more than 1.5U when stowed. This size allows for a 0.5U power bus for the power board, batteries, release mechanism, and payload interface, 1U for the stowed 16 panel array and structure, and the remaining 1.5U for payload and interfaces. A maximum mass of 3.5 kg is reserved for the XSAS system, leaving 1.5 kg for payload, reasonable for many CubeSat applications currently under consideration.

There are two flight configurations. The first is a stowed configuration where the panels are retracted like an accordion and constrained in all degrees of freedom by a release mechanism. The second is a deployed position where the panels are extended and constrained by hinge mechanisms and a scissor structure.

XSAS Performance Requirements

Subsystems requirements shape the design and interaction of the power system, structure, mechanisms, attitude control system (ACS), and ground systems. The following list details the top level sub-system requirements, followed by explanations of their application.

- XSAS shall provide at least 20 W beginning of life average continuous power
- Solar array shall have an active and redundant release mechanism
- Solar array shall have passive deployment and locking mechanisms
- Deployment and locking sequences shall apply zero shock to the power system and payload
- Once deployed, XSAS shall provide gravity gradient stabilization for payload operation
- Ground system shall be able to verify fully deployed configuration

Power system requirements impact the entire design of XSAS. While most CubeSat power requirements are limited to 5 W, XSAS shall supply 20 W of average continuous power during its sunlit orbit. As a result, its array needs to contain enough solar panels with highly efficient solar cells to produce this power. Additionally, the deployment mechanisms must be small enough to fit the required number of panels within the solar arrays 1U stowed volume budget.

The release mechanism is required to be redundant, robust, and reliable. As an active system, testing and verification is vital to the performance validation. Therefore, for testing purposes, the release mechanism shall be simple, inexpensive, and repeatable with a 10 minutes maximum reset time.

The hinge and deployment system must deploy the array passively, control the deployment rate, and lock the array into its open configuration. After initial estimates the entire hinge system is required to have less than a 3-mm height when folded in order to have enough vertical space for 16 solar panels. Hinge width and length also need to be minimized to ensure maximum available surface area, while still providing a reliable connection between panels. Finally, the performance of the array during deployment must be passively controlled at all times to eliminate shock on the structure and payload. This means additional mechanisms must be integrated to passively control the array's deployment orientation and rate.

Note the possibility of gravity gradient stabilization is an inherent quality of the deployed XSAS geometry in LEO. To take full advantage of this unique quality, the system's passive pointing accuracy must be considered in the structural design, mass, and volume budget. Since passive pointing accuracy is controlled by the center of gravity of the deployed system, suitable volume must be allotted for ballast or additional functional mass at the top of the array. Mission specific requirements may have a major impact on the application of this design and shall be considered when sizing the ballast hardware.

Fabrication Requirements

Fabrication requirements control the cost budget and manufacturing time of XSAS. The following list details the top level sub-system requirements and is followed by explanations of their application.

- XSAS shall include all commercial off-the-shelf (COTS) components and materials
- Any fabrication shall be done in house using available student accessible machinery
- Fabrication of the final XSAS prototype shall be completed and tested within 3.5 months

The purpose of these requirements is to restrict the cost of manufacturing a complete XSAS system. By limiting the mechanisms to COTS parts and materials, engineers can focus on the custom and creative integration of these parts. Additionally, mechanisms and components can be rapidly prototyped for testing and production. Lead times of custom parts will not impact the manufacturing time of any XSAS subsystem.

Simulations

Analytical simulations and trade studies were required to determine the quantitative requirements and behavior of the XSAS solar array and gravity gradient system. The solar array was sized based on a trade study between two types of solar cells with average on orbit power losses. The gravity gradient analysis was also completed using simplified disturbance models and the projected geometry and mass distribution of the deployed XSAS and payload. The following sections describe the details of each trade study.

Solar Cell Selection

According to volume constrains, the XSAS array can have as many as 16 panels. To determine the maximum power capacity for this array, a trade study was completed comparing Spectrolab Triangular Advanced Solar Cells (TASC) and Emcore 2nd Generation Triple Junction (BTJ) cells. The most obvious difference is the efficiency and price of each cell. An array composed of TASC cells is half the cost of a BTJ array with an efficiency of 27±3% and 28.5% [10] [11], respectively. Immediately, the additional cost

may outweigh the inconsistency in the efficiency of the TASC cells. The primary components of the trade study are included in Table 2 for average Low Earth Orbit (LEO) conditions.

All specific values for the BTJ and TASC cell properties were collected from references [10] and [11] at max power ($V_{mp} \times I_{mp}$) conditions. With solar arrays on each side of the deployed array, power can be collected throughout the entire sunlit orbit. However, because of the nadir orientation of the array, its solar incidence and therefore cell efficiency constantly change according to the cosine of the incidence angle. As a result, the primary power loss to the array is estimated by the average incidence angle over the sunlit orbit, or 43° at a 1000-km orbit. Based on these results it is obvious the BTJ cells, with an average power of 23.1 W (nearly 5 times traditional CubeSat solar arrays), are the better choice.

Table 2. Beginning of Life Solar Cell Trade Study for 1000-km LEO Orbit

		BTJ	TASC	
	Parameter	Value	Value	Units
Layout	Solar Cell Area	32.86	2.28	cm ²
	Solar Cells Per String	2	6	
	Parallel Strings (Facet)	1	4	
	Number of Panels	16	16	
Power	Cell Efficiency at Reference Temperature	28.5	27.0	%
	Reference Temperature	28.0	25.0	°C
	Maximum Power	32.8	23.6	W
	Temperature Loss Coefficient	-0.006	-0.021	%/°C
	Temperature Power Loss at 67°C [†]	-2.5	-12.7	%
	Incidence Angle Power Loss at 43 Deg [‡]	-26.8	-26.8	%
Net Max Power		32.0	20.6	W
Net Average Power		23.1	14.3	W

Attitude Control System

Beyond its obvious capabilities as a power generation tool, the XSAS system can provide enhancements to the CubeSat attitude control system by its very nature. By elongating the CubeSat along a single axis, the CubeSat will naturally begin to orient itself with its long axis perpendicular to the instantaneous tangent plane to the Earth underneath it. We can explore the relationship between length and this orientation tendency through equation 1:

$$\vec{N} = 3 \left(\frac{\mu}{R^3} \right)^2 \vec{r}_B \times (I \cdot \vec{r}_B), \quad (1)$$

where \vec{N} is gravity gradient torque, μ is the Earth's gravitational parameter, R is the orbital radius, \vec{r}_B is the zenith vector in body coordinates, and I is the diagonal inertial matrix in the body frame. This restoring torque causes the vehicle to return to a nadir pointing position should any disturbances occur (such as orbital motion, radiation pressure or magnetic torquing). It can easily be seen from the equations that no torque exists if the body is oriented nadir. If the body is tilted, however, and $I_x > I_z$ then the nadir position will be a stable equilibrium, and the vehicle will return to a nadir pointing position passively.

A complete design of XSAS must ensure that this restoring torque is greater than any of the lesser disturbances to assure pointing accuracy and mission success. Specifically in the case of the large flat shape of the solar array on XSAS, the torque caused by aerodynamic and solar radiation drag in LEO must be examined with the following equations:

[†] Temperature of a typical flat solar panel in LEO [9]

[‡] Cosine (average array solar incidence angle)

$$T_{sp} = \left\{ \frac{F_s}{c} A_s (1 + q) \cos i \right\} (c_{ps} - cg), \quad (2)$$

where T_{sp} is the solar radiation pressure torque, F_s is the solar constant, c is the speed of light, A_s is the surface area, q is the reflectance factor, i is the solar incidence angle, c_{ps} is the center of solar pressure, and cg is the center of gravity; and

$$T_a = \left\{ \frac{1}{2} \rho C_d A V^2 \right\} (c_{pa} - cg), \quad (3)$$

where T_a is the aerodynamic torque, ρ is the atmospheric density, C_d is the drag coefficient, A is the surface area normal to the direction of travel, V is velocity, and c_{pa} is the center of aerodynamic pressure.

From observation, the first term in Equations 2 and 3 is determined by the orientation and orbit of the spacecraft. Assuming these are constant, the second “static margin” terms, however, are controlled by the mass distribution of XSAS. By controlling its deployed cg position with a ballast or secondary payload, these terms can be minimized to ensure the gravity gradient stabilizing torque is dominant. Figure 2 displays the results from a simulation that estimates the nadir pointing error for a 180° orbit between poles at a range of LEO altitudes (500 to 2000 km). The simulation uses inputted mass and geometric values for an XSAS array, ballast, and payload. It assumes all restoring and disturbance torques are balanced to determine the stable nadir orientation.

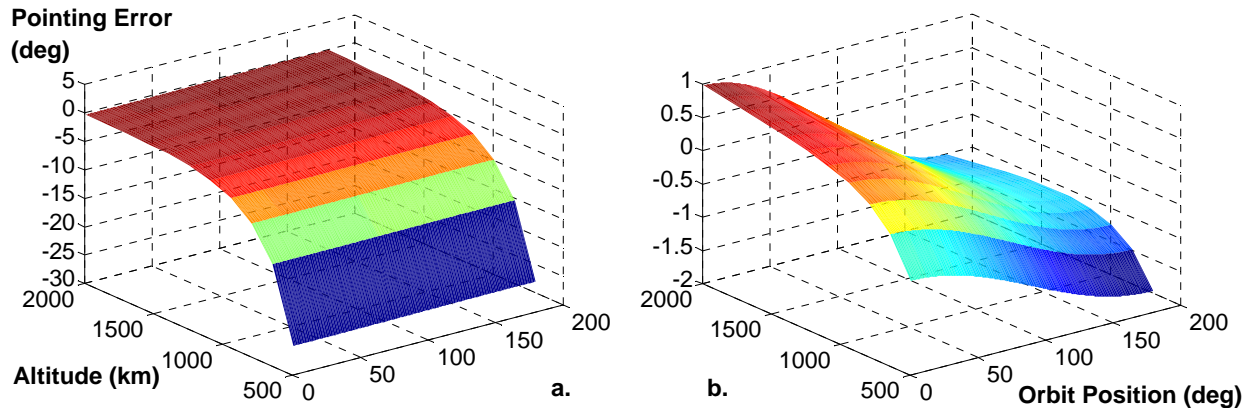


**Figure 2. Pointing Error from Balanced On-Orbit Torques:
(a) Current Mass Distribution; (b) Optimized Mass Distribution (Identical Axis Labels)**

Figure 2a and 2b display the difference between an unbalanced and balanced deployed mass distribution for a XSAS 3U CubeSat and target 1.5-kg payload. Condition 2a is dominated by aerodynamic effects at low altitudes, while 2b has both aerodynamic and solar radiation components. In fact, 2a must fly above 900 km to have a 5 degree minimum pointing error. Unfortunately 2a refers to the current design, while 2b represents an ideal, but over-budget, XSAS with an additional 0.7 kg of ballast. With this understanding, the next XSAS design must implement a more efficient distribution of ballast and payload mass.

Mechanisms

The overall layout of XSAS is defined by the aforementioned requirements and simulation results. However, it is in the mechanical design and integration of the mechanisms that validate the reality of XSAS beyond the simulation or theoretical concept. This however proved to be a non-trivial task with contradicting tight volume and revolutionary power requirements. Careful design of the primary

mechanisms: the release and deployment systems, was completed to ensure their successful integration. Modeling using Solidworks computer aided design software proved to be a very useful integration tool as it allows assemblies to move about realistic physical constraints. A three-panel, fully constrained XSAS CAD model was sufficient to capture all of the critical mechanical details. Figure 3 is a detailed view of the final April 2009 prototype CAD model. Each labeled component represents a sub-mechanism.

Table 3 lists the sub-mechanisms within each primary mechanism. The XSAS chassis is also included in the list because it interfaces directly with the deployment and release systems. The following subsections will describe the design, application, and functionality of these features.

Table 3. Sub-Mechanism Distribution

Mechanism	Sub-Mechanism			
Chassis	• Power Bus Structure	• Ballast Plate		
Release	• Dyneema Cutter	• Release Panels		
Deployment	• Hinge	• Array Panel	• Scissor System	• Rotary Damper

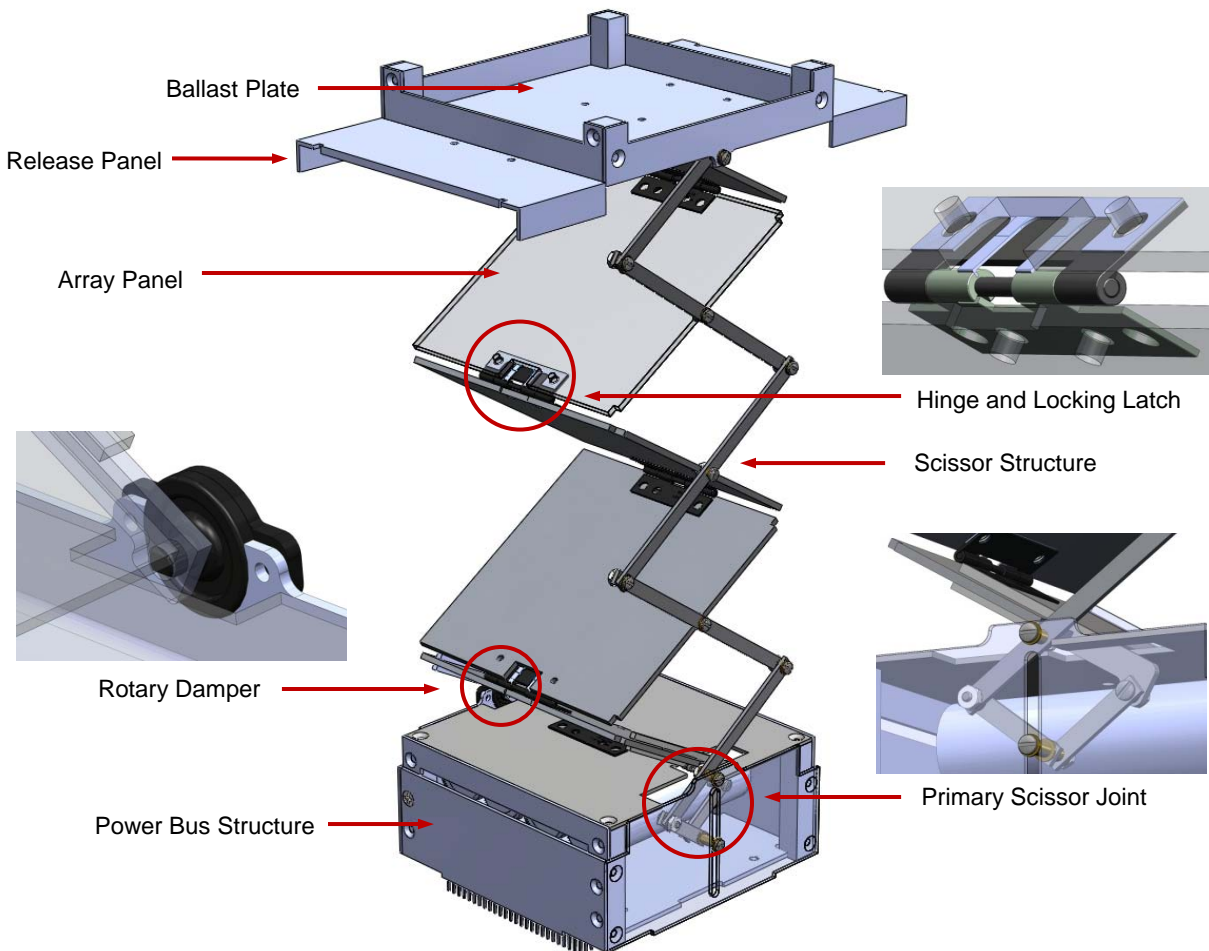


Figure 3. CAD Model and Key Design Features

Chassis

The XSAS chassis is composed of a power bus and ballast plate. The standardized geometry of COTS chassis makes them unsuitable for use on these components. As a result, the custom design of each focuses on the versatility and machinability of the structure.

The power bus idealizes this criterion in the design of the structure and internal space. It houses the release mechanisms, batteries, and power board, and also serves as the attachment between the payload bus and the array system. With connections to a variety of components that are either unknown or constantly changing in design, the layout of the bus will also need to change. Therefore the structure must be versatile and simple to modify. As a result, it is composed of removable panel walls fastened to aluminum posts. The individual panels are simple to machine, allowing single panels to be removed and modified without impact to the rest of the design. Additionally, removable panels permit easy access during assembly, integration, and testing. Finally, the solid aluminum posts allow for a continuous surface for mounting internal components. This method is also used for the fabrication of the ballast plate.

The ballast plate provides attachment volume for ballast mass and a standard interface to the P-POD deployment mechanism. The additional mass correlates the positions of the spacecraft's center of mass (c_m) and center of drag (c_d) to help control the passive ACS benefits of the deployed structure. The amount of mass is dependent on the geometry and mass distribution of the array and payload according to the gravity gradient stabilization theory described in the Simulations section of this paper.

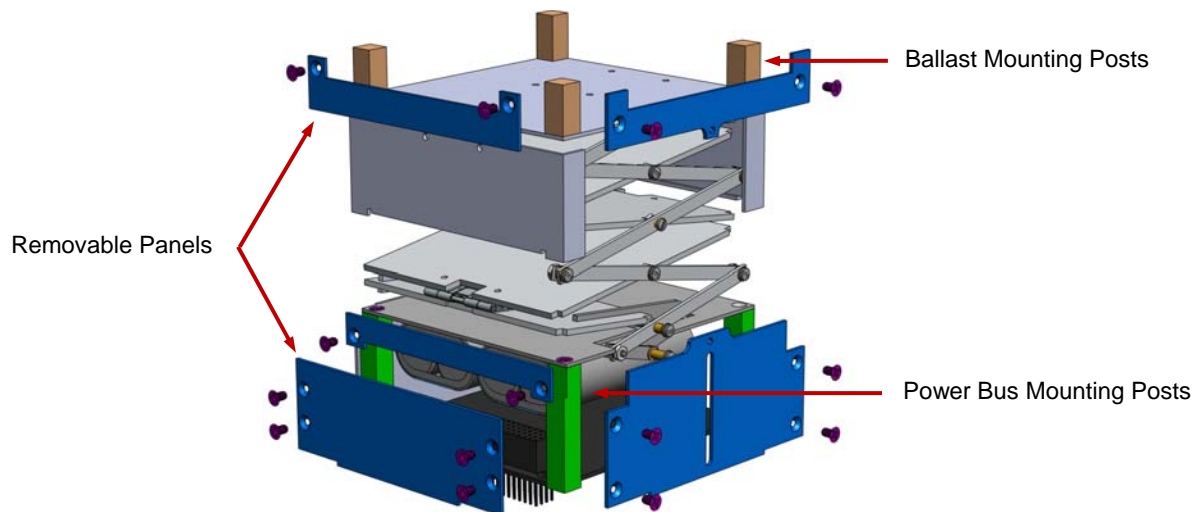


Figure 4. Exploded View of the Power Bus Showing Removable Panels and Mounting Posts

Release Mechanism

The release mechanism is composed of two hinged release panels and a cutter system. Motivations for the design and integration of each feature focus on low cost, low profile, and high reliability.

The resulting cutter system successfully incorporates each motivation. It is composed of 4 metal film resistors wired in parallel and a single line of Dyneema wire. The Dyneema wire is used to tether the release panels to the power bus structure. To do this, the wire is threaded between two holes on each release panel creating parallel lengths of wire that span the bus' interior. Each length then rests against two resistors mounted to the top surface of the bus.

To deploy the release panels, an on-board 9-V source is shorted across the resistor circuit. The resulting heat generated by the resistors cuts the wire allowing the release panels swing to open. Since one strand of Dyneema wire is used, only one resistor within the quadruple redundant array is required for a

successful release. Additionally, with the placement of the panel attachments and positioning of the resistors, the entire system requires a fraction of the available volume within the bus. Furthermore, the use of redundant resistors and Dyneema was implemented on the Delphi C3 nanosat mission [12] to deploy its solar arrays, proving the reliability of the inexpensive system.

The release panel design mimics the motivations used on the cutter system. Each panel is composed of a custom formed aluminum sheet and a single spring hinge. The geometry of the panels fully constrains the stowed array with minimal impact on the array panel dimensions. To accomplish this, each release panel has three folded edges called ribs. The side ribs will be referred to as ribs 1 and 2, and the bottom rib will be rib 3. This labeling is displayed in Figure 5. Ribs 1 and 2, and the lower portion of each panel fit within recessed areas on the power bus. This constrains the lateral translational degrees of freedom (DOF) of the array and rotational DOF about the vertical axis, z . Rib 3 is held within a slot in the power bus constraining the vertical translational DOF and rotational DOF about the x axis. The final rotational DOF about the y axis is constrained by the tension of the cutter system's Dyneema wire and the resulting interference of the panel and power bus. Once the system is released the spring hinge quickly rotates the release panels to the ballast plate. This prevents any interference with the deployment sequence of the array and also adds additional mass the ballast plate.

The panels are also designed to protect the solar array mechanisms and structures while stowed. The ribs create a constant surface along the edges of the stowed array to act as rails within the P-POD deployment mechanism. According to standard CubeSat requirements, the rails must cover at least 75% of the CubeSat length [5]. The release panels provide a nearly complete surface to satisfy this requirement.

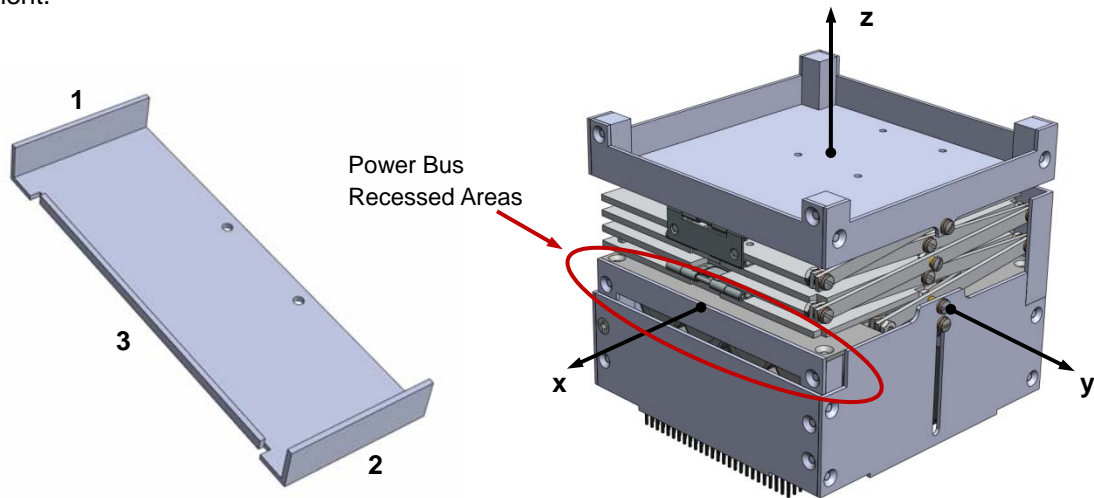


Figure 5. Release Panel Geometry and Constraint Method

Deployment Mechanism

The deployment mechanism is made up of the hinge system, array panel structure, scissor system, and rotary damper. Like previous mechanisms, the design of the deployment mechanism was non-trivial, needing numerous iterations to best satisfy the XSAS requirements. Each sub-mechanism is inspired from simple known concepts that have been creatively applied to the CubeSat geometry.

The hinge system is a compound mechanism that passively controls, deploys, and locks the solar array at each panel joint. The challenge was minimizing the vertical height of each compound hinge within the stowed 10cm length, as the height determined the number of solar panels in the array. The original design concept (Figure 6a) employed separate spring, damping, and locking hinges. This design did not meet COTS and size requirements. As a result, this arrangement would need custom designed components, which proved prohibitively expensive. The next iteration (Figure 6b) removed the damping hinge and

replaced the locking hinge with a plunger bolt. Again, failed size requirements and tolerance issues forced another redesign. The final two designs (Figure 6c,d) employ a modified COTS spring hinge mated with a custom locking latch. The end of each latch arm is bent at a 90 degree angle creating teeth. While stowed, these teeth rest on the outside of the hinge barrel, which pretensions the latch arms. During deployment, the teeth ride along the outside of the rotating barrel until they fall into slots machined into each hinge. This not only locks the hinge, but orients the open array at a predefined angle. In the case of XSAS, it is 180 degrees. Manufacturing constraints influenced the final redesign displayed in Figure 6d.

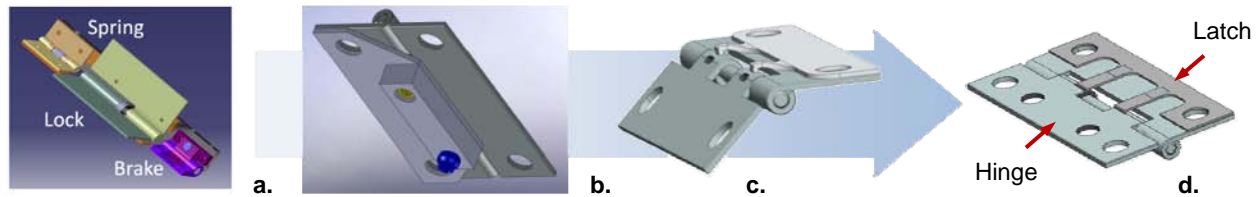


Figure 6. Hinge Design Evolution

The scissor system manages the orientation of the array during the deployment sequence. This concept incorporates inspirations from a common scissor lift. It is composed of two parts, the scissor structure and primary scissor joint. The structure coordinates a consistent deployment of each array panel and is fastened to only one side of the array, minimizing losses to the array panel area. The joint restricts the movements of the structure to a single vertical DOF. To control this vertical motion, the final joint connection slides within a channel cut into the bus panel wall. Using simulations from the CAD model, the joint arms are placed as close to the bus wall as possible as shown in Figure 7a. As a result, the joint does not impact the geometry of the array and has minimal impact on the volume within the power bus.

Additionally, the scissor joint provides a single point at which array can be controlled. Since the damping component of the hinge system was removed from the final design, a rotary damper is placed at the base of the array to control the deployment velocity. The damper uses viscous effects to counteract the velocity of the array as the damping constant increase with an increased rotational velocity.

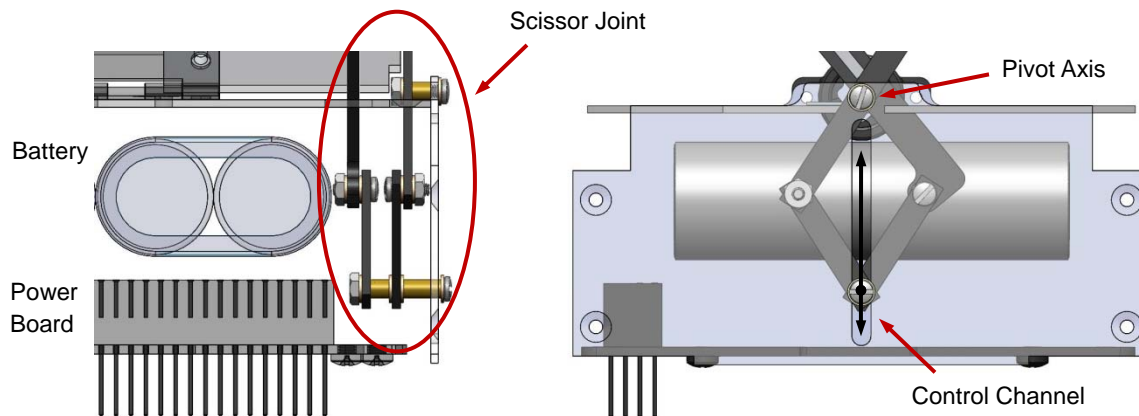


Figure 7. Scissor Joint Composition: a. Front Internal View; b. Side View

Successful assembly of each component is made possible by the geometry of the panel structure. Proper cutouts and hard point connections within each panel manage all connection and clearance requirements. This was designed confirmed through CAD simulations. Solar cells assembled on printed circuit board (PCB) can then be plated to the primary panel structure.

Hardware and Prototype

The primary goal of this first phase of the XSAS design was to create a prototype to demonstrate and study the manufacturing methods, integration, and functionality of the high risk mechanisms. Therefore the prototype serves primarily as a technology demonstrator rather than flight hardware. It was successfully tested using the aforementioned release and deployment system. The prototype and deployment sequence is displayed in Figure 9. This section describes the details of the hardware used.

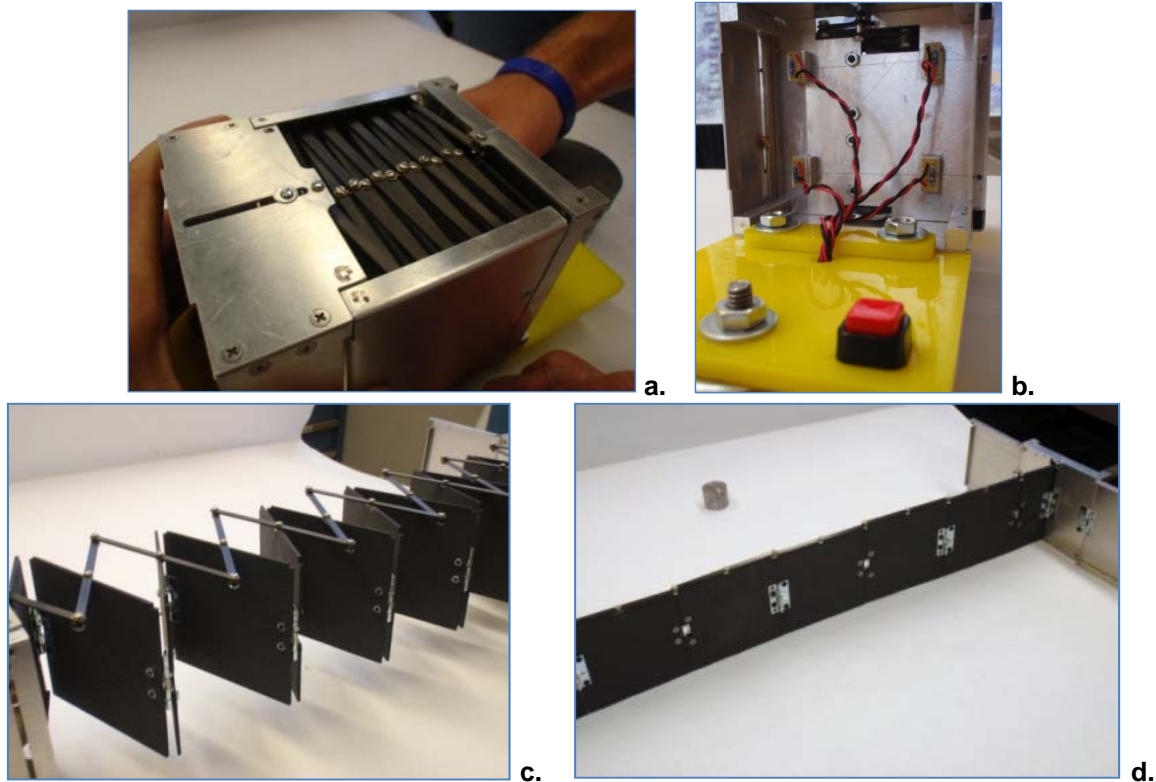


Figure 9. XSAS prototype deployment sequence: a. Stowed configuration; b. Metal film resistors positioned within power bus burn Dyneema wire restrains; c. Scissor structure evenly deploys panels; d. The completely deployed XSAS structure

All materials used on the XSAS prototype were purchased from stock supplies. Table 4 lists the materials used for each primary mechanism. Aluminum 7075 and aluminum 6061 are used for all chassis panels and posts respectively. The most obvious reason for this selection is aluminum's low density, corrosion resistance, and relatively high strength, which makes it widely used on spacecraft chassis. Additionally, each type of aluminum is approved for CubeSat structures by the CubeSat Requirements document [5]. Aluminum 5052 is used for the release panels because of its good formability properties. It is used by COTS CubeSat Kit structures, which are bent to optimize the stiffness and mass of the structure. Quasi-isometric 2-mm carbon fiber plate, manufactured by Dragonplate, is used for the solar panel structure to optimize the stiffness of the deployed panels. The profile of each material is design used CAD software and cut using a CNC waterjet cutter. Flat-head, countersunk machine screws are also used to join all exterior structural panels. This keeps a smooth exterior surface, preventing any interference with the P-POD deployment mechanism.

Table 4. List of Materials

Mechanism	Component	Material	Dimensions
Chassis	Panel	7075 Aluminum Plate	1.27 mm (0.05 in)
	Posts	6061 Aluminum Bar Stock	7.87 x 7.87 mm
Release Mechanism	Panel	5052 Aluminum Plate	1.27 mm (0.05 in)
Deployment	Panel	Quasi-iso Carbon Fiber Plate	2mm plate
	Scissor Arms	Unidirectional Carbon Fiber Bar	1.47 x 4.50 mm
	Locking Latch	304 Stainless Steel Shim Stock	0.254 mm (0.01in)
	Hinge	Low Carbon Steel	n/a

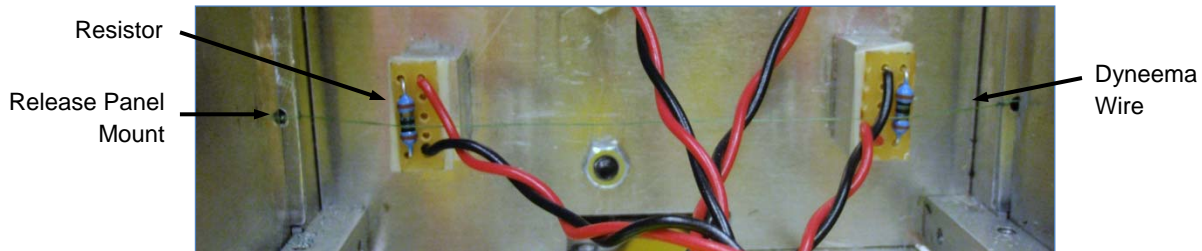


Figure 10. Assembled Release Panel Cutter Strand

Metal film resistors and Dyneema wire are used in the design of the XSAS release cutter mechanism. ¼ watt 10 Ω resistors were chosen. With such a low power rating each resistor is designed to handle only 28 mA with a 9-V power source. Instead, because of the low resistance, when the circuit is shorted, the resistor draws 900 mA, more than 32 times the rated value. This overload heats the resistors in excess of 150°C, the melting point of Dyneema wire, in 1 second. Aside from the low melting temperature, Dyneema was chosen because of its superior tensile strength, which is 15 times that of steel[§]. This allows the wire to be drawn tightly through the release panels while stowed, which has two benefits. First, it creates a snug and reliable fit between the panels and power bus; second, it produces a tight connection with the surface of the resistors. To ensure and intensify this connection, the resistors are mounted slightly below the level of the release panel mounting points. Figures 9b and 10 display the positioning of the resistors and threading of the Dyneema wire.

The spring hinges are COTS components manufactured by Guden. To make each hinge compatible with a locking latch, a 0.30-mm (0.012-in) jeweler’s saw was used to cut slots in the barrel of the hinge. The locking latch is created from water-jet cut 0.254-mm (0.010-in) stainless steel shim stock. Multipurpose stainless steel 304 was used because of its good formability properties and excellent corrosion resistance. The 0.0508-mm (0.002-in) excess tolerance on the slot ensured the latch tooth would successfully fall into the slot on each test. Once the latch is mated with the hinge, the entire system requires only 3.1 mm of vertical space. As a result, 16 stacked panels require 95 mm satisfying the volume and power requirement.

The scissor components are completely constructed from COTS materials and hardware. They were discovered as a design necessity through early prototypes. As a result, the structure and joint needed to be integrated into the design late in the process. To minimize its impact on the existing design the structure needed to be isolated to one side of XSAS. Unidirectional carbon fiber/epoxy rod, produced by a hobby supplier, presented an ideal solution for the structure. The carbon scissor arms are joined together and at the solar panels with stainless steel 2-56 machine screws and nuts. Brass washers are placed between the hardware and carbon surfaces to minimize fatigue on the composite. The scissor joint

[§] http://www.dsm.com/en_US/html/hpf/home_dyneema.htm

hardware is much more complicated. Stainless steel sleeves with a #2 inner diameter made it possible to stagger the locations of each arm. Again 2-56 hardware and brass washers are used.

Rotary dampers produced by ITW Delpro for the automotive industry were donated to the XSAS project. Unfortunately it was discovered through testing that these rotary dampers acted as a friction joint rather than a viscous damper. Although no COTS rotary damper was ever found for this application, it was included in the design to demonstrate an integration method for future development

Testing

Testing was limited to the observed bench-top performance and condition of each mechanism. To accomplish this, low-friction test carts, made of acrylic panels and captured ball bearing castors, were fabricated to provide the best bench-top method to observe the behavior of the system. XSAS is mounted on the carts with the hinge axis perpendicular to the table surface. Figure 11 displays the assembled test cart.

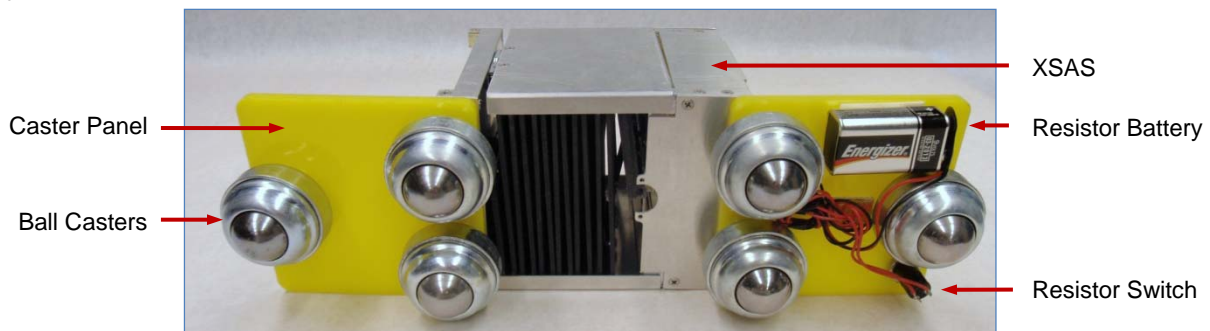


Figure 11. Assembled Test Cart (Bottom View)

This setup allows for minimally constrained 2DOF motion along a table surface isolating the controllability of the deployment system. To further validate the test conditions, the motion in and out of the test plane should be negligible even in orbit due to the inherent bending stiffness of the structure against the hinge axis. Additionally, to test the release mechanism the cutter resistors were wired to a switch and a 9-V battery on the bottom of the test cart. The switch and delay in the cutter allows the tester to activate the circuit and step back from the system, preventing them from impacting its performance.

The release system performed flawlessly during all attempts and the scissor system worked as planned to provide a consistent expansion of all array panels. Improvements focused on the redesigned of the hinge and locking system. Fatigue from multiple test trials permanently deformed the barrel hinges and locking prongs negating the required tolerances to ensure a locked hinge. Additionally, due to the strain and unidirectional layup of the scissor joint members, one of the arms split in half along its length. This failure points towards the use of metallic components for the joint structure since an improved layup could not be found in COTS components.

Conclusions and Future Work

While the concept of a deployable solar array such as XSAS is simple, its implementation is nontrivial, especially under the constraints of the CubeSat form. The analysis and simulations presented in this paper yielded a functional prototype of the XSAS mechanism. Additionally, analytical trades have characterized its power and ACS capabilities. Results proved extremely successful for a concept of this infancy. Successful, integration, deployment, and control of the array were achieved, proving the hardware could function within CubeSat volume and mass constraints. Moreover, estimated average and maximum power capabilities at 23 and 32 W, respectively, exceed initial design requirements.

As expected of a technology demonstrator for a new and novel design, the simulation and test results also revealed many improvements that can be made to the current system. Areas of focus address improvements to current hardware such as fatigue, tolerance, and thermal concerns with the hinge and locking mechanism, identification and integration of a damping mechanism, and improved gravity gradient capabilities with a more efficient mass distribution and payload interface. Additionally, new challenges such as the solar panel electrical integration, cross-panel wiring harness design, improved array orientation and structural analysis, and an understanding of the unconstrained release and deployment dynamics, will bring XSAS closer to flight hardware status.

The University of Michigan Student Space Systems Fabrication Laboratory (S3FL), an active student group, has taken on the XSAS concept for continued development. S3FL will focus on improved design and analysis of the mechanisms, structural mechanics, and deployment dynamics of a new XSAS prototype. This summer they will test the prototype in microgravity within NASA's Reduced Gravity Student Opportunities Program. This program allows selected teams to fly onboard the famed "Vomit Comet" to perform experiments in a controlled and unconstrained 6-DOF environment. This first microgravity flight will help in the dynamic analysis of the XSAS system and prepare for additional, future flights, supporting CubeSats in low Earth orbit.

Acknowledgements

The authors would like to thank the students of AE/AOSS 582 and 583 during the Fall 2008 and Winter 2009 school year for their dedicated efforts in supporting the XSAS project. In particular, Eric Kosmyrna made significant contributions to XSAS' development. Furthermore, the authors are grateful to the S3FL and XSAS Reduced Gravity Student Opportunities Program teams for continuing development and flying it onboard the "Vomit Comet".

References

1. Berry, LB and Brown, WD and Dawson, WP and Suenaga, EL and CA, H.A.C.O.E.L.S. and others, "Flexible Integrated Solar Cell Array", AFAPL-TR-67-100, Contract AF 33-(615)-2750, Aug. 1967, Space Systems Div., Hughes Aircraft Co, 1967.
2. _____, "Deployable Solar Array", US Patent 3,532,299, 1970.
3. Aguirre-Martinez, M. "Developments in deployable masts to support flexible solar arrays", CSA Illumina, p391-398, 1984.
4. Malone, P.K. and Williams, G.T., "inflatable solar array", Journal of Propulsion and Power, v12, n5, p866-872, 1996.
5. _____, "CubeSat Specifications", Available at: www.cubesat.org, 2009.
6. Rossberg, F., "Structural Design of a NPS CubeSat Launcher", Storming Media, 2008.
7. Koyama, M. and Suzuki, K. and Imamura, O. and Yamada, K., "Study on Mini Re-Entry System Using Deployable Membrane Aeroshell", Transactions of Space Technology Japan, v7, 2009.
8. Pearson, J. and Levin, E. and Oldson, J. and Carroll, J., "ElectroDynamic Delivery Experiment (EDDE)", AIP Conference Proceedings, p425-432, 2001.
9. Larson, W., Wertz, J., "Space Mission Analysis and Design", Microcosm Press, 1999.
10. _____, "Triple-Junction with Monolithic Diode (BTJM) High Efficiency Solar Cells for Space Applications", Emcore, Inc, Available at: http://www.emcore.com/assets/photovoltaics/Emcore+BTJM+Solar+Cell+Data+Sheet_May-07.pdf, 2010.
11. _____, "Triangular Advanced Solar Cells", Spectrolab, Available at: http://www.spectrolab.com/DataSheets/PV/PV_NM_TASC_ITJ.pdf, 2010.
12. _____. "Delphi C-3" TU Delft, Available at: <http://www.delfic3.nl/>, 2010.

Development of a Solar Array Drive Assembly for CubeSat

Mike Passaretti* and Ron Hayes*

Abstract

Small satellites and in particular CubeSats, have increasingly become more viable as platforms for payloads typically requiring much larger bus structures. As advances in technology make payloads and instruments for space missions smaller, lighter and more power efficient, a niche market is emerging from the university community to perform rapidly developed, low-cost missions on very small spacecraft - micro, nano, and picosatellites¹.

In just the last few years, imagingⁱⁱ, biologicalⁱⁱⁱ and new technology demonstration missions have been either proposed or have flown using variations of the CubeSat structure as a basis. As these missions have become more complex, and the CubeSat standard has increased in both size (number of cubes) and mass, available power has become an issue. Body-mounted solar cells provide a minimal amount of power; deployable arrays improve on that baseline but are still limited. To truly achieve maximum power, deployed tracked arrays are necessary. To this end, Honeybee Robotics Spacecraft Mechanisms Corporation, along with MMA of Nederland Colorado, has developed a solar array drive assembly (SADA) and deployable solar arrays specifically for CubeSat missions. In this paper, we discuss the development of the SADA.

Introduction

This SADA has been designed and prototyped specifically for CubeSat satellites. A CubeSat is a type of small satellite intended for cost-effective research in low Earth orbit space flights. A CubeSat comprises of a number of standardized modules or "U's" which measure exactly 10 cm³, weigh no more than 1 kilogram and are well known to use readily available system components. CubeSats also follow a standard which was pioneered by the California Polytechnic University and Stanford University in 1999.

Implementation of an articulated solar array drive addresses the demand for maximal power transfer from a given solar array assembly. In conjunction with a solar array assembly, the SADA further increases the effectiveness of "low-cost" CubeSat missions. A prototype SADA unit has been developed for demonstration purposes. The prototype was developed using sound aerospace engineering practices that pave the way to future flight units. To further enhance the performance of this system, this SADA will also be able to support autonomous sun-tracking. The SADA described herein is a simple, self contained, ultra-thin, low-power, stackable single actuator drive system. This self-contained system is designed to operate on approximately 500 mW of power while articulating the arrays, and less than 1 mW while the actuators and system are inactive. The SADA power system will be supplied from existing CubeSat power bus and can accept a range of voltages.

All of this innovative technology is specifically designed to fit in what used to be wasted payload space, a 6.5-mm "slice" of the CubeSat bus. Refer to Figure 1 for the location on the bus where this system is designed to reside.

* Honeybee Robotics Spacecraft Mechanisms Corporation, New York, NY

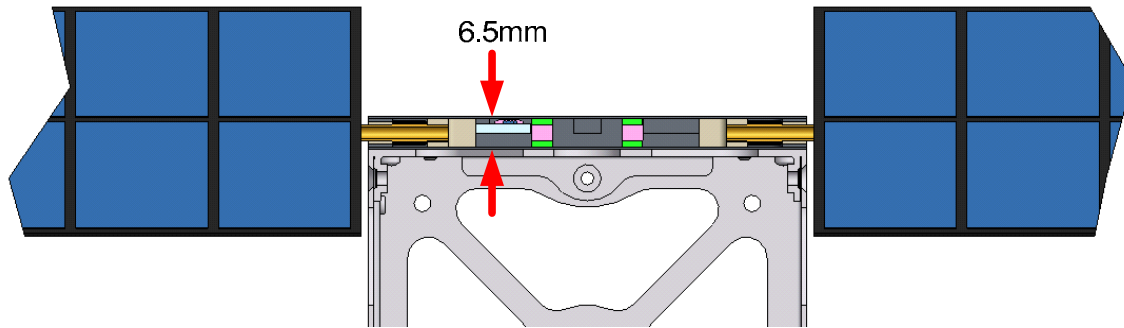


Figure 1: 6.5mm “slice” of CubeSat bus where SADA will integrate on the end of typical CubeSat structure.

Mechanical Description

The solar array drive assembly performs key system functions, rotating the solar arrays to keep them optimally oriented with respect to the Sun and providing a path for power transfer from the arrays to the CubeSat bus. The prototype system is shown in Figure 2. This prototype was specifically developed to make use of off-the-shelf technology to minimize the cost and complexity of the design.

Solar arrays are attached to either end of the SADA onto output shafts protruding from the unit. Cable-twists are used to carry power from the arrays and each wing has a dedicated cable-twist assembly. Cable-twists offer several advantages, but from an operational standpoint they need to be protected from over winding. To prevent over-winding, mechanical hard stops are implemented to limit the rotational travel of the output shafts. The SADA is designed to accommodate slip rings for continuous rotation if required, but the total number of circuits available for both power transfer options is limited due to the small height of the device. This became one of the major challenges in the electrical design.

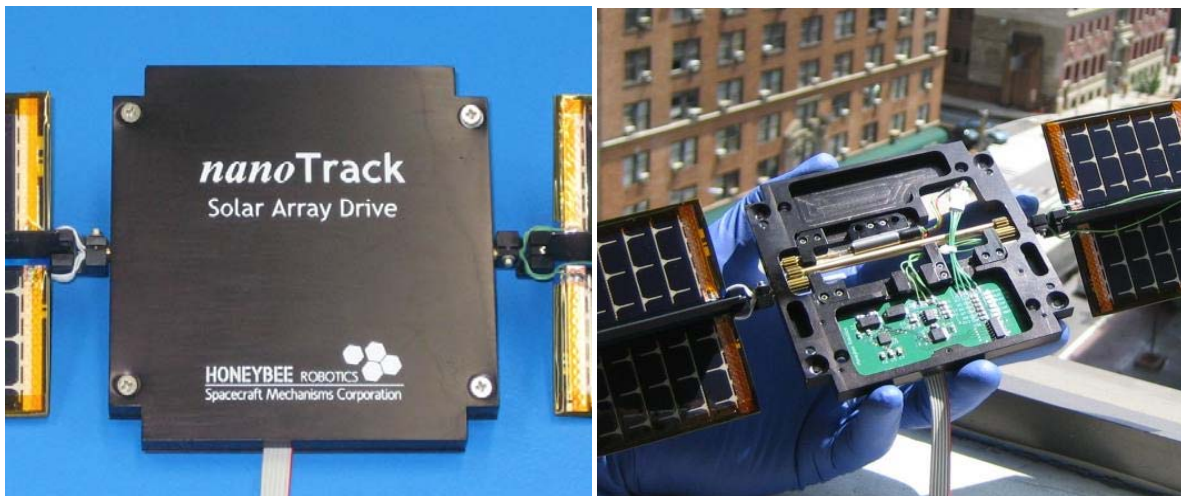


Figure 2: Prototype unit shown with cover on (left) and off (right) on top of Honeybee Robotics headquarters in Manhattan.

Small Satellite Electronics & Considerations

Very small cost-effective spacecraft such as CubeSats are well known to take advantage and are almost synonymous with employing the use of commercial-off-the-shelf electronic components. The benefits gained by designing from such volumes of commonly available and very inexpensive hardware, does not come without some added risk. The demanding environment of space in which all spacecraft are asked to operate in, brings with it exposure to several extreme factors, namely radiation.

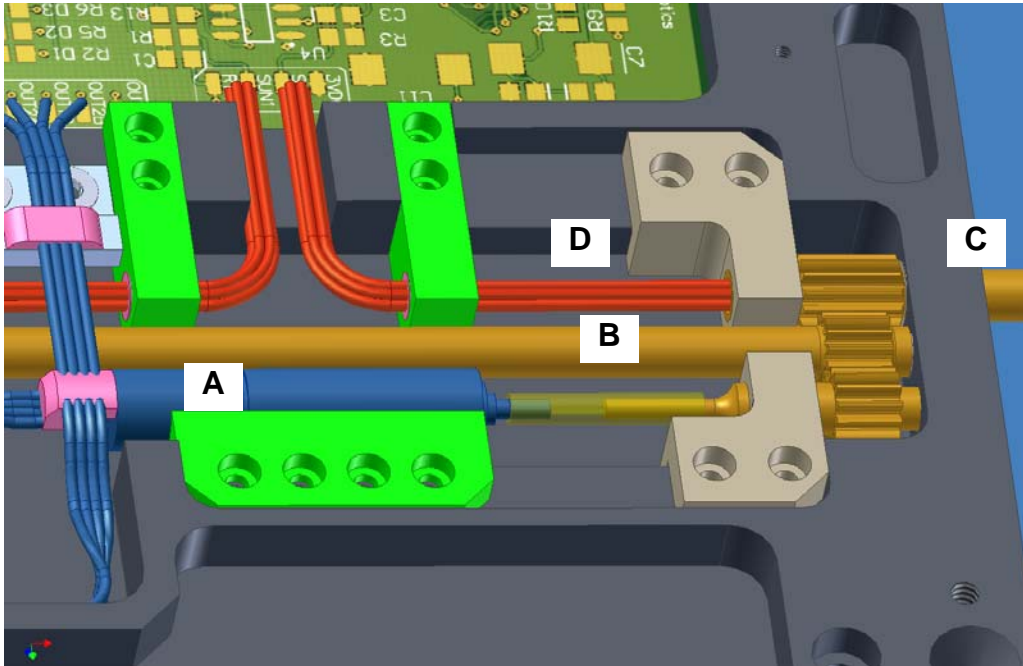


Figure 3: Details of drive train and power transfer sections. Stepper motor and multi-stage planetary transmission (A), idler gear shaft (B), output shaft and gear (C), and cable wrap (D).

Semiconductor based electronic components are inherently susceptible to unwanted effects of space radiation. These effects can be generally separated into two classes: cumulative and single event effects (SEE). The first class, cumulative effects are brought on gradually throughout the lifetime of exposure in a radiation rich environment. The upper limit on the cumulative amount of radiation a susceptible component can accept before failure is referred to as the total ionizing dose. Total ionizing dose is the measure of the cumulative dose of energy transferred into the material by radiation in the form of ionizing energy. Thorough testing and characterization of a component can be used to confidently assess its total ionizing dose. The second class, single event effects are quite different in that they can be attributed to the energy transferred by a single particle interacting with an electronic device. A device susceptible to SEE can therefore exhibit failure at any moment.

There are different types of SEE. Single event upsets are non-damaging soft errors. Single event upsets typically appear as transient signals, or as bit changes in memory stores. In contrast to single event upsets, which are only seen in software, there exists a counterpart in hardware, single event latch-up. Single event latch-ups can result in higher operating currents which can lead to component degradation and possible failure.

Radiation hardening, or “rad hard” for short, is a method of designing and testing electronic components such that they are resistant to the unwanted effects associated with the environment of high altitude flights above Earth or in outer space. The typical costs associated such “rad hard” devices are normally

high and are therefore only reserved for consideration when larger budgets are available. Traditionally space systems have been designed using a limited number of electronic components, whose limited variety can be attributed to availability of their radiation hardened versions. However, a migration from traditional rad hard components is currently underway, thanks to the commercialization of space. Space is no longer the sole domain of the world's largest governments, where programs are funded by enormous and eternal budgets aimed at fighting the cold war. Consequently, space manufacturers around the world are faced with a requirement to build satellites that are faster, better and cheaper than those made in the past.^{iv}

Another way of dealing with the unwanted effects of radiation and thereby still achieving "rad hard," is through clever hardware & software designs. Common techniques include cold-redundancy (only one processor powered at a time thereby minimizing risk of a SEE). Other techniques such as hot-redundancy are also employed in the case of memory access. Hot-redundancy utilizes voting schemes where the contents of triplet and physically separate memory stores are compared and voted upon using a "majority-wins" rule to confidently obtain a valid result. Similar techniques can be implemented in software for an added level of radiation hardness. The principle of triplet techniques can be used with data variables.

Over the years since this migration has taken place, select groups of readily available electronic components have made their way onto satellites and into space. The Texas Instruments MSP430 family of microcontrollers is one example of typically sought after processors that have been used over and over on CubeSat missions. Another example is the Atmel ATmega64 microcontrollers. As CubeSats are becoming more attractive to organizations and institutions, more and more commercial-off-the-shelf (COTS) type electronics are emerging as viable small satellite system components. Companies like Pumpkin Inc^v are now introducing products that are based on the widely available and commonly known 8051-, Microchip PIC24/dsPIC33 as possible design options for CubeSat engineers.

SADA Electrical System

The SADA's embedded control unit (ECU) was designed around a low-cost Texas Instruments MSP430F2013. The microcontroller (MCU) used was very simple but effective; having just enough memory to demonstrate the SADA's capabilities. While motor commutation was accomplished by the algorithm run on the MCU, the step sequences were translated to a motor driver IC. The motor driver IC was used to energize the coils of our bipolar stepper motor. The motor driver chosen was the Allegro MicroSystems A3906 low-voltage motor driver chip. Each output channel of this device is rated at 1A and the device itself can operate on voltages as low as 2.5VDC. The A3906 was chosen for its cost, availability and functionality and very small package (QFN-20, 4x4x1.5 mm). Other features of the device include internal thermal shutdown and under voltage lock-out. For power, a low-noise, low-drop-out (LDO) voltage regulator was chosen. The Linear Technologies LT1763 is capable of supplying 500 mA of output current with a LDO voltage of <300 mV. This LDO regulator is specifically designed for low power, battery applications.

The performance of the above mentioned electronic components are used to realize the core functions of the SADA's prototype ECU. The prototype ECU is comprised of the following major sub-systems: a spacecraft bus power translator module (LT1763), processor unit (MSP430) and the stepper motor translator (A3906). Refer to Figure 4 for the system block diagram. It should be noted that external memory stores as well as the spacecraft communication module were not implemented in the prototype ECU.

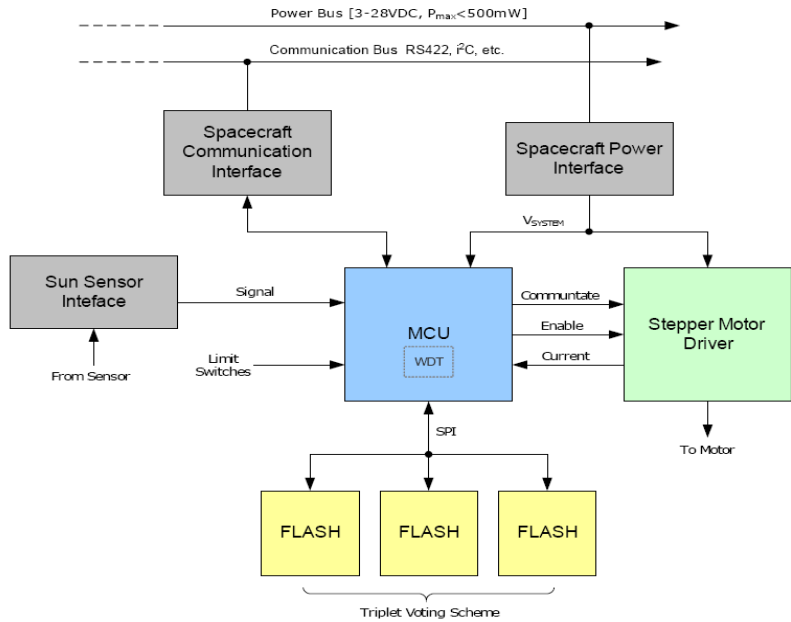


Figure 4: Block diagram of SADA drive and control electronics

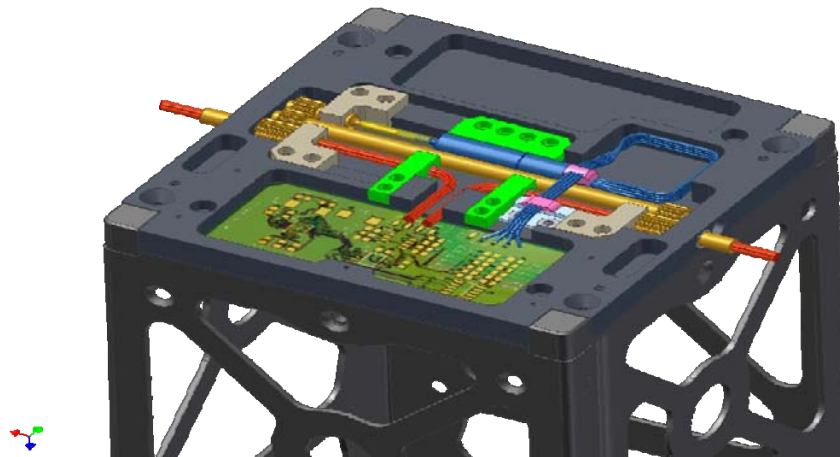


Figure 5: Inner workings of the prototype SADA shown on typical CubeSat structure. The drive fits into the typically unused space at the end of a standard frame (e.g. Pumpkin^V).

Electrical Controls

This SADA ECU is designed to enable Sun tracking in two possible modes of operation. While the spacecraft communication module was not included in the prototype, this first mode is intended to allow the SADA ECU to receive commands over the spacecraft communication bus for purposes such as Sun tracking. Typical Sun tracking are: “track”, “idle”, “stop” and “position.” If the ECU is not acting on commands via a host, it will default to an autonomous Sun tracking mode. In either mode of tracking, the host may request data from the SADA at any time. For the purposes of this first prototype, the device was always run in autonomous Sun tracking mode.

The SADA ECU is capable of entering into a “stand-by” mode while the system is inactive. In stand-by mode the system is still capable of receiving and reacting to commands from the host. This powerful

interrupt driven feature of the MCU unit chosen drastically reduces complexity of the software control system and greatly reduces the power consumption of the system. From a standpoint of consumption, the system will operate on approximately 500 mW while actively tracking and less than 1 mW while in stand-by.

The solar array position is controlled in an open-loop fashion. The motor current is limited by the stepper motor controller for thermal protection and power savings reasons. The motor current is also monitored by the MCU for increased perception from a controls standpoint. Motor steps are accumulated and limit switches (not shown in models) are used to reliably detect proximity of hard stops. The limit switches in conjunction with hard-stops are approximately 360° apart and allow for the angular position at the respective extremes to be known by the MCU. One of the limit-switch/hard-stops will be designated as the “home” position. This is the default starting point for rotation of the output shafts and attached solar arrays. The shaft is free to rotate and track the Sun (under command from either the host or via feedback from the Sun sensor) while under control of the MCU for approximately one full rotation. At the end of this rotation the next limit-switch/ hard-stop will be encountered. The system will recognize this limit and the array will be rotated back the “home” position to pick-up where it left off and begin tracking again. The process will be repeated on orbit, keeping the arrays pointed at the Sun to maintain optimal power levels on the solar arrays.

Sun Sensing

For purposes of the prototype, a very simple Sun sensor was created by using two inexpensive COTS photovoltaic (PV) cells. A “fence” or intra-bank barrier was positioned between the PV cells. In Figure 6, the action of the intra-bank barrier in determining Sun position is illustrated. In this diagram, it can be seen that as the angle of the light source (or Sun in this case) changes relative to the array it casts a shadow onto the cell bank furthest from it, causing a reduced output from that bank (or string). A photograph of the prototype sensor can be seen in Figure 7. A simple algorithm was written to interpret the overall effect of the system with an incident light source.

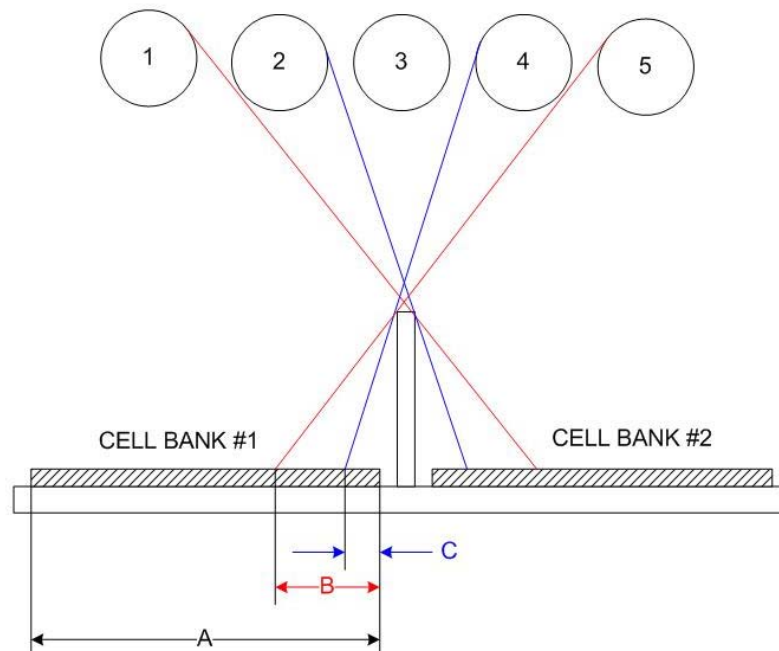


Figure 6: Illustration of Sun angle to obscured portion of cell banks. Note that of the total available area (represented by ‘A’) the obscured area (‘B’ and ‘C’) decreases as the light source becomes normal to the panel surface. By comparing the output of the two banks shown, we are able to determine gross array position relative to the Sun.

The algorithm was written and executed on the MSP430 MCU to accomplish a simple but effective Sun tracking mode. The 12-bit ADC on-chip peripheral provided by the MCU was used to sample and convert the loaded PV cell bank voltages. The ADC was called upon to sample both PV cell bank banks at approximately 1 kHz; this data product was then used by the algorithm to determine position. A “dead band” variable was defined and used to account for acceptable difference between the PV cell bank voltages. When the relative voltage between the two PV cell banks deviated by a value greater than the dead-band, the light-source’s angle of incidence is inferred and the direction in which the PV array is to be rotated is established. A sample of this algorithm is shown here:

```

GetDIRECTION( ) {
IF (SUNSENSE1 > (SUNSENSE2 + dead_band))
return CLOCKWISE;
IF (SUNSENSE1 < (SUNSENSE2 - dead_band))
return COUNTER_CLOCKWISE;
ELSE
return NO_MOTION;
}

```

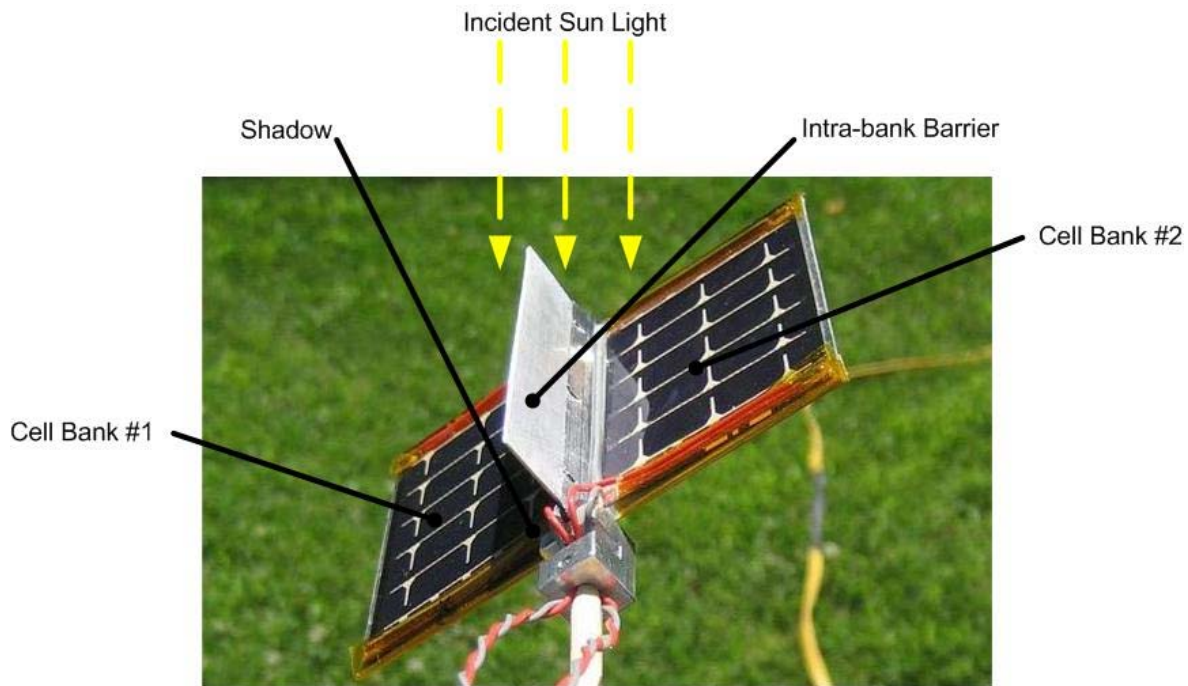


Figure 7: Prototype Intra-bank Barrier Test

Because the drive itself is so thin (6.5-mm thick) and so much is packed in the available space, there is little room for power transfer. Typically, devices used for transfer of power generated in the solar arrays into the body of a spacecraft have been either slip rings or twist capsules. Slip rings are devices that use sliding contacts on rotating rings to allow continuous rotation of the ring (typically it is this part that is connected to the arrays themselves). In this drive, the option exists to use either a slip ring or twist-device. Both are limited however, as the number of slip ring circuits and their current-carrying capacities are limited by the space available. Because of this, the method described above was developed to perform course sun tracking without additional sensors on the wing.

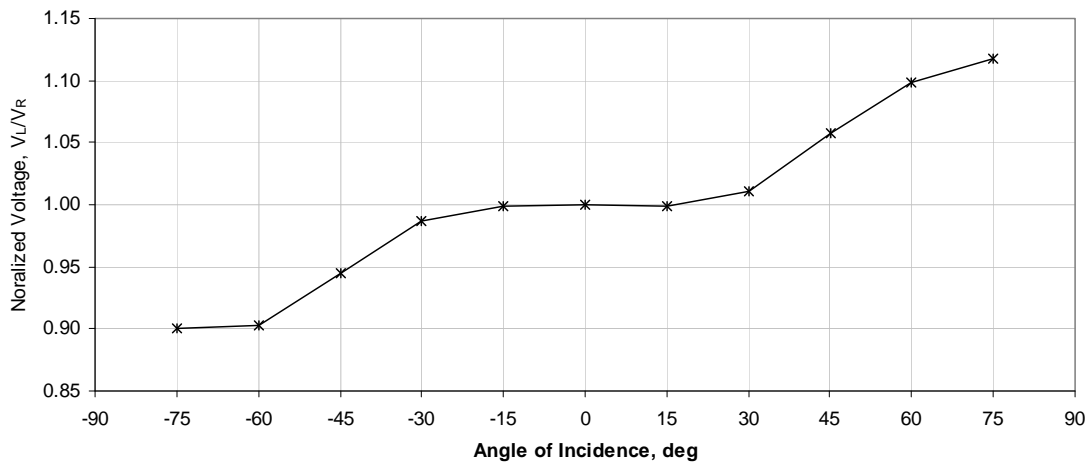
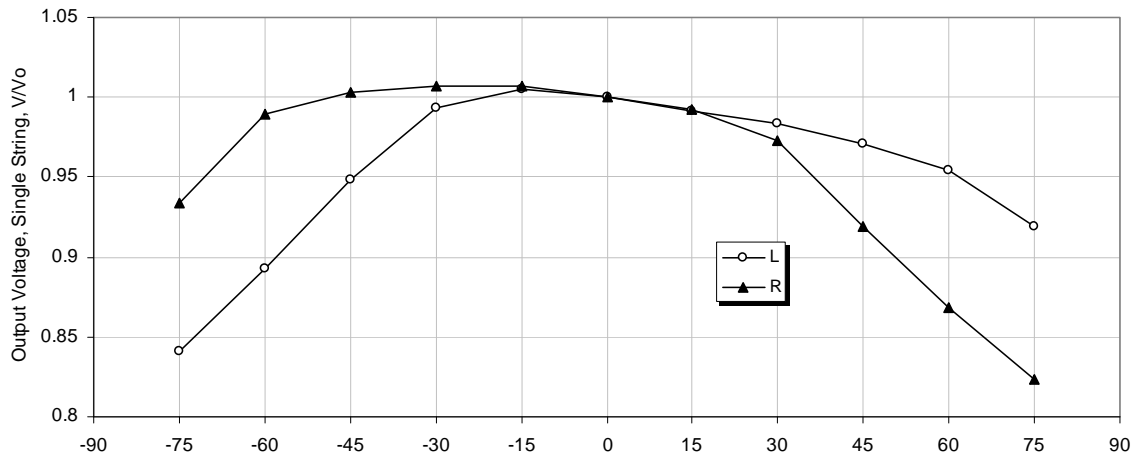


Figure 8: Characterization of breadboard solar array configuration with raised, intra-bank barrier. The top graph shows the output of the individual strings as a function of Sun (gimbal) position; the bottom graph shows the normalized voltage ratio.

Conclusions

The development of an application specific low-profile solar array drive assembly for CubeSats was successfully developed and demonstrated at SmallSat 2009. The problem of addressing the demand for increasingly more power on a CubeSat bus can be realized through implementation of this type of SADA.

The prototype ECU developed for the SADA described herein possessed only basic functionality and was done so intentionally for simplicity and demonstration-friendly purposes. It will be critical that future iterations of the ECU incorporate key sub-systems such as a communication bus, external memory stores, etc. Even further, these future ECU's should also include features also described herein; specifically for radiation hardening. While such aspects were decidedly foregone during the development of this first prototype, it is imperative that they be included in order for the electrical system to be tried as a viable flight unit.

A simplistic and cost-effective method for determining the angle of incidence of a light source (such as the Sun) was developed herein. Autonomous Sun tracking was realized by using PV cells (a common component to any satellite) and simple addition of a shadow-casting intra-bank barrier. While the method proved to be useful, it is acknowledged that a relatively large amount of error in achieving normal is unavoidable with such an effort. Higher accuracy COTS Sun sensors are available for the same purpose, with of course added but likely acceptable costs. Future work should include and effort to down-select and implement a COTS Sun sensor, while further work using the cost-effective

References

-
- ⁱ Toorian, A. et al. "The CubeSat Approach to Space Access" Aerospace Conference, 2008 IEEE, March 2008.
 - ⁱⁱ Blocker, A., et.al., "TINYSCOPE – The Feasibility of a 3-Axis Stabilized Earth Imaging CubeSat from LEO", 22nd Annual AIAA/USU Conference on Small Satellites, 2008.
 - ⁱⁱⁱ Lee, E., et.al., "The *.Sat CubeSat bus: When Three Cubes Meet", 19th Annual AIAA/USU Conference on Small Satellites, 2005.
 - ^{iv} Dowd, M. "How Rad Hard Do You Need? The Changing Approach to Space Parts Selection", Maxwell Technologies Microelectronics, 2002.
 - ^v <http://www.cubesatkit.com/>